

UNIVERSITY OF LATVIA
FACULTY OF CHEMISTRY



Agris Bērziņš

Doctoral thesis

**ON THE RATIONALIZATION OF THE FORMATION, STABILITY AND
PHASE TRANSITIONS OF PHARMACEUTICALLY ACTIVE SOLID
SUBSTANCE SOLVATES**

Supervisor: Prof., Dr. Chem. Andris Actiņš

Scientific advisor: Dr. Chem. Paul Hodgkinson

2015

The doctoral thesis was carried out at the Chair of Physical Chemistry, Department of Chemistry, University of Latvia, from 2011 to 2015, with previous elaboration foreruns, and at the Department of Chemistry, Durham University, from 2103 to 2014.



**LATVIJAS
UNIVERSITĀTE**
ANNO 1919

EIROPAS SAVIENĪBA

IEGULDĪJUMS TAVĀ NĀKOTNĒ

This work has been supported by the European Social Fund within the project «Support for Doctoral Studies at University of Latvia», and 2014 Ludo Frevel Crystallography Scholarship Award (ICDD).

The thesis contains the introduction, 3 chapters, reference list, 11 appendices.

Form of the thesis: dissertation in Chemistry, Physical Chemistry.

Supervisor: Prof., Dr. Chem., Andris Actiņš

Scientific advisor: Dr. Chem. Paul Hodgkinson

Reviewers:

- 1) Dr. chem., assoc. prof. Pēteris Mekšs, University of Latvia
- 2) Dr. chem., prof. Māris Turks, Riga Technical university.
- 3) Dr. fiz. Sergejs Beļakovs, Latvian Institute of Organic Synthesis

The thesis will be defended in a public session of the Promotional Committee of Chemistry, University of Latvia, at 16:00 on June 27, 2015 at the University of Latvia, Department of Chemistry, Kr. Valdemāra iela 48, lecture room 21.

The thesis and the summary of the thesis are available at the Library of the University of Latvia, Raiņa Blvd. 19.

ABSTRACT

In this doctoral thesis analysis of the solvate and polymorph landscape, solvate stability and phase transitions of active pharmaceutical ingredients are used to approach a possibility where the crystal structures could be used to completely understand and rationalize driving forces for solvate formation, stability and desolvation mechanism. A study of the dehydration of mildronate dihydrate is used to rationalize its dehydration mechanism. Solvate formation, stability and phase transitions of droperidol and benperidol is rationalized using analysis of molecular properties, crystal structures and computational calculations. Droperidol isostructural solvates are used to find a tool for rationalization of solvate thermal stability and explain the observed different solvent molecule arrangement and dynamics in their crystal structures.

TABLE OF CONTENTS

Introduction.....	7
Abbreviations	12
1 Literature review	13
1.1 Solid phases.....	13
1.1.1 Polymorphs.....	13
1.1.2 Solvates.....	14
1.2 Characterization of solvates and their stability	15
1.2.1 Thermodynamic stability of solvates.....	15
1.2.2 Arrangement and dynamics of solvent molecules.....	17
1.2.3 Characterization of crystal structure	19
1.2.4 Prediction of solvate formation.....	22
1.3 Desolvation process.....	24
1.3.1 Crystal structure aspects.....	24
1.3.2 Qualitative aspects	26
1.3.3 Quantitative aspects.....	28
1.4 Analytical methods for characterization of solvates and polymorphs.....	30
1.4.1 Crystal structure and PXRD.....	31
1.4.2 Solid state NMR spectroscopy.....	31
1.5 Solid state characterization of the studied compounds	33
1.5.1 Mildronate.....	33
1.5.2 Droperidol.....	34
1.5.3 Benperidol.....	34
2 Materials and methods	35
2.1 Materials.....	35
2.2 Sample preparation	35
2.3 Powder X-ray Diffraction.....	37
2.4 Single crystal X-ray diffraction	38
2.5 Thermal Analysis	38
2.6 Determination of desolvation kinetic parameters	40
2.7 Gravimetric determination of solvent content	40
2.8 Determination of lattice parameters of solvates with different solvent content	41
2.9 Crystal structure determination from PXRD data	41
2.10 Fourier transform infrared spectroscopy.....	42
2.11 Particle size analysis	42
2.12 Karl Fischer titration.....	42
2.13 Solid-state NMR.....	42

2.14	Theoretical calculations	43
3	Results and Discussion	46
3.1	Dehydration mechanism of mildronate dihydrate.....	46
3.1.1	Characterization of mildronate dihydrate dehydration.....	46
3.1.2	The relationship between crystal structures and the observed dehydration mechanism.....	48
3.1.3	Kinetic parameters of dehydration.....	50
3.1.4	Dehydration mechanism.....	51
3.1.5	Conclusions.....	53
3.2	Rationalization of mildronate dihydrate dehydration mechanism and determination of kinetic parameters by analyzing the effect of experimental and sample factors.....	54
3.2.1	Particle size effects evaluated from dehydration in isothermal and non-isothermal modes	54
3.2.2	Effect of the sample weight	58
3.2.3	Effect of the atmosphere.....	60
3.2.4	Effect of the sample history	61
3.2.5	Conclusions.....	62
3.3	Analysis of droperidol solvent formation and their characterization.....	64
3.3.1	Solvate screening.....	64
3.3.2	X-ray diffraction.....	64
3.3.3	Thermal characterization	66
3.3.4	Crystal structures of isostructural solvates.....	68
3.3.5	The interactions of solvent molecules in isostructural solvates.....	69
3.3.6	Fourier-Transform Infrared spectroscopy	71
3.3.7	Characterization of solvent content in isostructural solvates at different solvent activity	72
3.3.8	Characterization of changes in isostructural solvate structure at various solvent content	74
3.3.9	Water arrangement in a partially filled NSH structure	75
3.3.10	Analysis of the droperidol solvate formation	76
3.3.11	Conclusions.....	77
3.4	Comparison and Rationalization of Droperidol Isostructural Solvate Stability.....	79
3.4.1	Desolvation kinetics of droperidol solvates.....	79
3.4.2	Thermal stability of droperidol solvates	83
3.4.3	Quantitative comparison of solvate stability based on the crystal structure	84
3.4.4	Conclusions.....	89
3.5	Solid-state NMR and computational investigation of solvent molecule arrangement and dynamics in isostructural solvates of droperidol.....	90
3.5.1	Solvate characterisation using ¹³ C CPMAS spectra.....	90

3.5.2	Solvate characterisation using ¹⁵ N CPMAS spectra	94
3.5.3	Characterization of solvent dynamics in droperidol isostructural solvates	95
3.5.4	Theoretical analysis of the differences in solvent molecule behaviour	101
3.5.5	Conclusions	102
3.6	Structural Characterization and Rationalization of Formation, Stability, and Transformations of Benperidol Solvates	104
3.6.1	Crystallization	104
3.6.2	X-ray diffraction and thermal characterization of benperidol solvates	105
3.6.3	Characterization of benperidol solvate crystal structures	109
3.6.4	Fourier-Transform Infrared Spectroscopy	114
3.6.5	Characterization and rationalization of benperidol solvate desolvation	115
3.6.6	Rationalization of solvate stability and frequency of solvate formation in crystallization	118
3.6.7	The analysis of benperidol solvate formation	120
3.6.8	Conclusions	121
	Conclusions	123
	References	125
	Appendix 1	139
	Appendix 2	141
	Appendix 3	144
	Appendix 4	146
	Appendix 5	148
	Appendix 6	149
	Appendix 7	164
	Appendix 8	172
	Appendix 9	195
	Appendix 10	216
	Appendix 11	222

INTRODUCTION

Solvates are essential phase type of solid phases for organic molecules, and for pharmaceuticals in particular. They are likely to be obtained during the active pharmaceutical ingredient (API) manufacturing and can even be used as the API commercial form. Solvates typically appear during the API purification stage or processing stages, such as mixing and blending, wet granulation, lyophilisation, spray drying, etc., when APIs are exposed to solvents or solvent vapours¹⁻⁴. However, the stability of the solvates under an atmosphere without the corresponding solvent vapour is typically limited. Thus the solvate decomposition is likely to occur during the transportation or storage of the drug product. Therefore only hydrates are usually considered as a final drug product, although their dehydration is also possible. Moreover, high humidity during the transportation or storage can also lead to unexpected formation of a hydrate.

During the desolvation, new polymorphs can form, which can make formation of the solvate either undesirable, if polymorphs are unstable, or advantageous, as polymorphs inaccessible by crystallization can be obtained in such cases⁵⁻⁸.

Nevertheless, even nowadays it is not possible to predict the existence and stability of solvates for a particular compound, so this has to be explored during the development of an API. Moreover, there is not even an efficient scheme for fast and efficient detection of solvate formation and their stability for a given API molecule.

If a solvate forms in a crystallization process, it is likely that it is possible to obtain its crystals and therefore easily characterize its crystal structure. However, determination of the stability of particular solvate and phase transitions occurring during its desolvation is time-consuming and needs human resources and various analytical techniques.

By analysing the solvate and polymorph landscape, solvate stability and phase transitions of a well-explored API it would be possible to use the crystal structures for understanding and rationalizing driving forces for their formation, rationalizing their stability and desolvation mechanism. Accumulation and analysis of such an information can lead to general understanding of these relations, leading to a possibility of solvate engineering and prediction of the desolvation mechanism.

The **aim** of the study was to analyse the connection between crystal structure features of the studied API solvates and their stability, phase transitions and desolvation kinetics by searching for general regularities and the possibility to predict the formation, properties and phase transitions of the solvates.

To achieve the aim, the following **tasks** were proposed:

1. To determine the dehydration kinetic parameters of mildronate dihydrate from experiments in isothermal and nonisothermal mode.

2. To rationalize the dehydration mechanism of mildronate dihydrate by using qualitative and quantitative analysis of the crystal structure of mildronate phases, as well as data obtained from the study of dehydration kinetics.
3. To explore the polymorph and solvate landscape of chemically very similar APIs droperidol and benperidol by rationalizing the formation of their solvates, solvate properties, stability, and desolvation mechanism.
4. To characterize the desolvation kinetics and intermolecular interaction energies in droperidol isostructural solvates formed with water, methanol, ethanol, acetonitrile and nitromethane. Use this information to rationalize the relative stability of these solvates.
5. To rationalize the differences observed in the solvent molecule arrangement and behaviour in the droperidol isostructural solvates formed with water, methanol, ethanol, acetonitrile and nitromethane.

The scientific novelty of this work:

1. Crystalline structures has been linked to the properties, stability and desolvation mechanism of solvates. This has been achieved for solvates with completely different crystal structure features (isolated site and channel solvates with different solvent molecule linkage and role in the crystal structure) and different relationship between crystal structures of solvates and polymorphs (from similar to completely different). This is the only way to achieve general rationalization and prediction of the solvate properties using the crystal structures.
2. Solvate formation, stability and desolvation products has been rationalized for two APIs. This is a step forward to situation, where it would be possible to predict the formation, stability and desolvation mechanism of solvates for any particular molecule.
3. Computational calculations has been incorporated in the data analysis, rationalization and explanation of results as well as validation of hypothesis. Such approach leads to more reliable conclusions and reduces the amount of necessary experimental work.
4. Method for rationalization of solvate stability based on the solvent intermolecular interactions in the crystal structure has been developed and used for isostructural solvate system. By extending this to a general stoichiometric solvate systems general rationalization of the solvate stability would be possible.
5. It has been shown that by analysing the effect of different sample and environmental factors on the dehydration kinetic parameters it is possible to achieve information about the dehydration mechanism. Together with the interpretation of the dehydration mechanism in molecular level this leads to general understanding of the dehydration process.

6. New polymorphs and solvates of benperidol and droperidol have been discovered and characterized.

The practical significance of this work:

1. Prediction of the solvate formation can lead to faster selection of the solvents used for the processing of API, by therefore allowing this step to be more efficient and cost-effective.
2. Prediction of solvate stability and desolvation products can lead to faster and more effective decisions about possible complications during drug synthesis and usefulness of particular solvates.
3. General understanding of the desolvation mechanism can lead to fast and reliable prediction of the solvate stability in a given environmental conditions.

The findings of this research have been disclosed in six publications, and have been presented in nine international scientific conferences and four local scientific conferences.

List of original publications:

1. Bērziņš, A.; Actiņš, A., Dehydration of mildronate dihydrate: a study of structural transformations and kinetics. *CrystEngComm* **2014**, 16, (19), 3926–3934.
2. Bērziņš, A.; Actiņš, A., Effect of Experimental and Sample Factors on Dehydration Kinetics of Mildronate Dihydrate: Mechanism of Dehydration and Determination of Kinetic Parameters. *J. Pharm. Sci.* **2014**, 103, (6), 1747–1755.
3. Bērziņš, A.; Skarbulis, E.; Reķis, T.; Actiņš, A., On the Formation of Droperidol Solvates: Characterization of Structure and Properties. *Cryst. Growth Des.* **2014**, 14, (5), 2654–2664.
4. Bērziņš, A.; Reķis, T.; Actiņš, A., Comparison and Rationalization of Droperidol Isostructural Solvate Stability: An Experimental and Computational Study. *Cryst. Growth Des.* **2014**, 14, (7), 3639–3648.
5. Bērziņš, A.; Hodgkinson, P., Solid-state NMR and computational investigation of solvent molecule arrangement and dynamics in isostructural solvates of droperidol. *Solid State Nucl. Magn. Reson.* **2015**, 65, 12–20.
6. Bērziņš, A.; Skarbulis, E.; Actiņš, A., Structural characterization and rationalization of formation, stability, and transformations of benperidol solvates. *Cryst. Growth Des.* **2015**, 15, (5), 2337-2351.

Presentations in international conferences:

1. Bērziņš, A.; Actiņš, A.; Skarbulis, E., Stability and desolvation kinetics of droperidol hydrates and ethanol solvate studied by powder X-ray diffractometry and differential thermal analysis/thermogravimetry. In 10th Annual Pharmaceutical Powder X-ray Diffraction Symposium, May 16–19, 2011, Lyon, France.

2. Bērziņš, A.; Rēķis, T.; Actiņš, A., Kinetics and mechanism of mildronate dihydrate dehydration. In 12th International Conference on Pharmacy and Applied Physical Chemistry, May 6–9, 2012, Graz, Austria.
3. Bērziņš, A.; Actiņš, A.; Rēķis, T.; Sarceviča, I., Desolvation of droperidol isostructural solvates. In 11th Annual Pharmaceutical Powder X-ray Diffraction Symposium, May 15–18, 2012, Fort Myers, USA.
4. Bērziņš, A.; Skarbulis, E.; Actiņš, A., Preperation and Characterization of Benperidol Solvates and Polymorphs. In XVth Conference on Heterocycles in Bio-organic Chemistry, May 27–30, 2013, Riga, Latvia.
5. Bērziņš, A.; Actiņš, A.; Rēķis, T.; Skarbulis, E.; Sarceviča, I., Stability of Isostructural Solvates of Droperidol. In 7th Crystal Forms@Bologna, June 9–11, 2013, Bologna, Italy.
6. Bērziņš, A.; Actiņš, A., Computational study of the dehydration process of mildronate dihydrate. In 9th European Conference on Computational Chemistry, September 1–5, 2013, Sopron, Hungary.
7. Bērziņš, A.; Actiņš, A., Computational study of the intermolecular interaction energies in droperidol solvates. In 9th European Conference on Computational Chemistry, September 1–5, 2013, Sopron, Hungary.
8. Bērziņš, A.; Actiņš, A., Crystal structures of two molecules with small chemical structure difference. In 23rd Congress and General Assembly of the International Union of Crystallography, August 5–12, 2014, Montreal, Canada. Published in: *Acta Cryst.* **2014**, A70, C1686.
9. Bērziņš, A.; Hodgkinson, P., Solid-state NMR and computational investigation of solvent molecule arrangement and dynamics in isostructural solvates of droperidol. In SMARTER 4, September 1–4, 2014, Durham, UK.
10. Bērziņš, A.; Actiņš, A., Structural characterization and rationalization of formation, stability, and transformations of benperidol solvates. In 13th Annual Pharmaceutical Powder X-ray Diffraction Symposium, May 18–21, 2015, Bad Herrenalb, Germany.

Presentations in local conferences:

1. Bērziņš, A.; Actiņš, A.; Skarbulis, E., Droperidola dihidrāta un izostrukturālā nestehiometriskā solvāta X desolvatācijas kinētika un stabilitāte. In 69th University of Latvia conference, 2011, Riga, Latvia.
2. Bērziņš, A.; Actiņš, A., Farmaceutiski aktīvo vielu hidratu dehidratācijas kinētikas pētīšanas iespējas. In 70th University of Latvia conference, 2012, Riga, Latvia.
3. Bērziņš, A.; Actiņš, A., Dehydration of Mildronate dihydrate. In MSSC2012 - Ab Initio Modelling in Solid State Chemistry; September 17–21, 2012, London, UK.

4. Bērziņš, A.; Actiņš, A., Mildronāta dihidrāta dehidratācijas kinētika. In 71st University of Latvia conference, 2013, Riga, Latvia.
5. Bērziņš, A., Cietvielu KMR spektroskopijas lietošana farmaceutiski aktīvu molekulu pētījumos. In 73rd University of Latvia conference, 2015, Riga, Latvia.

Acknowledgment

I would like to express the deepest gratitude to his thesis supervisor professor, Dr. Chem Andris Actiņš for excellent guidance in my way to becoming an independent researcher, and to scientific advisor Dr. Chem. Paul Hodgkinson his first-class guidance, stimulating discussions and attention that I received during my time in the Durham University and after that.

Special thanks to all the supervised students, particularly Edgars Skarbulis and Toms Rēķis, for many useful ideas and results obtained during the cooperation period.

Special acknowledgment is given to the University of Latvia for financial support from the European Social Fund within the project «Support for Doctoral Studies at University of Latvia», and 2014 Ludo Frevel Crystallography Scholarship Award (ICDD).

ABBREVIATIONS

α	desolvation (dehydration) degree
AFM	atomic force microscopy
API	active pharmaceutical ingredient
CSD	Cambridge crystal structure database
DFT	density functional theory
DSC	differential scanning calorimetry
DTA	differential thermal analysis
Ea	activation energy
HSM	hot stage microscopy
PES	potential energy surface
PXRD	Powder X-ray diffraction
RF	radiofrequency
SCXRD	Single crystal X-ray diffraction
SEM	scanning electron microscopy
SSNMR	solid state NMR spectroscopy
TA	thermal analysis
TG	thermogravimetry
WET	water evaluation type
XRD	X-ray diffraction

1 LITERATURE REVIEW

1.1 Solid phases

APIs in the solid state can exist in numerous phases, which includes polymorphs (solid crystalline phases of the same compound with different arrangement and/or conformation of the molecules in the crystal lattice⁹), solvates (solid crystalline phases of a compound in which also solvent molecules are incorporated in the crystal structure¹⁰, sometimes designated as solvatomorphs¹⁰), co-crystals (solid crystalline phases composed of at least two solid neutral components present in definite stoichiometric amounts¹¹⁻¹³) and amorphous solids (phases lacking three-dimensional long-range molecular order, but possibly containing short-range order over several molecular dimensions¹⁴), see Figure 1.1. Solvates containing water in the crystal lattice are known as hydrates. Such phases can exist for neutral API molecules as well as their salts.

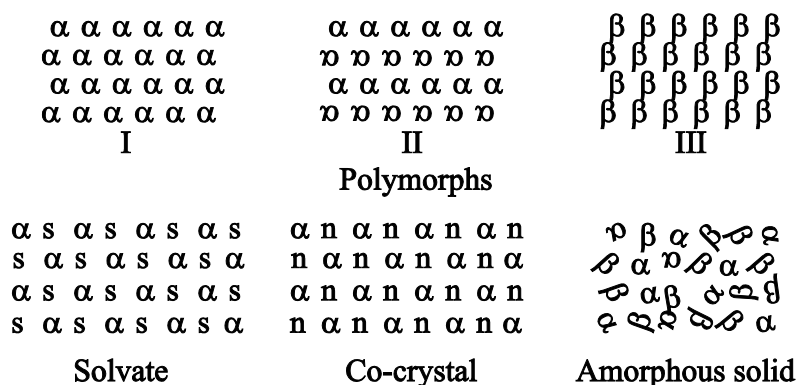


Figure 1.1. Different solid forms formed by molecular crystals (α and β are different conformers of API molecule, s = solvent molecules and n = molecules of neutral solid)¹⁵

The importance of polymorphism and solvatomorphism in pharmaceutical industry is showed by a fact, that 57% of compounds in the European Pharmacopeia are reported to exist in more than one phase, with 36% existing in different polymorphic forms, 29% forming hydrates and 10% forming other solvates in particular¹⁶.

It is well known that these different phases typically have different physical properties such as packing, thermodynamic, spectroscopic, kinetic, surface and mechanical properties, which therefore will affect drug stability and performance¹⁷. Under specified conditions only one phase is the thermodynamically stable one (except at an equilibrium conditions)¹⁸ and it is suggested to use this form as a final drug product^{19,20}. In practice, however, due to kinetic considerations, metastable forms can exist²¹, and these sometimes are selected as final drug products due to better solubility, intellectual property issues, or even because thermodynamically stable form has not been discovered yet²².

1.1.1 Polymorphs

In molecular crystals there are two different types of polymorphs: conformational (pairs I-III and II-III in Figure 1.1) and packing polymorphs (pair I-II in Figure 1.1)^{23, 24}. Packing

polymorphism arises from different possible packing arrangements of conformationally rigid molecules²⁴, whereas in conformational polymorphs conformationally flexible molecules adopt different conformations in the solid state²⁵, although this usually also include packing into different characteristic ways²³. Typically conformationally flexible molecules form more polymorphs than rigid molecules, and the number of polymorphs can reach up to ten (10 for ROY²⁶ and 9 for flufenamic acid²⁷).

Based on the relative thermodynamic stability polymorph pairs are divided in two types: two polymorphs are related enantiotropically if there is a transition temperature below the melting point of the lower melting polymorph, and therefore both of the polymorphs have temperature range where they are thermodynamically stable, whereas polymorphs are related monotropically, if only one of the polymorphs is thermodynamically stable in whole temperature interval up to its melting point^{9, 17, 28}.

Relative stability of polymorphs is determined by the relative stability of both conformers present in the crystal structure (typical energy difference is 1-8 kcal·mol⁻¹)²⁹ as well as the relative lattice energy (which is affected by the presence of intermolecular interactions as conventional hydrogen bonds (4-15 kcal·mol⁻¹), weak hydrogen bonds (1-4 kcal·mol⁻¹) and van der Waals and dispersive interactions (0.5-1.0 kcal·mol⁻¹)²⁵. As the differences of intramolecular and intermolecular interaction energy for polymorphs are very similar, both of these aspects will affect the relative total energy of the polymorphs^{25, 30}.

1.1.2 *Solvates*

Solvates typically are obtained during the API purification stage or the API processing stages, such as mixing and blending, wet granulation, lyophilisation, spray drying, etc., when APIs are exposed to solvents or solvent vapours¹⁻⁴. Moreover, solvates tend to crystallize more easily than solvent-free polymorphs because of the more efficient packing together with solvent molecules³¹.

Solvates are broadly classified as stoichiometric (where there is a definite ratio of solvent to molecule) and non-stoichiometric (where the ratio of solvent to molecule may vary continuously over a given range)^{10, 32}. The solvent in stoichiometric solvates is usually an integral part of the crystal structure and is essential for its maintenance, and their desolvation always lead to a different crystal structure or a disordered or amorphous state¹⁶.

In non-stoichiometric solvates solvent molecules are usually arranged in structure channels or other voids and does not significantly participate in the formation and stabilization of the crystal structure. Therefore the amount of solvent in the structure depends on the partial pressure of the solvent in the environment and on the temperature¹⁶. Nevertheless, the crystal structure of non-stoichiometric solvates usually forms only in the presence of the solvent¹⁶. If the non-stoichiometric solvate can be completely desolvated by obtaining a one-component phase with the same main structural characteristics, the obtained phase is called isomorphic desovate^{16, 33-35}.

Although such structures can sometimes be stable³⁶, they are typically unstable³³ or even collapse immediately after the removal of the solvent molecules^{27, 110}, and usually they easily binds the original or even another solvent molecules^{16, 33}.

It is common that the same host structure can incorporate different solvent molecules to form a set of isostructural solvates. This phenomenon is typical for non-stoichiometric channel solvates^{37, 38}, but is not limited to non-stoichiometric solvates^{8, 39, 40} nor to channel solvates⁴¹. The formation of isostructural solvates is typically driven by the presence of specific solvent-host interactions^{39, 41} or by the specific shape of the solvent molecule³⁷.

1.2 Characterization of solvates and their stability

1.2.1 Thermodynamic stability of solvates

Solvatomorphic system consists of at least two components (the substance and the solvent) and therefore variables as pressure, volume, temperature, and composition should be considered to describe the phases present in the system. A two-component phase diagram with eutectic and peritectic points (see Figure 1.2a) is characteristic for solvates. It shows that the solvate is the only stable crystalline phase at a compositions between the eutectic and the peritectic points below the curve. It has been shown that such phase diagram can cause complicated desolvation process, which appears as the dependence of the desolvation process on the experimental procedure and sample preparation (see Figure 1.2b)⁴². Closed sample pan, fast heating and big particles will result to the peritectic decomposition/melting of the solvate and appearance of the corresponding peak (1) in thermal analysis at the peritectic temperature (P), after which evaporation of liquid water will occur if the sample pan is open (2). In contrast, open pan, N₂ flow, slow heating and small particles will facilitate the nucleation and formation of the desolvate, and therefore appearance of conventional desolvation peak (3)⁴².

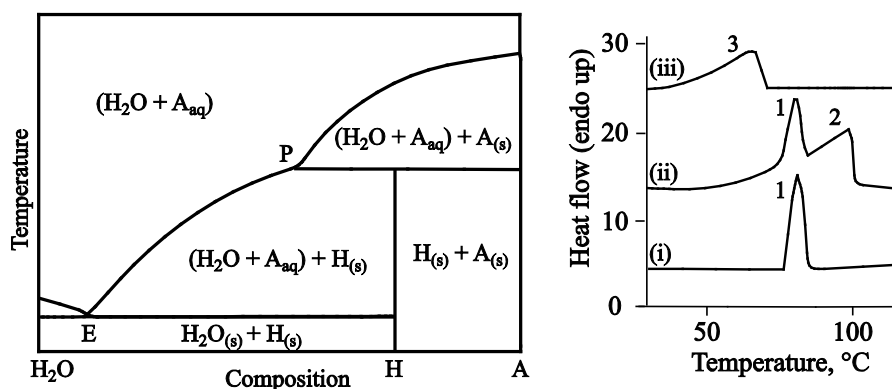
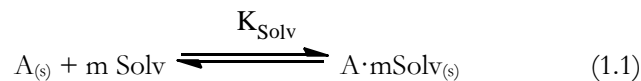


Figure 1.2. (a) Phase diagram of water and compound A showing an incongruently melting hydrate H⁴³ and (b) DSC curves of the dehydration of barbituric acid hydrate in (i) closed pan at 10 K·min⁻¹, (ii) pinholed pan at 10 K·min⁻¹, and (iii) closed pan at 2.5 K·min⁻¹.⁴²

Biphasic equilibria implies that the thermodynamic stability of the solvate will depend on the corresponding solvent vapour pressure¹⁰. Equilibrium between solvate and nonsolvated form

(Eq. (1.1)) can be described by Eq. (1.2), and in the case of pure solids in their standard states stability of the solvate at a given temperature depends only on the activity of the solvent:



$$K_{\text{Solv}} = \frac{a(A \cdot m \text{ Solv}_{(s)})}{a(A_{(s)})a(\text{Solv})^m} = a(\text{Solv})^{-m}, \quad (1.2)$$

where K_{Solv} is the equilibrium constant between the solvate and the nonsolvated phase and a is the activity of the corresponding phase^{10, 16, 44, 45}. Therefore stability of the solvates are determined by the temperature and the solvent activity in the surrounding medium⁴⁶⁻⁴⁹. With an exception of the hydrates, absence of the solvent vapour in the atmosphere makes all of the solvates thermodynamically unstable in ambient conditions^{10, 16}.

The stability of solvates at a given temperature is typically characterized by solvent sorption-desorption isotherms, in which solvent content dependence on the solvent activity (for water: relative humidity) is reported. There are several different types of isotherms observed for pharmaceutical solids⁵⁰, and two most characteristic types corresponding to stoichiometric and non-stoichiometric solvates are highlighted in Figure 1.3.

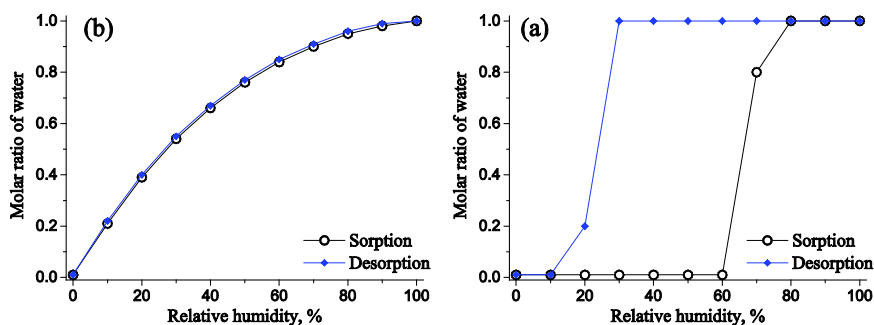


Figure 1.3. Solvent sorption-desorption isotherms characteristic for (a) stoichiometric and (b) non-stoichiometric solvates.

Isotherms of stoichiometric solvates are step-shaped with each step corresponding to well-defined water content. Typically in these isotherms there is a hysteresis (different solvent content at the same solvent activity in sorption and desorption isotherms). In isotherm of non-stoichiometric solvates, however, solvent content changes continuously within a certain solvent activity range and typically there is no hysteresis. However, there is no exact shape of isotherms corresponding to non-stoichiometric solvates, their shape depends on the crystal structure solvate and the strength of solvent-solvent and substance-solvent interactions. Various thermodynamic models describing non-stoichiometric solvents and their sorption-desorption isotherms have been reviewed⁵¹ and are summarized in Appendix 1.

Stability of a stoichiometric solvate can be characterized by the solvent activity (relative humidity for water) at which it starts to desolvate. However, the kinetics of desolvation usually does not allow to reach the equilibrium in a reasonable time and it depends on many variables. In

fact, this is one of the main factors responsible for the appearance of the hysteresis in the sorption-desorption isotherms. Thermodynamic stability is related to the solubility and therefore determination of the solubility in a chosen solvent can be used to fully characterize the stability of solvates and even compare it to other phases, provided no phase transition occurs during the solubility determination⁵². Solvate stability can as well be compared by constructing a phase diagram of solvate Gibbs energy dependence on the solvent activity⁵³.

The temperature effect on the stoichiometric solvate stability can be evaluated based on the phase diagram in coordinates $p_{\text{solv}} - T$, if the transition between the solvate and the nonsolvated phase occurs without significant hysteresis. In this case phase boundary between two phases can be found by determining the equilibrium solvent vapour pressure at various temperatures. From this phase boundary phase transition enthalpy can then be calculated using Gibbs-Helmholtz equation^{54, 55}.

1.2.2 Arrangement and dynamics of solvent molecules

As already stated, solvent molecules can have different role in the crystal structure, although in all cases they improve the stability of the crystal lattice¹⁰. This can be accomplished in three basic ways: firstly, solvent molecules can occupy isolated lattice positions, secondly, solvent molecules can occupy channels in the structure, and thirdly, solvent molecules (usually water) can associate with metal ions by being a part of a coordination complex or by forming a strong ionic bond. In the classification of hydrates such aspects as hydrogen bond strength and hydrogen bonding motifs can also be taken into account, although in practice both of these classifications usually can be associated with already mentioned three classes¹⁰.

In isolated site (discrete position) solvates solvent molecules (or solvent molecule clusters⁵⁶) are isolated from each other and bridge individual molecules or sheets of molecules¹⁰. These solvates are typically stoichiometric and removal of the solvent (desolvation) leads to destruction of the crystal structure⁵⁶. In TA these solvates show sharp desolvation endotherm and have narrow weight loss range⁴⁴.

In channels solvates solvent molecules included in the lattice are located in proximity to other solvent molecules in adjoining unit cells along a particular axis of the lattice¹⁰ and typically interact with each other⁴⁴. Although these solvates are usually non-stoichiometric¹⁶, depending on the hydrogen bonding and the size of the channel they can as well be stoichiometric⁵⁶. Removal of the solvent from channel solvates is easier and isostructural desolvate^{33, 35} or non-solvated phase with similar crystal structure can be obtained^{57, 58}. These solvates usually have wide weight loss range and broad endothermic peak in TA⁴⁴.

Most of the metal ion associated solvates are hydrates, and the interaction between the metal cation and the oxygen atoms of the bound water molecules are very strong, therefore these hydrates are very stable¹⁰ and have high dehydration temperatures⁴⁴.

However, picture of a static crystal structure is in fact wrong and the molecular level mobility should be included to gain full understanding of the crystal structure⁵⁹. Molecular motion can be associated with solid phase stability and phase transitions, and can be relatively easily studied using SSNMR⁶⁰. Although there are many functional groups which can exhibit intramolecular motion in the crystalline state (e.g. rotational diffusion of methyl group, 180° rotation of phenylene rings)⁵⁹⁻⁶¹ and affect the relative stability of the phase^{35, 62}, in case of solvates more interesting is the dynamics of the solvent molecules. It is shown that solvent molecules tend to be particularly mobile when they occupy structure channels and are weakly bounded to the host molecules⁶³⁻⁶⁵. However, also water molecules forming strong hydrogen bonds tend to experience C2 flips (exchanging the positions of the hydrogen atoms)⁶⁶⁻⁶⁸. Moreover, exchange of solvent molecules with solvent molecules from nearby atmosphere and exchange of hydrogen atoms between the solvent molecules and labile N-H and O-H sites in the host molecule is also taking part and have been studied using SSNMR and also Raman spectroscopy^{69, 58, 59}. Motion of the solvent molecules is typically studied by measuring relaxation time of individual ¹³C atoms³⁵ or common ¹H relaxation time⁷⁰ (as the mobility of solvent molecules usually drive the ¹H relaxation of the whole solid via spin diffusion⁷¹), line broadening⁶⁵ or spectra and its temperature dependence^{63, 72}. Another commonly used approach is a study of the spectra of deuterium labelled sample in which quadrupolar coupling parameters and T_1 relaxation time of deuterium atoms provide useful information about the dynamics of the corresponding sites^{63, 65, 73, 74}.

Characterization of the arrangement and dynamics of the solvent molecules in non-stoichiometric solvates with different solvent content is more complex^{10, 16}. Change of the solvent molecule amount in the solid phase and associated changes in the solvent site occupation factor⁷⁵,⁷⁶ usually introduce some changes in the solvent molecule arrangement and in the host structure itself. These typically include change of the channel size by therefore altering the lattice parameters (identifiable by PXRD as shift of the diffraction peaks^{56, 77, 78}, see Figure 1.4a) and unit cell volume (see Figure 1.4b) as well as changes in the molecular level mobility (identifiable by SSNMR)^{35, 79}. It has been shown that SSNMR can be more useful than XRD methods to understand structural changes and solvent molecule arrangement in such solvates^{73, 78-80}, especially if the crystal structure is not known^{81, 82}, as peak positions and width directly depends on the local chemical environment (and therefore the solvent content) and possible local disorder (see Figure 1.4c). Moreover, solvent dynamics can readily be identified and characterized. Besides, ²H spectra can even allow discrimination between bounded and surface solvent, which helps to rationalize the solvent sorption-desorption isotherms⁷⁴.

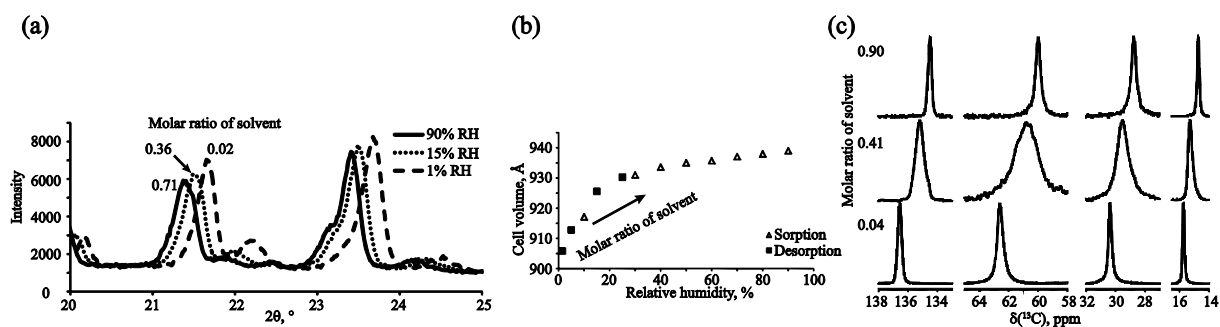


Figure 1.4. Effect of different water content in non-stoichiometric hydrate on (a) PXRD pattern⁸³, (b) unit cell volume⁸³, and (c) ^{13}C SSNMR spectra⁷⁹.

1.2.3 Characterization of crystal structure

Crystal structures can be characterized based on two partially separable features: molecular conformation and intermolecular interactions. Combination of all intermolecular interactions present in the structure leads to molecular packing, and this feature can be analysed separately. All of these features can be characterized qualitatively by comparing the geometrical parameters, as well as quantitatively by calculating and comparing the energy of different molecular conformations, intermolecular interactions or whole crystal lattices.

Molecular conformation. Molecular conformation is easily characterizable and comparable but is the least informative of the crystal structure features. Molecular conformation can be analysed qualitatively by comparing the values of any flexible torsion (dihedral) angles in the molecule^{8, 84}, or quantitatively, by calculating the energy differences between conformers^{30, 85} or by performing PES scan with respect to flexible torsion angles^{86, 87}. Such calculations nowadays typically are done at *ab initio* or DFT level. The similarity of the molecular conformation in different solid forms depends on the molecule flexibility and the energy differences between different conformers^{25, 88}. In general, conformational differences can appear as either significant differences in one or more torsion angles, or accumulation of a large number of small differences in torsion angles⁸⁸. Although analysis of the PES scan with respect to particular torsion angles can be used to evaluate the possibility of a molecule to adopt some particular conformation^{29, 30, 85, 89}, this cannot be used as the main factor, because the most favourable conformation can sometimes prevent the formation of energetically favourable intermolecular interactions⁹⁰. Therefore different intermolecular interactions in polymorphs and particularly in solvates, in which additional different structure building elements are introduced, can lead to a variety of different conformers present in the crystal structures, see Figure 1.5a^{8, 84, 91}.

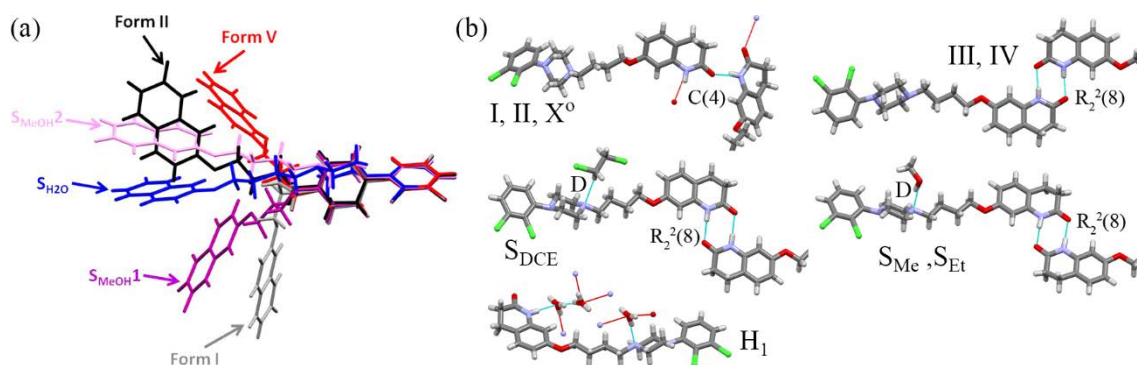


Figure 1.5. (a) Molecular conformation in different polymorphs and solvates of dehydro-aripiprazole⁸⁴ and (b) intermolecular interactions in different polymorphs and solvates of aripiprazole³⁴.

Intermolecular interactions. Although identification and geometrical characterization of strong intermolecular interactions is straightforward and conventionally used structure characterization tool, complete and comprehensive characterization of intermolecular interactions is more challenging. There are several possibilities for performing the characterization, starting from simple qualitative identification of the interactions and quantitative characterization of their geometrical parameters^{92,93}, quantitative characterization using Hirshfeld surfaces⁹⁴⁻⁹⁶, and finishing by quantification of all interaction energies in the crystal structure⁹⁷⁻⁹⁹, which was recently postulated as strongly suggested method to evaluate the relative importance of cohesion factors in crystals¹⁰⁰.

The most commonly characterized intermolecular interactions are strong hydrogen bonds, which are typically characterized by their geometrical parameters (distance and angle) as well as graph sets categorizing the interaction with respect to the hydrogen-bonding pattern formed. Graph set analysis divides hydrogen bonds in four patterns: chains (**C**), rings (**R**), intramolecular hydrogen-bonded patterns (**S**), and other finite patterns (**D**). Further analysis includes identification of motifs and higher level graph sets in cases when more than one different hydrogen bond is present in the structure^{9,101}. This analysis is of particular interest in supramolecular chemistry and crystal engineering^{9,101}. Identification of the characteristic hydrogen bonding pattern is still one of the most important information about the crystal structure and is used for fast evaluation of structure similarity. For example, three of aripiprazole polymorphs form hydrogen bonded catamers with graph set notation C(4), while other two forms hydrogen bonded dimers with graph set notation R₂²(8), see Figure 1.5b. The second pattern is observed also in three of the solvates, in which additional hydrogen bonds with solvent molecules are present, whereas in H₁ more complex and not easily characterizable higher level graph sets can be identified.

However, recently it has been emphasized^{99,100} that strong hydrogen bonds does not always determine stability of the crystal structure and also weaker interaction (e.g., weak hydrogen bonds and dispersion interactions) are important and therefore should be discussed. These interactions

can be visualized and analysed using commonly used structure visualization softwares (e.g. Mercury¹⁰²). Nevertheless, lately a tool, CrystalExplorer¹⁰³, for identification and characterization of all relevant intermolecular interactions have been provided. It generates Hirshfeld surface (0.5 isosurface where the electron distribution of a sum of spherical atoms for the molecule of interest is equal to the corresponding sum over the crystal) and maps different properties on this surface (e.g. curvedness, shape index, distance to the atoms)^{94,95}. The benefit of using Hirshfeld surface lies in the fact that the size and the shape of the Hirshfeld surface reflects the interplay between different atoms and intermolecular contacts in the crystal, and hence the surfaces reflect different intermolecular interactions⁹⁴, see Figure 1.6a. From this surface 2D Fingerprint plot can be generated, in which a summary of the frequency of each combination of d_e and d_i (distances from the surface to the nearest atoms outside and inside, respectively) across the surface is provided^{94,95} by thus providing a concise two-dimensional summary of intermolecular interactions in the crystal¹⁰⁴, see Figure 1.6b. Besides, this information can be decomposed into different interaction types by enabling analysis of their contributions and quantification of these different intermolecular interactions¹⁰⁴.

Nevertheless, the most straightforward way for evaluating the importance of the interactions is quantification of their energy. Nowadays this can be done relatively easily and this information can be obtained from fast but not always reliable force-field methods⁹⁷, slower and more limiting but reliable semi-empirical PIXEL methodology^{98, 105-107}, slow but usually the most accurate DFT or post-Hartree–Fock *ab initio* methods^{98, 108-110}, and even from the experimentally determined electron densities¹¹¹. In this way interaction energy between individual molecule pairs and its importance with respect to the total lattice energy can be evaluated^{30, 112, 113}, see Figure 1.6c. Comparison of pairwise interaction energy values can facilitate the understanding of formation of the crystal structures by analysing the occurrence frequency of molecule pairs interacting in a particular way^{99, 114-116}. Sum of the intermolecular interaction energy over all of the molecule pairs in the crystal is the lattice energy¹¹⁷. Comparison of the lattice energy allows determination of the stability of different crystal structures, if conformation energy is also taken into account^{30, 118}. However, one should not forget that these calculations represent the relative energy at 0 K^{100, 117} and temperature effect can be taken into account only by the analysis of the dynamics, which is computationally expensive and can be done by frequency calculations^{119, 120} or molecular dynamics simulations¹¹⁷.

Lately Hirshfeld surfaces, 2D fingerprint plots and interaction energy calculations has become a commonly used tools^{8, 110, 121-123} or even is the main tools in the characterization and comparison of crystal structure^{112, 113, 124, 125}. Examples of the use of these techniques for characterization of crystal structures of arylboronic azaester¹²⁶, arjunolic acid derivative¹²⁷ and 7-Hydroxy-4-methyl-2H-chromen-2-one¹¹² are given in Figure 1.6. Besides, more new tools for analysing crystal

structures are appearing, e.g., recently developed Full Interaction Maps allow visualisation of the intermolecular interaction preferences of a molecule in a particular conformation and qualitative analysis of how well interaction preferences are satisfied within the lattice¹²⁸.

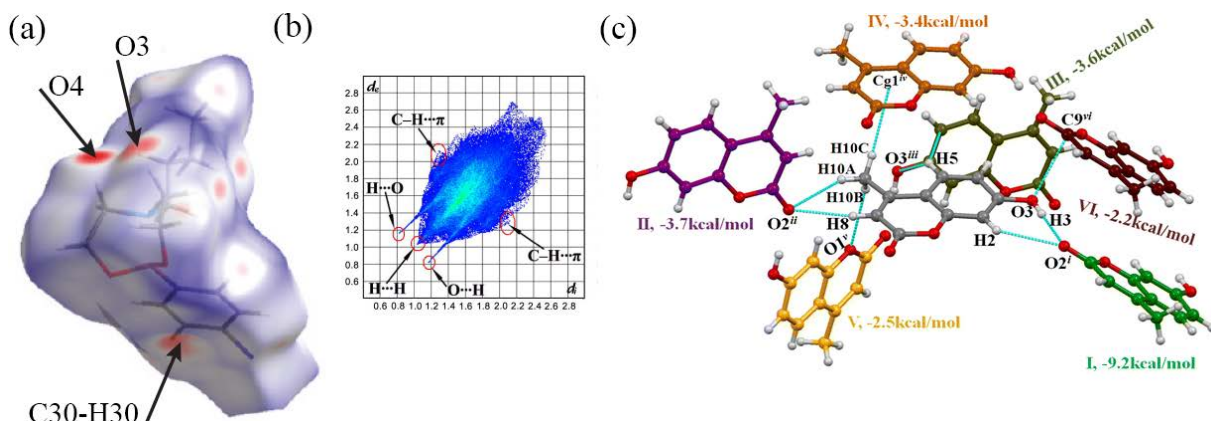


Figure 1.6. Characterization of intermolecular interactions using (a) Hirshfeld surfaces¹²⁶, (b) 2-D fingerprint plots¹²⁷, and (c) calculation of pairwise interaction energies¹¹².

Molecular packing. Analysis of all intermolecular interactions in the crystal structure leads to characterization of the molecular packing, which fully describes the arrangement of molecules with respect to all other molecules in the crystal structure. Similarities of molecular packing in different structures will appear in the case of coinciding intermolecular interactions, and depending on the level of the similarity can be either 0-D (isolated units such as dimers), 1-D (differently bundled identical rows), 2-D (differently stacked identical sheets) or 3-D (identical frameworks, in the case of isostructural phases)¹²⁹. The identification of such similarities can be done either by visually comparing crystal structures, or by using special software XPac, which searches for identical supramolecular constructs in the crystal structures, identifies and quantifies crystal structure similarity¹²⁹⁻¹³¹. This approach has been used for identification of the packing similarities in polymorphs and solvates^{8, 89, 123, 132} as well as in phases formed by structurally similar molecules¹³³.

Structural similarity based on the comparison of the whole crystal structure (therefore – molecular packing) can be quantified also using tools as dSNAP (compare geometrical parameters of the structure)¹³⁰, IsoQuest (compare PXRD patterns)^{130, 134} or Mercury¹⁰² Compack algorithm (compare the arrangement of the molecules surrounding the central molecule)¹³⁵.

1.2.4 Prediction of solvate formation

Understanding of the solvate formation is important in order to enable prediction of their formation and even their stability. Currently, it would be the most reasonable to make solvate predictions based on the solvent and host properties. Although structural features leading to the solvate formation have not been completely identified, there are two main scenarios in which solvent molecules tend to incorporate into the crystal lattice by forming solvates¹³⁶: a) potential intermolecular interactions between the molecules of the compound are not well satisfied and the

incorporation of solvent molecules provides a strong intermolecular interaction, or b) solvent inclusion in the crystal decreases the void space. In the first scenario, the solvate selectivity is typically based on their functionality, whereas it does not have to be so for the second scenario. However, most solvates include contributions from both of these driving forces, which can be viewed as lowering the crystal free energy primarily through electrostatic and van der Waals interactions, respectively. In more specific cases the solvent molecules can act as bridges between polar and apolar structure regions and/or serve the role of ligands completing the coordination around a metal ion³. It has also been concluded that solvate ability to involve multi-point recognition through hydrogen bonds strongly facilitates its stability¹³⁷.

More challenging is to understand the reasons for the formation of isostructural solvates, where the same host structure can incorporate different solvent molecules. There are cases where the formation of isostructural solvates can occur only from solvents with some specific interaction^{39, 41} or molecular shape³⁷, although it is common that such solvates form with very different solvent molecules located in structural channels^{8, 38, 138}.

Rationalization of the solvate formation can also be achieved by evaluating the properties of the solvent molecules. There are several studies in which the most commonly used solvents have been grouped by classifying them according to statistical analysis of four molecular descriptors¹³⁹ as well as hydrogen bond acceptor and donor propensity, polarity/dipolarity, dipole moment, and dielectric constant¹⁴⁰. Solvent classification according to their properties are given in Appendix 2.

Detailed analysis of the arrangement of water and methanol molecules in crystal structures deposited in the CSD has been performed by trying to understand structural features necessary for the crystallization of hydrates and methanol solvates, identifying the most frequent hydrogen bonding patterns and motifs^{141, 142} and the most common environments¹⁴³. Also various physical parameters have been correlated with the hydrate formation and it have been found that increase in the sum of the number of average donor and acceptor hydrogen bonds in the crystal structure causes an increase in the frequency of hydrates¹⁴⁴.

Despite the pessimistic feature promises¹⁴⁵, computational crystal structure prediction have evolved rapidly¹⁴⁶⁻¹⁴⁸ in the last ten years and recently it has been shown to be successful in specially organized tests^{149, 150} as well as during polymorph screening studies as a valuable tool to understand the formation possibility of particular polymorphs and their energetic relations^{132, 151-154}. Nevertheless, computational prediction of the solvate crystal structures is more challenging and until now predictions have been successful only in few cases mostly for relatively simple solvate systems^{149, 155-158}.

1.3 Desolvation process

1.3.1 *Crystal structure aspects*

It is well known that solvate stability and desolvation process is directly determined by the crystal structure of the solvate and the solvent molecule arrangement in particular^{73, 159, 160}. Crystal structure features are related with desolvation temperature and enthalpy, desolvation product, as well as desolvation kinetic model and activation energy. Therefore crystal structure aspects should be evaluated if the stability or the desolvation process of a solvate is studied.

Classification of solvates with respect to the desolvation mechanism. Besides establishing the role of the solvent molecules in the crystal structure (section 1.2.2), structural changes during the desolvation process are suggested as a tool for solvate classification. Although this has been presented only for the hydrates, the presented classification is directly transferable to solvates of any other solvent. From a crystallographic point of view one can arrive at a somewhat simplified scheme, anticipating one of the three situations: a) the crystal structure of the resulting anhydrous substance is identical or very similar to that of the original hydrate, b) the crystal collapses resulting an amorphous phase, and c) the crystal transforms into a fundamentally different crystal structure^{10, 161}. The drawbacks of this classification lies in the fact that it compares only the initial and the final crystal structures. Two more sophisticated theories have provided classification schemes which deals with this drawback. Nevertheless, the main conclusions are similar to those of previously mentioned simplified scheme.

First theory, so-called “Rouen 96 model”, divides hydrates into two general classes and several subclasses based on the changes in the structural information upon the dehydration, by analysing the possible release of water molecules, formation of anhydrous material and possible reorganization processes¹⁶², see Appendix 3. The second theory explores and reviews all possible structural changes during the dehydration, resulting in six water evaluation types (WET) of hydrates, which are based on the observed transformations¹⁶³. These WETs are described in Appendix 3.

Structural relation of a solvate and the corresponding desolvate. Rational outcome of the desolvation process commonly is the formation of structurally similar non-solvated structure. This can occur for stoichiometric isolated site solvates¹⁶⁴, and in particular for non-stoichiometric channels solvates³⁴. Such structural similarity of solvate and its desolvate is usually accompanied by relatively fast and easy solvation-desolvation process^{164, 165} and the particular desolvation product is favourable if compared with formation of any other structurally different non-solvated polymorph¹⁶⁵. Such structural similarities usually are easily identifiable, although sometimes they can be identified only in a complex molecular packing analysis⁸. If there are only slight structural changes during the desolvation, it is possible to develop a model of the desolvation mechanism by identifying conformation changes and molecule rearrangement^{42, 166}. Such model can be confirmed

using quantum chemistry calculations by optimizing the geometry of a solvate structure where the solvent molecules have been removed. If the structural changes are small enough, after optimization the geometry of the experimental desolvate will be obtained^{167, 168}. Although usually after the removal of the solvent molecules host molecules will rearrange to pack in a more compact way, some exceptions are reported where the unit cell size have increased after the desolvation¹⁶⁹.

However, not always there are structural similarities between the solvate and its desolvate, especially if the solvent molecules have crucial role in the stabilization of the crystal structure¹⁷⁰. This is also supported by some of the possible solvent evaluation types in which structural information is not retained during the desolvation^{162, 163}. Such a route explains some of the experimentally observed desolvation processes, e.g., the formation of thermodynamically unstable polymorph after the desolvation of R-cinacalcet hydrochloride, although thermodynamically stable polymorph has similar structure features to that of the solvate⁷, and the formation of only one of two energetically and structurally similar polymorphs after the dehydration of nitrofurantion monohydrate¹⁷¹.

In cases when solvent molecules in the crystal structure occupy different sites with different arrangement and different intermolecular interactions, desolvation can occur in multiple stages^{161, 169, 172, 173}. Using computational chemistry it is possible to calculate the sorption energy of the solvent molecules by thus evaluating the cohesion energy of each individual solvent molecule in the crystal structure⁸⁰. Particularly different cohesion energy and thus favourable multi step desolvation process is observed when solvent molecules in the structure occupy completely different environments, e.g. solvent molecules are located in structure channels and in isolated sites¹⁷⁴, or even are associated with metal ions¹⁰.

Effect of the structure on the desolvation process and kinetics. It is stated that the desolvation temperature and rate is associated with the solvent interaction energy (and enthalpy) in the structure¹⁷⁵. Usually the thermal stability of solvates is compared using the desolvation onset point or the desolvation rate at a given temperature or heating rate. In general, thermal stability should be a function of all the host-guest interactions, host-host interactions, and the intrinsic properties of the guest itself¹⁷⁵. Although it is stated¹⁷⁵ and shown experimentally^{85, 89} that the thermal stability of solvates correlates with the normal boiling point of the solvent, this can be true only if the solvent molecules are weakly bound to the host material and situated in open voids. In other cases the solvate stability should strongly depend on the solvent molecule accommodation in the host structure: the interaction energy between solvent and host molecules and the spatial characteristics⁸⁹. This is supported by the experimentally obtained order of the isostructural solvate thermal stability not matching the order of solvent boiling points^{63, 123} and explained by the presence of different solvent-host intermolecular interactions^{41, 170, 176, 177}, tight binding of the solvent molecules in the crystal cavities^{8, 38}, or steric effects hindering the desolvation¹³⁸.

This also explains the difference between the desolvation features of isolated site and channel solvates: desolvation rate of isolated site solvates below the desolvation temperature is very slow, but rapidly become fast when the desolvation temperature is reached as all of the solvent molecules in the structure have identical environment^{10, 44}. In contrast, the desolvation of channel solvates is continuous and have an onset at relatively low temperature. This is explained by generally accepted idea that all the hydrogen bonds of a given solvent molecule may get stronger as subsequent hydrogen bonds are formed. Thus, when one solvent molecule is taken away from this arrangement, the remaining solvent molecules become less strongly bound to the host system¹⁰.

Also crystal packing efficiency can be associated with solvent molecule interactions and therefore the solvate thermal stability¹³⁸. The relative sequence of the desolvation for different host structures can, in principle, be rationalized using factors as the presence and size of solvent tunnels, compactness of the crystal packing, hydrogen bonding, and other crystal packing factors^{160, 178}.

The desolvation mechanism (and kinetic model) is definitely related to the crystal structure of the solvate, and a study of structure transformations and desolvation kinetics can establish the desolvation mechanism^{90, 179-181}. In the presence of solvent channels in the structure, rate limiting step will be determined by the energy barrier associated with the disruption of the intermolecular interactions and the diffusion of solvent molecules¹⁸⁰⁻¹⁸². If the solvent molecules, however, are involved in structurally important intermolecular interactions and there are no solvent channels, the rate limiting step usually is the phase boundary advance towards the centre of the crystal⁹⁰. There also have been attempts to connect the crystal structure features and the desolvation E_a , by concluding that for the studied solvates E_a can be related to the solvent-host interaction energy¹⁸³. Moreover, it has been shown that the dehydration E_a of selected hydrates correlate with the dehydration onset temperature and therefore could be used to estimate their physical stability¹⁸⁴.

The presence of the solvent channels in the structure can be confirmed, if the microscopy analysis confirms anisotropic desolvation, as the desolvation in the channel direction will be favourable^{160, 185, 186} and the only rational explanation for desolvation in other directions is the cracking of the crystal due to different unit cell volume of the corresponding desolvate¹⁸⁵.

1.3.2 Qualitative aspects

Fundamentals of solid state transformations and their description. Solid state reactions are heterogeneous (as at least two solid phases are involved) and are more complicated than reactions in homogenous media, because of various possible rate limiting steps, such as nucleation, nuclei growth, diffusion, and interface advance¹⁸⁷⁻¹⁸⁹. Moreover, the kinetics often are affected by particle size and their geometrical shape¹⁹⁰. As the reaction usually occurs on the phase boundary, which is initiated at the defects in the crystal lattice or at crystal surfaces, edges, or corners, concentration does not relate to reactivity and conversion degree (or fraction converted) α is used instead. α takes values from 0 (no reaction has occurred) to 1 (reagent has reacted completely)¹⁹⁰.

The rate of a solid-state reaction can be described using Eq. 1.3, where k is the rate constant and $f(\alpha)$ is the differential reaction kinetic model or the rate law^{187, 188}.

$$\frac{d\alpha}{dt} = kf(\alpha) \quad (1.3)$$

Integration of Eq. 1.3 produces Eq. 1.4, where $g(\alpha)$ is the integral reaction kinetic model^{187, 188}.

$$g(\alpha) = kt \quad (1.4)$$

Above mentioned different rate limiting steps lead to a variety of kinetic models, the most common of which are summarized in Appendix 4^{90, 171, 187, 190-192}. These models are generally categorized by the underlying mechanistic assumptions as: a) Nucleation: the rate-limiting step is the formation and the growth of product nuclei. The nucleation rate is different from that of the nuclei growth. Nucleation models are divided in A and P models based on the relative rates of nucleation and nuclei growth. b) Geometrical contraction: nucleation is instantaneous throughout the surface and the rate-limiting step is the progression of the product layer from the surface to the crystal inward, which is different for various crystal morphologies. c) Diffusion: the rate-limiting step is the diffusion of the reactants into the reaction sites or the products away from the reaction sites. d) Other models: there are several other models, most often used of which are reaction-order models (analogous to homogenous kinetics), although in the solid state they usually are purely empirical¹⁹⁰.

Desolvation process and phase boundary. Desolvation can sometimes produce different products or can occur in multiple steps. Besides, the appearance of particular steps can depend on the desolvation conditions¹⁹³. Therefore the identification of the desolvation products and intermediates is a crucial step in characterization of the desolvation process¹⁵².

Chemical reactions and transformations in the solid state usually occur only in the phase boundary between the reactant and the product^{187, 188}. In the phase boundary changes as crystal structure decomposition, bond reorganization, recrystallization, diffusion of evolved gases etc. occurs. These processes can occur either simultaneously, or can be divided by space and/or time, which determine the desolvation mechanism and the desolvation products^{163, 187, 188, 194}. The study of phase boundaries are complicated as they are not accessible for direct examination in an undestructed form^{195, 196}. The phase boundary progresses (moves) into the unchanged reactant from a particular sites of the reaction initiation – nuclei – and the rate of the reaction is directly proportional to the total active contact surface between the reagent and the product. In the desolvation reactions nucleation usually occurs on the crystal surface and the phase boundary progresses inwards to the centre of the crystal, while the solvent is removed through the product layer¹⁹⁴. The rate of the phase boundary advance in different crystallographic directions is often different.

Nucleation is particularly important step in the desolvation process, as it is believed that it determines the desolvation onset temperature. Besides, this step controls the geometry (and therefore the kinetic model) of the desolvation process, and it often depends on the presence, concentration and location of the crystal defects^{163, 197}.

1.3.3 Quantitative aspects

Desolvation activation energy. Complete kinetic description of the solid state transformation is obtained only after the quantification of the rate constant dependence on the temperature and determination of the kinetic model¹⁹¹. The dependence of the rate constant on the temperature is usually described using the Arrhenius equation 1.5, where A is the frequency factor, E_a is the activation energy, T is the absolute temperature and R is the universal gas constant^{195, 198}.

$$k = A \cdot \exp\left(-\frac{E_a}{RT}\right) \quad (1.5)$$

The most common controversy in the solid state kinetics is the fact that the energy distribution of solid state reactions are suggested to differ from the Maxwell–Boltzmann distribution which is the basis of the Arrhenius equation. This has resulted a questioning of the physical significance of Arrhenius equation constants E_a and A^{187, 189, 195, 199}. However, later the bond reorganization and electron transitions in the reaction zone have been described with band theory, which takes into account that the energy in the crystal during the reaction is in the form of phonons and electronic energy. The description of the energy distribution for both phonons and electronic energy has shown that they have the same form as that of the Maxwell–Boltzmann distribution and therefore use of Eq. 1.5 is justified^{195, 196}.

Determination of the kinetic parameters. Kinetic parameters can be determined in two general ways: using model fitting methods and model free methods. Recent reviews emphasize that the model-free methods should be preferred, especially when analysing non-isothermal data^{190, 200}.

Model fitting methods are based on the fitting of the experimental data to various solid state kinetic models (see Appendix 4^{90, 171, 187, 190-192}). The kinetic model is determined from the best statistical fit, while the rate constant (for isothermal data) or the E_a and A (for non-isothermal data) are calculated from the correlation analysis. The E_a values for isothermal data are then determined from the Arrhenius plot. Use of these methods have been criticized, especially for the analysis of non-isothermal data²⁰¹⁻²⁰³. Nevertheless, they are still the most powerful and common tool for determination of the kinetic model from isothermal data^{186, 204, 205} and are widely used in the analysis of APIs^{172, 179}.

In the model free methods E_a is calculated without any modelistic assumptions. The most commonly used of these methods are isoconversional methods, where E_a is calculated at progressive conversion degree (α) values²⁰⁶ using data from multiple temperatures or heating rates²⁰⁷. These methods can be divided into two types – differential (most common of which is the

Friedman (FR)²⁰⁸ method) and integral (most common of which are average linear integral method (ALIM)²⁰⁹ and advanced isoconversional method (AIC)^{210, 211}) methods. Mathematical expressions used in the most common isoconversional methods are given in the Appendix 4.

The most common approach for determination of the kinetic model when E_a is determined with the isoconversional methods is the use of model fitting methods^{4, 15, 26} or the use of an integrated approach where these two method groups are combined^{90, 180, 212}. Methods from this integrated approach used to determine the kinetic model include but are not limited to: a) reconstruction of the integral or differential reaction model with independently obtained E_a (from isoconversional methods) and frequency factor (calculated from isokinetic relationship^{90, 180, 213}) values using Eq. 1.3, 1.4 and 1.5^{90, 180, 214}, b) use of algorithm provided in ALIM method²⁰⁹, and c) reduced time plots for isothermal data¹⁸⁸ and so-called “master plots” for non-isothermal data²¹⁵. The last two approaches, however, are less commonly used. Mathematical expressions used for determination of the kinetic model are given in the Appendix 4. However, one should keep in mind that although the choice of the kinetic model is generally based on statistical fit of the mathematical models to the data¹⁹⁰, the choice of a particular model should ideally be supported by other complementary techniques such as microscopy, spectroscopy, XRD, etc²¹⁶.

Effect of different factors on the desolvation kinetic parameters. As already mentioned, the desolvation kinetic parameters can be strongly affected by various sample and experimental factors and in some cases these factors can even have larger impact on the desolvation parameters than the crystal structure itself^{197, 217, 218}. Differences of the sample particle size^{180, 204, 205, 219, 220}, crystal habit²²¹, sample history²¹⁷, distribution and concentration of crystal defect²²², and seeding with the product¹⁸³ can result in different desolvation rate, E_a variation and even change the kinetic model. Besides these sample factors, all the mentioned kinetic parameters can be affected by experimental factors as solvent vapour pressure in the atmosphere^{187, 188, 204, 205, 223, 224}, inert gas flow rate^{187, 204}, vapour pressure of concurrent or inert solvent^{225, 226}, and sample weight^{219, 227}. Thus, for better understanding of the desolvation process and the calculated kinetic parameters, the effects of sample and experimental factors should be evaluated, and the kinetic parameters should be reported together with accurate experimental conditions and sample preparation procedure.

Various mechanistic features and sample factors can result deflections of the kinetic curves from those calculated using ideal kinetic models. Besides actual deviations from the kinetic model, these deflections can as well can be a result of averaging of the kinetic curve from reactions in various crystallographic directions^{194, 228} or from particles with different sizes^{194, 229}. Although mathematical expressions have been provided to take this into account^{194, 230}, in the absence of a convincing proof for a particular complication these equations are only empirical.

1.4 Analytical methods for characterization of solvates and polymorphs

Most common analytical methods for characterization and studies of API polymorphs and solvates are X-ray diffraction methods (SCXRD and PXRD which analyse features and changes of the crystal structures), thermal methods (DSC, TG and DTA which analyse the thermal effects and associated weight changes), vibrational spectroscopy (IR and Raman spectroscopy), solid state NMR spectroscopy (which analyse the magnetic environment of nuclei and the molecular level dynamics) and microscopic methods (which includes HSM, SEM, AFM and which characterize crystal shape, morphology and changes in these characteristics). Main information obtained from these methods is briefly summarized in Table 1.1. Basic principles of commonly used techniques is not reviewed and can be found in the corresponding textbooks^{14, 92, 231-238}. However, attention is paid to aspects of PXRD associated with the crystal structure determination as well as to less commonly used and described SSNMR.

Table 1.1. Information obtained from different analytical techniques for each type of solid phases¹⁵.

Phase	SCXRD	PXRD	IR/Raman spectroscopy	SSNMR spectroscopy	Thermal methods	Microscopy
Polymorphs	Same chemical composition. Unique unit cell parameters, molecular conformation and packing.	Unique diffraction peaks. Useful for determination of phase purity and crystallinity degree.	Characteristic spectra. Sensitive to hydrogen bonding.	Unique chemical shifts. Useful for determining phase purity, molecular mobility.	Unique mp, heat capacity, heats of fusion/transition, solubility. Useful for determining relative stability of forms.	Characteristic indices of refraction, birefringence, dispersion colour and crystal habit.
Solvates	Same as polymorphs.	Same as polymorphs.	Unique solvent bands. Shifted API bands. Sensitive to hydrogen bonding.	Unique solvent resonances. Shifted API resonances. Solvent mobility can be determined.	Low-temperature transitions due to desolvation (in TG – weight loss).	Same as polymorphs. Desolvation observable by HSM.
Isomorphic desolvates	NA	Diffraction pattern only slightly changed from parent solvates.	Solvent bands disappear. API bands shifted.	Solvent resonances disappear. API resonances shift.	Low-temperature desolvation absent. Events due to crystallization or lattice relaxation. Glass transition seen. Often followed by crystallization and melting. 'Fragility' related to width of T _g .	Birefringent microcrystalline domains, with cracks and fissures.
Amorphous solids	NA	No diffraction peaks.	Broadened spectra.	Broadened spectra.	Thermal behaviour indicative of phase diagram (e.g. mp-depression, eutectic melting, dissolution).	No birefringence, irregular particle shape.
Polymorphic mixtures	NA	Composite pattern of crystalline components.	Composite spectrum of all components.	Nuclei-specific composite spectrum of all components.		Composite of distinct crystalline and amorphous particles.

1.4.1 *Crystal structure and PXRD*

Peak positions and intensity in the PXRD pattern directly depends on the unit cell parameters and the crystal structure. Therefore changes in the PXRD pattern of a given phase is caused by the crystal structure changes. To determine the changes in the lattice parameters, PXRD pattern should be indexed, whereas to understand the crystal structure changes, crystal structure should be known. Lattice parameter changes can be identified from the changes in the peak positions, while lattice parameter optimization gives quantitative information about these changes. The most accurate approach for the lattice parameter optimization is the fitting of the whole PXRD pattern using whole powder pattern decomposition, where besides the lattice parameters also the parameters of peak profile function, particle size, strain, and peak asymmetry can be optimized²³². The most popular is the Pawley fitting, which is derived from the Rietveld refinement by removing the crystal structure data, and adding the possibility to refine an individual intensity for every expected Bragg peak²³⁹, and very similar Le Bail fitting²⁴⁰. These methods are implemented in lot of softwares, e.g., EXPO2014, TOPAS, Fox, DASH etc.

Recently the development of XRD equipment, as well as computational power and software have provided an opportunity to determine the crystal structure using only PXRD pattern. However, this is time consuming and not straightforward task, which is typically used only if the SCXRD analysis cannot be performed. Nevertheless, a lot of recent studies report crystal structures determined in this particular way, and the complexity of structures calculated in this way is constantly growing^{58, 241-244}. Two of the most commonly used structure determination algorithms are Monte Carlo Simulated Annealing and Parallel Tempering. The quality of the structural model is evaluated using Rietveld refinement: a least-squares fit of the calculated diffraction pattern to the experimental diffraction pattern using the weighted R-factor R_{wp} as a similarity quantification tool²⁴⁵⁻²⁴⁷.

1.4.2 *Solid state NMR spectroscopy*

The main differences between the NMR in the liquid state and the SSNMR is the lack of a rapid motion, which leads to very broad peaks due to chemical shift anisotropy (CSA) and unaveraged dipolar and quadrupolar (only for quadrupolar nuclei) couplings. Besides, T_1 relaxation time in the solid state is longer and may significantly differ for different atoms in the molecule (leading to longer experiment times), while linewidths are generally much broader (largely due to the effects of dipolar coupling)^{71, 248}.

Nevertheless, there are three techniques of considerable importance for obtaining high-quality, well-resolved spectra, especially from powdered samples. These are magic angle spinning (MAS), heteronuclear decoupling and cross polarization (CP), all of which are used to record most of typical SSNMR spectra⁷¹. MAS involves spinning the sample at 54.74° with respect to the external magnetic field \mathbf{B}_0 at rate up to 15kHz (or even 100 kHz for ^1H spectra) to average the CSA

and scale down the dipolar couplings (elimination of the dipolar coupling can occur only if the spinning rate is significantly faster than the strength of the dipolar interaction). Averaging of the CSA results in appearance of a peak at the isotropic chemical shift, as well as appearance of spinning sidebands (resonances spaced at intervals of the spin rate from the isotropic resonance frequency), if the spinning rate is not fast enough to completely average the CSA. Quadrupolar couplings are too large to be averaged out by the MAS, so numerous spinning sidebands will usually be seen in the spectra of quadrupolar nuclei.

^{13}C and ^{15}N homonuclear couplings are typically not a problem, whereas high-power ^1H decoupling should be used to eliminate the heteronuclear couplings by therefore significantly narrowing the peaks in ^{13}C and ^{15}N SSNMR spectra. In contrast, ^1H homonuclear dipolar couplings are problematic as they cannot be averaged out by MAS because of the strength of these interactions and the fact that ^1H chemical shift range is limited to ~ 15 ppm. Therefore to obtain reasonable quality ^1H SSNMR spectra specially designed pulse sequences for ^1H homonuclear decoupling are used in combination with ultra-fast MAS^{71, 248, 249}.

Another problem in SSNMR spectroscopy is that it is difficult to record a spectra of nuclei with low sensitivity (e.g., ^{13}C and ^{15}N) with good signal-to-noise ratio in a reasonable time. This can be overcome by using CP, which involves a transfer of magnetization from abundant ^1H (or, occasionally, ^{19}F) spins to dilute X ones, where X is any other spin- $\frac{1}{2}$ nucleus. There are two most apparent benefits for using CP sequence. First, the recycle delay is limited by the recovery of the ^1H magnetization and not that of the X spins. As usually $T_1^{\text{H}} \ll T_1^{\text{X}}$, the pulse sequence can be repeated much more rapidly than in a direct-excitation experiment, by thus significantly increasing the signal-to-noise ratio. Secondly, the gyromagnetic ratio of ^1H is 4 and 10 times higher than that of ^{13}C and ^{15}N , respectively, therefore the magnetization transfer results a signal enhancement by the same factor, which represents 16- and 100-fold reduction in experiment time^{71, 248, 249}.

The strength of SSNMR lies in its ability to analyse different nuclei, and in the fact that the chemical shift and the appearance of the signal depends on the chemical environment and the molecular level dynamics in the solid structure. Moreover, modern quantum chemistry calculations can be used to predict the chemical shift, its anisotropy, dipolar and quadrupolar couplings (most commonly used technique for this is GIPAW²⁵⁰⁻²⁵³, which is implemented in periodic *ab initio* codes CASTEP²⁵¹ and *QuantumEspresso*²⁵⁴), as well as to predict and analyse possible molecular level dynamics and its effect on the NMR parameters by using molecular dynamics. In contrast to the diffraction methods, local changes in the chemical environment will introduce changes in the spectra, which makes this method particularly useful for analysing isostructural phases. Besides, additional information can be obtained by performing spectral editing or 2D-spectroscopy experiments^{61, 71, 249}.

SSNMR spectra can be used to probe molecular dynamics in the timescale of the nucleus Larmor frequency (usually tens to hundreds of MHz), MAS and decoupling frequency (usually tens of kHz). Besides the spectra itself, useful information about the dynamics can also be obtained by measuring the relaxation times. SSNMR is particularly concerned with three types of the relaxation: a) spin–lattice relaxation (the process of regaining equilibrium of the z component of magnetization, characterized by relaxation time constant T_1), b) spin–spin relaxation (the process of regaining equilibrium of the xy component of magnetization, characterized by relaxation time constant T_2 and is directly related to the linewidth or lineshape of resonances), and c) spin–lattice relaxation in the rotating frame (which describes the return to equilibrium of transverse magnetization in the presence of an RF magnetic field in the same direction, is characterized by relaxation time constant $T_{1\rho}$ and is of particular interest in CP experiments). From these the first (T_1) and the third ($T_{1\rho}$) are commonly analysed and used to probe the dynamics in the corresponding timescale (tens to hundreds of MHz for T_1 and tens of kHz for $T_{1\rho}$). Although molecular motions in solids can be very complex and are often poorly understood, in simple cases T_1 and $T_{1\rho}$ pass through a well-defined minimum as the motional rate increases, with a tendency to increase toward infinity for very fast motions (as in mobile liquids) or very slow motions (as for rigid solids)⁷¹.

1.5 Solid state characterization of the studied compounds

1.5.1 Mildronate

Mildronate, 3-(1,1,1-trimethylhydrazin-1-ium-2-yl)propionate (Figure 1.7a), is a γ -butyrobetaine analogue, inhibitor of γ -butyrobetaine hydroxylase, and used as an anti-ischemic drug^{255, 256}. It is known to exist in a form of dihydrate²⁵⁷, monohydrate and anhydrous phase²⁵⁸. The crystal structures of all these phases are known. Dihydrate **DH** belongs to space group $P2_1/c$ ^{257, 259}, the monohydrate **MH** crystallizes in P-1 space group²⁶⁰, and water molecules in both hydrates are located in structural channels. The anhydrous phase **AP** belongs to $P2_1/n$ space group with empty channels present in the structure²⁶⁰. Mildronate is very hygroscopic and deliquesces if kept in high humidity²⁵⁸, which is explained by the presence of the channels in crystal structures in all of its crystal forms²⁶⁰. When heated in dry air, mildronate **DH** transforms into **AP**, whereas at elevated temperature and relatively high humidity it transforms into **MH**²⁵⁸.

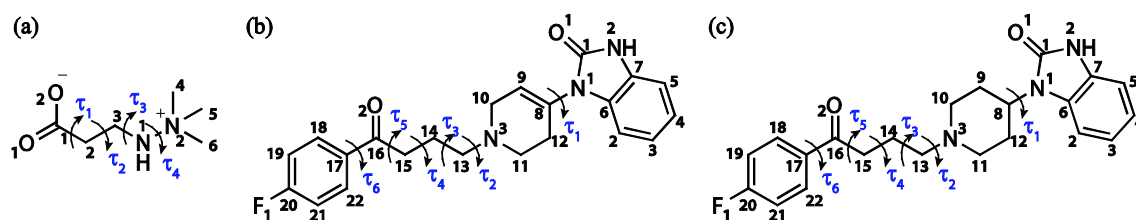


Figure 1.7. Molecular structure of (a) mildronate, (b) droperidol, and (c) benperidol with the numbering of non-hydrogen atoms and flexible torsion angles.

1.5.2 Droperidol

Droperidol, 1-{1-[4-(4-Fluorophenyl)-4-oxobutyl]-1,2,3,6-tetrahydro-4-pyridyl}-1,3-dihydro-2H-benzimidazol-2-one (Figure 1.7b), is a neuroleptic pharmaceutical. It is reported to exist in two polymorphic forms **I** and **II** (also labelled as ζ)^{261, 262} and three solvated forms: dihydrate **DH**^{262, 263}, non-stoichiometric hydrate **NSH** (also labelled as χ)^{261, 262, 264}, and ethanol solvate **S_{Et}**²⁶⁵. **NSH**, **II** and **I** can be identified by the melting points, which are reported to be 129°, 145° and 151°C respectively⁴¹. The crystal structures of the **DH**, **S_{Et}**, **NSH**, and polymorph **II** have been reported. It is determined that the **NSH** and **S_{Et}** are isostructural²⁶⁴. Although **NSH** is reported as hemihydrate²⁶¹, it is nonstoichiometric and the water content in its structure can change freely from 0 to 1²⁶⁴. **DH** is isolated site hydrate, whereas in both isostructural solvates solvent molecules are situated in the structural channels oriented along the *a*-axis. In polymorph **II** and in isostructural solvates droperidol forms hydrogen bonded amide homodimers. Additional structural stability for **II** is provided by two weak hydrogen bonds formed by the carbonyl group, whereas the structure of isostructural solvates is stabilized by three weak hydrogen bonds formed by the carbonyl group, tertiary nitrogen and fluorine, as well as by the hydrogen bond between the amide carbonyl group and the solvent molecules. **DH** structure, however, is stabilized by network of strong hydrogen bonds mediated by water molecules employing all the strong hydrogen bond donor and acceptor sites of droperidol. Molecular conformation of droperidol molecules in isostructural solvates and in **II** is very similar²⁵⁶.

1.5.3 Benperidol

Benperidol, (1-{1-[4-(4-fluorophenyl)-4-oxobutyl]piperidin-4-yl}-1,3-dihydro-2H-benzimidazol-2-one) (Figure 1.7c), is butyrophenone derivative, an antipsychotic, which can be used for the treatment of schizophrenia²⁶⁶. Its molecular structure is very similar to that of droperidol. Benperidol is reported to exist in three polymorphic forms **I**, **II** and **III**, a dihydrate **DH** and an ethanol solvate **S_{Et}**. These phases are characterized by PXRD peak positions and DSC traces⁴¹. Crystal structure has been reported only for polymorph **I**, which crystallizes in R-3 space group, in which six benperidol molecules are connected with N2-H \cdots N3 hydrogen bonds by forming a hydrogen boded ring R₆⁶⁽⁴⁸⁾²⁶⁷. Besides, later study reports the preparation procedures and IR spectra of benperidol crystalline forms by concluding that in part of them benperidol exists in an enol form, and that polymorph **III** actually is a mixture of polymorphs **I** and **II**²⁶⁸.

2 MATERIALS AND METHODS

2.1 Materials

Mildronate (purity >99%) was provided by JSC Grindeks (Riga, Latvia) and was confirmed as pure **DH** by PXRD. Droperidol (purity >99%) was obtained from JSC Grindeks. The sample consisted of polymorph **II**. Benperidol (purity >99%) was obtained from JSC Grindeks. The sample consisted of polymorph **I**.

Inorganic compounds and organic solvents of analytical grade were purchased from commercial sources and used without further purification (see Appendix 5).

2.2 Sample preparation

Mildronate dihydrate. Four samples differing by the preparation procedure and/or storage conditions were used. Samples were prepared by slowly crystallizing mildronate from water at 30 °C or by drying a paste obtained by adding a small amount of water to mildronate in mortar. The obtained samples were fractionated by pushing through sieves with mesh size 1300, 700, 350, 150, 67 and 40 μm, yielding a maximum of 7 fractions (the obtained particle size distribution for different fractions is given in Figure S3, Appendix 7). Part of the 150-350 μm and 350-700 μm fractions was slightly ground and then fractionated by pushing through sieves with mesh size 350, 150, 67 and 40 μm, and 5 fractions were thus obtained. Samples were stored at ambient temperature above saturated solutions of CH₃COOK (RH = 22.5%) or MgCl₂ (RH = 34%). More details of sample preparation procedures are given in the Appendix 7.

For studying the effect of mechanical compression on the dehydration kinetics of **DH**, approximately 30 mg of sample was inserted in a die with 13 mm diameter, and then compressed at 130, 370 and 740 MPa for one minute. Manual hydraulic press was used for compression of the samples. Right after the compression, the obtained tablet was either gently ground to obtain powder or divided into smaller pieces suitable for analysis with TG. Dehydration analyses were started immediately afterwards.

For studying the effect of prior history of dehydration/rehydration, the initial **DH** sample was dehydrated at 50°C temperature under N₂ flow. Then the dehydrated sample was stored at the ambient temperature in 22.5% relative humidity.

Solvent-based polymorph and solvate screening of droperidol and benperidol. The most popular solvents chosen from different solvent classes^{139, 140} (grouped according to physical and physicochemical properties) were selected for the crystallization of droperidol and benperidol. Saturated or concentrated solutions of droperidol or benperidol in all of the solvents were prepared at 40–130 °C depending on the boiling point of the solvent (see Table S1, Appendix 8 and Table S1, Appendix 11). The obtained solutions were then cooled down to –5°C. In the cases when no crystallization was observed, the solutions were slowly evaporated at 40°C or 50°C, while

preventing a complete evaporation. The obtained products were collected by filtration, air dried and characterized.

Droperidol. For studying the thermal stability of the solvates and recording their SSNMR spectra, samples were prepared as follows: saturated solutions of droperidol in methanol, ethanol, acetonitrile, and nitromethane were prepared at 60 – 90°C depending on the boiling point of the solvent. The solutions were then cooled down to –5 °C or –20 °C, giving **S_{Me}**, **S_{Et}**, **S_{ACN}**, and **S_{NM}**, respectively. Small amount of water (5-10%) was added to droperidol solution in acetone and the resulting solution was slowly partially evaporated at 50°C temperature, giving **NSH**. Solvates were stored in the mother liquor, filtered, dried and ground in a mortar for 30 s immediately before the analysis. **DH** was prepared by dissolving droperidol in acetone at 50 °C, cooling the solution to ~10 °C, slowly adding similar volume of water and then slowly partially evaporating the resulting solution at 5 °C. Droperidol polymorph **II** was obtained by recrystallizing the sample from acetone at 50 °C. The identity of all droperidol phases was confirmed using PXRD.

For a study of the desolvation kinetics, different sample preparation procedures were used. Four different types of **NSH** samples were obtained similarly as described above. Samples labelled as *Crystals I - IV* (the size of all of the dimensions was higher than 100 μm) were obtained by slowly evaporating the solution in a 100 mL conical flask, samples labelled *Small crystals I-III* (with the size below 100 μm for at least one of the dimensions) were obtained by evaporating the solution in a 250 mL conical flask, while samples labelled *Powder I-II* (with the size below 40 μm for all of the dimensions) were obtained when the solution was evaporated at 25 °C temperature from a Petri dish. The fourth type of samples was obtained by grinding the *Crystals II* in a mortar. More details on the preparation of each sample are given in Table S2, Appendix 9.

Organic solvates used for the kinetic study were prepared by obtaining saturated solutions of droperidol in the respective solvents at 60 – 90°C (depending on the boiling point of the solvent) and then cooling to –10 °C either slowly (obtaining crystals with the size of at least one of the dimensions below 100 μm, labelled *Small crystals*) or rapidly (obtaining powder samples with the particle size below 40 μm for all of the dimensions, and labelled *Powder*). Alternatively, well-ground polymorph **II** was suspended in the corresponding solvent at 50°C for 24 h, producing powdered solvate samples labelled *Suspension*. For the study of the desolvation kinetics of organic solvates under non-isothermal conditions, *Small crystals* were ground in a mortar for 1 minute.

Prior to the analysis, solvate samples were stored at ambient temperature in desiccators above saturated solution of K₂SO₄ (97% relative humidity) for **NSH** and 90% solution (mole fraction) of the corresponding solvent with glycerol (for alcohol solvates) or DMF (for acetonitrile and nitromethane solvates).

Deuterium-labelled droperidol solvates were prepared by grinding and then desolvating the original solvate at 50 °C over P₂O₅. The resulting sample was then placed in a closed container with

saturated D₂O or *d*₁-alcohol vapour. **NSH** with different D₂O content was obtained by storing the deuterium-labelled sample above D₂O to obtain monohydrate stoichiometry or above a saturated solution of MgCl₂ in D₂O to obtain approximately hemihydrate stoichiometry.

Benperidol. For studying the phase transitions and desolvation kinetics of the solvates, samples were prepared as follows: **S_{Et}**, **S_{Me}** and **S_{ACN}** were prepared by obtaining saturated solutions of benperidol in the respective solvents at 60–70 °C (depending on the boiling point of the solvent) and then cooling to –5 °C by obtaining crystals. Alternatively, well-ground polymorph **I** was suspended in the corresponding solvent at 50 °C for 24 h, producing powdered solvate samples. Similarly, **S_{EtOAc}**, **S_{NM}**, **S_{Benz}**, **HH** and **S_{DIOX}** were prepared by obtaining saturated or concentrated solutions of benperidol in the respective solvents (*o*-xylene containing traces of water for **HH**) at 70–90 °C (depending on the boiling point of the solvent) and then cooling to –5 °C by obtaining crystals (powder for **S_{DIOX}**). Fast cooling of the ethanol and methanol solutions produced small solvate crystals (the size of at least one of the dimensions was below 100 μm), while slow evaporation of these solutions at 50 °C produced large crystals (the size of all of the dimensions was higher than 200 μm). Polymorph **I** was prepared by recrystallization from isopropanol, using saturated solution at 70 °C and fast cooling to –5 °C. Polymorph **II** was prepared by slowly evaporating benperidol solution in isopropanol at 50 °C. **DH** crystals were obtained when a similar volume of water was slowly added to droperidol solution in acetone and the resulting solution was slowly evaporated at 50 °C temperature. Powdered **DH** was obtained when droperidol solution in acetone or DMF was poured into a large amount of water, by stirring the obtained suspension. **S_{CLF}** and **S_{TCC}** were prepared as in the crystal forms screening experiments.

Study of solvate stability. Stability of the solvates was determined at ambient conditions, by storing the solvate sample in desiccator over P₂O₅ at 30 °C, and at elevated temperatures by heating the samples in air thermostats. The heating temperature was selected based on the recorded DTA/TG curves. Phase transformations was identified using PXRD and, if necessary, DTA/TG as well.

2.3 Powder X-ray Diffraction

PXRD patterns were measured at ambient temperature on a D8 Advance (Bruker) diffractometer using copper radiation (CuK α) at a wavelength of 1.54180 Å. The tube voltage and current were set to 40 kV and 40 mA. The diffraction patterns of mildronate samples were recorded with a scintillation detector using a scanning speed 0.5s/0.02° from 3° to 30° in the 2 θ scale, the divergence and antiscattering slits were set at 1.0 mm, and the receiving slit was set at 0.6 mm. The diffraction patterns of droperidol and benperidol samples were recorded with a LynxEye position sensitive detector using a 0.2s/0.02° scanning speed (for phase identification) or 0.5s/0.02° (for lattice parameter determination) from 3° to 35° in 2 θ scale, the divergence slit was set at 0.6 mm

and the antiscattering slit was set at 8.0 mm. To prevent the atmospheric humidity effect and decomposition of the solvates, when necessary during the analysis the samples were covered with a 10 μm polyethylene film.

For crystal structure determination of benperidol phases, PXRD patterns were measured on a D8 Discover (Bruker) diffractometer at transmission geometry using Göbel Mirrors and a capillary sample stage. Other settings and equipment were identical to those used for D8 Advance. Samples were sealed in rotating (60 rpm) borosilicate glass capillaries of 0.5 mm outer diameter (Hilgenberg glass No. 10), and data were collected using 22s/0.01° (**III**), 25s/0.01° (**S_{Benz}**), or 36s/0.01° (**HH**) scanning speed from 2.5° (**S_{Benz}**) or 4.5° (**III** and **HH**) to 70° on 2 θ scale.

For variable temperature PXRD (VT-PXRD) of mildronate **DH**, D8 Advance (Bruker) diffractometer equipped with a MRI heating stage, Sol-X energy dispersive detector, automatically adjustable slits (1.0, 1.0 and 0.1 mm, respectively) and Soller collimators was used. The diffraction patterns were recorded using a scanning speed 4s/0.02° from 10° to 25° in the 2 θ scale. Stepwise temperature increase 1 °C per diffraction pattern was used from 30 to 60 °C, then 5 °C per diffraction pattern was used up to 80 °C. For VT-PXRD of droperidol and benperidol samples, D8 Discover (Bruker) diffractometer equipped with a MRI heating stage and LynxEye position sensitive detector was used. The diffraction patterns were recorded using a scanning speed 0.2s/0.02° from 3° to 30° in the 2 θ scale. Stepwise temperature increase 2 or 5 °C per diffraction pattern was used.

2.4 Single crystal X-ray diffraction

The single-crystal X-ray diffraction data for droperidol and benperidol phases were collected either at 173 K or 100 K on a Nonius Kappa CCD (Bruker) diffractometer, or at 120 K or 333 K on a SMART CCD 6000 (Bruker) diffractometer, both using Mo-K α radiation (graphite monochromator, $\lambda=0.71073\text{\AA}$) and Oxford Cryostream (Oxford Cryosystems) open-flow nitrogen cryostat for sample temperature control. The structure was solved by direct method and refined by full-matrix least squares on F^2 for all data using SHELXTL²⁶⁹ and OLEX2²⁷⁰ software or SHELX-97 suite²⁶⁹. All non-disordered non-hydrogen atoms were refined anisotropically. For disordered alcohol and ethyl acetate molecules a fixed value of site occupancy factor 0.5 was used.

The packing coefficients for crystal structures were calculated by PLATON⁹³. Mercury 3.3 software¹⁰² was used for crystal structure analysis and simulation of powder X-ray diffraction patterns based on crystal structure data.

2.5 Thermal Analysis

Differential scanning calorimetry. DSC patterns were recorded with a DSC 823e apparatus (Mettler Toledo), 5 – 10 mg of each sample was used for analysis. Samples were heated

in sealed aluminium pans at heating rate of $1\text{ }^{\circ}\text{C}\cdot\text{min}^{-1}$ or $5\text{ }^{\circ}\text{C}\cdot\text{min}^{-1}$ from $30\text{ }^{\circ}\text{C}$ to $120\text{ }^{\circ}\text{C}$ in static air atmosphere. Some of the samples were pinholed with hole diameter 0.5 mm .

Differential thermal analysis/thermogravimetry. DTA/TG analysis was performed with Exstar6000 TG/DTA6300 (SII Nanotechnology). Open aluminium pans were used. Heating of samples from 30 to $200\text{ }^{\circ}\text{C}$ ($120\text{ }^{\circ}\text{C}$ for mildronate) was performed at a $5\text{ }^{\circ}\cdot\text{min}^{-1}$ ($0.5, 1, 2, 3, 4$ and $5\text{ }^{\circ}\cdot\text{min}^{-1}$ for mildronate) heating rate. Samples of $5\text{-}10\text{ mg}$ mass were used, and the nitrogen flow rate was $100\pm 10\text{ mL}\cdot\text{min}^{-1}$ ($80\pm 10\text{ mL}\cdot\text{min}^{-1}$ for mildronate).

Study of the desolvation kinetics. For studying the desolvation kinetics, TG analysis in open aluminium pans was performed with Exstar6000 TG/DTA6300 (SII Nanotechnology). For studying the desolvation kinetics in non-isothermal mode, samples were heated with heating rates of $0.5, 1, 2, 3, 4$ and $5\text{ }^{\circ}\text{C}\cdot\text{min}^{-1}$ for mildronate and with variable heating rates in the range from 0.1 to $3\text{ }^{\circ}\text{C}\cdot\text{min}^{-1}$ for droperidol. The nitrogen flow rate was $80\pm 10\text{ mL}\cdot\text{min}^{-1}$ for mildronate and $300\pm 20\text{ mL}\cdot\text{min}^{-1}$ for droperidol. The sample weight for mildronate was $7.0\pm 0.5\text{ mg}$. For mildronate the effects of sample size and nitrogen flow rate were determined at additional data points, where the sample weight was 3 or 15 mg , and nitrogen flow rate was 30 or $300\text{ mL}\cdot\text{min}^{-1}$.

Desolvation kinetics were studied also in the isothermal mode at the temperature range from 25 to $80\text{ }^{\circ}\text{C}$ for mildronate, 20 to $125\text{ }^{\circ}\text{C}$ for droperidol and 30 to $110\text{ }^{\circ}\text{C}$ for benperidol with a step of $5\text{ }^{\circ}\text{C}$. The heater unit was preset to the required temperature before the insertion of the sample. For each sample, desolvation was performed at eight (for mildronate) and four to eight (for droperidol and benperidol) different temperatures selected according to the desolvation rate, which depended on the analysed solvate and the particle size. For droperidol and benperidol the nitrogen flow rate was $100\pm 10\text{ mL}\cdot\text{min}^{-1}$. For mildronate the sample weight was $7.0\pm 0.5\text{ mg}$, and nitrogen flow rate was $80\pm 10\text{ mL}\cdot\text{min}^{-1}$. The effects of sample weight and nitrogen flow rate were determined at additional data points, where the sample weight was $2, 4, 6, 8, 10\text{ mg}$, and nitrogen flow rate was $0, 45, 200,$ and $300\text{ mL}\cdot\text{min}^{-1}$.

For studying the dehydration at controlled water vapour pressure, a system previously described in the literature²⁷¹ was used for providing specific water vapour activity. Dry and moist nitrogen gas was mixed in a Gas controller unit (SII) at selected flow rates. The combined flow rate was $300\text{ mL}\cdot\text{min}^{-1}$. The relative humidity was measured with a TFH 620 (Ebro) humidity meter, which was previously calibrated using saturated solutions of NaCl and MgCl_2 .

Hot stage microscopy. For HSM, a Laborlux 12 PolS (Leitz) polarized light microscope equipped with a heating stage and a Newtronic heating control module was used. The heating rate was $5\text{ }^{\circ}\text{C}\cdot\text{min}^{-1}$. Images were acquired with Leica Application Suite software from a DFC450 (Leica) digital microscope camera.

2.6 Determination of desolvation kinetic parameters

For isothermal experiments, both model-free and model-based methods were used, but for non-isothermal experiments only model-free kinetic analysis was performed²⁰⁰. For isothermal experiments, data sets of α – time were obtained with $\Delta\alpha = 0.02$ at each temperature. Temperature stability during the reaction was evaluated and further analysis was performed in the conversion degree region where temperature change was smaller than 0.3 degrees for all used temperatures. For non-isothermal experiments, data sets of α – temperature and time were obtained with $\Delta\alpha = 0.02$ for each heating rate. By using results from both experimental modes, E_a was calculated with isoconversional methods: Friedman (FR)²⁰⁸, average linear integral method (ALIM)²⁰⁹ and advanced isoconversional method (AIC)^{210, 211}. For the first two methods E_a was calculated from the slope of the line in corresponding coordinates for α values with step size 0.02^{208, 209}, but for AIC method the parameter $\Phi(E_a)$ was minimized with MS Excel Solver, obtaining E_a for α values with step size 0.1^{210, 211}. Confidence intervals for the calculated E_a values were evaluated from the slope error of the line used for calculation of E_a with the FR method. Kinetic model determination was performed with ALIM²⁰⁹ and reaction progress was reconstructed in the coordinates $g(\alpha) - \alpha$ ^{180, 272} and $f(\alpha) - \alpha$ ^{90, 180, 272}. Besides, kinetic model determination for isothermal experiments was performed with reduced time plots¹⁸⁸, but for non-isothermal experiments from master plots using the parameter $Z(\alpha)$ ²¹⁵. Most often used solid-state kinetic models were included in the analysis^{90, 171, 190, 191}.

For isothermal experiments model fitting methods were used as well. The kinetic model was determined from linearization of the experimental points in coordinates $g(\alpha) - \text{time}$, and model with the best linear fit was selected from the list of most often used solid-state kinetic models^{90, 171, 190, 191}. The dehydration rate constants were subsequently determined by plotting experimental data points in the coordinates $\alpha - \text{time}$ and fitting theoretical lines modelled from selected kinetic models to the experimental points. The sum of squared differences between experimental and theoretically calculated α values was minimized with MS Excel Solver. If more than one model was selected for this procedure, then the best model was identified by the smallest sum of least squares. The E_a values were then determined from the Arrhenius plot.

More details are given in Appendix 4.

2.7 Gravimetric determination of solvent content

Solvent content was determined for droperidol non-stoichiometric solvates stored in desiccators with controlled solvent activity in the vapour phase. To provide a variety of relative humidity (RH) values for determination of water content in **NSH**, saturated salt solutions and P_2O_5 were used. The salts used for this experiment and the corresponding RH values were: LiBr (6%), LiCl (11%), CH_3CO_2K (23%), $MgCl_2$ (32%), NaBr (56%), KI (68%), NaCl (75%), KCl (84%), K_2SO_4 (97%), and also P_2O_5 ($\sim 0\%$)²⁷³. To provide a variety of ethanol, methanol, acetonitrile, and

nitromethane vapour activity, solutions with different compositions of the corresponding solvents and glycerol for methanol and ethanol, and glycerol and dimethylformamide for acetonitrile and nitromethane were prepared. The solvent activity in the vapour phase was estimated by the Raoult's law. All desiccators were thermostated at $30.0 \pm 0.5^\circ\text{C}$ and the sample containers were weighed on analytical balance ($d=0.1$ mg). Further experimental details are given in Appendix 8.

Similar procedure was used for recording sorption-desorption isotherm of mildronate. **DH** and **AP** samples were placed in humidity chambers thermostated at $25 \pm 1^\circ\text{C}$ where the relative humidity was provided with saturated salt solutions and P_2O_5 (see above) and their weight was controlled using analytical balance ($d=0.1$ mg) until no notable change of weight was observed. At the end of the experiment, the phase composition of each sample was determined with PXRD.

2.8 Determination of lattice parameters of solvates with different solvent content

The PXRD patterns were determined for droperidol solvates with different solvent content. Samples identical to those used for gravimetric solvent content determination were used. Both samples were stored together, and thus the solvent content was assumed to be identical. The lattice parameters of the fully solvated non-stoichiometric solvates was determined at ambient temperature with *LP-Search* algorithm in *TOPAS 4.2*²⁷⁴ using lattice parameters determined at 173 K in SCXRD measurements as the initial guess. The lattice parameters of the non-stoichiometric solvates with different solvent content were determined by performing the Pawley refinement in *TOPAS 4.2* by relaxing the lattice parameters and the crystallite size parameter.

2.9 Crystal structure determination from PXRD data

The PXRD patterns were indexed for the first 20-25 peaks, using DICVOL04²⁷⁵ (implemented in WinPLOTR software²⁷⁶) and SVD indexing algorithms²⁷⁷ (implemented in TOPAS v4.2). Space group determination was carried out using a statistical assessment of systematic absences, and Z' was determined based on density considerations. Structure solutions were performed by Monte Carlo/Simulated annealing technique implemented in Expo2014^{278, 279}, using a rigid model, flexible about the dihedral angles τ_{1-6} and $\tau_{\text{Benz}1}$ and $\tau_{\text{Benz}2}$ (Figure S7, Appendix 11) for benzyl alcohol molecule by also determining the center of mass location and molecular orientation. The initial geometries of benperidol molecule as in crystal structures of polymorph **I** (for \mathbf{S}_{Benz}) and \mathbf{S}_{ACN} (for **HH** and **III**) were used. For the structure of **HH**, oxygen atoms of water molecules were kept in the special positions, and the initial unit cell with water molecules was taken from the CSD (Refcode AMCHCA²⁸⁰). The initial geometry of benzyl alcohol molecule was taken from the CSD (Refcode FEBCUL²⁸¹). The final refinements were carried out by the Rietveld method, maintaining the rigid bodies introduced at the structure solution stage. The background was modelled by a 20th-order polynomial function of the Chebyshev type; peak profiles were

described by the Pearson VII function and a common (refinable) isotropic thermal factor was attributed to all non-hydrogen atoms, while that of hydrogen atoms was assumed to be 1.2 times higher.

2.10 Fourier transform infrared spectroscopy

The ATR-FTIR spectra were collected for neat solids on a Frontier FTIR (PerkinElmer) spectrometer equipped with a Universal ATR Sampling Accessory with a diamond window. The spectra were recorded from 650 to 4000 cm^{-1} at a 2 cm^{-1} spectral resolution with 16 scans.

2.11 Particle size analysis

A Mastersizer 2000 (Malvern Instruments) laser diffraction instrument was used for particle size analysis. Integration time was 3000 ms. The measurement range was set to 0.020 – 2000 μm , and 59 counting channels were used. For sample dispersion nitrogen with 1.0 bar pressure was used. All measurements were carried out three times and the average particle size distribution was calculated.

2.12 Karl Fischer titration

A 836 Titrando (Metrohm) Karl Fischer volumetric titrator was used for the determination of water content in the samples. Approximately 100–200 mg portions of each sample were weighed on an analytical balance ($d=0.1$ mg) and titrated with Hydranal Composite 5 (Fluka).

2.13 Solid-state NMR

High-resolution solid-state NMR spectra were obtained using either a Avance III HD spectrometer (Bruker) operating at 125.67 MHz for ^{13}C (499.72 MHz for ^1H) and 76.71 MHz for ^2H with a 4.0 mm (rotor o.d.) MAS probe, or a VNMRs 400 spectrometer (Varian), operating at 40.53 MHz for ^{15}N (399.88 MHz for ^1H) with a 6.0 mm (rotor o.d.) MAS probe. ^{15}N spectra were recorded at ambient temperature, whereas ^{13}C and ^2H spectra were recorded at controlled temperatures from 20 $^{\circ}\text{C}$ down to -45 $^{\circ}\text{C}$. Note that these are set temperatures that do not attempt to correct for sample heating under magic-angle spinning; these are estimated to be of the order of +5, +8 and +15 $^{\circ}\text{C}$ for the ^2H , ^{15}N and ^{13}C spectra respectively.

^{13}C and ^{15}N spectra were obtained under MAS conditions using cross polarization (CP) with the following conditions: recycle delay 7–30 s for **NSH**, **S_{Me}** and **S_{Et}**, and 120–180 s for **S_{ACN}**, and **S_{NM}**, contact time 0.5–2 ms, a sample spin rate of 13 kHz for ^{13}C and 6.8 kHz for ^{15}N spectra, and acquiring 300–1000 transients for ^{13}C and 440–3600 transients for ^{15}N (depending on relaxation delays). SPINAL64 with 78 kHz ^1H nutation rate and TPPM with 55.6 kHz nutation rate were used for heteronuclear decoupling of the ^{13}C and ^{15}N spectra respectively. Spectra were referenced with respect to external neat TMS for ^{13}C or neat nitromethane for ^{15}N by setting the high-frequency signal from a replacement sample of adamantane to 38.4 ppm or the nitrate signal from a replacement sample of solid ammonium nitrate to -5.1 ppm, and typically processed with an

apodisation function corresponding to a 20 Hz Lorentzian line-broadening prior to Fourier transformation. ^{13}C linewidths were determined by fitting the peaks to a mixed Lorentzian/Gaussian lineshape in the Bruker TopSpin software.

Carbon-13 T_1 values were estimated from direct-excitation spectra with recycle delays of 0.2–180 s, while more accurate measurements were made using saturation-recovery experiments with recovery delays of 0.1 ms – 90 s. 12 pulses separated with a 10 ms delay were used for saturation of the ^{13}C magnetization. 200–240 repetitions were accumulated, with a spinning rate of 13 kHz and ^1H decoupling nutation rate of 71 kHz. T_1 values from variable recycle delay experiments were calculated by fitting peak heights to a simple rising exponential function using Excel Solver. T_1 values from saturation-recovery experiments were determined in TopSpin by fitting integrated peak areas to a rising exponential. Note that measurement of the relaxation times for the CH_3 of \mathbf{S}_{Et} in particular were complicated by transient Nuclear Overhauser effects²⁸²; this is discussed further in the Appendix 10.

^2H MAS spectra were acquired without proton decoupling with 10 kHz spinning rate and 10 s recycle delay, acquiring 1000–10000 transients (depending on time available). T_1 relaxation times were estimated with short experiments (50–100 repetitions) with the recycle delay varying up to 10 s or 30 s using 7–9 increments. T_1 values were estimated by fitting peak heights to a simple rising exponential function as above. Bandsape analysis of the spinning sidebands was performed in Gsim²⁸³ / pNMRsim²⁸⁴ by simultaneously fitting the peak linewidths (using a Lorentzian lineshape function) and quadrupolar coupling parameters from both ND and solvent sites. Flat baselines, which are significant for fitting, were typically obtained by discarding the data points before the first rotary echo for signals obtained on-resonance. Alternatively, the baseline roll was suppressed using spline fitting in TopSpin.

2.14 Theoretical calculations

Geometry optimization and energy calculation of the crystal structures. The starting geometries of all droperidol and benperidol phases and mildronate \mathbf{DH} were obtained from SCXRD experimental data²⁵⁹, while that of mildronate \mathbf{AP} was used as determined from PXRD data²⁶⁰ and then corrected in *Gaussian09* at the B3LYP/6-31G level, see Appendix 6. Since the solvent molecules in droperidol \mathbf{S}_{Me} and \mathbf{S}_{Et} are disordered over two orientations related by inversion symmetry, the starting geometries of \mathbf{S}_{Me} and \mathbf{S}_{Et} without disorder were prepared by discarding one of the solvent molecule orientations, by thus creating a structure in the P1 space group with two symmetrically individual droperidol molecules. The starting geometry for droperidol \mathbf{ISD} was obtained by removing the water molecules from the \mathbf{NSH} structure. Geometry optimization of crystal structures were performed in *CRYSTAL09*²⁸⁵ and in CASTEP²⁵¹. Calculations in *CRYSTAL09* were performed at the B3LYP-D*^{277, 286} level using 6-31G(d,p) basis set^{287, 288}, dispersion interactions were treated using Grimme dispersion correction model²⁸⁹

modified as described in the literature^{98, 286, 290}. All of the obtained energies were corrected for basis set superposition error by the counterpoise method²⁹¹. The calculations in CASTEP were performed with the PBE²⁹² functional using on-the-fly generated ultrasoft pseudopotentials and cut-off energy of 600 eV. Dispersion interactions were treated using semiempirical dispersion correction schemes of Grimme (G06)²⁸⁹ and Tkatchenko-Scheffler (TS)²⁹³. Crystal structure optimization was performed by employing three different procedures – by relaxing only the hydrogen atoms (HO), by relaxing all atoms (ALL), and by relaxing all atoms and the unit cell parameters (UC) – using three different calculation methods: PBE+TS (HO, ALL and UC) and PBE+G06 (UC) in CASTEP, as well as B3LYP-D* (UC) in CRYSTAL09. Identical input geometries were used for all of the calculation methods.

Geometry optimizations of droperidol solvate doubled unit cells (see Appendix 9 and Section 3.5.4) with adjacent solvent molecules in the same or opposing directions were performed both with the pure PBE functional and also using the TS dispersion correction scheme²⁹³. The orientation of the solvent molecule was inverted by manually adjusting the atomic coordinates on one solvent molecule prior to full geometry optimisation. Structures where adjacent alcohol molecules were oriented in opposite directions were used to confirm the validity of the ordered model of **S_{Me}** and **S_{Et}** by calculating the intermolecular interaction energy of the solvent molecules (see Appendix 9).

Frequency calculation^{294, 295} was performed in CRYSTAL09 for mildronate structures after the full geometry optimization in order to calculate the zero-point vibration correction and thermal correction on the total energy.

Calculations in Gaussian 09. Single molecule and molecular cluster energy calculation and geometry optimization were performed in Gaussian 09²⁹⁶. The potential energy surface (PES) scans with respect to one dihedral angle were performed at the MP2/6-31G(d,p) or B3LYP/6-311G(d,p) level with step size of 10°, while PES scans with respect to two dihedral angles were performed at the B3LYP/6-31G level with step size 15° for each dihedral angle. For this analysis mildronate molecule was extracted from nonoptimized **DH** structure with atom coordinates as in the literature, from **AP** structure corrected at the B3LYP/6-31G level (see Appendix 6), as well as from droperidol **NSH** and benperidol **S_{ACN}** structures optimized in CASTEP.

The molecular volumes of selected solvent molecules were calculated in Gaussian 09²⁹⁶ after the geometry optimization at the B3LYP/6-311G(d,p) level using Grimme's dispersion correction²⁹⁷.

Simulation of IR spectra was performed by extracting a characteristic molecular fragment representing the intermolecular interactions (amide homodimers for **II** and **S_{ACN}**, six benperidol molecule ring for **I**, chain consisting of three benperidol and two alcohol molecules for **S_{Me}** and **S_{Benz}**, and a fragment of three benperidol and one water molecule for **HH**). Geometry optimization

and frequency calculation was performed at PM6 level, and the obtained frequencies were multiplied by a scale factor 0.953²⁹⁸.

Calculation of the intermolecular interaction energy. The interaction energies between pairs of molecules were calculated in *Gaussian 09*²⁹⁶ using the B3LYP and M06-2X²⁹⁹ functionals and 6-311G(d,p) basis set to molecular geometries directly extracted from the crystal structures after the geometry optimization. The basis set superposition error was corrected using the counterpoise method. For B3LYP calculations the Grimme dispersion correction method was used²⁹⁷. The interaction energy was calculated as the difference between the total energy of the dimer and the corresponding isolated molecules. The total interaction energy values were calculated as a sum of all pairwise interaction energies (without the correction for double counting of identical interactions) for molecule pairs having contacts shorter than the given cut-off distance, see Table 3.16.

Calculation of the lattice energy. Lattice energy calculations were performed with semi-empirical PIXEL⁹⁷ methodology (code provided in the CLP software suite), which also provides information about pairwise intermolecular interaction energies. This code enables decomposition of total lattice energy and pairwise interaction energy into electrostatic, polarization, dispersion and repulsion contributions. Empirical parameters for calculations were used as provided in the literature^{97, 300}. The atom positions for the purposes of this calculation were obtained by standard procedure using *RETCIF* and *RETCOR* modules. Hydrogen atom positions were either renormalized or optimized by *CASTEP*. Molecular electron density calculations were performed in *Gaussian 09*²⁹⁶ at the MP2/6-31G(d,p) level using standard grid parameters. Condensation level 4 and cutoff distance 35-45Å depending on the molecule size were used.

Calculation of chemical shift. Chemical shift calculations were carried out using the GIPAW method implemented in *CASTEP*²⁵⁰⁻²⁵³, after geometry optimization of the droperidol crystal structures determined at 173 K. Since the first principles calculations cannot be applied to disordered structures, starting structures of \mathbf{S}_{Me} and \mathbf{S}_{Et} without disorder were prepared in two ways: (a) both structures were solved in the *P1* space group with ordered solvent and (b) *P1* structures were derived from the reported $\bar{P}1$ structures by discarding one of the solvent molecule orientations. Calculations were performed with the PBE²⁹² functional using on-the-fly generated ultrasoft pseudopotentials and a cut-off energy of 600 eV, with integrals taken over the Brillouin zone using a Monkhorst-Pack grid of a minimum k-point sampling of 0.05 Å⁻¹. Two approaches were used for geometry optimization: optimization of hydrogen atom positions only and optimization of all atomic positions. Unit cell parameters were fixed to the values determined from X-ray diffraction studies in both cases. The computed ¹³C and ¹⁵N chemical shifts were referenced by linear regression of computed shielding values to the experimental shifts²⁵².

3 RESULTS AND DISCUSSION

3.1 Dehydration mechanism of mildronate dihydrate

When heated in dry air, mildronate **DH** transforms into **AP**, whereas at high temperature and relatively high humidity it transforms into **MH**²⁵⁸. However, the dehydration mechanism of the **DH**, the only stable mildronate form in ambient conditions, has not yet been examined. Understanding the mechanism of such dehydration is important for the systematic study of the dehydration processes of pharmaceutical materials⁵⁸. The aims of this study thus were: a) to determine the dehydration mechanism of mildronate **DH**; b) to establish the reasons for the observed one step dehydration process of mildronate **DH** directly to the **AP**, and c) to calculate the dehydration kinetic parameters and relate them to the dehydration mechanism and the crystal structure of **DH**.

3.1.1 Characterization of mildronate dihydrate dehydration

It was determined that at 25 °C temperature **DH** was stable in the relative humidity interval from 6 to 50%, but dehydrated to **AP** at humidity below 6%. Thus it was confirmed that **MH** was not thermodynamically stable at any of the examined conditions. It was observed that the dehydration of **DH** at various temperatures gave **AP** as the only product, implying that the dehydration of **DH** was a one step process. In order to confirm this dehydration mechanism, we analyzed dehydration of **DH** with VT-PXRD under air atmosphere. The temperature in the range where dehydration was observed in other experiments was raised with 1°C step size per diffraction pattern, until complete dehydration was observed. Diffraction patterns for those temperatures where phase transition was observed are given in Figure 3.1. It can be seen that at $p(\text{H}_2\text{O}) = 1.1 \text{ kPa}$, relative humidity 40% at 22 °C, dehydration started at 57 °C temperature, which was identified by appearance of the **AP** peaks (marked with blue triangles). Formation of **MH** was not observed in this experiment, nor in other similar experiments. The characteristic diffraction peak position for **MH** would be at 12.0 ° and 16.6 ° in 2θ scale.

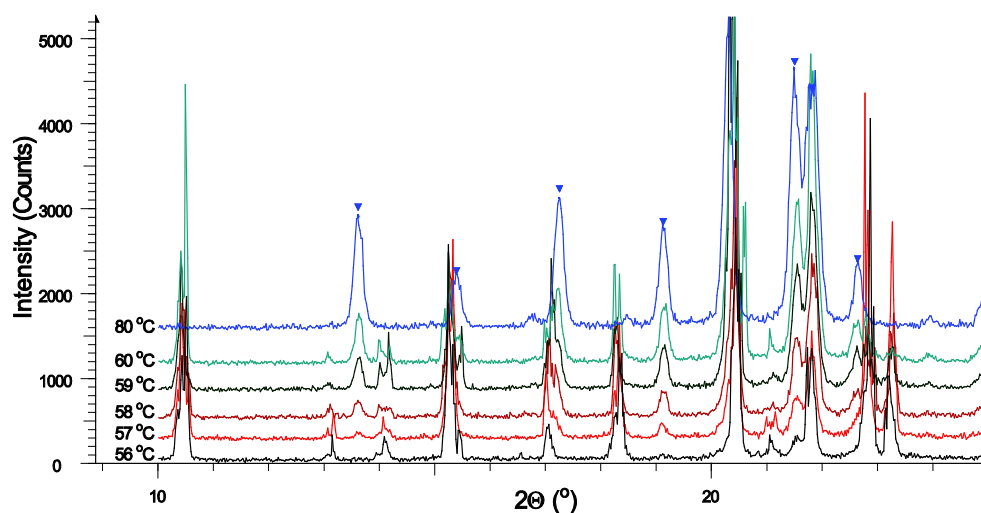


Figure 3.1. VT-PXRD patterns of mildronate **DH** dehydration.

Dehydration of **DH** samples was analyzed with DSC in closed and pinholed sample holders and with DTA/TG in open pans under nitrogen flow. In DTA analysis one or two overlapping endothermic peaks appeared with dehydration starting at 45-55 °C. The second endothermic effect was always observed as a relatively narrow peak at 86-88 °C and above this temperature the weight loss rate noticeably decreased. The temperature of first peak was affected by the heating rate and the particle size, whereas these parameters did not affect the temperature of the second peak (see Figure 3.2). When **DH** samples were analyzed with DSC, dehydration was observed as a narrow signal with peak temperature of 88-90 °C, regardless of the hole in the container (see Figure 3.2). From various experiments (9 scans for particle size fractions from <40 μm up to 350-700 μm) the enthalpy of the observed process was calculated as $31.8 \pm 0.9 \text{ kJ} \cdot \text{mol}^{-1}$.

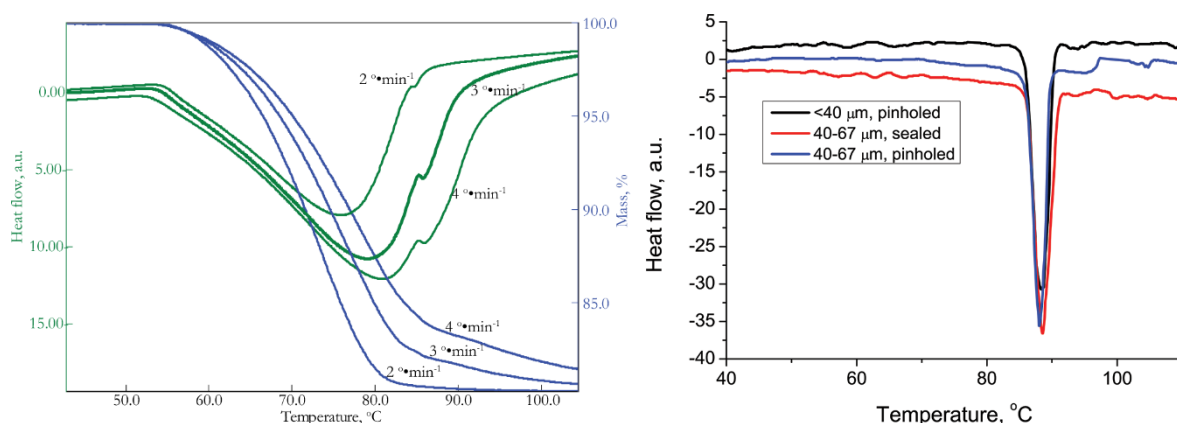


Figure 3.2. DTA/TG curves of mildronate **DH** fraction 67-150 μm at various heating rates (on the left) and DSC curves of mildronate **DH** at heating rate $5 \text{ }^{\circ}\text{C} \cdot \text{min}^{-1}$ (on the right).

From the obtained data it can be concluded that the observed endothermic process in the DSC scans under static air atmosphere was melting/peritectic decomposition of the **DH**. This explains the observed enthalpy value ($31.8 \pm 0.9 \text{ kJ} \cdot \text{mol}^{-1}$), which was too low even for the evaporation of two water molecules (vaporization enthalpy of water at the corresponding temperature is $41.6 \text{ kJ} \cdot \text{mol}^{-1}$)³⁰¹. This was obvious for closed pans, and the explanation for pinholed pans was that the size of the hole was too small for evaporation of the evolved water during the analysis. However, when **DH** was heated in DTA/TG instrument on open pans, nucleation of **AP** started at lower temperatures and water was lost much more effectively. Thus the dehydration of the **DH** was finished before reaching the melting temperature in cases when the heating rate was slow enough and/or particles were small enough. By using the DTA data it was calculated that the dehydration enthalpy of the **DH** was $120 \pm 10 \text{ kJ} \cdot \text{mol}^{-1}$, corresponding to the sum of the crystal hydrate decomposition and water vaporization enthalpies (DTA was calibrated with substances having known melting and dehydration enthalpy values).

If complete dehydration was not reached until the melting temperature in the DTA scans, then a melting/peritectic decomposition process was also observed. This was supported from

HSM study of two samples with different particle sizes (see Appendix 6) and by decrease of the weight loss rate.

Phase composition of the samples obtained after and during DTA/TG analysis was determined with PXRD. It was found that for samples where dehydration was observed as a one step process (complete dehydration was reached below 86 – 88 °C), the only phase which formed during and after the dehydration was **AP**. The results of PXRD and thermal analysis thus indicated that **AP** formed as the only product in a one-step dehydration process. However, when dehydration was slower (and also the melting/peritectic decomposition signal appeared in DTA) during and after the second endothermic dehydration peak (at temperatures above 90 °C), **MH** was sometimes also detected as one of the phases. Nevertheless, after exceeding the melting temperature, formation of **MH** occurred due to the crystallization of mildronate from solution or solid phase transition from the **AP** in the presence of liquid water. This observation agreed with the previously reported fact that **MH** was stable only at elevated temperature²⁵⁸.

3.1.2 The relationship between crystal structures and the observed dehydration mechanism

The dehydration of **DH** resulted in the formation of **AP** instead of **MH**. This observation could be related to the similarity of the crystal structures of **DH** and **AP**. To explore this theory, we analyzed the structures of three crystalline phases formed by mildronate.

Mildronate molecules in the structures of **DH** and **MH** adopted the same conformation and were characterized by the same hydrogen bonding motif different from that in the **AP** structure. Thus, from this analysis, crystal structures of **DH** and **MH** appeared to be similar²⁶⁰.

However, analysis of molecular packing in the crystal structures of **DH**, **AP** and **MH** showed that structures of **DH** and **AP** were similar and consisted of four mildronate molecules notated A, B, C and D (each generated by one of four symmetry operations corresponding to P2₁/c or P2₁/n space group). In **DH** these molecules were grouped around hydrogen bonded graph set ring R₄⁴(8) formed by water molecules (see Figure S12 in Appendix 6). Each of the four molecules A, B, C and D formed a hydrogen bonded molecule pair with the molecules A', B', C' and D', respectively. Similarly arranged four pairs of molecules A-A', B-B', C-C' and D-D' could be identified in the crystal structure of **AP** as well (see Figure 3.3). However, in this structure between these molecules there was an empty channel, and molecule pairs were packed more tightly. Besides this, there were significant changes in molecular conformation (τ_1 and τ_2 , see Appendix 6) and hydrogen bonds between the molecule pairs A and A', B and B' etc were lost, but new hydrogen bonds formed between molecules A and D, and between B and C, thus forming C(6) chains (see Figure S12 in Appendix 6). Therefore, inversion-related antiparallel molecule pairs occurred in the crystal

structures of **DH** and **AP**. Two such antiparallel pairs (A-A' and C-C') were situated perpendicularly to two other (B-B' and C-C').

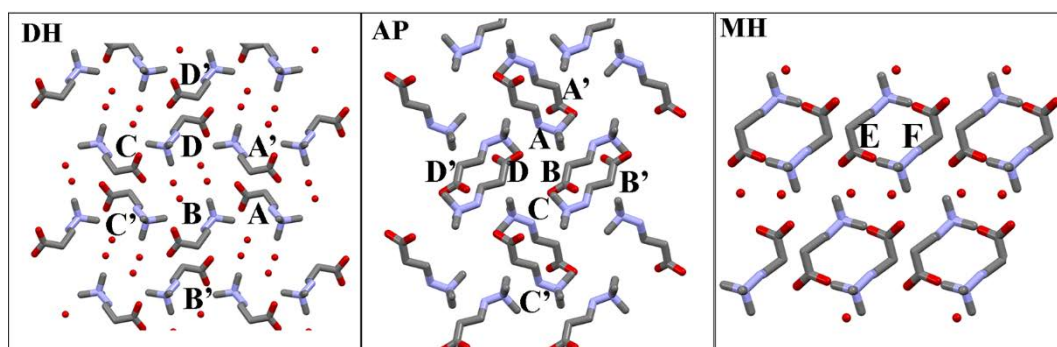


Figure 3.3. Molecular packing in the crystalline forms of mildronate (hydrogen atoms have been omitted for clarity).

In the crystal structure of **MH**, inversion-related antiparallel molecule pairs E-F were packed parallel to other such pairs, resulting in layers of mildronate molecules (see Figure 3.3). These layers were interconnected by hydrogen bonds mediated by water molecules (see Figure S12 in Appendix 6). Although hydrogen bonded antiparallel molecule pairs with the same molecular conformation were present in both hydrates, these pairs in the **MH** structure were packed in different way. Therefore, the molecule conformation can be associated with hydrogen bonding motif and/or the presence of the hydrogen bonds with water molecules but not with the molecule packing.

Thus, it was shown that the transformation from **DH** to **AP** was associated with only minor changes in packing of the mildronate molecules. At the same time, the transformation from **DH** structure to **MH** was connected with important reorganization of mildronate molecular packing, which could occur only during destructive dehydration followed by crystallization of a new phase. Thus it can be seen that transition from **DH** to **AP** should be an easy one-step process, and not connected with formation of **MH** as an intermediate step. However, dehydration did not occur as a single crystal to single crystal transition. It can be concluded that structure reorganization was important enough to introduce cracking and thus **AP** was produced as a polycrystalline powder.

Based on the structural analyzes, we provide a mechanism of water elimination and structure reorganization explaining the observed dehydration of **DH** to **AP**. Due to the presence of large channels containing all of the water molecules, it was likely that the first step in the dehydration process represented escape of water by emptying of the channels (see 1 in Figure 3.4). After this step, conformation change (2) and molecule translation (3) occurred, forming **AP** as the final product. Although separated in the Figure 3.4 for the clarity, most probably both of these processes happened simultaneously and were associated with disappearance of the hydrogen bonded molecule pairs and formation of new hydrogen bonds observed in **AP** structure.

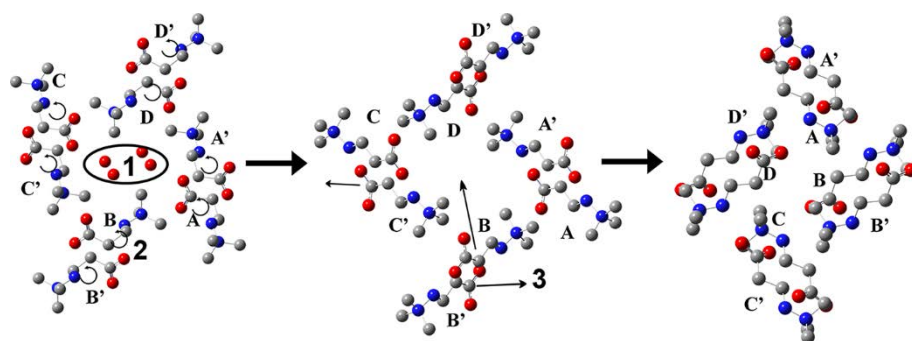


Figure 3.4. Schematic representation of structural reorganizations during the transition from **DH** to **AP**.

Thus, based on the dehydration process classification according to structural changes during the dehydration, dehydration of the **DH** could be classified as a) a water evolution type WET3 with direct formation of **AP** crystalline phase after the dehydration¹⁶³ and b) cooperative release of water followed by the cooperative rearrangement, thus belonging to the class II-Coop.-Reorg.¹⁶², according to the two systems described in literature.

3.1.3 Kinetic parameters of dehydration

Particle size. Dehydration of **DH** was studied for samples with different particle sizes. Particle size distribution for different **DH** fractions is given in Figure S1 in Appendix 6. PXRD was used to determine that in all of the cases **AP** was obtained as the only dehydration product. The dehydration E_a value for each fraction was calculated from isothermal experiments and are shown in Figure 3.5.

From Figure 3.5 it can be seen that E_a of the samples with particle size up to 350 μm was $75 \pm 3 \text{ kJ} \cdot \text{mol}^{-1}$, but for particles larger than 350 μm there was a significant decrease of the E_a caused by increasing the particle size. Most probably this decrease of the E_a for larger particles was due to diffusion control. When considering water vapor escape through a thick product layer, the rate becomes diffusion limited for some critical particle size, and this effect grows upon further increase in the particle size.

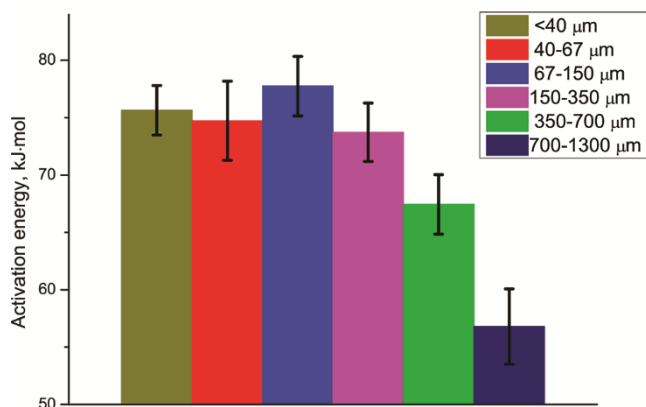


Figure 3.5. Dehydration activation energy for different fractions of **DH**.

It was determined that the most appropriate kinetic model for dehydration of fractions with particle size below 150 μm was the one-dimensional phase boundary model R1, but for particle size above 350 μm it was the two-dimensional phase boundary model R2. Kinetic models R1 and R2 both describe phase boundary controlled reactions with different dimensionality. This result fits with the observations from hot stage microscopy where dehydration process initiated on the single crystal surface and then reaction boundary progressed inwards to the crystal interior. It has been mentioned in the literature¹⁶³ that the typical thickness of the reaction interface is 10 – 150 μm , so for smaller particles the only rate limiting step can be formation and advance of this interface towards the crystal interior from only one energetically more favourable direction. However, the formation of the phase boundary for bigger particles (applicable in this case where the average particle diameter was above 350 μm) was complete when there still was a lot of **DH** present. Thus the rate limiting step could also involve reaction interface advancement from other crystal faces, which could be described by a two dimensional phase boundary mechanism.

Sample weight. Dehydration of **DH** <40 μm fraction was studied for samples with different weight. It was determined that the dehydration rate decreased when the sample weight was increased. The reason for the decrease of the rate constant by increasing the sample weight can be due to the slower vapor diffusion through the sample layer, which limits the total dehydration rate. Dehydration E_a dependence on the sample weight was calculated as well and the obtained results are shown in Figure 3.6. It is apparent that the E_a decreased by increasing the sample weight. Such an effect can be the result of increased contribution from the bulk diffusion effect upon increasing the sample weight as the E_a of the diffusion step typically is smaller than that of the phase boundary reaction and more contribution from the diffusion would be observed by increasing the sample weight.

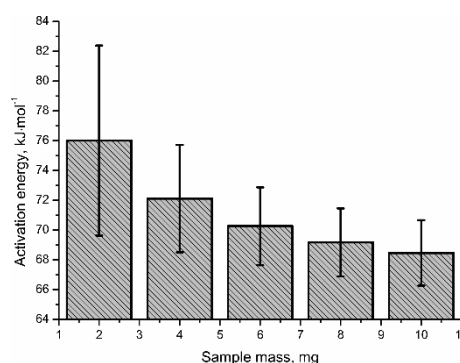


Figure 3.6. Dehydration activation energy dependence on sample weight for the <40 μm fraction.

3.1.4 Dehydration mechanism

There are large channels containing water molecules along the *a*-axis^{257, 259} in the **DH** structure. Thus, we suggested that during the dehydration of mildronate **DH**, water molecules escaped through these channels. It has been postulated that if the dehydration environment is

controlled by nitrogen flow with relative humidity close to zero, then the water molecule diffusion to the crystal surface should not control dehydration rate¹⁸¹, as it appeared for mildronate **DH** where dehydration kinetics were described by the models R1 and R2. Thus it can be concluded that the rate limiting step should be hydrogen bond dissociation and/or molecular conformation change and reorganization. From the PES analysis it was determined that the energy necessary for molecular conformation changes was at least three times lower than the dehydration E_a (see Appendix 6). Thus it can be predicted that the rate limiting step most probably is the disruption of the hydrogen bonding network, or separation of mildronate molecules paired through hydrogen bonds in the crystal structure of **DH**²⁵⁷.

However, it was also found that besides phase boundary advance other factors limited the rate of dehydration: a) diffusion rate of water outside of the crystal and b) diffusion of water from the inside of the powder. By changing the particle size and sample weight influence of these rate limiting steps could be modified. However, based on the results from kinetic model determination, phase boundary advance was the main rate limiting step.

Based on the crystal structure it can be suggested that for small particles the phase boundary advance during the dehydration of **DH** occurred along the *a*-axis and complete dehydration was reached by phase boundary advance only in this direction. The dehydration rate could thus be described with a one-dimensional phase boundary reaction model. However, for particles with larger size than 350 μm , dehydration most probably occurred also in the second energetically favourable direction. This can be described by the movement of the reaction interface also perpendicularly to the channels where water molecules are situated in the **DH** crystal structure. As a result the dehydration could be described by a two-dimensional phase boundary reaction model. It is possible that evolving of water in the direction perpendicular to the water channels is hindered, thus contribution from the diffusion increased in this case, and the dehydration E_a decreased as observed for samples where R2 was determined as the most appropriate kinetic model. Schematic representation of the dehydration process and the rate limiting steps are given in Figure 3.7.

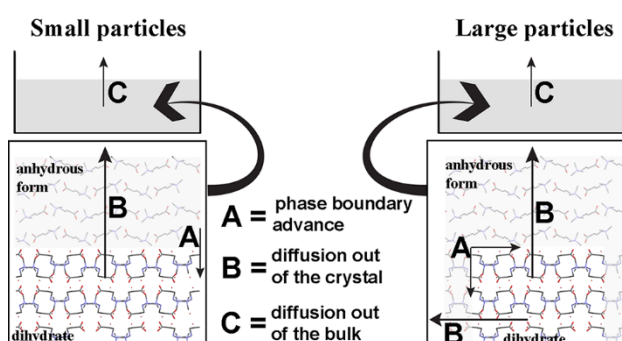


Figure 3.7. Schematic representation of the dehydration process and the rate limiting steps

3.1.5 Conclusions

The mechanism of mildronate dihydrate (**DH**) dehydration was analyzed according to various experimental methods, and it was determined that dehydration of the **DH** is a single-step process leading directly to the anhydrous form (**AP**). By analyzing the crystal structures of the **DH**, **MH** and **AP** it was determined that, in contrast to the similar molecular conformation and hydrogen bonding patterns in **DH** and **MH**, molecular packing in the **DH** and **AP** structures was also similar, thus explaining the one-step dehydration of the **DH** directly to **AP**.

The dehydration of the mildronate **DH** was linked to the escape of water molecules through structural channels, as molecule conformation changes and molecule translation. Thus, dehydration of the **DH** could be classified as a) WET3 with direct formation of **AP** crystalline phase after the dehydration¹⁶³ and b) class II-Coop.-Reorg.¹⁶².

The dehydration E_a of **DH** was $75 \pm 3 \text{ kJ} \cdot \text{mol}^{-1}$ for particles with diameter below $350 \text{ }\mu\text{m}$ but it decreased for larger particles due to the increasing effect of water diffusion out of the particle. The kinetic model best describing the dehydration of particles smaller than $150 \text{ }\mu\text{m}$ was R1, while for particles larger than $350 \text{ }\mu\text{m}$ it was the R2 model. This change was associated with the altered dimensionality of the phase boundary movement towards the center of the crystal.

By analyzing the sample weight effect on the dehydration, a decrease of the reaction rate and the dehydration E_a were observed by increasing the sample weight. This decrease was associated with increasing contribution from the water diffusion out of the powdered sample.

3.2 Rationalization of mildronate dihydrate dehydration mechanism and determination of kinetic parameters by analyzing the effect of experimental and sample factors

The effects of various sample and experimental factors on the dehydration process of API hydrates have been investigated in a number of papers^{180, 219, 220, 271, 302-304}. By studying the dehydration mechanism of mildronate **DH** (section 3.1) it was observed that dehydration kinetic parameters depended on particle size and sample weight. However, this represent only two sample and experimental factors studied for one sample in isothermal mode.

In this section a) the possibilities of determining the dehydration kinetic parameters of mildronate hydrate **DH** by both isothermal and non-isothermal methods were explored, b) the effect of various sample and experimental factors on the dehydration activation energy and kinetic model were studied in depth, c) variations of kinetic parameters were used for understanding the dehydration mechanism and d) optimal conditions for determining the dehydration kinetic parameters were selected.

Investigation of the sample and experimental factors in both isothermal and non-isothermal modes allowed us to compare the influence of each factor on the results obtained in both modes. Moreover, evaluation of various factors allowed the identification of the most appropriate sample and experimental factors for performing reliable determination of the dehydration kinetic parameters.

Matching E_a values were obtained with all the calculation methods for each sample in each particular experiment. For representation of the model-free method results, E_a values calculated with Friedman's method were used in this section. In each of the cases a certain kinetic model was determined as the most appropriate according to all methods, unless stated otherwise.

PXRD was used to determine that **AP** was obtained as a dehydration product. However, in samples where the dehydration continued after the melting/peritectic decomposition point, **MH** was also detected, even though its formation was not associated with direct dehydration of the **DH**, see section 3.1.

It was determined that sample preparation procedure and storage conditions had no effect on the examined kinetic parameters. For example, the similarity of the dehydration E_a for fractions up to 150-350 μm of all the samples can be evaluated from Figure S4 in Appendix 7. The sample particle size in this section is reported according to the mesh sizes used for their preparation.

3.2.1 Particle size effects evaluated from dehydration in isothermal and non-isothermal modes

To evaluate the possibility of determining the dehydration kinetics of **DH** under isothermal and non-isothermal modes, as well as for the evaluation of the particle size effects, E_a and kinetic

models from dehydration experiments of different **DH** particle size fractions in both modes were calculated and compared. Particle size distribution for different **DH** fractions is given in Figure S3 in Appendix 7. It was observed that by increasing the particle size, the dehydration process slowed, and the dehydration rate constant correspondingly decreased in isothermal mode, while the dehydration starting and finishing temperatures increased in the non-isothermal mode. This is due to the fact that for smaller particles there was more surface area accessible to dehydration than that for larger particles. Nevertheless, it was observed that the dehydration rate expressed as fraction converted per one degree was similar for all sample fractions in the non-isothermal mode, whereas more detailed study identified that the fraction of $<40\ \mu\text{m}$ showed an exception from these trends (see Appendix 7).

In section 3.1 it is already stated that dehydration E_a of the **DH** samples with particle size up to $350\ \mu\text{m}$ is almost the same, but for particles larger than $350\ \mu\text{m}$ there is a significant decrease of the E_a by increasing the particle size, explained by diffusion control. Here the dehydration E_a was calculated with isoconversional methods from both isothermal and non-isothermal experiments. The obtained dehydration E_a as a function of conversion degree α for samples with various particle sizes are shown in Figure 3.8.

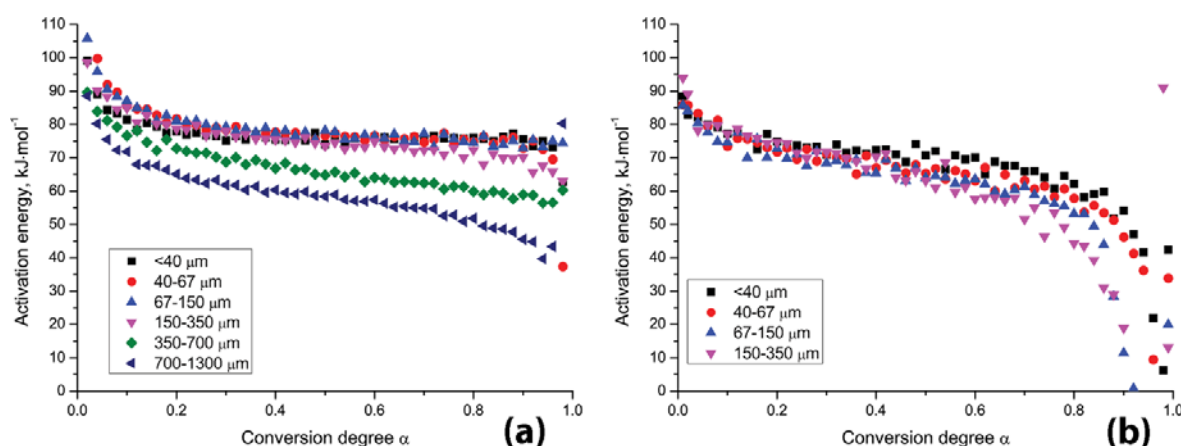


Figure 3.8. Dehydration activation energy – conversion degree plot for various **DH** fractions obtained (a) from isothermal experiments and (b) from non-isothermal experiments.

From the isothermal experiments shown in the Figure 3.8(a) it was confirmed that E_a of the samples with particle size up to $350\ \mu\text{m}$ was the same, whereas it decreased by further increasing the particle size. From the non-isothermal experiments shown in Figure 3.8(b), it was possible to identify differences in the final part of the $E_a - \alpha$ plots for fractions with particle size up to $350\ \mu\text{m}$.

In Figure 3.9, the dehydration $E_a - \alpha$ plots calculated from isothermal and non-isothermal experiments for the $40\text{-}67\ \mu\text{m}$ fraction are shown. It can be seen that the E_a values calculated from both modes were the same at the start of the reaction, within the limits of experimental error, and a small decrease of the values was observed by increasing the conversion degree. This decrease was explained by the fact that the higher dehydration E_a at the start of reaction was caused by nucleation of the product phase¹⁷¹ or by the reversibility of the dehydration reaction²⁷².

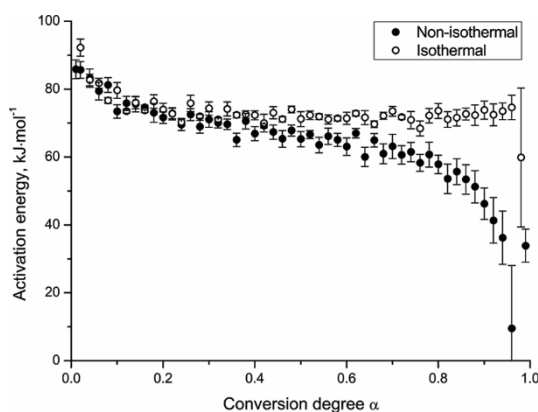


Figure 3.9. An activation energy - conversion degree plot for dehydration of the 40-67 μm fraction calculated from isothermal and non-isothermal experiments.

After this initial decrease, E_a values calculated from isothermal experiments in the α interval from 0.2 to 0.8 were almost constant. However, the E_a values obtained from non-isothermal experiment were constant only for a small α interval and after that started to decrease slowly by increasing α . This decrease became faster when the conversion degree approached 1.

Similar results were obtained also when other fractions were compared, although there typically was some divergence of the E_a values at the beginning of the dehydration reaction. Comparison of the obtained E_a values in isothermal and non-isothermal experiments for the fractions from $<40 \mu\text{m}$ up to $150\text{-}350 \mu\text{m}$ is given in Figure 3.10. In this diagram, the bottom and the top of the presented column corresponds to the lowest and highest dehydration E_a values in α interval from 0.2 to 0.7. The color change point corresponds to the average E_a value in this interval.

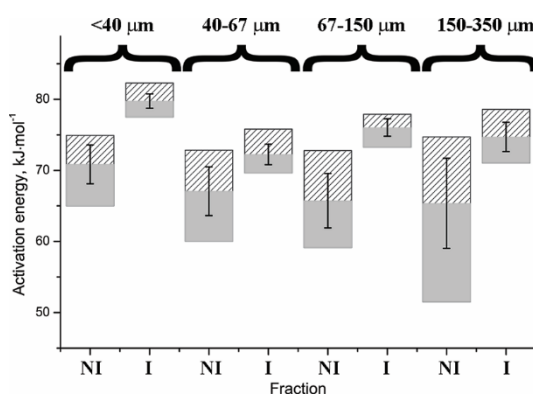


Figure 3.10. Minimum, maximum and the average value of the dehydration activation energy calculated from non-isothermal (NI) and isothermal (I) experiments for the $<40 \mu\text{m}$, $40\text{-}67 \mu\text{m}$, $67\text{-}150 \mu\text{m}$, and $150\text{-}350 \mu\text{m}$ fractions.

The Figure 3.10 clearly illustrates that in all cases the average, minimum and maximum values of dehydration E_a were higher for isothermal experiments. Also, for non-isothermal experiments the E_a value changed more within the conversion degree interval from 0.2 to 0.7, because E_a decreased at higher conversion degree, as presented in Figure 3.8(b) and Figure 3.9. Moreover, in non-isothermal experiments the range of E_a values in this α interval became wider by increasing the particle size. These results can easily be connected with Figure 3.8, where the E_a values are

constant for fractions up to 150-350 μm in isothermal experiments and decrease in non-isothermal experiments. Furthermore, this decrease was faster for larger particles.

The temperature range at which the dehydration reaction was examined in both experimental modes for each **DH** fraction is given in Table S1 in Appendix 7. It is evident that higher temperatures were used in non-isothermal experiments. Moreover, the E_a values for non-isothermal experiments at high conversion degrees were calculated from data measured at higher temperatures, explaining the differences in E_a values presented in Figure 3.9. Thus the decrease of E_a by increasing α suggested that at higher temperatures the energy of the rate limiting step was different, or contribution from a different rate limiting step became apparent. The more pronounced decrease of the E_a for larger particles in non-isothermal experiments could easily be associated with slower dehydration, which led to higher dehydration temperature. Moreover, in order to reach complete dehydration at every experimentally used heating rate for the fractions with 67-150 μm and 150-350 μm particle size, samples were heated above the melting/peritectic decomposition point at 88-92 $^{\circ}\text{C}$. The conversion degree at which this point was reached for the fastest heating rate is given in Table S1 in Appendix 7. It is clear that data obtained above melting point cannot be used for calculation of the dehydration E_a . Thus, E_a obtained above this conversion degree could not be considered purely as dehydration E_a , because some of the data used for its calculation was not actually from the dehydration process. For the 150-350 μm fraction this α value was as low as 0.55, thus explaining the significantly lower minimum E_a value in Figure 3.10.

Thus, also for non-isothermal experiments E_a was not dependent on the particle size for fractions with particle size up to 350 μm . Unfortunately, it was not possible to reliably calculate the E_a of the samples with particle size above 350 μm , because the evolution of water above the melting point caused problems in most of the experiments. Thus, E_a decrease for fractions with particle size above 350 μm was not demonstrated in non-isothermal experiments.

As can be seen from Figure 3.8(a), small decrease of the E_a by increasing the α was observed in isothermal experiments for the 350-700 μm and 700-1300 μm fractions. This cannot be explained by the higher temperature, because dehydration of the 350-700 μm fraction was examined at the same conditions as the fractions with smaller particle size. As already mentioned, decrease of the average E_a for these two fractions was associated with the increased diffusion of water out of the particles. Thus it was possible that the diffusion effect slightly increased during the dehydration, and in this way E_a decreased by increasing α , as shown in Figure 3.8(a). Therefore the decrease of the E_a resulting from increased contribution of water diffusion was due to the fact that water molecules had to travel a longer distance to leave the particle, or due to the possible phase boundary advance in directions perpendicular to the water channels (see Section 3.1), which was observed for larger particles, especially at the end of the reaction when all of the hydrate was surrounded by a thick **AP** layer.

The most appropriate kinetic models for the dehydration process were determined for all of the samples with various particle sizes under both isothermal and non-isothermal conditions, as well as for samples where the influence of other factors was examined. The obtained results are presented in Table 3.1. It is visible that the dehydration of fractions with particle size below 150 μm was best described by the one-dimensional phase boundary model R1, whereas that of fractions with particle size above 350 μm was best described by the two-dimensional phase boundary model R2. This is consistent with results presented in Section 3.1. The other examined experimental and sample factors did not change the dehydration kinetic model. However, for all of the analyzed samples there were deviations from the most appropriate kinetic model at the beginning and the end of the dehydration process. Deviations at the beginning can be associated with stabilization of the temperature or heating rate, while at the end there may have been actual deviations from the chosen model associated with either a) a certain degree of diffusion control or b) the fact that the escape of the last water molecules can occur in other directions rather than those associated with the main movement of the phase boundary¹⁸⁰. The reason for different kinetic models determined for different particle size fractions is associated with change of the dimensionality of the phase boundary movement, see Section 3.1. Although it can be seen that the same dehydration kinetic model for all of the analyzed samples was found both from isothermal and non-isothermal experiments, determination of the kinetic model from isothermal experiments was more straightforward and it was possible to make a selection more convincingly.

Table 3.1. The most appropriate dehydration kinetic model for different **DH** fractions, determined by studying the effect of various sample and experimental factors.

Study	<40 μm - 67-150 μm	150-350 μm	350-700 μm	700-1300 μm , >1300 μm
Isothermal mode ¹	R1	R1/R2	R2	R2
Non-isothermal mode ¹	R1	R2	R2	-
Sample weight	R1	R1	R2	-
Atmosphere	R1	-	-	-
Dehydration/rehydration	R1	-	-	-
Mechanical compression ²	R1	-	-	-

¹ – Study of the particle size effect,

² – Results from dehydration of the powdered sample under isothermal mode.

3.2.2 *Effect of the sample weight*

In Section 3.1 it was already stated that the dehydration rate of the **DH** decreased for larger samples, due to the slower vapor diffusion through the sample layer. By carrying out more detailed investigation it was observed that the reciprocal dehydration rate constant determined with model fitting methods was linearly dependent on the sample weight (see Figure 3.11). It can be seen that the slope was decreasing if the temperature was raised, showing that the sample weight had a more pronounced effect on the dehydration rate constant at lower temperatures. This probably was

because of slower water diffusion from the sample volume at lower temperatures. However, it was concluded that the particle size did not have an effect on the slope, although the slopes determined for 40-67 μm and 350-700 μm fractions were different than that for the rest of the fractions. For the 40-67 μm fraction this could be due to random errors, but for the 350-700 μm fraction this was due to the different kinetic model used, producing different rate constant values and thus changing the slope (see Table 3.1). Increase of the intercept (thus, decrease of the dehydration rate) by increasing the particle size was due to the slower dehydration rate of the larger particles, as discussed previously.

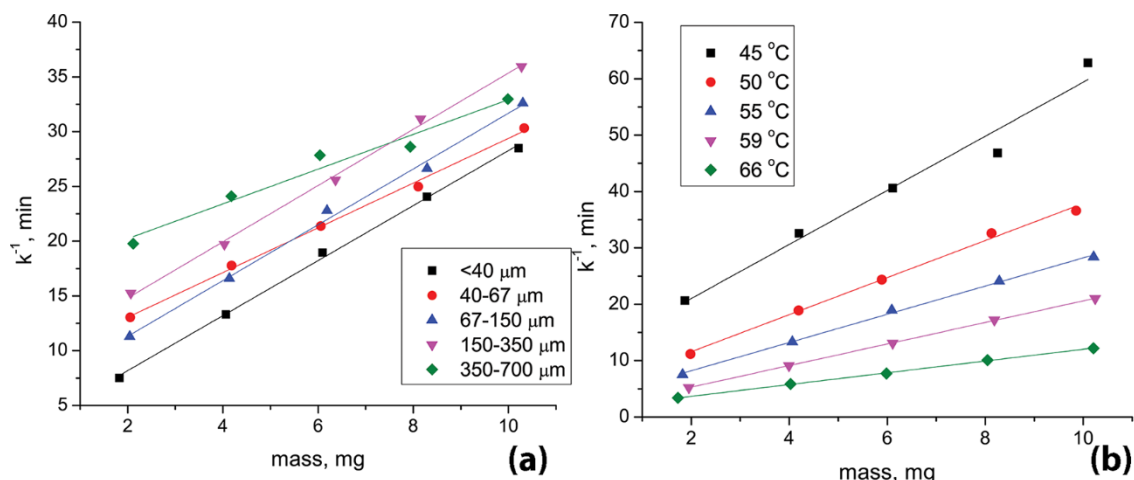


Figure 3.11. Sample weight effect on the reciprocal dehydration rate constant of mildronate DH: (a) different fractions at 55 °C temperature and (b) <40 μm fraction at different temperatures.

In Section 3.1 it was also stated that the dehydration E_a determined under isothermal conditions decreased by increasing the sample weight due to increasing contribution from the bulk diffusion effect. In this work the effect of the sample weight on the dehydration E_a was measured in both isothermal and non-isothermal conditions, and the obtained E_a dependence on α for samples of various weight is shown in Figure 3.12.

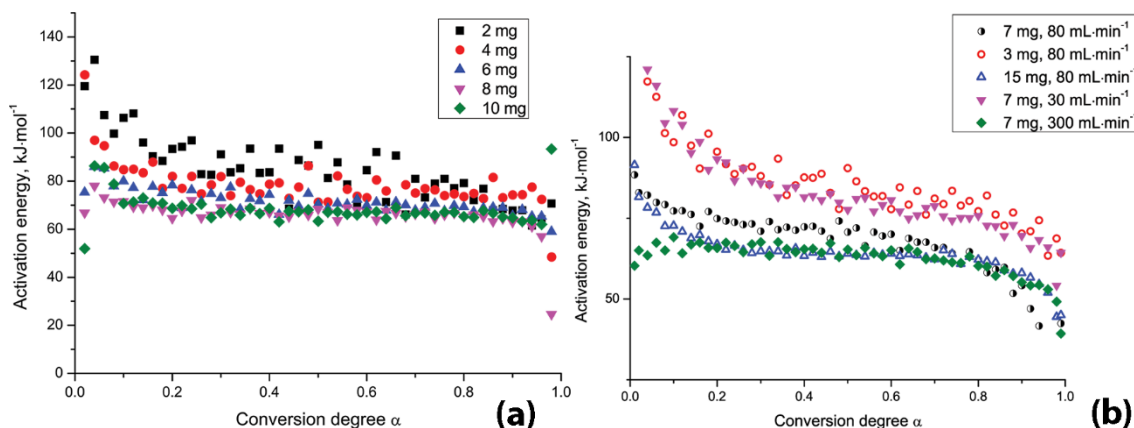


Figure 3.12. Dehydration activation energy dependence on (a) sample weight for the <40 μm fraction in isothermal experiments and (b) sample weight (empty markers) and nitrogen flow rate (filled markers) for the <40 μm fraction in non-isothermal experiments.

Decrease of the dehydration E_a by increasing the sample weight was observed in both experimental modes. By changing the sample weight from 2 mg to 15 mg, dehydration E_a changed from 84 to 64 $\text{kJ}\cdot\text{mol}^{-1}$. These E_a values were in accordance with the Figure 3.6 and showed that larger samples gave even smaller dehydration E_a . From the obtained results it was evaluated that sample weights of 2, 3, and 4 mg were not appropriate for accurate study of the dehydration kinetics because of the elevated random error in calculated E_a values. However, by using excessively large samples, unacceptable diffusion effects would appear, so samples of moderate weight are preferable. Thus both experimental modes could easily be used for the evaluation of the sample weight effect on the dehydration rate and E_a , although results obtained under non-isothermal mode were complicated by the sample weight unrelated E_a changes, the reason for which is already discussed.

3.2.3 Effect of the atmosphere

Experiments with dehydration of **DH** $<40\mu\text{m}$ fraction were carried out under nitrogen gas flow at various flow rates. It was determined that by increasing the N_2 flow rate increased the dehydration reaction rate. This is because the rate of reversible dehydration was enhanced noticeably when the evolved vapor was promptly removed from the sample. The same effect was found in non-isothermal mode as well. However, changes of the nitrogen flow had less effect on the dehydration rate, compared to changes in other factors (like particle size, sample weight and water vapor content in the atmosphere). From the results obtained under non-isothermal conditions, dehydration E_a was calculated and the obtained results are shown in Figure 3.12 (b). Although the increase of the nitrogen flow resulted in faster dehydration, it did not noticeably reduce the contribution from the step associated with the water diffusion out of the sample which would result in a lower E_a value. On the contrary, the dehydration E_a decreased when the N_2 flow rate was increased. The magnitude of the E_a changes was similar to that introduced by the sample weight variation. These results suggested that the increased N_2 flow provided for a more efficient removal of water from the bulk of **DH** particles, most probably resulting in an increase of the contribution from the water vapor diffusion from the **DH** particles. Thus, the observed total dehydration E_a decreased because the E_a of water vapor diffusion from the particles was lower than that of the phase boundary advance. The Figure 3.12 (b) indicates that with $300\text{ mL}\cdot\text{min}^{-1}$ N_2 flow the calculated dehydration E_a values did not show initial decrease at low α values as observed in all the other cases. This initial decrease was therefore most probably associated with the reversibility of the dehydration reaction, and faster nitrogen flow precluded this effect.

The effect of variable water vapor pressure on the dehydration of **DH** was evaluated as well. It was observed that the dehydration rate decreased with increasing water vapor pressure at a given temperature, and the rate constant dependence on water vapor pressure could be approximated with straight line. This observation can be associated with the reversibility of the dehydration

reaction. The observation of a linear dehydration rate decrease suggested that the presence of water in the vapor phase did not change the dehydration mechanism. By using dehydration curves recorded at different temperatures for a particular relative humidity, the dehydration E_a dependence on the relative humidity was calculated, and the results are shown in Figure 3.13. It is visible that the dehydration E_a did not depend on the relative humidity. This confirms that the presence of water did not change the dehydration mechanism and did not introduce any changes in the dehydration rate limiting step energy at the reaction interface. However, the three highest relative humidity levels used had a high uncertainty, which could be related to slow dehydration where other factors could play a major role in the determination of the dehydration rate and the fact that the **AP** and **DH** phase boundary has a slight temperature dependence²⁵⁸.

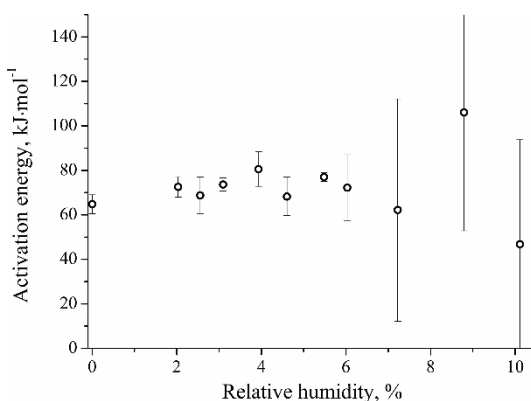


Figure 3.13. The dependence of the dehydration activation energy on the relative humidity for the <40 μm fraction.

3.2.4 Effect of the sample history

The considered aspects of sample history were a) previous dehydration/rehydration of the sample and b) mechanical compression. It was observed that repeated dehydration of previously dehydrated/rehydrated samples occurred faster and the dehydration E_a was lower. This effect could result from the cracking of the crystals and formation of channels through which water escape was facilitated during the repeated dehydration as well as due to the formation of internal defects allowing for an easier phase boundary advance. Also it was possible that previous dehydration/rehydration reduced the particle size, allowing faster dehydration in the second dehydration cycle³⁰⁴. However, reduction of the particle size alone would not explain the decrease of the dehydration E_a .

It was observed that the mechanical compression (in terms of enhanced crystal defects and stress) had no effect on the dehydration E_a and the kinetic model. However, these defects promoted the initiation of the dehydration process, which was clearly observed as lower dehydration starting temperatures in non-isothermal experiments. When dehydration of compressed tablets was performed, water evolution from samples was more difficult compared to powdered samples, thus the dehydration rate was reduced, as observed both in isothermal and non-

isothermal experiments. Extended discussion about the obtained results for mechanically compressed samples can be found in the Appendix 7.

3.2.5 Conclusions

It was possible to obtain comparable E_a values and the same kinetic model for the dehydration of mildronate **DH** in both isothermal and non-isothermal mode. However, both the obtained results and experimental procedures were more complicated when experiments were performed in non-isothermal mode. Firstly, there was a decrease of dehydration E_a at high conversion degree values, either due to different contributions from various rate limiting steps at different temperatures, or due to altered E_a of rate limiting step at high temperatures. Secondly, dehydration process should be complete before reaching the melting/peritectic decomposition point for every employed heating rate. Thus in non-isothermal mode it was possible to analyse only sufficiently small particles, therefore the possibility to study the particle size effect was limited. Moreover, obtained results were complicated by the E_a changes not directly caused by the change of the particle size. For fast identification of the possible complications and for setting up the dehydration kinetic study, results obtained from thermal analysis should be used to get insight about the appropriate temperature interval for the study.

Particle size influenced both the dehydration rate and E_a . This factor should therefore be controlled and sample with narrow particle size distribution would be preferred for the dehydration kinetic study. Although in isothermal mode it was possible to study the dehydration of all prepared fractions, small variation in dehydration E_a was observed for particles with size above 350 μm , because of the changing diffusion contribution, and <40 μm fraction showed deviation from typical dehydration behaviour.

Study of the experimental factor effects revealed that very low sample weight resulted in elevated random error for dehydration E_a , whereas very high sample weight increased the diffusion contribution. Increase in the nitrogen flow decreased the dehydration E_a suggesting that the contribution from water diffusion out of the particles was possibly increased by this change. Relative humidity did not affect the dehydration E_a , thus the presence of water at the reaction interface did not change the energy of the dehydration rate limiting step.

Although sample preparation and storage did not show an effect on the examined dehydration parameters, sample history did. Thus, in order to perform a kinetic study, the sample should be handled carefully prior to dehydration experiments, in order not to induce any physical changes.

As the dehydration E_a is affected by the diffusion of the water out of the particle and the kinetic model is affected by the phase boundary advance in other directions than those along the water channels, the particle morphology can be an important factor affecting these kinetic parameters. In this study we used samples with particles lacking a characteristic morphology, which

had crystallized as a particle aggregate. However, it is possible that other crystallization procedures can produce particles with different characteristic morphologies showing different dehydration kinetics.

For the determination of diffusion-independent kinetic parameters characterizing the main **DH** dehydration mechanism, an isothermal experimental mode should be selected, with moderate particle size (narrow range within 40-150 μm) and sample weight (6-8 mg), and nitrogen flow providing effective removal of the evolved water ($\sim 100 \text{ mL}\cdot\text{min}^{-1}$) should be used. Sample preparation and handling should be done carefully. Such conditions would preclude the detection of the sample property and experimental factor effects, thus limiting the study of the dehydration mechanism. However, parameters obtained through such approach would be characteristic of the **DH** dehydration. Nevertheless, if one wants to study the dehydration mechanism, effects of various sample and experimental factors should be investigated.

Of course, the study of dehydration mechanisms through the influence of various sample and experimental factors on the kinetic parameters is not limited to mildronate **DH**. Thus, a similar study could easily reveal essential information about the dehydration mechanism of other organic and inorganic hydrates, as well as provide conditions for determining the main dehydration mechanism characterizing dehydration kinetic parameters.

3.3 Analysis of droperidol solvent formation and their characterization

In this section we tried to understand and rationalize the solvate formation of droperidol. Therefore we crystallized droperidol from solvents belonging to different solvent classes to investigate the possibility of forming new solvates, and we also characterized the structure and physiochemical properties of all droperidol solvates. We tried to rationalize solvate formation based on the solvate structure and solvent and droperidol properties. Besides, we characterized the solvent role and interactions in solvate structures and the water molecule arrangement in a partially filled **NSH** structure.

3.3.1 Solvate screening

A crystal form screening of droperidol was performed by selecting the most commonly used solvents covering different solvent classes based on classification according to statistical analysis of four molecular descriptors¹³⁹ and hydrogen bond acceptor and donor propensity, polarity/dipolarity, dipole moment, and dielectric constant¹⁴⁰. Solvents used for the screening and the crystal forms obtained after the crystallization are given in Table S1 in Appendix 8. It can be seen that besides the already known polymorphic forms **I** and **II**, hydrates **NSH** and **DH**, and the ethanol solvate **S_{Et}**, eight new crystalline forms were obtained from methanol, acetonitrile, nitromethane, chloroform, dichloromethane, carbon tetrachloride, 1,4-dioxane, and toluene. All of the obtained crystal forms were characterized by PXRD and thermal methods and were found to be droperidol solvates and were labelled as **S_{Me}**, **S_{ACN}**, **S_{NM}**, **S_{CLEF}**, **S_{DCM}**, **S_{CTC}**, **S_{DIOX}** and **S_{TOL}** respectively. Crystals suitable for SCXRD analyses were obtained only from methanol, acetonitrile, and nitromethane. Besides, all of the analyses were performed also with the poorly characterized solvated forms **NSH**, **S_{Et}** and **DH**.

3.3.2 X-ray diffraction

PXRD patterns of all the obtained solvated forms are given in the Figure 3.14. It can be seen that the diffraction peak positions of the new solvates **S_{Me}**, **S_{ACN}**, **S_{NM}**, **S_{DCM}** and **S_{CLEF}** were very similar and almost matched those of **NSH** and **S_{Et}**, suggesting the isostructurality of all these solvated forms. However, PXRD patterns of **S_{TCC}**, **S_{DIOX}**, and **S_{TOL}** exhibited different characteristic features and differed also from the PXRD patterns of all other known droperidol forms.

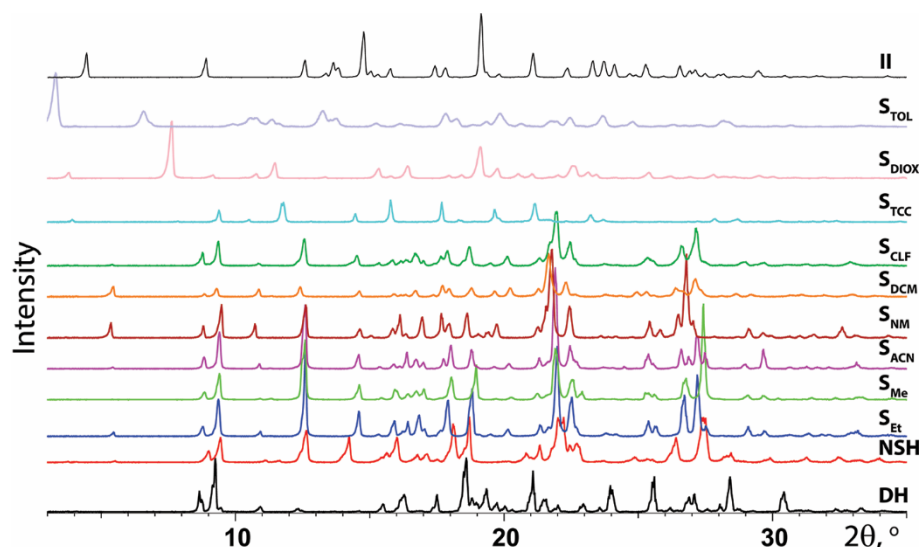


Figure 3.14. PXRD patterns of the droperidol solvates and polymorph II.

A crystal structure determination for the newly prepared S_{Me} , S_{ACN} , S_{NM} , and also S_{Et} and NSH was performed and the obtained crystallographic data are given in Table 3.2. The crystal structures of NSH and S_{Et} were consistent with those already reported^{261, 265}, and the newly prepared solvates S_{Me} , S_{ACN} , and S_{NM} were isostructural to NSH and S_{Et} as already suggested by the PXRD patterns (a more detailed discussion is given further). In this study the NSH was determined to be of monohydrate stoichiometry (the previously published hemihydrate stoichiometry²⁶¹ is explained by its nonstoichiometric behaviour²⁶⁴), whereas S_{Et} , S_{Me} , S_{ACN} , and S_{NM} crystallized as hemisolvates (although monoethanol solvate was reported²⁶⁵, both the published²⁶⁵ and our determined crystal structures corresponded to a hemimethanol solvate).

Table 3.2. Crystallographic data for the droperidol solvates (S_{ACN} , S_{NM} , S_{Me} , NSH , and ISD).

Solvate	S_{ACN}	S_{NM}	S_{Me}	NSH -mono	NSH -hemi	ISD
Empirical formula	$(C_{22}H_{22}FN_3O_2)_2 \cdot C_2H_3N$	$(C_{22}H_{22}FN_3O_2)_2 \cdot CH_3NO_2$	$C_{22}H_{22}FN_3O_{22} \cdot 0.5CH_4O$	$C_{22}H_{22}FN_3O_2 \cdot H_2O$	$C_{22}H_{22}FN_3O_2 \cdot 0.5H_2O$	$C_{22}H_{22}FN_3O_2$
M_r	399.96	409.95	395.45	397.44	388.43	379.43
Crystal system	triclinic	triclinic	triclinic	triclinic	triclinic	triclinic
Space group	P1	P1	$P\bar{1}$	$P\bar{1}$	$P\bar{1}$	$P\bar{1}$
Temperature	173	173	120	120	120	333
a (Å)	6.0870(2)	6.06730(10)	6.0504(5)	6.3199(4)	6.2743(3)	6.2780(3)
b (Å)	10.2177(3)	10.1884(3)	10.2207(8)	10.1525(7)	10.1560(6)	10.0865(4)
c (Å)	16.2642(6)	16.4237(5)	16.1100(14)	15.7463(11)	15.7786(9)	16.3969(7)
α (°)	101.2051(11)	99.8303(13)	101.397(2)	102.691(2)	102.253(2)	103.0980(10)
β (°)	92.7447(10)	92.2880(12)	93.445(3)	91.775(2)	92.501(2)	92.8550(10)
γ (°)	96.7569(19)	95.6243(18)	97.022(2)	100.403(2)	99.460(2)	99.4190(10)
V (Å ³)	982.78(6)	993.86(4)	965.62(14)	966.81(11)	965.95(9)	993.57(7)
Z^a	2	2	2	2	2	2
μ (mm ⁻¹)	0.094	0.099	0.096	0.098	0.095	0.089
D_{calc} (g cm ⁻³)	1.352	1.370	1.360	1.365	1.335	1.268
no. of parameters	533	542	350	353	353	342
reflns collected	5243	5245	16568	12518	12520	11524
reflns ($I > 2\sigma$)	3644	3649	5392	5357	5375	4788
wR (all data)	0.1285	0.1346	0.1512	0.1721	0.1635	0.1558
final R ($I > 2\sigma$)	0.0526	0.0546	0.0534	0.0600	0.0556	0.0486
GOF	1.012	1.023	1.011	1.073	1.030	1.020
Packing coef.	0.705	0.704	0.717b	0.714		0.659

^a – Based on droperidol as the molecular entity.

^b – Calculated for structure where solvent molecules were ordered.

An overlay of the PXRD patterns obtained experimentally and simulated from crystal structure data confirmed the identity of the polycrystalline phases.

3.3.3 Thermal characterization

The DTA/TG curves of all isostructural solvates were almost the same (see Figure 3.15): desolvation of these solvates occurred over a wide temperature range, which started at ambient temperature without a characteristic sharp endothermic effect associated with the desolvation process, thus suggesting that all of these solvates are non-stoichiometric. When the temperature was increased to 115 – 130°C, melting occurred as confirmed by hot stage microscopy (HSM). Desolvation of these solvates occurred at different rates and at the heating rate 5°·min⁻¹ the forms **S_{Et}**, **S_{ACN}**, **S_{NM}** and **S_{CLF}** were not completely desolvated before melting, and thus the melting endotherm appeared together with a rapid loss of the rest of solvent. After the melting, recrystallization occurred by forming polymorph **I** as identified by the melting point in the DTA curves. The recrystallization was also observed in the HSM study.

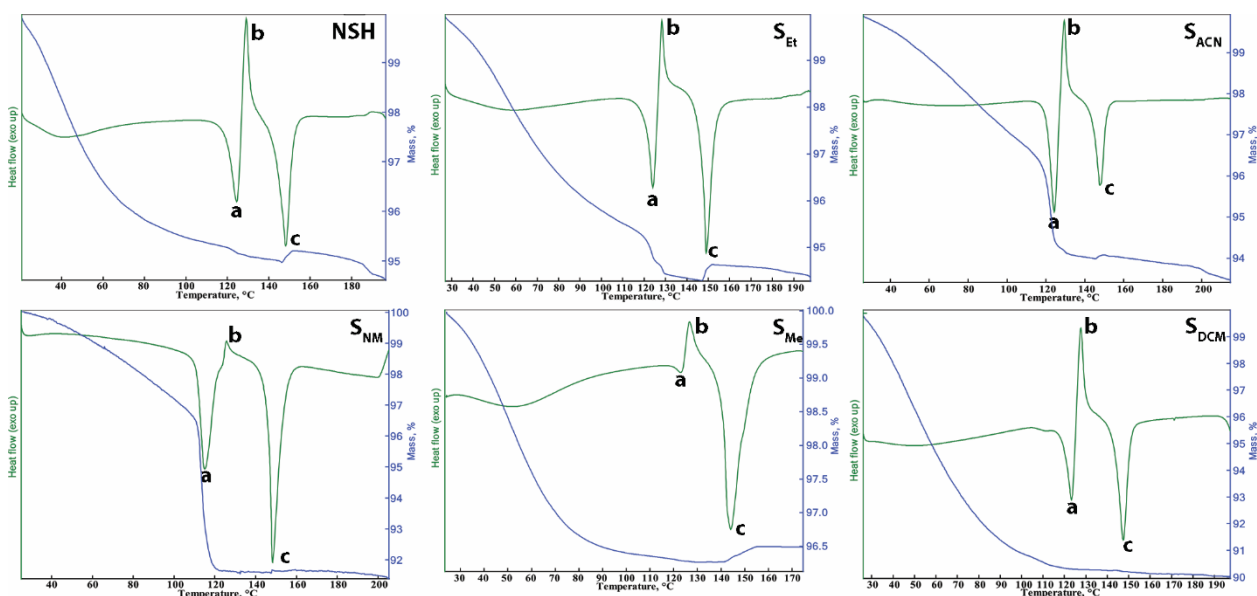


Figure 3.15. The DTA and TG curves of the droperidol isostructural solvates showing (a) the melting of solvate and/or **ISD**, (b) recrystallization, and (c) melting of the resulting polymorph **I**.

Desolvation products of all the solvates were analysed with PXRD, the obtained diffraction patterns are given in Figure 3.16. By combining the PXRD and DTA/TG data it was determined that all of the isostructural solvates can be desolvated before melting (by heating at 100°C for a maximum of 2 days).

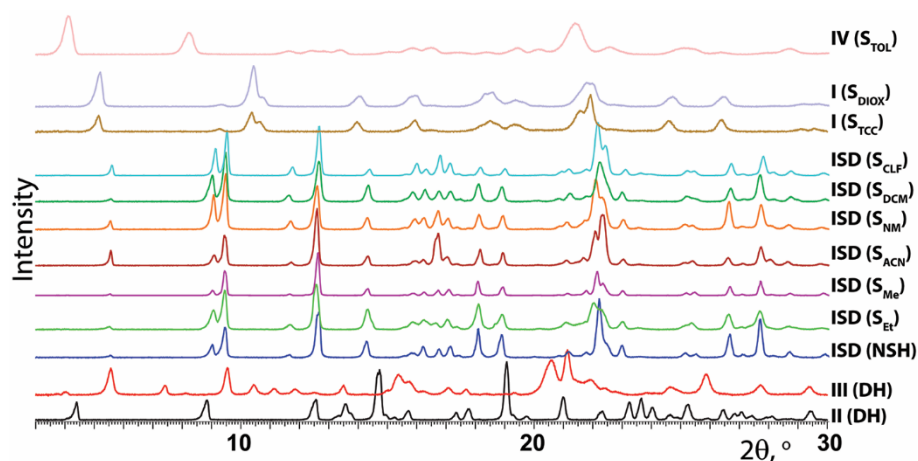


Figure 3.16. PXRD patterns of the desolvation products of the droperidol solvates.

From Figure 3.16 it can be identified that desolvation of isostructural solvates produced a phase with only slightly different PXRD pattern: the isostructural desolvate (**ISD**). This was confirmed also by the structure determination of completely dehydrated **NSH** crystals (see Table 3.2). The formation of isostructural desolvate supports the fact that isostructural solvates are non-stoichiometric.

Solvent stoichiometry was determined from TG curves, and the obtained results are given in Table 3.3. The obtained results were consistent with the solvent stoichiometry determined by SCXRD. The differences between the observed and calculated solvent content in isostructural solvates are associated with their non-stoichiometric behaviour. The stoichiometry of **S_{DCM}** and **S_{CLEF}** was determined only from TG data. Based on measurements from at least three different samples, **S_{DCM}** was found to be a hemisolvate, whereas the stoichiometry of **S_{CLEF}** was unclear because the highest obtained solvent : droperidol ratio was only 1:3.

Table 3.3. Physicochemical data for the droperidol isostructural solvates.

Solvate	Calculated weight loss, %	Observed weight loss, %	$T_{\text{desolvation}}^{\text{a}}$, °C (peak)	Resulting phase
NSH	4.5 ^b	2.5-4.8 ^c	124	ISD
S_{Me}	4.2 ^d	3.5-4.5	124	ISD
S_{Et}	6.1 ^d	5.1-6.6	125-127	ISD
S_{ACN}	5.4 ^d	4.9-6.0	124-129	ISD
S_{NM}	8.0 ^d	8.2-8.9	113-115	ISD
S_{DCM}	11.2 ^d	5.5-11.0	123-124	ISD
S_{CLEF}	15.7 ^d	5.5-9.5	123-126	ISD

^a – melting peak of the solvate or resulting **ISD**

^b - for monosolvate stoichiometry

^c – depended on the storage conditions

^d – for hemisolvate stoichiometry

Desolvation of **S_{TCC}** and **S_{DIOX}** produced the polymorph **I**, **S_{TOL}** produced a new polymorph **IV** and that of **DH** depended on the sample and produced either the polymorph **II** or a new polymorph **III**.

Schematic representation of solvate preparation and phase transformations upon heating are given in Figure 3.17.

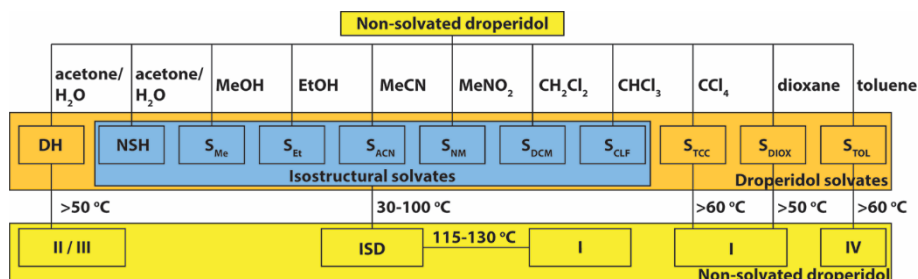


Figure 3.17. Schematic representation of the droperidol solvate preparation and phase transformations upon their heating.

3.3.4 Crystal structures of isostructural solvates

NSH, **S_{Et}**, and **S_{Me}** crystallize in $P\bar{1}$ space group (see Table 3.2) with one droperidol molecule and a water molecule or half of a disordered alcohol molecule respectively, in agreement with the already reported structures^{261,265}. However, **S_{ACN}** and **S_{NM}** crystallize in the $P1$ space group with two droperidol molecules and a solvent molecule in the unit cell. Both droperidol molecules in these two solvates are inversion related, thus only the asymmetric solvent molecule breaks centrosymmetry of the whole crystal structure. Therefore the conformation of both droperidol molecules in the unit cell is the same (by taking into account the inversion symmetry). As already mentioned, despite the different space groups, all these droperidol solvates are isostructural and the solvent molecules are situated in the channels positioned along the a -axis (see Figure 3.18 and Appendix 8).

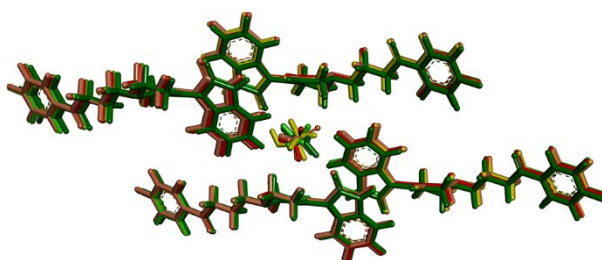


Figure 3.18. Overlay of the crystal structures of isostructural droperidol solvates.

In these solvates all of the acetonitrile and nitromethane molecules pointed in only one direction. Although the methanol and ethanol molecules are asymmetric, the disorder of these solvent molecules allowed description of **S_{Et}** and **S_{Me}** in $P\bar{1}$ space group. The type of structural disorder with regard to the solvent molecules and its causes were further investigated using solid-state NMR and theoretical calculations, and is given in Section 3.5.

The 2D fingerprint plots (calculated from the Hirshfeld surfaces^{96,104} in *CrystalExplorer 3.1*¹⁰⁵) of droperidol molecules from all of the solvates were almost the same, and were dominated by the interactions between the droperidol molecules themselves. Thus the solvent had only a minor role in the crystal structure, and therefore it was reasonable that isostructural solvates with quite different solvent molecules could form.

3.3.5 The interactions of solvent molecules in isostructural solvates

In order to understand the differences between the isostructural solvates, as well as the reasons for their stability, intermolecular interactions of solvent molecules were analysed. Solvates can be divided based on the presence (in **NSH**, **S_{Me}**, and **S_{Et}**) or absence (in **S_{ACN}** and **S_{NM}**) of strong hydrogen bonds between the solvent and the droperidol molecule oxygen atom O1 in the benzimidazolone moiety. Although the disorder of solvent molecules complicated the characterization of this interaction in **S_{Me}** and **S_{Et}**, hydrogen bond parameters were characteristic to a strong hydrogen bond with the O1···O3 distance 2.81-2.91 Å, where the longest distance was in **S_{Me}** (see Table 3.4).

Table 3.4. Geometrical parameters for the intermolecular interactions of solvent molecules in droperidol solvates **S_{Me}**, **S_{Et}**, **S_{ACN}**, **S_{NM}**, and **NSH**

	Interaction ^a	X-H (Å)	H···A (Å)	D···A (Å)	D-H···A (°)
S_{Me}	O3-H···O1 ^b	1.13	1.87	2.91	150
	O3···H-C9 ^c	0.97	2.80	3.51	130
	C23-H···O1 ^d	0.96	2.46	3.36	156
S_{Et}	O3-H···O1 ^d	0.82	2.53	2.81	102
	O3···H-C5 ^e	0.93	2.64	3.41	140
	C24-H···C9 ^f	0.95	2.99	3.85	151
	C24-H···O1 ^f	0.97	2.92	3.51	120
S_{ACN}	C23-H···O1 _A ^g	0.96	2.68	3.41	133
	C23-H···C9 _B ^b	0.96	2.97	3.92	169
	N4···H-C5 _A ^c	0.93	2.80	3.70	162
	N4···H-C5 _B ^g	0.93	2.83	3.60	140
S_{NM}	C23-H···O1 _A ^h	0.96	2.44	3.31	150
	C23-H···C9 _B ^b	0.96	2.90	3.86	178
	O3···H-C5 _A ^b	0.93	2.70	3.42	135
	O3···H-C10 _A ^h	0.97	2.52	3.29	135
	O3···H-C11 _A ^h	0.97	2.66	3.51	147
	O3···H-C4 _A ^e	0.93	2.64	3.42	143
	O4···H-C9 _B ^c	0.93	2.66	3.16	115
	O4···H-C10 _B ^c	0.97	2.72	3.13	106
	O4···H-C4 _B ^g	0.93	2.67	3.28	124
	O4···H-C5 _B ^g	0.93	2.66	3.26	123
NSH	O3-H···O1 ^b	0.85	1.99	2.83	171
	O3-H···O3 ⁱ	0.85	2.22	2.86	131
	O3···H-C9 ^c	0.95	2.73	3.38	127

^a - cutoff parameter: van der Waals radii + 0.1 Å. Symmetry codes: ^b x, y, z; ^c 1+x, y, z;

^d 1-x, 1-y, -z; ^e -1+x, y, z; ^f -1+x, -1+y, z; ^g 1+x, 1+y, z; ^h x, 1+y, z; ⁱ 2-x, -y, -z.

There were slightly different interactions between alkyl residues of alcohol molecules and droperidol molecules: in both solvates the O3 atom was an acceptor of hydrogen bond from different droperidol hydrogen atoms, and the methyl group of the methanol was a hydrogen bond donor for a much shorter interaction than in ethanol (see Table 3.4).

There was no strong hydrogen bond between droperidol and acetonitrile or nitromethane. Nevertheless, these molecules formed numerous weak hydrogen bonds and dispersion interaction with droperidol molecules (see Table 3.4), therefore providing sufficient interactions to allow the formation of a stable solvate.

The only strong intermolecular interaction between solvent molecules was observed in **NSH** where two water molecules formed hydrogen bond by connecting two droperidol molecules via an O1...O3...O3...O1 linkage²⁶¹ across the channel.

Hirshfeld surface 2D fingerprint plots of the solvent molecules representing the intermolecular interactions are given in Figure 3.19. For this analysis crystal structures of **S_{Me}** and **S_{Et}** with ordered solvent molecules after optimization of hydrogen atom positions were used.

From the solvent molecule 2D fingerprint plots it was possible to determined that interactions of both alcohol molecules were different, although both were dominated by the strong hydrogen bond O3-H...O1. Despite the different functional groups in acetonitrile and nitromethane, and the seemingly different interactions of nitrile and nitro groups (see Table 3.4), the interactions represented in 2D fingerprint plots, although differently shaped, were very similar. This suggests that the properties of **S_{ACN}** and **S_{NM}** could be similar. Therefore, besides a strong hydrogen bond connecting alcohols in **S_{Me}** and **S_{Et}**, the stability of these solvates and that of **S_{ACN}** and **S_{NM}** was provided by weak hydrogen bonds and dispersion interactions. As could be expected, interactions of water molecules in **NSH** were dominated only by strong hydrogen bonds. However, unusual relative arrangement of water molecules (see Figure S14 in Appendix 8) introduced unusually shaped broad representation of hydrogen-hydrogen interactions between both water molecules.

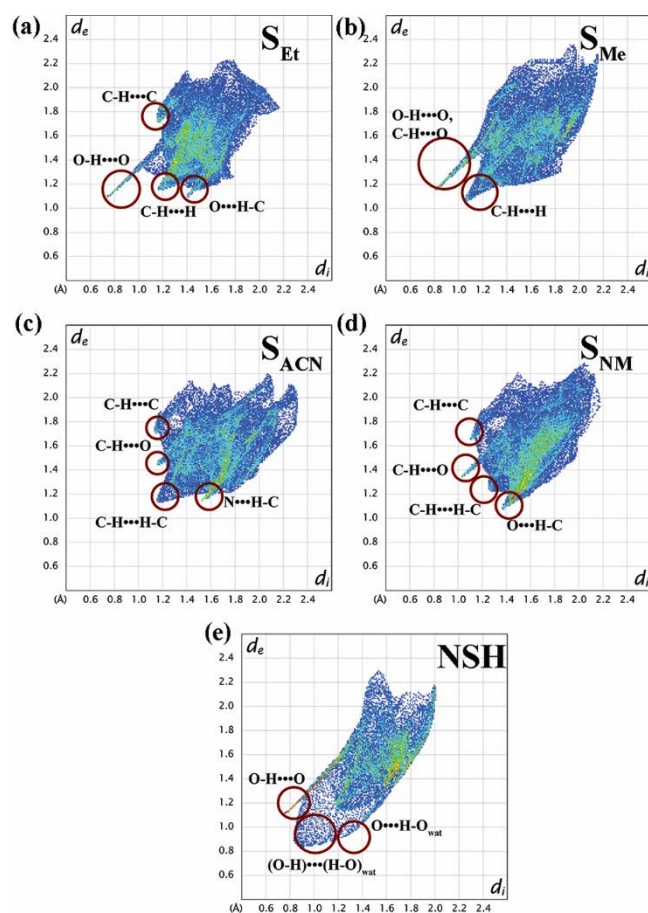


Figure 3.19. Hirshfeld surface 2D fingerprint plots of solvent molecules in droperidol isostructural solvates, where d_e is the distance from a point on the surface to the nearest nucleus outside the surface and d_i represents the distance from a point on the surface to the nearest nucleus inside the surface^{96, 104}.

3.3.6 Fourier-Transform Infrared spectroscopy

ATR-FTIR spectra of the solvates are presented in Figure 3.20. Besides the few peaks appearing due to the presence of different solvent molecules, the spectra of these solvates were almost identical, confirming their isostructurality. However, noticeable differences characterizing the structure of solvates appeared in the carboxyl group stretching and O-H stretching regions. There were two distinct peaks with almost the same intensity in the carboxyl group stretching region for **S_{NM}**, **S_{ACN}**, and **S_{DCM}**. However, the higher frequency peak ($\sim 1692\text{ cm}^{-1}$) was observed as a shoulder on the lower frequency peak ($\sim 1682\text{ cm}^{-1}$) for **S_{Me}**, **S_{CLF}**, **S_{Et}**, and **NSH**. At the same time there was sharp peak at $3468\text{--}3475\text{ cm}^{-1}$ for **S_{Et}**, **S_{Me}**, and **S_{CLF}**, and at 3499 cm^{-1} for **NSH** corresponding to the O-H (in alcohols and water) and C-H (in chloroform) stretching bands, respectively.

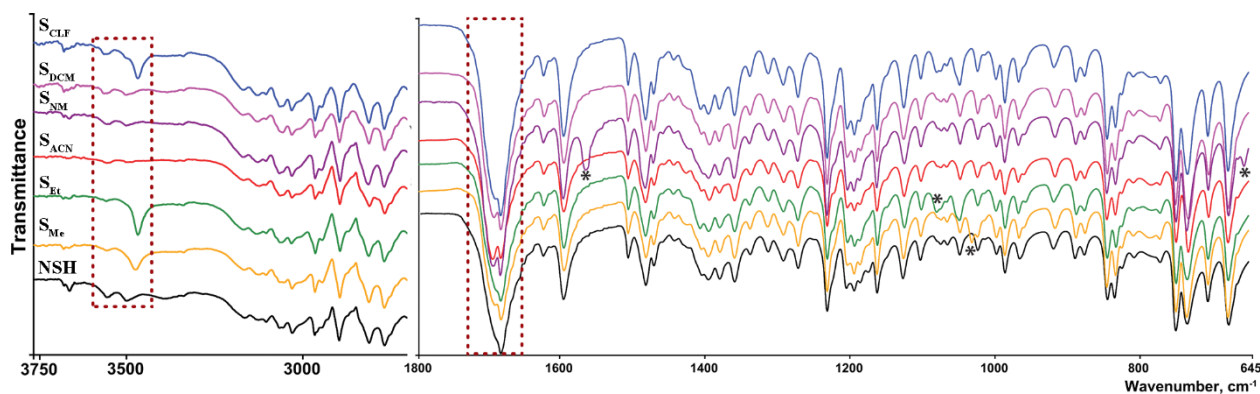


Figure 3.20. FTIR spectra of the droperidol isostructural solvates with dashed rectangle highlighting the most differing spectral regions and asterisks marking the bands due to the solvent molecules.

Thus, based on the similarities in IR spectra in the O-H and C-H stretching regions and in the C=O stretching region, it can be concluded that chloroform molecule also forms hydrogen bond with droperidol molecules similarly to water and alcohol molecules, whereas the solvent interactions in S_{DCM} are more similar to those in S_{NM} and S_{ACN} .

3.3.7 Characterization of solvent content in isostructural solvates at different solvent activity

The non-stoichiometric behaviour of the solvates and the presence of solvent channels suggested that solvent content in the structure (ϵ) should be dependent on the solvent activity¹⁰. To investigate this, **NSH**, S_{Et} , S_{Me} , S_{ACN} , and S_{NM} were stored under atmosphere with different solvent activity, obtaining the sorption-desorption isotherms of the corresponding solvents. Water sorption-desorption isotherm of **NSH** is shown in Figure 3.21. The highest water content corresponds to monohydrate stoichiometry and lowering of the RH gradually decreased the water content ϵ by completely dehydrating the **NSH** and obtaining **ISD** at $\approx 0\%$ RH.

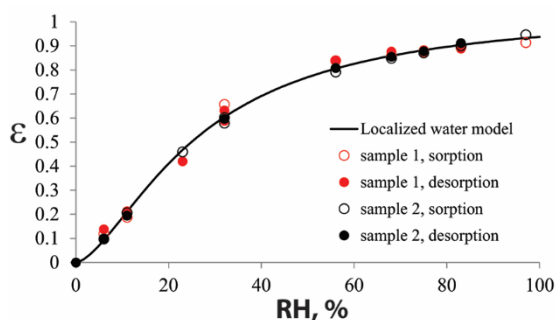


Figure 3.21. Water sorption-desorption isotherm of NSH from two sample sorption and desorption cycles, and localized water model describing the experimental points.

A study of the other four solvate sorption-desorption isotherms revealed that uptake of the solvent also was gradual but occurred at much lower solvent activity: most of the solvent uptake had already had taken place when solvent activity reached 0.02 and maximum solvate stoichiometry ($\epsilon \approx 0.5$) was reached at solvent activity 0.1. The resulting sorption-desorption isotherm of S_{Me} is

given in Figure 3.22, but those of S_{Et} , S_{ACN} , and S_{NM} are in Appendix 8. The initial parts of the isotherms for all solvates are given in Figure 3.23.

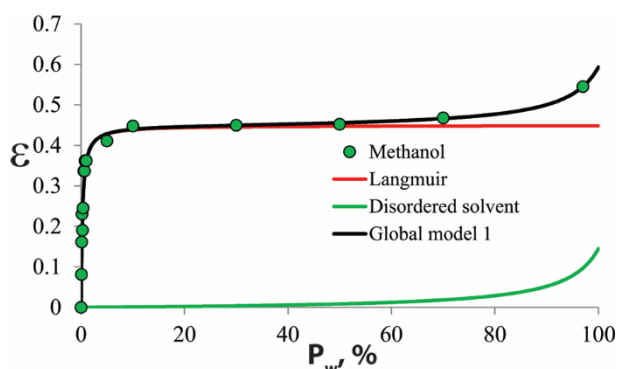


Figure 3.22. Methanol sorption-desorption isotherm of S_{Me} . The black line corresponds to global isotherm model formed by combination of Langmuir isotherm (red line) and disordered solvent model⁵¹ (green line).

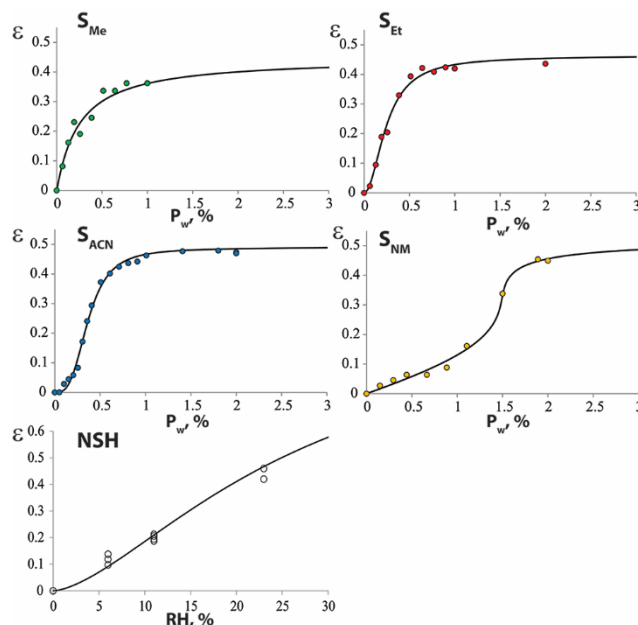


Figure 3.23. Initial part of the droperidol isostructural solvate sorption-desorption isotherms where circles indicate experimental solvent content ϵ and lines represent the best theoretical model (Langmuir isotherm (S_{Me}) and general localized solvent model⁵¹ with constant activity coefficients (NSH , S_{Et} and S_{ACN}) or activity coefficients described by 3rd order Margules equation (S_{NM}). For NSH a 10 times larger solvent activity region is shown.

In order to compare the obtained isotherms, thermodynamic models were used to describe the obtained data points, thus characterizing the thermodynamics of the solvates themselves⁵¹. The sorption-desorption isotherm of NSH was fitted with general localized water model with constant activity coefficients (see Figure 3.21, parameters used for all the fittings are given in Appendix 8), whereas those of all organic solvates were described as a combination of a) localized solvent model describing solvent in the structural channels and b) disordered solvent model describing the adsorbed solvent⁵¹ (see Appendix 8). Localized solvent in the sorption-desorption isotherm of S_{Me}

was fitted with Langmuir isotherm and that in **S_{Et}** with general localized solvent model with constant activity coefficients. The sorption-desorption isotherms of **S_{ACN}** and **S_{NM}** clearly did not correspond to Langmuir isotherm because of the hindered solvent absorption at very low solvent activity and thus sigmoidal shape (see Figure 3.23). The **S_{ACN}** isotherm was fitted with a general localized solvent model (usage of variable activity coefficients only slightly improved the fit), whereas that of **S_{NM}** could be fitted only using localized solvent model with variable activity coefficients described by Margules equations. The differences between the isotherms are associated with the presence or absence of interactions between solvent molecules in two adjacent solvent sites positioned along the *a*-axis as well as the solvent molecule size differences (see Appendix 8). As the solvent molecules have well located crystallographic sites, the use of the Langmuir model or localized solvent model for describing the change of these molecules in the channels is in accordance with the assumptions for these models.

3.3.8 Characterization of changes in isostructural solvate structure at various solvent content

The PXRD patterns of solvates with various solvent content were recorded. By increasing the solvent content, continuous displacement of diffraction peaks to mostly lower 2θ values occurred (insertion of the solvent molecules increased the cell volume and thus the interplanar spacing), and continuous intensity changes of some peaks were observed. The peak positions changed gradually, thus confirming the continuity of structural changes, and it was possible to calculate the dependence of lattice parameters on the solvent content (ϵ) for these solvates. The obtained results confirmed gradual changes of the crystal structure (see Figure 3.24). The differences between **NSH** and other solvates observed from changes of the diffraction peak positions were reflected in the calculated lattice parameters: the direction and amplitude of the lattice parameter changes was almost identical for all solvates except for the **NSH** (see Figure 3.24).

These differences of the lattice parameter change clearly could be associated with the formation of hydrogen bonds mediated by water molecules, with these bonds providing links between droperidol molecules situated across structural channels. Therefore the decrease of the cell length *c* and the angle α , with concurrent increase of the angle γ in **NSH** was due to the geometric effects driven by the formation of this linkage. The decrease of the cell length *a* for other solvates most probably can be associated with the presence of solvent - solvent interactions in the channels, but the size of the solvent molecules caused the increase of the cell lengths *b* and *c*.

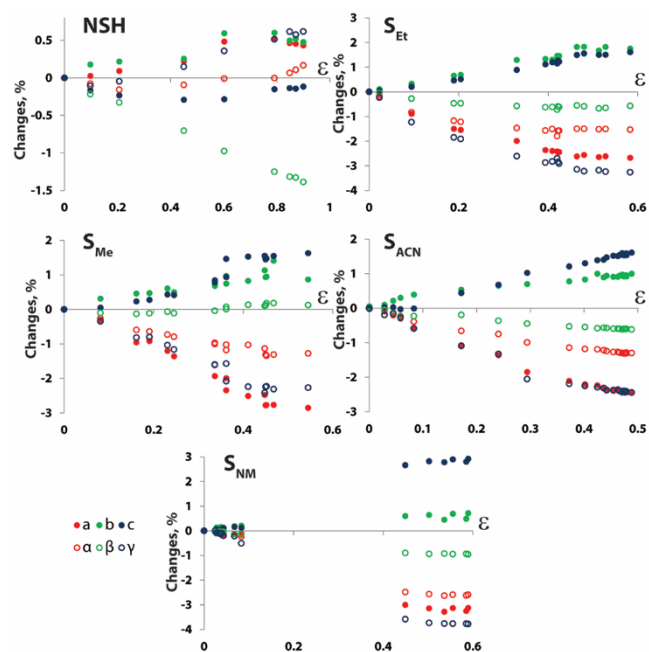


Figure 3.24. Lattice parameter dependence on the solvent content (ϵ) in the isostructural solvates of droperidol.

3.3.9 Water arrangement in a partially filled NSH structure

In this study the crystal structures of **NSH** with three different levels of water content were determined: the monohydrate (120 K, obtained from synthesis), the hemihydrate (120 K, obtained by storing a sample at 30-40% RH), and the anhydrous form or **ISD** (333 K, obtained by storing a sample at 0% RH, or heating the sample). The intermolecular interaction geometry of droperidol molecules was only slightly affected by the water content.

The hydrogen bonding parameters determined for water mediated hydrogen bond linkage $O1 \cdots O3 \cdots O3 \cdots O1$ are given in Table 3.5. In this study, both of the hydrogen atoms were located for the case of monohydrate stoichiometry, therefore confirming that between two water molecules there is a hydrogen bond with unusual geometry (see Figure S14 in Appendix 8).

Table 3.5. Geometrical parameters for the hydrogen bond linkage provided by water molecules in **NSH** with mono- and hemi-hydrate stoichiometry.

ϵ	Temp., °C	$O1 \cdots O3$, Å	$O3 \cdots O3$, Å	$O1-O3-O3$, °	$O1 \cdots O1$, Å
1	120	2.83	2.86	109	7.11
	173	2.85	2.83	109	7.14
0.5	120	2.85	2.86	108	7.13
	298 ²⁶¹	2.85	2.76	111	7.16

The geometrical parameters for the $O3-H \cdots O1$ and $O3-H \cdots O3$ hydrogen bonds were the same for both stoichiometries. Therefore the removal of water occurred by simultaneously losing both hydrogen bonded water molecules from some of the channel sites instead of losing water molecules from one of the O3 positions and thus losing hydrogen bond linkage across the channel. This water molecule arrangement in **NSH** with stoichiometry below 1 was also supported by the

absence of a significant increase in the equivalent isotropic displacement parameter of water oxygen for hemihydrate stoichiometry (thus confirming that water retains two hydrogen bonds also for this stoichiometry), by the energy calculations (hemihydrate structure with hydrogen bonded water molecules was energetically favourable by 2 - 4.5 kJ per mole of water), lattice parameter changes (this arrangement explained the observed lattice parameter changes), and the recorded sorption-desorption isotherms corresponding to the presence of only equivalent water absorption sites in the structure. More details are given in the Appendix 8.

We therefore conclude that the difference observed in the solvent uptake at a given solvent activity in the **NSH** sorption-desorption isotherm (see Figure 3.23) can be associated with the absorption of water through an insertion of two hydrogen-bonded molecules at one site, which theoretically is a lower probability process compared to the absorption of one solvent molecule, as in the rest of the solvates.

3.3.10 Analysis of the droperidol solvate formation

While it should not be assumed that all of the potentially existing solvates have been identified, the crystallization from 30 solvents selected from various solvent classes should ensure the discovery of most of the stable solvated forms. Interestingly, five of the newly prepared solvated phases were isostructural to the already known **NSH** and **S_{Et}**. Thus, although droperidol solvates can be obtained with ten solvents, only five distinct solvated crystal structures were obtained: **DH**, **S_{TCC}**, **S_{DIOX}**, **S_{TOL}** and the “isostructural solvate”, where the latter one formed from a variety of different solvents. Therefore three questions can be raised to understand the solvate formation of droperidol: a) what is the reason for the formation of only these five structures, b) why the isostructural solvates were obtained from such a wide range of solvents, and c) which solvents can form isostructural solvates?

Unfortunately, the lack of information regarding the **S_{TCC}**, **S_{DIOX}**, and **S_{TOL}** crystal structures prevents a thorough answer to the first question. It is stated that one of the driving forces for solvate formation can be a mismatch of the hydrogen bond donors and acceptors in a molecule³⁰⁵. Although the molecule of droperidol contains three strong hydrogen bond acceptors (HBA) and only one hydrogen bond donor (HBD), this HBD deficiency was compensated only in the **DH** structure. In isostructural solvates the solvent molecules did not compensate the HBD deficiency, and it is not theoretically possible also in the structures of **S_{TCC}**, **S_{DIOX}**, and **S_{TOL}**. Therefore it can be concluded that the formation of droperidol solvates can be associated with the fact that molecules cannot pack with a sufficient efficiency and solvent molecules act as void fillers in these structures. This is supported by the fact that the packing index of the thermodynamically stable polymorph II is 0.675, which is only slightly higher than that of **ISD** at 333 K (0.659) where there are empty channels, but significantly lower than that of the isostructural solvates (0.704 – 0.717).

The reason for the formation of isostructural solvates is the stability of this structure. The calculation of both the total and lattice energy showed that the structures of **II** and **ISD** have almost the same energy at 0 K (the energy of **ISD** is even slightly favourable), and only the higher density of the polymorph **II** makes it thermodynamically stable at elevated temperature. Therefore this structure is not necessarily characterized by a high solvent selectivity, and the criteria for solvate formation most probably are a) the ability to form sufficiently efficient droperidol - solvent interactions, and b) the solvent molecules should fit into the channels by not significantly disturbing the packing of droperidol molecules.

By evaluating the properties of solvents forming isostructural solvates, it was noticed that three solvates formed with aprotic polar solvents (acetonitrile, nitromethane, and dichloromethane), three formed with hydrogen bond donors (water, methanol, and ethanol), and the last one formed with chloroform that can be classified both as a hydrogen bond donor and aprotic polar solvent, depending on the classification scheme¹³⁹. However, the classification of solvents according to these two groups clearly is not the main factor affecting the formation of the solvates (see Table S1, Appendix 8), although the formation of strong hydrogen bonds apparently is one of the driving forces. A better explanation of isostructural solvate formation can be achieved by taking into account a more detailed solvent classification based on various physical and physicochemical properties¹⁴⁰. Isostructural solvates were obtained from solvents belonging to groups 3 (mostly alcohols), 7 (mostly halocarbons), 9 (nitriles and nitromethane), and 15 (water)¹⁴⁰. Therefore only solvents from these groups were able to form energetically favourable interactions with the functional groups of droperidol molecules located around the structure channel.

Nevertheless, the second important factor for the formation of isostructural solvates clearly is the size (and shape) of solvent molecules. Thus, only the smallest molecules from the solvent groups 3, 7, and 9 formed isostructural solvates, which was confirmed by the calculation of molar volume (see Table S14 in Appendix 8). The largest solvent molecule forming an isostructural solvate with droperidol is chloroform (the size of which is even higher than that of some solvents not able to form isostructural solvates with droperidol), explaining the solvent content in the **S_{CLF}** phase observed by TG measurements to be below 0.5-stoichiometry. In contrast, the small size of water molecule and its ability to form inter-water hydrogen bonds enabled the formation of a monohydrate.

3.3.11 Conclusions

Crystallization of droperidol from 30 different solvents produced eight new solvates from methanol, acetonitrile, nitromethane, chloroform, dichloromethane, carbon tetrachloride, 1,4-dioxane, and toluene, while the desolvation of droperidol solvates produced two new polymorphs **III** and **IV**. Droperidol solvates obtained from methanol, ethanol, acetonitrile, nitromethane, dichloromethane, chloroform, and water are nonstoichiometric and isostructural. The solvent

content in these solvates can reach up to 0.5 equivalents (with the exception of **NSH**, that can reach monohydrate stoichiometry), and desolvation of these solvates produces an isostructural desolvate.

The crystal structures of five of these solvates were determined, proving that the droperidol molecule arrangement was isostructural despite the crystal structure description in both the centrosymmetric $P\bar{1}$ (**NSH**, **S_{Me}** and **S_{Et}**) and non-centrosymmetric P1 (**S_{ACN}** and **S_{NM}**) space group. The different space group determined for solvates with organic solvents was due to the disorder of methanol and ethanol molecules. The stability of isostructural solvates was mainly provided by the interactions between droperidol molecules themselves, while the solvent molecules were located in the structural channels and formed strong and/or weak hydrogen bonds with the droperidol molecules. Based on the IR spectra it was concluded that the chloroform molecules in **S_{CLF}** formed hydrogen bonds with droperidol molecules.

The solvent sorption-desorption isotherms of **NSH**, **S_{Me}**, **S_{Et}**, **S_{ACN}**, and **S_{NM}** showed that the solvent molecule content in the solvate could be described with a localized solvent model and there was no interaction between the solvent sites in **S_{Me}**. For **NSH**, **S_{Et}**, **S_{ACN}**, and **S_{NM}** the solvent interactions and the larger molecule size complicated the shape of the sorption isotherm. It was proved that the solvent content variation in the channels resulted in linear changes of the lattice parameters, therefore the transformation of the crystal structure was gradual. The lattice parameter changes and the solvent uptake at a given solvent activity in **NSH** significantly differed from those in the rest of the solvates. This was due to the formation of water molecule mediated hydrogen bond linkage across the structural channels and the simultaneous occupation of both of these hydrogen bonded water molecule positions.

The analysis of the solvate formation revealed that the driving force for droperidol solvate formation was the inability of droperidol molecules to pack efficiently, thus the solvent molecules acted as a void fillers, with the exception of **DH**, where water molecules provided an HBD function matching the excess HBA functions in the molecule of droperidol. The stability of the isostructural solvate structure was rationalized by the very effective interactions between droperidol molecules, explaining the fact that no specific interaction with solvate was necessary to maintain the crystal structure of the isostructural solvate. Therefore isostructural solvates can be obtained with solvents fitting in the channels and providing sufficiently effective intermolecular interactions with droperidol. By analysing the solvent classification it was concluded that these solvates can be obtained with the smallest solvent molecules from the solvent groups 3, 7, and 9, as well as from water¹⁴⁰, and the formation of strong hydrogen bonds is one of the driving forces for solvate formation.

3.4 Comparison and Rationalization of Droperidol Isostructural Solvate Stability

In this section we have tried to rationalize the solvate stability with respect to the desolvation based on their crystal structures and to select an appropriate tool for experimental comparison of the solvate stability by studying droperidol isostructural solvates. Solvate stability was compared theoretically by calculating the intermolecular interactions in the solvate structure and experimentally by determining the solvate thermal stability, desolvation kinetics, and by analyzing in Section 3.3 given solvent sorption-desorption isotherms. Isostructural solvates of droperidol are useful for such study as they retain the crystal structure after the desolvation, and thus it is possible to avoid the effects of any other factors on the solvate stability and desolvation process.

3.4.1 Desolvation kinetics of droperidol solvates

Firstly, the stability of droperidol isostructural solvates was compared by determining their desolvation kinetic parameters. The desolvation kinetics was studied in both isothermal and nonisothermal modes. Various samples were analyzed in the isothermal mode (including the crystals of **NSH**, **S_{Me}**, and **S_{Et}**), while in the nonisothermal conditions only a well-ground sample was analyzed for each solvate. The E_a values were calculated by using isoconversional method only, to allow the identification and characterization of possible complexity of the desolvation process²⁰⁰ and to identify the possible complications and errors associated with the experimental variables (most importantly, the sample, its mass and packing)¹⁹⁰ which can easily affect the results, especially for the desolvation process of non-stoichiometric solvates.

Desolvation activation energy. A total of 11 different **NSH** samples were analyzed in isothermal mode and the calculated activation energy values had a relatively high dispersion (see Table 3.6).

Table 3.6. Summary of the **NSH** desolvation kinetic parameters in isothermal mode.

Sample	Crystallization conditions ^a	E_a , kJ·mol ⁻¹	E_a - α dependence	Kinetic model ^b	Temperatures used, °C
<i>Crystals I</i>	50 °C/5%/100 mL	38±20	↓	F3/2, D5	60-100
<i>Crystals II</i>	50 °C/5%/100 mL	55±20	(↓)	D5, D3	70-110
<i>Crystals III</i>	50 °C/10%/100 mL	47±13	↓	F1	40-90
<i>Crystals IV</i>	50 °C/50%/100 mL	49±10	↓	F3/2, D3, D5	50-100
<i>Small crystals I</i>	50 °C/5%/250 mL	54±11	(↓)	F2, D5	60-120
<i>Small crystals II</i>	50 °C/5%/250 mL	66±7	–	F3/2, F1	25-50
<i>Small crystals III</i>	50 °C/10%/250 mL	60±20	–	F1	35-60
<i>Crystals II</i> ground for 10 s ^c	-	68±7	–	D5, F2	25-70
<i>Crystals II</i> ground for 1 min	-	65±10	–	F3/2, F2	25-70
<i>Powder I</i>	25 °C/5%/Petri dish	54±12	↓	F2, F3/2	25-50
<i>Powder II</i>	25 °C/10%/Petri dish	56±10	–	F3/2, F1	20-60
Summary		56±10	–	modified D5	20-120

^a – Temperature for the evaporation, volume percent of the water in the solution and volume of the conical flask used for the evaporation

^b – For each individual sample only commonly used kinetic models were included in the selection.

However, no direct relationship between the dehydration E_a (or kinetic model) and the sample particle size was observed. It was confirmed that the samples with smaller particle size dehydrated faster at a given temperature (see Table 3.6), and it was determined that unground samples showed higher variation of apparent E_a with α , while the average E_a values were in the same range as those determined for samples without E_a variation (see Table 3.6). The average dehydration E_a of **NSH** was calculated to be $56 \pm 10 \text{ kJ}\cdot\text{mol}^{-1}$.

The determination of the desolvation E_a was less straightforward for the organic solvates of droperidol. Firstly, for some of the samples complications arose due to almost identical desolvation rate at each temperature in the beginning of the reaction. This was observed for the samples with the smallest particles and could be due to the rapid escape of the solvent molecules close to the surface and with only minor temperature dependence, and for small particles there were many such solvent molecules. Secondly, a higher E_a variation from sample to sample and also higher apparent variation by the fraction desolvated was observed (see Table S2 in Appendix 9). This most probably was a result of lower reproducibility of the sample conditions and a stronger effect of different sample and experimental factors on the obtained results. Thirdly, the desolvation of **S_{ACN}** and **S_{NM}** in the selected conditions could be analyzed only at temperatures very close to the melting point of these solvates, see Section 3.3. This resulted in a very high desolvation rate dependence on the temperature, which produced unexpectedly high calculated E_a values. This most probably was a result of the change of the desolvation mechanism at temperatures close to the melting point, therefore the calculated E_a values most probably did not actually represent the activation energy of the desolvation process. This assumption was supported by the relatively lower E_a values obtained for the **S_{ACN}** sample that was analyzed at slightly lower temperatures (see Table S2 in Appendix 9). The average desolvation E_a values for all droperidol solvates are given in Table 3.7.

Table 3.7. Kinetic parameters for the desolvation of droperidol solvates.

Solvate	Isothermal mode		Nonisothermal mode	
	E_a , $\text{kJ}\cdot\text{mol}^{-1}$	Model	E_a , $\text{kJ}\cdot\text{mol}^{-1}$	Model
NSH	56 ± 10		-	-
S_{Me}	50 ± 13		65 ± 10	D5
S_{Et}	53 ± 15	Modified D5	51 ± 15	D1, D4
S_{NM}	- ^a		57 ± 5	D5
S_{ACN}	- ^a		60 ± 15	D5

^a – desolvation mechanism changed at a temperature close to the melting point of the solvate.

In order to bring more clarity about the desolvation kinetics of droperidol solvates with organic molecules, these solvates were studied also in nonisothermal mode using well ground

samples and a higher nitrogen flow rate. Although these results were also complicated by the apparent variation of E_a with the fraction desolvated and by the high uncertainty of the E_a values, the determined average desolvation E_a value for all four solvates was similar (50-65 $\text{kJ}\cdot\text{mol}^{-1}$) and almost the same as that of **NSH** in the isothermal mode (see Table 3.7). Therefore it was concluded that a) desolvation activation energy of all the droperidol solvates is almost the same and is 57 ± 15 $\text{kJ}\cdot\text{mol}^{-1}$, and b) in isothermal mode very high E_a calculated for desolvation of **S_{ACN}** and **S_{NM}** was due to the analysis at the temperatures close to the melting point and not because of actually higher desolvation E_a .

The identical desolvation E_a values did not allow to use this parameter for the comparison of solvate stability.

Kinetic model. Determination of the desolvation kinetic model of droperidol solvates was not straightforward and none of the commonly cited^{171, 187, 191, 192, 303} kinetic models (see Table A5) derived from the rate dependence on the nuclei formation and growth, interface advance, diffusion and/or geometrical shape of the particles were able to convincingly and satisfactorily describe the desolvation kinetic curves recorded in isothermal mode. However, the shape of the desolvation kinetic curves was similar to those of diffusion (D5 and D3) and reaction order (F3/2, F1 and F2) models. The arrangement of the solvent molecules in the structural channels, the absence of structural changes during the desolvation (Section 3.3), and the similarity of the shape of diffusion and reaction order model kinetic curves suggested that the rate limiting step in the desolvation process for all droperidol solvates was the diffusion of the solvent molecules out of the crystals. However, the exact diffusion mechanism appeared to be slightly different for different solvates, different samples, or even different conditions used. The deviation from the classical diffusion mechanisms could be due to the lattice parameter shrinkage during the loss of the solvent resulting in the reduction of the channel cross section area, which could change the diffusion coefficient during the desolvation process.

Besides, it was observed that the desolvation kinetic curves of **S_{ACN}** and **S_{NM}** at highest used temperatures were significantly different from diffusion-controlled kinetic curves and could be fitted by the nucleation and nuclei growth models (see Table S2 in Appendix 9). This observation confirmed the already stated hypothesis that at temperatures close to the melting point desolvation mechanism of these solvates differed from that at the lower temperatures. Moreover, at temperatures close to the melting temperature partial melting of the sample and desolvation from the melt could occur, thus changing the desolvation mechanism.

Nevertheless, the most appropriate kinetic model fitting most of the kinetic curves was the Zhuravlev equation D5^{306, 307}. This kinetic model has been modified^{308, 309} based on the changing diffusion activation energy during the reaction, giving the Eq. 3.1.

$$N \cdot \left[(1 - \alpha)^{-1/3} - 1 \right]^2 = kt^n \quad (3.1)$$

This modification, however, could as well represent the changing diffusion coefficient during the reaction or even the effect of a hindered conversion of the largest particles appearing due to a broad particle size distribution. It was found that all of the kinetic curves describing the desolvation of droperidol solvates in isothermal mode could be fitted with this modified Zhuravlev equation (see Figure 3.25 and S13 in Appendix 9). Note that an additional normalization constant N was introduced in this equation in order to compensate for the possible effects from either slight absorption of the solvent at the surface, or very slow approach to complete conversion due to the presence of a few very large particles.

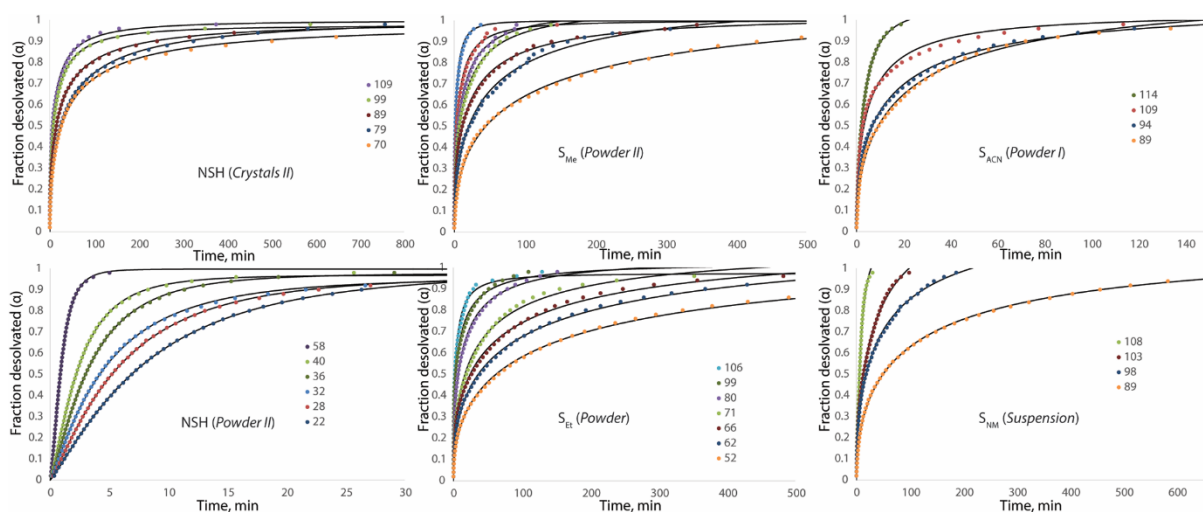


Figure 3.25. Desolvation kinetic curves of droperidol isostructural solvate samples at various temperatures in the isothermal mode. Theoretical curves calculated using the modified D5 model (Eq. 3.1) are shown with black lines.

Although the fit of the data with Eq. 3.1 could as well be empirical, the obtained description of desolvation of all droperidol solvates can not be a coincidence, proving that the rate limiting step in this desolvation process is the diffusion. This conclusion is also supported by the fact that the desolvation E_a of all of the solvates was the same, which can easily be true for diffusion limited desolvation, but is less likely to be true for other rate controlling mechanisms, because of the different interaction energy between the solvent and the droperidol molecules. Furthermore, also in the nonisothermal mode the desolvation process was best described by diffusion models, with the most appropriate one being D5 in particular.

Moreover, the diffusion as the rate limiting step was also confirmed by analyzing the desolvation of **NSH**, **S_{Me}**, and **S_{Et}** crystals by HSM, as the desolvation before melting (up to 120 °C) did not introduce any apparent changes to the crystal, except for the appearance of defects due to the cracking of the crystals or slight distortion of the molecular layers close to the crystal surface, which was most probably associated with the reduction of the unit cell size.

3.4.2 Thermal stability of droperidol solvates

Although the desolvation kinetic parameters were almost the same for all droperidol isostructural solvates, the solvate thermal stability was not equal. It was not possible to compare the desolvation onset temperature as the desolvation occurred over a wide temperature range and the nonstoichiometric behavior produced very broad and indistinct desolvation endotherm (see Figure 3.26). Therefore, the thermal stability of the droperidol solvates was evaluated from the experimental results characterizing the desolvation rate of the solvates in both isothermal and nonisothermal mode using TG curves and PXRD patterns recorded during the desolvation. The determination of the solvate stability in nonisothermal mode was complicated by the solvate melting due to the relatively slow desolvation process, during which a complete rapid desolvation from the melt occurred (see Figure 3.26). In this study it was possible to identify separate melting peaks for the solvates (a in Figure 3.26) and the melting or phase transition peak of **ISD** (b in Figure 3.26). Although in our previous experiments both of these processes were not distinguishable, in Table 3.3 reported melting points were consistent with those determined here. It was observed that **S_{NM}** had the lowest melting point, while **S_{Me}** had the highest melting point. Therefore the thermal stability of the solvates was evaluated from the desolvation curves before the melting point of solvate, as the melting point did not characterize the thermal stability of solvate with respect to the desolvation.

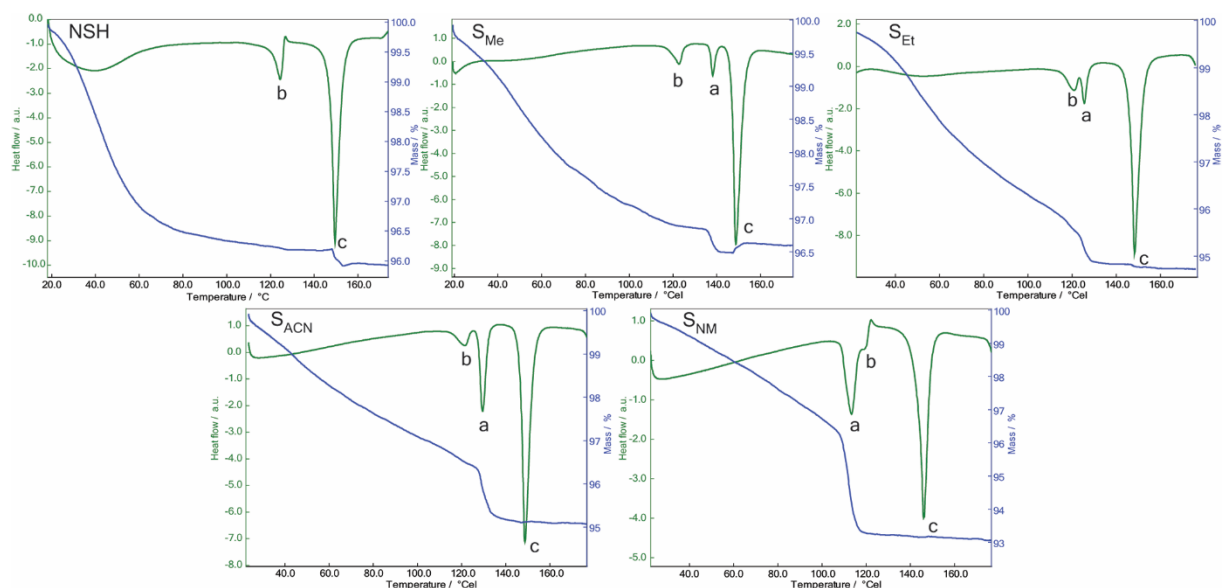


Figure 3.26. The DTA and TG curves of the droperidol isostructural solvates showing (a) the melting of solvate, (b) the melting of **ISD** or its phase transition to **I**, and (c) the melting of the resulting polymorph **I**.

Although the criteria for evaluation of the thermal stability were straightforward, the sample preparation appeared to be the crucial aspect to determine the thermal stability (as can be identified from the dehydration temperature of different **NSH** samples, Table 3.6). Thus, the obtained results were not completely unambiguous, although identical sample preparation was used to obtain all of

the data for this comparison. Nevertheless, the presented conclusions are based on separate experiments using different samples, and therefore are reliable.

Nonisothermal (Figure 3.27) and isothermal (Figure S17 in Appendix 9) heating of ground droperidol isostructural solvates showed that it is possible to rationalize their thermal stability: the least stable was **NSH**, while the most stable was **S_{NM}**. Although the thermal stability of **S_{Me}**, **S_{Et}**, and **S_{ACN}** was more similar and the established stability order slightly differed in some of the experiments, most of the experiments showed that from these three phases the least stable was **S_{Me}** and the most stable was **S_{ACN}**.

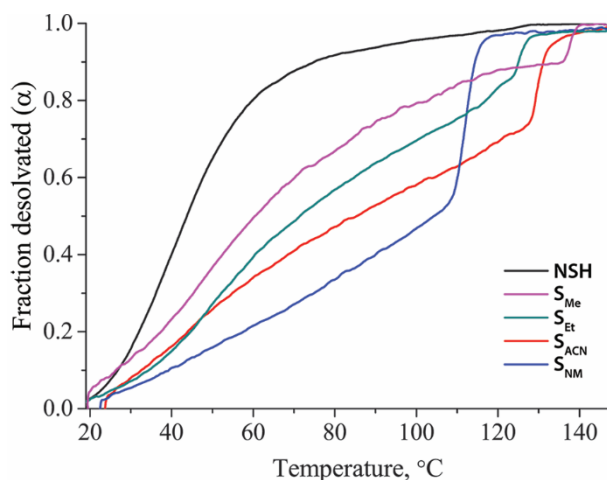


Figure 3.27. Desolvation kinetic curves of droperidol isostructural solvates in nonisothermal mode at the heating rate of $5^{\circ}\cdot\text{min}^{-1}$.

The same order of thermal stability was confirmed also by monitoring the PXRD patterns during the isothermal solvate desolvation and by analyzing the curves recorded during the study of the desolvation kinetics in the nonisothermal mode. Therefore, based on the data obtained from all of the performed experiments, it was possible to determine the relative thermal stability of droperidol isostructural solvates, which increased in the following order:



3.4.3 Quantitative comparison of solvate stability based on the crystal structure

In the crystal structure of droperidol solvates, the solvent molecules and droperidol molecules are connected with strong and/or weak hydrogen bonds. It is clear that the stability of the solvates can not be associated with the presence of strong hydrogen bonds, because in the most stable solvates **S_{ACN}** and **S_{NM}** the acetonitrile and nitromethane molecules form only weak hydrogen bonds with the droperidol molecules. Therefore, in order to rationalize the relative stability of the droperidol solvates, solvent-droperidol, solvent-solvent, and also droperidol-droperidol intermolecular interaction energy values were calculated in *Gaussian 09*. Before the calculation of the interaction energy, geometry optimization of the crystal structures was performed. To obtain comparable results, crystal structures of all five solvates determined at 173 K were used for the calculations. As it is not possible to take into account the degree of disorder, the alcohol molecules

in the crystal structures of S_{Me} and S_{Et} were oriented in one of their two possible positions for crystal structure optimization and calculation of the interaction energy.

Characterization of the droperidol-droperidol intermolecular interaction energy.

Droperidol-droperidol interaction energy in all solvates was evaluated based on droperidol molecule interactions with 10 closest droperidol molecules designated by the letters A – G (see Figure 3.28, symmetrically equivalent interactions were designated with the same letter). The calculated interaction energy for these droperidol molecule pairs, as well as the total droperidol-droperidol interaction energy from these ten interactions is given in the Appendix 9. From these calculations it was concluded that the intermolecular interactions between droperidol molecules as well as their energy were almost the same in all of these solvates and did not depend on the crystal structure optimization method. Therefore, different solvent molecules in the channels did not introduce significant changes in the droperidol-droperidol molecule arrangement, although some minor differences of the interaction energy values occurred.

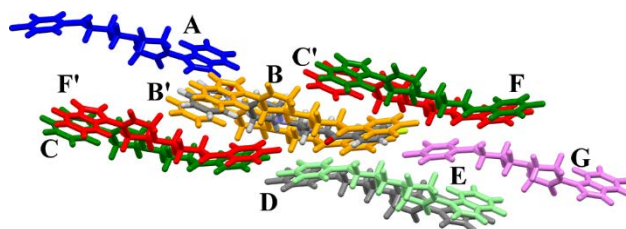


Figure 3.28. The arrangement of the central droperidol molecule and ten closest droperidol molecules surrounding it, that was used for the evaluation of pairwise droperidol-droperidol interaction energy values in the droperidol isostructural solvates.

Characterization of the intermolecular interaction energy of solvent molecules. The presence of various functional groups in the solvent molecules and different arrangement of these molecules in the crystal structure prevented a direct comparison of the intermolecular interaction energy for solvent-droperidol molecule pairs in different solvates. Nevertheless, the interaction energy was calculated between the solvent molecule and up to 8 droperidol molecules, as well as the closest solvent molecules. These interactions with droperidol molecules were designated by Greek alphabet letters α to θ and solvent-solvent interactions were designated by ι and κ (see Figure 3.29), and the calculated values are given in the Appendix 9.

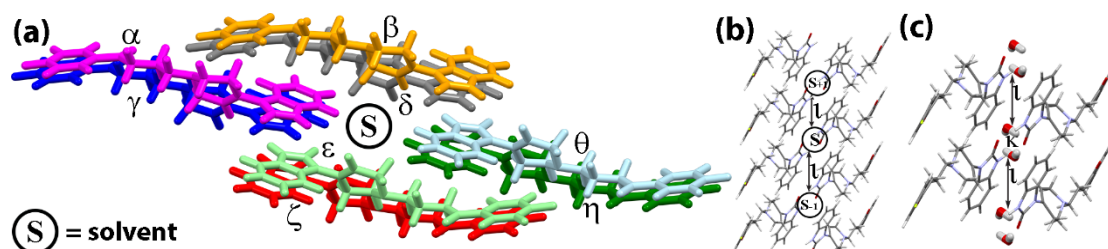


Figure 3.29. The arrangement of (a) solvent-droperidol molecule pairs and solvent-solvent molecule pairs in (b) organic solvates and (c) **NSH**, corresponding to all energetically relevant solvent interactions in the droperidol isostructural solvates.

Most of the molecule pairs were characterized by negative interaction energy and therefore corresponded to energetically favorable interactions, while few pairs were characterized by slightly positive interaction energy and corresponded to energetically unfavorable interactions, which was shown to be a common phenomenon and was explained by the existence of a crystal structure in a state where the energy minimum was reached for the whole multi-molecular system, and not individual molecule pairs¹¹⁵.

It was observed that the calculated interaction energy for all of the molecule pairs at the B3LYP-D level was more negative than that calculated at the M06-2X level. This difference for interactions between droperidol and solvent molecules was less than $6.5 \text{ kJ}\cdot\text{mol}^{-1}$ with no direct correlation with the magnitude of the interaction energy (although it was noticed that B3LYP-D typically overestimated the magnitude of the interaction energy for pairs in which it was small). Therefore the total solvent interaction energy (a sum of all solvent-droperidol and solvent-solvent interaction energies) calculated at the M06-2X level was also less negative (see Table 3.8). The results obtained by using M06-2X are considered to be more accurate, as it has been shown that this empirical exchange-correlation functional performs better for the description of the noncovalent interactions, compared to the more commonly used dispersion corrected B3LYP-D functional^{310,311}. Moreover, the better accuracy of the interaction energies calculated at the M06-2X level also was supported by a better agreement to the interaction energy values calculated with PIXEL code (see Appendix 9). Unfortunately, it was not possible to use the PIXEL code for the calculation of the intermolecular interaction energy in droperidol organic solvates due to the presence of three symmetry independent molecules in the unit cell.

The differences in crystal structure geometry obtained after different optimization methods were also reflected in the calculated interaction energy values. Therefore, there were only slight differences of interaction energy values for the individual molecule pairs (typically below $2.0 \text{ kJ}\cdot\text{mol}^{-1}$) and for total solvent interaction energy (below $6.4 \text{ kJ}\cdot\text{mol}^{-1}$) in \mathbf{S}_{ACN} , \mathbf{S}_{NM} , and \mathbf{S}_{Et} structures after all structure optimization methods (see Table 3.8).

Table 3.8. The total solvent interaction energy (in $\text{kJ}\cdot\text{mol}^{-1}$) values calculated in *Gaussian 09* after different structure optimization methods for isostructural solvates of droperidol.

		\mathbf{S}_{NM}	\mathbf{S}_{ACN}	\mathbf{S}_{Et}	\mathbf{S}_{Me}	\mathbf{NSH}
B3LYP-D	1	-104.4	-92.9	-96.5	-81.3	-71.1
	2	-101.6	-94.1	-95.6	-82.3	-75.7
	3	-103.3	-95.1	-95.7	-81.4	-77.3
	4	-97.4	-90.3	-91.1	-82.8	-72.0
	5	-98.9	-92.6	-96.2	-76.4	-69.4
M06-2X	1	-82.8	-72.0	-69.3	-64.6	-59.7
	2	-80.4	-74.3	-68.0	-64.6	-65.1
	3	-82.9	-76.1	-68.8	-65.6	-66.6
	4	-76.6	-71.0	-67.6	-67.6	-57.0
	5	-75.4	-70.7	-69.2	-50.5	-62.6

1 – PBE+TS HO in *CASTEP*, 2 – PBE+TS ALL in *CASTEP*, 3 – PBE+TS UC in *CASTEP*, 4 – PBE+G06 UC in *CASTEP* and 5 – B3LYP-D* UC in *CRYSTAL09*.

The same applied also to the differently optimized structures of \mathbf{S}_{Me} , except for that optimized at the B3LYP-D* level. The different water molecule arrangements in \mathbf{NSH} after different geometry optimization methods also showed up as differences in the water interaction energy values. Further discussion is given in the Appendix 9.

From all three optimization procedures at the PBE+TS level in *CASTEP*, the calculated average total solvent interaction energy per one mole of solvent for all droperidol solvates is presented in Figure 3.30. From these results it follows that the total solvent interaction energy becomes more negative in the following order:

$$\mathbf{NSH} > \mathbf{S}_{Me} > (\mathbf{S}_{Et}, \mathbf{S}_{ACN}) > \mathbf{S}_{NM},$$

where the sequence between the \mathbf{S}_{Et} and \mathbf{S}_{ACN} depended on the interaction energy calculation level (at the B3LYP-D level the calculated total solvent intermolecular interaction energy was higher in \mathbf{S}_{Et} , whereas at the M06-2X level the calculated energy was higher in \mathbf{S}_{ACN}), but not on the crystal structure optimization method (although full relaxation of the crystal structure reduced at the B3LYP-D level calculated energy difference between \mathbf{S}_{Et} and \mathbf{S}_{ACN}). Therefore, the \mathbf{S}_{NM} was predicted to be the most stable solvate with respect to the loss of the solvent molecule, as this process would require disruption of energetically favored interactions, while the \mathbf{NSH} was predicted to be the least stable one.

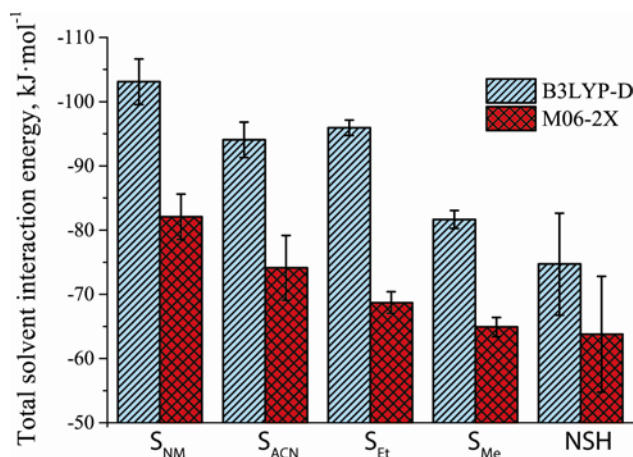


Figure 3.30. The average total solvent interaction energy calculated in *Gaussian 09* after geometry optimization at the PBE+TS level in *CASTEP* for all isostructural solvates of droperidol.

It was also noticed that in \mathbf{S}_{NM} and \mathbf{S}_{ACN} an important contribution to the total solvent interaction energy was provided by the solvent-solvent interactions, whereas they had only a minor contribution for the alcohol solvates (see Table 3.9). This is logical, as the acetonitrile and nitromethane molecules have the greatest length and do not have a specific orientation of the polar end (in alcohol molecules this end is hydrogen bonded to the benzimidazolone moiety of droperidol). Besides, the contribution from the interactions with other solvent molecules in the

total interaction energy increased when the interaction energy calculation level was changed from B3LYP-D to M06-2X, which appeared to be one of the main factors affecting the change of the order of the total solvent interaction energy for S_{ACN} and S_{Et} .

Logically, due to the presence of a strong hydrogen bond between two water molecules, water-water interaction energy had a relatively high contribution to the total interactions involving water molecules.

Table 3.9. The average solvent-solvent interaction energy (in $\text{kJ}\cdot\text{mol}^{-1}$) and its contribution to the total solvent interaction energy calculated in *Gaussian 09* at the M06-2X level after the structure optimization at the PBE+TS level in *CASTEP* for isostructural solvates of droperidol.

		S_{NM}	S_{ACN}	S_{Et}	S_{Mc}	NSH
B3LYP-D	E (solv-solv)	-8.5	-11.1	-1.8	-1.3	-15.4
	Contribution, %	16.9	23.9	3.9	3.3	20.6
M06-2X	E (solv-solv)	-8.5	-10.7	-1.5	-1.2	-15.4
	Contribution, %	21.4	29.5	4.3	4.0	24.2

Summary and comparison to the experimental results. The calculated total solvent interaction energy at the M06-2X level became more negative in the following order:

$$NSH > S_{Mc} > S_{Et} > S_{ACN} > S_{NM}.$$

Thus, the theoretically predicted order of the stability of solvates based on the total solvent interaction energy at the M06-2X level is opposite, compared to this sequence. This order is identical to that observed for the thermal stability of these solvates, which should not come as a surprise, as during the desolvation only solvent-droperidol and solvent-solvent interactions are disrupted, while the rest of the crystal structure is maintained. Therefore, the calculation of the total solvent interaction energy at the M06-2X level in this system can be used to rationalize and predict the thermal stability of solvates.

Although the total solvent interaction energy in NSH was very similar to that of S_{Mc} , the thermal stability of these two solvates was quite different. This most probably could be associated with the small size of water molecules allowing an easier dehydration and the fact that the dehydration occurs by simultaneously losing the hydrogen bonded molecule pair (see Section 3.3), therefore the water-water interaction between the hydrogen bonded water molecules actually did not stabilize the NSH against the dehydration.

Interestingly, it was noted that the order of the solvate melting points correlated with the calculated total droperidol-droperidol interaction energy values (see Table S17 in Appendix 9). Although such a small interaction energy value difference ($8\text{-}9 \text{ kJ}\cdot\text{mol}^{-1}$) are unlikely to introduce significant melting point differences ($>20^\circ\text{C}$), it would be reasonable that the solvate melting point would be associated with the droperidol-droperidol interactions and therefore the stability of the crystal lattice.

Although the thermal stability of the organic solvates increased in the same order as the boiling points of the respective solvents, this should be considered only a coincidence as the interactions of solvent molecules in the solvates are completely different than those in their liquid states.

Although the experimental stability of the solvates can also be compared using the sorption-desorption isotherms, which would provide an information about the thermodynamic stability, the solvent content in the initial part of the isotherm representing the solvent sorption at a given solvent vapor activity increased in the order **NSH** < **S_{NM}** < **S_{ACN}** < **S_{Et}** < **S_{Me}** (see Section 3.3 and Figure S22 in Appendix 9). Therefore it appeared that the solvent content was determined by the steric factors of solvent molecules, and not by the intermolecular interactions. The only exception was the **NSH**, which had the lowest solvent content at any given activity, although the significant difference, if compared to other solvents, cannot be explained exclusively by the lower total energy of intermolecular interactions involving water molecules.

3.4.4 Conclusions

The study of the desolvation kinetics of droperidol isostructural solvates revealed that the desolvation activation energy of all these solvates was almost the same ($57 \pm 15 \text{ kJ} \cdot \text{mol}^{-1}$) and the desolvation process was diffusion limited and the desolvation curves could be fitted using the modified Zhuravlev equation.

The thermal stability of the solvates determined from the desolvation rate in both isothermal and nonisothermal mode could be successfully used as a solvate stability comparison and ranging tool for the droperidol solvates. The calculation of the intermolecular interaction energies in droperidol solvates showed that it was possible to rationalize and predict the thermal stability order of solvates by using a sum of the solvate-droperidol and solvate-solvate interaction energies.

Although this solvate system can be used to understand the general trends in the characterization and rationalization of the solvate stability, we conclude that a) crystal structure does not substantially change during the desolvation, and b) droperidol-droperidol interaction energy in all solvates is almost the same, which makes this system a relatively simple model. Complications associated with a) different host-host interaction energy and b) the energy necessary for the crystal structure change during the desolvation will arise when a general stoichiometric solvate system is considered. Therefore, additional studies are necessary to obtain more general understanding of the solvate stability.

3.5 Solid-state NMR and computational investigation of solvent molecule arrangement and dynamics in isostructural solvates of droperidol

Although isostructural in terms of the host droperidol structure, droperidol isostructural solvates are unusual in that they fall into three categories. Firstly, the **NSH** crystal structure is centrosymmetric with one droperidol and one water molecule in the asymmetric unit. The isotropic displacement parameter for the water oxygen at 120 K is three times higher than for other non-hydrogen atoms, and it was not possible to locate all the water hydrogen atoms for structures determined at 173 K or above, see Section 3.3, suggesting that the water molecules are slightly disordered. Secondly, the **S_{Me}** and **S_{Et}** structures refine with centrosymmetry, with one droperidol and half a disordered alcohol molecule in the asymmetric unit. Therefore only one of the two droperidols in the unit cell is hydrogen bonded to the alcohol molecule, and taking into account disorder between two orientations related by inversion symmetry is necessary for a satisfactory refinement within the $P\bar{1}$ space group. Thirdly, the **S_{ACN}** and **S_{NM}** are non-centrosymmetric, with two droperidol and one ordered solvent molecules in the asymmetric unit.

In this section we use ^{13}C , ^{15}N and ^2H solid-state NMR to determine and characterize the differences between these five droperidol isostructural solvates. This includes the identification and characterization of the molecular motion in **NSH**, **S_{Me}** and **S_{Et}**, to explain the slight disorder of water molecule in **NSH** and to distinguish between static vs. dynamic disorder in the alcohol solvates. Theoretical calculations are used to rationalize the differences in the molecular motion of the solvent molecules.

3.5.1 Solvate characterisation using ^{13}C CPMAS spectra

Figure 3.31 shows the ^{13}C CPMAS spectra of the solvates, with the peak positions given in Table 3.10. The resonances of the solvent molecules are readily identified (see labels), except for the methyl group signal of ethanol and the quaternary carbon of acetonitrile, as these overlap with the peaks of droperidol. Bearing in mind that the spectra were recorded under CP conditions, and so are not strictly quantitative, the intensity of the solvent peaks is consistently around two times lower than that of the droperidol CH_2 peaks, consistent with a 0.5 solvate stoichiometry. CP spectra with short (10–50 μs) contact times were recorded to identify the carbon atoms directly attached to hydrogen; the peaks absent in these spectra and thus associated with quaternary carbon atoms are marked with arrows in Figure 3.31.

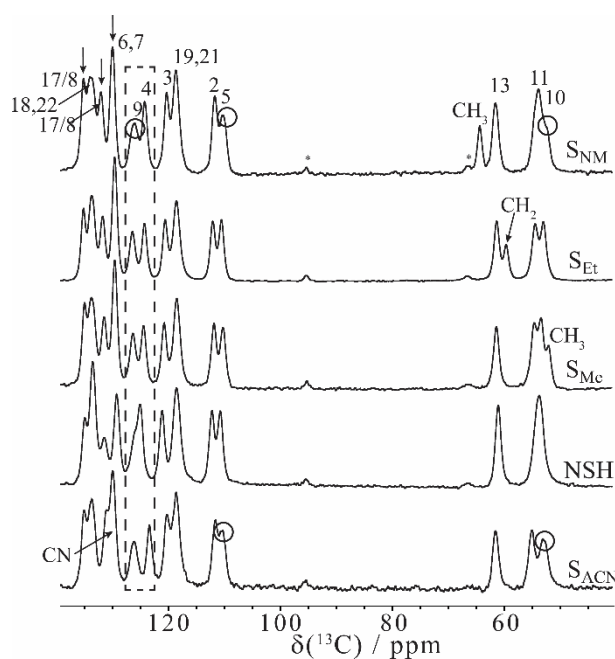


Figure 3.31. 50–135 ppm region of the ^{13}C CPMAS spectra of the droperidol isostructural solvates together with peak assignment. Spinning sidebands are marked with asterisks, signals absent in short CP contact time experiments are marked with arrows, and signals in the \mathbf{S}_{ACN} and \mathbf{S}_{NM} spectra showing evidence of splitting are circled. Full spectra are given in Figure S2 in Appendix 10.

As would be expected, the \mathbf{NSH} spectrum is consistent with one unique droperidol molecule in the asymmetric unit. However, the \mathbf{S}_{Mc} and \mathbf{S}_{Et} spectra also do not show clear evidence of distinct droperidol molecules in the crystal structure, one hydrogen-bonded to the solvent, and one not. Only slight splitting of some peaks, circled in Figure 3.31, is observed in the spectra of \mathbf{S}_{ACN} and \mathbf{S}_{NM} , which would be consistent with having two slightly different droperidol molecules in the asymmetric unit.

To help assign the peaks, GIPAW calculations of the NMR parameters were performed for all solvates after geometry optimization. The results, after rescaling each set of the calculated shieldings against the experimental chemical shifts, are presented in Table 3.10. Different isotropic shielding values were calculated for the same carbon atom where inequivalent droperidol molecules are present in the asymmetric unit (\mathbf{S}_{Mc} , \mathbf{S}_{Et} , \mathbf{S}_{ACN} and \mathbf{S}_{NM}). It was observed that these differences were quite large (up to 6.8 ppm, with an average difference of 2–3 ppm, depending on the solvate) when only hydrogen atom positions were relaxed for structures solved in the $P1$ space group. Relaxing all atomic positions during the geometry optimization decreased the average difference to 0.5 ppm. Since this is clearly in better agreement with the experimental results, only the structures obtained by all atom optimization were used in further calculations, and average values of the calculated shieldings of corresponding atoms were used when making comparisons with experimental data. The maximum difference of up to 2–3 ppm is observed for C9 and C10, which is consistent with their proximity to the solvent molecules. These results imply that solution of the

XRD results in *P1* has “exaggerated” the asymmetry between the droperidol molecules; relaxing all the atomic positions results in increased local symmetry and better agreement with the experimental NMR data.

As might be expected, the situation was reversed for the structures originally solved in $\bar{P}1$ space group (\mathbf{S}_{Me} and \mathbf{S}_{Et}). With only optimization of the hydrogen atom positions, the droperidol environments remain essentially identical and only small maximal (1.6 to 2.2 ppm) and average (0.3 – 0.45 ppm) differences were observed for equivalent carbon shifts in the two droperidol molecules. Several of these shifts, both for solvent and droperidol sites, however, deviated significantly from the experimentally observed values. Relaxation of all atoms resulted in almost identical chemical shifts to those calculated after all-atom optimization of structures solved in *P1*.

The most significant differences between the ^{13}C spectra are observed for the C4 and C9, marked by a dashed rectangle in Figure 3.31; these again are close to the solvent molecules. This observation was consistent with the GIPAW calculations, where the highest difference between the average chemical shifts for different solvates were predicted to be for C9 (2.7 ppm), C4 (1.8 ppm) as well as for C8 (3.0 ppm), see Table 3.10. Overall, however, the spectra of solvates are very similar, showing the different solvent molecules introduce significant changes in the local chemical environment of the droperidol molecules.

Taking into account the previously identified signals from quaternary carbons and solvent atoms, the obtained shielding values after all atom optimization were plotted *versus* the observed chemical shifts, illustrated in Figure 3.32 for \mathbf{S}_{Et} . As observed previously^{72, 252} and justified theoretically³¹², these plots had a non-unity slope. Linear regression was used to reference the mean experimental shift to the mean computed shielding, and to rescale the calculated shifts. These plots allowed the majority of the signals to be assigned, as indicated in Figure 3.31, with the exceptions of strongly overlapped peaks in the region 127–135 ppm, indicated by the rectangle in Figure 3.32. These ambiguities are not, however, significant for the purposes of this study. Further details of the assignment are given in Table 3.10. In each case, a smaller RMS deviation between calculated and experimental values was observed when all atomic positions were refined.

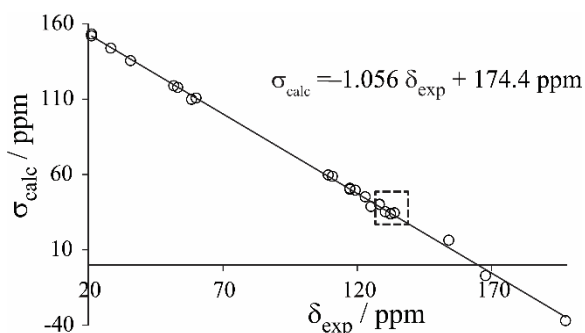


Figure 3.32. Calculated ^{13}C isotropic shielding (averaged over equivalent carbons) values *versus* observed chemical shifts in droperidol \mathbf{S}_{Et} . The dashed rectangle marks the region where the peak assignment is ambiguous.

Table 3.10. Assigned experimental peak maxima (in ppm) in ^{13}C CPMAS spectra and (rescaled) average calculated ^{13}C chemical shifts after all atom optimisation.

Carbon	NSH			S_{Me}			S_{Et}			S_{ACN}			S_{NM}			$\Delta\delta_{\text{Calc}}^{\text{b}}$
	δ_{Exp}	δ_{all}		δ_{Exp}	δ_{all}	diff. ^a	δ_{Exp}	δ_{all}	diff. ^a	δ_{Exp}	δ_{all}	diff. ^a	δ_{Exp}	δ_{all}	diff. ^a	
C16^c	197.6	199.9	197.5	199.9	0.1	197.5	199.8	0.1	197.6	200.2	0.2	197.5	199.7	0.0	0.5	
C20^{c,d}	167.5	171.5	167.7	171.7	0.0	167.7	171.6	0.1	167.7	171.9	0.0	167.6	171.6	0.0	0.4	
C1^e	154.0	149.2	154.1	149.5	0.3	154.1	149.3	0.1	154.1	149.8	0.2	154.2	149.7	0.4	0.6	
C17/C8^{c,e}	133.6	131.4 ^f	133.6	131.4 ^g	1.4	133.8	132.1 ^g	0.6	133.7	131.4 ^f	0.0	133.9	132.9 ^g	0.8	0.1 ^f	
C18		132.7		133.0	0.2		132.9	0.2		132.8	0.0		133.3	0.1	0.5	
C22	132.2	132.4	132.4^h	132.6	0.1	132.4	132.7	0.4	132.3	133.3	0.0	132.7^h	132.6	0.2	0.9	
C17/C8^{c,e}	130.1	130.0 ^g	130.2	131.3 ^f	0.1	130.4	131.4 ^f	0.0	129.8	131.3 ^g	0.2	130.7	131.5 ^f	0.0	3.0 ^g	
C6^c		127.1		127.1	0.4		127.0	0.4		127.2	0.5		127.4	0.2	0.4	
C7^c	127.9	126.3	128.3	126.6	0.1	128.3	126.7	0.3	128.6	127.2	0.3	128.6	127.3	0.3	1.1	
C9	124.7	130.0	125.0	128.4	3.2	125.1	128.2	1.2	124.8	128.0	1.3	124.6^h	127.3	2.1	2.7	
C4	123.7	122.9	123.1	122.0	1.3	123.0	122.1	0.9	122.1	121.0	0.2	122.9	122.3	0.3	1.8	
C3	119.8	118.1	119.4	118.0	0.3	119.3	117.9	0.3	118.9	117.4	0.1	119.0	117.5	0.0	0.6	
C19		117.3		117.6	0.5		117.4	0.5		117.6	0.0		117.6	0.3	0.3	
C21	117.2	116.5	117.2	116.7	0.0	117.3	116.7	0.4	117.3	116.8	0.0	117.3	116.8	0.0	0.4	
C2ⁱ	110.9	108.7	110.5	108.9	0.6	110.8	109.2	0.6	110.3	108.6	0.1	110.4	108.8	0.2	0.6	
C5ⁱ	109.4	109.0	108.9	107.5	1.3	109.2	108.3	1.1	109.0^h	107.7	0.7	108.9^h	107.7	0.9	1.5	
C13	59.8	60.3	60.1	60.1	0.0	60.0	60.1	1.2	60.3	60.2	0.5	60.3	60.5	1.1	0.4	
C11ⁱ		53.8		53.6	1.0		53.4	0.6		53.9	0.4		53.2	1.2	0.7	
C10ⁱ	52.4	53.2	52.1	53.0	0.6	51.7	52.3	2.1	51.8^h	51.8	1.0	52.6^h	52.9	2.1	1.5	
C15	35.3	36.1	35.5	36.1	0.0	35.6	36.6	0.0	35.6	36.5	0.0	35.9	37.2	0.1	1.1	
C12	28.4	28.2	28.4	28.8	0.2	28.3	28.7	0.2	28.0	28.0	0.2	28.4	29.1	0.3	1.1	
C14	21.3	21.0	21.3	21.0	0.2	21.1	21.1	0.0	21.2	20.9	0.0	21.1	21.2	0.0	0.3	
CH₃^{solv}			50.8	52.2		21.1	19.8		4.2	6.0		63.1	62.5			
CH₂/CN^{solv}						58.3	60.9		128.6/ 129.8^j	128.3						
RMSD^k		2.06		1.83			1.79			1.81			1.65			

^a Difference in calculated chemical shift between two chemically equivalent atoms in the unit cell. Significant differences (greater than 0.7 ppm) are highlighted in grey (dark grey if larger than 2 ppm).

^b Difference between the highest and lowest calculated chemical shifts from the same atom in all five solvates.

^c Non-protonated carbons identified from short contact time CP spectrum.

^d Signal split by J-coupling to ^{19}F , with $^1J_{\text{CF}} = 278\text{--}280$ Hz in **NSH**, **S_{Me}**, **S_{Et}** and **S_{ACN}** and $^1J_{\text{CF}} = 265$ Hz in **S_{NM}**.

^e High variation in CASTEP calculated chemical shifts for these two atoms in different solvates prevents unambiguous assignment.

^f Given value is for C17 (calculated).

^g Given value is for C8 (calculated).

^h Signal is slightly split.

ⁱ Peak separation of C2 and C5, as well as that of C10 and C11 is too small for unambiguous assignment, but consistent relative position in GIPAW calculations for all solvates (with the exception of C2 and C5 in **NSH**) and the splitting of C5 and C10 peaks support this assignment.

^j Experimental peak position uncertain, but peak intensities and GIPAW calculations suggest that nitrile carbon corresponds to one of these peaks.

^k Root mean square difference between experimental and calculated chemical shifts.

The experimental spectra show only slight evidence of splitting for a few peaks in \mathbf{S}_{ACN} and \mathbf{S}_{NM} corresponding to carbon atoms C5, C9 and C10, which are all close to the solvent molecules. The differences between peak maxima were at most 0.5 ppm, but these particular carbon atoms also show the highest splitting in the GIPAW-calculated chemical shifts, see Table 3.10. Observing the line splitting is complicated by the relatively broad linewidths; the widths of the peaks in the spectra of droperidol isostructural solvates were 0.75–1.15 ppm, whereas peak widths in the ^{13}C spectra of droperidol dihydrate and form **II** were only 0.32–0.70 ppm under the same conditions. This difference in linewidths can not be explained by the presence of two slightly different droperidol molecules in the unit cell, as the linewidths of the organic solvates was identical to that of **NSH**, where there is a single droperidol molecule in the asymmetric unit. The “line-broadening factors” associated with the anisotropy of the bulk magnetic susceptibility (ABMS) for powder samples³¹³ were determined using the magnetic susceptibility tensor calculated by CASTEP-NMR. This was found to be ~ 3.6 ppm for the isostructural solvates and ~ 1.7 ppm for both form **II** and dihydrate, suggesting that the width of the lines in the solvate spectra is associated with a large ABMS, making it intrinsically difficult to resolve overlapped resonances.

3.5.2 Solvate characterisation using ^{15}N CPMAS spectra

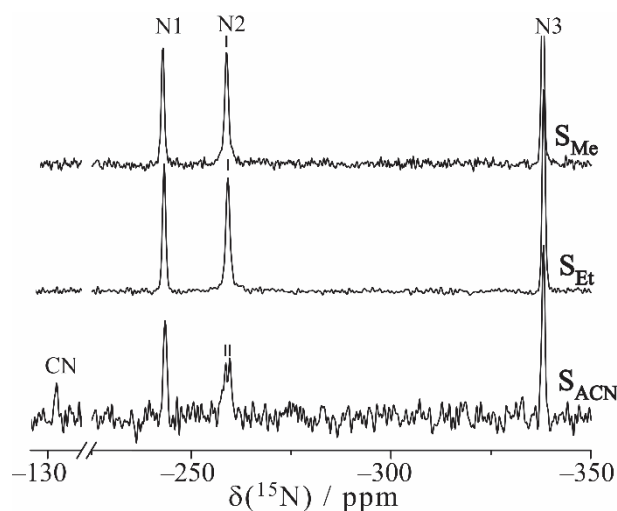


Figure 3.33. ^{15}N CPMAS spectra of droperidol solvates \mathbf{S}_{Et} , \mathbf{S}_{Me} and \mathbf{S}_{ACN} , showing the splitting of the N2 peak in the spectrum of \mathbf{S}_{ACN} . The lower signal-to-noise ratio of the \mathbf{S}_{ACN} spectrum reflects the much longer recycle delay needed for this sample (120 s, compared to 15 and 25 s for \mathbf{S}_{Et} and \mathbf{S}_{Me} respectively) and consequently a much reduced number of acquisitions compared to the alcohol solvates (440 compared to 3628 and 2308 respectively).

As shown in Figure 3.33, ^{15}N CPMAS spectra were recorded for the \mathbf{S}_{Et} , \mathbf{S}_{Me} and \mathbf{S}_{ACN} solvates, and peaks assigned based on the GIPAW calculations. Both \mathbf{S}_{Et} and \mathbf{S}_{Me} show sharp lines from all three nitrogen atoms, whereas the line from N2 – the only nitrogen atom close to the solvent – was split (or significantly broadened) in \mathbf{S}_{ACN} , indicating two distinct local environments. This confirms that the acetonitrile breaks the local symmetry of droperidol molecules, consistent

with the determined crystal structure. The experimental and GIPAW-calculated ^{15}N chemical shift differences are almost the same, 1.0 and 0.8 ppm respectively. The alcohol molecules are strongly hydrogen-bonded with the droperidol O1 atom, thus affecting the strength of the intermolecular hydrogen bond between droperidol molecules $\text{N2-H}\cdots\text{O1}$ and the calculated chemical shift difference for N2 is significantly higher in \mathbf{S}_{Me} and \mathbf{S}_{Et} , 1.6 and 3.2 ppm respectively. In contrast to \mathbf{S}_{ACN} , only one, somewhat broader, line is observed in the ^{15}N spectrum for the alcohol solvates (45–50 Hz for N2 compared to 35–40 Hz for other nitrogen resonances). This strongly suggests that the alcohol molecules in \mathbf{S}_{Me} and \mathbf{S}_{Et} are dynamically disordered, resulting in a single resonance. Although the ^{15}N spectra were much more demanding to acquire, they are more sensitive in this case to the very subtle symmetry breaking involved.

3.5.3 Characterization of solvent dynamics in droperidol isostructural solvates

The evidence from the ^{13}C and ^{15}N CPMAS spectra acquired at ambient temperature, combined with the crystal structure determinations, suggests that the solvent molecules are dynamic in \mathbf{S}_{Me} and \mathbf{S}_{Et} . The crystal structure of \mathbf{NSH} also shows evidence of disordered water molecules. ^{13}C and ^2H MAS spectra of \mathbf{S}_{Et} , \mathbf{S}_{Me} and \mathbf{NSH} as a function of temperature are used here to try to characterize the solvent dynamics.

Solvates with organic solvents. It can be seen in Figure 3.34 that the ethanol CH_2 group signal (highlighted with an arrow) in the CPMAS spectrum (solid lines) of \mathbf{S}_{Et} broadens when the temperature is reduced to $-15\text{ }^\circ\text{C}$ and has lost most of its intensity at $-40\text{ }^\circ\text{C}$. These changes are reversible and consistent with the presence of dynamics. Experiments with different contact times, confirmed that the low intensity of this peak is related to its broad nature rather than, for example, rapid $T_{1\rho}$ relaxation. The broad CH_2 peak is more easily observed in the ^{13}C direct-excitation spectra (dashed lines). The most likely mechanism for the broadening is interference between the modulation of NMR parameters by dynamics and the ^1H decoupling^{59, 314}, implying that the dynamics of the ethanol CH_2 are on the order of 10s kHz around $-40\text{ }^\circ\text{C}$. It was also noticed that the build-up of the ethanol CH_2 group signal during cross-polarisation at $20\text{ }^\circ\text{C}$ was significantly slower than that of CH_2 carbons of droperidol (see Figure S8 in Appendix 10). This implies that the heteronuclear CH dipolar couplings are partially averaged by dynamics on the timescale of 10s of kHz or faster.

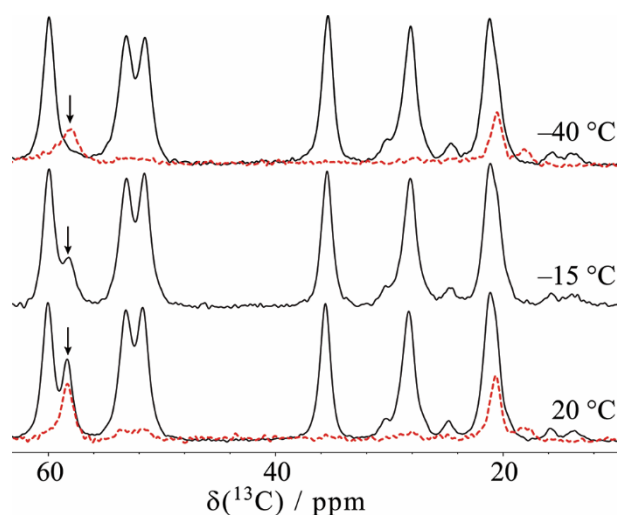


Figure 3.34. ^{13}C CPMAS (solid lines) and direct-excitation (dashed lines, 20 °C and -40 °C) spectra of S_{Et} at different temperatures. The signal from ethanol CH_2 is marked with an arrow.

The ^{13}C T_1 relaxation times measured as a function of temperature provide further insight into the dynamics of the ethanol molecules. These are tabulated in Table S2 in Appendix 10 and plotted in Figure 3.35. The relaxation times of both ethanol carbon atoms are relatively short e.g. 1.04 s for the CH_2 and 0.8 s for the CH_3 at 20 °C, compared to at least 50 s for the carbon atoms in droperidol. The steady decrease in T_1 relaxation time of the CH_3 carbon with decreasing temperature is consistent with the approach towards a T_1 minimum. Assuming Arrhenius-type behaviour, fitting the linear regime (i.e. excluding the data point at -40 °C) gives an activation barrier, E_a , of 15.1 ± 0.6 kJ mol $^{-1}$. This is a typical value for rotational diffusion of the methyl group^{60, 70, 315}, although it should be noted that a more extensive data set encompassing the T_1 minimum would provide much more robust figures. The interpretation of the CH_2 carbon data is less straightforward, but its rapid relaxation implies that there are significant local dynamics of the CH_2 over the full temperature range. While ^{13}C relaxation rates will be dominated by dipolar relaxation driven by modulations of the CH heteronuclear couplings, there will also be a contribution from cross-relaxation to any rapidly relaxing ^1H spins. Faster ^1H T_1 relaxation at lower temperatures allowed the recycle delays to be reduced from 12 s at 20 °C to 6 s at -40 °C, suggesting that the decrease in the ^{13}C T_1 of the CH_2 in the low-temperature limit may be related to faster cross-relaxation to ^1H (associated with the methyl group re-orientation). The ^{13}C T_1 of the CH_2 also decreases in the high temperature limit, where the methyl group dynamics is not contributing so effectively to T_1 relaxation. This suggests that there are additional dynamic processes that become more effective at driving the spin-lattice relaxation in the high temperature regime (and so are likely to have higher activation barrier than methyl rotation). Such processes would need to be of the order of the ^{13}C Larmor frequency (in this case 125 MHz) at 20 °C, which could also be consistent with a process that is of the order of 10s kHz at -40 °C (as observed via the spectra).

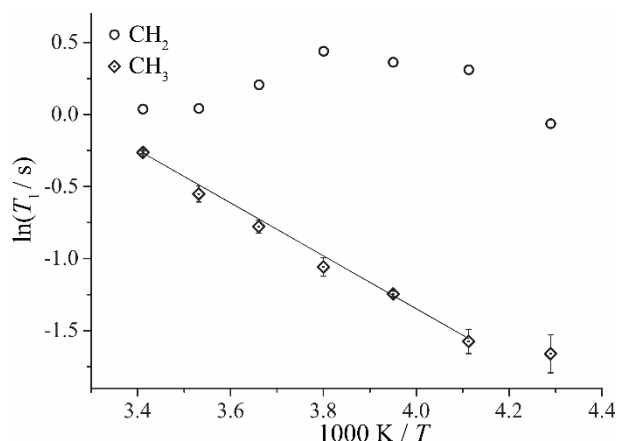


Figure 3.35. ^{13}C T_1 relaxation times for the ethanol carbons of \mathbf{S}_{Et} as a function of inverse temperature. The one-standard-deviation error bars on the fitting of CH_2 T_1 values are of the order of the size of symbols used.

The T_1 relaxation times of methyl group carbons in methanol and acetonitrile molecules are much longer than in the ethanol solvate, 5.1 and 17 s at 20 °C respectively (see Table S2 in Appendix 10), and show the opposite temperature dependence (i.e. decreasing with increasing temperature). Bearing in mind the difficulties of interpreting relaxation data at some distance from the T_1 minimum, this suggests that the barrier for methyl group re-orientation in these solvates (and the acetonitrile solvate in particular) is significantly higher, and that the T_1 minimum is well above ambient temperature. There is also no evidence for additional high-frequency motions.

The ^2H MAS spectra of the alcohol solvates prepared from d_1 -alcohols were very similar, showing resonances both from the deuterated solvent, at about 4.0 ppm, and the labile NH site of droperidol, at about 10.5 ppm. Figure 3.36 shows the spectra for \mathbf{S}_{Et} ; and spectra of \mathbf{S}_{Me} is almost identical. Fitting the bandshape from both of the deuterium sites, quadrupolar coupling parameters were determined in pNMRsim²⁸⁴. The quadrupolar coupling parameters for the alcohol OD determined from the spectra at 20 °C were found to be the same within experimental error, $\chi = 206$ kHz, $\eta = 0.17$. The fitted quadrupolar coupling constants were slightly larger at -45 °C: $\chi = 211$ kHz for \mathbf{S}_{Me} and 222 kHz for \mathbf{S}_{Et} , with $\eta = 0.17$. The uncertainties on χ and η are estimated to be 2 kHz and 0.02 respectively, on the basis of duplicate measurements and different processing methods used to obtain flat spectral baselines. These parameters are consistent with values calculated by the GIPAW calculations, $\chi = 244\text{--}246$ kHz, $\eta = 0.15$, but reduced by high frequency motions of increasing amplitude as the temperature is increased³¹⁶. Note that flipping of the solvent molecules through the inversion centre will not change the quadrupolar coupling tensor orientation and so would not have a direct effect on the spectrum.

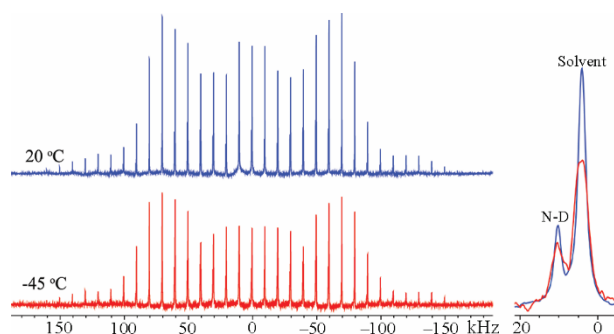


Figure 3.36. ^2H MAS spectra at a spinning rate of 10 kHz for S_{Et} at 20 and $-45\text{ }^\circ\text{C}$, with the centreband region expanded on the right.

In contrast to the ^2H spectra, which might suggest that the solvent molecules are essentially static, the ^2H T_1 relaxation times for the alcohol OD group were short (estimated to be 0.1 – 0.3 s) at both measurement temperatures ($-45\text{ }^\circ\text{C}$ and $20\text{ }^\circ\text{C}$). Again, a simple flip of solvent molecules through an inversion centre cannot itself explain the fast relaxation, since the quadrupolar tensor is left unchanged. This implies that multiple high-frequency processes are active, resulting in fast relaxation rates that are not significantly temperature dependent, i.e. there is no single motional process creating a well-defined T_1 minimum. We have previously observed small amplitude motions that are large enough to drive relaxation but too small to significantly average the quadrupolar coupling constant⁷⁰. The crystal structure solution and the averaged chemical environments for the droperidol molecules in the unit cell indicate that the solvent molecules are also flipping orientations, but the ^2H NMR data and the ^{13}C relaxation times are not sensitive to this process. The most likely scenario is that the alcohol molecules are relatively dynamic within their lattice sites and also occasionally flip over to the equivalent site related by the inversion symmetry.

Nonstoichiometric hydrate. Reduction of the temperature to $-40\text{ }^\circ\text{C}$ noticeably changed the ^{13}C CPMAS spectra of **NSH**, Figure 3.37. The largest changes are for the signals from C9 and C4, both of which are close to the water molecules – C9 is even weakly hydrogen bonded with the water (see Section 3.3) – suggesting changes in the dynamics and/or average structure of the water molecules. The relatively short (largely temperature independent) ^1H T_1 relaxation time of about 15 s observed in the ^{13}C CP experiments is consistent with motion of the water molecules; droperidol phases without mobile solvent molecules, S_{ACN} , S_{NM} , polymorph **II** and dihydrate, showed T_1 values in excess of 2 min, which is more typical of molecular solids lacking methyl groups to drive relaxation.

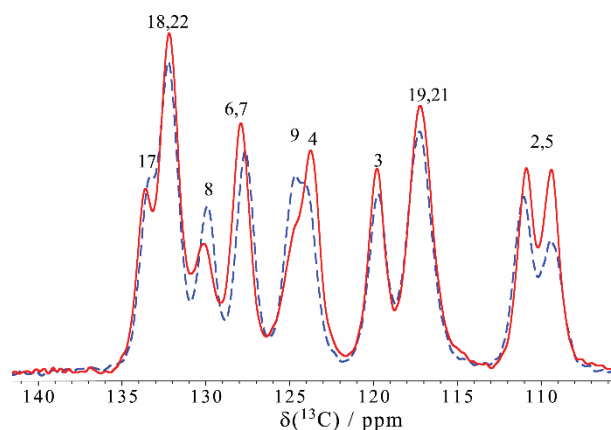


Figure 3.37. ^{13}C CPMAS spectra of **NSH** at 20 °C (solid line) and -40 °C (dashed line).

Figure 3.38 shows ^2H MAS spectra of **NSH** prepared from D_2O as a function of temperature. Very different bandshapes and temperature dependence are observed compared to the alcohol solvates. The water signal in **NSH** has narrower bandshape with partially averaged quadrupolar coupling parameters: χ was 84 ± 3 kHz, while η was more variable, in the range 0.6 to 1.0, depending both on water content and temperature. This dependence on the water content presumably reflects changes in the overall dynamics with the degree of occupancy of water sites. While the possibility of distinct populations of static vs. dynamic water molecules can be ruled out, it is difficult to distinguish whether there is a distribution of similar water environments or a single averaged water environment with fast exchange between sites. Reducing the temperature clearly broadens the lines corresponding to D_2O , Figure 3.38 (b), implying the water is highly dynamic at ambient temperature and that some aspect of the dynamics is being slowed to the 10s kHz frequency scale at -45 °C. The overall quadrupolar coupling constants are somewhat lower than those typically reported for water molecules undergoing rapid C2 flips⁶⁶⁻⁶⁸, suggesting that the overall dynamics is more complex. Moreover a simple C2 flip motion would produce η values of unity and would not explain the relatively high displacement parameters for water oxygen site observed in XRD. As would be expected, the ^2H T_1 relaxation times for the water sites are very short, estimated to be <0.1 s from experiments with variable recycle delays. T_1 relaxation times of ND sites were 1–3 s, comparable to values observed for deuterium sites without high-frequency dynamics. The larger intensity of the ND signal in Figure 3.38 (a), probably reflects that the fact that the hemihydrate sample was stored for longer in the D_2O atmosphere than the monohydrate sample.

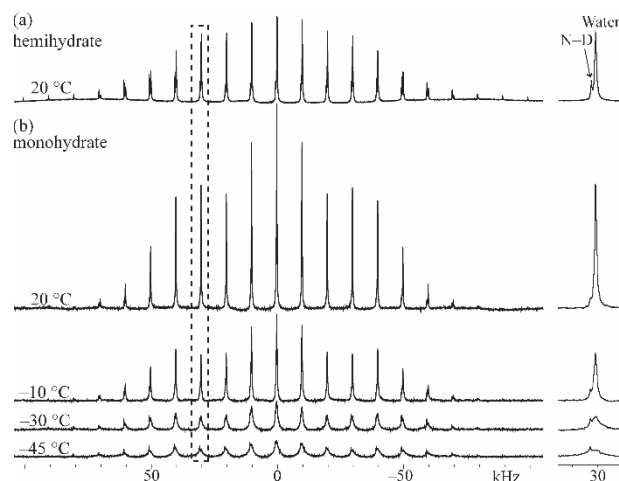


Figure 3.38. ^2H MAS spectra at a spinning rate of 10 kHz of **NSH** with (a) hemihydrate stoichiometry at 20 °C, and (b) monohydrate stoichiometry at different temperatures. The insets show the spinning sideband at about 30 kHz (marked with dashed rectangle), as the ND signal is clearer here than in the centreband. The spectra have the same vertical scale.

To quantify the motional broadening seen in Figure 3.38, the linewidths of the D_2O peaks (LW) were determined from the bandshape fitting of the spinning sideband manifold. The motional broadening was estimated by subtracting the width of the ND resonance ($LW_0 = 160$ Hz), which is assumed to be unaffected by the water dynamics. The plot of linewidth due to motional broadening⁶⁵ against inverse temperature, Figure 3.39, is linear over this temperature range allowing an Arrhenius-type activation barrier to be determined, $E_a = 25 \pm 3$ kJ mol⁻¹. Note that in this fast exchange limit, the constant of proportionality between the motional broadening and the rate of dynamics is related in a non-trivial way to the quadrupolar parameters and motional mechanism. Moreover, the physical significance of the derived activation parameter is limited given both the non-trivial nature of the motion and the restricted temperature range covered.

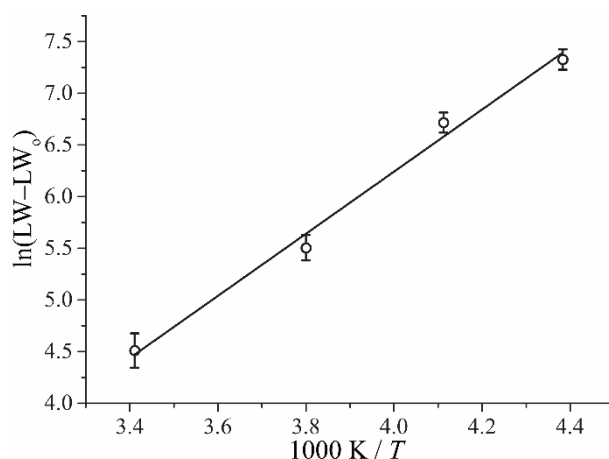


Figure 3.39. Estimated motional line broadening of the ^2H D_2O resonance of **NSH** as a function of inverse temperature. The “error bar” indicates the maximum and minimum linewidths observed using different methods for bandshape fitting / baseline roll suppression (see Section 2.13).

3.5.4 Theoretical analysis of the differences in solvent molecule behaviour

In order to rationalize the observed differences in the solvent molecule dynamics between the different droperidol solvates, the energy difference was determined between structures where all the solvent molecules in a channel point in the same direction and where adjacent solvent molecules point in opposite directions. As a first step, the orientation of the solvent molecule in each hemisolvate crystal structure was approximately reversed and geometry optimization in CASTEP used to relax all the atomic positions. The tiny energy differences of up to 0.3 kJ cell⁻¹ (equivalent about 3×10^{-7} of the total cell energy) between the energies of these nominally identical unit cells gives an estimate of the “error bar” in this type of calculation. The unit cell dimensions were then doubled in the solvent channel (*a*-axis) direction and the orientation of one solvent molecule was reversed. The energy differences (per unit cell / droperidol molecule) between the “same direction” and “opposite direction” structures after full geometry optimization, with and without dispersion correction, are shown in Table 3.11. It can be seen that the cell energies are essentially the same for **S_{Et}**, particularly when the dispersion-corrected functional is used. In contrast, the “same direction” structure is slightly energetically more favourable for **S_{Me}**, and is significantly more energetically favourable for **S_{NM}** and **S_{ACN}**.

Table 3.11. Increase in unit cell total energy (in kJ cell⁻¹) of droperidol solvates when adjacent solvent molecules are positioned in the opposite direction, with and without dispersion correction (+TS).

Solvate	S_{Et}	S_{Me}	S_{NM}	S_{ACN}
PBE	-1.5	2.9	9.9	26.3
PBE+TS	-0.4	3.7	12.6	26.9

Pairwise interaction energies were also calculated to provide insight into the energetics of different relative solvent orientations. Interaction energies (the difference in energy between two separated molecules and their dimer) were calculated using *Gaussian 09* between one solvent molecule and the two solvent and eight droperidol molecules that surround the chosen solvent molecule. The co-ordinates of these ten molecular pairs were extracted from the optimized “same direction” and “opposite direction” crystal structures, and the overall interaction energy approximated as the sum of these ten pairwise interaction energies. In the case of the “opposite direction” structure, adjacent solvent molecules can either be oriented “head-to-head” (HH) or “tail-to-tail” (TT), see Figure S11 in Appendix 10, along the *a*-axis direction. As required from the inversion symmetry, the total interaction energy of the solvent with its surroundings is the same, within the calculation accuracy, for the two solvent arrangements in “opposite direction” structure. As shown in Figure 3.40, the total interaction energy is essentially identical for the “same direction” and “opposite direction” structures in the case of **S_{Et}**. In contrast, the interaction energies are much more favourable for the “same direction” structure for **S_{NM}** and **S_{ACN}**. These trends are fully

consistent with the pattern of total unit cell energies as observed above. As shown in Figure 3.40 and tabulated in Table S5 in Appendix 10, the most significant factor (at least 87%) contributing to the difference in interaction energies are the solvent-solvent interactions. The solvent-solvent interactions are always attractive in the “same direction” structure, whereas the interactions between nitromethane and acetonitrile molecules change by 13–18 kJ mol⁻¹ from attractive to repulsive in the “opposite direction” structure.

These results provide a straightforward rationalisation of the absence of solvent disorder in the **S_{ACN}** and **S_{NM}** solvates – where there is a strong energetic preference for the solvent molecules to be consistently oriented – and the presence of solvent molecule disorder in **S_{Me}** and **S_{Et}**, where there is little energetic preference for a consistent orientation.

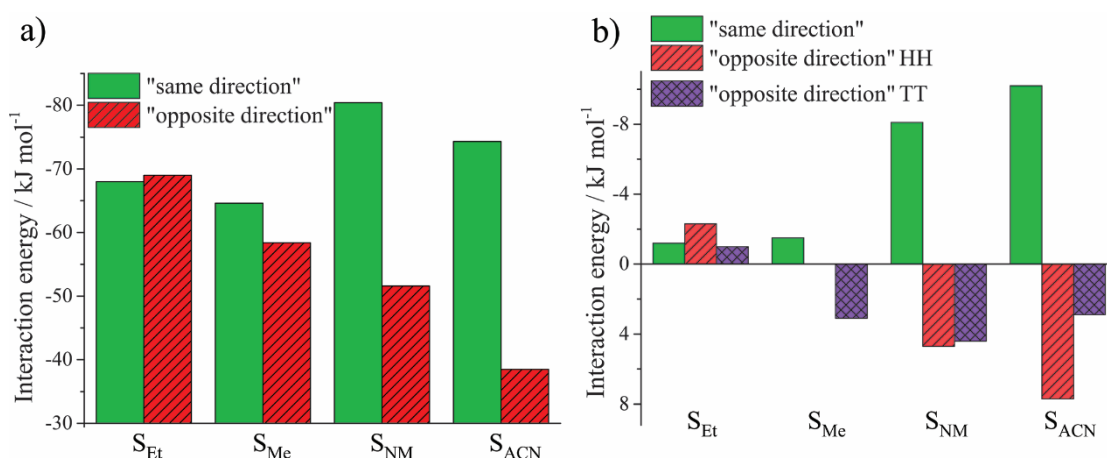


Figure 3.40. Calculated (a) total pair-wise interaction energies of solvent molecules and (b) solvent-solvent interaction energies, in “same direction” and “opposite direction” droperidol solvate structures.

3.5.5 Conclusions

The ¹³C CPMAS solid-state NMR spectra of a set of isostructural solvates of droperidol (**NSH**, **S_{Me}**, **S_{Et}**, **S_{ACN}** and **S_{NM}**) confirm that the solvent molecules have only minor effect on the chemical environment of the droperidol molecules. The relatively broad linewidths, which make it difficult to resolve the inequivalence of the droperidol molecules in the **S_{ACN}** and **S_{NM}** solvates, can be explained by high anisotropy of the bulk magnetic susceptibility. The nature of the disorder was somewhat easier to resolve in the ¹⁵N CPMAS spectra, where dynamic disorder in the **S_{Me}** and **S_{Et}** results a single sharp set of peak for the droperidol nitrogen sites.

Variable-temperature ¹³C and ²H spectra and measurements of spin-lattice relaxation times allow the characterization of the solvent molecule dynamics in **NSH**, **S_{Me}** and **S_{Et}**. The motion of the alcohol molecules in **S_{Me}** and **S_{Et}** contains dynamics of relatively high-frequency (on the order of 10s MHz to drive ²H and ¹³C *T*₁ relaxation), but of limited amplitude (given the minimal averaging of the ²H quadrupolar parameters). The absence of well-defined *T*₁ minima suggests that this is a complex motion. The dynamics also includes components on the 10s kHz frequency scale

(observed via the ^{13}C spectra) and allows for occasional flipping over to the equivalent state related by the inversion symmetry, although the rate of this process cannot be estimated with any precision; the ^{15}N spectra set a lower limit of about 40 Hz at ambient temperature (corresponding to collapsing a frequency difference of about 1 ppm at 40.53 MHz ^{15}N Larmor frequency). The motion of the water molecules in **NSH** is also expected to be a composite motion, resulting in greater averaging of the NMR parameters than a simple C2 flip between equivalent positions, with an estimated C2 flip rate on the order of 10s kHz in $-45\text{ }^\circ\text{C}$ temperature, although an Arrhenius-type activation barrier of $E_a = 25 \pm 3\text{ kJ mol}^{-1}$ could be estimated in this case.

The computational simulations help to rationalise these observations. There is little energy difference between initial and final states for inverting the orientation of the alcohol molecule in the **S_{Me}** and **S_{Et}** solvates. Although the barrier to inversion may be relatively high, this means that the solvent molecules appear to be disordered between the two symmetry-equivalent positions over the timescale of the XRD and NMR experiments. In contrast, the unfavourable energetics associated with adjacent acetonitrile and nitromethane molecules having opposite directions means that the **S_{ACN}** and **S_{NM}** are strongly ordered on the NMR and XRD timescales. These unfavourable energetics are mostly associated with solvent-solvent interaction energies.

3.6 Structural Characterization and Rationalization of Formation, Stability, and Transformations of Benperidol Solvates

A study of the solvate formation of droperidol (Section 3.3) showed that it exists as four polymorphs and eleven solvates. Benperidol is very similar to droperidol and also has three strong hydrogen bond acceptors and only one hydrogen bond donor, suggesting it could be a promiscuous solvate former³⁰⁵. In this study we tried to explore, understand, and rationalize the benperidol solvate formation, stability, and phase transformations. Benperidol was crystallized from solvents belonging to different solvent classes, the obtained solvates were characterized, and their crystal structures, as well as solvent and benperidol properties were used to rationalize their formation. The desolvation process and products were rationalized based on crystal structure and relative stability of non-solvated forms. Crystal structures of solvates were compared to rationalize the relative stability of solvates and the observed frequency of the solvate formation in the crystallization experiments.

3.6.1 Crystallization

Benperidol was crystallized from a range of solvents selected to represent different solvent classes based on classification according to statistical analysis of four molecular descriptors¹³⁹, as well as hydrogen bond acceptor and donor propensity, polarity/dipolarity, dipole moment, and dielectric constant¹⁴⁰. In these experiments no new benperidol polymorphs were obtained, see Table S1, Appendix 11. Moreover, in our experiments it was not possible to obtain polymorph **III** neither from *n*-heptane as described in the literature²⁶², nor from any other solvent. From most of the solvents polymorph **I** was obtained. In accordance to previous studies^{262, 268}, it was possible to crystallize polymorph **II** from isopropanol. However, the precipitation of the solid product from isopropanol usually initiated shortly after cooling the solution, and polymorph **I** was obtained instead.

Nevertheless, besides the already reported solvates **DH** and **S_{Et}**^{262, 268}, nine new solvates were obtained in crystallization experiments from methanol, acetonitrile, ethyl acetate, nitromethane, 1,4-dioxane, toluene/*o*-xylene, benzyl alcohol, carbon tetrachloride, and chloroform (labelled as **S_{Me}**, **S_{ACN}**, **S_{EtOAc}**, **S_{NM}**, **S_{DIOX}**, **HH**, **S_{Benz}**, **S_{TCC}**, and **S_{CLF}**, respectively). In this study, the first seven of these solvates, as well as the poorly explored solvated forms **S_{Et}** and **DH** were characterized using PXRD patterns, DTA/TG analysis, and IR spectra, while their desolvation products were also identified, and the desolvation process was characterized. Preparation of solvates **S_{TCC}** and **S_{CLF}** was complicated by the formation of side-products and poor reproducibility, so these solvates were characterized only using PXRD and DTA/TG analysis. Crystals suitable for SCXRD measurements were obtained for polymorph **II** and solvates **DH**, **S_{Et}**, **S_{Me}**, **S_{ACN}**, and **S_{EtOAc}**.

Additionally, attempts were made to solve the crystal structures of the rest of the phases by using the recorded PXRD patterns, with success for **HH**, **S_{Benz}**, and the polymorph **III**.

3.6.2 X-ray diffraction and thermal characterization of benperidol solvates

The PXRD patterns of all the obtained solvated forms are given in Figure 3.41.

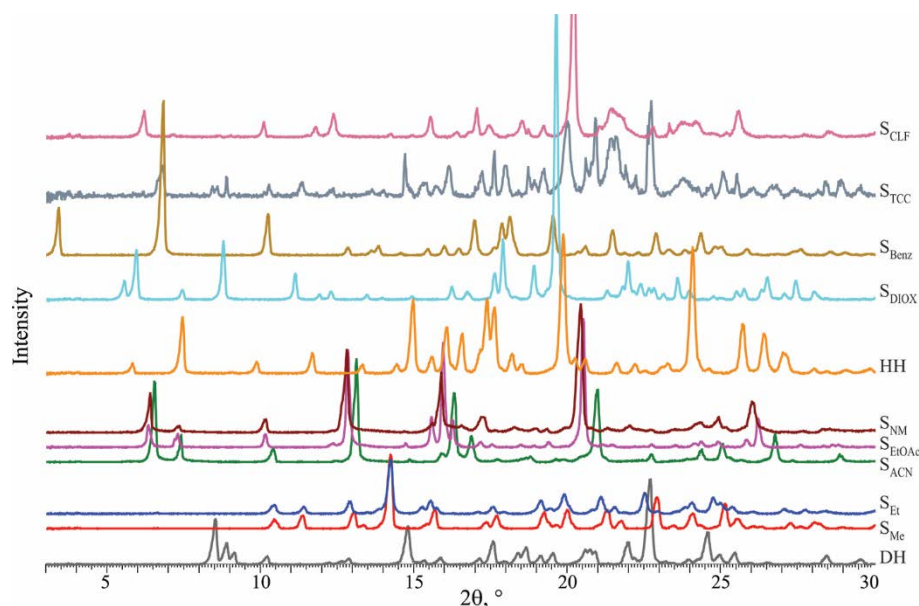


Figure 3.41. PXRD patterns of the benperidol solvates.

It can be seen that the diffraction peak positions of solvates **S_{Me}** and **S_{Et}** were very similar. The same was found also for solvates **S_{ACN}**, **S_{EtOAc}**, and **S_{NM}**. These similarities suggest the formation of two sets of benperidol isostructural solvates: type 1 solvates (**S_{Me}** and **S_{Et}**), and type 2 solvates (**S_{ACN}**, **S_{EtOAc}**, and **S_{NM}**). The PXRD patterns of **HH**, **S_{Benz}**, **S_{DIOX}**, and **S_{TCC}**, however, exhibited different characteristic features, which also differed from those in PXRD patterns of all other known benperidol forms. The PXRD pattern of **S_{CLF}**, however, was similar to that of type 2 solvates, suggesting that this solvate probably also belongs to this type, although poor quality of the pattern did not allow to draw an absolute conclusion.

The DTA/TG curves of the benperidol solvates are shown in Figure 3.42. Although this method allowed to confirm **S_{TCC}** and **S_{CLF}** as solvates, the obtained curves cannot be assured to be characteristic for pure phases.

The desolvation of **DH** and **HH** appeared to be a simple one step process with characteristic desolvation endothermic peak associated with the weight loss. The curves of other solvates, however, showed complex desolvation process. Type 1 and type 2 solvates usually showed two endothermic peaks associated with the weight loss. This suggests that the desolvation occurred in two stages, or other complications were encountered during the desolvation. It was shown that the second desolvation peak corresponded to peritectic desolvation and/or melting, see Section 3.6.5. Although the desolvation of **S_{Benz}** most probably was also a one step process, it appeared to be complicated by the difficult evaporation of benzyl alcohol ($T_b = 205.3\text{ }^\circ\text{C}$).

Desolvation products of the solvates were analyzed using PXRD and are given in Table 3.12.

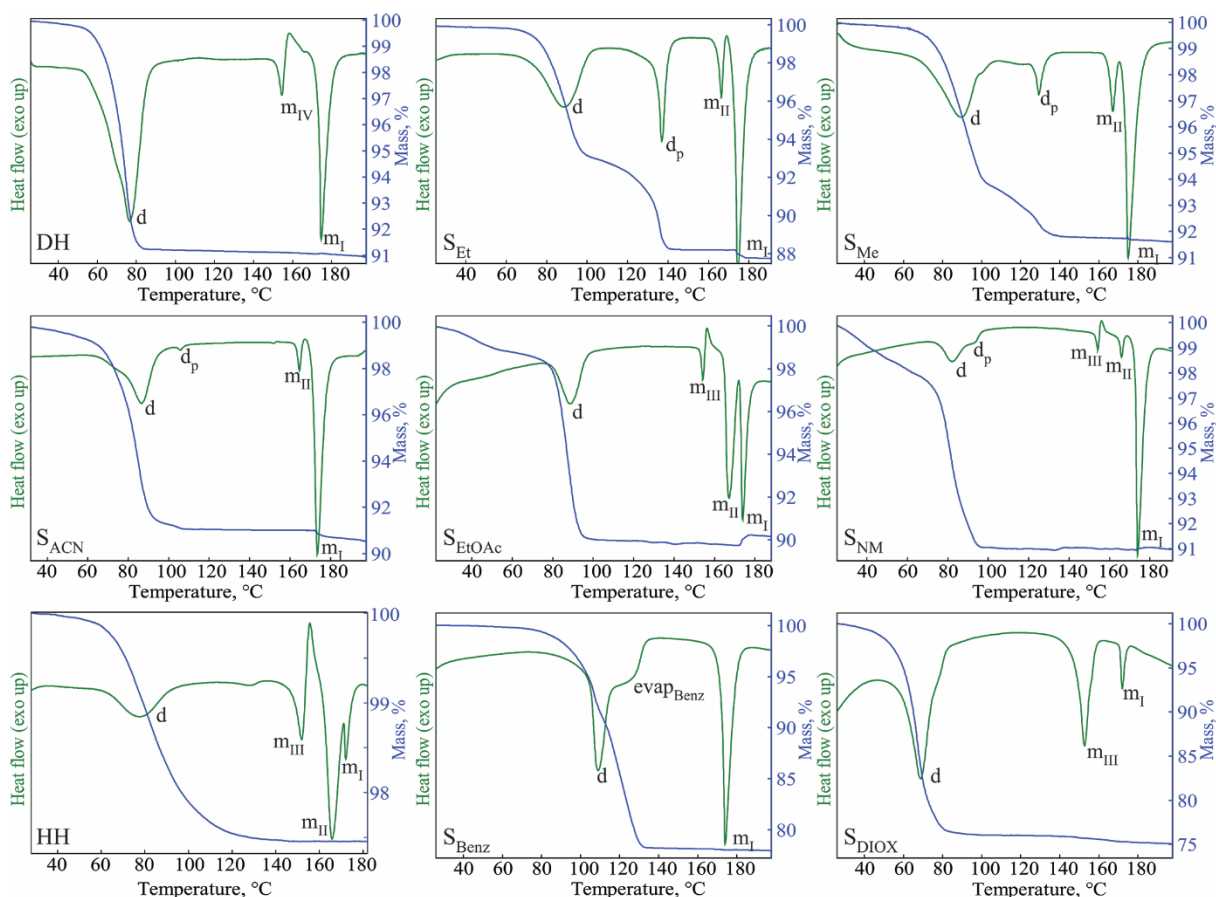


Figure 3.42. The DTA and TG curves of benperidol solvates. d – desolvation, d_p – peritectic desolvation and/or melting, m_{I-IV} – melting of polymorphs I – IV, and $evap_{Benz}$ – evaporation of benzyl alcohol.

Table 3.12. Weight loss observed during the desolvation of benperidol solvates and the obtained desolvation products.

Solvate	Ratio	Calculated weight loss, %	Observed weight loss, %	$T_{desolvation}, ^\circ C$ (peak)	Resulting phase
DH	1:2	8.6	8.8 (9.0) ^a	77	(V, IV)/(II, I) ^c
S_{Me}	1:1	7.8	7.9	89, 129 ^b	II/I ^c
S_{Et}	1:1	10.8	11.6	87, 137 ^b	II/I ^c
S_{ACN}	1:1	9.7	8.1-9.5 ^d	86, 106 ^b	III/I ^c
S_{NM}	1:0.5	7.4	6.9-9.0 ^d	82, ~95 ^b	III/I ^c
S_{EtOAc}	1:0.5	10.4	8.5-9.8 ^d	88	III/I ^c
HH	1:0.5	2.3	2.0–2.5 (2.1) ^a	89	III/I ^c
S_{Benz}	1:1	22.1	21.8	109	I
S_{DIOX}	1:1.5	25.7	24.5	69	III/I ^c
S_{TCC}	1:1	16.8	16–22	66, 88	IV, V, II, I
S_{CLF}	1:0.5	13.5	10–17	76	III/I

^a – the water content determined by Karl Fischer titration is given in parentheses.

^b – the second value is peritectic decomposition and/or melting temperature.

^c – see discussion in Section 3.6.5.

^d – the first number is the weight loss after the appearance of the desolvation peak in the DTA, and the second number is the total weight loss.

Besides the polymorphs **I** and **II** obtained in the crystallization, desolvation of type 2 solvates, **HH**, **S_{DIOX}**, and **S_{CLF}** produced the polymorph **III** described in the literature²⁶², whereas the desolvation of **DH** produced new polymorphs **IV** and **V**. The PXRD patterns of benperidol polymorphs are given in Figure S2, Appendix 11, while the DTA curves are given in Figure S3, Appendix 11.

Therefore, the existence of polymorph **III** as described in the literature²⁶² has been confirmed²⁶⁸, although it is not clear whether it is possible to obtain it as described²⁶², because in our study it was obtained only in the desolvation process.

The stoichiometry of the solvates was calculated from the weight loss in TG curves. The **DH** phase was confirmed to be a dihydrate, whereas **S_{Et}** was determined to be an ethanol monosolvate, in contrast to the reported ethanol disolvate stoichiometry²⁶². With regard the isostructural type 2 solvates, the **S_{ACN}** phase was monosolvate, whereas **S_{NM}** and **S_{EtOAc}** appeared to be hemisolvates. Both TG and KF titration confirmed that **HH** is a hemihydrate. Repeated measurements suggested that **S_{DIOX}** is a sesquisolvate, although this should be interpreted cautiously.

Crystal structures of benperidol polymorph **II**, and solvates **DH**, **S_{Et}**, **S_{Me}**, **S_{ACN}**, and **S_{EtOAc}** were determined from SCXRD measurements at 173 K or 100 K (**S_{EtOAc}**), while those of polymorph **III**, as well as solvates **HH** and **S_{Benz}** were determined from PXRD data collected in transmission mode at ambient temperature. The obtained crystallographic data are given in Table 3.13. An overlay of the experimental data and PXRD patterns simulated from crystal structure data confirmed the identity of the polycrystalline phases. The correctness of the structures calculated from PXRD patterns was confirmed by the good agreement between experimental and calculated diffraction patterns (see Figure 3.43), as well as by the geometry optimization in CASTEP introducing only small changes in the crystal structure. Polymorphs **II** and **III** crystallized in the space group $P\bar{1}$ with three molecules or one molecule in the asymmetric unit, respectively. The **DH** form crystallized in the $P2_1/n$ space group, **S_{Et}** and **S_{Me}** were isostructural and crystallized in the $P2_1/c$ space group, **S_{ACN}** and **S_{EtOAc}** were isostructural and crystallized in the $P\bar{1}$ space group, **HH** crystallized in the $C2/c$ space group, and **S_{Benz}** - in the $Pbca$ space group. The asymmetric units of all solvated forms contained one benperidol molecule and two (**DH**), one (**S_{Me}**, **S_{Et}**, **S_{ACN}**, and **S_{Benz}**), or one half (**HH** and **S_{EtOAc}**) solvent molecules. In the **HH** form, the oxygen atom of water molecule was at a special position, and the ethyl acetate molecule in **S_{EtOAc}** was disordered over two symmetrically related positions. The solvent stoichiometry determined from this analysis was consistent with that determined from TG analysis.

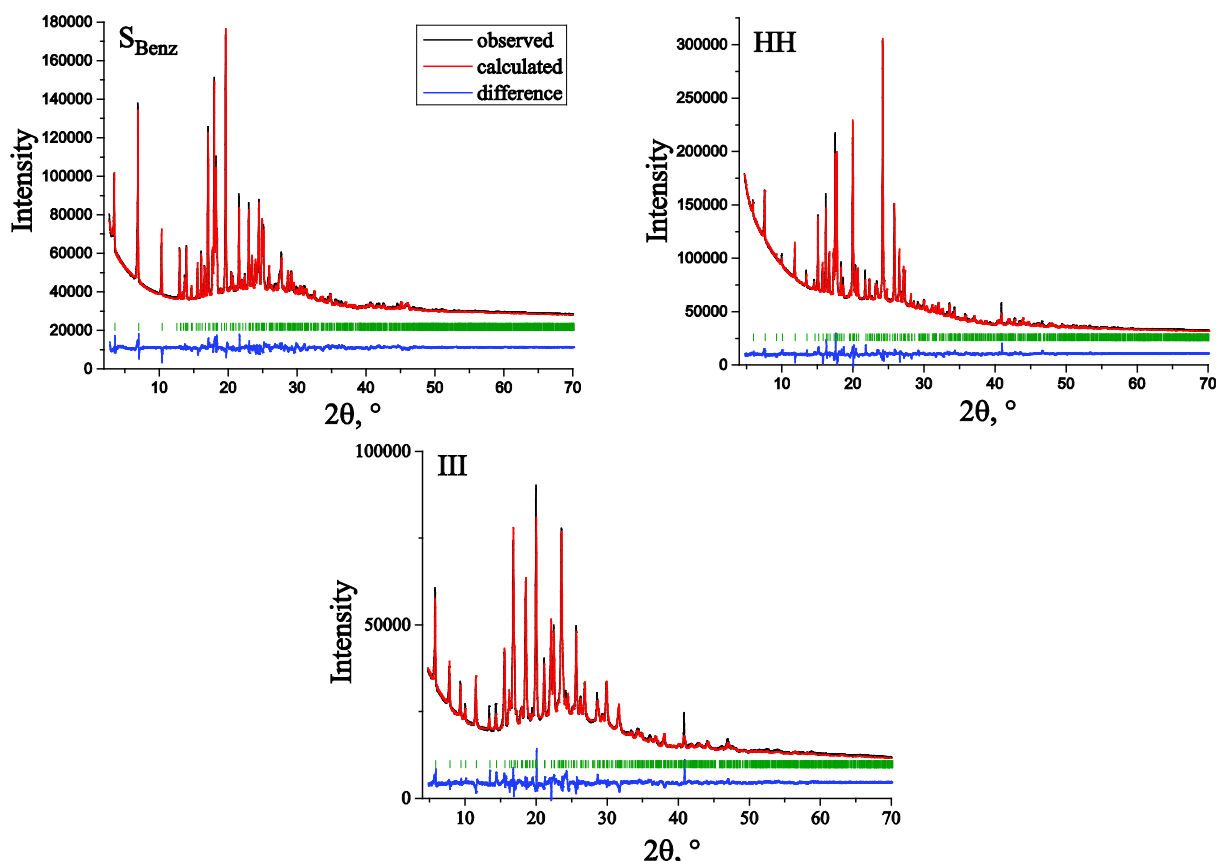


Figure 3.43. Experimental (black), calculated (red), and difference (dark blue) PXR D profiles from the final Rietveld refinement of various benperidol forms.

Table 3.13. Crystallographic data for the benperidol phases **II**, **DH**, **S_{Et}**, **S_{Me}**, **S_{ACN}**, **S_{EtOAc}**, **HH**, **S_{Benz}**, and **III**.

Solvate	II	DH	S_{Et}	S_{Me}	S_{ACN}	S_{EtOAc}	HH	S_{Benz}	III
Empirical formula	C ₂₂ H ₂₄ FN ₃ O ₂	C ₂₂ H ₂₄ FN ₃ O ₂ · 2H ₂ O	C ₂₂ H ₂₄ FN ₃ O ₂ · C ₂ H ₆ O	C ₂₂ H ₂₄ FN ₃ O ₂ · CH ₄ O	C ₂₂ H ₂₄ FN ₃ O ₂ · C ₂ H ₃ N	C ₂₂ H ₂₄ FN ₃ O ₂ · 0.5C ₄ H ₈ O ₂	C ₂₂ H ₂₄ FN ₃ O ₂ · 0.5H ₂ O	C ₂₂ H ₂₄ FN ₃ O ₂ · C ₇ H ₈ O	C ₂₂ H ₂₄ FN ₃ O ₂
M _r	381.44	417.48	427.51	413.48	422.49	425.49	390.45	489.58	381.44
Crystal system	triclinic	monoclinic	monoclinic	monoclinic	triclinic	triclinic	monoclinic	orthorhombic	triclinic
Space group	$\bar{P}1$	$P2_1/n$	$P2_1/c$	$P2_1/c$	$\bar{P}1$	$\bar{P}1$	$C2/c$	$Pbca$	$\bar{P}1$
a (Å)	10.8417(3)	11.0595(3)	15.0684(3)	15.1097(4)	5.56500(10)	5.4228(3)	36.7342(7)	13.7193(4)	15.61501(10)
b (Å)	16.2903(4)	9.3896(2)	10.8602(3)	10.7200(3)	14.1256(4)	14.6014(8)	5.58581(10)	51.6467(20)	11.48189(8)
c (Å)	17.9497(5)	20.4456(6)	15.2555(4)	15.3070(5)	15.0478(5)	14.8045(10)	23.6629(5)	7.43071(20)	5.45694(30)
α (°)	66.7233(11)	90	90	90	109.2583(13)	109.936(3)	90	90	86.627(3)
β (°)	87.0069(10)	91.7206(11)	117.6353(9)	119.3538(13)	90.9875(13)	90.199(2)	124.8680(8)	90	96.618(6)
γ (°)	85.0074(16)	90	90	90	100.071(2)	100.322(3)	90	90	94.435(5)
V (Å ³)	2900.55(13)	2122.20(10)	2211.69(9)	2161.04(11)	1095.91(5)	1081.50(11)	3983.71(14)	5265.07(30)	967.71(6)
Z/Z'	6/3	4/1	4/1	4/1	2/1	2/1	8/1	8/1	2/1
T, K	173(2)	173(2)	173(2)	173(2)	173(2)	100(2)	298(3)	298(3)	298(3)
wR (all data)	0.1616	0.196	0.1415	0.1997	0.1126	0.1992			
final R (I > 2σ) ^a	0.0765	0.048	0.0543	0.0644	0.0460	0.0751			
GOF	1.013	1.243	1.028	0.972	1.018	1.030			
R _{wp}							0.02897	0.03356	0.03686
R _p							0.01721	0.02427	0.0243
R _{exp}							0.00520	0.00734	0.00816
Pacing coef.	0.682	0.689	0.684	0.672	0.681	0.690	0.675	0.651	0.681

^a For the **DH** form I > 3σ.

3.6.3 Characterization of benperidol solvate crystal structures

Analysis of the crystal structures revealed that the conformation differences appear as different values of the dihedral angles $\tau_1 - \tau_6$, although the oxobutyl side chain ($\tau_3 - \tau_6$) tends to be linear. Interestingly, molecular conformation of benperidol in polymorphs **I** and **III**, as well as that in all of its solvates is quite similar, but different from all three benperidol molecules in the polymorph **II**, with the most apparent difference observed for the value of τ_1 (see Figure 3.44 (a) and Table 3.14). The molecular conformation of all three symmetrically independent molecules in **II** (designated as A, B, and C) was different, with slight variations in the conformations of A and C, and significant variations in the dihedral angles τ_2 and τ_4 for molecule B. As already mentioned, besides the identical conformations observed in the isostructural solvates **S_{Me}** and **S_{Et}** as well as in **S_{ACN}** and **S_{EtOAc}**, the conformation of all solvates and polymorph **III** were nearly identical, with the exception of **S_{Benz}**, which had a noticeable deviation of the dihedral angles τ_2 and τ_4 (see Figure 3.44(b) and Table 3.14). It should, however, be mentioned that the geometry optimization in CASTEP changed the geometry of oxobutyl side chain by making it more similar to that in the rest of the solvates. Therefore, the overall conformation differences of benperidol were small if compared to other molecules with similar conformational degrees of freedom^{84,91}, and the observed structural diversity resulted from different intermolecular interaction possibilities producing different molecular packing.

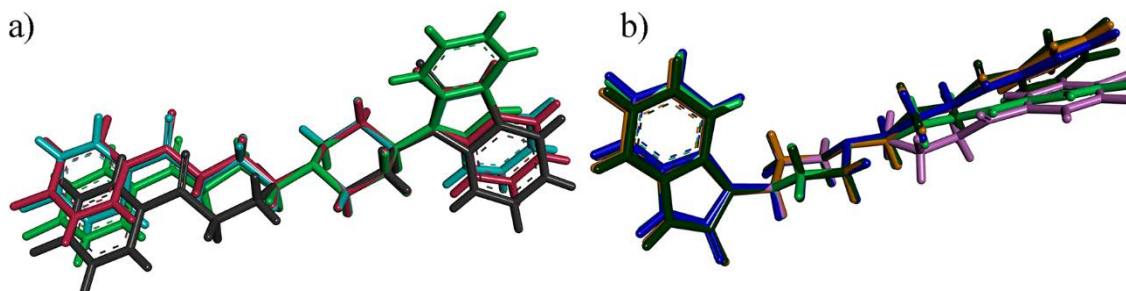


Figure 3.44. An overlay of benperidol molecules in a) polymorphs (**I**: green, **II_A**: red, **II_B**: dark grey, **II_C**: cyan), b) solvates (**DH**: dark blue, **S_{Et}**: dark green, **S_{ACN}**: orange, **S_{Benz}**: pink) and polymorph **I** (green).

Table 3.14. Dihedral angles (in degrees) of benperidol in its polymorphs and solvates.

	I ²⁶⁷	II_A	II_B	II_C	DH	S_{Et}	S_{ACN}	HH	S_{Benz}	III
τ_1	-124.03	74.00	92.67	64.60	-108.82	-108.29	-113.17	-114.21	-123.07	-108.93
τ_2	-60.75	-157.37	-68.78	-156.47	-60.65	-72.75	-71.46	-72.09	-21.19	-75.32
τ_3	-172.82	175.51	-177.09	-177.98	-167.59	-176.74	-169.39	-148.24	-165.54	-162.38
τ_4	-166.14	171.94	74.07	175.18	-175.91	-179.91	-174.13	-152.45	138.78	-165.18
τ_5	-176.79	-179.31	-172.78	-173.37	179.6	-179.58	-175.07	163.25	172.75	177.45
τ_6	-177.47	155.52	161.46	-177.79	-178.83	178.82	-178.18	169.07	-149.71	170.13

The analysis of strong hydrogen bonding pattern showed that benperidol molecules in the polymorph **I** formed N2-H \cdots N3 bonds creating a ring of 6 molecules characterized by $R_6^6(48)$ graph set, whereas all three molecules in **II** formed amide homodimers linked by N2-H \cdots O1 bonds and characterized by $R_2^2(8)$ graph set (see Figure 3.45 and Table 3.15).

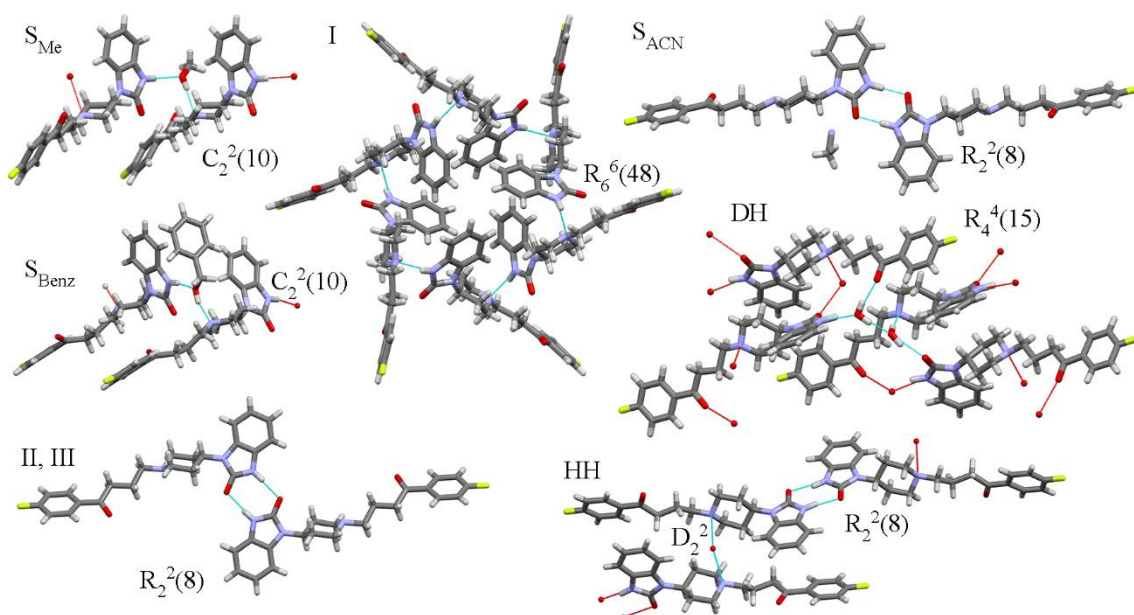


Figure 3.45. Hydrogen bond patterns observed in crystal forms of benperidol.

Table 3.15. Geometrical parameters of the strong hydrogen bonds in benperidol polymorphs and solvates.

Phase	Interaction	Distance, Å			D-H \cdots A, °	Graph set
		X-H	H \cdots A	D \cdots A		
I ²⁶⁷	N2-H \cdots N3			2.883		$R_6^6(48)$
II	N2A-H \cdots O1A	0.86	1.96	2.800(3)	165	$R_2^2(8)$
	N2B-H \cdots O1C	0.86	1.95	2.779(3)	161	$R_2^2(8)$
	N2C-H \cdots O1B	0.86	2.03	2.881(3)	171	$R_2^2(8)$
III	N2-H \cdots O1	0.91	1.97	2.866(9)	167	$R_2^2(8)$
S_{Me}	N2-H \cdots O3	0.86	1.97	2.783(3)	157	$C_2^2(10)$
	O3-H \cdots N3	0.82	2.00	2.806(3)	169	
S_{Et}	N2-H \cdots O3	0.90	1.91	2.7872(19)	164	$C_2^2(10)$
	O3-H \cdots N3	0.82	1.98	2.7931(19)	175	
S_{Benz}	N2-H \cdots O3	0.86	1.99	2.841(7)	169	$C_2^2(10)$
	O3-H \cdots N3	0.90	1.75	2.625(8)	162	
S_{AcN}	N2-H \cdots O1	0.89	1.91	2.7978(16)	177	$R_2^2(8)$
S_{EtOAc}	N2-H \cdots O1	0.86	1.93	2.776(4)	172	$R_2^2(8)$
DH	O4-H \cdots O3	0.92	1.85	2.7271(19)	159	} $R_4^4(15)$
	O4-H \cdots O2	0.85	2.02	2.8597(19)	168	
	N2-H \cdots O4	0.97	1.86	2.7629(18)	153	
	O3-H \cdots O1	0.9	1.98	2.8385(17)	159	
	O3-H \cdots N3	0.87	1.95	2.8122(18)	174	
HH	N2-H \cdots O1	0.90	1.90	2.787(8)	165	$R_2^2(8)$
	O3-H \cdots N3			3.005(15)		D_2^2

The observed conformation differences in benperidol polymorphs, however, could not be purely associated with the difference in strong hydrogen bonds, as benperidol molecules were arranged in amide homodimers also in the form **III**. Nevertheless, other intermolecular interactions in this form were completely different from those in both **II** and **I**.

Although the incorporation of proton donating alcohol molecules in the crystal lattice can provide a possibility for the formation of additional strong hydrogen bonds, only one hydrogen bond acceptor N3 in both type 1 solvates and in \mathbf{S}_{Benz} is employed in similar hydrogen bonding connection with N2-H as observed in form **I**, with alcohol O-H group inserted between the benperidol molecules, and therefore creating two strong hydrogen bonds. However, infinite hydrogen bonded chains $C_2^2(10)$ are formed in these structures. The alcohol molecules in these solvates are positioned in structural voids which can be joined in zigzag shaped channels. However, the diameter of the channel in the narrowest place is smaller than that of the solvent molecules, and alcohol molecules are involved in the formation of the main hydrogen bonding pattern, so these solvates cannot be classified as channel solvates.

In the **HH** and **DH** forms, however, the presence of the water molecules provided for the formation of one additional hydrogen bond in **HH** by employing an additional hydrogen bond acceptor of benperidol molecule, and an efficient hydrogen bonding in **DH** by employing all hydrogen bond acceptors of benperidol. In the **HH** form, benperidol molecules existed as amide homodimers, whereas in the **DH** form benperidol molecules were linked to each other by strong hydrogen bonds via water molecules, and directly interacted only by weak interactions. In these structures, the water molecules were situated in isolated structural cavities, so both of the hydrates were isolated site hydrates.

The insertion of acetonitrile and ethyl acetate molecules, however, could not provide a basis for the emergence of additional strong hydrogen bonds. Benperidol molecules in type 2 solvates formed amide homodimers characterized by $R_2^2(8)$ graph set. The solvent molecules were located in structural channels and interacted with benperidol molecules only by weak hydrogen bonds and dispersion forces. The type 2 solvates thus were typical channel solvates. As ethyl acetate ($81.4 \text{ cm}^3 \cdot \text{mol}^{-1}$) molecules are much larger than acetonitrile ($37.9 \text{ cm}^3 \cdot \text{mol}^{-1}$) molecules, the size of the channel apparently is too small to accommodate 1 equivalent of ethyl acetate, explaining the different stoichiometry observed in type 2 solvates. Ethyl acetate molecules, however, did not occupy the two adjacent solvent sites in one channel but rather two sites from the nearby partially connected channels, see Figure S18, Appendix 11. Interestingly, the molecular size calculation and computational simulation showed that the crystal structure of \mathbf{S}_{NM} should be identical to that of \mathbf{S}_{ACN} with monosolvate stoichiometry (see Appendix 11). This could be explained by a partial desolvation before the experiment, which is supported by the slow desolvation at the beginning of

the TG curve for type 2 solvates (particularly for **S_{NM}**, see Figure 3.42), and can be explained by the fact that solvent molecules are located in the channel and their escape is therefore relatively easy.

A more detailed comparison of the intermolecular interactions was performed through the analysis of weak interactions and 2D fingerprint plots of Hirshfeld surfaces, which summarized the information about intermolecular interactions^{96,104}, see Figure 3.46 and Table S4, Appendix 11. The program Crystal Explorer 3.1¹⁰⁵ was used for calculations. Overall, weak hydrogen bonds were the most typical weak intermolecular interactions in crystal structures of benperidol forms, and mostly were formed by O2 (in all structures except type 1 solvates and **DH**), O1 (in **I**, type 1 solvates, **II**, **S_{Benz}**, and **DH**), and F1 (in **II**, **III**, type 1 solvates, **S_{Benz}**, and **HH**), while not by N3 (probably because of the shape and packing of the molecules). In the crystal structure of **I**, **II**, **DH**, and **S_{Benz}** a noticeable role was played also by other weak interactions (mainly CH \cdots π). In the Hirshfeld surface fingerprint plots, a similarity was observed between the benperidol molecules forming amide homodimers in **II**, **III**, type 2 solvates, and **HH** (except for the spike associated with the O3-H \cdots N3 bond). The plot of **S_{Benz}** is different from those of type 1 solvates, clearly identifying structural differences, whereas it is similar to that of polymorph **I**, suggesting structural similarity with it. The structural similarity between **I** and **S_{Benz}** is also identified from the presence of similar weak intermolecular interactions. Due to the dominance of strong hydrogen bonding pattern involving water molecules in **DH**, its plot completely differs from that of all other phases.

Interestingly, a common feature of the fingerprint plots of polymorphs **I** and **II** is the presence of a number of longer contacts (notice the points at high d_i and d_e values in Figure 3.46) if compared to the solvates, indicating less efficient packing. This is also supported by the presence of small structural voids (2.2% and 1.4% of the volume, respectively, but too small to accommodate residual solvent molecules) in the structure of both of these polymorphs, as determined using PLATON and visualized in Mercury.

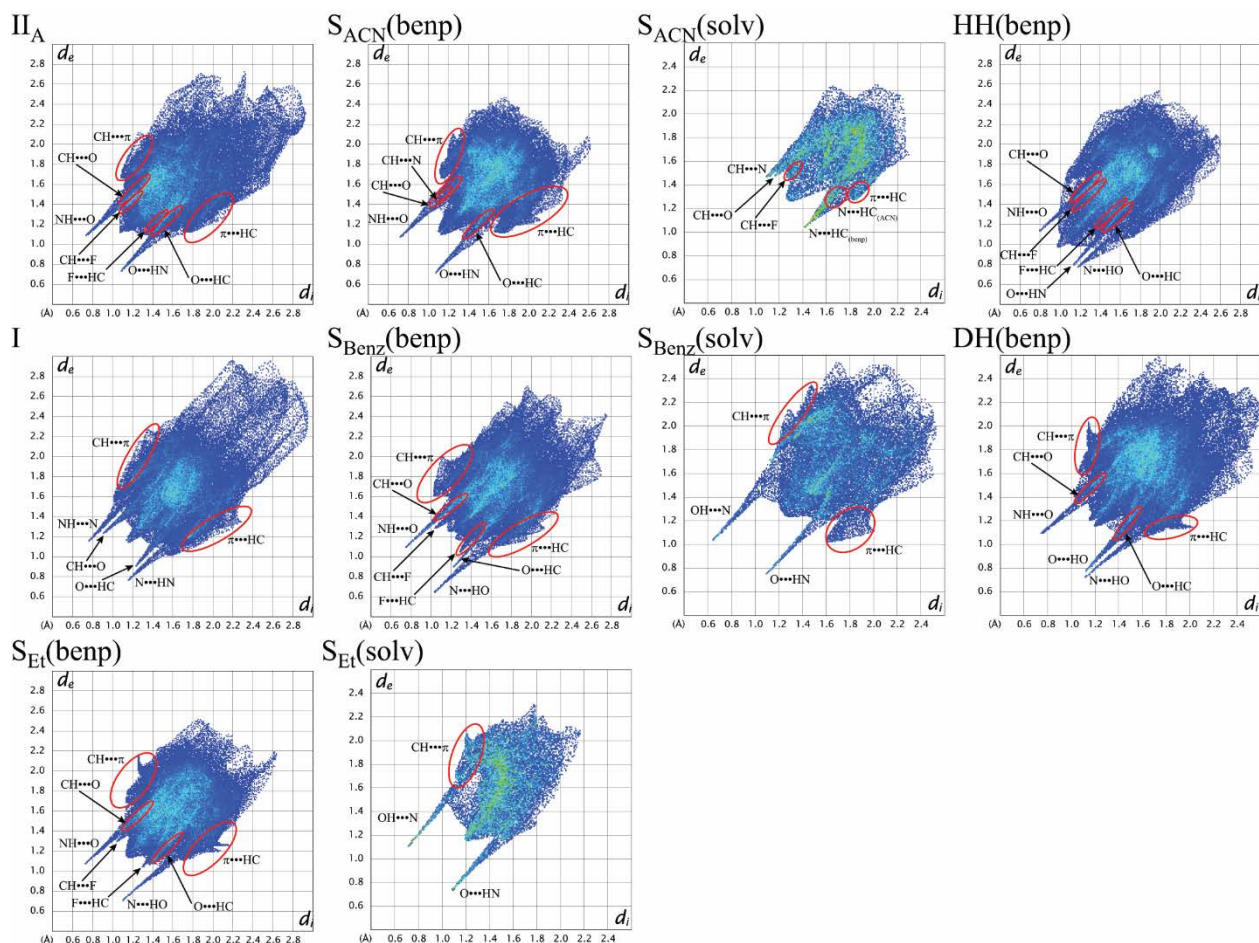


Figure 3.46. The 2D fingerprint plots of Hirshfeld surfaces for selected molecules in benperidol polymorphs and solvates.

Analysis of the molecular packing was performed in Mercury and using XPac code^{129, 131}. It was determined that the only forms showing clear similarity of molecular packing (except for the isostructural solvates) were **III** with **HH** and type 2 solvates, in which the benperidol molecules were packed in a similar manner (see Figure 3.47) by forming identical 2D supramolecular constructs – infinite layers of molecules parallel to (110) in **III**, (011) in type 2 solvates, and (20 $\bar{1}$) in **HH**, see blue and green layers in Figure 3.47. The similarity of **HH** and type 2 solvates, however, is lower, and the only identical 1D supramolecular construct (finite layers formed from amide homodimers as shown with red in Figure 3.47) was identified because of the presence of solvent molecules distorting the molecular packing. Similarly formed hydrogen bonded molecular chains forming similar double layers were observed also in all alcohol solvates, with small differences due to different molecular conformation. However, these double layers were stacked differently in S_{Benz} , therefore making this structure different from those of type 1 solvates. Despite the similarity of intermolecular interactions and Hirshfeld surfaces when comparing **I** and S_{Benz} , no obvious similarity in the molecular packing of these two forms could be identified. All other benperidol forms did not show identifiable packing similarities, see Figure 3.47 and Figure S19, Appendix 11.

Interestingly, it was noticed that benperidol molecule layers could be identified in all solvated forms, whereas molecular packing of the two stable polymorphs **I** and **II** was more complex.

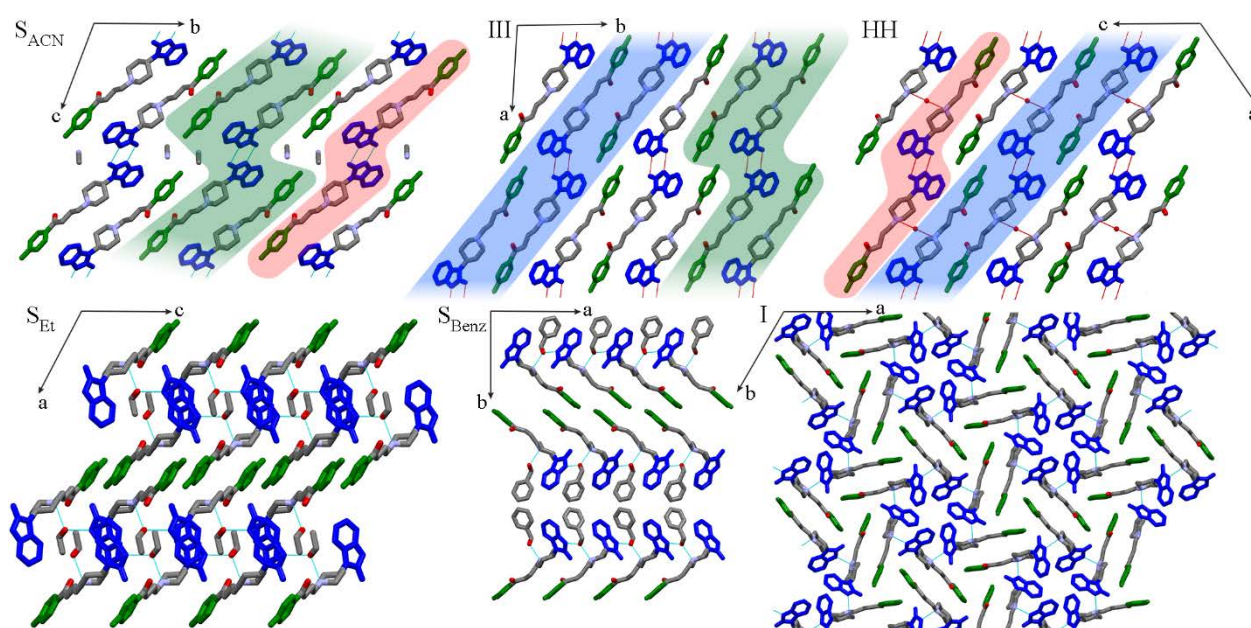


Figure 3.47. Molecular packing in benperidol polymorphs and solvates. Benzimidazolone moiety is in blue, and fluorophenyl moiety is in green color. Green, blue and red layers represent identical supramolecular constructs identified in the crystal structures. Hydrogen atoms have been omitted for clarity.

3.6.4 *Fourier-Transform Infrared Spectroscopy*

The FTIR spectra confirmed the already identified isostructurality within type 1, as well as type 2 solvates. Individual solvates, however, could be identified by the presence of particular bands from different solvent molecules, see Figure 3.48. Also, the already identified similarity of molecular packing in the polymorph **III**, hydrate **HH**, and less explicitly in type 2 solvates, as well similarity between the polymorph **I** and **S_{Benz}** identified by intermolecular interaction analysis was reflected as similarity of their IR spectra. No clear similarities, however, were observed between **DH** and polymorph **V** (see Figure S5, Appendix 11), suggesting that there is no direct structural relation between these forms, although this can also be explained by the significant changes introduced in benperidol molecular environment by removal of the water molecules. Interestingly, the IR spectra of polymorphs **IV** and **V** are slightly similar, suggesting that structural rearrangements during the transition from **V** to **IV** could be quite limited in magnitude.

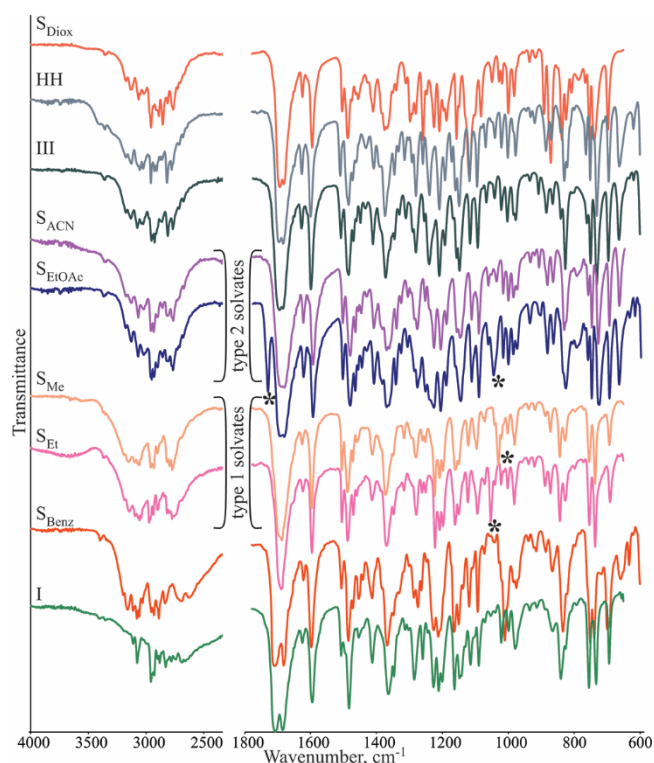


Figure 3.48. FTIR spectra of the benperidol solvates and polymorphs **I** and **III**. Asterisks mark the most characteristic bands from the solvent molecules in isostructural solvates.

The most easily noticeable difference in the IR spectra was the position of the carbonyl group stretching bands, as two peaks (at ~ 1708 and ~ 1684 cm^{-1}) appearing for the polymorph **I** and **S_{Benz}**, whereas two indistinguishable or slightly split peaks (at $\sim 1696 - 1683$ cm^{-1}) appeared for other polymorphs and solvates. By using computational methods it was shown that the position of amide carbonyl stretching band was significantly affected by the hydrogen bonding, with the N2-H \cdots N3 and N2-H \cdots O3 hydrogen bonds in **I** and **S_{Benz}** observed at ~ 1710 cm^{-1} , while the N2-H \cdots O1 and N2-H \cdots O3 hydrogen bonds in other benperidol phases were observed at ~ 1695 cm^{-1} vibrational frequency.

3.6.5 Characterization and rationalization of benperidol solvate desolvation

Dihydrate. The TG analysis and PXRD patterns showed that the dehydration of **DH** occurred in one stage. However, the dehydration products of **DH** depended on the sample and its preparation. Dehydration of fine **DH** powder at 30°C over P_2O_5 resulted in the formation of polymorph **V**. At elevated temperature (above 40°C), the polymorph **V** transformed to polymorph **IV**. However, when **DH** crystals were dehydrated, polymorph **II** or a mixture of **II** and **I** was obtained. This could be explained by slower water escape from the crystal, which could lead to recrystallization of the product in thermodynamically preferred polymorphs **II** and **I** (see Appendix 11) These polymorphs also typically appeared when powdered **DH** obtained by grinding its crystals was dehydrated, and could be explained by the nucleation of polymorphs **II** and **I** during grinding. The fact that water molecules had a crucial role in the stabilization of the crystal structure

implies that the dehydration most probably involved complete structural collapse, followed by recrystallization to a completely different crystal structure, which explains the possibility of forming different dehydration products.

Type 1 solvates. The PXRD measurements and crystal structure analysis indicated that the presence of two endothermic peaks in the desolvation process of **S_{Me}** and **S_{Et}** (Figure 3.42) cannot be associated with the formation of a desolvation intermediate. Besides, a change of the sample particle size affected the contribution from each peak. Therefore, the appearance of two peaks apparently resulted from different desolvation rates associated with the molecules located at different distances from the surface of the crystals. The first peak was associated with the desolvation of solvate close to the surface, for which the escape of solvent molecules was relatively easy. The amount of solvate desolvated in this way depended on the particle size. The further desolvation, however, slowed down because of the hindered escape of solvent molecules through the product phase. Nevertheless, the desolvation slowly continued at increased temperature. The second desolvation peak appeared when a fast and complete desolvation occurred by reaching the peritectic decomposition/melting point of the solvate at 129°C for **S_{Me}**, and at 137°C for **S_{Et}**. Therefore the desolvation profile depended both on the particle size and on the heating rate (see Figure 3.49).

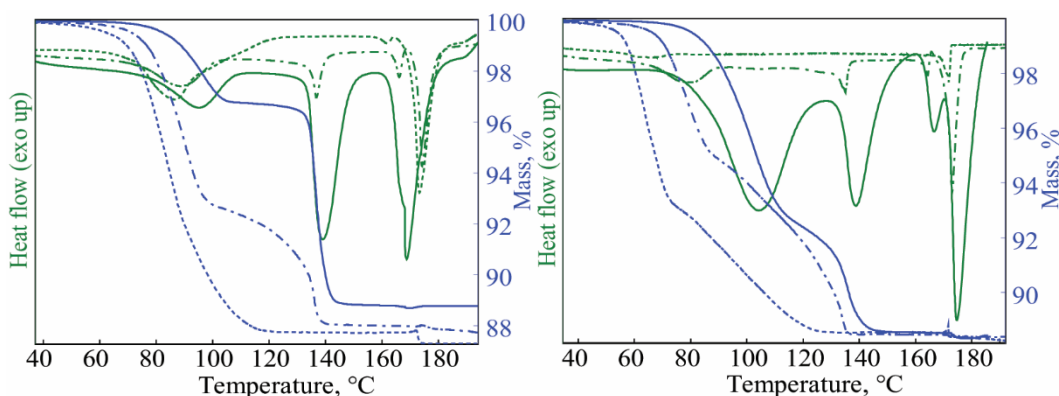


Figure 3.49. The effect of particle size (on the left, solid lines – large crystals, dashed – small crystals, dotted – well ground powder) and the heating rate (on the right, solid lines – $20^{\circ}\cdot\text{min}^{-1}$, dashed – $2^{\circ}\cdot\text{min}^{-1}$, dotted – $0.2^{\circ}\cdot\text{min}^{-1}$) on the desolvation of **S_{Et}**.

The desolvation product in most cases was the structurally different polymorph **II**. Nevertheless, when desolvation was performed with solvates prepared by suspending technique, or with large solvate crystals, a mixture of polymorphs **II** and **I** was obtained in both desolvation stages, although it was noticed that slow desolvation at low temperature facilitated the formation of polymorph **II**, while fast desolvation at high temperature facilitated the formation of **I**. The formation of polymorph **I** can be explained by the presence of small nuclei of **I** in the solvates obtained by suspending technique, as well as the recrystallization from retained or condensed solvent in large crystals, as **I** is the thermodynamically stable polymorph at temperatures required

for the desolvation process. This was supported by the observation that seeding of **S_{Me}** with 5% of **I** led to the formation of pure **I** after desolvation. Moreover, the crystallization of polymorph **I** from ethanol solution, as well as the occurrence of peritectic decomposition and/or melting was confirmed by a hot-stage microscopy experiment.

Type 2 solvates. Similarly to the type 1 solvates, thermal analysis of **S_{ACN}** with various particle sizes showed that the second desolvation peak (at 106°C in Figure 3.42) corresponded to the peritectic melting and/or decomposition of this solvate. The desolvation process of these solvates usually produced a mixture of polymorphs **III** and **I**, with smaller particle size and lower temperatures facilitating the formation of **III**. The desolvation of these solvates was easy and occurred even by grinding at ambient conditions in a mortar, producing **III** with low crystallinity. This relatively easy desolvation can be explained by the presence of solvent channels and the absence of strong benperidol-solvent interactions facilitating the solvent removal process. The appearance of polymorph **I** as a desolvation product most probably occurred in the presence of nuclei of this thermodynamically stable polymorph or in a recrystallization process from acetonitrile solution in the case when large crystals were desolvated.

Other solvates. Dehydration of **HH** over P_2O_5 at 30°C produced pure **III**, while dehydration at elevated temperature produced besides **III** also the polymorph **I**. Desolvation of **S_{Benz}** both at elevated temperature and at ambient temperature produced only the polymorph **I**. Desolvation of **S_{DIOX}** produced the polymorph **III** or **HH**, depending on the conditions.

Structural characterization of benperidol solvate desolvation. A summary of the most characteristic phase transitions occurring during the desolvation of solvates is given in Figure 3.50.

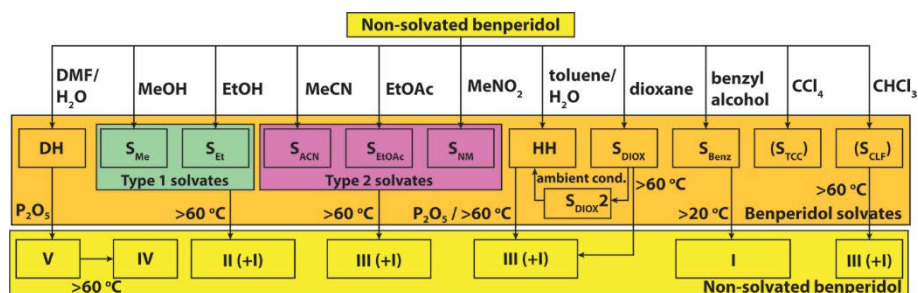


Figure 3.50. A schematic representation of benperidol solvate preparation and the phase transformations occurring during their desolvation.

By analyzing these phase transitions in association with the crystal structure data and phase stability of polymorphs, it was concluded that two driving forces determined the obtained desolvation product: a) structural similarity between the solvate and the obtained polymorph, and b) thermodynamic stability of the resulting polymorph. The only solvate clearly producing only one desolvation product was **S_{Benz}**, which formed only the thermodynamically stable polymorph **I**. Besides, strong similarity of intermolecular interactions was observed in both of these phases. Although type 2 solvates and **HH** showed clear structural similarity with polymorph **III**, which

usually was their main desolvation product, hardly ever it appeared without polymorph **I** as minor component. The formation of polymorph **I** was enhanced in situations facilitating the formation of thermodynamically stable polymorph: at high temperatures and in the case of large solvate crystals, when recrystallization from trapped solvent was possible. Similar effects facilitating the formation of **I** were observed also in the desolvation of type 1 solvates, and in that case further supported by the observation that seeding with **I** produced **I** as the only desolvation product. For type 1 solvates, however, no structural similarities with the main desolvation product **II** could be observed.

Similar observations as for type 2 solvates were made also for the desolvation of **DH**, although in that case the main desolvation product was the unstable polymorph **V**, and the thermodynamically stable byproducts were polymorphs **II** and **I**. In this case, however, structural similarity between **DH** and **V** could not be determined.

3.6.6 Rationalization of solvate stability and frequency of solvate formation in crystallization

The solvate stability was compared using the lattice energies and pairwise intermolecular interaction energies. The results obtained for structures where atom positions were relaxed in *CASTEP* are given in Table 3.16. As shown previously, the results from semi-empirical PIXEL code had similar accuracy to those from DFT-D methods⁹⁸, while results from empirical AA-CLP are less accurate and are given only to compare the lattice energy of solvates with more than two molecules in the asymmetric unit. Total pairwise interaction energy values were less conclusive than the lattice energies, especially those calculated for benperidol-benperidol interactions, as they did not take into account the energetically relevant long-range interactions. However, they allowed an approximate evaluation of the contribution from benperidol and solvent molecule interactions in the lattice energies and gave a fast insight into the relative stability of solvates with similar structures.

Table 3.16. The lattice energy and total pairwise interaction energy (in $\text{kJ}\cdot\text{mol}^{-1}$) for benperidol solvates.

Solvate	Lattice energy		Total pairwise interaction energy		
	PIXEL	AA-CLP	benperidol ^a	solvent ^b	
DH	–	–99.3	–227.1	–86.1 / –79.4 ^c	
HH	–84.3	–65.6	–269.7	–44.7	
S_{Benz}	–130.7	–109.5	–167.8	–151.9	
type 1	S_{Me}	–119.9	–107.4	–245.7	–92.9
	S_{Et}	–124.3	–121.9	–223.0	–104.9
type 2	S_{ACN}	–110.7	–116.0	–295.6	–53.5
	S_{EtOAc}	–	–137.6	–301.1 / –301.8 ^c	–60.9
	S_{NM}	–108.2	–119.7	–273.5	–75.8

^a – the sum of all pairwise benperidol-benperidol interaction energies with cutoff distance equal to the sum of vdW radii + 0.3 Å.

^b – the sum of all pairwise solvent-benperidol and solvent-solvent interaction energies with cutoff distance equal to the sum of vdW radii + 1.6 Å.

^d – for each water molecule (in **DH**) or benperidol molecule (in **S_{EtOAc}**) in the asymmetric unit.

The higher lattice energy of **S_{Et}** compared to that of **S_{Me}** apparently explains the higher stability of this solvate, as observed by its higher peritectic desolvation and/or melting point (see Table 3.12) and higher desolvation E_a , see Appendix 11.

Logically, by comparing the interaction energies in type 1 solvates with those in **S_{Benz}**, it is observed that an increase in the size of the solvent molecule increase the contribution of the total pairwise solvent interaction energy to the lattice energy, while the contribution from the total pairwise benperidol interaction energy decrease due to the larger separation of these molecules.

Although the thermal stability of type 2 solvates is very similar, crystallization from acetonitrile always resulted in the formation of **S_{ACN}**, whereas crystallization from ethyl acetate mainly produced pure polymorph **I**. Moreover, **S_{NM}** was obtained only once. Besides, **S_{ACN}** was obtained also in slurry experiments, whereas preparation of the other two solvates using this approach was not possible. The lattice energy of **S_{ACN}** was slightly more negative than that of **S_{NM}**, and the pairwise interaction energies between benperidol molecules in the crystal structure of **S_{NM}** were less efficient (due to the larger size of nitromethane molecule). This theoretically can lead to hindered formation of **S_{NM}**, as the formation of its crystals is energetically less favored, compared to the formation of **S_{ACN}** crystals. Due to the different stoichiometry, reliable comparison with **S_{EtOAc}** was possible only using pairwise interaction energies, which showed that the ethyl acetate molecule in this structure did not form as efficient interactions as acetonitrile or nitromethane molecules, explaining the complications with its crystallization. Nevertheless, it should not be forgotten that the crystallization product can also be associated with the molecular interactions in the liquid state, and it is theoretically possible that ethyl acetate and nitromethane somehow facilitate the crystallization of polymorph **I**.

The easier desolvation of type 2 solvates, compared to the type 1 solvates, is explained by the presence of solvent channels and weaker interaction energies experienced by the solvent molecules⁸⁹.

Although all the strong hydrogen bonds in **DH** structure are formed with or between water molecules, interactions between benperidol molecules in the form of weak hydrogen bonds and dispersion forces contributed more to the lattice energy. Nevertheless, the overall interactions in **DH** were energetically more favored than those in **HH**, which apparently explain the fact that this is the most stable of benperidol hydrates. Therefore, the facile crystallization of **DH** can be

explained by a more efficient hydrogen bond network, while the formation of **HH** was possible only under the conditions with a very low water activity and in the presence of specific solvent molecules, probably providing for the formation of favorable benperidol molecule associates.

3.6.7 *The analysis of benperidol solvate formation*

Crystallization of benperidol from a range of 31 solvents selected from various solvent classes resulted in the formation of 11 solvates. Nevertheless, **S_{EtOAc}** and **S_{NM}** were obtained only in some crystallization experiments from the respective solvents, hemihydrate crystallized only from xylene and toluene containing traces of water, and repeated preparation of **S_{CLF}** and **S_{TCC}** was complicated. These observations suggest that discovery of additional benperidol solvates with the studied solvents is theoretically possible. Nevertheless, the obtained amount of solvates and the knowledge of benperidol and solvent properties, as well as the elucidation of solvate crystal structure allowed to rationalize the formation of benperidol solvates.

Generally it was concluded that solvates formed with solvent molecules representing different solvent classes: hydrogen bond donors (type 1 solvates, **HH**, and **DH**), aprotic polar solvents (type 2 solvates, **S_{CLF}**), aromatic apolar or lightly polar solvents (**S_{Benz}**; although benzyl alcohol is a hydrogen bond donor, its ability to form dispersion interactions appeared to be even more important for the formation of this solvate), and aprotic polar electron pair donor (**S_{DIOX}**). Even though the crystal structures of some of the solvates are not known, it was possible to conclude that the solvent molecules in all solvates employed features (strong or weak hydrogen bonds, dispersion interactions) characteristic of the corresponding solvent class. More detailed classification of solvents did not provide additional clarification for the solvate formation of benperidol, as type 1 solvates formed from solvents belonging to group 3, type 2 solvates from solvents from groups 2 and 9, and other solvates were obtained from solvents belonging to groups 1, 7, 10, 11, and 15¹⁴⁰ (see Table S1, Appendix 11).

As already mentioned, although the solvates were obtained with four different hydrogen bond donors, only in both hydrates the additional hydrogen bond acceptor sites of benperidol molecule were employed. Therefore, the formation of hydrates was directly explained by the advantages of a more efficient hydrogen bonding network. The formation of alcohol solvates, however, was not driven purely by this feature, although the presence of strong benperidol-solvent hydrogen bonds definitely provided stability for these structures. The solvent molecules in other solvates could not participate in strong hydrogen bonds, but provided new, weak interactions and allowed energetically favourable packing of benperidol molecules with the solvent molecules. Interestingly, although there were some voids in the crystal structures of both polymorphs **I** and **II**, which were not observed in any of the solvate structures, the packing index of solvates was generally the same as that in the polymorphs, see Table 3.13. Nevertheless, the presence of voids

and complex structural patterns in the crystals of stable benperidol polymorphs (six-molecule rings in **I**, see Figure 3.45, and $Z'=3$ for **II**) suggested that energetically efficient packing is complicated for phases consisting of benperidol molecules only. The presence of certain functional groups in the benperidol molecule, however, provides possibilities for efficient interactions with solvent molecules containing different functional groups. These appear to be the two main reasons for the formation of such a wide range of benperidol solvates with various solvent molecules.

The appearance of two isostructural solvate groups suggests that in the case of some particular solvent properties, solvent molecules are incorporated in identical crystal structures. The comparison of these structures shows that both the specific interactions provided by solvent, as well as the size of the solvent molecules are important factors. Therefore, small hydrogen bond donating alcohol molecules form type 1 solvates, whereas aprotic polar donors and acceptors of weak hydrogen bonds with appropriate molecular size and shape form type 2 solvates.

3.6.8 Conclusions

Crystallization of benperidol from various solvents produced nine new solvates containing methanol, acetonitrile, ethyl acetate, nitromethane, 1,4-dioxane, water, benzyl alcohol, carbon tetrachloride, and chloroform, while the desolvation of benperidol solvates produced two new polymorphs **IV** and **V**. It was determined that benperidol forms two sets of isostructural solvates: type 1 (with methanol and ethanol) and type 2 (with acetonitrile, nitromethane, and ethyl acetate). Infrequent formation of some of the solvates, however, showed that the existence of a certain solvate cannot guarantee its facile formation and discovery, even if there are isostructural solvates forming easily.

It was determined that the main reason for the formation of various benperidol crystal structures was the diverse possibilities of molecular packing, resulting in different intermolecular interactions, whereas the molecular conformation of benperidol was typically very similar. A comparison of the crystal structures of benperidol phases showed that the only structures showing clear similarities of molecular packing were the polymorph **III**, hemihydrate **HH**, and type 2 solvates, while similarities of intermolecular interactions were observed also for **S_{Benz}** and polymorph **I**.

Desolvation studies of benperidol solvates showed that the stability of solvates can be associated with the intermolecular interactions in the crystal structure, while the structures of desolvation products were determined through an interplay of structural similarity and thermodynamic stability of the resulting polymorphs, and each of these factors could become dominant due to sample preparation procedures or experimental conditions.

The inability of benperidol molecules to pack efficiently without solvent was found to be the main reason for solvate formation, whereas the presence of specific functional groups in benperidol

molecule enabled the formation of a wide range of stable solvate structures containing various solvent molecules. This is similar to the properties for droperidol solvates, although less structural variation was observed in the case of droperidol solvates, Section 3.3. Nevertheless, theoretical prediction of benperidol solvates would be quite complicated as it would be difficult to predict the energetically favorable packing for each particular solvate. The formation of both benperidol hydrates, however, was driven by the compensation for hydrogen bond donor deficiency in benperidol molecules.

By using both sets of isostructural solvates it was proved that both the possible interactions and the size of the solvent molecules were important factors in solvate formation. The solvate structures of benperidol, however, were more interaction-specific, if compared to those of droperidol, which formed only one set of isostructural solvates with at least 7 very different solvents, Section 3.3. In the formation of type 2 solvates, both the size and shape of the solvent molecules appeared to be relevant, as two nearby partially connected channels could be occupied by smaller molecules in each of the channel (as in \mathbf{S}_{ACN} and \mathbf{S}_{NM}), or by larger molecules occupying both of the channels (\mathbf{S}_{EtOAc}).

CONCLUSIONS

1. The dehydration of mildronate **DH** is a single step process leading directly to the anhydrous form **AP**. This is explained by similar mildronate molecule packing in both of these structures. The dehydration occurs as escape of the water molecules through structural channels, molecular conformation changes and molecular translation of mildronate molecules.
2. The dehydration of mildronate **DH** can be described with 1D phase boundary reaction with E_a is $75 \pm 3 \text{ kJ} \cdot \text{mol}^{-1}$. Based on the crystal structure it can be suggested that for small particles the phase boundary advancement during the dehydration occurred along the *a*-axis.
3. Comparable dehydration kinetic parameters of mildronate dihydrate was obtained in both isothermal and nonisothermal mode. However, both the interpretation of obtained results and experimental procedures were more complicated when experiments were performed in nonisothermal mode.
4. Different sample and environmental factors, particularly particle size, sample weight, nitrogen flow rate and sample history affected not only the dehydration rate, but also the dehydration E_a and kinetic model. Study of the effect of these factors revealed that the dimensionality of the phase boundary advance can increase to 2D for large particles, and change of some of the factors showed that also a) the diffusion of water outside the crystal and b) diffusion of water from the inside of the powder could limit this dehydration process.
5. The driving force for droperidol solvate formation was the inability of droperidol molecules to pack efficiently; thus the solvent molecules acted as a void fillers, with the exception of droperidol **DH**, where water molecules provided a hydrogen bond donor function matching the excess hydrogen bond acceptor functions in the molecule of droperidol.
6. The stability of droperidol isostructural solvate structure was rationalized by the very effective interactions between droperidol molecules, explaining the fact that no specific interaction with solvate was necessary to maintain the crystal structure of the isostructural solvate. Therefore, droperidol isostructural solvates can be obtained with solvents fitting in the channels and providing sufficiently effective intermolecular interactions with droperidol.
7. The study of the desolvation kinetics of droperidol isostructural solvates revealed that the desolvation E_a of all of these solvates was almost the same ($57 \pm 15 \text{ kJ} \cdot \text{mol}^{-1}$) and the desolvation process was diffusion limited, and the desolvation curves could be fitted using the modified Zhuravlev equation.
8. The thermal stability of the solvates determined from the desolvation rate in both isothermal and nonisothermal modes could be successfully used as a solvate stability comparison and

ranging tool for the droperidol solvates. The calculation of the intermolecular interaction energies in droperidol solvates showed that it was possible to rationalize and predict the thermal stability order of solvates by using a sum of the solvate–droperidol and solvate–solvate interaction energies.

9. Using solid-state NMR spectroscopy it was determined that solvent molecules in droperidol isostructural solvates **NSH**, **S_{Me}** and **S_{Et}** are dynamic, whereas in **S_{ACN}** and **S_{NM}** are static and ordered. The alcohol molecules are relatively dynamic within their lattice sites and also occasionally flip over to the equivalent site related by the inversion symmetry. Also water molecules experience complex motion consisting of C2 flips and some other type of motion, with total estimated $E_a = 25 \pm 3 \text{ kJ mol}^{-1}$.
10. Differences in the presence of solvent molecule dynamics in droperidol isostructural solvates with organic solvents was rationalized using total energy and intermolecular interaction energy: for **S_{Et}** and **S_{Me}** there was little energy difference between structures where all solvent molecules pointed in one direction and adjacent solvent molecules pointed in opposite directions, whereas for **S_{ACN}** and **S_{NM}** the first structures were highly favourable.
11. The formation of wide range of solvates for benperidol was mainly due to the inability of the benperidol molecules to pack efficiently without solvent, while incorporation of solvent molecules allowed energetically efficient molecule packing. Solvate formation was observed with solvents providing specific intermolecular interactions and having appropriate size and shape. Also for benperidol excess of benperidol hydrogen bond acceptor functions was compensated only in the hydrates.
12. The stability of benperidol solvates was determined by the intermolecular interactions in the crystal structure, while the desolvation products was determined in an interplay of structural similarity and thermodynamic stability of the resulting polymorph, and each of both factors could be made dominant by sample preparation and experimental conditions.

REFERENCES

- (1) Chavez, K. J.; Guevara, M.; Rousseau, R. W., Characterization of Solvates Formed by Sodium Naproxen and an Homologous Series of Alcohols. *Cryst. Growth Des.* **2010**, 10, (8), 3372-3377.
- (2) Fujii, K.; Aoki, M.; Uekusa, H., Solid-State Hydration/Dehydration of Erythromycin A Investigated by ab Initio Powder X-ray Diffraction Analysis: Stoichiometric and Nonstoichiometric Dehydrated Hydrate. *Cryst. Growth Des.* **2013**, 13, (5), 2060-2066.
- (3) Guguta, C.; Eeuwijk, I.; Smits, J. M. M.; de Gelder, R., Structural Diversity of Ethinyl Estradiol Solvates. *Cryst. Growth Des.* **2008**, 8, (3), 823-831.
- (4) Herbstein, F. H., Diversity Amidst Similarity: A Multidisciplinary Approach to Phase Relationships, Solvates, and Polymorphs. *Cryst. Growth Des.* **2004**, 4, (6), 1419-1429.
- (5) Schmidt, A. C.; Niederwanger, V.; Griesser, U. J., Solid-state forms of prilocaine hydrochloride. *J. Therm. Anal. Calorim.* **2004**, 77, (2), 639-652.
- (6) Giron, D., Thermal analysis and calorimetric methods in the characterisation of polymorphs and solvates. *Thermochim. Acta* **1995**, 248, (0), 1-59.
- (7) Braun, D. E.; Kahlenberg, V.; Gelbrich, T.; Ludescher, J.; Griesser, U. J., Solid state characterisation of four solvates of R-cinacalcet hydrochloride. *CrystEngComm* **2008**, 10, (11), 1617-1625.
- (8) Braun, D. E.; Gelbrich, T.; Kahlenberg, V.; Tessadri, R.; Wieser, J.; Griesser, U. J., Stability of Solvates and Packing Systematics of Nine Crystal Forms of the Antipsychotic Drug Aripiprazole. *Cryst. Growth Des.* **2009**, 9, (2), 1054-1065.
- (9) Bernstein, J., *Polymorphism in Molecular Crystals*. Oxford University Press: Oxford, 2002.
- (10) Brittain, H. G.; Morris, K. R.; Boerrigter, S. X. M., Structural Aspects of Solvatomorphic Systems. In *Polymorphism in pharmaceutical solids*, Brittain, H. G., Ed. Informa Healthcare: New York, 2009; pp 233-281.
- (11) Aitipamula, S.; Chow, P. S.; Tan, R. B. H., Polymorphism in cocrystals: a review and assessment of its significance. *CrystEngComm* **2014**, 16, (17), 3451-3465.
- (12) Blagden, N.; Coles, S. J.; Berry, D. J., Pharmaceutical co-crystals - are we there yet? *CrystEngComm* **2014**, 16, (26), 5753-5761.
- (13) Shan, N.; Zaworotko, M. J., The role of cocrystals in pharmaceutical science. *Drug Discov. Today* **2008**, 13, (9-10), 440-446.
- (14) Hilfiker, R., *Polymorphism in the pharmaceutical industry*. ed.; Wiley-VCH Verlag GmbH & Co, KGaA.: Weinheim 2006; p 414.
- (15) Yu, L.; Reutzel, S. M.; Stephenson, G. A., Physical characterization of polymorphic drugs: an integrated characterization strategy. *Pharm. Sci. Technol. Today* **1998**, 1, 118-127.
- (16) Griesser, U. J., The Importance of Solvates. In *Polymorphism in the Pharmaceutical Industry*, Hilfiker, R., Ed. WILEY-VCH Verlag GmbH & Co. KGaA: Weinheim, 2006; pp 211-233.
- (17) Brittain, H. G., Theory and Principles of Polymorphic Systems. In *Polymorphism in Pharmaceutical Solids*, pp 1-23.
- (18) Burger, A.; Ramberger, R., On the polymorphism of pharmaceuticals and other molecular crystals. I. *Microchim. Acta* **1979**, 72, (3), 259-271.
- (19) Yu, L.; Furness, M. S.; Raw, A.; Outlaw, K. W.; Nashed, N.; Ramos, E.; Miller, S. F.; Adams, R.; Fang, F.; Patel, R.; Holcombe, F., Jr.; Chiu, Y.-y.; Hussain, A., Scientific Considerations of Pharmaceutical Solid Polymorphism in Abbreviated New Drug Applications. *Pharm. Res.* **2003**, 20, (4), 531-536.
- (20) Campeta, A. M.; Chekal, B. P.; Abramov, Y. A.; Meenan, P. A.; Henson, M. J.; Shi, B.; Singer, R. A.; Horspool, K. R., Development of a targeted polymorph screening approach for a complex polymorphic and highly solvating API. *J. Pharm. Sci.* **2010**, 99, (9), 3874-3886.
- (21) Braga, D.; Grepioni, F.; Maini, L.; Polito, M., Crystal Polymorphism and Multiple Crystal Forms. In *Molecular Networks*, Hosseini, M. W., Ed. Springer Berlin Heidelberg: 2009; Vol. 132, pp 87-95.
- (22) Bauer, J.; Spanton, S.; Henry, R.; Quick, J.; Dziki, W.; Porter, W.; Morris, J., Ritonavir: An Extraordinary Example of Conformational Polymorphism. *Pharm. Res.* **2001**, 18, (6), 859-866.
- (23) Brittain, H. G.; Byrn, S. R.; Lee, E., Structural Aspects of Polymorphism. In *Polymorphism in Pharmaceutical Solids*, pp 185-232.
- (24) Lee, A. Y.; Erdemir, D.; Myerson, A. S., Crystal Polymorphism in Chemical Process Development. *Annual Review of Chemical and Biomolecular Engineering* **2011**, 2, (1), 259-280.
- (25) Nangia, A., Conformational polymorphism in organic crystals. *Acc. Chem. Res.* **2008**, 41, (5), 595-604.

- (26) Yu, L., Polymorphism in Molecular Solids: An Extraordinary System of Red, Orange, and Yellow Crystals. *Acc. Chem. Res.* **2010**, 43, (9), 1257-1266.
- (27) López-Mejías, V.; Kampf, J. W.; Matzger, A. J., Nonamorphism in Flufenamic Acid and a New Record for a Polymorphic Compound with Solved Structures. *J. Am. Chem. Soc.* **2012**, 134, (24), 9872-9875.
- (28) Purohit, R.; Venugopalan, P., Polymorphism: An overview. *Resonance* **2009**, 14, (9), 882-893.
- (29) Buttar, D.; H. Charlton, M.; Docherty, R.; Starbuck, J., Theoretical investigations of conformational aspects of polymorphism. Part 1: o-acetamidobenzamide. *Journal of the Chemical Society, Perkin Transactions 2* **1998**, (4), 763-772.
- (30) Dunitz, J. D.; Gavezzotti, A., Toward a Quantitative Description of Crystal Packing in Terms of Molecular Pairs: Application to the Hexamorphic Crystal System, 5-Methyl-2-[(2-nitrophenyl)amino]-3-thiophenecarbonitrile†. *Cryst. Growth Des.* **2005**, 5, (6), 2180-2189.
- (31) Vippagunta, S. R.; Brittain, H. G.; Grant, D. J. W., Crystalline solids. *Adv. Drug Delivery Rev.* **2001**, 48, 3-26.
- (32) Vippagunta, S.; Brittain, H.; Grant, D., Crystalline solids. *Adv. Drug Delivery Rev.* **2001**, 48, (1), 3-26.
- (33) Stephenson, G.; Groleau, E.; Kleemann, R.; Xu, W.; Rigsbee, D., Formation of isomorphic desolvates: Creating a molecular vacuum. *J. Pharm. Sci.* **1998**, 87, (5), 536-542.
- (34) Stephenson, G. A.; Diseroad, B. A., Structural relationship and desolvation behavior of cromolyn, cefazolin and fenoprofen sodium hydrates. *Int. J. Pharm.* **2000**, 198, (2), 167-177.
- (35) Te, R. L.; Griesser, U. J.; Morris, K. R.; Byrn, S. R.; Stowell, J. G., X-ray Diffraction and Solid-State NMR Investigation of the Single-Crystal to Single-Crystal Dehydration of Thiamine Hydrochloride Monohydrate. *Cryst. Growth Des.* **2003**, 3, (6), 997-1004.
- (36) Murphy, B. J.; Casteel, M. J.; Samas, B.; Krzyzaniak, J. F., Thermodynamic stability considerations for isostructural hydrates. *J. Pharm. Sci.* **2012**, 101, (4), 1486-1495.
- (37) Hosokawa, T.; Datta, S.; Sheth, A. R.; Brooks, N. R.; Young Jr, V. G.; Grant, D. J. W., Isostructurality among five solvates of phenylbutazone. *Cryst. Growth Des.* **2004**, 4, (6), 1195-1201.
- (38) Banerjee, R.; Bhatt, P. M.; Desiraju, G. R., Solvates of Sildenafil Saccharinate. A New Host Material. *Cryst. Growth Des.* **2006**, 6, (6), 1468-1478.
- (39) Stieger, N.; Liebenberg, W.; Wessels, J.; Samsodien, H.; Caira, M., Channel inclusion of primary alcohols in isostructural solvates of the antiretroviral nevirapine: an X-ray and thermal analysis study. *Struct. Chem.* **2010**, 21, (4), 771-777.
- (40) Schultheiss, N.; Smit, J. P.; Hanko, J. A., Three isostructural solvates of finasteride and their solid-state characterization. *Eur. J. Pharm. Sci.* **2009**, 38, (5), 498-503.
- (41) Caira, M. R.; Bettinetti, G.; Sorrenti, M., Structural relationships, thermal properties, and physicochemical characterization of anhydrous and solvated crystalline forms of tetroxoprim. *J. Pharm. Sci.* **2002**, 91, (2), 467-481.
- (42) Zencirci, N.; Gstrein, E.; Langes, C.; Griesser, U., Temperature- and moisture-dependent phase changes in crystal forms of barbituric acid. *Thermochim. Acta* **2009**, 485, (1-2), 33-42.
- (43) Morris, K. R.; Griesser, U. J.; Eckhardt, C. J.; Stowell, J. G., Theoretical approaches to physical transformations of active pharmaceutical ingredients during manufacturing processes. *Adv. Drug Delivery Rev.* **2001**, 48, 91-114.
- (44) Tian, F.; Qu, H.; Zimmermann, A.; Munk, T.; Jørgensen, A. C.; Rantanen, J., Factors affecting crystallization of hydrates. *J. Pharm. Pharmacol.* **2010**, 62, (11), 1534-1546.
- (45) Laurent, S.; Couture, F.; Girard, C., Thermodynamical and Chemical Behavior of a Solid Hydrate during Drying. *Drying Technol.* **2013**, 31, (9), 1029-1048.
- (46) Zhu, H.; Yuen, C.; Grant, D. J. W., Influence of water activity in organic solvent + water mixtures on the nature of the crystallizing drug phase. 1. Theophylline. *Int. J. Pharm.* **1996**, 135, (1-2), 151-160.
- (47) Ticehurst, M. D.; Storey, R. A.; Watt, C., Application of slurry bridging experiments at controlled water activities to predict the solid-state conversion between anhydrous and hydrated forms using theophylline as a model drug. *Int. J. Pharm.* **2002**, 247, (1-2), 1-10.
- (48) Ledwidge, M. T.; Corrigan, O. I., Effects of environmental factors on the dehydration of diclofenac HEP dihydrate and theophylline monohydrate. *Int. J. Pharm.* **1997**, 147, (1), 41-49.
- (49) Krzyzaniak, J. F.; Williams, G. R.; Ni, N., Identification of phase boundaries in anhydrate/hydrate systems. *J. Pharm. Sci.* **2007**, 96, (5), 1270-1281.

- (50) Reutzel-Edens, S. M.; Newman, A. W., Physical Characterization of Hygroscopicity in Pharmaceutical Solids. In *Polymorphism*, Wiley-VCH Verlag GmbH & Co. KGaA: 2006; pp 235-258.
- (51) Authelin, J., Thermodynamics of non-stoichiometric pharmaceutical hydrates. *Int. J. Pharm.* **2005**, 303, (1-2), 37-53.
- (52) Shefter, E.; Higuchi, T., Dissolution behavior of crystalline solvated and nonsolvated forms of some pharmaceuticals. *J. Pharm. Sci.* **1963**, 52, (8), 781-791.
- (53) Rager, T.; Geoffroy, A.; Hilfiker, R.; Storey, J. M. D., The crystalline state of methylene blue: a zoo of hydrates. *Phys. Chem. Chem. Phys.* **2012**, 14, (22), 8074-8082.
- (54) Bērziņš, A.; Actiņš, A.; P.Kreišmanis, J., Hydration and dehydration kinetics of xylazine hydrochloride. *Pharm. Dev. Technol.* **2009**, 14, (4), 388-399.
- (55) Blumberga, A.; Actiņš, A., Thermodynamic stability of crystalline modifications of zopiclone. *Latv. J. Chem.* **2005**, (2), 111-118.
- (56) Fucke, K.; Steed, J. W., X-ray and Neutron Diffraction in the Study of Organic Crystalline Hydrates. *Water* **2010**, 2, 333-350.
- (57) Fujii, K.; Ashida, Y.; Uekusa, H.; Guo, F.; Harris, K. D. M., Selective transformation pathways between crystalline forms of an organic material established from powder X-ray diffraction analysis. *Chem. Commun.* **2010**, 46, (24), 4264-4266.
- (58) Fujii, K.; Uekusa, H.; Itoda, N.; Yonemochi, E.; Terada, K., Mechanism of Dehydration–Hydration Processes of Lisinopril Dihydrate Investigated by ab Initio Powder X-ray Diffraction Analysis. *Cryst. Growth Des.* **2012**, 12, (12), 6165-6172.
- (59) Hodgkinson, P., Intramolecular Motion in Crystalline Organic Solids. In *NMR Crystallography*, Harris, R. K.; Wasylshen, R. E.; Duer, M. J., Eds. Wiley: 2009.
- (60) Carignani, E.; Borsacchi, S.; Geppi, M., Dynamics by Solid-State NMR: Detailed Study of Ibuprofen Na Salt and Comparison with Ibuprofen. *J. Phys. Chem. A* **2011**, 115, (32), 8783-8790.
- (61) Harris, R. K., NMR studies of organic polymorphs & solvates. *Analyst* **2006**, 131, (3), 351-373.
- (62) Dempah, K.; Barich, D.; Kaushal, A.; Zong, Z.; Desai, S.; Suryanarayanan, R.; Kirsch, L.; Munson, E., Investigating Gabapentin Polymorphism Using Solid-State NMR Spectroscopy. *AAPS PharmSciTech* **2013**, 14, (1), 19-28.
- (63) Byard, S.; Abraham, A.; Boulton, P. J. T.; Harris, R. K.; Hodgkinson, P., A multi-technique approach to the study of structural stability and desolvation of two unusual channel hydrate solvates of finasteride. *J. Pharm. Sci.* **2012**, 101, (1), 176-186.
- (64) Dracinsky, M.; Sala, M.; Hodgkinson, P., Dynamics of water molecules and sodium ions in solid hydrates of nucleotides. *CrystEngComm* **2014**, 16, (29), 6756-6764.
- (65) Hogg, N. H. M.; Boulton, P. J. T.; Zorin, V. E.; Harris, R. K.; Hodgkinson, P., Use of rotary echoes in magic-angle spinning NMR for the quantitative study of molecular dynamics. *Chem. Phys. Lett.* **2009**, 475, (1-3), 58-63.
- (66) Vold, R. R., Deuterium NMR studies of dynamics in solids and liquid crystals. In *Nuclear Magnetic Resonance Probes of Molecular Dynamics*, ed.; Tycko, R., Ed. 1994; pp 27-112.
- (67) Soda, G.; Chiba, T., Deuteron Magnetic Resonance Study of Cupric Sulfate Pentahydrate. *J. Chem. Phys.* **1969**, 50, (1), 439-455.
- (68) Chiba, T.; Soda, G., Deuteron Quadrupole Interactions in Two Modifications of Oxalic Acid Dihydrate Crystal. *Bull. Chem. Soc. Jpn.* **1971**, 44, (6), 1703-1704.
- (69) Ahlqvist, M. U. A.; Taylor, L. S., Water dynamics in channel hydrates investigated using H/D exchange. *Int. J. Pharm.* **2002**, 241, (2), 253-261.
- (70) Apperley, D. C.; Markwell, A. F.; Frantsuzov, I.; Ilott, A. J.; Harris, R. K.; Hodgkinson, P., NMR characterisation of dynamics in solvates and desolvates of formoterol fumarate. *Phys. Chem. Chem. Phys.* **2013**, 15, (17), 6422-6430.
- (71) Apperley, D. C.; Harris, R. K.; Hodgkinson, P., *Solid state nmr: Basic principles & practice*. ed.; Momentum: 2012.
- (72) Apperley, D. C.; Markwell, A. F.; Harris, R. K.; Hodgkinson, P., NMR characterisation of structure in solvates and polymorphs of formoterol fumarate. *Magn. Reson. Chem.* **2012**, 50, (10), 680-690.
- (73) Vogt, F. G.; Brum, J.; Katrincic, L. M.; Flach, A.; Socha, J. M.; Goodman, R. M.; Haltiwanger, R. C., Physical, Crystallographic, and Spectroscopic Characterization of a Crystalline Pharmaceutical Hydrate: Understanding the Role of Water. *Cryst. Growth Des.* **2006**, 6, (10), 2333-2354.
- (74) Vogt, F. G.; Copley, R. C. B.; Mueller, R. L.; Spoons, G. P.; Cacchio, T. N.; Carlton, R. A.; Katrincic, L. M.; Kennady, J. M.; Parsons, S.; Chetina, O. V., Isomorphism, Disorder, and Hydration in

- the Crystal Structures of Racemic and Single-Enantiomer Carvedilol Phosphate. *Cryst. Growth Des.* **2010**, *10*, (6), 2713-2733.
- (75) Steiner, T.; Koellner, G., Crystalline .beta.-Cyclodextrin Hydrate at Various Humidities: Fast, Continuous, and Reversible Dehydration Studied by X-ray Diffraction. *J. Am. Chem. Soc.* **1994**, *116*, (12), 5122-5128.
- (76) Chen, L. R.; Young Jr, V. G.; Lechuga-Ballesteros, D.; Grant, D. J. W., Solid-state behavior of cromolyn sodium hydrates. *J. Pharm. Sci.* **1999**, *88*, (11), 1191-1200.
- (77) Evans, J. S. O.; Radosavljevic Evans, I., Beyond classical applications of powder diffraction. *Chem. Soc. Rev.* **2004**, *33*, (8), 539-547.
- (78) Kiang, Y. H.; Cheung, E.; Stephens, P. W.; Nagapudi, K., Structural Studies of a Nonstoichiometric Channel Hydrate Using High-Resolution X-ray Powder Diffraction, Solid-State Nuclear Magnetic Resonance, and Moisture Sorption Methods. *J. Pharm. Sci.* **2014**, n/a-n/a.
- (79) Chakravarty, P.; Berendt, R. T.; Munson, E. J.; Young, V. G.; Govindarajan, R.; Suryanarayanan, R., Insights into the dehydration behavior of thiamine hydrochloride (Vitamin B1) hydrates: Part I. *J. Pharm. Sci.* **2010**, *99*, (2), 816-827.
- (80) Kang, F.; Vogt, F. G.; Brum, J.; Forcino, R.; Copley, R. C. B.; Williams, G.; Carlton, R., Effect of Particle Size and Morphology on the Dehydration Mechanism of a Non-Stoichiometric Hydrate. *Cryst. Growth Des.* **2011**, *12*, (1), 60-74.
- (81) Apperley, D. C.; Basford, P. A.; Dallman, C. I.; Harris, R. K.; Kinns, M.; Marshall, P. V.; Swanson, A. G., Nuclear magnetic resonance investigation of the interaction of water vapor with sildenafil citrate in the solid state. *J. Pharm. Sci.* **2005**, *94*, (3), 516-523.
- (82) Vogt, F. G.; Dell'Orco, P. C.; Diederich, A. M.; Su, Q.; Wood, J. L.; Zuber, G. E.; Katrincic, L. M.; Mueller, R. L.; Busby, D. J.; DeBrosse, C. W., A study of variable hydration states in topotecan hydrochloride. *J. Pharm. Biomed. Anal.* **2006**, *40*, (5), 1080-1088.
- (83) Pina, M. F.; Pinto, J. F.; Sousa, J. J.; Fábíán, L.; Zhao, M.; Craig, D. Q. M., Identification and Characterization of Stoichiometric and Nonstoichiometric Hydrate Forms of Paroxetine HCl: Reversible Changes in Crystal Dimensions as a Function of Water Absorption. *Mol. Pharm.* **2012**, *9*, (12), 3515-3525.
- (84) Zeidan, T. A.; Trotta, J. T.; Chiarella, R. A.; Oliveira, M. A.; Hickey, M. B.; Almarsson, Ö.; Remenar, J. F., Polymorphism of Dehydro-Aripiprazole, the Active Metabolite of the Antipsychotic Drug Aripiprazole (Abilify). *Cryst. Growth Des.* **2013**, *13*, (5), 2036-2046.
- (85) Aitipamula, S.; Chow, P. S.; Tan, R. B. H., Solvates and a monohydrate of N4-acetylsulfamerazine: Structural, thermochemical, and computational analysis. *J. Mol. Struct.* **2011**, *1005*, (1-3), 134-140.
- (86) Nanubolu, J. B.; Sridhar, B.; Babu, V. S. P.; Jagadeesh, B.; Ravikumar, K., Sixth polymorph of aripiprazole - an antipsychotic drug. *CrystEngComm* **2012**, *14*, (14), 4677-4685.
- (87) Surov, A. O.; Bui, C. T.; Proshin, A. N.; Roussel, P.; Idrissi, A.; Perlovich, G. L., Novel 1,2,4-Thiadiazole Derivatives: Crystal Structure, Conformational Analysis, Hydrogen Bond Networks, Calculations, and Thermodynamic Characteristics of Crystal Lattices. *J. Phys. Chem. B* **2013**, *117*, (36), 10414-10429.
- (88) Bernstein, J., Conformational polymorphism: intra- and intermolecular energetics. In *Polymorphism in Molecular Crystals*, Bernstein, J., Ed. Oxford University Press: Oxford, 2002; pp 151-187.
- (89) Zencirci, N.; Griesser, U. J.; Gelbrich, T.; Kahlenberg, V.; Jetti, R. K. R.; Apperley, D. C.; Harris, R. K., New Solvates of an Old Drug Compound (Phenobarbital): Structure and Stability. *J. Phys. Chem. B* **2014**.
- (90) Sheth, A. R.; Zhou, D.; Muller, F. X.; Grant, D. J. W., Dehydration kinetics of piroxicam monohydrate and relationship to lattice energy and structure. *J. Pharm. Sci.* **2004**, *93*, (12), 3013-3026.
- (91) Braun, D. E.; Gelbrich, T.; Kahlenberg, V.; Tessadri, R.; Wieser, J.; Griesser, U. J., Conformational polymorphism in aripiprazole: Preparation, stability and structure of five modifications. *J. Pharm. Sci.* **2009**, *98*, (6), 2010-2026.
- (92) Blake, A. J.; Clegg, W.; Cole, J. M.; Evans, J. S. O.; Main, P.; Parsons, S.; Watkin, D. J., *Crystal structure analysis: principles and practice*. ed.; Oxford University Press: 2009; Vol. 13.
- (93) Spek, A. L., Structure validation in chemical crystallography. *Acta Crystallogr., Sect. D* **2009**, *65*, (2), 148-155.
- (94) McKinnon, J. J.; Fabbiani, F. P. A.; Spackman, M. A., Comparison of Polymorphic Molecular Crystal Structures through Hirshfeld Surface Analysis. *Cryst. Growth Des.* **2007**, *7*, (4), 755-769.
- (95) McKinnon, J. J.; Spackman, M. A.; Mitchell, A. S., Novel tools for visualizing and exploring intermolecular interactions in molecular crystals. *Acta Crystallogr. B* **2004**, *60*, (6), 627-668.

- (96) Spackman, M. A.; Jayatilaka, D., Hirshfeld surface analysis. *CrystEngComm* **2009**, 11, (1), 19-32.
- (97) Gavezzotti, A., Efficient computer modeling of organic materials. The atom-atom, Coulomb-London-Pauli (AA-CLP) model for intermolecular electrostatic-polarization, dispersion and repulsion energies. *New J. Chem.* **2011**, 35, (7), 1360-1368.
- (98) Maschio, L.; Civalieri, B.; Ugliengo, P.; Gavezzotti, A., Intermolecular Interaction Energies in Molecular Crystals: Comparison and Agreement of Localized Møller–Plesset 2, Dispersion-Corrected Density Functional, and Classical Empirical Two-Body Calculations. *J. Phys. Chem. A* **2011**, 115, (41), 11179-11186.
- (99) Dunitz, J. D.; Gavezzotti, A., Molecular Recognition in Organic Crystals: Directed Intermolecular Bonds or Nonlocalized Bonding? *Angew. Chem., Int. Ed.* **2005**, 44, (12), 1766-1787.
- (100) Gavezzotti, A., Computational Studies of Crystal Structure and Bonding. *Top. Curr. Chem.* **2012**, 315, 1-32.
- (101) Bernstein, J.; Davis, R. E.; Shimoni, L.; Chang, N.-L., Patterns in Hydrogen Bonding: Functionality and Graph Set Analysis in Crystals. *Angewandte Chemie International Edition in English* **1995**, 34, (15), 1555-1573.
- (102) Macrae, C. F.; Bruno, I. J.; Chisholm, J. A.; Edgington, P. R.; McCabe, P.; Pidcock, E.; Rodriguez-Monge, L.; Taylor, R.; van de Streek, J.; Wood, P. A., Mercury CSD 2.0 - new features for the visualization and investigation of crystal structures. *J. Appl. Crystallogr.* **2008**, 41, (2), 466-470.
- (103) Wolff, S. K.; Grimwood, D. J.; McKinnon, J. J.; Turner, M. J.; Jayatilaka, D.; Spackman, M. A. *CrystalExplorer (Version 3.1)*, University of Western Australia: 2012.
- (104) McKinnon, J. J.; Jayatilaka, D.; Spackman, M. A., Towards quantitative analysis of intermolecular interactions with Hirshfeld surfaces. *Chem. Commun.* **2007**, (37), 3814-3816.
- (105) Gavezzotti, A., Calculation of Intermolecular Interaction Energies by Direct Numerical Integration over Electron Densities. I. Electrostatic and Polarization Energies in Molecular Crystals. *The Journal of Physical Chemistry B* **2002**, 106, (16), 4145-4154.
- (106) Gavezzotti, A., Calculation of Intermolecular Interaction Energies by Direct Numerical Integration over Electron Densities. 2. An Improved Polarization Model and the Evaluation of Dispersion and Repulsion Energies. *The Journal of Physical Chemistry B* **2003**, 107, (10), 2344-2353.
- (107) Gavezzotti, A., Calculation of lattice energies of organic crystals: the PIXEL integration method in comparison with more traditional methods. *Z. Kristallogr.* **2005**, 220, (5-6-2005), 499-510.
- (108) Dudenko, D. V.; Yates, J. R.; Harris, K. D. M.; Brown, S. P., An NMR crystallography DFT-D approach to analyse the role of intermolecular hydrogen bonding and [small pi]-[small pi] interactions in driving cocrystallisation of indomethacin and nicotinamide. *CrystEngComm* **2013**, 15, (43), 8797-8807.
- (109) Mafra, L.; Santos, S. M.; Siegel, R.; Alves, I.; Almeida Paz, F. A.; Dudenko, D.; Spiess, H. W., Packing Interactions in Hydrated and Anhydrous Forms of the Antibiotic Ciprofloxacin: a Solid-State NMR, X-ray Diffraction, and Computer Simulation Study. *J. Am. Chem. Soc.* **2011**, 134, (1), 71-74.
- (110) Durka, K.; Jarzemska, K. N.; Kamiński, R.; Luliński, S.; Serwatowski, J.; Woźniak, K., Structural and Energetic Landscape of Fluorinated 1,4-Phenylenediboronic Acids. *Cryst. Growth Des.* **2012**, 12, (7), 3720-3734.
- (111) Jarzemska, K. N.; Hoser, A. A.; Kamiński, R.; Madsen, A. Ø.; Durka, K.; Woźniak, K., Combined Experimental and Computational Studies of Pyrazinamide and Nicotinamide in the Context of Crystal Engineering and Thermodynamics. *Cryst. Growth Des.* **2014**, 14, (7), 3453-3465.
- (112) Panini, P.; Venugopala, K. N.; Odhav, B.; Chopra, D., Quantitative Analysis of Intermolecular Interactions in 7-Hydroxy-4-methyl-2H-chromen-2-one and Its Hydrate. *Proceedings of the National Academy of Sciences, India Section A: Physical Sciences* **2014**, 84, (2), 281-295.
- (113) Hoser, A. A.; Kaminski, D. M.; Matwijczuk, A.; Niewiadomy, A.; Gagos, M.; Wozniak, K., On polymorphism of 2-(4-fluorophenylamino)-5-(2,4-dihydroxybenzeno)-1,3,4-thiadiazole (FABT) DMSO solvates. *CrystEngComm* **2013**, 15, (10), 1978-1988.
- (114) Gavezzotti, A., Towards a realistic model for the quantitative evaluation of intermolecular potentials and for the rationalization of organic crystal structures. Part II. Crystal energy landscapes. *CrystEngComm* **2003**, 5, (77), 439-446.
- (115) Gavezzotti, A., The lines-of-force landscape of interactions between molecules in crystals; cohesive versus tolerant and 'collateral damage' contact. *Acta Crystallogr., Sect. B* **2010**, 66, (3), 396-406.
- (116) Gavezzotti, A., Quantitative Ranking of Crystal Packing Modes by Systematic Calculations on Potential Energies and Vibrational Amplitudes of Molecular Dimers. *J. Chem. Theory Comput.* **2005**, 1, (5), 834-840.
- (117) Price, S. L.; Price, L. S., Modelling Intermolecular Forces for Organic Crystal Structure Prediction

- Intermolecular Forces and Clusters I. In Wales, D., Ed. Springer Berlin / Heidelberg: 2005; Vol. 115, pp 81-123.
- (118) Karamertzanis, P. G.; Day, G. M.; Welch, G. W. A.; Kendrick, J.; Leusen, F. J. J.; Neumann, M. A.; Price, S. L., Modeling the interplay of inter- and intramolecular hydrogen bonding in conformational polymorphs. *The Journal of Chemical Physics* **2008**, 128, (24), -.
- (119) Otero-de-la-Roza, A.; Johnson, E. R., A benchmark for non-covalent interactions in solids. *The Journal of Chemical Physics* **2012**, 137, (5), -.
- (120) Salahinejad, M.; Le, T. C.; Winkler, D. A., Capturing the Crystal: Prediction of Enthalpy of Sublimation, Crystal Lattice Energy, and Melting Points of Organic Compounds. *J. Chem. Inf. Model.* **2013**, 53, (1), 223-229.
- (121) Kamiński, D. M.; Hoser, A. A.; Gagó, M.; Matwijczuk, A.; Arczewska, M.; Niewiadomy, A.; Wozniak, K., Solvatomorphism of 2-(4-Fluorophenylamino)-5-(2,4-dihydroxybenzeno)-1,3,4-thiadiazole Chloride. *Cryst. Growth Des.* **2010**, 10, (8), 3480-3488.
- (122) Mazur, L.; Jarzemska, K. N.; Kamiński, R.; Woźniak, K.; Pindelska, E.; Zielińska-Pisklak, M., Substituent and Solvent Effects on Intermolecular Interactions in Crystals of N-Acylhydrazone Derivatives: Single-Crystal X-ray, Solid-State NMR, and Computational Studies. *Cryst. Growth Des.* **2014**, 14, (5), 2263-2281.
- (123) Braun, D. E.; Gelbrich, T.; Jetti, R. K. R.; Kahlenberg, V.; Price, S. L.; Griesser, U. J., Colored Polymorphs: Thermochemical and Structural Features of N-Picryl- p-toluidine Polymorphs and Solvates. *Cryst. Growth Des.* **2008**, 8, (6), 1977-1989.
- (124) Dey, D.; Shripanavar, C. S.; Banerjee, K.; Chopra, D., Quantitative Crystal Structure Analysis of (E)-1-[(2-Chloro-1,3-thiazol-5-yl)methyl]-3-methyl-2-nitroguanidine. *Journal of Crystallography* **2014**, 2014, 8.
- (125) Maloney, A. G. P.; Wood, P. A.; Parsons, S., Competition between hydrogen bonding and dispersion interactions in the crystal structures of the primary amines. *CrystEngComm* **2014**, 16, (19), 3867-3882.
- (126) Durka, K.; Hoser, A. A.; Kamiński, R.; Luliński, S.; Serwatowski, J.; Koźmiński, W.; Woźniak, K., Polymorphism of a Model Arylboronic Azaester: Combined Experimental and Computational Studies. *Cryst. Growth Des.* **2011**, 11, (5), 1835-1845.
- (127) Seth, S. K.; Maity, G. C.; Kar, T., Structural elucidation, Hirshfeld surface analysis and quantum mechanical study of para-nitro benzylidene methyl arjunolate. *J. Mol. Struct.* **2011**, 1000, (1-3), 120-126.
- (128) Wood, P. A.; Olsson, T. S. G.; Cole, J. C.; Cottrell, S. J.; Feeder, N.; Galek, P. T. A.; Groom, C. R.; Pidcock, E., Evaluation of molecular crystal structures using Full Interaction Maps. *CrystEngComm* **2013**, 15, (1), 65-72.
- (129) Gelbrich, T.; Hursthouse, M. B., A versatile procedure for the identification, description and quantification of structural similarity in molecular crystals. *CrystEngComm* **2005**, 7, (53), 324-336.
- (130) Bond, A. D., The Role of the Cambridge Structural Database in Crystal Engineering. In *Organic crystal engineering: frontiers in crystal engineering*, Tiekink, E. R. T.; Vittal, J.; Zaworotko, M., Eds. John Wiley & Sons, Ltd.: Wiltshire, 2010; pp 1-42.
- (131) Gelbrich, T., The Xpac program for comparing molecular packing. *IUCr Newsllett.* **2006**, (7), 39-44.
- (132) Braun, D. E.; McMahon, J. A.; Koztecki, L. H.; Price, S. L.; Reutzel-Edens, S. M., Contrasting Polymorphism of Related Small Molecule Drugs Correlated and Guided by the Computed Crystal Energy Landscape. *Cryst. Growth Des.* **2014**.
- (133) Gelbrich, T.; Hursthouse, M. B., Systematic investigation of the relationships between 25 crystal structures containing the carbamazepine molecule or a close analogue: a case study of the XPac method. *CrystEngComm* **2006**, 8, (6), 448-460.
- (134) Gelder, R., Quantifying the Similarity of Crystal Structures. *IUCr Newsllett.* **2006**, (7), 59-69.
- (135) Chisholm, J. A.; Motherwell, S., COMPACT: a program for identifying crystal structure similarity using distances. *J. Appl. Crystallogr.* **2005**, 38, (1), 228-231.
- (136) Price, C. P.; Glick, G. D.; Matzger, A. J., Dissecting the Behavior of a Promiscuous Solvate Former. *Angew. Chem., Int. Ed.* **2006**, 45, (13), 2062-2066.
- (137) Nangia, A.; Desiraju, G., Pseudopolymorphism: occurrences of hydrogen bonding organic solvents in molecular crystals. *Chem. Commun.* **1999**, 1999, (7), 605-606.
- (138) Zhang, Q.; Lu, L.; Dai, W.; Mei, X., Polymorphism and isomorphism of Huperzine A solvates: structure, properties and form transformation. *CrystEngComm* **2014**, 16, 1919-1926.

- (139) Gramatica, P.; Navas, N.; Todeschini, R., Classification of organic solvents and modelling of their physico-chemical properties by chemometric methods using different sets of molecular descriptors. *Trends Anal. Chem.* **1999**, 18, (7), 461-471.
- (140) Gu, C.-H.; Li, H.; Gandhi, R. B.; Raghavan, K., Grouping solvents by statistical analysis of solvent property parameters: implication to polymorph screening. *Int. J. Pharm.* **2004**, 283, (1–2), 117-125.
- (141) Infantes, L.; Chisholm, J.; Motherwell, S., Extended motifs from water and chemical functional groups in organic molecular crystals. *CrystEngComm* **2003**, 5, (85), 480-486.
- (142) Brychczynska, M.; Davey, R. J.; Pidcock, E., A study of methanol solvates using the Cambridge structural database. *New J. Chem.* **2008**, 32, (10), 1754-1760.
- (143) Gillon, A. L.; Feeder, N.; Davey, R. J.; Storey, R., Hydration in Molecular Crystals A Cambridge Structural Database Analysis. *Cryst. Growth Des.* **2003**, 3, (5), 663-673.
- (144) Infantes, L.; Fabian, L.; Motherwell, W. D. S., Organic crystal hydrates: what are the important factors for formation. *CrystEngComm* **2007**, 9, (1), 65-71.
- (145) Gavezzotti, A., Are Crystal Structures Predictable? *Acc. Chem. Res.* **1994**, 27, (10), 309-314.
- (146) Price, S. L., Predicting crystal structures of organic compounds. *Chem. Soc. Rev.* **2014**, 2098-2111.
- (147) Day, G. M., Current approaches to predicting molecular organic crystal structures. *Crystallogr. Rev.* **2011**, 17, (1), 3-52.
- (148) Price, S., Why don't we find more polymorphs? *Acta Crystallogr., Sect. B* **2013**, 69, (4), 313-328.
- (149) Bardwell, D. A.; Adjiman, C. S.; Arnautova, Y. A.; Bartashevich, E.; Boerrigter, S. X. M.; Braun, D. E.; Cruz-Cabeza, A. J.; Day, G. M.; Della Valle, R. G.; Desiraju, G. R.; van Eijck, B. P.; Facelli, J. C.; Ferraro, M. B.; Grillo, D.; Habgood, M.; Hofmann, D. W. M.; Hofmann, F.; Jose, K. V. J.; Karamertzanis, P. G.; Kazantsev, A. V.; Kendrick, J.; Kuleshova, L. N.; Leusen, F. J. J.; Maleev, A. V.; Misquitta, A. J.; Mohamed, S.; Needs, R. J.; Neumann, M. A.; Nikylov, D.; Orendt, A. M.; Pal, R.; Pantelides, C. C.; Pickard, C. J.; Price, L. S.; Price, S. L.; Scheraga, H. A.; van de Streek, J.; Thakur, T. S.; Tiwari, S.; Venuti, E.; Zhitkov, I. K., Towards crystal structure prediction of complex organic compounds - a report on the fifth blind test. *Acta Crystallogr., Sect. B* **2011**, 67, (6), 535-551.
- (150) Kazantsev, A. V.; Karamertzanis, P. G.; Adjiman, C. S.; Pantelides, C. C.; Price, S. L.; Galek, P. T. A.; Day, G. M.; Cruz-Cabeza, A. J., Successful prediction of a model pharmaceutical in the fifth blind test of crystal structure prediction. *Int. J. Pharm.* **2011**, 418, (2), 168-178.
- (151) Ismail, S. Z.; Anderton, C. L.; Copley, R. C. B.; Price, L. S.; Price, S. L., Evaluating a Crystal Energy Landscape in the Context of Industrial Polymorph Screening. *Cryst. Growth Des.* **2013**, 13, (6), 2396-2406.
- (152) Kendrick, J.; Stephenson, G. A.; Neumann, M. A.; Leusen, F. J. J., Crystal Structure Prediction of a Flexible Molecule of Pharmaceutical Interest with Unusual Polymorphic Behavior. *Cryst. Growth Des.* **2013**, 13, (2), 581-589.
- (153) Baias, M.; Dumez, J.-N.; Svensson, P. H.; Schantz, S.; Day, G. M.; Emsley, L., De Novo Determination of the Crystal Structure of a Large Drug Molecule by Crystal Structure Prediction-Based Powder NMR Crystallography. *J. Am. Chem. Soc.* **2013**, 135, (46), 17501-17507.
- (154) Eddleston, M. D.; Hejczyk, K. E.; Bithell, E. G.; Day, G. M.; Jones, W., Polymorph Identification and Crystal Structure Determination by a Combined Crystal Structure Prediction and Transmission Electron Microscopy Approach. *Chem. Eur. J.* **2013**, 19, (24), 7874-7882.
- (155) Braun, D. E.; Tocher, D. A.; Price, S. L.; Griesser, U. J., The Complexity of Hydration of Phloroglucinol: A Comprehensive Structural and Thermodynamic Characterization. *J. Phys. Chem. B* **2012**, 116, (13), 3961-3972.
- (156) Braun, D. E.; Karamertzanis, P. G.; Price, S. L., Which, if any, hydrates will crystallise? Predicting hydrate formation of two dihydroxybenzoic acids. *Chem. Commun.* **2011**, 47, (19), 5443-5445.
- (157) Hulme, A. T.; Price, S. L., Toward the Prediction of Organic Hydrate Crystal Structures. *J. Chem. Theory Comput.* **2007**, 3, (4), 1597-1608.
- (158) Cruz-Cabeza, A. J.; Karki, S.; Fabian, L.; Friscic, T.; Day, G. M.; Jones, W., Predicting stoichiometry and structure of solvates. *Chem. Commun.* **2010**, 46, (13), 2224-2226.
- (159) Byrn, S. R.; Pfeiffer, R. R.; Stowell, J. G., *Solid State Chemistry of Drugs*. 2nd edn. ed.; SSCI, Inc.: West Lafayette, IN, 1999; p 754.
- (160) Perrier, P.; Byrn, S. R., Influence of crystal packing on the solid-state desolvation of purine and pyrimidine hydrates: loss of water of crystallization from thymine monohydrate, cytosine monohydrate, 5-nitouracil monohydrate, and 2'-deoxyadenosine monohydrate. *J. Org. Chem.* **1982**, 47, (24), 4671-4676.
- (161) Mimura, H.; Kitamura, S.; Kitagawa, T.; Kohda, S., Characterization of the non-stoichiometric and isomorphic hydration and solvation in FK041 clathrate. *Colloids Surf., B* **2002**, 26, (4), 397-406.

- (162) Petit, S.; Coquerel, G., Mechanism of Several Solid–Solid Transformations between Dihydrated and Anhydrous Copper(II) 8-Hydroxyquinolinates. Proposition for a Unified Model for the Dehydration of Molecular Crystals. *Chem. Mater.* **1996**, *8*, (9), 2247-2258.
- (163) Galwey, A., Structure and order in thermal dehydrations of crystalline solids. *Thermochim. Acta* **2000**, *355*, (1-2), 181-238.
- (164) Shankland, N.; David, W. I. F.; Shankland, K.; Kennedy, A. R.; Frampton, C. S.; Florence, A. J., Structural transformations in zopiclone. *Chem. Commun.* **2001**, (21), 2204-2205.
- (165) Fujii, K.; Uekusa, H.; Itoda, N.; Hasegawa, G.; Yonemochi, E.; Terada, K.; Pan, Z.; Harris, K. D. M., Physicochemical Understanding of Polymorphism and Solid-State Dehydration/Rehydration Processes for the Pharmaceutical Material Acrinol, by Ab Initio Powder X-ray Diffraction Analysis and Other Techniques. *J. Phys. Chem. C* **2009**, *114*, (1), 580-586.
- (166) Czapik, A.; Konowalska, H.; Gdaniec, M., p-Phenylenediamine and its dihydrate: two-dimensional isomorphism and mechanism of the dehydration process, and N-H...N and N-H...[pi] interactions. *Acta Crystallogr., Sect. C* **2010**, *66*, (3), o128-o132.
- (167) Guguta, C.; Meeke, H.; de Gelder, R., Crystal Structure of Aspartame Anhydrate from Powder Diffraction Data. Structural Aspects of the Dehydration Process of Aspartame. *Cryst. Growth Des.* **2006**, *6*, (12), 2686-2692.
- (168) Guguta, C.; Meeke, H.; de Gelder, R., The hydration/dehydration behavior of aspartame revisited. *J. Pharm. Biomed. Anal.* **2008**, *46*, (4), 617-624.
- (169) Guguta, C.; van Eck, E. R. H.; de Gelder, R., Structural Insight into the Dehydration and Hydration Behavior of Naltrexone and Naloxone Hydrochloride. Dehydration-Induced Expansion versus Contraction. *Cryst. Growth Des.* **2009**, *9*, (8), 3384-3395.
- (170) Aitipamula, S.; Chow, P. S.; Tan, R. B. H., Solvates and polymorphic phase transformations of 2-chloro-4-nitrobenzoic acid. *CrystEngComm* **2011**, *13*, (3), 1037-1045.
- (171) Koradia, V.; de Diego, H. L.; Elema, M. R.; Rantanen, J., Integrated approach to study the dehydration kinetics of nitrofurantoin monohydrate. *J. Pharm. Sci.* **2010**, *99*, (9), 3966-3976.
- (172) Zhu, H.; Xu, J.; Varlashkin, P.; Long, S.; Kidd, C., Dehydration, hydration behavior, and structural analysis of fenoprofen calcium*. *J. Pharm. Sci.* **2001**, *90*, (7), 845-859.
- (173) Gillon, A. L.; Davey, R. J.; Storey, R.; Feeder, N.; Nichols, G.; Dent, G.; Apperley, D. C., Solid State Dehydration Processes: Mechanism of Water Loss from Crystalline Inosine Dihydrate. *The Journal of Physical Chemistry B* **2005**, *109*, (11), 5341-5347.
- (174) Suzuki, T.; Araki, T.; Kitaoka, H.; Terada, K., Characterization of Non-stoichiometric Hydration and the Dehydration Behavior of Sitafloxacin Hydrate. *Chem. Pharm. Bull.* **2012**, *60*, (1), 45.
- (175) Nassimbeni, L. R., Physicochemical Aspects of Host–Guest Compounds. *Acc. Chem. Res.* **2003**, *36*, (8), 631-637.
- (176) Aitipamula, S.; Chow, P. S.; Tan, R. B. H., Polymorphs and Solvates of a Cocrystal Involving an Analgesic Drug, Ethenzamide, and 3,5-Dinitrobenzoic Acid. *Cryst. Growth Des.* **2010**, *10*, (5), 2229-2238.
- (177) Bettinetti, G. P.; Caira, M. R.; Sorrenti, M.; Catenacci, L.; Ghirardi, M.; Fábíán, L., Thermal studies of solvent exchange in isostructural solvates of a tetroxoprim-sulfametrole complex. *J. Therm. Anal. Calorim.* **2004**, *77*, (2), 695-708.
- (178) Nagase, H.; Ogawa, N.; Endo, T.; Shiro, M.; Ueda, H.; Sakurai, M., Crystal Structure of an Anhydrous Form of Trehalose: Structure of Water Channels of Trehalose Polymorphism. *The Journal of Physical Chemistry B* **2008**, *112*, (30), 9105-9111.
- (179) Malaj, L.; Censi, R.; Martino, P. D., Mechanisms for dehydration of three sodium naproxen hydrates. *Cryst. Growth Des.* **2009**, *9*, (5), 2128-2136.
- (180) Zhou, D.; Schmitt, E. A.; Zhang, G. G. Z.; Law, D.; Wight, C. A.; Vyazovkin, S.; Grant, D. J. W., Model-free treatment of the dehydration kinetics of nedocromil sodium trihydrate. *J. Pharm. Sci.* **2003**, *92*, (7), 1367-1376.
- (181) Dong, Z.; Salsbury, J. S.; Zhou, D.; Munson, E. J.; Schroeder, S. A.; Prakash, I.; Vyazovkin, S.; Wight, C. A.; Grant, D. J. W., Dehydration kinetics of neotame monohydrate. *J. Pharm. Sci.* **2002**, *91*, (6), 1423-1431.
- (182) Alkhamis, K. A.; Salem, M. S.; Obaidat, R. M., Comparison between dehydration and desolvation kinetics of fluconazole monohydrate and fluconazole ethylacetate solvate using three different methods. *J. Pharm. Sci.* **2006**, *95*, (4), 859-870.
- (183) Joshi, V.; Morris, K. R.; Byrn, S. R.; Carvajal, M. T., Evaluation of the Use of Ea (Activation Energy) as a Quantitative Indicator of Physical Stability of Indomethacin Solvates: Methanolate and Tertiary Butyl Alcohol Solvate. *Cryst. Growth Des.* **2009**, *9*, (8), 3359-3366.

- (184) Shimanovich, R.; Cooke, M.; Peterson, M. L., A rapid approach to the preliminary assessment of the physical stability of pharmaceutical hydrates. *J. Pharm. Sci.* **2012**, 101, (10), 4013-4017.
- (185) Kim, Y.-s.; Paskow, H. C.; Rousseau, R. W., Propagation of Solid-State Transformations by Dehydration and Stabilization of Pseudopolymorphic Crystals of Sodium Naproxen. *Cryst. Growth Des.* **2005**, 5, (4), 1623-1632.
- (186) Zellelow, A. Z.; Kim, K.-H.; Sours, R. E.; Swift, J. A., Solid-State Dehydration of Uric Acid Dihydrate. *Cryst. Growth Des.* **2009**, 10, (1), 418-425.
- (187) Galwey, A. K.; Brown, M. E., *Thermal Decomposition of Ionic Solids*. ed.; Elsevier: Amsterdam, 1999; p 598.
- (188) Bamford, C. H.; Tipper, C. F. H., *Reactions in the Solid State*. ed.; Elsevier: Amsterdam, 1980; p 340.
- (189) Houston, P., *Chemical kinetics and reaction dynamics*. ed.; McGraw-Hill Boston, MA: 2001.
- (190) Khawam, A.; Flanagan, D. R., Basics and applications of solid-state kinetics: A pharmaceutical perspective. *J. Pharm. Sci.* **2006**, 95, (3), 472-498.
- (191) Khawam, A.; Flanagan, D. R., Solid-State Kinetic Models: Basics and Mathematical Fundamentals. *J. Phys. Chem. B* **2006**, 110, (35), 17315-17328.
- (192) Dickinson, C. F.; Heal, G. R., Solid-liquid diffusion controlled rate equations. *Thermochim. Acta* **1999**, 340-341, (0), 89-103.
- (193) Giron, D.; Goldbronn, C.; Mutz, M.; Pfeffer, S.; Piechon, P.; Schwab, P., Solid State Characterizations of Pharmaceutical Hydrates. *J. Therm. Anal. Calorim.* **2002**, 68, (2), 453-465.
- (194) Koga, N.; Tanaka, H., A physico-geometric approach to the kinetics of solid-state reactions as exemplified by the thermal dehydration and decomposition of inorganic solids. *Thermochim. Acta* **2002**, 388, (1-2), 41-61.
- (195) Galwey, A. K.; Brown, M. E., Application of the Arrhenius equation to solid state kinetics: can this be justified? *Thermochim. Acta* **2002**, 386, (1), 91-98.
- (196) Galwey, A. K.; Brown, M. E., A Theoretical Justification for the Application of the Arrhenius Equation to Kinetics of Solid State Reactions (Mainly Ionic Crystals). *Proceedings of the Royal Society of London. Series A: Mathematical and Physical Sciences* **1995**, 450, (1940), 501-512.
- (197) Galwey, A.; Brown, M., Solid-state Decompositions—Stagnation or Progress? *J. Therm. Anal. Calorim.* **2000**, 60, (3), 863-877.
- (198) Laidler, K. J., The development of the Arrhenius equation. *J. Chem. Educ.* **1984**, 61, (6), 494.
- (199) Anderson, H. C., *Thermal Analysis*. ed.; Chem. Inst. Canada: Toronto, 1967.
- (200) Vyazovkin, S.; Burnham, A. K.; Criado, J. M.; Pérez-Maqueda, L. A.; Popescu, C.; Sbirrazzuoli, N., ICTAC Kinetics Committee recommendations for performing kinetic computations on thermal analysis data. *Thermochim. Acta* **2011**, 520, (1-2), 1-19.
- (201) Brown, M. E.; Maciejewski, M.; Vyazovkin, S.; Nomen, R.; Sempere, J.; Burnham, A.; Opfermann, J.; Strey, R.; Anderson, H. L.; Kemmler, A.; Keuleers, R.; Janssens, J.; Desseyn, H. O.; Li, C.-R.; Tang, T. B.; Roduit, B.; Malek, J.; Mitsunashi, T., Computational aspects of kinetic analysis: Part A: The ICTAC kinetics project-data, methods and results. *Thermochim. Acta* **2000**, 355, (1-2), 125-143.
- (202) Vyazovkin, S.; Wight, C. A., Model-free and model-fitting approaches to kinetic analysis of isothermal and nonisothermal data. *Thermochim. Acta* **1999**, 340-341, 53-68.
- (203) Dickinson, C. F.; Heal, G. R., A review of the ICTAC kinetics project, 2000: Part 2. Non-isothermal results. *Thermochim. Acta* **2009**, 494, (1-2), 15-25.
- (204) Okoth, M. O.; Vrcelj, R. M.; Sheen, D. B.; Sherwood, J. N., Hydration studies of a simple molecular solid. *CrystEngComm* **2012**, 14, (5), 1602-1612.
- (205) Okoth, M. O.; Vrcelj, R. M.; Sheen, D. B.; Sherwood, J. N., Dehydration mechanism of a small molecular solid: 5-nitouracil hydrate. *CrystEngComm* **2013**, 15, (40), 8202-8213.
- (206) Šimon, P., Isoconversional methods. *J. Therm. Anal. Calorim.* **2004**, 76, (1), 123-132.
- (207) Zsakó, J., Kinetic analysis of thermogravimetric data. *J. Therm. Anal. Calorim.* **1996**, 46, (6), 1845-1864.
- (208) Friedman, H. L., Kinetics of thermal degradation of char-forming plastics from thermogravimetry. Application to a phenolic plastic. *J. Polym. Sci. C* **1964**, 6, 183-195.
- (209) Ortega, A., A simple and precise linear integral method for isoconversional data. *Thermochim. Acta* **2008**, 474, (1-2), 81-86.
- (210) Vyazovkin, S., Evaluation of activation energy of thermally stimulated solid-state reactions under arbitrary variation of temperature. *J. Comput. Chem.* **1997**, 18, (3), 393-402.
- (211) Vyazovkin, S., Modification of the integral isoconversional method to account for variation in the activation energy. *J. Comput. Chem.* **2001**, 22, (2), 178-183.

- (212) Khawam, A.; Flanagan, D. R., Complementary Use of Model-Free and Modelistic Methods in the Analysis of Solid-State Kinetics. *J. Phys. Chem. B* **2005**, 109, (20), 10073-10080.
- (213) Koga, N., A review of the mutual dependence of Arrhenius parameters evaluated by the thermoanalytical study of solid-state reactions: The kinetic compensation effect. *Thermochim. Acta* **1994**, 244, 1-20.
- (214) Vyazovkin, S. V.; Lesnikovich, A. I., Estimation of the pre-exponential factor in the isoconversional calculation of effective kinetic parameters. *Thermochim. Acta* **1988**, 128, 297-300.
- (215) Ortega, A., The kinetics of solid-state reactions toward consensus, Part 2: Fitting kinetics data in dynamic conventional thermal analysis. *Int. J. Chem. Kinet.* **2002**, 34, (3), 193-208.
- (216) Brown, M. E., *Introduction to thermal analysis: techniques and applications*. ed.; Springer: 2001; Vol. 1.
- (217) Galwey, A., What can we learn about the mechanisms of thermal decompositions of solids from kinetic measurements? *J. Therm. Anal. Calorim.* **2008**, 92, (3), 967-983.
- (218) Galwey, A. K., Is the science of thermal analysis kinetics based on solid foundations?: A literature appraisal. *Thermochim. Acta* **2004**, 413, (1-2), 139-183.
- (219) Agbada, C. O.; York, P., Dehydration of theophylline monohydrate powder -- effects of particle size and sample weight. *Int. J. Pharm.* **1994**, 106, (1), 33-40.
- (220) Taylor, L.; York, P., Effect of particle size and temperature on the dehydration kinetics of trehalose dihydrate. *Int. J. Pharm.* **1998**, 167, (1-2), 215-221.
- (221) Burnett, D. J.; Malde, N.; Naderi, M.; Acharya, M. In *Surface Energy distributions of Pharmaceutical Materials*, 11th International Conference on Pharmacy and Applied Physical Chemistry, Innsbruck, Austria, 2010; Innsbruck, Austria, 2010.
- (222) Brown, M. E.; Brown, R. E., Kinetic aspects of the thermal stability of ionic solids. *Thermochim. Acta* **2000**, 357, 133-140.
- (223) Han, J.; Suryanarayanan, R., A method for the rapid evaluation of the physical stability of pharmaceutical hydrates. *Thermochim. Acta* **1999**, 329, (2), 163-170.
- (224) Brown, M.; Gallagher, P., *Handbook of thermal analysis and calorimetry: Recent advances, techniques and applications*. ed.; Elsevier Science Ltd: London, 2007; Vol. V, p 756.
- (225) Chakravarty, P.; Suryanarayanan, R., Characterization and Structure Analysis of Thiamine Hydrochloride Methanol Solvate. *Cryst. Growth Des.* **2010**, 10, (10), 4414-4420.
- (226) Khoo, J. Y.; Williams, D. R.; Heng, J. Y. Y., Dehydration Kinetics of Pharmaceutical Hydrate: Effects of Environmental Conditions and Crystal Forms. *Drying Technol.* **2010**, 28, (10), 1164-1169.
- (227) L'Vov, B. V.; Novichikhin, A. V.; Dyakov, A. O., Mechanism of thermal decomposition of magnesium hydroxide. *Thermochim. Acta* **1998**, 315, (2), 135-143.
- (228) Ozao, R.; Ochiai, M., Fractal reaction in solids - reaction functions reconsidered. *Nippon Seramikkusu Kyokai Gakujutsu Ronbunshi / Journal of the Ceramic Society of Japan* **1993**, 101, (1171), 263-267.
- (229) Koga, N.; Tanaka, H., Effect of sample mass on the kinetics of thermal decomposition of a solid - II. Isothermal dehydration of Li₂SO₄·H₂O. *J. Therm. Anal.* **1993**, 40, (3), 1173-1179.
- (230) Koga, N., Physico-geometric kinetics of solid-state reactions by thermal analyses. *J. Therm. Anal. Calorim.* **1997**, 49, (1), 45-56.
- (231) Hammond, C., *The basics of crystallography and diffraction*. ed.; Oxford University Press Oxford: 2009.
- (232) Dinnebier, R. E.; Billinge, S. J. L., *Powder Diffraction Theory and Practice*. ed.; The Royal Society of Chemistry: Cambridge, 2008; p 582.
- (233) Brittain, H. G., *Spectroscopy of Pharmaceutical Solids*. Taylor & Francis Group: New York, 2006.
- (234) Duer, M. J., *Solid state NMR spectroscopy: principles and applications*. ed.; John Wiley & Sons: Berlin, 2008.
- (235) Carlton, R. A., *Pharmaceutical microscopy*. ed.; Springer: New York, 2011; p 321.
- (236) Craig, D. Q.; Reading, M., *Thermal analysis of pharmaceuticals*. ed.; CRC press: London, 2006; p 400.
- (237) Gabbott, P., *Principles and applications of thermal analysis*. ed.; John Wiley & Sons: Singapore, 2008.
- (238) Brittain, H. G., *Polymorphism in pharmaceutical solids*. 2nd ed.; Informa Healthcare: London, 2009; p 640.
- (239) Pawley, G., Unit-cell refinement from powder diffraction scans. *J. Appl. Crystallogr.* **1981**, 14, (6), 357-361.
- (240) Le Bail, A.; Duroy, H.; Fourquet, J. L., Ab-initio structure determination of LiSbWO₆ by X-ray powder diffraction. *Mater. Res. Bull.* **1988**, 23, (3), 447-452.
- (241) Martí-Rujas, J.; Islam, N.; Hashizume, D.; Izumi, F.; Fujita, M.; Kawano, M., Dramatic Structural Rearrangements in Porous Coordination Networks. *J. Am. Chem. Soc.* **2011**, 133, (15), 5853-5860.

- (242) Guo, F.; Zhang, M.-Q.; Famulari, A.; Marti-Rujas, J., Solid state transformations in stoichiometric hydrogen bonded molecular salts: ionic interconversion and dehydration processes. *CrystEngComm* **2013**, *15*, (31), 6237-6243.
- (243) Dudenko, D. V.; Williams, P. A.; Hughes, C. E.; Antzutkin, O. N.; Velaga, S. P.; Brown, S. P.; Harris, K. D. M., Exploiting the Synergy of Powder X-ray Diffraction and Solid-State NMR Spectroscopy in Structure Determination of Organic Molecular Solids. *The Journal of Physical Chemistry C* **2013**, *117*, (23), 12258-12265.
- (244) Braga, D.; Grepioni, F.; Chelazzi, L.; Campana, M.; Confortini, D.; Viscomi, G. C., The structure-property relationship of four crystal forms of rifaximin. *CrystEngComm* **2012**, *14*, (20), 6404-6411.
- (245) Datta, S.; Grant, D. J. W., Crystal structures of drugs: advances in determination, prediction and engineering. *Nat. Rev. Drug Discov.* **2004**, *3*, (1), 42-57.
- (246) David, W. I. F.; Shankland, K.; McCusker, L. B.; Baerlocher, C., *Structure determination from powder diffraction data*. ed.; Oxford University Press: New York, 2006; p 337.
- (247) Harris, K. D. M.; Tremayne, M., Crystals structure determination from powder diffraction data. *Chem. Mater.* **1996**, *8*, 2554-2570.
- (248) Tishmack, P. A., Solid-state nuclear magnetic resonance spectroscopy. In *Polymorphism in pharmaceutical solids*, Brittain, H. G., Ed. Informa Healthcare: New York, 2009; pp 381-435.
- (249) Laws, D. D.; Bitter, H.-M. L.; Jerschow, A., Solid-State NMR Spectroscopic Methods in Chemistry. *Angewandte Chemie International Edition* **2002**, *41*, (17), 3096-3129.
- (250) Pickard, C. J.; Mauri, F., All-electron magnetic response with pseudopotentials: NMR chemical shifts. *Phys. Rev. B* **2001**, *63*, (24), 245101.
- (251) Clark, S. J.; Segall, M. D.; Pickard, C. J.; Hasnip, P. J.; Probert, M. I.; Refson, K.; Payne, M. C., First principles methods using CASTEP. *Z. Kristallogr.* **2005**, *220*, (5/6/2005), 567-570.
- (252) Harris, R. K.; Hodgkinson, P.; Pickard, C. J.; Yates, J. R.; Zorin, V., Chemical shift computations on a crystallographic basis: some reflections and comments. *Magn. Reson. Chem.* **2007**, *45*, (S1), S174-S186.
- (253) Yates, J. R.; Pickard, C. J.; Mauri, F., Calculation of NMR chemical shifts for extended systems using ultrasoft pseudopotentials. *Phys. Rev. B* **2007**, *76*, (2), 024401.
- (254) Paolo, G.; Stefano, B.; Nicola, B.; Matteo, C.; Roberto, C.; Carlo, C.; Davide, C.; Guido, L. C.; Matteo, C.; Ismaila, D.; Andrea Dal, C.; Stefano de, G.; Stefano, F.; Guido, F.; Ralph, G.; Uwe, G.; Christos, G.; Anton, K.; Michele, L.; Layla, M.-S.; Nicola, M.; Francesco, M.; Riccardo, M.; Stefano, P.; Alfredo, P.; Lorenzo, P.; Carlo, S.; Sandro, S.; Gabriele, S.; Ari, P. S.; Alexander, S.; Paolo, U.; Renata, M. W., QUANTUM ESPRESSO: a modular and open-source software project for quantum simulations of materials. *J. Phys.: Condens. Matter* **2009**, *21*, (39), 395502.
- (255) Kalviņš, I.; Stonāns, I., 3-(2, 2, 2-trimethylhydrazinium) propionate salts for treating ischemic heart disease. In ed.; WO Patent WO/2009/071586: 2009.
- (256) Simkhovich, B. Z.; Shutenko, Z. V.; Meirena, D. V.; Khagi, K. B.; Mezapuke, R. J.; Molodchina, T. N.; Kalvins, I. J.; Lukevics, E., 3-(2,2,2-Trimethylhydrazinium)propionate(thp)-a novel [gamma]-butyrobetaine hydroxylase inhibitor with cardioprotective properties. *Biochem. Pharmacol.* **1988**, *37*, (2), 195-202.
- (257) Kemme, A.; Bleidelis, J.; Kalvins, I.; Eremeev, A., Molecular-Crystalline Structure Of 3-(2,2, 2-Trimethylhydrazinio)Propionate Dihydrate C₆H₁₄N₂O₂.2H₂O. *Latv PSR Zinat Akad Vestis* **1983**, *2*, 215.
- (258) Veldre, K.; Actiņš, A.; Kalniņa, A. In *Thermal Stability of 3-(2,2,2-trimethylhydrazine)propionate*, Solid State Chemistry 2010, Prague, 2010; Prague, 2010; p 231.
- (259) Mishnev, A.; Kalvins, I.; Aleksejeva, L.; Lebedev, A. In *Structure of Mildronate, its Pharmaceutical Salts and Cocrystals*, XXII Congress and General Assembly of the International Union of Crystallography, Madrid, Spain, 22-30 August, 2011; Madrid, Spain, 2011; p MS53.P23.
- (260) Zvirgzdiņš, A.; Veldre, K.; Actiņš, A., Structures of Mildronate Polymorphic and Pseudopolymorphic Forms. *Latv. J. Chem.* **2011**, *50*, (1), 64-72.
- (261) Actins, A.; Araj, R.; Belakovs, S.; Orola, L.; Veidis, M., The Crystal and Molecular Structure of a Polymorph and a Pseudo-Polymorph of Droperidol. *J. Chem. Crystallogr.* **2008**, *38*, (3), 169-174.
- (262) Azibi, M.; Draguet-Brughmas, M.; Bouche, R., Polymorphisme des butyrophenones: benperidol et droperidol. *Pharm. Acta Helv.* **1982**, *57*, (7), 182-188.
- (263) Blaton, N. M.; Peeters, O. M.; De Ranter, C. J., 1-{1-[4-(4-Fluorophenyl)-4-oxobutyl]-1,2,3,6-tetrahydro-4-pyridyl}-1,3-dihydro-2H-benzimidazol-2-one dihydrate (Dehydrobenzperidol®). *Acta Crystallogr., Sect. B* **1980**, *36*, (11), 2828-2830.
- (264) Orola, L. Synthesis, structure and properties of crystalline forms of some active pharmaceutical ingredients. Riga Technical University, Riga, 2010.

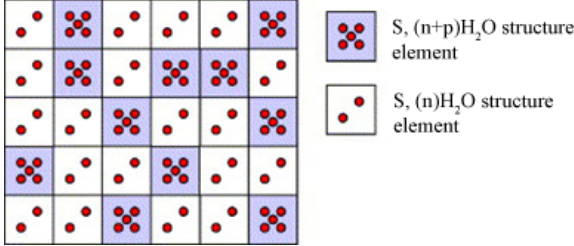
- (265) Klein, C. L.; Welch, J.; Southall, L. C., Structure of droperidol-ethanol (1/1). *Acta Crystallogr., Sect. C* **1989**, 45, (4), 650-653.
- (266) Bobon, J.; Collard, J.; Lecoq, R., Benperidol and promazine: a "double blind" comparative study in mental geriatrics. *Acta Neurol. Belg.* **1963**, 63, 839.
- (267) Declercq, J. P.; Germain, G.; Koch, M. H. J., 1-{1-[3-(p-Fluorobenzoyl)propyl]-4-piperidyl}-2-benzimidazolinone (benperidol). *Acta Crystallogr., Sect. B* **1973**, 29, (10), 2311-2313.
- (268) Gassim, A. E. H.; Girgis Takia, P.; James, K. C., Polymorphism and possible intramolecular bonding in benperidol. *Int. J. Pharm.* **1986**, 34, (1-2), 23-28.
- (269) Sheldrick, G., A short history of SHELX. *Acta Crystallogr., Sect. A* **2008**, 64, (1), 112-122.
- (270) Dolomanov, O. V.; Bourhis, L. J.; Gildea, R. J.; Howard, J. A. K.; Puschmann, H., OLEX2: a complete structure solution, refinement and analysis program. *J. Appl. Crystallogr.* **2009**, 42, (2), 339-341.
- (271) Han, J.; Suryanarayanan, R., Influence of Environmental Conditions on the Kinetics and Mechanism of Dehydration of Carbamazepine Dihydrate. *Pharm. Dev. Technol.* **1998**, 3, (4), 587-596.
- (272) Vyazovkin, S.; Wight, C. A., Kinetics in Solids. *Annu. Rev. Phys. Chem.* **1997**, 48, (1), 125-149.
- (273) Greenspan, L., Humidity fixed points of binary saturated aqueous solutions. *J. Res. Nat. Bur. Stand., Sect. A* **1977**, 81A, 89-96.
- (274) TOPAS, version 4.2; Bruker AXS: Karlsruhe, Germany, 2009.
- (275) Boultif, A.; Louer, D., Powder pattern indexing with the dichotomy method. *J. Appl. Crystallogr.* **2004**, 37, (5), 724-731.
- (276) Roisnel, T.; Rodríguez-Carvajal, J. In *WinPLOTR: a windows tool for powder diffraction pattern analysis*, Mater. Sci. Forum, 2001; Transtec Publications; 1999: 2001; pp 118-123.
- (277) Coelho, A., Indexing of powder diffraction patterns by iterative use of singular value decomposition. *J. Appl. Crystallogr.* **2003**, 36, (1), 86-95.
- (278) Altomare, A.; Camalli, M.; Cuocci, C.; Giacovazzo, C.; Moliterni, A.; Rizzi, R., EXPO2009: structure solution by powder data in direct and reciprocal space. *J. Appl. Crystallogr.* **2009**, 42, (6), 1197-1202.
- (279) Altomare, A.; Cuocci, C.; Giacovazzo, C.; Moliterni, A.; Rizzi, R.; Corriero, N.; Falcicchio, A., EXPO2013: a kit of tools for phasing crystal structures from powder data. *J. Appl. Crystallogr.* **2013**, 46, (4), 1231-1235.
- (280) Yamazaki, K.; Watanabe, A.; Moroi, R.; Sano, M., The structure of cis-4-(aminomethyl)cyclohexanecarboxylic acid (cis-AMCHA) hemihydrate. *Acta Crystallogr., Sect. B* **1981**, 37, (7), 1447-1449.
- (281) Kawahata, M.; Yamaguchi, K.; Ishikawa, T., o-Bisguanidinobenzene, a Powerful Hydrogen Acceptor: Crystal Structures of Organic Complexes with Benzoic Acid, Phenol, and Benzyl Alcohol. *Cryst. Growth Des.* **2005**, 5, (1), 373-377.
- (282) Findlay, A.; Harris, R. K., Measurement of nuclear overhauser enhancements in polymeric films. *J. Magn. Reson.* **1990**, 87, (3), 605-609.
- (283) Zorin, V. *Gsim – a visualisation and processing program for solid-state NMR*, URL: <http://gsim.sourceforge.net>; 2013.
- (284) Hodgkinson, P. *pNMRsim: a general simulation program for large problems in solid-state NMR*, URL: <http://www.dur.ac.uk/paul.hodgkinson/pNMRsim>; 2013.
- (285) Dovesi, R.; Saunders, V.; Roetti, C.; Orlando, R.; Zicovich-Wilson, C.; Pascale, F.; Civalleri, B.; Doll, K.; Harrison, N.; Bush, I. *CRYSTAL09*, University of Torino, Torino, Italy: 2009.
- (286) Civalleri, B.; Zicovich-Wilson, C. M.; Valenzano, L.; Ugliengo, P., B3LYP augmented with an empirical dispersion term (B3LYP-D*) as applied to molecular crystals. *CrystEngComm* **2008**, 10, (4), 405-410.
- (287) Gatti, C.; Saunders, V. R.; Roetti, C., Crystal field effects on the topological properties of the electron density in molecular crystals: The case of urea. *J. Chem. Phys.* **1994**, 101, (12), 10686-10696.
- (288) Spackman, M. A.; Mitchell, A. S., Basis set choice and basis set superposition error (BSSE) in periodic Hartree-Fock calculations on molecular crystals. *Phys. Chem. Chem. Phys.* **2001**, 3, (8), 1518-1523.
- (289) Grimme, S., Semiempirical GGA-type density functional constructed with a long-range dispersion correction. *J. Comput. Chem.* **2006**, 27, (15), 1787-1799.
- (290) Zicovich-Wilson, C. M.; Kirtman, B.; Civalleri, B.; Ramirez-Solis, A., Periodic density functional theory calculations for 3-dimensional polyacetylene with empirical dispersion terms. *Phys. Chem. Chem. Phys.* **2010**, 12, (13), 3289-3293.
- (291) Boys, S. F.; Bernardi, F., The calculation of small molecular interactions by the differences of separate total energies. Some procedures with reduced errors. *Mol. Phys.* **1970**, 19, (4), 553-566.

- (292) Perdew, J. P.; Burke, K.; Ernzerhof, M., Generalized Gradient Approximation Made Simple. *Phys. Rev. Lett.* **1996**, 77, (18), 3865-3868.
- (293) Tkatchenko, A.; Scheffler, M., Accurate Molecular Van Der Waals Interactions from Ground-State Electron Density and Free-Atom Reference Data. *Phys. Rev. Lett.* **2009**, 102, (7), 073005.
- (294) Pascale, F.; Zicovich-Wilson, C. M.; López Gejo, F.; Civalleri, B.; Orlando, R.; Dovesi, R., The calculation of the vibrational frequencies of crystalline compounds and its implementation in the CRYSTAL code. *J. Comput. Chem.* **2004**, 25, (6), 888-897.
- (295) Zicovich-Wilson, C. M.; Pascale, F.; Roetti, C.; Saunders, V. R.; Orlando, R.; Dovesi, R., Calculation of the vibration frequencies of α -quartz: The effect of Hamiltonian and basis set. *J. Comput. Chem.* **2004**, 25, (15), 1873-1881.
- (296) Frisch, M. J.; Trucks, G. W.; Schlegel, H. B.; Scuseria, G. E.; Robb, M. A.; Cheeseman, J. R.; Scalmani, G.; Barone, V.; Mennucci, B.; Petersson, G. A.; Nakatsuji, H.; Caricato, M.; Li, X.; Hratchian, H. P.; Izmaylov, A. F.; Bloino, J.; Zheng, G.; Sonnenberg, J. L.; Hada, M.; Ehara, M.; Toyota, K.; Fukuda, R.; Hasegawa, J.; Ishida, M.; Nakajima, T.; Honda, Y.; Kitao, O.; Nakai, H.; Vreven, T.; Montgomery, J. A. J.; Peralta, J. E.; Ogliaro, F.; Bearpark, M.; Heyd, J. J.; Brothers, E.; Kudin, K. N.; Staroverov, V. N.; Kobayashi, R.; Normand, J.; Raghavachari, K.; Rendell, A.; Burant, J. C.; Iyengar, S. S.; Tomasi, J.; Cossi, M.; Rega, N.; Millam, J. M.; Klene, M.; Knox, J. E.; Cross, J. B.; Bakken, V.; Adamo, C.; Jaramillo, J.; Gomperts, R.; Stratmann, R. E.; Yazyev, O.; Austin, A. J.; Cammi, R.; Pomelli, C.; Ochterski, J. W.; Martin, R. L.; Morokuma, K.; Zakrzewski, V. G.; Voth, G. A.; Salvador, P.; Dannenberg, J. J.; Dapprich, S.; Daniels, A. D.; Farkas, O.; Foresman, J. B.; Ortiz, J. V.; Cioslowski, J.; Fox, D. J. *Gaussian 09*, Gaussian Inc., Wallingford, CT: 2009.
- (297) Grimme, S.; Antony, J.; Ehrlich, S.; Krieg, H., A consistent and accurate ab initio parametrization of density functional dispersion correction (DFT-D) for the 94 elements H-Pu. *J. Chem. Phys.* **2010**, 132, (15), 154104.
- (298) Alecu, I. M.; Zheng, J.; Zhao, Y.; Truhlar, D. G., Computational Thermochemistry: Scale Factor Databases and Scale Factors for Vibrational Frequencies Obtained from Electronic Model Chemistries. *J. Chem. Theory Comput.* **2010**, 6, (9), 2872-2887.
- (299) Zhao, Y.; Truhlar, D., The M06 suite of density functionals for main group thermochemistry, thermochemical kinetics, noncovalent interactions, excited states, and transition elements: two new functionals and systematic testing of four M06-class functionals and 12 other functionals. *Theor. Chem. Acc.* **2008**, 120, (1-3), 215-241.
- (300) Gavezzotti, A. *The Coulomb - London - Pauli (CLP) model of intermolecular interaction. Description and user's manual*, 2012.
- (301) Lide, D., *CRC Handbook of Chemistry and Physics, 87th edition*. Taylor & Francis Group: London, 2006.
- (302) Khoo, J. Y.; Williams, D. R.; Heng, J. Y. Y., Dehydration Kinetics of Pharmaceutical Hydrate: Effects of Environmental Conditions and Crystal Forms. *Drying Technol.* **2010**, 28, (10-12), 1164-1169.
- (303) Zellelow, A. Z.; Kim, K.-H.; Sours, R. E.; Swift, J. A., Solid-State Dehydration of Uric Acid Dihydrate. *Cryst. Growth Des.* **2010**, 10, (1), 418-425.
- (304) Zhu, H.; Grant, D. J. W., Dehydration behavior of nedocromil magnesium pentahydrate. *Int. J. Pharm.* **2001**, 215, (1-2), 251-262.
- (305) Tessler, L.; Goldberg, I., Crystal Structures of Aripiprazole, a New Anti-psychotic Drug, and of its Inclusion Compounds with Methanol, Ethanol and Water. *J. Inclusion Phenom. Macrocyclic Chem.* **2006**, 55, (3-4), 255-261.
- (306) Zhuravlev, V. F.; Lesokhin, I. G.; Templeman, R. G., Kinetics of the formation of calcium aluminates and the role of mineralizers. *J. Appl. Chem. (USSR)* **1948**, 21, 887-902.
- (307) Šesták, J.; Šatava, V.; Wendlandt, W. W., The study of heterogeneous processes by thermal analysis. *Thermochim. Acta* **1973**, 7, (5), 333-556.
- (308) Malecki, A.; Komornicki, S.; Prochowska-Klisch, B., *Bull. Pol. Acad. Sci.: Chemistry* **1981**, 29, 455.
- (309) Malecki, A.; Prochowska-Klisch, B.; Gajerski, R., Another Approach to the Modified Zhuravlev Equation on the Basis of the Oxidation of V2O4 and V6O13. *J. Therm. Anal. Calorim.* **1998**, 54, (1), 25-34.
- (310) Maranzana, A.; Giordana, A.; Indarto, A.; Tonachini, G.; Barone, V.; Causà, M.; Pavone, M., Density functional theory study of the interaction of vinyl radical, ethyne, and ethene with benzene, aimed to define an affordable computational level to investigate stability trends in large van der Waals complexes. *J. Chem. Phys.* **2013**, 139, (24), 244306.
- (311) Zhao, Y.; Truhlar, D. G., Density Functionals with Broad Applicability in Chemistry. *Acc. Chem. Res.* **2008**, 41, (2), 157-167.

- (312) Dračinský, M.; Hodgkinson, P., Effects of Quantum Nuclear Delocalisation on NMR Parameters from Path Integral Molecular Dynamics. *Chem. Eur. J.* **2014**, 20, (8), 2201-2207.
- (313) Robbins, A. J.; Ng, W. T. K.; Jochym, D.; Keal, T. W.; Clark, S. J.; Tozer, D. J.; Hodgkinson, P., Combining insights from solid-state NMR and first principles calculation: applications to the ¹⁹F NMR of octafluoronaphthalene. *Phys. Chem. Chem. Phys.* **2007**, 9, (19), 2389-2396.
- (314) Rothwell, W. P.; Waugh, J. S., Transverse relaxation of dipolar coupled spin systems under rf irradiation: Detecting motions in solids. *J. Chem. Phys.* **1981**, 74, (5), 2721-2732.
- (315) Horsewill, A. J., Quantum tunnelling aspects of methyl group rotation studied by NMR. *Prog. Nucl. Magn. Reson. Spectrosc.* **1999**, 35, (4), 359-389.
- (316) Dracinsky, M.; Hodgkinson, P., A molecular dynamics study of the effects of fast molecular motions on solid-state NMR parameters. *CrystEngComm* **2013**, 15, (43), 8705-8712.

Appendix 1.

Table A1. Thermodynamic models for non-stoichiometric hydrates and the the corresponding water sorption-desorption isotherms.

Model	Characterization of the model	Basic equations	Equations for sorption the sorption-desorption isotherms
A	<p><u>Substitution solid solution of a (n+p)-hydrate in a n-hydrate.</u> This model can describe only crystalline solids where water molecules are considered to be in fixed ordered locations in the crystal lattice.</p> 	<p>Equilibrium: $\langle S, (n+p)H_2O \rangle \leftrightarrow \langle S, (n)H_2O \rangle + p H_2O$</p> <p>Water content: $\varepsilon - n = \frac{y_1 p \cdot P_W^p}{K_A(T) + \frac{y_1}{y_2} P_W^p}$ $\varepsilon - n = \frac{y_1 p \cdot P_W^p}{K_A(T) + \frac{y_1}{y_2} P_W^p}$</p> <p>$\varepsilon$ – amount of water sorbed (in moles) per mole of substance, n and p – amount of water, y_1 and y_2 – activity coefficients of n and (n+p)-hydrates, P_W – equilibrium water partial pressure, K_A – equilibrium constant at temperature T.</p>	<p>a) Henry's law: if $p = 1$ and P_W is close to 0, $\varepsilon - n \approx \frac{1}{y_2^\infty K_A(T)} P_W$</p> <p>b) Langmuir isotherm: if $y = \text{const.}$, $p = 1$ $\varepsilon - n = p \frac{a P_W}{1 + a P_W}, \text{ where}$ $a = \frac{y_1}{y_2 K_A(T)}$</p> <p>c) Activity coefficients models: Activity coefficients are evaluated by the Margules method. Mathematical expressions for the case when $n=0$ and Margules' equations of second order are used: $P_W = K_A(T) \frac{\varepsilon}{p - \varepsilon} \left(\exp \left(\frac{A_{12}}{RT} \left(1 - 2 \frac{\varepsilon}{p} \right) \right) \right)^{\frac{1}{q}}$</p> <p>For the case when $n=0$ and Margules' equations of third order are used: $P_W = K_A(T) \frac{\varepsilon}{p - \varepsilon} \left(\exp \left(\ln \frac{y_1}{y_2} \right) \right)^{\frac{1}{q}}$ $\ln \frac{y_1}{y_2} = \left[\frac{1}{RT} \left(\left(\frac{\varepsilon}{p} \right)^2 A_{12} + 2 \left(\frac{\varepsilon}{p} \right)^2 (A_{21} - A_{12}) \left(\frac{p - \varepsilon}{p} \right) - \left(\left(\frac{p - \varepsilon}{p} \right)^2 A_{21} + 2 \left(\frac{p - \varepsilon}{p} \right)^2 (A_{12} - A_{21}) \left(\frac{\varepsilon}{p} \right) \right) \right]$</p>
B	<p><u>Crystallographic vacant location.</u> Also this model can describe only crystalline solids where water molecules are considered to be in fixed ordered locations in the crystal lattice. An additional assumption is that the water molecules are associated into clusters of q molecules on well-defined crystallographic sites in the skeleton of the n-hydrate.</p>	<p>Equilibrium: $\langle H_2O \rangle_q \leftrightarrow q H_2O + \langle \dots \rangle_q$</p> <p>Water content: $\varepsilon = n + \frac{y_1 p \cdot P_W^q}{K_B(T) + \frac{y_1}{y_2} P_W^q}$</p>	<p>For the case when $n=0$ and Margules' equations of third order are used: $P_W = K_A(T) \frac{\varepsilon}{p - \varepsilon} \left(\exp \left(\ln \frac{y_1}{y_2} \right) \right)^{\frac{1}{q}}$ $\ln \frac{y_1}{y_2} = \left[\frac{1}{RT} \left(\left(\frac{\varepsilon}{p} \right)^2 A_{12} + 2 \left(\frac{\varepsilon}{p} \right)^2 (A_{21} - A_{12}) \left(\frac{p - \varepsilon}{p} \right) - \left(\left(\frac{p - \varepsilon}{p} \right)^2 A_{21} + 2 \left(\frac{p - \varepsilon}{p} \right)^2 (A_{12} - A_{21}) \left(\frac{\varepsilon}{p} \right) \right) \right]$</p>

	<p>●● Water molecules cluster on crystallographic site</p> <p>○○ Free adsorption site</p>		<p>where A_{ij} – constants reflecting the interaction between n and $(n + p)$-hydrates.</p>
C	<p><u>Non-stoichiometric hydrates with disordered water distribution.</u></p> <p>In this model a partition equilibrium of water between the vapor phase and the solid solution is assumed. The solid can either be crystalline or amorphous. Molecules can be associated in clusters of q molecules. As no position or interaction with a site is assumed, this model describes disordered water molecules. Depending on the energy difference between the low energy and the high-energy positions ΔE, the relative concentration of molecules in the high and the low energy state will vary as $\exp(-(\Delta E/kT))$. Therefore, if the difference in energy is small compared to the thermal agitation, the molecules can easily move to the upper band and the system is disordered; elsewhere the molecules are mainly trapped in sharp energy minima and the system is ordered. Note that ΔE should be equal to the activation energy for diffusion.</p> <p>(a) Ordered system</p> <p>(b) Disordered system</p>	<p>Equilibrium: $q[H_2O] \leftrightarrow \langle\langle H_2O \rangle\rangle_q$</p> <p>Water content: $\varepsilon = n + \frac{q \left(\frac{P_W}{P_W^o(T)} \right)^q}{y_2 - \left(\frac{P_W}{P_W^o(T)} \right)^q}$</p> <p>where $\left(\frac{P_W}{P_W^o(T)} \right)$ is the relative humidity.</p>	<p>In general form isotherm can be written as:</p> $\varepsilon = n + \frac{q \left(\frac{P_W}{P_W^o(T)} \right)^q}{y_2 - \left(\frac{P_W}{P_W^o(T)} \right)^q}$ <p>When Margules' equations of second order are used:</p> $\left(\frac{P_W}{P_W^o(T)} \right) = \frac{\varepsilon - n}{1 + \varepsilon + n} e^{\left(\frac{A_{12}}{RT(1 + \varepsilon - n)} \right)}$

Appendix 2. Classification of solvents.

Table A2. Solvent classification using the k -nearest neighbour classification method¹³⁹.

ID	Solvent	A	B	C	ID	Solvent	A	B	C	ID	Solvent	A	B	C
1	acetic acid	4	4	4	52	diethylene glycol	4	4	4	103	nitrobenzene	1	1	1
2	acetic anhydride	1	1	1	53	diethyl ether	3	3/5	3	104	nitroethane	1	1	1
3	acetone	1	1	1	54	di-isopropyl ether	5	5	3	105	nitromethane	1	1	1
4	acetonitrile	1	1	1	55	1,2-dimethoxyethane	3	1/3	3	106	n-octane	5	5	5
5	acetophenone	2	2	2	56	N,N-dimethylacetamide	1	1	1	107	1-octanol	4	4	4
6	acetylacetone	2	1	1	57	N,N-dimethylaniline	1	1	1	108	n-pentane	5	5	5
7	2-aminoethanol	4	4	4	58	3,3-dimethyl-2-butanone	1	1	1	109	1-pentanol	4	4	4
8	aniline	1	1	1	59	N,N-dimethylformamide	1	1	1	110	2-pentanol	4	4	4
9	anisole	2	2	2	60	2,4-dimethylpyridine	1	1	1	111	3-pentanol	4	4	4
10	benzaldehyde	2	2	2	61	2,6-dimethylpyridine	1	1	1	112	2-pentanone	1	1	1
11	benzene	2	2	2	62	dimethylsulfoxide	1	1	1	113	3-pentanone	1	1	1
12	benzonitrile	1	1	1	63	2,6-dimethyl-4-heptanone	1	1	1	114	pentyl acetate	1	1	1
13	benzyl alcohol	2	2	2	64	2,4-dimethyl-3-pentanone	1	1	1	115	phenetole	2	2	2
14	bromobenzene	2	2	2	65	1,4-dioxane	1	1	3	116	phenol	2	2	2
15	1-bromobutane	3	3	3	66	diphenyl ether	2	2	2	117	3-picoline	1	1	1
16	bromoethane	3	1/3	3	67	di-n-propyl ether	5	5	3	118	4-picoline	1	1	1
17	1-butanol	4	4	4	68	DMEU	1	1	1	119	piperidine	4	4	4
18	2-butanol	4	4	4	69	DMPU	1	1	1	120	1-propanol	4	4	4
19	2-butanone	1	1	1	70	ethanol	4	4	4	121	2-propanol	4	4	4
20	n-butyl acetate	1	1	1	71	ethyl acetate	1	1	1	122	n-propylamine	4	4	4
21	n-butylamine	4	4	4	72	ethyl benzoate	2	2	2	123	propyl formate	1	1	1
22	butyronitrile	1	1	1	73	ethyl formate	1	1	1	124	propylene carbonate	1	1	1
23	carbon disulfide	2	2/5	5	74	ethyl propionate	1	1	1	125	propionitrile	1	1	1
24	carbon tetrachloride	5	4	4	75	ethylenediamine	4	4	4	126	pyridine	1	1	1
25	chlorobenzene	2	2	2	76	ethylene glycol	4	4	4	127	pyrrolidine	4	4	4

26	1-chlorobutane	3	3	3	77	fluorobenzene	2	2	2	128	quinoline	1	1	1
27	chloroform	4	4/1/3	3	78	formamide	4	4	4	129	styrene	2	2	2
28	1-chloropropane	3	3/1	3	79	furfuryl alcohol	1	2/4	2	130	sulfolane	1	1	1
29	2-chloropropane	3	3/1	3	80	glycerol	4	4	4	131	tert.-butyl alcohol	4	4	4
30	m-cresol	2	2	2	81	n-heptane	5	5	5	132	tert.-butyl methyl ether	3	5/3	3
31	cyclohexane	5	5	5	82	HMPTA	1	1	1	133	TEGDME	1	1/3	3
32	cyclohexanol	4	4	4	83	n-hexane	5	5	5	134	1,1,2,2-tetrachloroethane	1	3	1
33	cyclohexanone	1	1	1	84	1-hexanol	4	4	4	135	tetrachloroethylene	5	4/2	5
34	cyclohexene	2	5/2	5	85	iodobenzene	2	2	2	136	tetraethylene glycol	4	4	4
35	cyclopentane	5	5	5	86	iodoethane	3	1/3	3	137	tetrahydrofuran	3	3	3
36	cyclopentanone	1	1	1	87	isobutyl alcohol	4	4	4	138	1,1,3,3-tetramethyl urea	1	1	1
37	cis-decaline	5	5	5	88	iso-octane	5	5	5	139	toluene	2	2	2
38	n-decane	5	5	5	89	mesitylene	2	2	2	140	tributylamine	3	3	3
39	DEGDEE	3	3/1	3	90	methanol	4	4	4	141	1,1,1-trichloroethane	1	1	1
40	DEGDME	1	1/3	3	91	methyl acetate	1	1	1	142	trichloroethylene	1	1	1
41	dibenzyl ether	2	2	2	92	methyl benzoate	2	2	2	143	triethylamine	3	3	3
42	di-n-butyl ether	5	5/3	3	93	2-methyl-2-butanol	4	4	4	144	triethylene glycol	4	4	4
43	m-dichlorobenzene	2	2	2	94	3-methyl-1-butanol	4	4	4	145	trifluoroacetic acid	4	4	4
44	o-dichlorobenzene	2	2	2	95	3-methyl-2-butanone	1	1	1	146	2,2,2-trifluoroethanol	4	4	4
45	1,2-dichloroethane	1	1	1	96	methyl formate	1	1	1	147	trimethylene glycol	4	4	4
46	1,1-dichloroethane	1	1	1	97	4-methyl-2-pentanone	1	1	1	148	2,4,6-trimethylpyridine	1	1	1
47	1,1-dichloroethylene	1	1	1	98	2-methoxyethanol	4	4	4	149	m-xylene	2	2	2
48	Z-1,2-dichloroethylene	1	1	1	99	N-methylacetamide	1	1	1	150	o-xylene	2	2	2
49	dichloromethane	1	1	1	100	N-methylformamide	1	1	1	151	p-xylene	2	2	2
50	diethylamine	4	4	4	101	N-methyl-pyrrolidin-2-one	1	1	1	152	water	4	4	4
51	diethyl carbonate	1	1	1	102	morpholine	1	4/1	4					

A: KNN classification; B: CP-ANN-1 classification; C: CP-ANN-2 classification (see original publication¹³⁹). 1: Class 1, aprotic polar (AP); 2: Class 2, aromatic apolar or lightly polar (AALP); 3: Class 3, electron pair donors (EPD); 4: Class 4, hydrogen bond donors (HBD); 5: Class 5, aliphatic aprotic apolar (AAA).

Table A3. Solvent classification based on the cluster analysis of following solvent property parameters: hydrogen bond acceptor propensity, hydrogen bond donor propensity, polarity/dipolarity, dipole moment, and dielectric constant¹⁴⁰.

Group 1	n-Dodecane (0.0), n-decane (0.1), Cyclohexane (0.1), n-octane (0.1), n-hexane (0.2), n-heptane (0.2), cis-decalin (0.2), n-pentane (0.2), carbon tetrachloride (0.3), tetrachloroethene (0.3)
Group 2	Ethyl acetate (0.2), diethyl sulfide (0.4), propyl ethanoate (0.6), methyl benzoate (0.8), methyl ethanoate (0.8), butyl ethanoate (1.1), tetrahydrofuran (1.4), methyl tertiary-butyl ether (1.6), diethyl ether (1.9), ethyl formate (2.3), diisopropyl ether (2.8), methyl methanoate (2.8), dibutylether (3.1), dimethyl disulfide (3.5)
Group 3	2-methyl-1-propanol (0.3), 2-butanol (0.5), 1-butanol (0.9), 2-methoxyethanol (1.1), 1-pentanol (1.3), 2-propanol (2.8), 2-methyl-2-propanol (4.0), 1-propanol (4.1), 1-octanol (6.6), ethanol (8.4), morpholine (9.0), butylamine (11.9), methanol (16.2)
Group 4	m-Xylene (0.1), p-xylene (0.1), benzene (0.1), mesitylene (0.2), carbon disulfide (0.3), toluene (0.3)
Group 5	2-hexanone (0.0), cyclopentanone (0.8), 2-pentanone (1.1), pyridine (1.2), 4-methyl-2-pentanone (1.2), cyclohexanone (1.5), 4-methylpyridine (2.2), 2-heptanone (2.5), 3-pentanone (2.7), acetophenone (3.4), butanone (4.1), 2,4-dimethylpyridine (4.7), acetone (6.4), 2,6-dimethylpyridine (7.0)
Group 6	N,N-dimethylacetamide (0.8), N,N-dimethylformamide (1.3), N-methyl-2-pyrrolidone (6.3), dimethylsulfoxide (8.3)
Group 7	1-iodobutane (0.4), chlorobenzene (0.6), fluorobenzene (0.8), 1,1,1-trichloroethane (0.9), dibromomethane (1.0), diiodomethane (1.0), 1,2-dibromoethane (1.4), chloroform (1.6), iodobenzene (1.7), anisole (2.0), bromoform (2.1), ethyl phenyl ether (2.1), dichloromethane (2.7), trichloroethene (2.9), 1,1-dichloroethane (3.8), o-dichlorobenzene (3.9), 1,2-dichloroethane (3.9)
Group 8	Acetic acid (0.1), propanoic acid (2.8), pentanoic acid (3.5), m-cresol (6.2)
Group 9	Propanenitrile (1.0), benzonitrile (4.7), acetonitrile (5.4), butanenitrile (6.0), nitromethane (6.3)
Group 10	Benzyl alcohol (2.8), aniline (2.8)
Group 11	Triethylamine (0.4), 1,4-dioxane (0.4)
Group 12	Formic acid (4.9), ethylene glycol (4.9)
Group 13	Diethylamine
Group 14	Glycerol
Group 15	Water

The Euclidean distance of each solvent to the centre of the corresponding group is provided in the parentheses.

Appendix 3. Classification of the dehydration process with respect to the crystal structure changes.

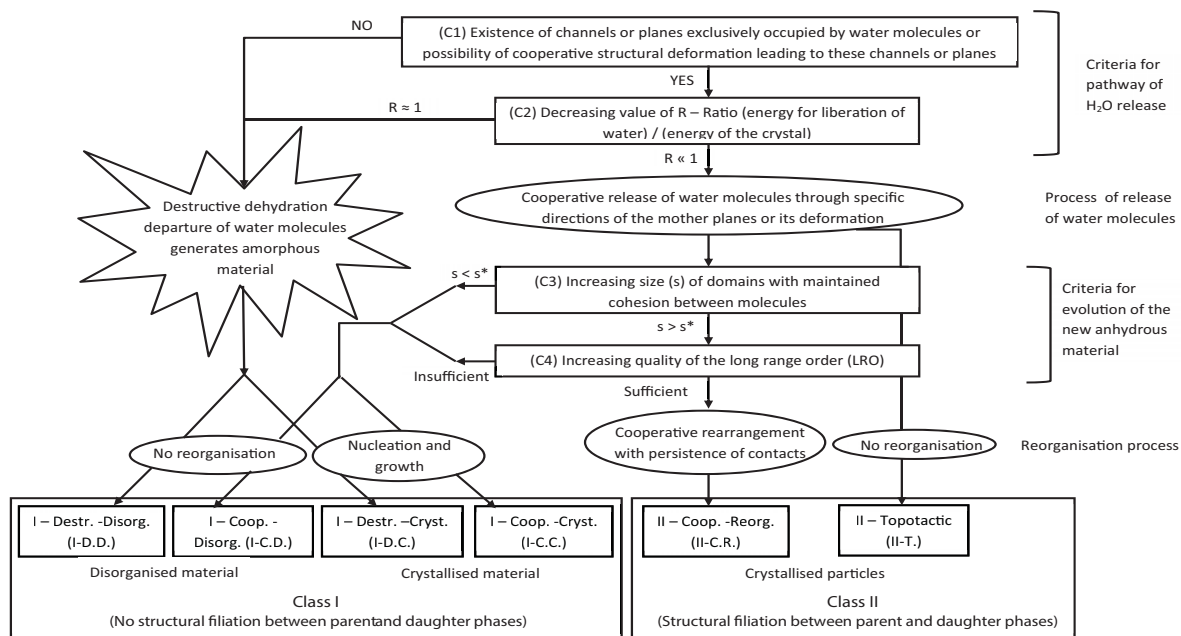


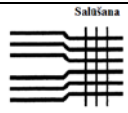

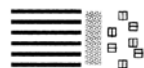

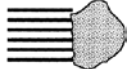


Figure A1. "Rouen 96 model" for classification of hydrates according to the dehydration process¹⁶².

Table A4. Water evaluation types (WET) with the corresponding representation of phase boundary¹⁶³.

WET	Criteria	Characterization of structure and phase boundary	Phase boundary	Reaction rate controls
WET1	Crystal structure maintained (no geometric rate controls)	Crystal spacing unchanged by dehydration.		1A – diffusion, 1B – desorption from a surface.
WET2	Diffusion across an adherent barrier layer	Topotactic reaction. Lattice spacing reduced on dehydration without cracking.		Diffusion and (possible) geometric factor.
WET3	Interface advance. Nucleation and growth, or contracting envelope	a) Topotactic reaction. Crystal spacings changed sufficiently to cause cracking within the reaction zone.		Interface reaction and geometric control.
		b) Product recrystallization. Reaction may or may not be topotactic.		
		c) Amorphous product that subsequently recrystallizes.		
		d) Amorphous product that does not recrystallize.		
WET4	Homogeneous reactions in crystals	a) Release of water is blocked by the product layer until the internal pressure leads to explosive disintegration.		a) explosive disintegration.
		b) Change of the water vapour pressure leads to systematic change in the lattice parameters.		b) progressive structural change.
		c) Changes occur at sites randomly distributed in the crystal, without regard to their position.		c) homogeneous intracrystalline chemical change.
WET5	Melting and formation of impervious outer layer	a) During dehydration of large crystals fast release of water from the crystal surface occur. b) Dehydration of powder initially produces amorphous phase which melts before recrystallization.		Untypical kinetic characteristics.
WET6	Comprehensive melting	Melting may be accompanied by reactions other than the dehydrations.		Chemical reaction and/or diffusion.

Appendix 4. Kinetic models and kinetic parameter determination methods commonly used in the analysis of solid state kinetics.

Table A5. Solid-state integral rate expressions $g(\alpha)$ for the most often used solid-state kinetic models^{90, 171, 187, 190-192}.

Model	$g(\alpha)$	Model	$g(\alpha)$
Nucleation models		Diffusion models	
Power law (P2)	$\alpha^{1/2}$	1-D diffusion (D1)	$\alpha^2/2$
Power law (P3)	$\alpha^{1/3}$	2-D diffusion (D2)	$\alpha + (1 - \alpha) \ln(1 - \alpha)$
Power law (P4)	$\alpha^{1/4}$	3-D diffusion – Jander (D3)	$\left[1 - (1 - \alpha)^{1/3}\right]^2$
Avrami-Erofeyev (A3/2)	$[-\ln(1 - \alpha)]^{2/3}$	Ginstling-Brounshtein (D4)	$\left[1 - \frac{2}{3}\alpha - (1 - \alpha)^{2/3}\right]$
Avrami-Erofeyev (A2)	$[-\ln(1 - \alpha)]^{1/2}$	Zhuravlev (D5)	$\left[(1 - \alpha)^{-1/3} - 1\right]^2$
Avrami-Erofeyev (A3)	$[-\ln(1 - \alpha)]^{1/3}$	Reaction-order models	
Avrami-Erofeyev (A4)	$[-\ln(1 - \alpha)]^{1/4}$	First-order (F1)	$-\ln(1 - \alpha)$
Prout-Tompkins (B1)	$\ln\left[\frac{\alpha}{1 - \alpha}\right]$	1.5-order (F3/2)	$2\left(\frac{1}{(1 - \alpha)^{1/2}} - 1\right)$
Geometrical contraction models		Second-order (F2)	$\frac{1}{(1 - \alpha)} - 1$
Contracting disk (R1)	α	Third-order (F3)	$0.5((1 - \alpha)^{-2} - 1)$
Contracting area (R2)	$\left[1 - (1 - \alpha)^{1/2}\right]$		
Contracting volume (R3)	$\left[1 - (1 - \alpha)^{1/3}\right]$		

Table A6. Mathematical expressions used in the most common isoconversional methods.

Method	Equation	Procedure
Friedman (FR) ²⁰⁸	$\ln\left(\frac{d\alpha}{dt}\right)_\alpha = \ln(A \cdot f(\alpha))_\alpha - \frac{E_{a\alpha}}{RT_\alpha}$	E _a is calculated from desolvation curves recorded at different heating rates using the slope of the line in coordinates $\ln\left(\frac{d\alpha}{dt}\right) - T^{-1}$ for α values with step size 0.02.
Average linear integral method (ALIM) ²⁰⁹	$-\ln \Delta t = -\ln \Delta g(\alpha) + \ln A_\alpha - \frac{E_{a,\alpha}}{RT(t)}$	E _a is calculated from desolvation curves recorded at different heating rates using the slope of the line in coordinates $-\ln \Delta t - T^{-1}$ for α values with step size 0.02.
Advanced isoconversional method (AIC) ^{210, 211}	$J(E_{a\alpha}, T_i(t_\alpha)) = \int_{t_{\alpha-\Delta\alpha}}^{t_\alpha} e^{\frac{-E_{a,\alpha}}{RT(t)}} dt$ $\sum_i^n \sum_{j \neq i}^n \left[\frac{J(E_{a\alpha}, T_i(t_\alpha))}{J(E_{a\alpha}, T_j(t_\alpha))} \right] = \min$	Desolvation curves are recorded at different heating rates. Parameter $\Phi(E_a)$ is then calculated and minimized with MS Excel Solver, obtaining E _a for α values with step size 0.1

Table A7. Mathematical expressions used for determination of the kinetic models.

Method	Procedure
Model fitting method	This method is used only for isothermal data. Two approaches have been used. Firstly, experimental points for a particular desolvation curve is plotted in coordinates $g(\alpha) - time$ and model with the best linear fit is selected. Secondly, experimental points for a particular desolvation curve and theoretical lines modelled from selected kinetic models are plotted in the coordinates $\alpha - time$. The sum of squared differences between the experimental and theoretically calculated α values is minimized with MS Excel Solver. The best model is identified by the smallest sum of least squares.
Average linear integral method (ALIM) ²⁰⁹	Experimental data points are linearized as in ALIM method, Table 6: $-\ln \Delta t = -\ln \Delta g(\alpha) + \ln A_\alpha - \frac{E_{a,\alpha}}{RT(t)}$ The intercept I _α of this line is calculated and for each kinetic model following linear relationship is constructed by using previously determined E _a values: $\ln \Delta g(\alpha) + I_\alpha = bE_{a,\alpha} + c$ Model with the best linear fit is selected.
Reconstruction of the integral or differential reaction model ^{72, 157, 186}	Kinetic model $g(\alpha)$ or $f(\alpha)$ is reconstructed from experimentally determined E _a and A values, using Equations 1.3, 1.4 and 1.5. For reconstruction of integral kinetic model $g(\alpha)$ numerical integration is used. Frequency factor A is calculated using isokinetic relationship: $\ln A = bE_a + c$ Where b and c are determined from the ALIM method described above. Theoretical model best fitting with the constructed curve is selected.
Reduced time plots ¹⁸⁸	This method is used for isothermal data. This approach uses the fact that for the correct kinetic model a curve constructed from the experimental ratio $t(\alpha)/t(0.5)$ should match with the curve constructed from the ratio $g(\alpha)/g(0.5)$: $\frac{g(\alpha)}{g(0.5)} = \frac{t(\alpha)}{t(0.5)}$ Theoretical model with curve best fitting to the constructed curve is selected.
“Master plots” ²¹⁵	This method is used for non-isothermal data. For a particular desolvation curve parameter Z(α) is calculated and plotted: $Z(\alpha) = \frac{d\alpha/dt}{\beta} h(x)T$ where β is the heating rate and h(x) is the temperature integral. Curves for theoretical models are constructed using equation: $Z(\alpha) = f(\alpha)f(\alpha)$ Theoretical model with curve best fitting to the constructed curve is selected.

Appendix 5.

Table A8. Characterization of inorganic compounds and solvents used.

Compound	Purity	Manufacturer
Solvents		
acetone	>99.5%	Penta
acetonitrile	>99.9%	Fluka
benzyl alcohol	>99%	Alfa Aesa
1-butanol	>99.5%	Penta
butanone	>99.5%	Sigma-Aldrich
butyl acetate	>99%	Alfa Aesa
<i>tert</i> -butyl methyl ether	>99.9%	Alfa Aesa
carbon tetrachloride	>99.8%	Merck
chloroform	>99%	Alfa Aesa
Cyclohexane	>99%	Alfa Aesa
cyclohexanol	>99%	Alfa Aesa
cyclohexanone	>99%	Alfa Aesa
1,1-dichloroethane	>98%	Реахим
dichloromethane	99.7%	Alfa Aesa
dimethylsulfoxide	>99%, USP	Penta
1,4-dioxane	>99.9%	Sigma-Aldrich
ethanol	99.97%	LABSCAN
ethyl acetate	>99.5%	Penta
glycerine	>98%, Ph. Eur.	Penta
isobutanol	>99%	Alfa Aesa
isopropyl acetate	>99%	Alfa Aesa
Methanol	>99.8%	Fluka
N,N-dimethylformamide	>98%	Penta
<i>n</i> -heptane	>98%	Реахим
<i>n</i> -hexane	>98%	Реахим
nitromethane	>98%	Merck
3-pentanone	>99%	Merck
1-propanol	>99.5%	Penta
2-propanol	>99.5%	Alfa Aesa
tetrahydrofuran	>99.5%	Немпур
toluene	>98%	Реахим
<i>o</i> -xylene	>98%	Реахим
ethanol-d1	99.5 atom % D	Sigma-Aldrich
methanol-d1	99.5 atom % D	Sigma-Aldrich
D ₂ O	99.9 atom % D	Sigma-Aldrich
water	Deionised in the laboratory using Crystal 5, conductivity <0.2 μS	
Inorganic compounds		
CH ₃ CO ₂ K	>99%	Реахим
K ₂ SO ₄	>99%	Реахим
KCl	100%	НПО ЭКРОС
KI	>99%	Реахим
LiBr	>99%	Sigma-Aldrich
LiCl	>98%	Penta
MgCl ₂	>99%	Реахим
N ₂ (compressed gas)	>99.99%, technical	AGA
NaBr	>98%, Ph. Eur.	Penta
NaCl	>99%	Реахим
P ₂ O ₅	>98%	Реахим

Analysis of the particle size distribution

A Mastersizer 2000 (Malvern) laser diffraction instrument was used for particle size analysis. Integration time was 3000 ms. The measurement range was set to 0.020 – 2000 μm , and 59 counting channels were used. For sample dispersion nitrogen with 1.0 bar pressure was used. All measurements were carried out three times and the average value was used.

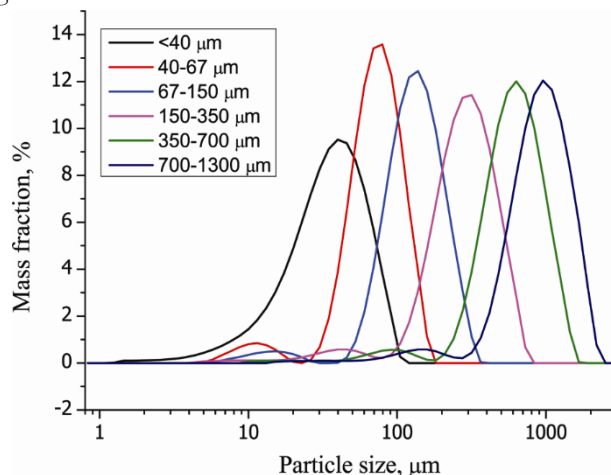


Figure S1. Particle size distribution of different fractions of mildronate dihydrate sample

Moisture Sorption-Desorption isotherm

Mildronate **AP** was used for acquiring a sorption isotherm. **AP** was prepared by heating **DH** at 100 °C temperature. Approximately 0.8 g of sample was weighed in each of ten containers. These containers were placed in humidity chambers where the relative humidity was provided with saturated salt solutions and phosphorus pentoxide. The salts used for this experiment and the corresponding relative humidity values were LiBr (6%), LiCl (11%), $\text{CH}_3\text{CO}_2\text{K}$ (23%), MgCl_2 (32%), NaBr (56%), KI (68%), NaCl (75%), KCl (84%), K_2SO_4 (97%) and also P_2O_5 (~0%)¹. Humidity chambers were thermostated at 25 ± 1 °C temperature and containers were weighed on analytical balance ($d=0.1$ mg) until no notable change of mass was observed (except for containers where sample deliquesced). At the end of the experiment, the phase composition of each sample was determined with PXRD. For desorption isotherm, approximately 0.8 g of mildronate **DH** sample stored at 22.5% relative humidity was weighed into containers and inserted in the previously described humidity chambers up to relative the humidity of 32%. The same analytical procedure as described for sorption isotherm was used. Inorganic compounds for relative humidity control were purchased from commercial sources and used without further purification.

From sorption-desorption isotherm of mildronate at 25 °C temperature it was observed that **DH** was stable in the relative humidity interval from 6 to 50% (See Figure S2). Dehydration of **DH** was observed only at 0% relative humidity and **AP** was obtained as the product. By using **AP** as a starting material, it was observed that a small amount of **DH** formed at 6% relative humidity (~10% of the **AP** transformed into the **DH** over 2 months), while fast transition to **DH** occurred at a higher humidity. By PXRD it was determined that samples contained either **AP** or **DH**. This confirmed² that **MH** was not thermodynamically stable at any of the examined conditions. However, continuous monitoring of the phase transition was not done. Thus, it was not possible to exclude the **MH** as a possible transition state in the transformation from **DH** to **AP** or vice versa.

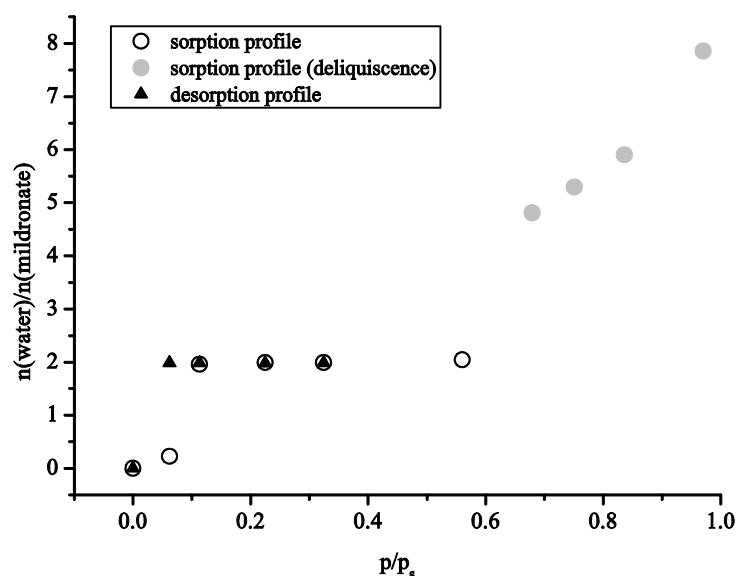


Figure S2. Sorption – desorption isotherm of mildronate (water content is given after storing for 2 months)

Study of the mildronate DH dehydration

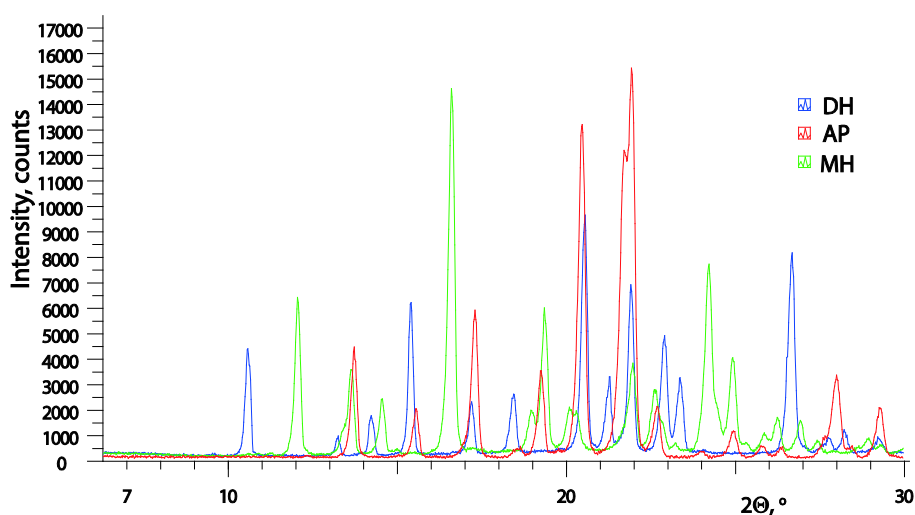


Figure S3. PXRD patterns of mildronate dihydrate (**DH**), monohydrate (**MH**) and anhydrous phase (**AP**)

Dehydration of **DH** samples with different particle sizes (the particle size distribution for various fractions is given in Figure S1) was performed during DTA/TG experiments at a heating rate of $1\text{ }^{\circ}\text{C}\cdot\text{min}^{-1}$ in open pans under nitrogen flow. One endothermic peak appeared with dehydration starting temperature below $50\text{ }^{\circ}\text{C}$ and the peak thermal effect around $60\text{--}65\text{ }^{\circ}\text{C}$ (See Figure S4 (b)). For both of these characteristic dehydration temperatures, a significant impact of particle size was observed – dehydration of smaller particles was faster than that of bigger particles at the same heating rate. When analysis of the same samples was performed at a higher heating rate, the dehydration thermal effect was split in two parts (See Figure 3). The second endothermic effect was observed as a relatively sharp peak at $86\text{--}88\text{ }^{\circ}\text{C}$. The temperature of this second maximum was not affected by the heating rate or the particle size, and it contributed more at higher heating rates and larger particle sizes. Changing the atmosphere from nitrogen flow to static air increased the dehydration starting temperature and the maximum temperature, while also increasing the contribution from this second maximum. It was also observed that for large particle sizes (above $350\text{ }\mu\text{m}$) after appearance of this second maximum the dehydration rate dropped dramatically, and breaches appeared in the TG line (See Figure S5).

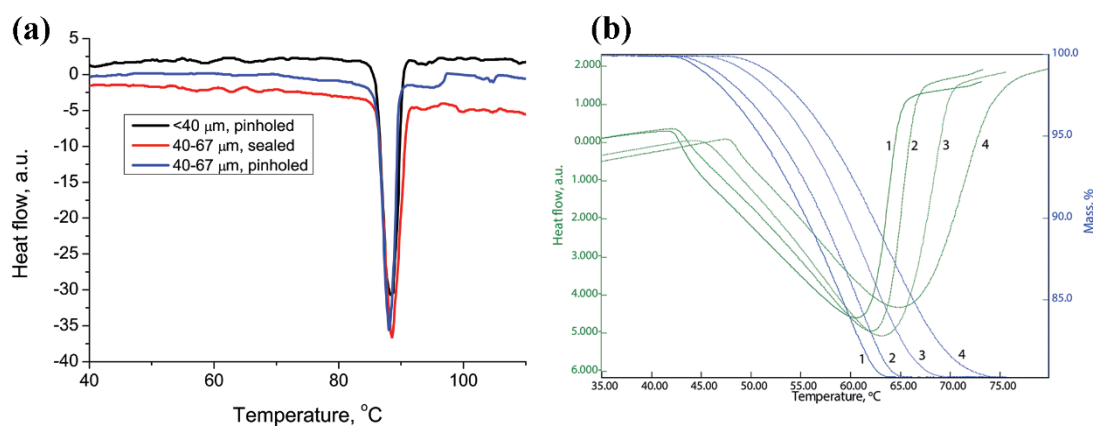


Figure S4. a) DSC curves of ildronate **DH** at heating rate $5\text{ °C}\cdot\text{min}^{-1}$ and b) DTA/TG curves of mildronate **DH** at heating rate $1\text{ °C}\cdot\text{min}^{-1}$ for fractions 1) $<40\text{ }\mu\text{m}$, 2) $40\text{-}67\text{ }\mu\text{m}$, 3) $67\text{-}150\text{ }\mu\text{m}$ and 4) $150\text{-}350\text{ }\mu\text{m}$.

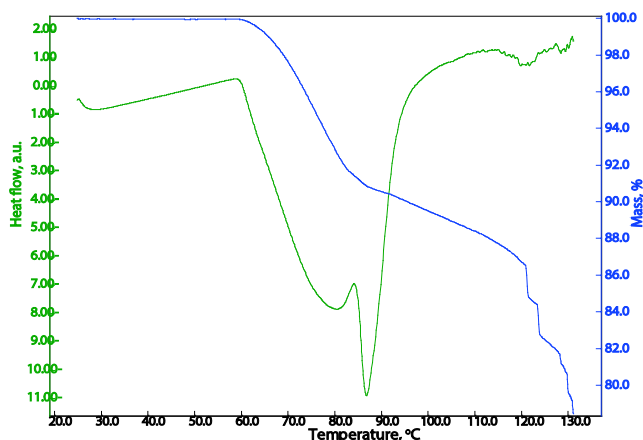


Figure S5. DTA/TG curves of mildronate **DH** at a heating rate of $4\text{ °C}\cdot\text{min}^{-1}$ for fraction $>350\text{ }\mu\text{m}$

The effect of the atmosphere on the dehydration starting temperature and the temperature of peak dehydration rate could be easily explained by the fact that dehydration process was affected by the moisture content in the atmosphere. By providing a dry nitrogen flow, water was effectively removed from the sample, thus enhancing the dehydration rate. The effect of heating rate could be associated with the total heating time, thus a higher conversion degree for given temperature was obtained with slower heating rates. The observation that smaller particles dehydrated faster can be associated with the larger surface to mass ratio and it is known that dehydration reactions typically start on the surface where the dehydration is enhanced³.

It was determined that the only factor affecting the dehydration peak position and shape in the DSC experiments was the heating rate. When the heating rate was $1\text{ °C}\cdot\text{min}^{-1}$, dehydration starting temperature decreased to the same value as was observed in the VT-PXRD experiment, although a sharp peak at 87 °C was still observed (See Figure S6).

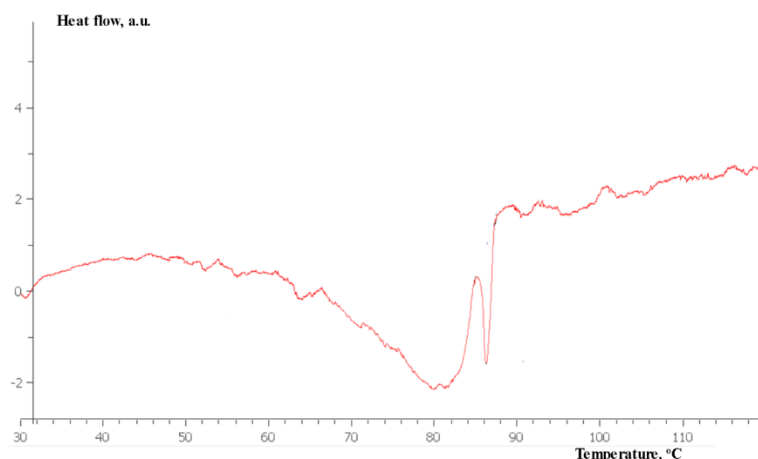


Figure S6. DSC curve of mildronate **DH** sample for fraction of 67-150 μm (with heating rate 1°min^{-1})

In order to get more insight into the processes occurring during the dehydration of **DH** and to explain observations from thermal analysis, dehydration of 67-150 μm and 350-700 μm **DH** fractions was analysed with hot stage polarized light microscopy. When particles from the 67-150 μm fraction were heated at the rate of 8°min^{-1} , sample darkening was observed at 70 $^\circ\text{C}$ temperature and no further changes were observed until the temperature of 140 $^\circ\text{C}$ was reached (see Figure S7). When particles from the 350-700 μm fraction were analysed, the sample darkened at 72 $^\circ\text{C}$. When the temperature reached almost 90 $^\circ\text{C}$, emanation of liquid water was observed from most of the crystals, and this process continued upon further heating of the sample. Bubbling of evolved water was observed above 100 $^\circ\text{C}$, and the bubbling intensified upon further increasing of the temperature. In some of the experiments within the temperature interval of 115 – 130 $^\circ\text{C}$ some of the crystals from the 350-700 μm fraction even exploded.

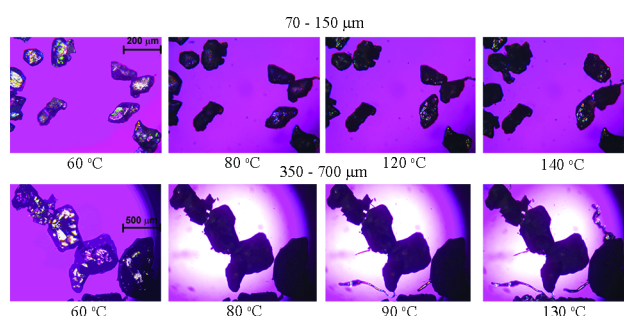


Figure S7. Polarized light photomicrographs of the dehydration process of mildronate **DH** (70-150 μm and 350-700 μm fractions).

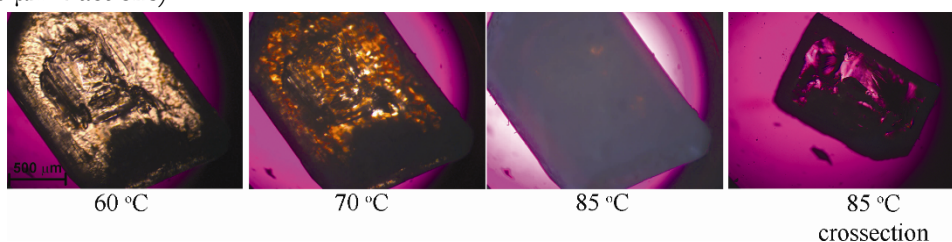


Figure S8. Polarized light photomicrographs of the dehydration process of mildronate **DH** single crystal at 60 – 85 $^\circ\text{C}$ and the cross section of the crystal after the heating.

Thus, above the peritectic temperature mildronate water solution formed by abruptly slowing down the dehydration process, as observed in DTA/TG scans. Crystal explosion most probably happened due to the fact that the newly formed **AP** surrounded the crystal, which temporarily blocked the release of water. After the peritectic temperature was reached, liquid water was released in the interior of the particle. Water was not able to escape the particle, and increasing the temperature led to a pressure increase, followed by disruption of the particle. This observation agrees with the appearance of branches in DTA/TG curves for larger particle sizes.

Parameters for calculations in *CRYSTAL09*

The level of accuracy in evaluating the Coulomb and exchange series was controlled by five thresholds⁴, for which values 10^{-8} , 10^{-7} , 10^{-7} , 10^{-7} and 10^{-24} were used as suggested in the literature⁵, in order to avoid numerical instabilities in computing the exact exchange contributions. For numerical integration of the density (75, 974)_p, an extra-large grid was adopted⁴. The irreducible Brillouin zone was sampled using 170 k-points (the shrinking factor⁴ of the reciprocal space net was set to 8). Levshift function with level shift of 1 hartree without locking was used in order to reach the convergence in energy. Full crystal structure optimization was done with analytical gradients for the unit cell. For optimization procedure, the space group symmetry of the original crystal structures was retained. Convergence criteria for geometry optimization were as follows: maximum energy gradient/component = 0.00045, RMS energy gradient/component = 0.0003, maximum displacement/component = 0.0018, RMS displacement/component = 0.0012, threshold for energy change = $0.1 \cdot 10^{-6}$, all in a.u.

Crystal structure correction

The crystal structures of **AP** and **MH** had previously been determined from PXRD data, thus only positions of non-hydrogen atoms were reported⁶. Moreover, the reported bond distances of carboxyl group oxygen atoms were not optimized but left as in non-conjugated systems⁶. The structural information for **AP** and **MH** was taken from the literature⁶ and improvements in the following order were applied: 1) hydrogen atoms were added, 2) molecular cluster consisting of a central molecule surrounded by 12 closest neighbour molecules was prepared. Positions of central molecule's carboxyl group oxygen atoms O1 and O2, hydrogen atom bounded to nitrogen H1, hydrogen atoms of water molecules H15, H16 (in **MH** and **DH**), H17 and H18 (in **DH**), to central molecule's N-H intermolecular hydrogen bonded oxygen (O1' in **AP** and O2' in **MH**), the hydrogen bound to central molecule's carboxyl group (H1'') and hydrogen atoms of water molecule H15'' and H16'' (in **MH**) (See Fig. S2) were optimized at the B3LYP/6-31G level in *Gaussian09*⁷. It should be remarked that the dihedral angle τ_1 was altered after this operation. 3) Positions of all hydrogen atoms of the central molecule were optimized at the B3LYP/6-31G level in *Gaussian09*⁷. For further calculations, the corrected structure of **AP** and **MH** was used. Corrected **DH** structure was used only for extraction of mildronate molecules to calculate the intramolecular energy.

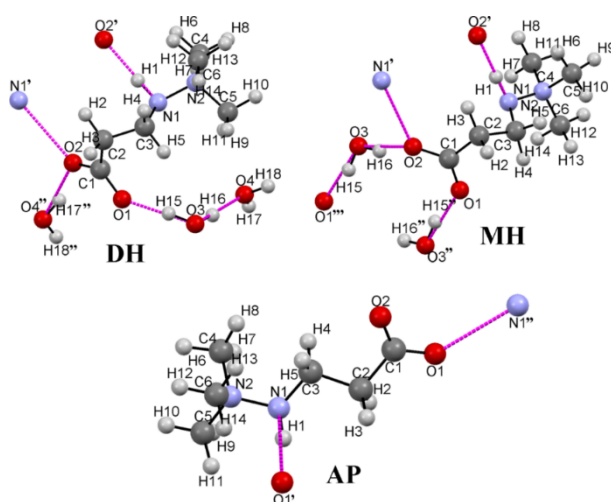


Figure S9. Labeling scheme for atoms in crystal structures of **DH**, **MH** and **AP** used for atom position optimization in *Gaussian09*

The values of bond distances, angles, and dihedral angles, which were changed during the crystal structure correction in *Gaussian09* in all three structures, are given in Table 1S. All atom positions in fractional coordinates after optimization are given in Table 2S. By comparing the obtained data with the results from crystal structure optimization in *CRYSTAL09*, it can be seen that there were only minor differences, meaning that the procedure performed in *Gaussian09* was reliable and the corrected crystal structures were suitable for further use.

Table S1. Original and final values of mildronate molecule bond lengths, angles and torsion angles affected by crystal structure correction in *Gaussian09* at the B3LYP/6-31G level and after full structure optimization in *CRYSTAL09* at the B3LYP-D*/6-31G(d,p) level

Parameter	AP			MH		DH		
	Original ⁶	Optimized ^a	Optimized ^b	Original ⁶	Optimized ^a	Original ⁸	Optimized ^a	Optimized ^b
d(O1-C1)	1.21	1.275	1.270	1.21	1.279	1.257	1.276	1.258
d(O2-C1)	1.36	1.255	1.258	1.36	1.307	1.267	1.307	1.275
d(N1-H14)	-	1.013	1.035	-	1.010	0.919	1.045	1.032
Angle(O1-C1-O2)	1.20	124.7	125.65	120.0	123.1	123.7	123.1	123.3
Angle(O1-C1-C2)	1.20	119.9	115.64	120.0	118.2	118.5	120.4	119.2
Angle(C3-N1-H1)	-	111.1	109.21	-	111.6	108.9	109.4	108.1
Torsion(O1-C1-C2-C3)	175.1	-156.2	-179.6	45.3	47.8	51.4	49.0	52.8
Torsion(C2-C3-N1-H1)	-	55.3	63.14	-	48.0	57.0	52.2	52.3

^a – optimization of central molecule in molecule cluster in *Gaussian09* at the B3LYP/6-31G level

^b – full crystal structure optimization in *CRYSTAL09* at the B3LYP-D*/6-31G(d,p) level

Table S2. Fractional coordinates of all atoms after crystal structure correction in *Gaussian09* and full structure optimization in *CRYSTAL09*

Code	<i>Gaussian09</i>									<i>CRYSTAL09</i>					
Form	AP			MH			DH			AP			DH		
O1	0.7805	1.1208	0.8543	0.7081	0.2152	0.6783	0.4451	0.1202	0.6766	0.7576	1.1022	0.8876	0.4562	0.1272	-0.3267
C1	0.7252	1.0653	0.7254	0.6518	0.3032	0.5596	0.3205	0.0811	0.5923	0.7214	1.0680	0.7349	0.3237	0.0845	-0.4084
O2	0.6117	1.0986	0.6356	0.7478	0.4510	0.3868	0.2144	0.1498	0.5172	0.6201	1.1154	0.6394	0.2020	0.1509	-0.4803
C2	0.7986	0.9477	0.6916	0.4686	0.2253	0.6141	0.3011	-0.0520	0.5702	0.8133	0.9603	0.6635	0.3096	-0.0537	-0.4255
H2	0.9200	0.9523	0.7236	0.4548	0.1026	0.5797	0.1738	-0.0681	0.5010	0.9374	0.9831	0.6658	0.1827	-0.0753	-0.4975
H3	0.7494	0.8823	0.7738	0.4306	0.3223	0.5180	0.4360	-0.0805	0.5480	0.7984	0.8867	0.7561	0.4503	-0.0830	-0.4432
C3	0.7743	0.9158	0.5035	0.3549	0.1695	0.8540	0.2797	-0.1270	0.6653	0.7693	0.9207	0.4791	0.2899	-0.1273	-0.3265
H5	0.8168	0.9878	0.4295	0.2309	0.0770	0.9000	0.3941	-0.1022	0.7380	0.8002	0.9910	0.3867	0.4067	-0.0990	-0.2525
H4	0.6530	0.9068	0.4739	0.4104	0.0935	0.9434	0.2993	-0.2203	0.6478	0.6433	0.9068	0.4698	0.3131	-0.2236	-0.3419
N1	0.8651	0.8103	0.4644	0.3399	0.3331	0.8985	0.0795	-0.1003	0.6808	0.8630	0.8146	0.4376	0.0863	-0.1014	-0.3129
H1	0.8388	0.7432	0.5433	0.3113	0.4208	0.7920	-0.0293	-0.1124	0.6081	0.8331	0.7471	0.5238	-0.0216	-0.1165	-0.3871
N2	0.8415	0.7676	0.2946	0.2170	0.2947	1.1123	0.0215	-0.1773	0.7602	0.8322	0.7605	0.2657	0.0246	-0.1808	-0.2347

C5	0.9502	0.6713	0.2645	0.0460	0.1992	1.1544	0.1400	-0.1432	0.8706	0.9457	0.6584	0.2550	0.1439	-0.1466	-0.1198
C4	0.8684	0.8616	0.1701	0.2160	0.4676	1.1370	-0.1965	-0.1520	0.7471	0.6667	0.7160	0.2461	-0.1986	-0.1541	-0.2519
C6	0.6832	0.7231	0.2708	0.2602	0.1838	1.2696	0.0452	-0.3075	0.7430	0.8691	0.8458	0.1191	0.0501	-0.3156	-0.2522
H9	1.0646	0.7067	0.2763	-0.0478	0.2010	1.3020	0.2934	-0.1736	0.8836	1.0619	0.6969	0.2640	0.1360	-0.0483	-0.1106
H10	0.9316	0.6364	0.1383	0.0331	0.0581	1.1748	0.0739	-0.1856	0.9288	0.9301	0.6136	0.1301	0.3024	-0.1751	-0.1054
H11	0.9341	0.6047	0.3599	0.0242	0.2693	1.0214	0.1364	-0.0477	0.8788	0.9219	0.5999	0.3659	0.0758	-0.1936	-0.0634
H12	0.6699	0.6893	0.1430	0.1719	0.1744	1.4277	-0.2774	-0.1797	0.6664	0.5836	0.7885	0.2655	-0.2158	-0.0573	-0.2382
H13	0.5999	0.7918	0.2871	0.2533	0.0493	1.2670	-0.2150	-0.0575	0.7565	0.6471	0.6477	0.3450	-0.2789	-0.1784	-0.3360
H14	0.6650	0.6551	0.3631	0.3890	0.2553	1.2306	-0.2475	-0.2034	0.8062	0.6555	0.6807	0.1140	-0.2555	-0.2097	-0.1962
H6	0.8658	0.8220	0.0454	0.1202	0.4406	1.2975	-0.0330	-0.3291	0.6602	0.9870	0.8802	0.1356	0.2126	-0.3374	-0.2272
H7	0.9812	0.8979	0.1929	0.3404	0.5367	1.1131	-0.0231	-0.3549	0.7977	0.7832	0.9171	0.1166	-0.0218	-0.3371	-0.3381
H8	0.7794	0.9267	0.1756	0.1862	0.5515	1.0191	0.2036	-0.3291	0.7620	0.8638	0.7941	-0.0014	-0.0268	-0.3658	-0.2016
O3				0.9950	0.7438	0.3183	0.5994	0.0778	0.8884				-0.3996	0.0736	-0.1124
H15				1.1007	0.7378	0.3308	0.5402	0.0876	0.8098				-0.4575	0.0837	-0.1920
H16				0.9141	0.6252	0.3580	0.4964	0.1029	0.9270				0.4896	0.0980	-0.0806
O4							0.3112	0.1251	0.9945				0.3017	0.1222	-0.0181
H17							0.2773	0.2048	1.0179				0.2762	0.2031	0.0095
H18							0.3248	0.0573	1.0463				0.3276	0.0612	0.0413

^a – optimization of central molecule in molecule cluster in Gaussian09 at the B3LYP/6-31G level, lattice parameters unchanged

^b – full crystal structure optimization in CRYSTAL09 at the B3LYP-D*/6-31G(d,p) level, lattice parameters given in Table 1

Analysis of the molecule conformation and hydrogen bonding

It is already stated that conformation of mildronate molecule is almost the same for the **DH** and **MH** (see Table S3). Torsion angles O1-C1-C2-C3 (τ_1) and C1-C2-C3-N1 (τ_2) in **AP** are significantly different than those in **DH** and **MH**. Hydrogen bond geometry of **DH**, **MH** and **AP** is presented in Table S4. Geometry of hydrogen bonds in **MH** and **AP** structures was determined after structure correction at the B3LYP level. Analysis of hydrogen bonding motifs in crystal structure showed that inversion related mildronate moieties in crystal structures of **DH** and **MH** form N1-H1 \cdots O2 hydrogen bonded dimers with graph set $R_2^2(12)$ (See Figure S10 (a)). Additionally, mildronate carboxyl groups and water molecules in **MH** form O-H \cdots O hydrogen bonds with second order graph set $R_4^4(12)$ (See Fig. S11). In crystal structure of **DH** four water molecules form hydrogen bonded $R_4^4(8)$ motifs (See Fig. S11). Water molecules are connected to mildronate molecules by infinite $C_3^3(8)$ and $C_3^4(12)$ chains (See Fig. S11). In **AP** crystal structure mildronate molecules form N1-H1 \cdots O1 hydrogen bonded chains designated by C(6) graph set (See Figure S10 (b)).

Table S3. Torsion angle values of the mildronate molecule in all three crystal structures

Angle	O1-C1-C2-C3, τ_1 , °	C1-C2-C3-N1, τ_2 , °	C2-C3-N1-N2, τ_3 , °	C3-N1-N2-C4, τ_4 , °
DH ⁸	51.4	69.4	172.1	-169.2
MH ⁶	45.3	74.6	171.5	179.2
AP ⁶	175.1	171.6	175.5	54.0
AP _{corr} ^a	-156.2	171.6	175.5	54.0

^a – optimization of central molecule in molecule cluster in Gaussian09 at the B3LYP/6-31G level

Table S4. The geometric parameters and graph set assignments of hydrogen bonds in mildronate crystalline phases

Hydrogen bond	Symmetry	D-H, Å	H \cdots A, Å	D-A, Å	\angle DHA, °	Graph set notation
DH						
N1—H1 \cdots O2	-x, -y, 1-z	0.919	2.004	2.920	175.5	$R_2^2(12)$
O4—H18 \cdots O3	1-x,-y,2-z	0.988	1.775	2.728	161.1	} $R_4^4(8)$
O3—H16 \cdots O4	x,y,z	1.171	1.594	2.760	173.5	
O4—H17 \cdots O2	x,1/2-y,1/2+z	0.777	0.955	2.714	165.4	
O3—H15 \cdots O1	x,y,z	0.786	1.941	2.719	170.3	
MH						
N1—H1 \cdots O2	1-x,1-y,1-z	1.040	1.742	2.779	1774.4	$R_2^2(12)$
O3—H16 \cdots O2	x,y,z	0.991	1.782	2.748	164.1	} $R_4^4(12)$
O3—H15 \cdots O1	2-x,1-y,1-z	1.002	1.675	2.657	165.6	
AP						
N1—H1 \cdots O1	1,5-x,1/2+y,1,5-z	1,013	1,925	2.894	159.0	C(6)

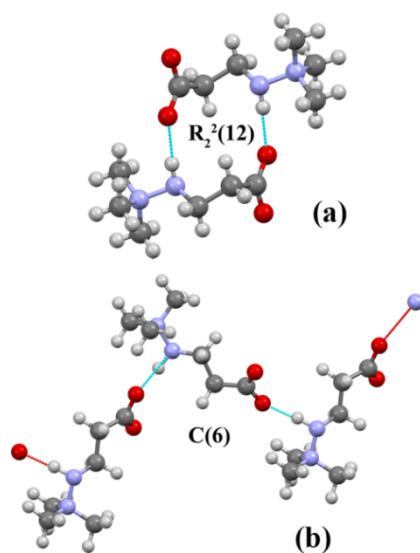


Figure S10. Hydrogen bonding motif connecting mildronate molecules (a) in **DH** and **MH** and (b) in **AP**

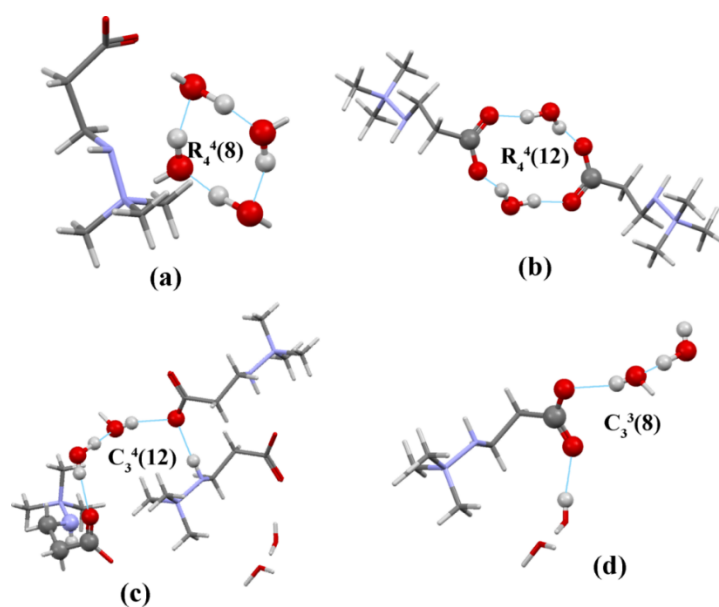


Figure S11. Hydrogen bonding motif formed by water molecules in **DH** (a), and by water and mildronate molecules in **MH** (b) and **DH** (c and d)

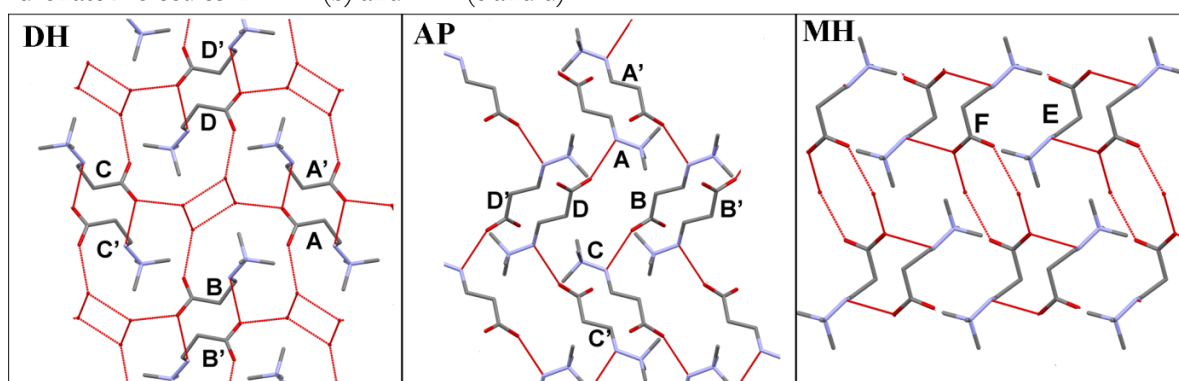


Figure S12. Molecular packing and hydrogen bonding network in the crystalline forms of mildronate (hydrogen atoms have been omitted for clarity).

Analysis of the potential energy surface (PES) scans

In order to examine the potential energy surface (PES) of observed conformations with respect to other available conformations all four torsion angles were scanned at the MP2/6-31G(d,p) level with step size of 10° while conformation for the rest of the molecule was maintained as observed whether in DH or AP structure. For this analysis mildronate molecule was extracted from nonoptimized DH structure with atom coordinates as in the literature and from AP structure corrected at the B3LYP/6-31G level. PES scans with marked torsion angles as observed in experimental structures are presented in Figure S13. It can be seen that the form of PES scans with respect to the same torsion angle slightly depends on the conformation of the rest of the molecule although the positions of minimums and maximums are generally at the same angles.

Minimums in the PES scan with respect to torsion angle τ_1 (Figure S13) can be associated with C3-H...O1 (in experimental DH structure) and C3-H...O2 (in experimental AP structure) interaction while maximums are associated with intramolecular interactions N1...O1 and N1...O2. In the scan with respect to torsion angle τ_2 global minimum is observed when intramolecular hydrogen bonding N1-H...O1 (in DH) and N1-H...O2 (in AP) is present, maximum at $\tau_2 = 0$ is related to eclipsed conformation where N1...O1(8) interaction is observed but local minimums are due to C3-H...O1 (in DH) and C3-H...O2 (in AP) intramolecular interaction. Energy difference between global minimum and global maximum is higher in AP structure due to shorter distances in observed interactions. Experimental structures correspond to different local energy minimums. Energy maximums in τ_3 scan is associated with close C1-H...H-C4 and C1-H...H-C6 interaction in AP and with methyl group close interaction with carboxyl group and with close C1-H...H-C5 and C1-H...H-C6 interaction in DH. Although it seems that from $\tau_3 = 100$ to -100 there is a plateau with the same energy, closer look reveals that AP is located in global energy minimum while DH in local minimum. Energy scan of τ_4 corresponds to conformational energy diagram for rotation around single bond with observed crystal structures situated in global energy minimums.

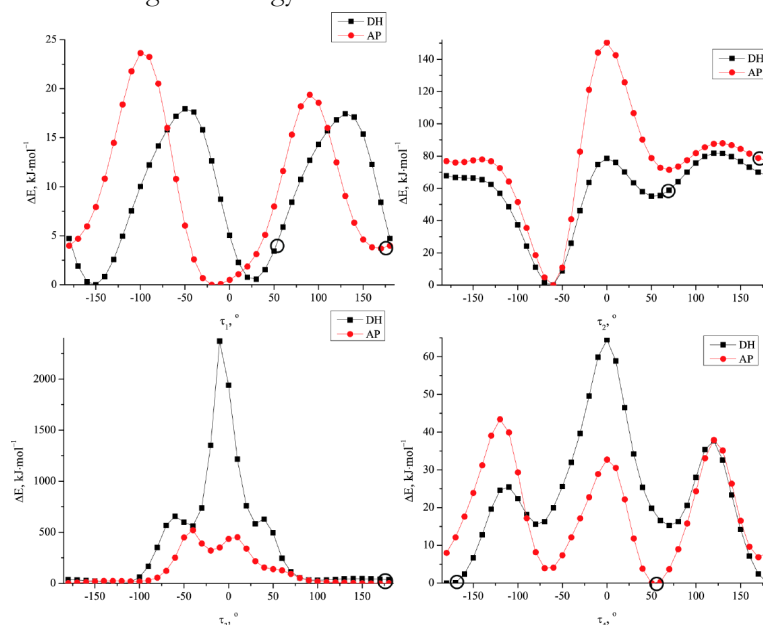


Figure S13. PES scans of mildronate molecule with respect to one torsion angle (the rest of the molecule was fixed at conformation observed in **DH** or **AP** structure)

By analysing the PES graphs with respect to one dihedral angle, it was calculated that the energy barrier necessary for conformation changes during the transition from **DH** to **AP** was 15 kJ·mol⁻¹ for changing τ_1 , 10-25 kJ·mol⁻¹ for changing τ_2 , and 30-40 kJ·mol⁻¹ for changing τ_4 . From these results it can be seen that the activation energy necessary for conformation changes was slightly lower than typical energy barriers in phase transitions.

To more realistically evaluate the activation energy necessary for transformation of molecular conformation, PES graphs with respect to two dihedral angles were created as well. In this transition from **DH** to **AP**, where the dihedral angles τ_3 and τ_4 did not change, a pathway where simultaneous changes dihedral angles $\tau_1 - \tau_2$ could be important.

PES with respect to two adjacent torsion angle change of all three adjacent torsion angle combinations were performed at the B3LYP/6-31G level with step size 15° for each dihedral angle and it was observed that PES for torsion angles τ_1 - τ_2 and τ_2 - τ_3 are basically the same for **DH** and **AP** conformations while PES scan for torsion angle τ_3 - τ_4 changes is different for both structures. All three PES scans for **DH** structure and τ_3 - τ_4 scan for **AP** is showed in Figure S14 but the rest two scans for **AP** structure are shown in Figure S15. Energy minimums observed in PES scan with respect to τ_1 - τ_2 1 and 1' and minimum 2 in scan with respect to τ_2 - τ_3 corresponds to intramolecular hydrogen bond N1-H··O1(O2), but minimum 3 corresponds to weak intramolecular hydrogen bond C5-H··O1 in **DH** and C3-H··O2 in **AP**. Energy maximum in PES scan with respect to τ_1 - τ_2 corresponds to N1··O1 and N1··O2 interaction. In scan with respect to τ_1 - τ_2 **DH** and **AP** structures are located in local energy minimums and changes from one conformation to second one is associated with energy barrier 20 kJ·mol⁻¹. In PES scan with respect to τ_3 - τ_4 conformation as in **AP** structure corresponds to global minimum without specific interaction. However, in **DH** global minimum 4 corresponds to C5-H··O1 interaction. Energy maximums in PES scans with respect to τ_2 - τ_3 and τ_3 - τ_4 correspond to unrealistic overlapping of atoms or unrealistically short intramolecular distances explaining huge energy difference comparing with observed conformations.

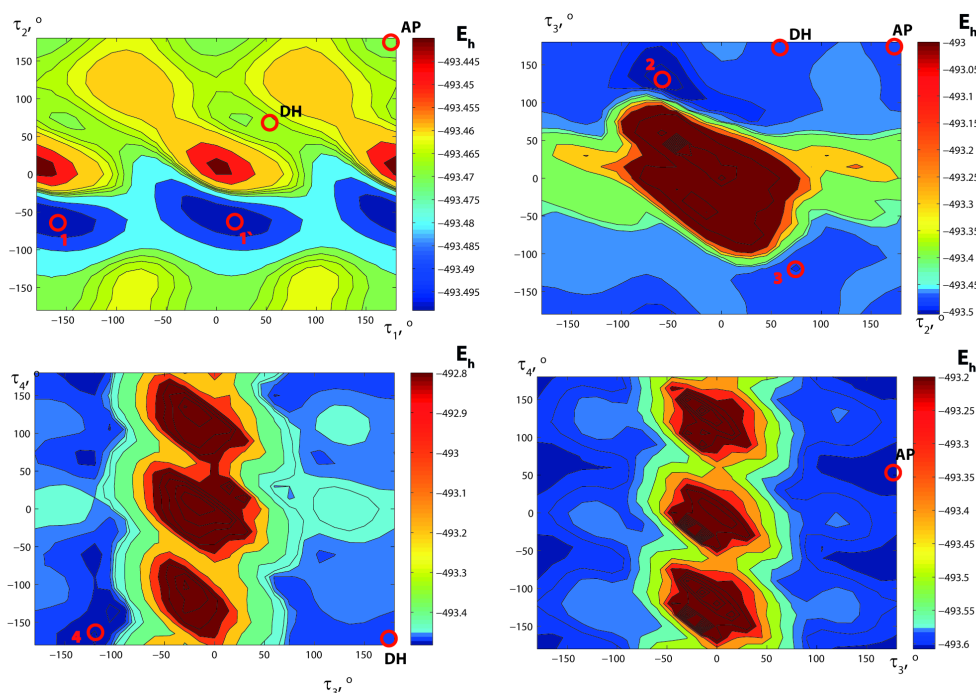


Figure S14. PES scans of mildronate molecule with respect to two adjacent torsion angles while the rest of the molecule was fixed at conformation observed in **DH** structure (except bottom right where the rest of the molecule had conformation as in **AP** structure)

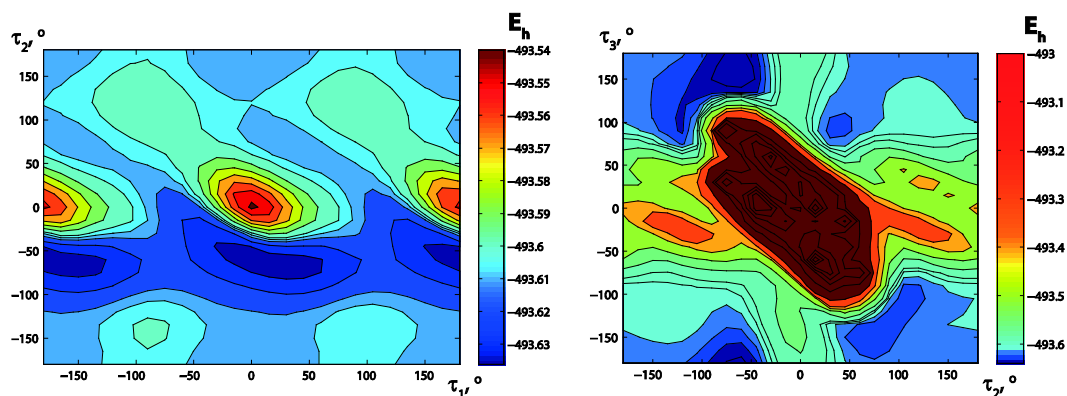


Figure S15. PES scans of mildronate molecule where two adjacent torsion angles were changed while the rest of the molecule was fixed at conformation observed in **AP** structure

Optimization of the molecule conformation of mildronate in DH and AP structures

Torsion angle optimization of mildronate molecule surrounded by 12 closest molecules was performed in *Gaussian09* at the B3LYP/6-31G level for both **DH** and **AP** structures. This procedure was repeated several times by updating the conformation of surrounding molecules with the goal to prove that observed conformation is the most stable in the experimental crystal structures. Full crystal structure optimization of both **DH** and **AP** was performed in *CRYSTAL09*. Results are shown in Table S5.

Table S5. Optimized torsion angles of mildronate molecules in **DH** and **AP** structures

Angle	$\tau_1, ^\circ$	$\tau_2, ^\circ$	$\tau_3, ^\circ$	$\tau_4, ^\circ$
DH				
Original ⁸	51.4	69.4	172.1	-169.2
HF/STO3G 3rd iteration	58.7	71.5	172.5	-170.6
HF/6-31G 1st iteration	55.0	66.0	176.4	-165.5
HF/6-31G 2nd iteration	53.9	67.7	175.2	-165.0
B3LYP-D* <i>CRYSTAL09</i>	52.8	68.9	169.3	-169.0
AP				
Original ^{6,a}	175.1	171.6	175.5	54.0
HF/STO3G 3rd iteration	-158.9	-177.7	177.1	55.4
HF/6-31G 1st iteration	-158.4	176.6	172.0	51.7
HF/6-31G 2nd iteration	-162.3	173.3	175.0	53.9
B3LYP-D* <i>CRYSTAL09</i>	-179.6	-177.4	177.9	61.6

^a – Torsion angle values from the literature⁶ were used while all other parameters were used from crystal structure corrected in *Gaussian09* at the B3LYP level.

Torsion angles in *Gaussian09* calculations have been changed by less than 5° with one exception of τ_1 of **AP** structure which has been changed by more than 20° while after calculations in *CRYSTAL09* changes up to 10° for **AP** structure were observed. It should be remembered that similar torsion angle τ_1 value for **AP** structure was obtained also when full oxygen and hydrogen atom position optimization in the molecule cluster was performed during structure correction in *Gaussian09*. Such a big change can be explained by previous optimization of oxygen atom bond distance and angle in such a way changing molecular environment. Differences between results from both calculation methods are associated with more accurate periodic boundary approach in *CRYSTAL09* and different calculation levels used. Also it can be seen that after full optimization in *CRYSTAL09* only minor changes in conformation of mildronate molecules in **DH** structure are introduced thus confirming that the **AP** crystal

structure probably is less accurate due to the determination from the PXRD data. Thus it can be seen that molecule conformation observed in crystal structures correspond to energy minimum in crystalline environment.

Interaction energy of hydrogen bonded molecule pairs

To compare the intermolecular energy of the **AP** and **DHWW** structures, at first the hydrogen bonding energy of mildronate molecules in the crystal structure was calculated. The interaction energy between hydrogen bonded molecules is shown in Table S6. However, it should be noted that in **DHWW** two hydrogen bonds formed between two molecules while in **AP** each molecule formed two hydrogen bonds, each with a different molecule. Thus, the interaction energy given in Table S6 corresponded to two hydrogen-bonds in the **DHWW** structure, but only one hydrogen bond in the **AP** structure, so the energy value obtained for **DHWW** was related to one hydrogen bond. It can be seen that the total interaction energy of two molecules was more favourable in the **DHWW** structure. By analysing the contribution from different types of interactions, it was concluded that the Coulomb energy dominated in both of these dimers, which was already expected for a molecule with highly polar groups, especially because mildronate molecule is a zwitterion. It can also be evaluated that all four energy types contributed similarly to the total energy of dimers from both structures and the main differences in the total energy resulted from more negative Coulomb energy in **DHWW** structure and small differences of other energy types.

Table S6. Interaction energy of hydrogen bonded molecule pairs in **AP**, **DHWW** and **MHWW** crystal structures.

Phase	Symmetry operation	d , Å ^a	E_{col} , kJ·mol ⁻¹	E_{pol} , kJ·mol ⁻¹	E_{disp} , kJ·mol ⁻¹	E_{rep} , kJ·mol ⁻¹	E_{tot} , kJ·mol ⁻¹
AP	1,5-x, -1/2+y, 1,5-z	7.09	-111.0	-42.7	-18.2	49.5	-122.4
DHWW	-x, -y, 1-z	4.96	-238.4	-80.0	-36.6	89.5	-265.5
	Per 1 hydrogen bond:		-119.2	-40.0	-18.3	44.75	-132.75
MHWW	1-x, 1-y, 1-z	4.91	-273.3	-98.0	-40.1	143.8	-267.7
	Per 1 hydrogen bond:		-136.7	-49.0	-20.1	71.9	-133.9

^a - d , is distance between mass centers of the molecules, Å

Additionally, interaction energy of mildronate molecule dimer in **MH** structure was calculated and given in Table S6. By comparing the interaction energy of mildronate dimers in **DH** and **MH** structures, it can be seen that the total interaction energy is the same, although components slightly differed – Coulomb and polarization energy terms were more negative for **MH** and the repulsion energy term was more positive. This result could be associated with the fact that molecules in hydrogen bonded pairs in the **MH** structure were situated closer to each other.

Energy of optimized and non-optimized crystal structures

The obtained lattice energy for both structures is given in Table S7. As expected for non-optimized crystal structures, by both calculation methods it was determined that the lattice energy of **AP** was lower than that of **DHWW** by 33.0 kJ·mol⁻¹ (from *PIXEL*) and 20.4 kJ·mol⁻¹ (from *CRYSTAL09*), due to the large empty channels in the **DHWW** structure. By comparing the contribution from lattice energy components calculated with *PIXEL*, it can be seen that the Coulomb, polarization and dispersion energy was more negative in **AP** structure, while repulsion energy was lower in the **DHWW** structure. This could be explained by the fact that molecules in **AP** were packed more compactly than in non-optimized **DHWW** structure.

Table S7. Crystal lattice energy and its components calculated with *PIXEL* and lattice energy corrected for basis set superposition error, calculated with *CRYSTAL09* for the original (SP) and optimized (OP) **AP** and **DHWW** structures.

	E_{Coul} , kJ·mol ⁻¹	E_{Pol} , kJ·mol ⁻¹	E_{Disp} , kJ·mol ⁻¹	E_{Rep} , kJ·mol ⁻¹	E_{Tot} , kJ·mol ⁻¹
AP					
PIXEL _{SP}	-278.9	-79.8	-110.5	160.7	-308.4
CRYSTAL09 _{SP}					-330.4
CRYSTAL09 _{OP}					-334.9
DHWW					
PIXEL _{SP}	-222.1	-58.4	-73.5	78.6	-275.4
CRYSTAL09 _{SP}					-309.5
CRYSTAL09 _{OP}					-320.9

In order to allow for possible reorganization in the **DHWW** structure after the water loss, crystal structure optimization was carried out with the *ab initio* code *CRYSTAL09*. Moreover, optimization was performed also for **AP**, to ensure that both structures are compared at the same conditions, because optimization (temperature-less relaxation) of the structure determined at room temperature led to cell shrinkage⁹).

After the optimization reduction in the cell volume for both structures was observed. Although the cell volume reduction was larger after optimization of the **DHWW** structure, crystallographic density of the **AP** was higher, which can be explained by the relatively large empty channels still present in the optimized **DHWW** structure.

By comparing the lattice energy of optimized crystal structures with that for non-optimized crystal structures (see Table S7), a decrease of the lattice energy was observed for both crystal structures. As may be predicted, reduction of the **DHWW** lattice energy was bigger than that for **AP**, although lattice energy of optimized **AP** structure was still energetically favourable.

The total crystal structure energy and lattice parameters obtained by structure optimization are given in Table S8, and fractional atom coordinates are given in Table S2. The addition of zero-point vibration and thermal correction to the calculated total energy did not alter the energy difference significantly. After this correction the **AP** was still energetically more favourable by 9.7 kJ·mol⁻¹.

Table S8. The total energy and lattice parameters obtained after the crystal structure optimization in *CRYSTAL09* for the structures of **AP** and **DHWW**.

	AP	DHWW
Energy, Hartree	-496.7405	-496.7363
E(AP)-E(DHWW), kJ·mol ⁻¹	-11.0	-
a, Å	8.5616	6.7874
b, Å	11.2490	11.1558
c, Å	7.6354	11.7025
β, °	89.26	111.63
d, g·cm ⁻¹	1.320	1.178
V	735.307	823.687
ΔV, %	-5.2	-15.8

The total energy of **DHWW** was very similar to that of **AP**, so this theoretical structure could not be considered as completely unrealistic and it may represent a transition structure during the dehydration process.

References

1. L. Greenspan, *J. Res. Nat. Bur. Stand., Sect. A*, 1977, **81A**, 89-96.
2. K. Veldre, A. Actiņš and A. Kalniņa, Thermal Stability of 3-(2,2,2-trimethylhydrazine)propionate, Solid State Chemistry 2010, Prague, 2010.
3. A. Galwey, *Thermochim. Acta*, 2000, **355**, 181-238.
4. R. Dovesi, V. Saunders, C. Roetti, R. Orlando, C. Zicovich-Wilson, F. Pascale, B. Civalleri, K. Doll, N. Harrison and I. Bush, CRYSTAL09, University of Torino, Torino, Italy, 2009.
5. C. M. Zicovich-Wilson, B. Kirtman, B. Civalleri and A. Ramirez-Solis, *Phys. Chem. Chem. Phys.*, 2010, **12**, 3289-3293.
6. A. Zvirgzdiņš, K. Veldre and A. Actiņš, *Latv. J. Chem.*, 2011, **50**, 64-72.
7. M. J. Frisch, G. W. Trucks, H. B. Schlegel, G. E. Scuseria, M. A. Robb, J. R. Cheeseman, G. Scalmani, V. M. Barone, B., G. A. Petersson, H. Nakatsuji, M. Caricato, X. Li, H. P. Hratchian, A. F. Izmaylov, J. Bloino, G. Zheng, J. L. Sonnenberg, M. Hada, M. Ehara, K. Toyota, R. Fukuda, J. Hasegawa, M. Ishida, T. Nakajima, Y. Honda, O. Kitao, H. Nakai, T. Vreven, J. A. J. Montgomery, J. E. Peralta, F. Ogliaro, M. Bearpark, J. J. Heyd, E. Brothers, K. N. Kudin, V. N. Staroverov, R. Kobayashi, J. Normand, K. Raghavachari, A. Rendell, J. C. Burant, S. S. Iyengar, J. Tomasi, M. Cossi, N. Rega, J. M. Millam, M. Klene, J. E. Knox, J. B. Cross, V. Bakken, C. Adamo, J. Jaramillo, R. Gomperts, R. E. Stratmann, O. Yazyev, A. J. Austin, R. Cammi, C. Pomelli, J. W. Ochterski, R. L. Martin, K. Morokuma, V. G. Zakrzewski, G. A. Voth, P. Salvador, J. J. Dannenberg, S. Dapprich, A. D. Daniels, O. Farkas, J. B. Foresman, J. V. Ortiz, J. Cioslowski and D. J. Fox, Gaussian 09, Gaussian Inc., Wallingford, CT, 2009.
8. A. Mishnev, I. Kalvins, L. Aleksejeva and A. Lebedev, Structure of Mildronate, its Pharmaceutical Salts and Cocrystals, XXII Congress and General Assembly of the International Union of Crystallography, Madrid, Spain, 2011.
9. A. Gavezzotti, *New J. Chem.*, 2011, **35**, 1360-1368.

Physicochemical evaluation of mildronate dihydrate

When crystallized from water or water containing solutions, mildronate crystallizes as a dihydrate **DH**. Thermogravimetrically determined water content is 19.7-20.0% (theoretical water content: 19.7 %). It is already reported¹ that **DH** is stable and at ambient temperature dehydration occurs only when the relative humidity (RH) was almost 0%. However, **DH** is highly hygroscopic: humidity induced changes appeared already at 56% RH and sample deliquesced when RH was 68% or higher. Therefore sample should be stored at 11 – 32% RH.

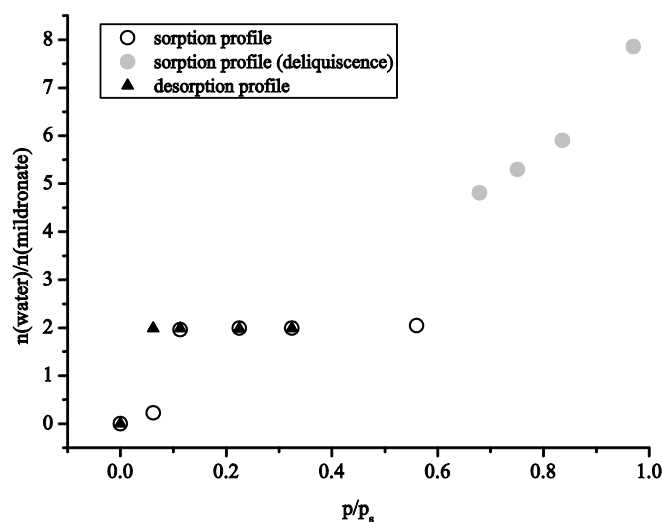


Figure S1. Sorption – desorption isotherm of mildronate (water content is given after storing for 2 months)¹

Dehydration process and dehydration profiles of mildronate dihydrate

A study of the **DH** dehydration process is already published¹. It was shown that the dehydration of **DH** in an open atmosphere can result in two processes: dehydration process initiating at 40 – 60 °C (depending on the sample and experimental conditions) and the melting/peritectic decomposition process occurring at 86-88 °C (if the dehydration was not already finished). Therefore, depending on the particle size, atmosphere and heating rate two situations were possible: a) dehydration finished before reaching the melting/peritectic decomposition temperature and only the thermal effect of the dehydration showed up (see Fig. S2 a), or b) dehydration did not finish before reaching the melting/peritectic decomposition temperature and thermal effect of both dehydration and melting/peritectic decomposition showed up (as for highest heating rates in Fig. S2 b). Phase composition analysis showed that in the first case the only phases present in the sample during the dehydration process was **DH** and anhydrous phase **AP** (see Fig. S2 c), whereas in the second case this was true only up to the reaching of the melting/peritectic decomposition temperature (see Fig. S2 d). In the second case above the 86-88 °C temperature (after appearance of the second endotherm) sample contained a mixture of all three known mildronate phases: **DH**, **AP** and a small amount of monohydrate **MH** (see Fig. S2 e, **MH** is marked with red asterisks). Formation of **MH** occurred due to the crystallization of mildronate from solution or solid phase transition from the **AP** in the presence of liquid water¹.

¹ - Bērziņš A, Actiņš A. 2014. Dehydration of mildronate dihydrate: a study of structural transformations and kinetics. *CrystEngComm*, DOI: 10.1039/C3CE42077A.

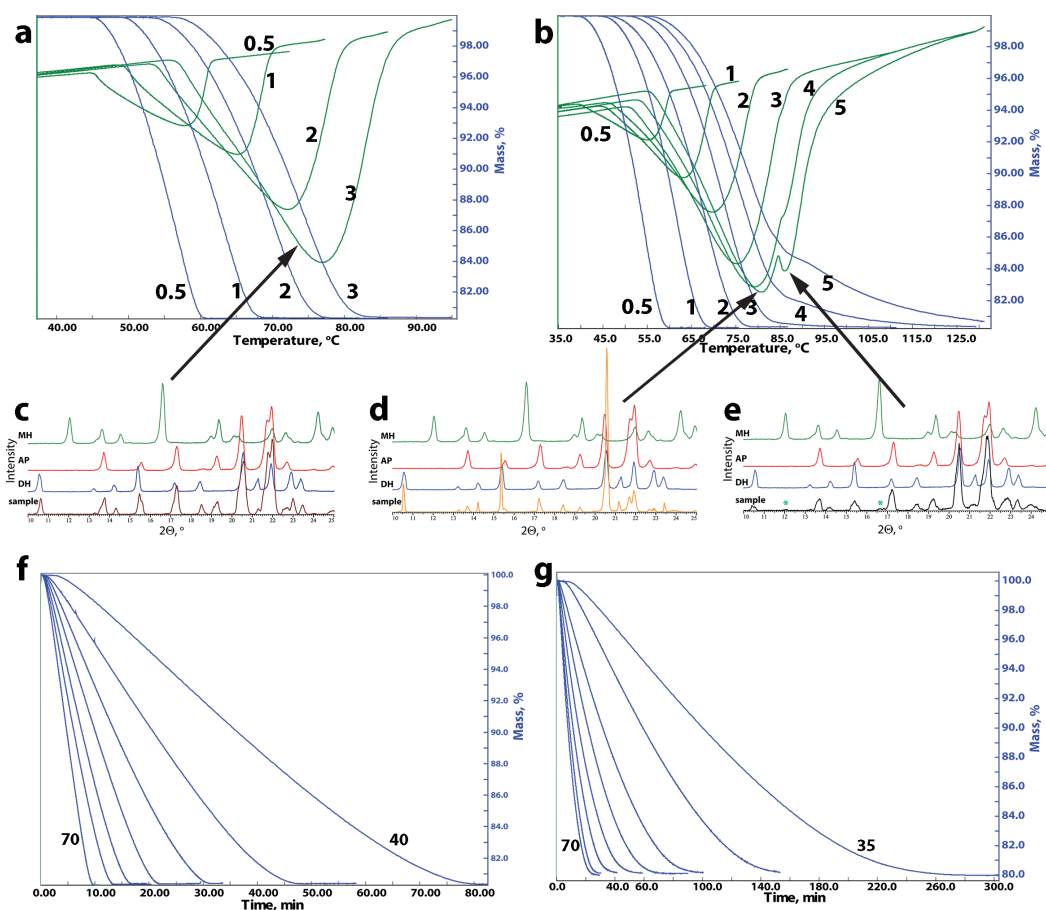


Figure S2. Dehydration DTA (in green) and TG (in blue) curves of mildronate **DH** fractions a) $<40\ \mu\text{m}$ and b) $67\text{--}150\ \mu\text{m}$ in non-isothermal mode (with corresponding heating rates in $^{\circ}\text{C}\cdot\text{min}^{-1}$), and fractions f) $40\text{--}67\ \mu\text{m}$ and g) $350\text{--}700\ \mu\text{m}$ in isothermal mode (temperature increases from right to left with $5\ ^{\circ}\text{C}$ step, minimum and maximum temperature is given in $^{\circ}\text{C}$). c) – e) shows PXRD pattern of the sample during the non-isothermal dehydration process and PXRD patterns of pure **DH**, **AP** and **MH**.

The dehydration profiles in the isothermal experiments are shown in Fig. S2 f and g.

Sample preparation

Totally 4 samples differing in the preparation method and storage conditions were used. Sample A was prepared in mortar by adding a small amount of water to mildronate, so that a paste formed, which was allowed to dry in the ambient conditions. The obtained sample was then fractionated by pushing through sieves with mesh size 350, 150, 67 and $40\ \mu\text{m}$, thus obtaining 5 fractions. Part of the fraction with particle size above $150\ \mu\text{m}$ was gently ground and fractionated in the same manner, yielding the sample A2. Both samples A and A2 were stored above saturated magnesium chloride solution at ambient temperature (relative humidity 34%). Sample B was prepared by slowly crystallizing mildronate from water at $30\ ^{\circ}\text{C}$. The obtained crystals were fractionated by pushing through sieves with mesh size 1300, 700, 350, 150, 67 and $40\ \mu\text{m}$, yielding 7 fractions (the obtained particle size distribution for different fractions of sample B is given in Figure S1). Part of the fractions $150\text{--}350\ \mu\text{m}$ and $350\text{--}700\ \mu\text{m}$ was slightly ground and fractionated by pushing through sieves with mesh size 350, 150, 67 and $40\ \mu\text{m}$, and 5 fractions of sample C were thus obtained. Samples B and C were stored above saturated solution of potassium acetate in ambient temperature (relative humidity 22.5%). All four samples were used for determination of the dehydration kinetic parameters.

All of the non-isothermal experiments were carried out using sample A (study of the particle size, sample weight, N_2 flow rate and mechanical compression effect) and sample A2 (study of the particle size effect). Sample A was also used to study the particle size effect in isothermal mode. Sample B was used to study the particle size, sample weight, N_2 flow rate, relative humidity, previous dehydration-rehydration

and mechanical compression effect in isothermal mode. Sample C was used only to study the particle size effect in isothermal mode.

Analysis of particle size distribution

Particle size distribution of all sample B fractions is given in Figure S1. It can be seen that in every fraction there were particles with smaller and bigger sizes than corresponding mesh sizes used for their preparation. Presence of the bigger particles most probably was due to the fact that either particles were not perfectly round and smallest of their dimensions was less than the mesh size or that during the particle size determination particles formed aggregates and size of this aggregates was determined. The presence of the smaller particles suggested that longer sieving time was necessary for better separation of fractions or that during fractionation there was an attraction between the particles and the size of formed aggregate was bigger than the corresponding mesh size used. However, for sample indication in the text fractions are named after the mesh sizes used for their preparation.

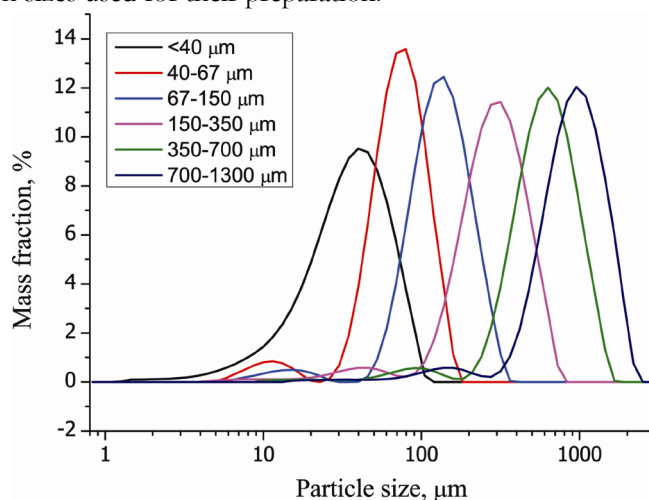


Figure S3. Particle size distribution for different fractions of sample B.

Effect of the particle size, sample preparation and storage conditions

Particle size, sample preparation and storage condition effect on the E_a for fractions up to 150-350 μm can be evaluated from Figure S2, where the average E_a values in conversion degree interval from 0.2 to 0.7 are shown. As it is shown in the section 3.1., E_a values calculated from non-isothermal experiments were lower than those calculated from isothermal experiments. It is obvious that the particle size had no effect on the dehydration E_a value for fractions with particle size below 350 μm . Besides this, also sample preparation and storage had no effect on the E_a .

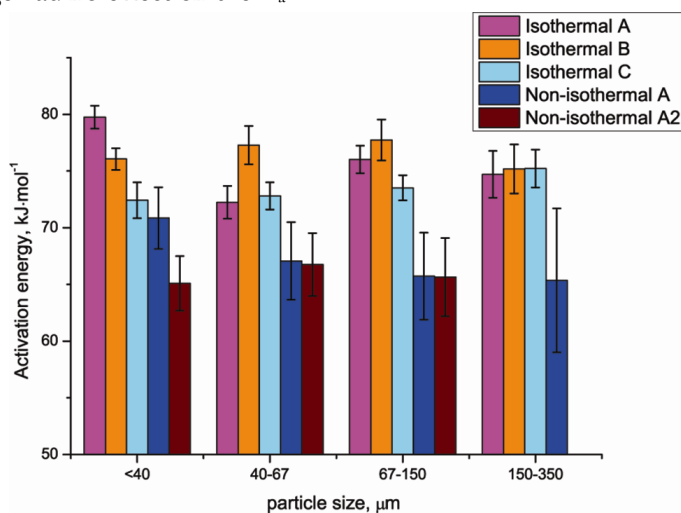


Figure S4. Particle size, sample preparation and storage effect on the average dehydration activation energy.

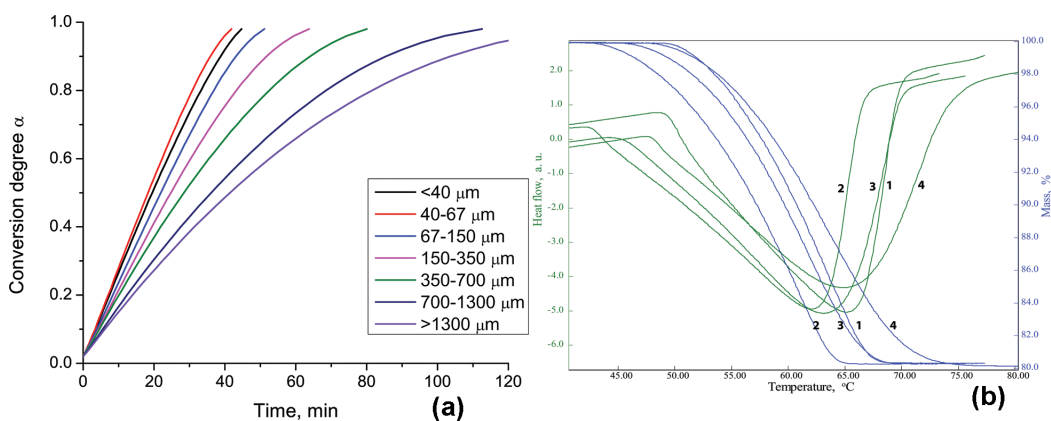


Figure S5. Dehydration kinetic curves of mildronate **DH** various fractions a) in isothermal mode and b) in non-isothermal mode (where fractions are marked as follows: 1 = <math><40 \mu\text{m}</math>, 2 = $40-67 \mu\text{m}$, 3 = $67-150 \mu\text{m}$, and 4 = $150-350 \mu\text{m}$). For better clarity time in a) was set to 0 at $\alpha = 0.02$ for each fraction due to the small differences in the actual initiation times.

<math><40 \mu\text{m}</math> fraction dehydrated slower than the $40-67 \mu\text{m}$ fraction in isothermal experiments, and its dehydration starting temperature was higher than that of fractions with bigger particle sizes in non-isothermal experiments (see Fig. S3). The reason for the slower dehydration rate of the <math><40 \mu\text{m}</math> fraction, as observed in isothermal mode for the same temperature, could be the agglomeration of small particles, thus slowing down the dehydration process on the common surfaces and complicating the escape of water vapor. In the non-isothermal mode the dehydration rate of the <math><40 \mu\text{m}</math> fraction was the fastest, but only because its dehydration starting temperature was the highest of all analyzed fractions. The higher dehydration starting temperature probably was observed due to the low occurrence of crystal defects on the surface of very small particles limiting the number of dehydration reaction initiation centers, or the dehydration was delayed by the slow escape of water vapor from the aggregates formed^{52, 53}. However, once the dehydration was successfully initiated, the temperature was already higher than that for the other fractions, thus explaining the higher dehydration rate.

Table S1. Temperature intervals used for the dehydration kinetic analysis of the different fractions of mildronate **DH**.

Fraction	Temperature interval		α_{melt}
	Isothermal mode	Non-isothermal mode	
<math><40 \mu\text{m}</math>	35-67	45-90	0.97
$40-67 \mu\text{m}$	35-67	40-85	0.98
$67-150 \mu\text{m}$	35-67	40-110 ¹	0.80
$150-350 \mu\text{m}$	35-67	45-(130) ^{1,2}	0.55
$350-700 \mu\text{m}$	36-69	45-(130) ²	
$700-1300 \mu\text{m}$	46-78	-	

¹ – Melting/peritectic decomposition point was reached and endothermic peak corresponding to melting/peritectic decomposition appeared in the DTA curve.

² – Complete transformation was not reached for the highest heating rates due to the fact that after the melting/peritectic decomposition point dehydration rate slowed down.

α_{melt} – conversion degree at which the melting/peritectic decomposition point was reached for the highest heating rate in non-isothermal mode.

Table S2. Conversion degree at which melting/peritectic decomposition point in non-isothermal experiments was reached for each **DH** fraction at each heating rate.

Heating rate, °·min ⁻¹	0.5	1	2	3	4	5
<40 μm	-	-	-	-	-	0.97
40-67 μm	-	-	-	-	-	0.98
67-150 μm	-	-	-	0.99	0.91	0.80
150-350 μm	-	-	0.96	0.83	0.68	0.55
350-700 μm	-	-	0.86	0.70	0.61	0.49

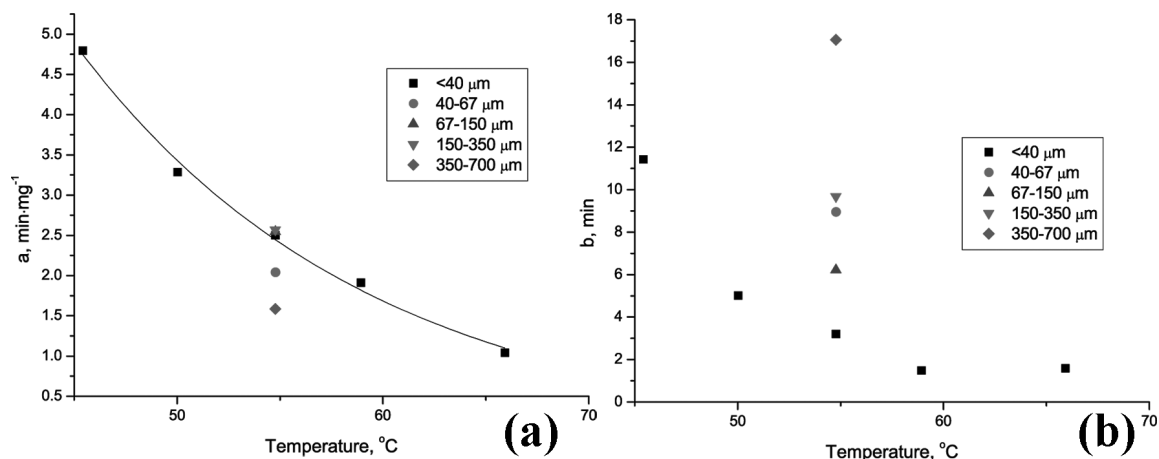


Figure S6. (a) Slope and (b) intercept of the straight line characterizing the dependence of the reciprocal dehydration rate constant on the sample weight for the <40μm fraction at various temperatures and for the 40-67μm, 67-150μm, 150-350μm, and 350-700μm fractions at 55 °C temperature.

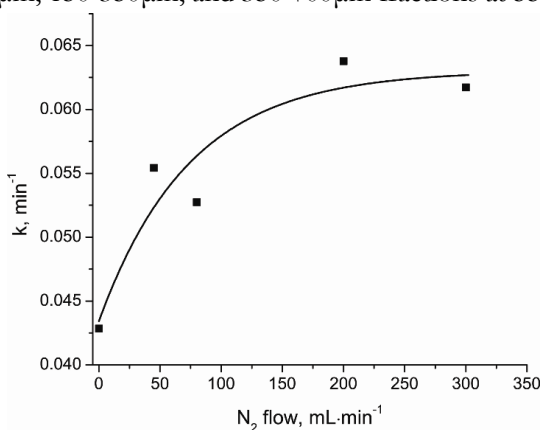


Figure S7. Nitrogen flow rate effect on the dehydration rate constant of the mildronate **DH** fraction <40 μm at 55 °C temperature.

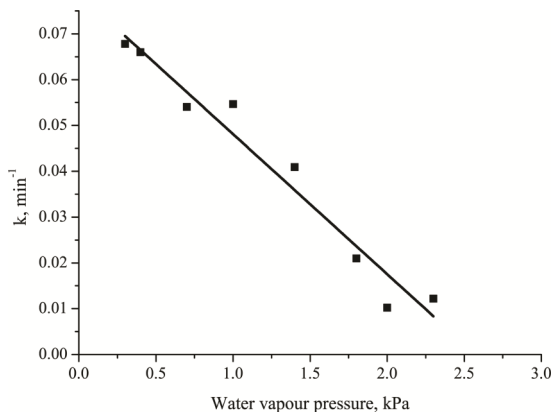


Figure S8. Effect of the water vapor pressure on the dehydration rate constant of the mildronate **DH** fraction <40 μm at 70 °C temperature.

Effect of the previous dehydration-rehydration

Dehydration E_a obtained for fresh samples and previously dehydrated and rehydrated samples are shown in Figure S6.

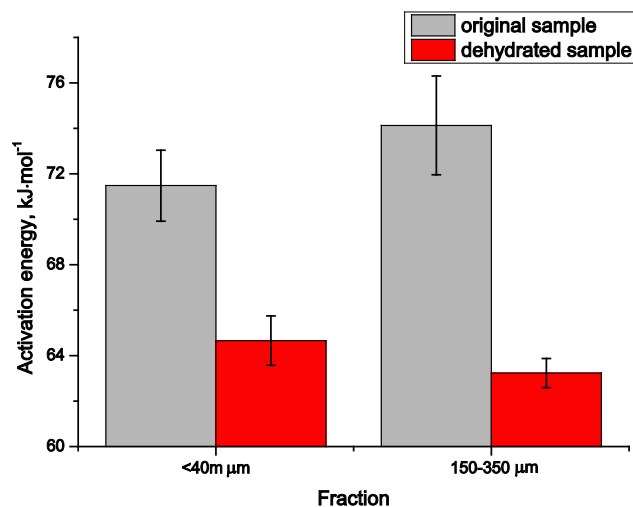


Figure S9. Dehydration activation energy of the different fractions of the **DH** original sample and sample which was previously dehydrated and rehydrated.

Effect of the mechanical compression

By analyzing the effect of mechanical compression on the dehydration rate, E_a and kinetic model, two different approaches have been used: a) tablets obtained after the compression were disassembled with mortar and pestle, and the obtained powder was analyzed; b) tablets were analyzed directly.

By comparing the dehydration rate of compressed and original **DH** samples in isothermal experiments it was concluded that the dehydration rate of compressed powder samples were comparable to uncompressed samples and no characteristic trend was observed. However, dehydration rate of tablets was slower than that of uncompressed powdered samples, but no dependence on the applied mechanical pressure was observed. In non-isothermal experiments it was observed that the dehydration of compressed samples started at lower temperature, but the dehydration rate was slower, so complete dehydration of the uncompressed samples was achieved faster. However, also in this case no relationship between the applied pressure and the dehydration starting temperature or the rate was found.

Dehydration E_a values of both mechanically compressed and the original **DH** samples in both experimental modes are shown in Figure S7. It can be seen that there was no obvious relationship between E_a and neither pressure applied or the sample form (powder or tablet). The small differences of the dehydration E_a value for powder samples could be a random error or due to the changes in particle size after breaking the tablet. Although fraction <40 μm compressed with 370 and 740 MPa and dehydrated as a tablet in isothermal mode showed lower dehydration E_a than the same sample dehydrated as a powder, and lower E_a values were obtained also for samples dehydrated as a tablets in non-isothermal mode, this did not represent an E_a decrease due to the compression, because in non-isothermal mode obtained E_a values generally were lower than those obtained under isothermal mode (as discussed in section 3.1.), and the standard deviation of E_a for samples analysed as a tablets was higher, suggesting that the decrease of the E_a obtained for fraction <40 μm in isothermal mode may be coincidental.

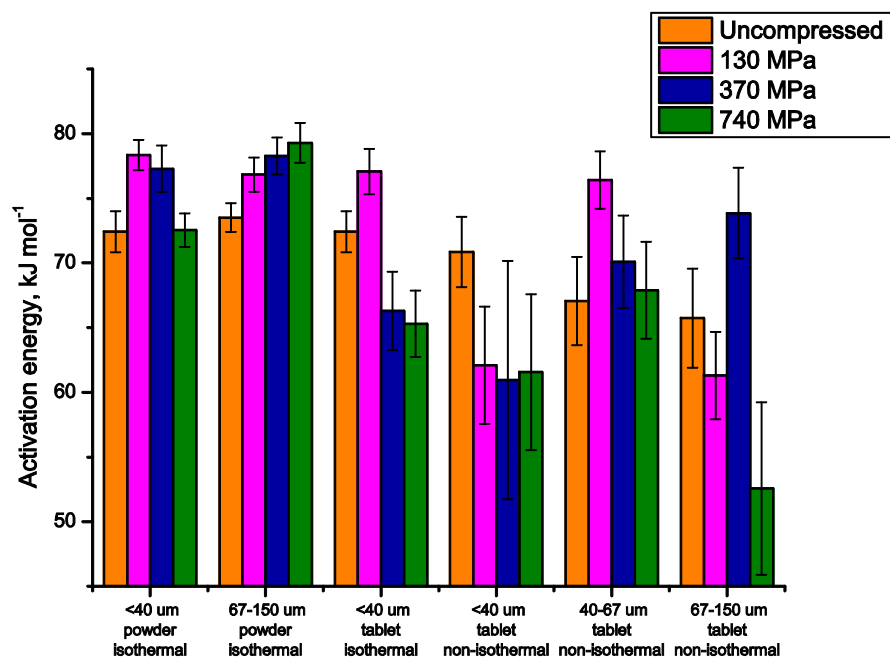


Figure S10. Mechanical compression effect on the average dehydration activation energy of the midronate **DH** in isothermal mode and in non-isothermal mode.

Besides the dehydration E_a , also the kinetic model was determined for all the analysed samples (See Table S3). For powder samples the same kinetic model R1 as for uncompressed samples was determined. However, for the tablet samples determination of the kinetic model was not straightforward. For many of these samples R2 was determined as the most appropriate model, although for some of the samples R1 or Avrami-Erofeev models showed a better fit. It was already stated that dehydration of the particles larger than 350 μm was best described with kinetic model R2. During the mechanical compression, the smaller particles were compressed tightly so it may be possible that the same effect on the dehydration rate control as for larger size particles was achieved. This theory was partly supported by the measurement of the particle size distribution of the compressed samples after the disassembling the tablets (see Figure S8). It can be seen that after compression the average particle diameter grew noticeably for fraction <40 μm , while a small decrease of the average particle size and widening of the particle size distribution was observed for the fraction 67-150 μm . This can be associated with the formation of particle associates for smaller fractions and reduction of particle size for bigger particles. However, as mentioned, particle size analysis was carried out after disassembling the tablet while the dehydration kinetic model R2 was obtained when dehydration was carried out for compressed tablet where particles were in close contact to each other.

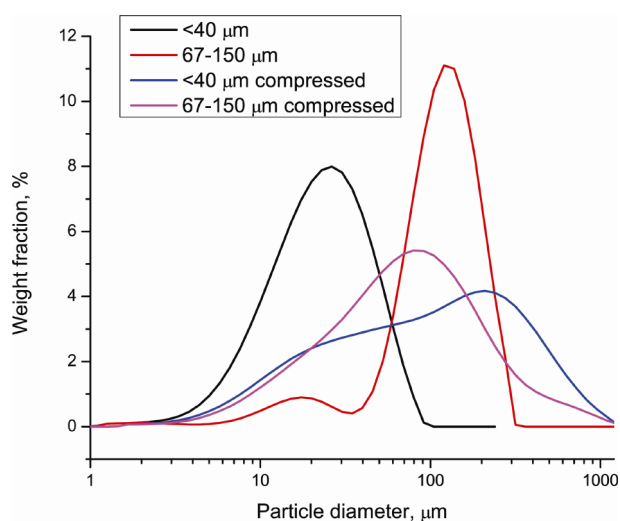


Figure S11. Particle size distribution for fractions <40 μm and 67-150 μm before and after the compression with 370 MPa pressure.

Table S3. The most appropriate dehydration kinetic model for different **DH** samples determined by studying the effect of mechanical compression

Method	Sample	Fraction	130 MPa	370 MPa	740 MPa
Isothermal	Powder	<40 μm	R1	R1	R1
		67-150 μm	R1	R1	R1
	Tablet	<40 μm	R2, A3/2	R2, A3/2	R2, A3/2
Non- isothermal	Tablet	<40 μm	R1, R2	R2	R2
		40-67 μm	R2, A3/2	R2	R2, R1
		67-150 μm	R2, R1	R2	R1, R2

Appendix 8. Supplementary Information for publication “On the formation of droperidol solvates: characterization of structure and properties”

PREPARATION AND CHARACTERIZATION OF DROPERIDOL SOLVATES

Table S1. Crystal forms obtained after the crystallization of droperidol from different solvents

Solvent	Classification ¹	Group ²	Temperature, °C	Phase
Cyclohexane	AAA	1	70 ^a	II
<i>n</i> -hexane	AAA	1	60 ^a	II
carbon tetrachloride	HBD	1	70	S_{TCC}
Ethyl acetate	AP	2	70	II
Butyl acetate	AP	2	90	II
tetrahydrofuran	EPD	2	60	II/I
methyl tertiary-butyl ether	EPD / AAA	2	50 ^a	II
<i>iso</i> -propyl acetate	AP	2	90	II
1-butanol	HBD	3	90	II
2-propanol	HBD	3	70	II
1-propanol	HBD	3	90	II
ethanol	HBD	3	70	S_{Et}
methanol	HBD	3	60	S_{Me}
toluene	AALP	4	90	S_{TOL}
<i>o</i> -xylene	AALP	4	90	II
cyclohexanone	AP	5	130	II
3-pentanone	AP	5	90	II
butanone	AP	5	70	II
acetone	AP	5	50	II
<i>N,N</i> -dimethylformamide	AP	6	130	no crystallization
dimethylsulfoxide	AP	6	130	no crystallization
chloroform	EPD / HBD / AP	7	50	S_{CLF}
dichloromethane	AP	7	40	S_{DCM}
1,1-dichloroethane	AP	7	70	II
acetonitrile	AP	9	80	S_{ACN}
nitromethane	AP	9	80	S_{NM}
Benzyl alcohol	AALP	10	130	no crystallization
1,4-dioxane	AP / EPD	11	90	S_{DIOX}
Water	HBD	15	-	NSH / DH
cyclohexanol	HBD	-	130	II

Bold – droperidol solvate was obtained, **Blue bold** – new droperidol solvate was obtained, **Gold shading** – isostructural droperidol solvates, ^a – solution was partially evaporated at 50 °C temperature

Classifications: AP = aprotic polar, AALP = aromatic apolar or lightly polar, EPD = electron pair donors, HBD = hydrogen bond donors, AAA = aliphatic aprotic apolar.

Groups are based on cluster analysis of following solvent parameters: hydrogen bond acceptor propensity, hydrogen bond donor propensity, polarity/dipolarity, dipole moment, and dielectric constant, and contain various solvents with similar properties (except for: group 13 = diethylamine, group 14 = glycerol, and group 15 = water).

Powdered **DH** was obtained when droperidol solution in acetone or DMF was poured into a large amount of cold water, by stirring the obtained suspension. **DH** crystals were obtained when a similar volume of cold water was slowly added to cold droperidol solution in acetone and the resulting solution was slowly evaporated at 50°C temperature. However, when a small amount of water (5-10%) was added to droperidol solution in acetone and the resulting solution was slowly evaporated at 50°C temperature, **NSH** crystals were obtained.

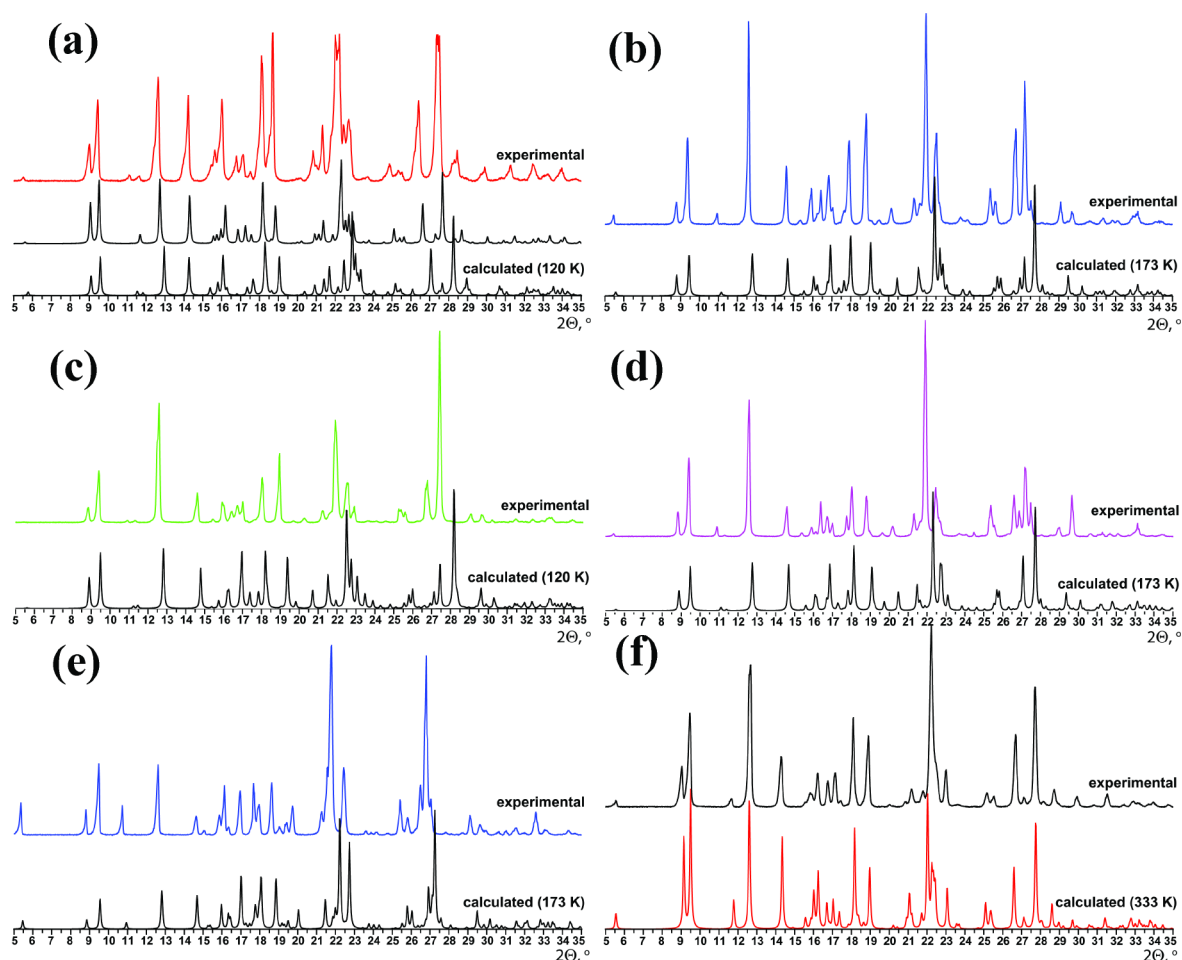


Figure S1. Overlay of the experimental and from crystal structure data simulated PXRD patterns for droperidol solvates a) **NSH**, b) **SEt**, c) **SMe**, d) **SACN**, e) **SNM** and f) **ISD**.

In Fig. S1 observed differences in peak positions was due to the different temperature used for the crystal structure determination and experimental PXRD measurements, whereas the intensity differences between calculated and experimental PXRD patterns suggested the presence of preferred orientation.

The PXRD patterns of isostructural solvates showed obvious intensity differences for some of the first diffraction peaks. Miller indices corresponding to these peaks were 001, 002, and 011 (see Figure S2). These crystallographic planes are positioned along the solvent channels and thus changes in the diffraction peak intensity are associated with the presence of different solvent molecules and their different arrangement in the solvate structure.

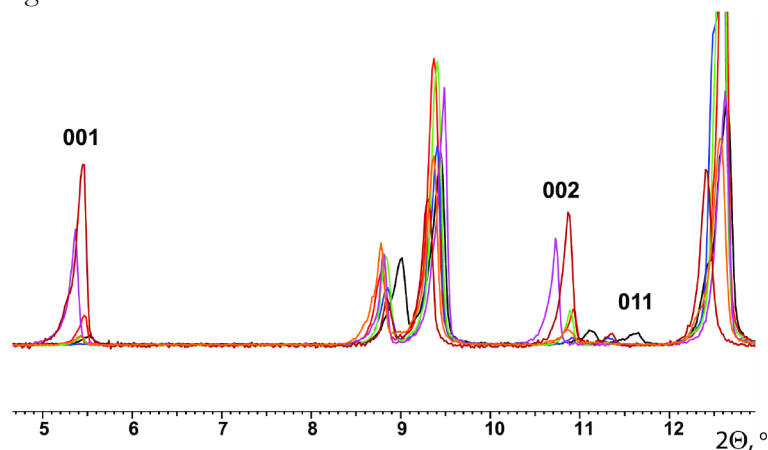


Figure S2. Overlay of the initial part of the droperidol isostructural solvate (**NSH** is black, **SMe** is blue, **SEt** is red, **SACN** is green, **SNM** is purple, **SDCM** is brown, and **SCLF** is orange) PXRD patterns. For three of the peaks corresponding Miller indexes are indicated.

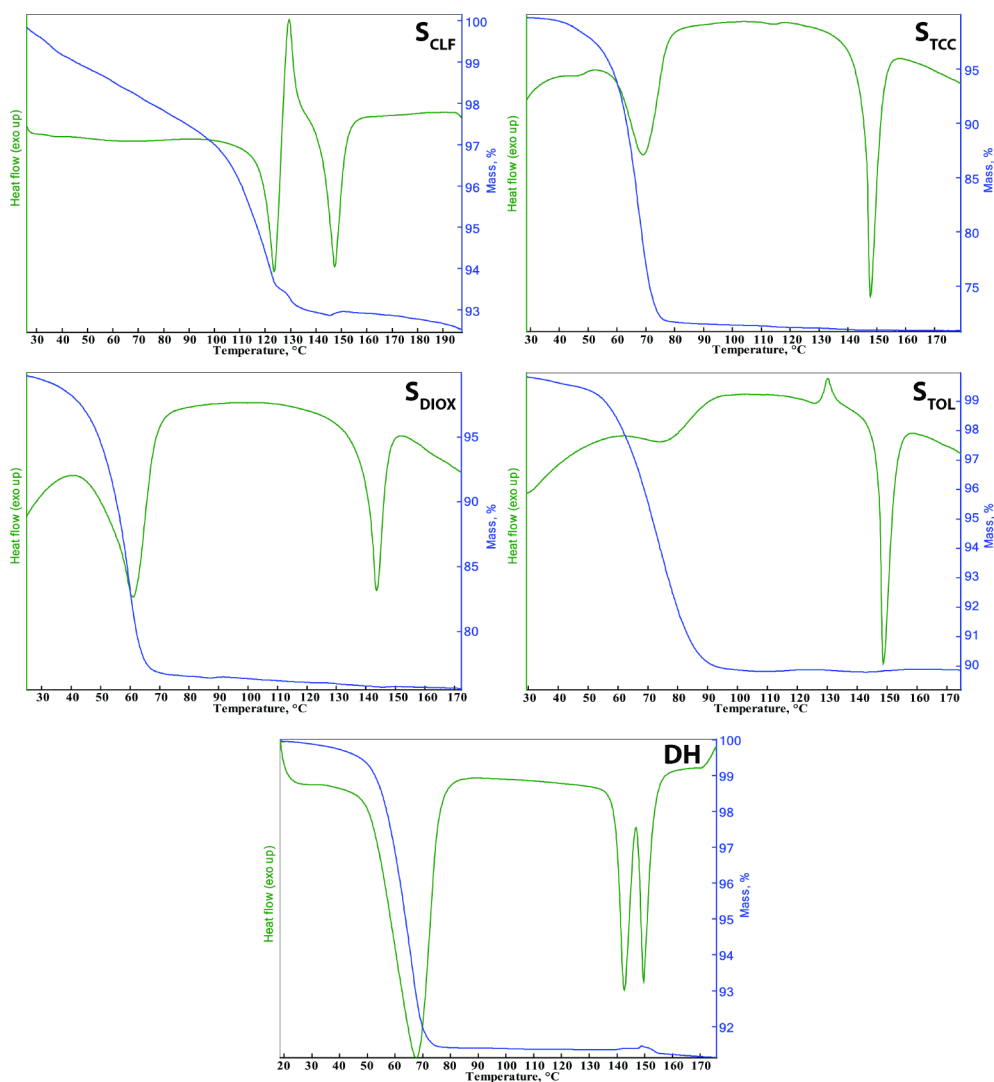


Fig. S3. DTA and TG curves of the droperidol solvates S_{CLF} , S_{TCC} , S_{DIOX} , S_{TOL} , and DH .

Although desolvation of isostructural solvates produced an identical desolvated phase, the observed melting points of partially desolvates solvates presented in Figure 3 were different: for most of the isostructural solvates it was 123–129°C (see Table 2), whereas that of S_{NM} was lower by 10°C. Although S_{NM} had the highest solvent content in the structure upon reaching the melting, a relationship between the solvent amount and the melting point was not observed neither for S_{NM} , no for any other of the isostructural solvates. Therefore the melting point most probably depended on the properties of solvent in the solvate structure.

Desolvation of S_{TCC} , S_{DIOX} , S_{TOL} , and DH (see Fig. S3) occurred over a smaller temperature interval with a characteristic desolvation endotherm in the DTA curve typical of stoichiometric solvates, with the peak maximum at 60 – 75°C (see Table S2). From the TG curves S_{TCC} and S_{DIOX} were determined to be monosolvates, whereas S_{TOL} was a hemisolvate.

Table S2. Physicochemical data for some of the droperidol solvates.

Solvate	Calculated weight loss, %	Observed weight loss, %	$T_{desolvation}, ^\circ C$ (peak)	Resulting phase
S_{TCC}	28.8 ^a	28.0	69	I
S_{DIOX}	19.5 ^a	22.5	61	I
S_{TOL}	10.4 ^b	9.6	74	IV
DH	8.7 ^c	8.5	67	II / III

^a - for monosolvate stoichiometry

^b - for hemisolvate stoichiometry

^c - for dihydrate stoichiometry

For HSM, a Laborlux 12 PolS (Leitz) polarized light microscope equipped with a heating stage and a Newtronic heating control module was used. The heating rate was $5^{\circ}\cdot\text{min}^{-1}$. Images were acquired with Leica Application Suite software from a DFC450 (Leica) digital microscope camera.

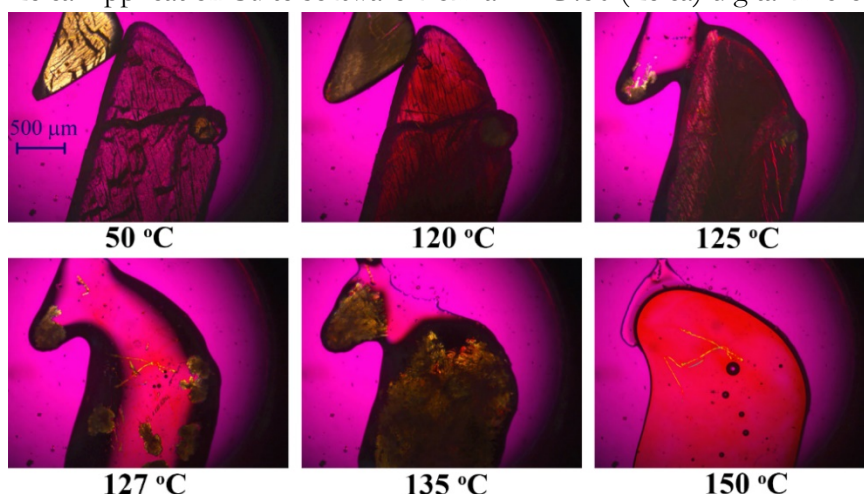


Figure S4. HSM photomicrographs of the droperidol **NSH** upon the heating.

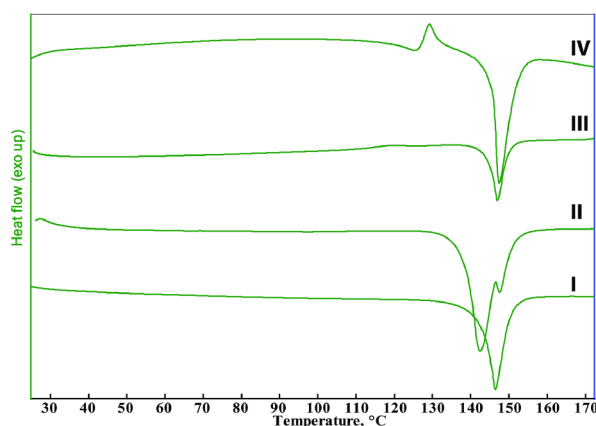


Fig. S5. DTA curves of the droperidol polymorphs.

Table S3. Crystallographic data of droperidol solvates **S_{Me}**, **S_{Et}** and **NSH** determined at 173 K

Solvate	S_{Me}	NSH	S_{Et}
Empirical formula	$(\text{C}_{22}\text{H}_{22}\text{FN}_3\text{O}_2)_2\cdot\text{CH}_4\text{O}$	$\text{C}_{22}\text{H}_{22}\text{FN}_3\text{O}_2\cdot\text{H}_2\text{O}$	$(\text{C}_{22}\text{H}_{22}\text{FN}_3\text{O}_2)_2\cdot\text{C}_2\text{H}_6\text{O}$
M_r	395.45	397.44	402.47
Crystal system	triclinic	triclinic	triclinic
Space group	$P\bar{1}$	$P\bar{1}$	$P\bar{1}$
Temperature	173	173	173
a (Å)	6.0671(2)	6.2936(2)	6.08400(10)
b (Å)	10.2183(4)	10.1673(4)	10.2978(3)
c (Å)	16.2078(8)	15.9173(4)	16.1737(5)
α (°)	101.3130(10)	102.6133(18)	100.9299(10)
β (°)	93.208(2)	91.8553(19)	92.6382(10)
γ (°)	96.996(2)	99.9459(16)	95.9415(15)
V (Å ³)	974.65(7)	976.41(6)	987.35(4)
Z ^a	2	2	2
μ (mm ⁻¹)	0.095	0.097	0.096
D _{calc} (g cm ⁻³)	1.347	1.348	1.354
no. of parameters	275	262	274
reflns collected	4401	3828	5220
reflns (I > 2 σ)	2618	3106	3784
wR (all data)	0.1955	0.1333	0.1402
final R (I > 2 σ)	0.0661	0.0472	0.0518
GOF	1.043	1.002	1.036
Packing coef.			0.708 ^b

^a – Based on droperidol as the molecular entity.

^b – Calculated for structure where solvent molecules were ordered.

CRYSTAL STRUCTURE ANALYSIS OF DROPERIDOL ISOSTRUCTURAL SOLVATES

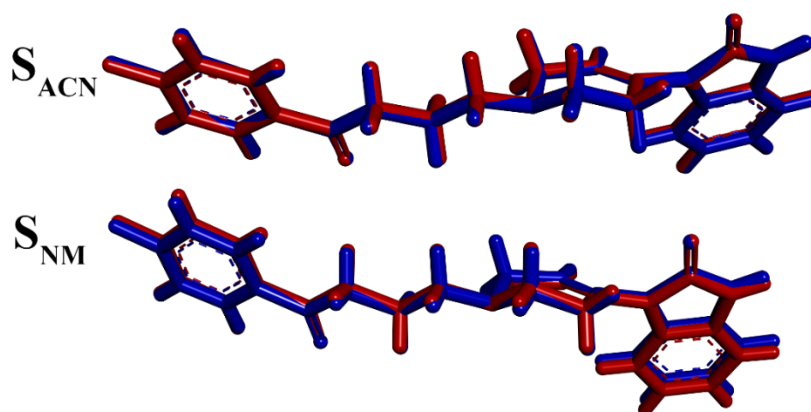


Fig. S6. Overlay of both droperidol molecules in the unit cell in S_{ACN} and S_{NM} structures (one of the molecules is inverted).

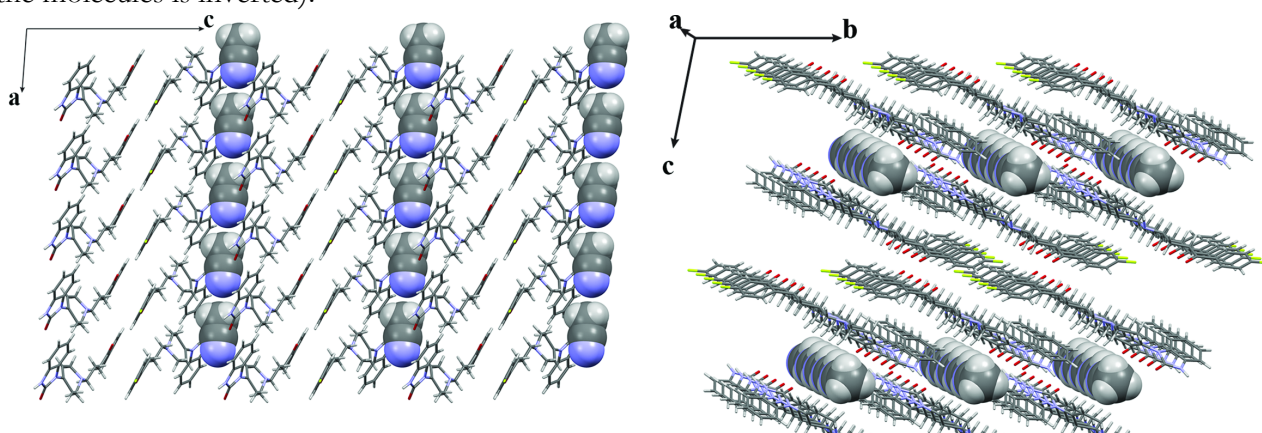


Fig. S7. Crystal structure of the droperidol solvate S_{ACN} representing the solvent molecule arrangement in isostructural solvate channels.

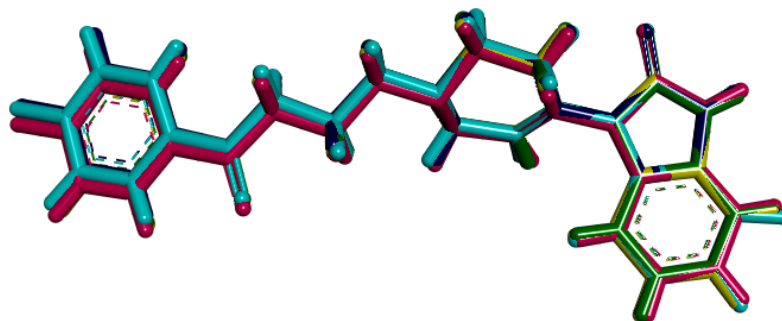


Fig. S8 Overlay of the droperidol molecules from the crystal structures of isostructural solvates NSH , S_{Et} , S_{Me} , S_{ACN} , and S_{NM} .

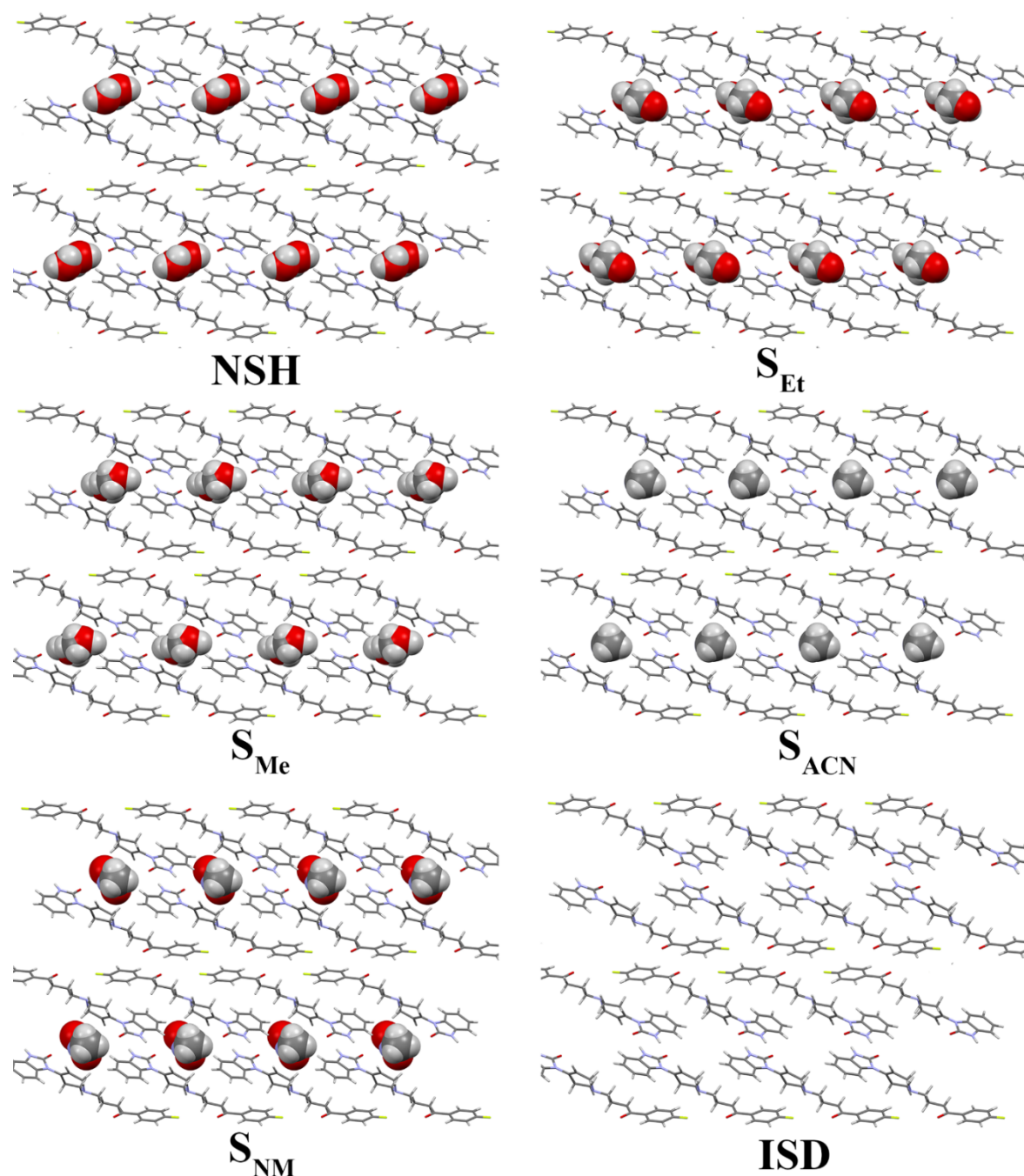


Fig. S9. Packing diagrams of droperidol isostructural solvates. Solvent molecules are showed in *Spacefill* style.

Table S4. Torsion angles ($^{\circ}$) characterizing the droperdiol molecule conformation in isostructural solvates

Torsion angle	NSH	S _{Me}	S _{Et}	S _{ACN}		S _{NM}	
				A	B	A	B
O2-C16-C15-C14	11.4	11.6	10.2	-12.7	9.4	-10.9	11.0
C16-C15-C14-C13	178.0	-179.2	179.9	179.5	179.4	179.6	179.6
C15-C14-C13-N3	-176.3	-175.7	-175.6	176.5	-175.5	174.3	-174.0
C14-C13-N3-C11	-170.3	-169.8	-170.9	171.4	-171.0	172.6	-170.2
C14-C13-N3-C10	67.3	68.9	67.4	-65.7	67.4	-65.7	67.2
C1-N1-C8-C9	124.1	122.6	123.1	-124.0	122.5	-122.4	121.7
C1-N1-C8-C12	-59.1	-60.3	-59.3	60.8	-58.5	61.6	-61.4

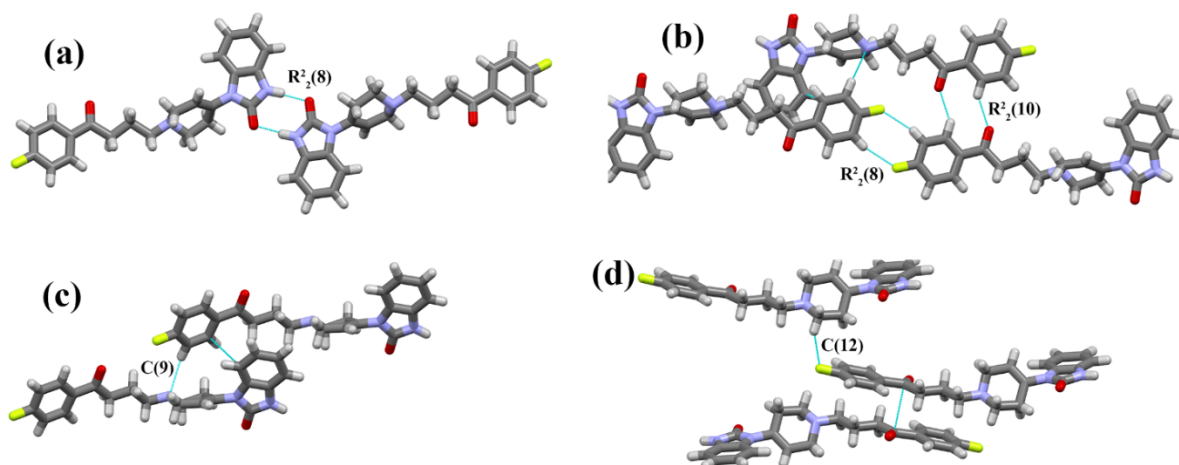


Fig. S10. Intermolecular interactions of droperidol molecules in isostructural solvates.

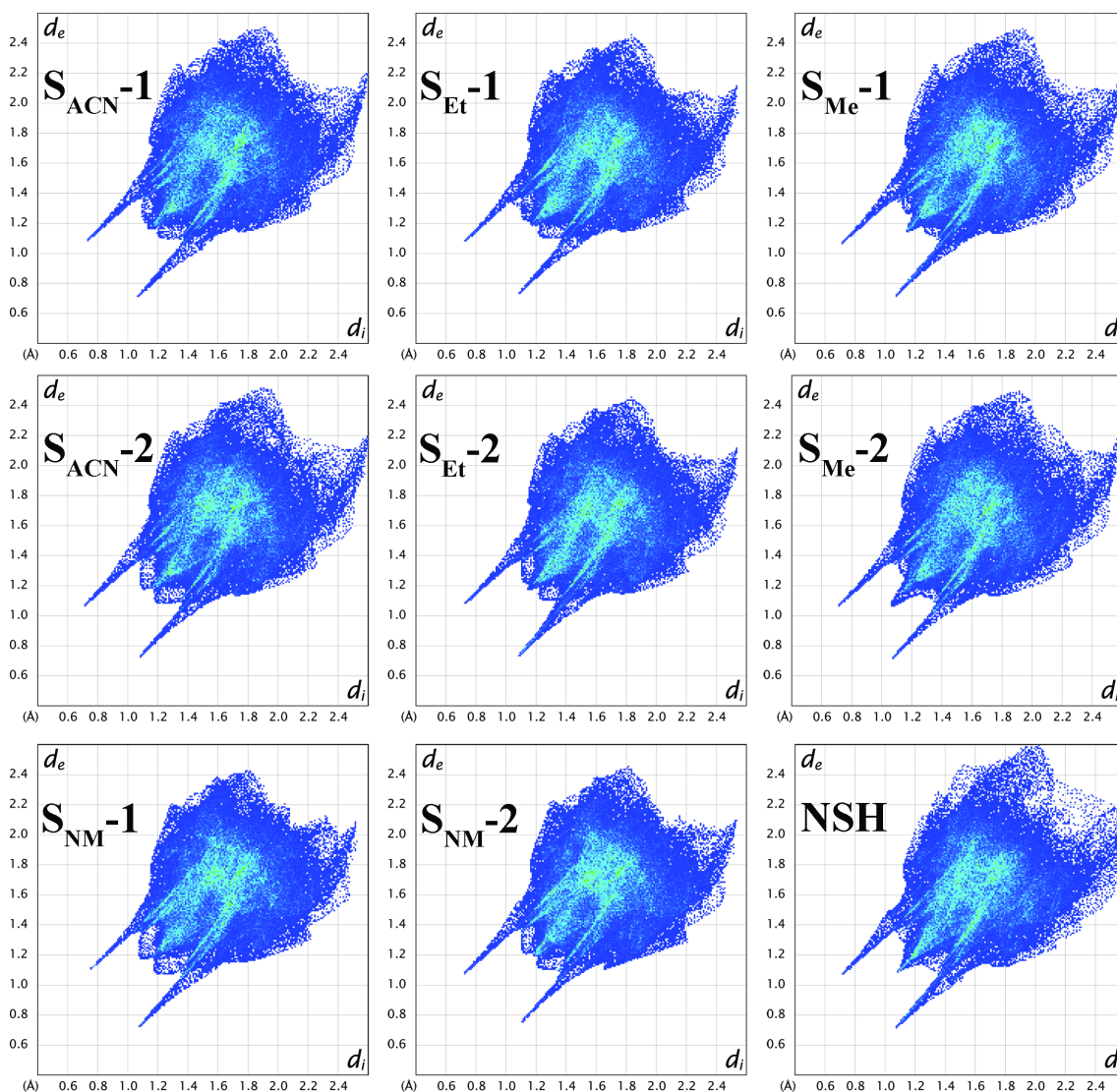


Fig. S11. Hirshfeld surface 2D fingerprint plots of droperidol molecules in isostructural solvates. Symmetrically different molecules in S_{ACN} , S_{NM} , S_{Me} and S_{Et} are designated with 1 and 2.

It was noted that alcohol molecule ordering in crystal structures of S_{Me} and S_{Et} is a good representation provided that the energy of both orientations is the same and solvent molecule reorientation does not affect the adjacent unit cells. This is explored and confirmed in our next study.

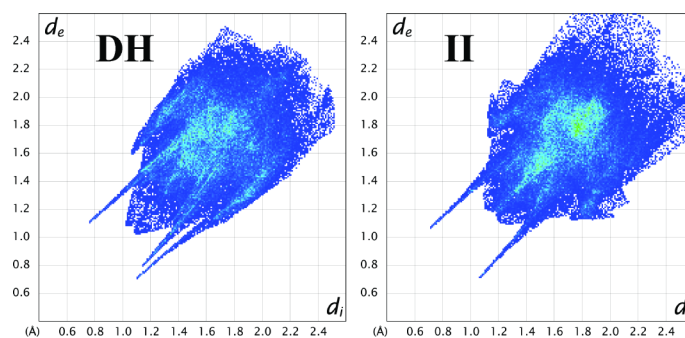


Fig. S12. Hirshfeld surface 2D fingerprint plots of droperidol molecules in **DH** and polymorph **II**.

Table S5. Geometrical parameters of strong hydrogen bonds in **S_{Me}**, **S_{Et}** and **NSH** crystal structures after all atom geometry optimization in *CASTEP* (unit cell parameters were fixed to the experimental values)

Solvate	Interaction	X-H (Å)	H···A (Å)	D···A (Å)	D-H···A (°)
S_{Me}	O3-H···O1	0.99	1.88	2.83	163
S_{Et}	O3-H···O1	0.98	1.81	2.78	166
NSH	O3-H···O1	0.99	1.79	2.76	167
	O3-H···O3	0.98	2.27	2.91	121

By comparing the position of solvent oxygen atom in these three crystal structures (both in the experimental data and after geometry optimization), it was determined that its orientation with respect to droperidol molecules was the same in **NSH** and **S_{Me}**, whereas it was different in **S_{Et}** (see Fig S13), probably due to the steric effects of the rest of the ethanol molecule. These differences led to the formation of different interactions between alkyl residues of alcohol molecules and droperidol molecules.

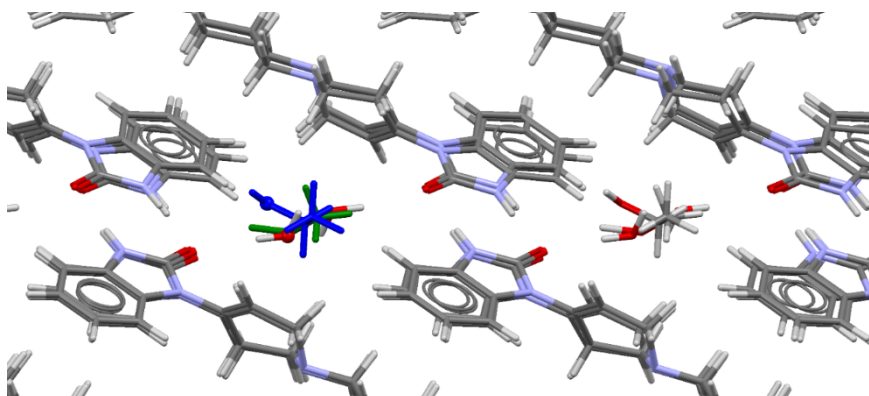


Fig S13. Overlay of the crystal structures of **NSH**, **S_{Me}** and **S_{Et}** showing solvent molecule orientation. Ethanol molecule in channel on the left has blue colour and methanol has green colour. Oxygen atom in all three solvents in this channel is showed as enlarged balls. Hydrogen atom positions are not optimized.

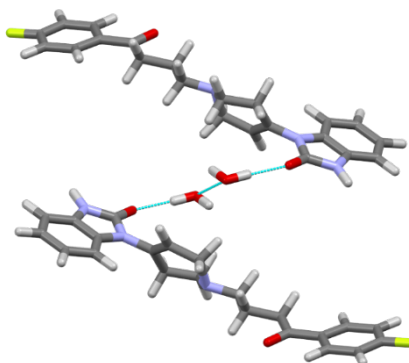


Fig. S14. Geometrical representation of water molecule provided hydrogen bond linkage across the structure channel in **NSH**.

FOURIER-TRANSFORM INFRARED SPECTROSCOPY

IR spectra of **NSH**, **DH**, **S_{TCC}**, **S_{DIOX}** and **S_{TOL}** and polymorphs (see Fig. S15 and S16) showed characteristic features and thus can be used to confirm the identity of these phases. It was noticed that spectra of **S_{TOL}** and polymorph **IV** was very similar (see Fig. S17) thus suggesting that local environment of droperidol molecules in these two phases is similar, as the crystal structure similarity of the solvate and its desolvation product is a very common phenomenon³⁻⁷.

Table S6. FTIR bands characterizing the isostructural solvates of droperidol

NSH	S_{Me}	S_{Et}	S_{ACN}	S_{NM}	S_{CLF}	S_{DCM}
3662				3663	3678	3678
3554	3557	3557		3555	3559	3561
3499				3500		3503
	3475	3468			3468	
3105	3105	3131	3125	3129	3129	3129
3062	3063	3063	3064	3066	3063	3060
3031	3032	3033	3032	3032	3032	3032
2966	2967	2966	2966	2966	2966	2965
2898	2896	2896	2896	2896	2897	2897
2813	2814	2814	2812	2816	2814	2814
2769	2770	2770	2769	2770	2770	2769
	1682	1683	1693	1692	1684	1691
	1682	1682	1682	1682	1684	1681
1623	1623	1622	1622	1623	1623	1622
1595	1594	1594	1594	1595	1595	1594
				1564		
1505	1506	1505	1506	1506	1506	1506
1481	1481	1482	1482	1483	1482	1481
1470	1470	1470	1470	1471	1471	1471
1443	1442	1443	1443	1442	1443	1442
1404	1405	1406	1404	1402	1406	1405
1395	1395	1395	1394	1395	1395	1394
1380	1379	1380	1380	1380	1380	1380
1359	1359	1359	1359	1360	1359	1359
1338	1338	1338	1337	1339	1338	1338
1313	1313	1312	1312	1312	1313	1313
1292	1292	1292	1291	1291	1292	1291
1271	1271	1272	1272	1272	1272	1271
1231	1231	1231	1231	1231	1231	1231
1205	1203	1203	1203	1203	1203	1203
1194	1194	1193	1194	1195	1194	1194
1162	1162	1162	1162	1163	1162	1162
1127	1126	1125	1125	1125	1126	1126
1103	1102	1101	1102	1102	1102	1102
1075	1074	1082	1075	1074	1078	1074
1066	1066	1066	1067	1066	1066	1066
1048	1048	1049	1048	1048	1049	1048
	1032					
1023	1024	1023	1024	1023	1024	1023
998	998	998	998	998	998	998
986	986	986	986	986	986	986
966	967	967	968	967	967	967
919	917	919	917	917	918	917
889	888	887	888	888	888	887
877	876	876	876	876	876	876
845	845	845	845	845	845	845
835	833	833	834	834	834	834
809	809	809	809	810	809	809
772	773	772	772	772	772	772
750	750	750	750	750	750	751
735	735	735	733	735	734	733
706	706	706	705	706	706	705
677	678	678	678	678	678	678
				656		

In green the most differing spectral regions are highlighted and in red bands due to the solvent molecules are marked.

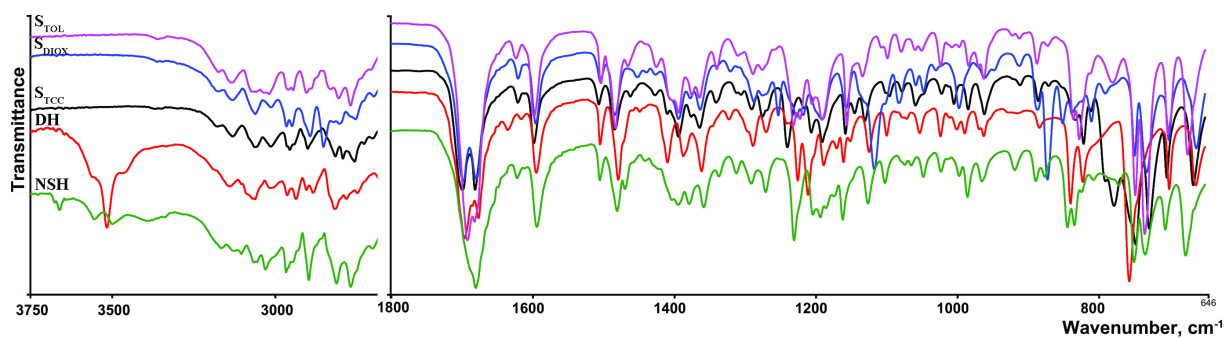


Fig. S15. FTIR spectra of droperidol solvates **NSH**, **DH**, **S_{TCC}**, **S_{DIOX}** and **S_{TOL}**.

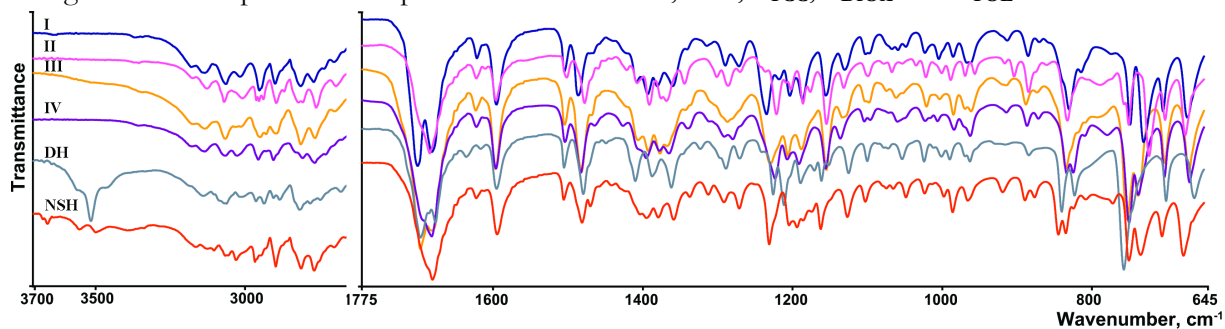


Fig. S16. FTIR spectra of droperidol polymorphs **I**, **II**, **III** and **IV** as well as solvates **NSH** and **DH**.

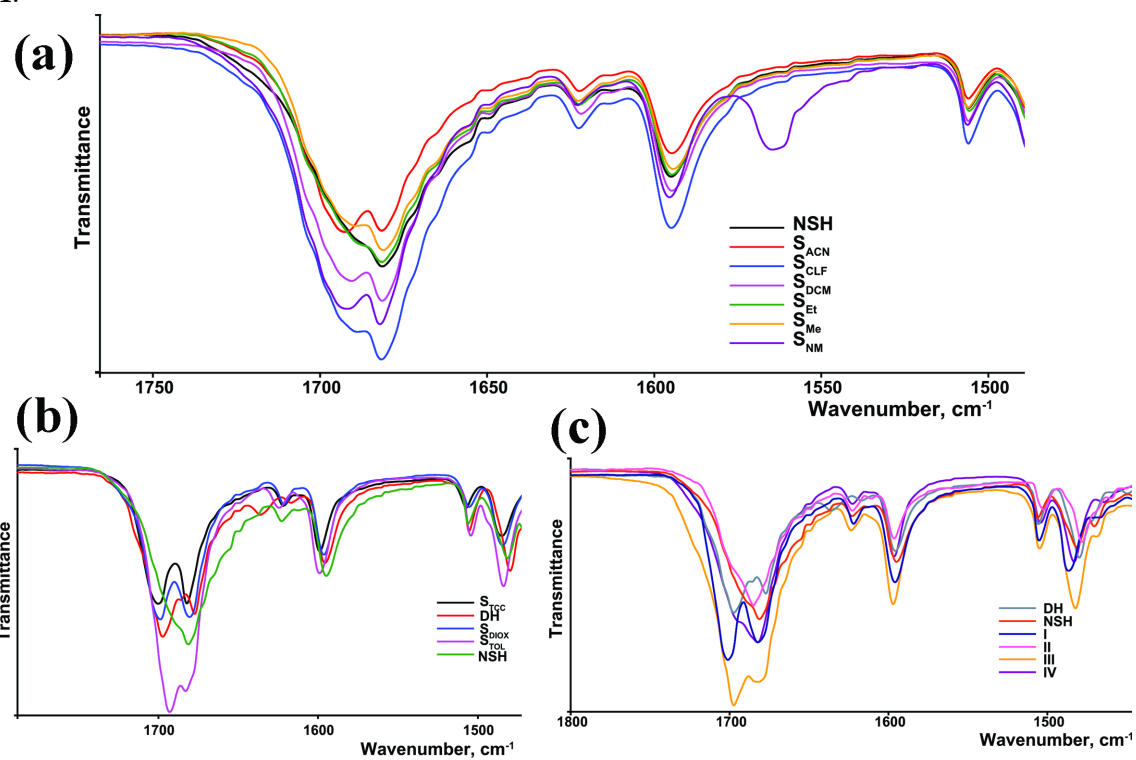


Fig. S17. FTIR spectra region 1500 – 1750 cm^{-1} for a) droperidol isostructural solvates, b) droperidol solvates **NSH**, **DH**, **S_{TCC}**, **S_{DIOX}** and **S_{TOL}** and c) droperidol polymorphs **I**, **II**, **III** and **IV** as well as solvates **NSH** and **DH**.

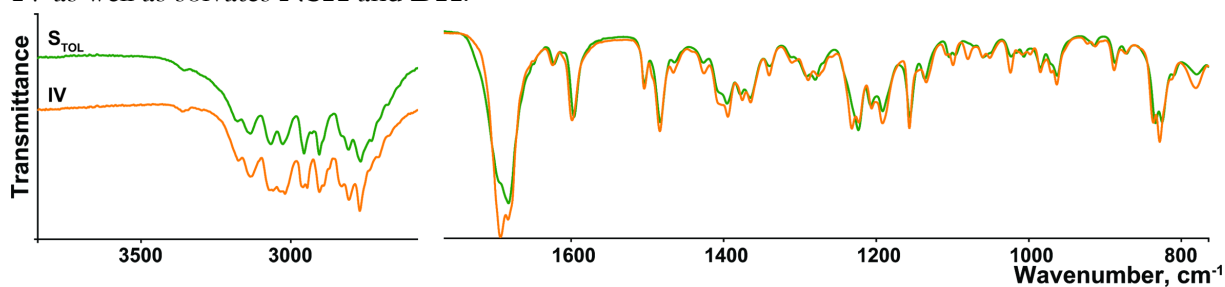


Fig. S18. FTIR spectra of droperidol solvate **S_{TOL}** and polymorph **IV**.

SOLVENT SORPTION-DESORPTION ISOTHERMS OF DROPERIDOL SOLVATES

For determination of organic solvent content in non-stoichiometric solvates in atmosphere with very low solvent vapour pressure, desiccators with glycerol (for methanol and ethanol) and glycerol and dimethylformamide (for acetonitrile and nitromethane) were prepared and a small amount of corresponding solvents were added by portions.

For determination of the water content in **NSH** approximately 0.35 g of the **NSH** sample was weighted in two containers which initially were placed in 0% and 32% RH. After the stabilization of the sample mass, the samples were moved to the desiccators with adjacent relative humidity. In this way full sorption-desorption cycle was recorded for both samples.

For determination of the organic solvent content in non-stoichiometric solvates, firstly corresponding solvate was desolvated on the P_2O_5 at ambient temperature. Then approximately 0.25 – 0.35 g of corresponding desolvated solvate was weighted in two sample containers which initially were placed in desiccators with 0 and 20% mole fraction of the corresponding solvent. After the stabilization of the sample mass the samples were moved to desiccators with adjacent solvent mole fraction. In this way full sorption-desorption cycle was recorded for both samples. For studies of the solvent sorption in atmosphere with very low solvent vapour pressure, approximately 0.25 – 0.35 g of corresponding desolvated solvate was weighted in container, which were placed in the desiccator prepared as described above. After the stabilization of the sample mass, portion of the corresponding solvent was added to the desiccator corresponding to addition of 0.05 – 0.2% solvent mole fraction.

It can be seen that the sorption-desorption isotherm does not exhibit a hysteresis. Besides, it was not found that the amount of solvent absorbed or desorbed would be dependent on the sorption-desorption cycle number.

Although the data points for solvates with organic solvent were obtained in two stages, they formed common sorption-desorption isotherm (the reversibility and hysteresis was not checked for solvent activity below 0.02). Reliability of the obtained data can be evaluated from isotherm of S_{ACN} where data obtained from four experiments with four different samples formed one isotherm without noticeable deviations, as clearly illustrated in Fig. S22.

When S_{ACN} and S_{NM} were stored in the desiccators with corresponding solvent activity above 0.5 for more than 5 days, samples got wet because of the solvent vapor adsorption and condensation on the sample. Therefore, the solvent amount in the sample was dependent on the storage time.

It was observed that at a high solvent activity all organic solvates sorbed more solvent than the corresponding solvent content determined from SCXRD and TG analysis. Although it is theoretically possible that additional solvent molecules were randomly placed in the structural channels, the additional solvent was in fact adsorbed on the powder surface. This was supported by the results from PXRD where no diffraction pattern changes were observed for these over-stoichiometric solvent content changes.

Localized solvent in solvent sorption-desorption isotherms of droperidol solvates **NSH**, S_{Me} , S_{Et} , S_{ACN} and S_{NM} were fitted with a) Langmuir isotherm, b) general localized solvent model with constant activity coefficients and c) general localized solvent model with variable activity coefficients described with c1) 2nd order Margules equation and c2) 3rd order Margules equation. Usage of the variable activity coefficients allowed the analysis of the isotherm only in limited solvent content range because of the computational specifics. For Langmuir isotherm and general localized solvent model with constant activity coefficients also solvent adsorption was described mathematically using disordered solvent model. It is noted that the disordered solvent model originally was provided for characterization of the solvent molecules absorbed in the solid phase⁸. However, equations corresponding to that also are able to describe the solvent adsorbed on the sample surface.

For fitting used mathematical equations⁸ and parameters characterizing the theoretical isotherm for each of the four used general models are given in a) Eq. 1 and Table S7, b) Eq. 2 and Table S8, c1) Eq. 3 and Table S9, and c2) Eq. 4 and 5 and Table S10, respectively. Fitting was performed by using the least-squares method to optimize the compatibility between theoretical and experimental data using the Excel add-in Solve by optimizing the parameters in the theoretical mathematical models.

For **NSH** all points were included in the calculation of Root-mean-square deviation RMSD, but for **S_{Me}** data up to $P_w = 5\%$, for **S_{Et}** up to $P_w = 2\%$, for **S_{ACN}** up to $P_w = 2\%$ and for **S_{NM}** up to $P_w = 5\%$ were used.

$$\varepsilon = p \frac{aP_w}{1 + aP_w} + Q \frac{P_w}{\gamma_2 + P_w} \quad (1)$$

Table S7. Parameters characterizing the Langmuir isotherm fitting the experimental droperidol solvate sorption-desorption isotherms.

	Localized water		Disordered water		RMSD
	p	a	Q	γ_2	
NSH	1.49	1.93	-	-	0.040
S _{Me}	0.449	398	0.0096	1.07	0.021
S _{Et}	0.511	340	0.013	1.13	0.043
S _{ACN}	0.58	220	-	-	0.068
S _{NM}	0.69	47	-	-	0.068

$$\varepsilon = \frac{\frac{\gamma_1}{\gamma_2} p P_w^q}{K(II) + \frac{\gamma_1}{\gamma_2} P_w^q} + Q \frac{P_w}{\gamma_2 + P_w} \quad (2)$$

Table S8. Parameters characterizing the general localized solvent model with constant activity coefficients fitting the experimental droperidol solvate sorption-desorption isotherms.

	Localized water				Disordered water		RMSD
	γ_1/γ_2	p	K(II)	q	Q	γ_2	
NSH	345	1.05	42.4	1.58	-	-	0.020
S _{Me}	34.8	0.447	0.0727	1.03	0.012	1.08	0.021
S _{Et}	344	0.459	0.00206	2.01	185	1570	0.0017
S _{ACN}	1930	0.483	$3.16 \cdot 10^{-5}$	3.20	274	1230	0.0029
S _{NM}	1920	0.513	$3.19 \cdot 10^{-5}$	4.12	345	874	0.0090

$$P_w = K(II) \frac{\varepsilon}{p - \varepsilon} \left(\exp \left(\frac{A_{12}}{RT} \left(1 - 2 \frac{\varepsilon}{p} \right) \right) \right)^{\frac{1}{q}} \quad (3)$$

Table S9. Parameters characterizing the general localized solvent model with variable activity coefficients described using 2nd order Margules' equation fitting the experimental droperidol solvate sorption-desorption isotherms.

	p	q	K(II)	A_{12}/RT	RMSD
NSH	1.09	1.20	55.2	0.39	
S _{Me}	0.421	1.00	0.239	0.683	0.0075
S _{Et}	0.447	1.00	0.240	1.62	0.0092
S _{ACN}	0.505	1.00	0.391	1.55	0.0038
S _{NM}	0.526	1.00	1.18	1.76	0.0079

$$P_w = K(II) \frac{\varepsilon}{p - \varepsilon} \left(\exp \left(\ln \frac{\gamma_1}{\gamma_2} \right) \right)^{\frac{1}{q}} \quad (4)$$

$$\ln \frac{\gamma_1}{\gamma_2} = \left[\frac{1}{RT} \left(\left(\frac{\varepsilon}{p} \right)^2 A_{12} + 2 \left(\frac{\varepsilon}{p} \right)^2 (A_{21} - A_{12}) \left(\frac{p - \varepsilon}{p} \right) - \left(\left(\frac{p - \varepsilon}{p} \right)^2 A_{21} + 2 \left(\frac{p - \varepsilon}{p} \right)^2 (A_{12} - A_{21}) \left(\frac{\varepsilon}{p} \right) \right) \right] \quad (5)$$

Table S10. Parameters characterizing the general localized solvent model with variable activity coefficients described using 3rd order Margules' equation fitting the experimental droperidol solvate sorption-desorption isotherms.

	ρ	q	$K(\text{II})$	A_{12}/RT	A_{21}/RT	RMSD
NSH	1.19	1.00	35.8	0.230	0.875	
S_{Me}	0.420	1.00	0.203	0.720	0	0.0045
S_{Et}	0.446	1.00	0.212	1.66	0.746	0.0027
S_{ACN}	0.509	1.00	0.402	1.41	1.80	0.0016
S_{NM}	0.520	1.00	1.19	2.12	1.37	0.0015

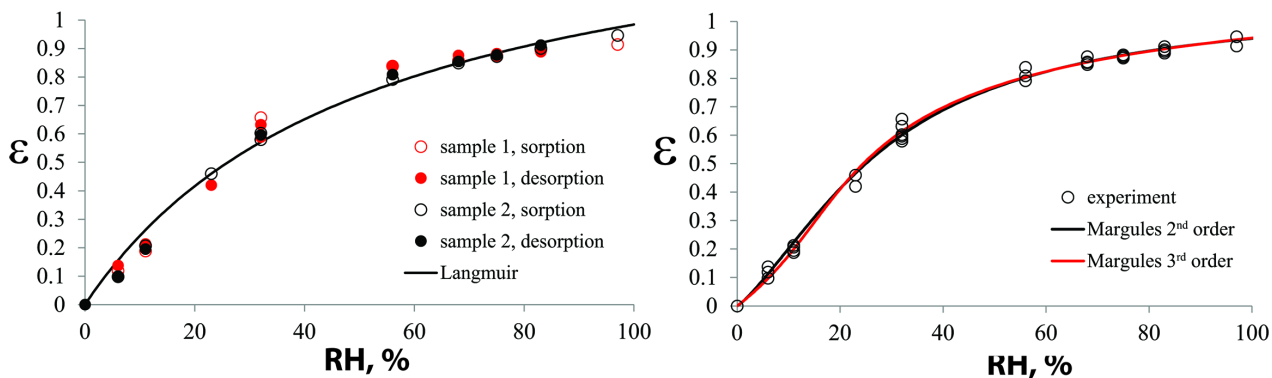


Fig. S19. Water sorption-desorption isotherm of **NSH** described using Langmuir isotherm (on the left) and localized solvent model with variable activity coefficients (on the right).

When the experimental **NSH** sorption-desorption data were fitted with Langmuir isotherm, reasonable fit was obtained (RMSD was 2 times higher than that for general localized water model). However, it was clear that this model only roughly described the characteristic water content dependence on the relative humidity.

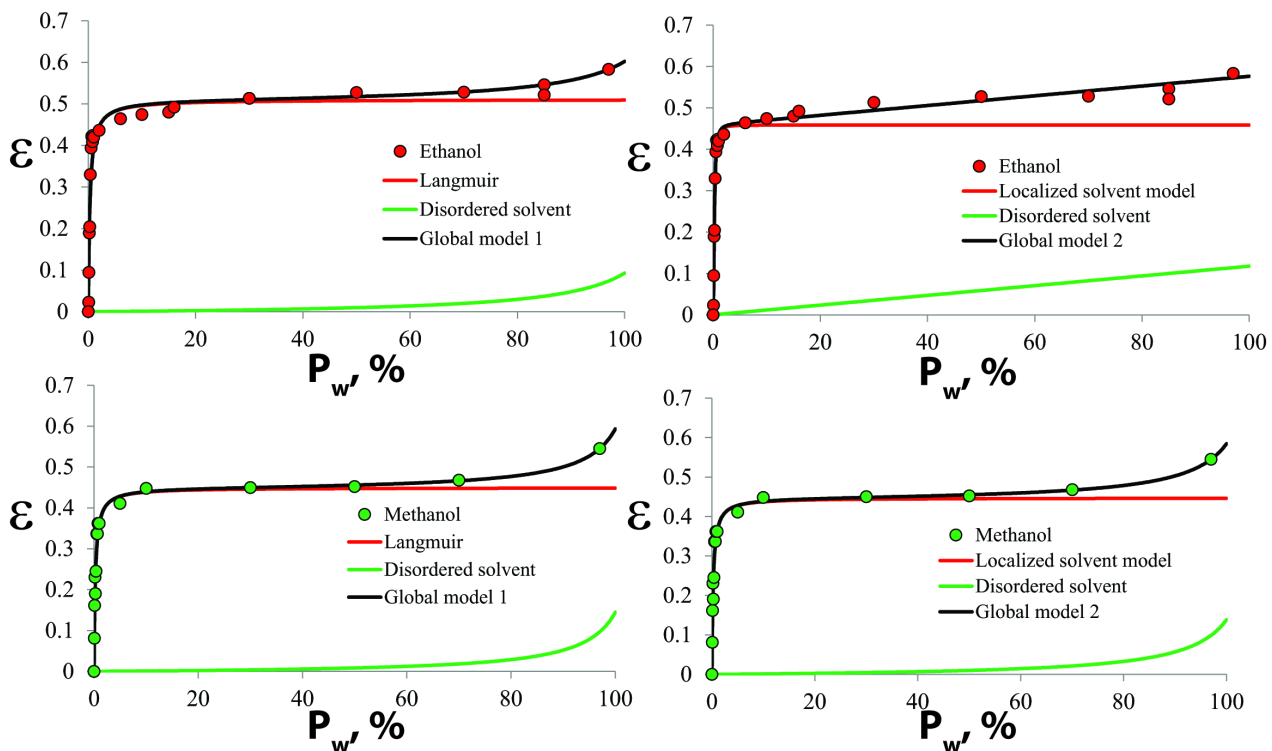


Fig. S20. Solvent sorption-desorption isotherm of S_{Me} and S_{Et} described using Langmuir isotherm (on the left) and localized solvent model with constant activity coefficients (on the right).

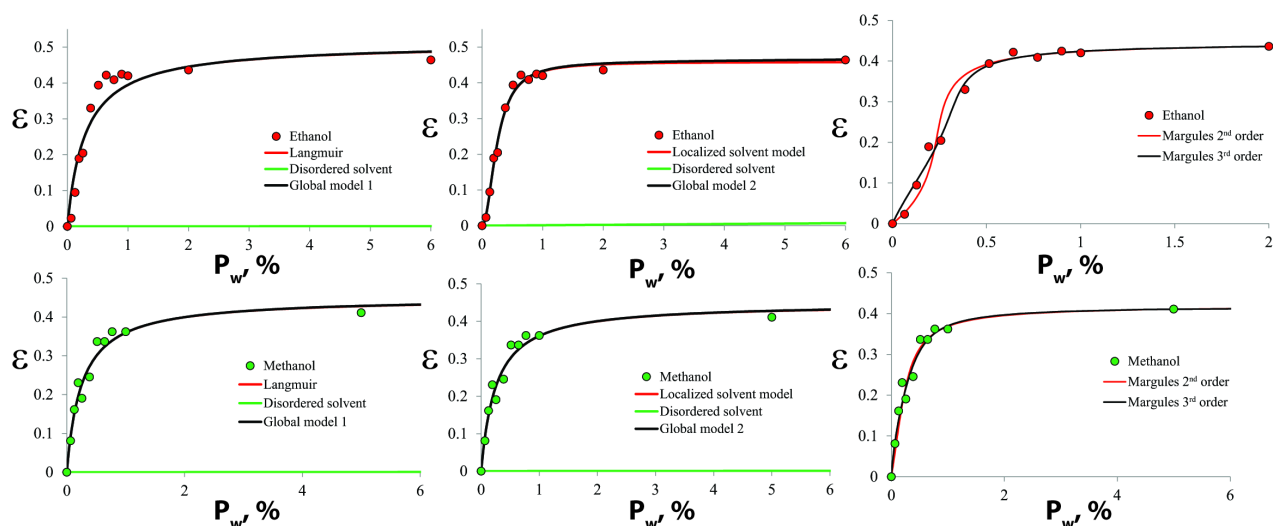


Fig. S21. Initial part of the solvent sorption-desorption isotherm of S_{Me} and S_{Et} described using Langmuir isotherm (on the left) and localized solvent model with constant (in the middle) and variable (on the right) activity coefficients.

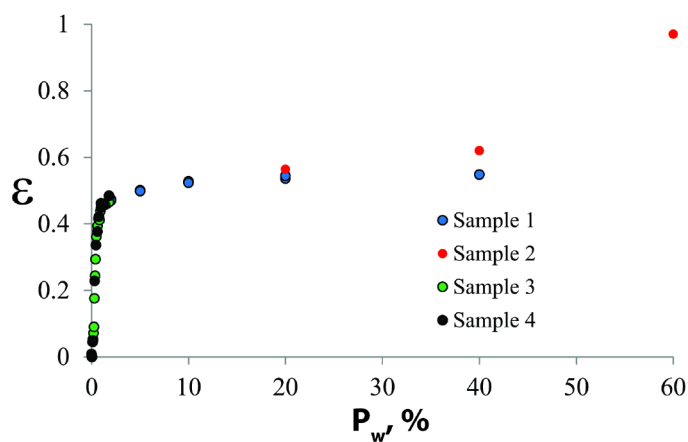


Fig. S22. Solvent sorption-desorption isotherm of S_{ACN} from two sample (1 and 2) solvent sorption and desorption measurements and two sample (3 and 4) solvent sorption measurements.

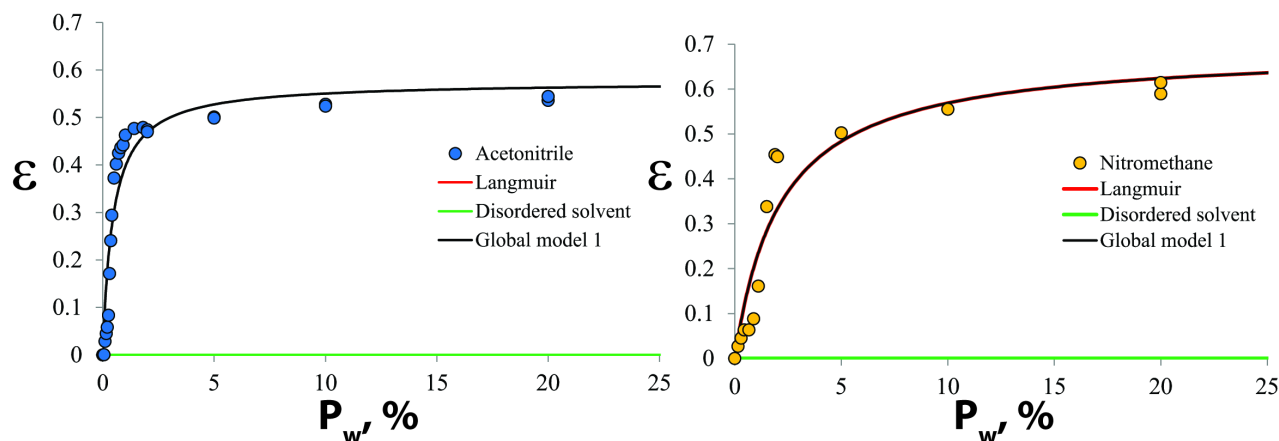


Fig. S23. Solvent sorption-desorption isotherm of S_{ACN} and S_{NM} described using Langmuir isotherm.

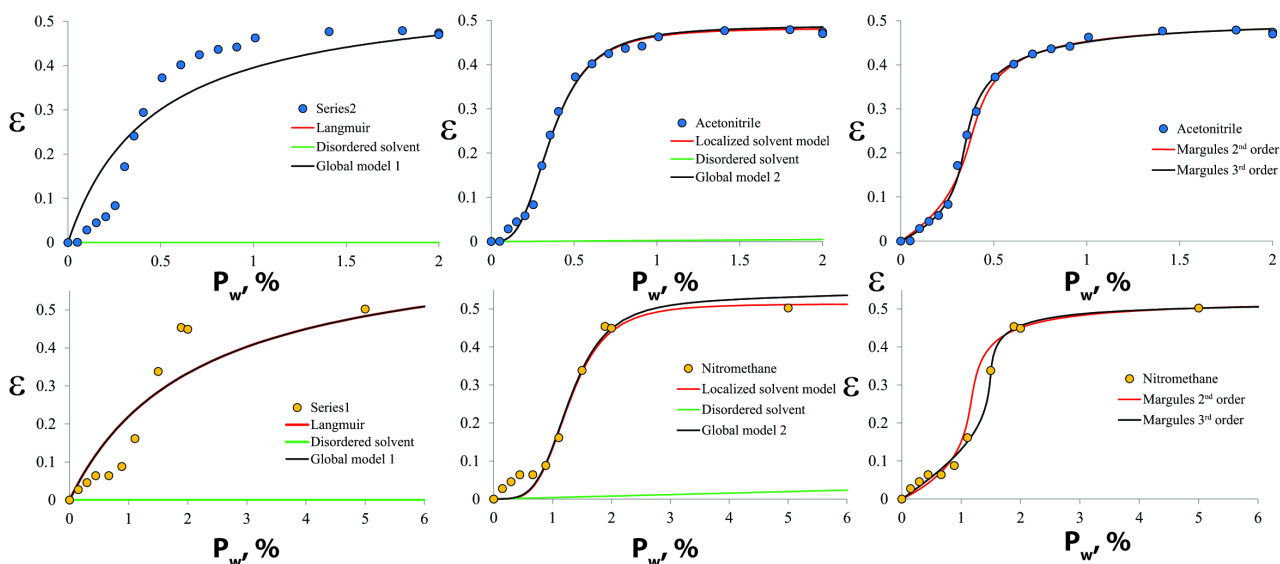


Fig. S24. Initial part of the solvent sorption-desorption isotherm of S_{ACN} and S_{NM} described using Langmuir isotherm (on the left) and localized solvent model with constant (in the middle) and variable (on the right) activity coefficients. Although almost ideal fit for the sorption-desorption isotherm of S_{NM} was obtained using 3rd order Margules equation, the meaning of this is open to discussion because of the experimental complications which arose during recording the sorption-desorption isotherm of S_{NM} (see the further discussion).

Apparently the small size of methanol molecules caused the lack of interactions between solvent molecules in two adjacent solvent sites positioned along a -axis and therefore their sorption in S_{Me} was described with a Langmuir isotherm. However, this was not true for the rest of the four solvates. Although the solvent uptake in the channels at a given solvent activity completely differed between NSH and the other solvates, all of these solvates showed lower solvent uptake for very low solvent activity values, probably because of the interaction between solvent molecules situated at two adjacent solvent sites. Nevertheless, based on the isotherms, this interaction was relatively weak in NSH and S_{Et} . The hindered solvent uptake period was the longest for S_{NM} , and variable activity coefficients had to be used to describe its isotherm. Therefore the larger size of nitromethane most probably prevented this solvent molecule from entering into the channels at very low solvent content in the atmosphere and only the reaching of some critical amount allowed more sudden structural changes by allowing easier insertion of additional solvent molecules. This can be also partially true for ethanol and acetonitrile molecules.

It was noticed that maximum solvent content in the channels (described by the localized solvent model) did not reach 0.5 stoichiometry as determined from the SCXRD data for S_{Me} . This could be explained by either actually lower solvent content in the structure or by the fact that all of the solvent did not leave the solvate and solvent content actually did not reach zero in this isotherm. However, sorption-desorption isotherm of S_{NM} showed higher solvent content because of the effective solvent adsorption process on the solvate particles even at relatively low solvent content in the atmosphere, as suggested by the obtained fitting results (see Fig. S24).

DROPERIDOL ISOSTRUCTURAL SOLVATE STRUCTURE WITH DIFFERENT SOLVENT CONTENT

Gradual changes of the PXRD patterns were observed when all of the solvates were stored in desiccators with different corresponding solvent activity in the atmosphere (see Fig. S25 – S29) and also when fully solvated S_{ACN} and S_{NM} were desolvated above the P_2O_5 (see Fig. S30 and S31).

The most noticeable peak intensity differences in the PXRD patterns of droperidol solvates with different solvent content (see Fig. S25 – S31) was associated to the peaks corresponding to Miller indices 001, 002 and 011 (see Fig. S2). It was already noted that these peaks are associated with the

planes along the solvent channels in the structure, thus, the change of the solvent molecule amount in the channels introduced the intensity changes. Moreover, the intensity of the peak 001 decreased by increasing the solvent content until the peak completely disappears at solvent content around $x = 0.5$. However, when solvent content was increased even more, intensity of this peak again increased. This was most obvious for NSH where 001 peak was absent for water stoichiometry 0.5-0.6. Changes of the other peak intensity (for example, $10\bar{2}$, 021 , and $1\bar{1}0$) was observed as well. However, these changes were not as apparent as those occurring with the first peaks and were not identified for all of the solvates.

It was noticed that the peak shift observed for the **NSH** was different from that occurring with the rest of the solvates, suggesting that different crystal structure changes occurred when water molecules entered the crystal structure, compared to the insertion of other solvent molecules.

The PXRD patterns of **S_{ACN}** obviously showed that the amount of solvent correlated with the diffraction peak shifts and therefore also with the changes in crystal structure: smaller changes in the solvent content at the initial phase of the sorption-desorption isotherm were consistent with smaller changes in the diffraction peak positions.

In the case of **S_{NM}**, after the initial changes of the lattice parameters there was no further gradual peak position shift, but peaks at the positions characteristic of a fully solvated **S_{NM}** phase appeared instead (see Fig. S29). Thus, it can be concluded that two phases were actually present during the sorption: a phase with nitromethane content around 0.15 equivalents, and a phase with nitromethane content of 0.5 equivalents. This suggests that two data points in the presented sorption-desorption isotherm within the solvent content interval of 0.15 – 0.4 equivalents (see Figure 11) did not actually correspond to the thermodynamic solvent content in the solvate, but rather to the kinetic solvent content in the phase mixture. Moreover, after fitting a sorption-desorption isotherm, the obtained constants reflecting the solvent - droperidol interaction according to the activity coefficient model also suggested that phase separation was possible for this particular case⁸.

It should be noted that such gradual structural changes were observed only when the solvent content changes in the solvate occurred slowly. However, when the solvates were desolvated at elevated temperature, the changes of solvent content were too fast for gradual structural changes to take place, and a two phase mixture was observed during the desolvation process.

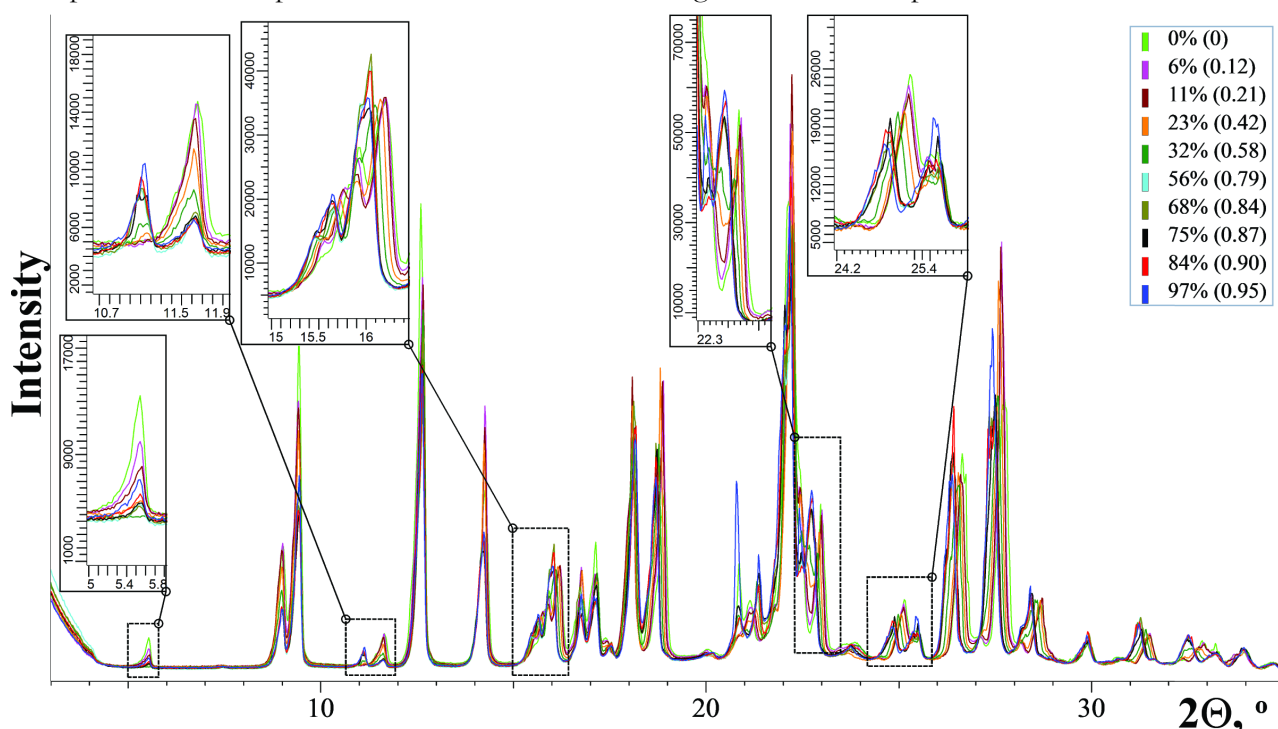


Fig. S25. PXRD patterns of **NSH** with different water content in the structure (given in brackets) obtained by storing the sample in different RH.

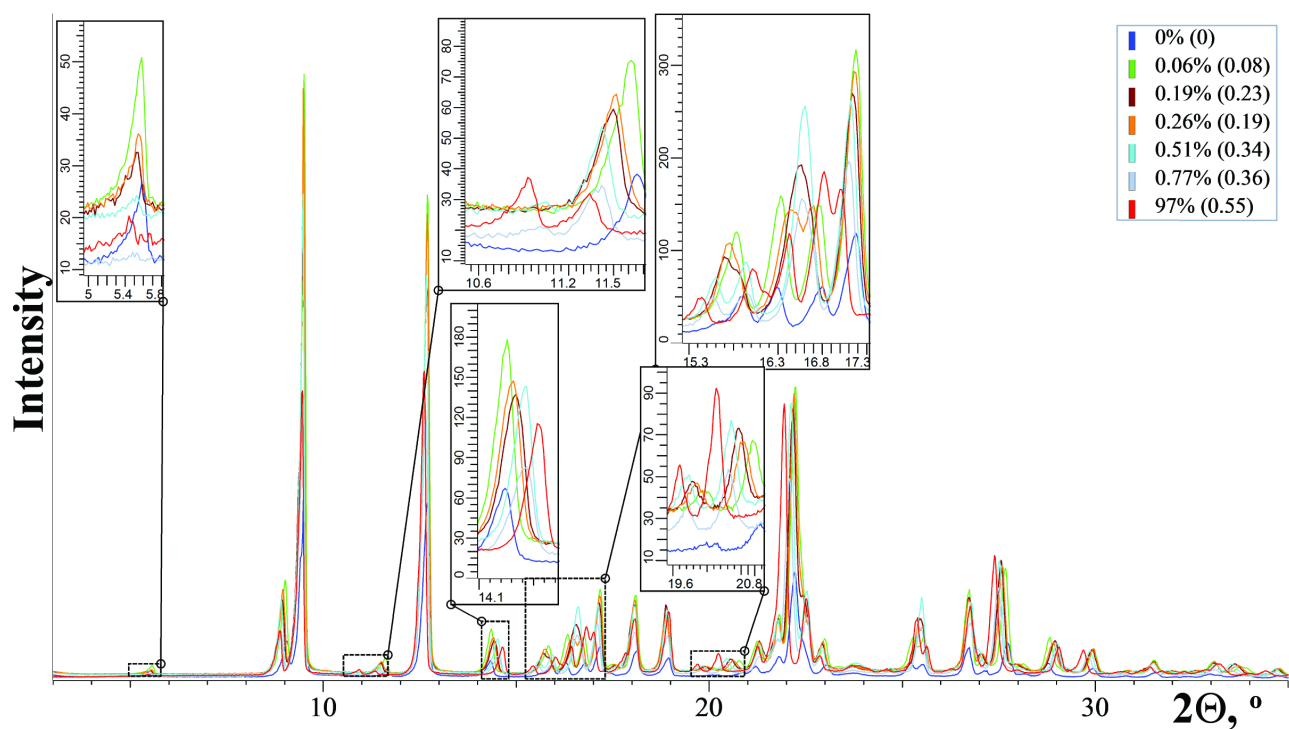


Fig. S26. PXRD patterns of S_{Me} with different methanol content in the structure (given in brackets) obtained by storing the sample in the atmosphere with different methanol activity.

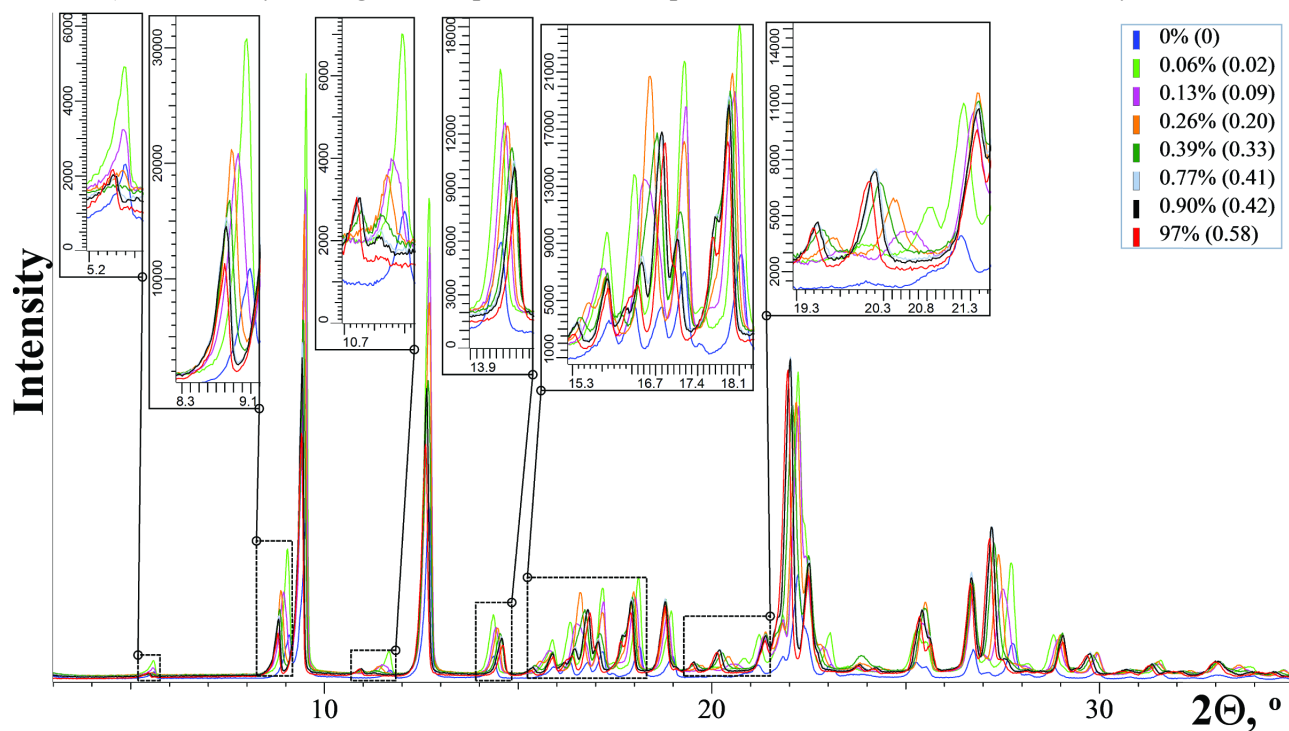


Fig. S27. PXRD patterns of S_{Et} with different ethanol content in the structure (given in brackets) obtained by storing the sample in the atmosphere with different ethanol activity.

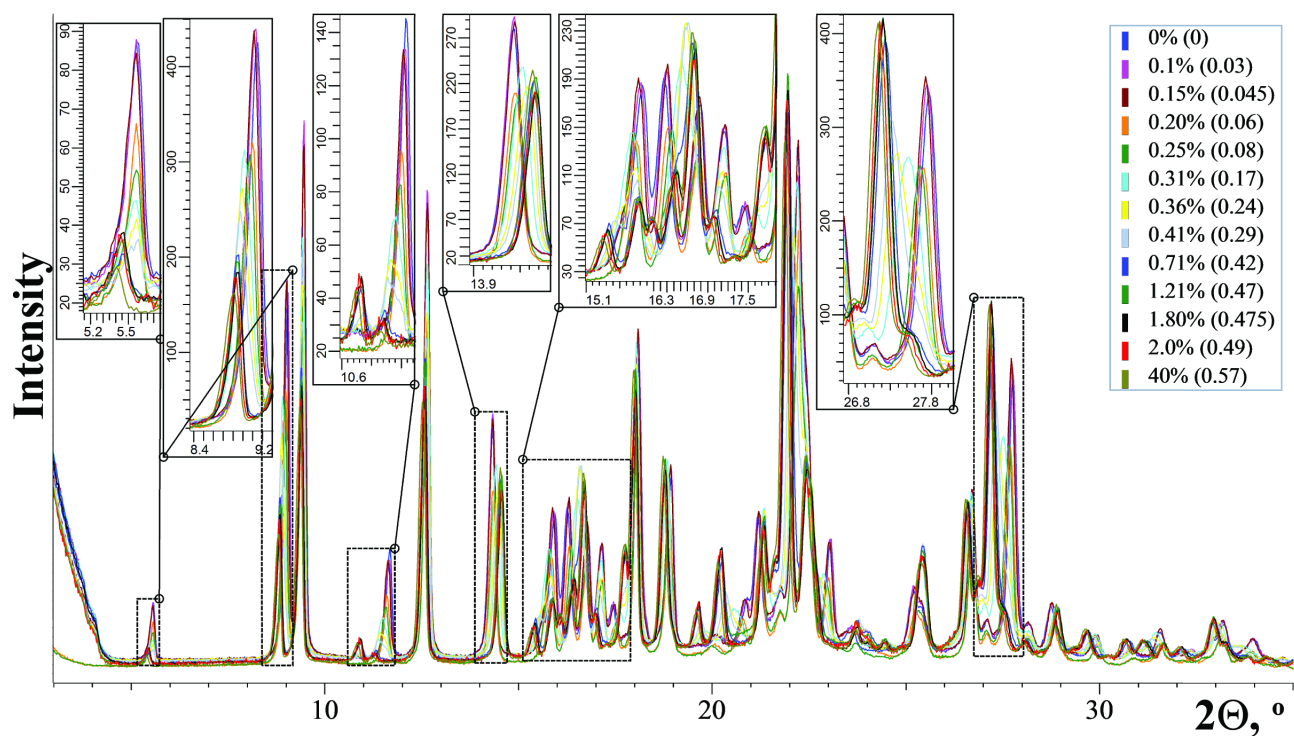


Fig. S28. PXRD patterns of S_{ACN} with different acetonitrile content in the structure (given in brackets) obtained by storing the sample in the atmosphere with different acetonitrile activity.

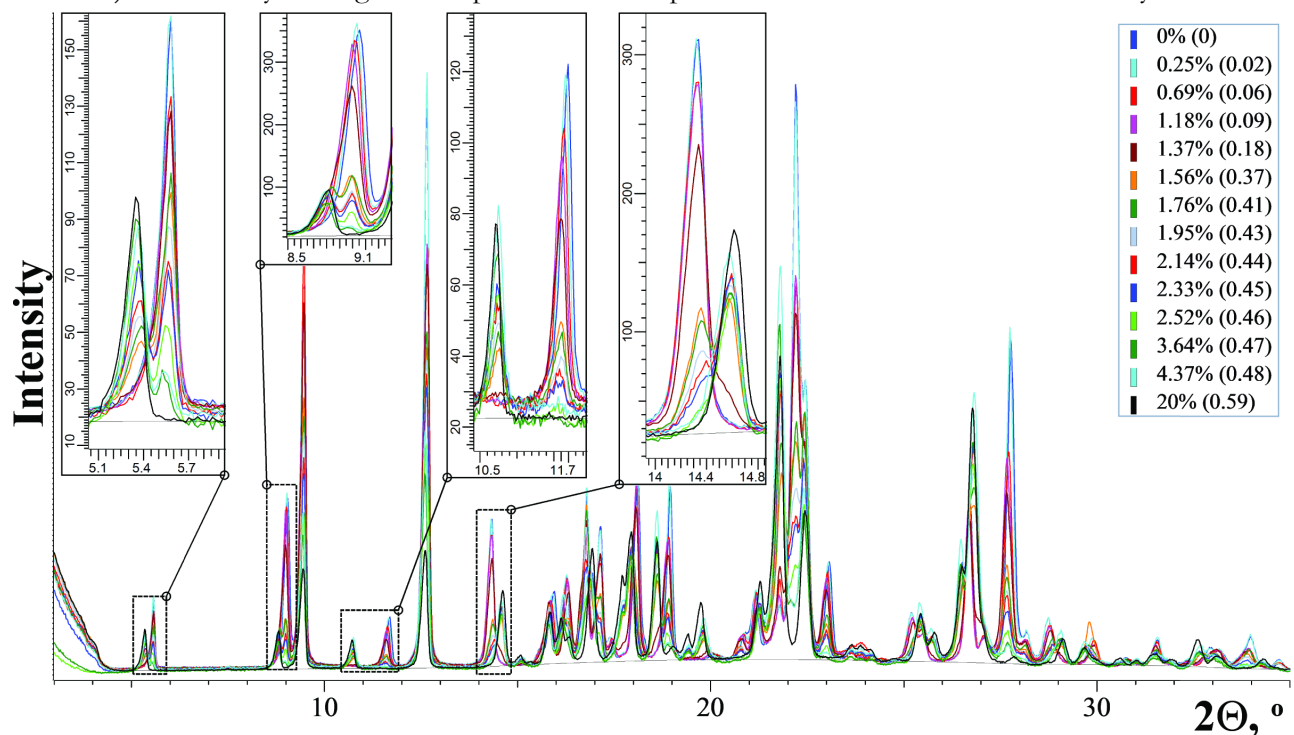


Fig. S29. PXRD patterns of S_{NM} with different nitromethane content in the structure (given in brackets) obtained by storing the sample in the atmosphere with different nitromethane activity.

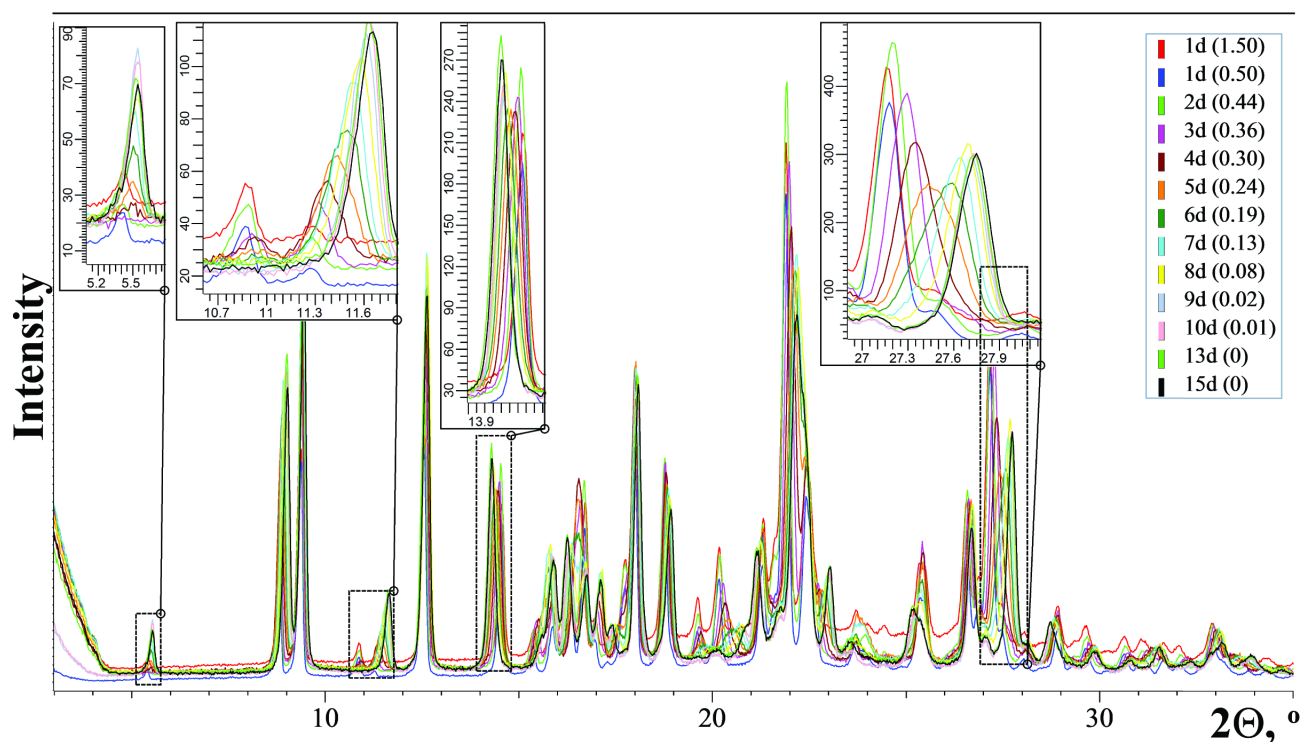


Fig. S30. PXRD patterns of S_{ACN} with different acetonitrile content in the structure (given in brackets) obtained by storing fully solvated sample at 50 °C temperature above the P_2O_5 for different amount of time.

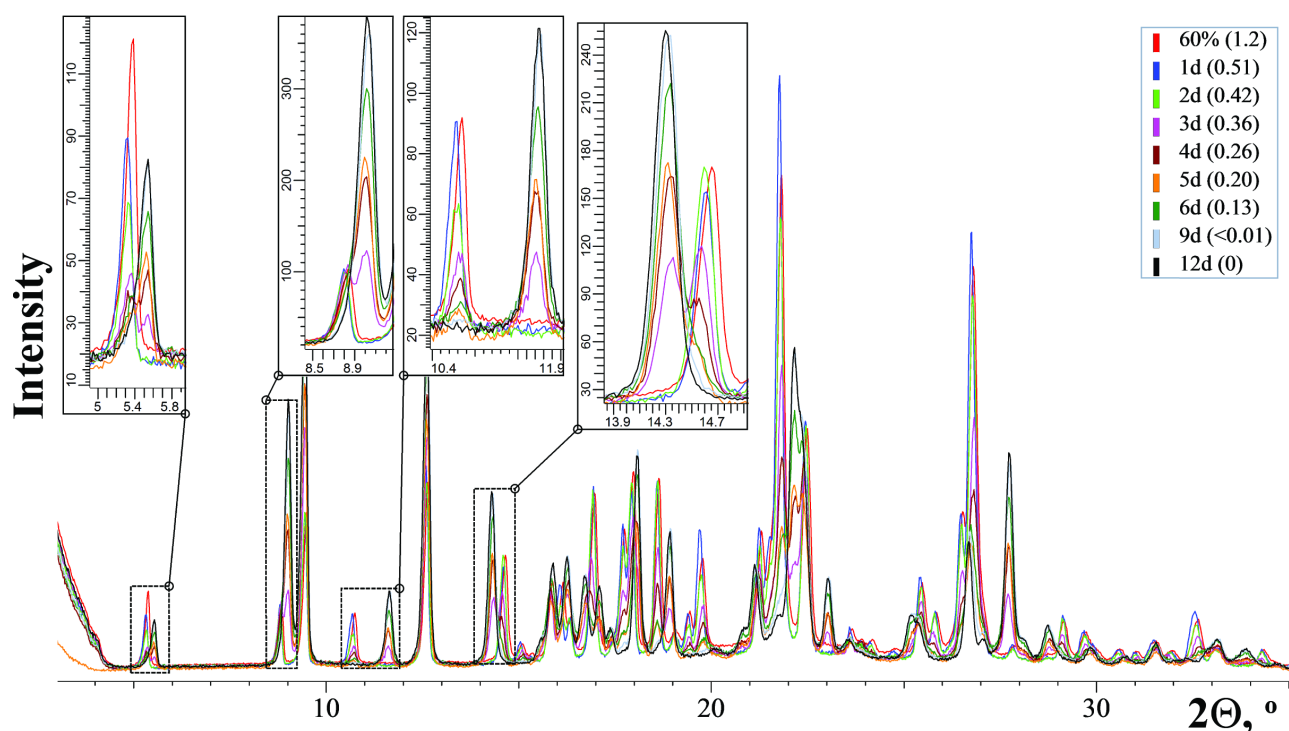


Fig. S31. PXRD patterns of S_{NM} with different nitromethane content in the structure (given in brackets) obtained by storing fully solvated sample at 50 °C temperature above the P_2O_5 for different amount of time.

An increase of the solvent content increased the **NSH** cell length a and the angle γ , while the same parameters decreased for other solvates. The cell length c at the same time exhibited the opposite trend (see Table S11). Moreover, the directions of changes in the lattice parameters c and α were reversed when the water content increased above 0.5 equivalents, although the cell volume and calculated density still increased gradually (see Fig. S32).

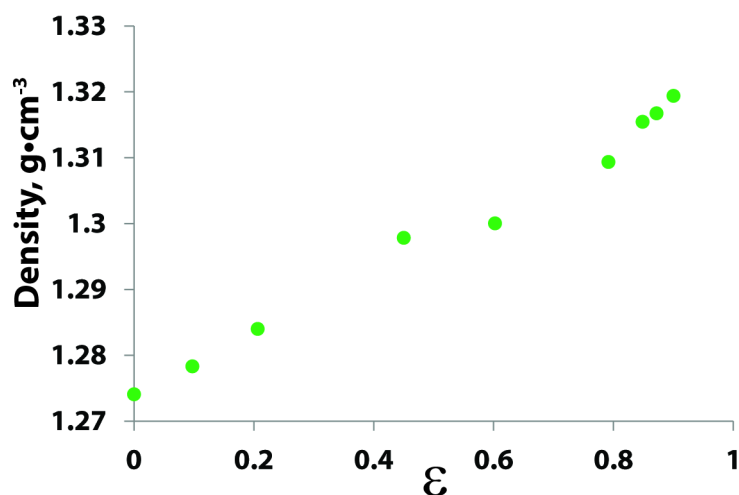


Fig. S32. Calculated density of **NSH** with different water content in the structure.

Table S11. Direction of the lattice parameter change by increasing the solvent content in the structure of droperidol isostructural solvates.

Parameter	NSH	NSH	S_{Me}	S_{Et}	S_{ACN}	S_{NM}
	(up to 0.5 stoichiometry)	(above 0.5 stoichiometry)				
a	↑	↑	↓	↓	↓	↓
b	↑	↑	↑	↑	↑	↑
c	↓	↑	↑	↑	↑	↑
α	↓	↑	↓	↓	↓	↓
β	↓	↓	-	↓	↓	↓
γ	↑	↑	↓	↓	↓	↓

WATER ARRANGEMENT IN A PARTIALLY FILLED NSH STRUCTURE

It was determined that the removal of water from **NSH** structure occurred by simultaneously losing both hydrogen bonded water molecules from some of the channel sites.

Firstly, this arrangement of water molecules explained the observed lattice parameter changes for **NSH** with different water content. If the first water molecules entering the channel would not link the droperidol molecules across the channel, a different lattice parameter change should be observed. Formation of the $O1 \cdots O1$ hydrogen bond linkage clearly explains the decrease of lattice parameters c , α , and β , and the insertion of water molecules above 0.5 stoichiometry increases the interaction of non-bonded water molecules positioned along the a -direction, most probably affecting the further lattice parameter changes for c and α . Moreover, the simulation of lattice parameter changes for **NSH** structure with different water content also confirmed that this water molecule arrangement should result in an observed lattice parameter behaviour with changes in the effects of water content on c and α at $\epsilon \approx 0.5$ (see Fig. S33).

Lattice parameter calculation in *CASTEP* was performed by creating a supercell from **NSH** unit cell repeated 2 times (for $\epsilon = 0.5$) or 5 times (for $\epsilon = 0.2, 0.4, 0.6$ and 0.8) in the a -direction and removing the water molecules to obtain the necessary water content. Then full geometry optimization of the obtained structures were performed. Lattice parameter a was calculated by dividing the obtained length of the supercell a edge 2 or 5 times respectively. Lattice parameters for $\epsilon = 1$ and $\epsilon = 0$ were calculated by performing identical geometry optimization of **NSH** structure with none or both of the water molecules removed.

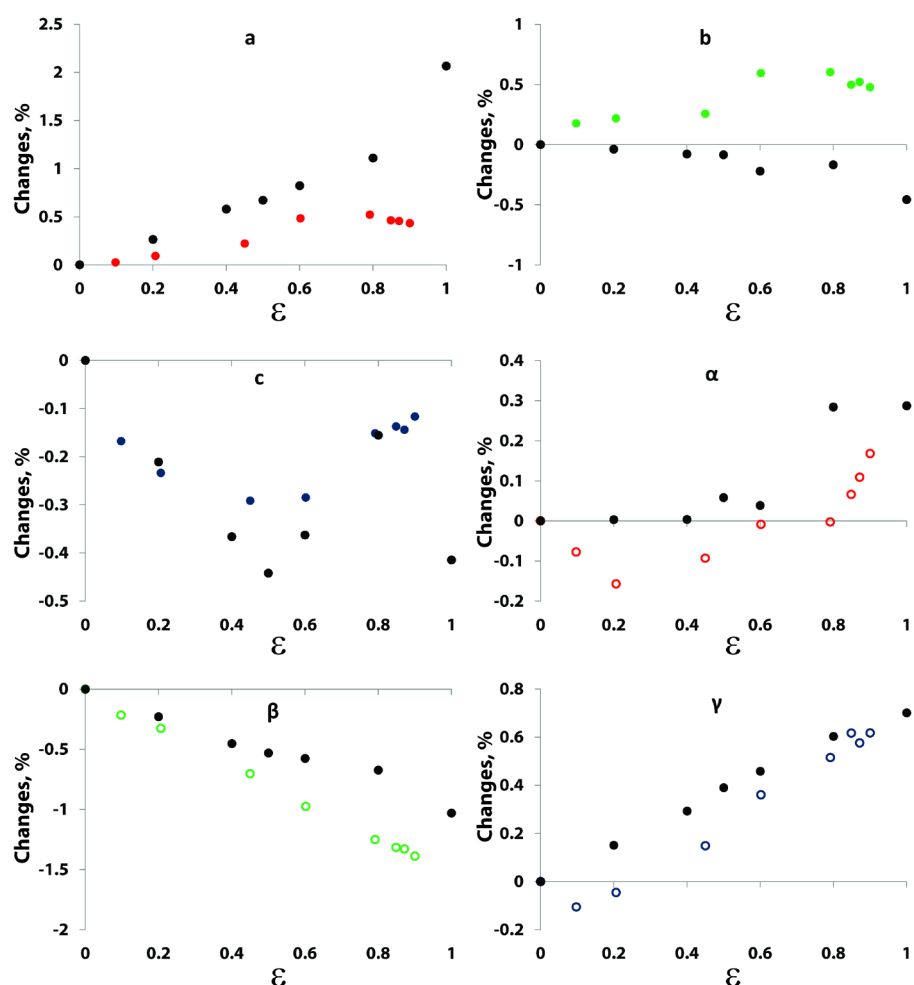


Fig. S33. Experimental (coloured as in Figure 12) and in *CASTEP* calculated (black filled circles) lattice parameter changes for **NSH** with different water content.

Secondly, the hemihydrate structure double-sized in the *a*-direction with two hydrogen bonded water molecules was slightly energetically favourable compared to that where the water molecules were positioned so that this hydrogen bond was lost (by 2 - 4.5 kJ per mole of water depending on the arrangement of water molecules in the second case, see Fig. S34).

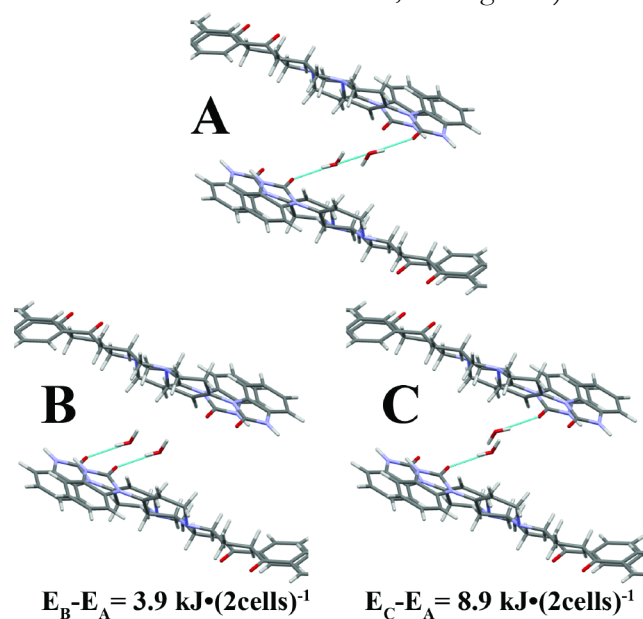


Fig. S34. Geometry and relative energy for three possible water arrangements in 2 times extended (in *a*-direction) **NSH** unit cell with hemihydrate stoichiometry.

Thirdly, the geometrical parameters for the O3-H···O1 and O3-H···O3 hydrogen bonds were the same for both stoichiometries. Slightly increased distances in **ISD** are associated with the expansion of the unit cell due to the increased temperature during the measurements, see Table 1).

Interestingly, the equivalent isotropic displacement parameters in the hemihydrate structure had increased for all of the atoms, thus suggesting that the structure is more ordered when the solvent molecules fully occupy the channels. The displacement parameters of **ISD** measured at 333K were significantly higher than those in the structures with water both at 120K and even in 298K⁹, thus suggesting that a complete loss of solvent makes the structure even more disordered, as already noted for channel hydrates¹⁰. It should be noted that the hydrogen positions for hemihydrate stoichiometry could not be located in the difference Fourier map and were placed in the calculated positions.

It was also observed that there were almost no changes in geometry parameters for other droperidol interactions, as presented in Table S12.

Table S12. Geometrical parameters for droperidol-droperidol intermolecular interactions in experimental **NSH** structures with different water content

Stoichiometry	Interaction	X-H (Å)	H···A (Å)	D···A (Å)	D-H···A (°)
1	N2-H···O1	0.97	1.82	2.79	175
	C19-H···N3	0.97	2.56	3.49	159
	C22-H···O2	0.99	2.49	3.29	138
	C21-H···F1	1.01	2.54	3.50	158
0.5	N2-H···O1	0.92	1.87	2.79	175
	C19-H···N3	0.96	2.57	3.48	157
	C22-H···O2	0.98	2.51	3.28	136
	C21-H···F1	1.01	2.54	3.50	158
0 (ISD)	N2-H···O1	0.95	1.87	2.81	173
	C19-H···N3	0.99	2.58	3.53	161
	C22-H···O2	0.99	2.56	3.35	136
	C21-H···F1	0.99	2.56	3.49	158

Fourthly, the water sorption-desorption isotherm was represented with a smooth line corresponding to a localized water model, which is possible only if all of the solvent sites are equivalent. Therefore both of the hydrogen-bonded water molecule positions should be regarded as one absorption site.

EVALUATION OF THE DROPERIDOL ISOSTRUCTURAL SOLVATE FORMATION

Lattice and total energy of polymorph **II** and **ISD** were compared after the geometry optimization in *CASTEP*. Geometry optimization was performed by optimizing all atom positions (ALL) or all atom positions and the lattice parameters (FULL). Total energy was calculated in *CASTEP*, but lattice energy was calculated in *PIXEL*. It was observed that both lattice and total energy of **ISD** was slightly lower than that of polymorph **II**. However, the instability of the **ISD** at ambient and elevated temperature can be due to its lower density which could result the reduction of the **ISD** relative thermodynamic stability by increasing the temperature up to ambient temperature and above.

Table S13. Comparison of total energy, lattice energy and density of **ISD** and polymorph **II**

		ALL	FULL
$E_{\text{ISD}} - E_{\text{II}}$	E_{total}	-0.45	-0.33
$\text{kcal} \cdot \text{mol}^{-1}$	E_{lattice}	-0.59	-0.53
$d, \text{g} \cdot \text{cm}^{-3}$	II	1.31	1.36
	ISD	1.27	1.32

Table S14. Solvent molecule molar volume calculated with *Gaussian09*

Solvent	Molar volume, $\text{cm}^3 \cdot \text{mol}^{-1}$
Water	12.842
Methanol	25.69
Acetonitrile	37.9
Ethanol	42.012
Nitromethane	48.07
Propionitrile	48.791
Dichloromethane	49.603
Propanol-2	60.177
1,2-dichloroethane	64.753
Propanol-1	67.384
Chloroform	69.072
1,1-dichloroethane	73.598
Tetrachlorocarbon	96.705

Shading – solvates from which the isostructural droperidol solvates formed.

It can be seen that molar volume of chloroform exceeds that of the next biggest solvent molecules forming isostructural solvates by $20 \text{ cm}^3 \cdot \text{mol}^{-1}$ and that of propanol-2, propanol-1, and 1,2-dichloroethane does not form the isostructural solvates. This could be explained by the ability of chloroform to form multiple hydrogen bonds with multiple droperidol molecules and probably also by the round shape of this molecule. In the same time both alcohol molecules and probably also the 1,2-dichloroethane can not form so efficient intermolecular interactions (except for the hydrogen bond with OH in alcohols and Cl in 1,2-dichloroethane), and also the shape of the alcohol molecules impede the solvate formation. Almost linear shape of the propionitrile prevents formation of its solvate as even smaller linear acetonitrile molecule completely occupies the space in the channels along the *a*-direction.

REFERENCES

- (1) Gramatica, P.; Navas, N.; Todeschini, R. *Trends Anal. Chem.* **1999**, 18, (7), 461-471.
- (2) Gu, C.-H.; Li, H.; Gandhi, R. B.; Raghavan, K. *Int. J. Pharm.* **2004**, 283, (1–2), 117-125.
- (3) Fujii, K.; Uekusa, H.; Itoda, N.; Hasegawa, G.; Yonemochi, E.; Terada, K.; Pan, Z.; Harris, K. D. M. *J. Phys. Chem. C* **2009**, 114, (1), 580-586.
- (4) Guguta, C.; Meeke, H.; de Gelder, R. *J. Pharm. Biomed. Anal.* **2008**, 46, (4), 617-624.
- (5) Fujii, K.; Aoki, M.; Uekusa, H. *Cryst. Growth Des.* **2013**, 13, (5), 2060-2066.
- (6) Fujii, K.; Uekusa, H.; Itoda, N.; Yonemochi, E.; Terada, K. *Cryst. Growth Des.* **2012**, 12, (12), 6165-6172.
- (7) Bērziņš, A.; Actiņš, A. *CrystEngComm* **2014**, submitted.
- (8) Authelin, J. *Int. J. Pharm.* **2005**, 303, (1-2), 37-53.
- (9) Actins, A.; Araj, R.; Belakovs, S.; Orola, L.; Veidis, M. *J. Chem. Crystallogr.* **2008**, 38, (3), 169-174.
- (10) Stephenson, G.; Groleau, E.; Kleemann, R.; Xu, W.; Riggsbee, D. *J. Pharm. Sci.* **1998**, 87, (5), 536-542.

CHARACTERIZATION OF SOLVATES

Table S1. Crystallographic data of the droperidol solvates **NSH**, **S_{Me}**, **S_{Et}**, **S_{ACN}**, and **S_{NM}**¹

Solvate	S_{ACN}	S_{NM}	S_{Me}	NSH	S_{Et}
Empirical formula	(C ₂₂ H ₂₂ FN ₃ O ₂) ₂ · C ₂ H ₃ N	(C ₂₂ H ₂₂ FN ₃ O ₂) ₂ · CH ₃ NO ₂	C ₂₂ H ₂₂ FN ₃ O ₂₂ · 0.5CH ₄ O	C ₂₂ H ₂₂ FN ₃ O ₂ · H ₂ O	(C ₂₂ H ₂₂ FN ₃ O ₂) ₂ · C ₂ H ₆ O
M _r	399.96	409.95	395.45	397.44	402.47
Crystal system	triclinic	triclinic	triclinic	triclinic	triclinic
Space group	<i>P</i> 1	<i>P</i> 1	<i>P</i> $\bar{1}$	<i>P</i> $\bar{1}$	<i>P</i> $\bar{1}$
Temperature	173	173	173	173	173
a (Å)	6.0870(2)	6.06730(10)	6.0671(2)	6.2936(2)	6.08400(10)
b (Å)	10.2177(3)	10.1884(3)	10.2183(4)	10.1673(4)	10.2978(3)
c (Å)	16.2642(6)	16.4237(5)	16.2078(8)	15.9173(4)	16.1737(5)
α (°)	101.2051(11)	99.8303(13)	101.3130(10)	102.6133(18)	100.9299(10)
β (°)	92.7447(10)	92.2880(12)	93.208(2)	91.8553(19)	92.6382(10)
γ (°)	96.7569(19)	95.6243(18)	96.996(2)	99.9459(16)	95.9415(15)
V (Å ³)	982.78(6)	993.86(4)	974.65(7)	976.41(6)	987.35(4)
Z ^a	2	2	2	2	2

^a – Based on droperidol as the molecular entity.

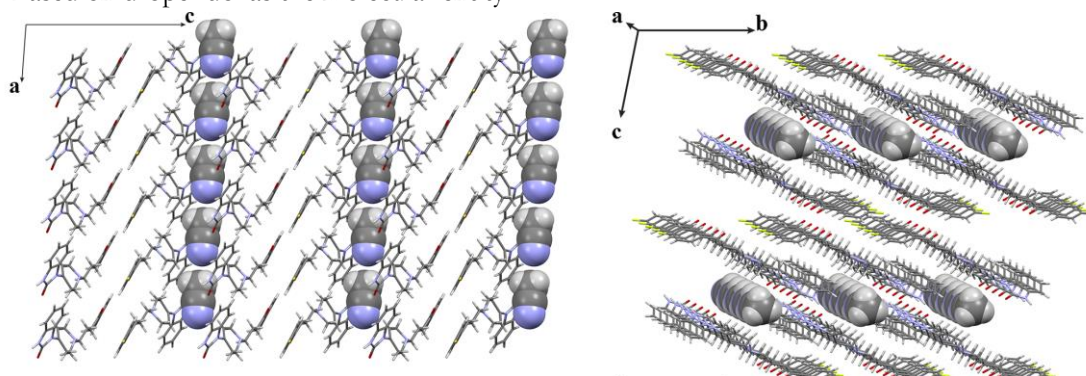


Fig. S1. Crystal structure of the droperidol solvate **S_{ACN}** representing the solvent molecule arrangement in isostructural solvate channels.

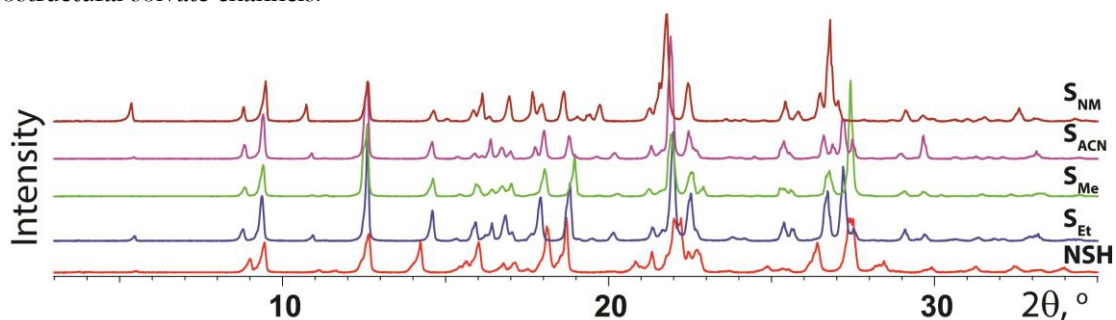


Fig. S2. PXRD patterns of the droperidol isostructural solvates.

DESOLVATION ACTIVATION ENERGY

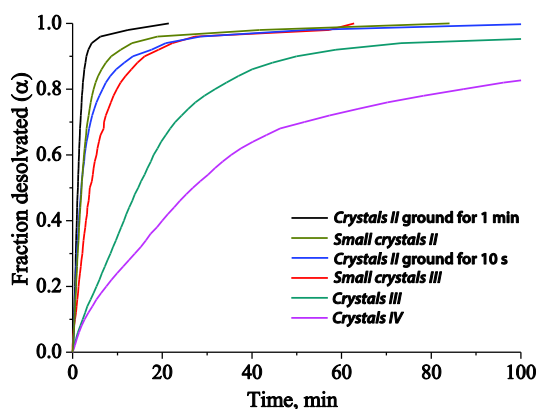


Fig. S3. The dehydration kinetic curves of various NSH samples in isothermal mode at 60°C.

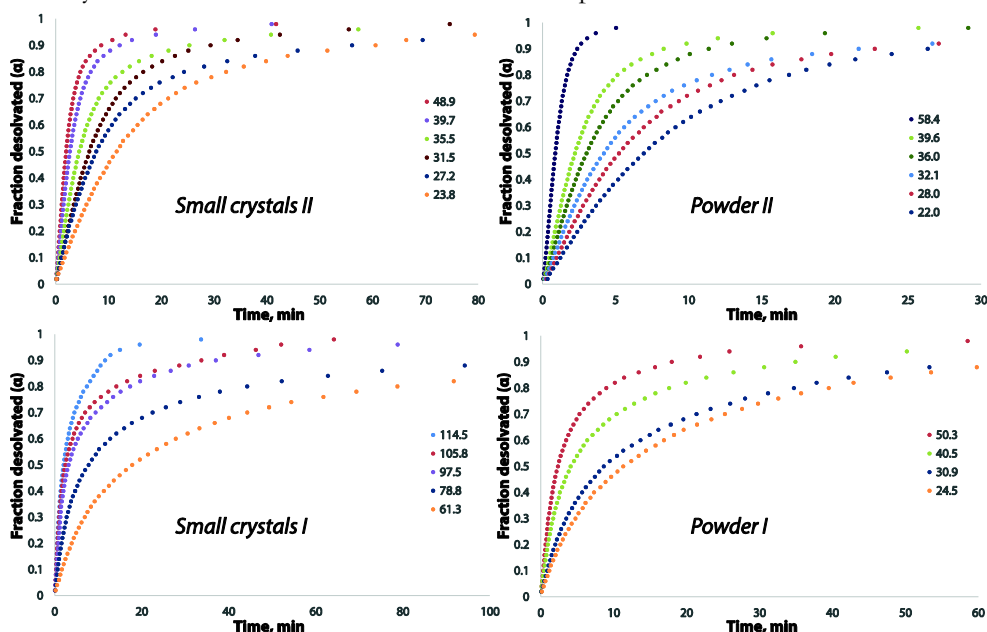


Fig. S4. Dehydration kinetic curves of different NSH samples at different temperatures in isothermal mode.

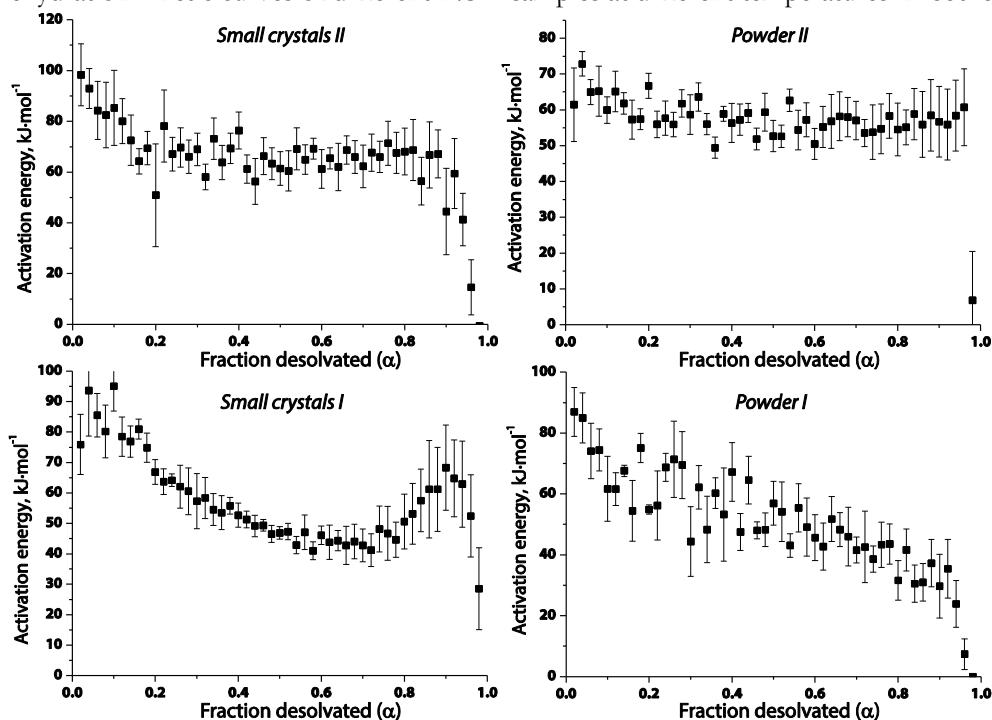


Fig. S5. Dehydration activation energy at different α values for different NSH samples in isothermal mode.

Table S2. Summary of droperidol organic solvate desolvation kinetic parameters in isothermal mode.

Solvate	Sample	E_a , $\text{kJ}\cdot\text{mol}^{-1}$	E_a - α dependence	Kinetic model ^a	Temperatures used, °C
S_{Me}	<i>Powder I</i>	50 ± 13	—	D5	50-100
	<i>Powder II</i>	52 ± 7	—	D5	40-110
	<i>Suspension</i>	46 ± 12	↓	F, D	45-90
	<i>Small crystals</i>	21 ± 10	—	A3/2, R2	40-100
S_{Et}	<i>Powder</i>	61 ± 14	↓	D, F3/2	50-110
	<i>Small crystals</i>	45 ± 10	—	A3/2, R3	40-110
S_{ACN}	<i>Powder I</i>	$100\pm 20^{\text{b}}$	—	D5	90-115
	<i>Powder II</i>	$490\pm 130^{\text{b}}$	—	D5, D3 A2 ^c	113-125
S_{NM}	<i>Powder I</i>	$400\pm 50^{\text{b}}$	—	D, F	90-120
	<i>Powder II</i>	$380\pm 60^{\text{b}}$	↑	D5, A3/2 ^c	100-115
	<i>Suspension</i>	$190\pm 60^{\text{b}}$	—	D5, D3, A3/2 ^c	90-110

^a – For each individual sample only commonly used kinetic models were included in the selection (see Table S4).

^b – Only apparent E_a value, which does not characterize the actual desolvation process.

^c – At highest used temperatures.

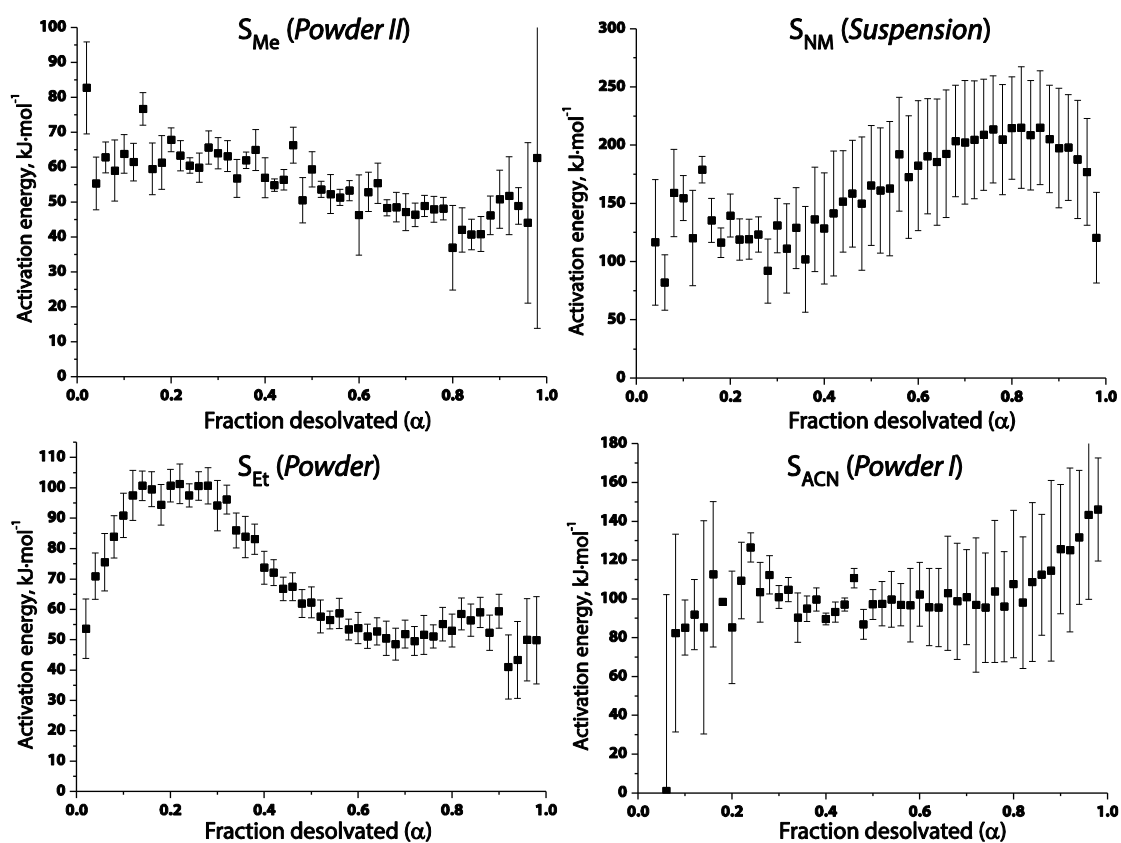


Fig. S6. Desolvation activation energy at different α values for droperidol solvate samples in isothermal mode.

Decrease (or growth) of the desolvation E_a values by increasing the fraction desolvated is only apparent and is a result from the wide particle size distribution or slight change of the desolvation mechanism during the reaction which thus affects the desolvation curves and therefore results in the changes of the calculated E_a values.

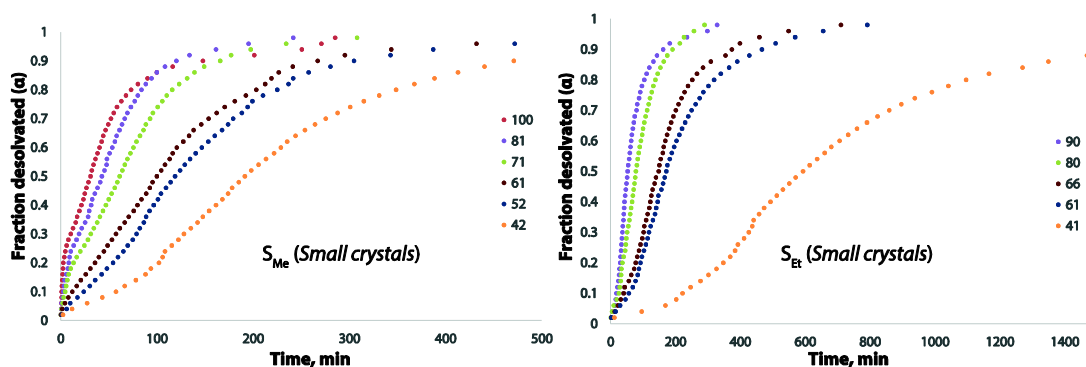


Fig. S7. Desolvation kinetic curves of crystalline S_{Me} and S_{Et} samples at different temperatures in isothermal mode.

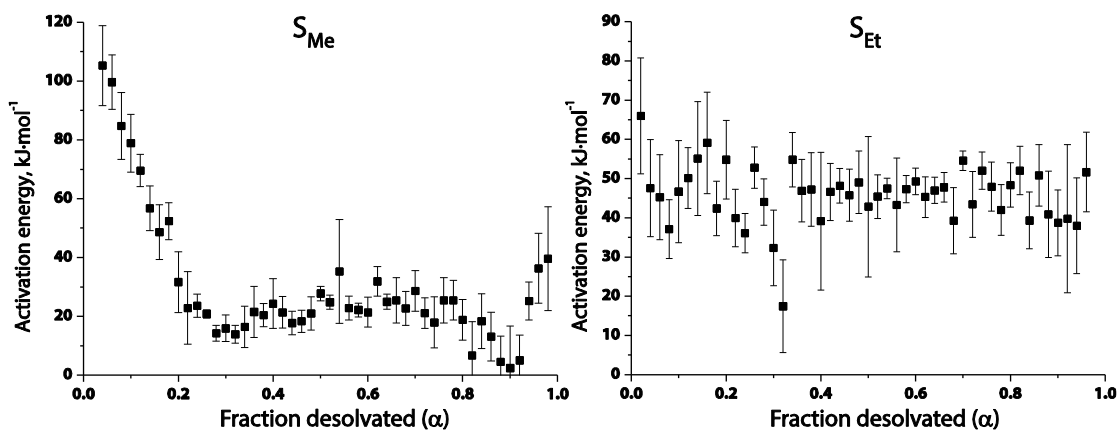


Fig. S8. Desolvation activation energy at different α values for crystalline S_{Me} and S_{Et} samples in isothermal mode.

Although one of the reasons for slower desolvation in isothermal experiments (which led to usage of such a high temperatures) might be lower nitrogen flow than that used in nonisothermal mode, most probably the main reason for the differences was associated with the sample preparation and storage.

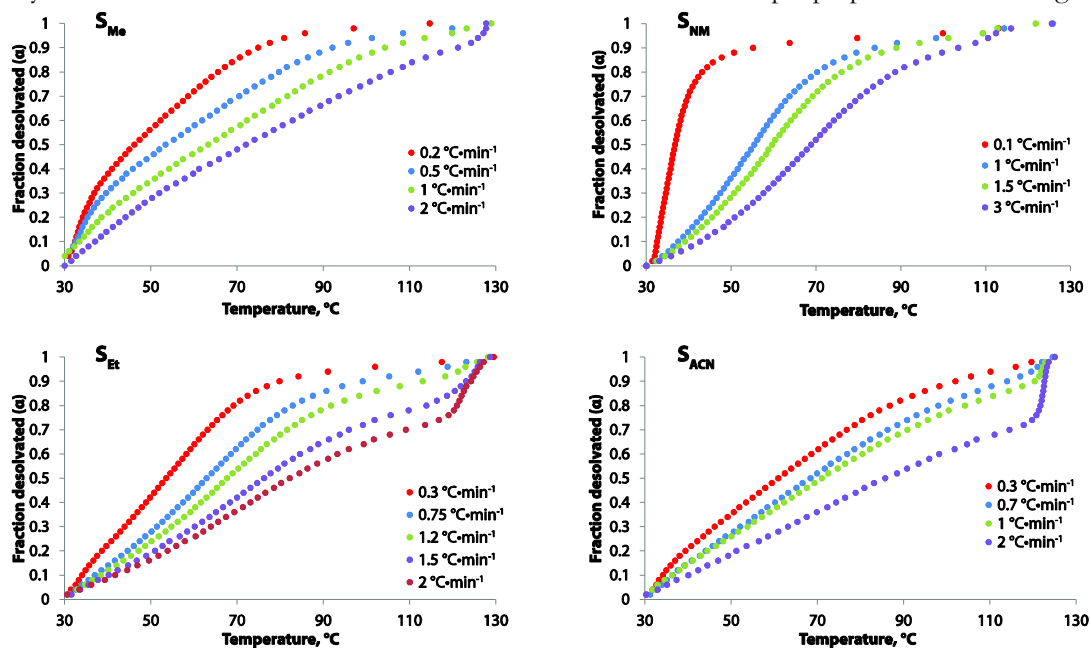


Fig. S9. Desolvation kinetic curves of droperidol solvate samples at different heating rates in nonisothermal mode.

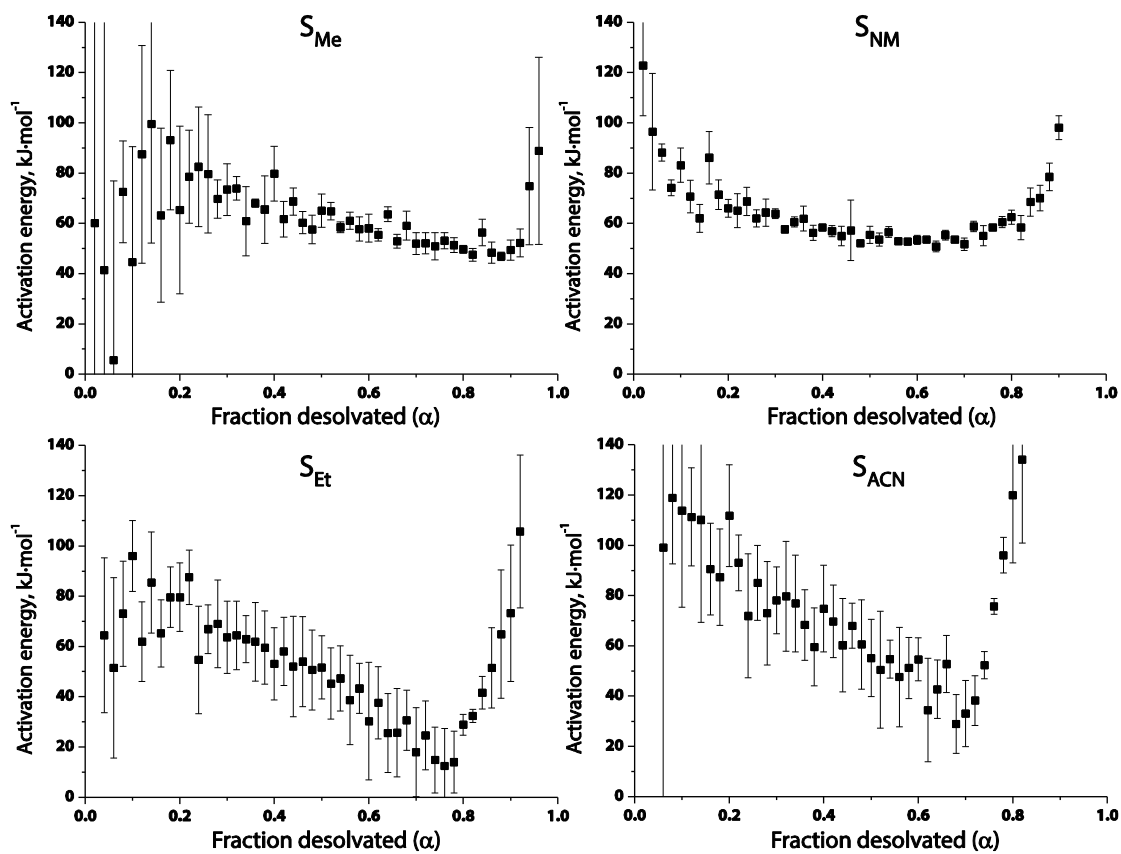


Fig. S10. Desolvation activation energy at different α values for droperidol solvate samples in nonisothermal mode.

DESOLVATION KINETIC MODEL

Table S3. Solid-state integral expressions $g(\alpha)$ for the most often used different reaction models²⁻⁷

Model	$g(\alpha)$	Model	$g(\alpha)$
Nucleation models		Diffusion models	
Power law (P2)	$\alpha^{1/2}$	1-D diffusion (D1)	$\alpha^2/2$
Power law (P3)	$\alpha^{1/3}$	2-D diffusion (D2)	$\alpha + (1-\alpha)\ln(1-\alpha)$
Power law (P4)	$\alpha^{1/4}$	3-D diffusion – Jander (D3)	$\left[1 - (1-\alpha)^{1/3}\right]^2$
Avrami-Erofeyev (A3/2)	$[-\ln(1-\alpha)]^{2/3}$	Ginstling-Brounshtein (D4)	$\left[1 - \frac{2}{3}\alpha - (1-\alpha)^{2/3}\right]$
Avrami-Erofeyev (A2)	$[-\ln(1-\alpha)]^{1/2}$	Zhuravlev (D5)	$\left[(1-\alpha)^{-1/3} - 1\right]^2$
Avrami-Erofeyev (A3)	$[-\ln(1-\alpha)]^{1/3}$	Reaction-order models	
Avrami-Erofeyev (A4)	$[-\ln(1-\alpha)]^{1/4}$	First-order (F1)	$-\ln(1-\alpha)$
Prout-Tompkins (B1)	$\ln\left[\frac{\alpha}{1-\alpha}\right]$	1.5-order (F3/2)	$2\left(\frac{1}{(1-\alpha)^{-1/2}} - 1\right)$
Geometrical contraction models		Second-order (F2)	$\frac{1}{(1-\alpha)} - 1$
Contracting disk (R1)	α	Third-order (F3)	$0.5\left((1-\alpha)^{-2} - 1\right)$
Contracting area (R2)	$\left[1 - (1-\alpha)^{1/2}\right]$		
Contracting volume (R3)	$\left[1 - (1-\alpha)^{1/3}\right]$		

Table S4. Correlation coefficients R^2 of fitting nonisothermal dehydration data of droperidol solvates with diffusion models (other models generally showed smaller R^2 values) according to the average linear integral method⁸.

	D1	D2	D3	D4	D5
S_{Me}	0.987	0.991	0.995	0.992	0.998
S_{Et}	0.9999	0.9998	0.9996	0.9997	0.9987
S_{NM}	0.993	0.994	0.995	0.994	0.996
S_{ACN}	0.996	0.997	0.997	0.997	0.998

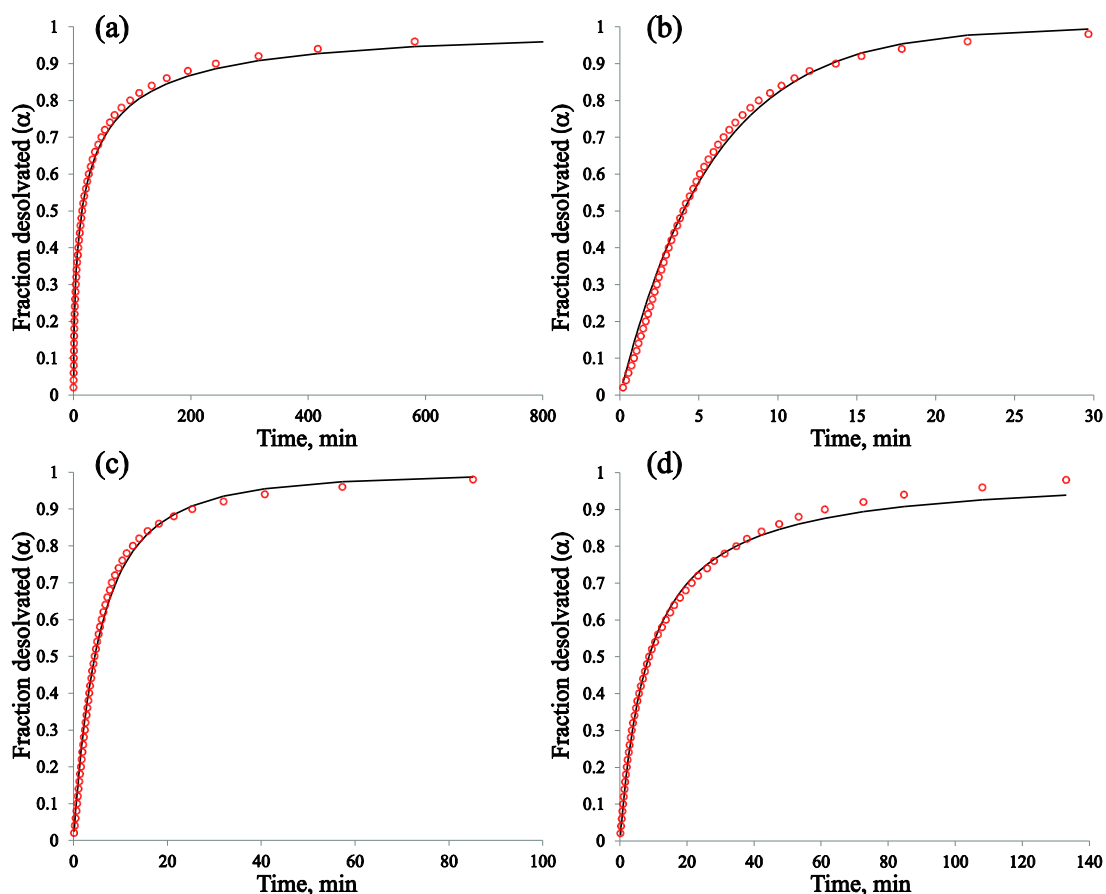


Fig. S11. Fit of the dehydration kinetic curves of different **NSH** samples with different kinetic models in isothermal mode: a) dehydration of *Crystals I* at 90 °C fitted with D5 model, b) dehydration of *Crystals III* at 80 °C fitted with F1 model, c) dehydration of *Small crystals II* at 35 °C fitted with F3/2 model, and d) dehydration of *Powder I* at 30 °C fitted with F2 model.

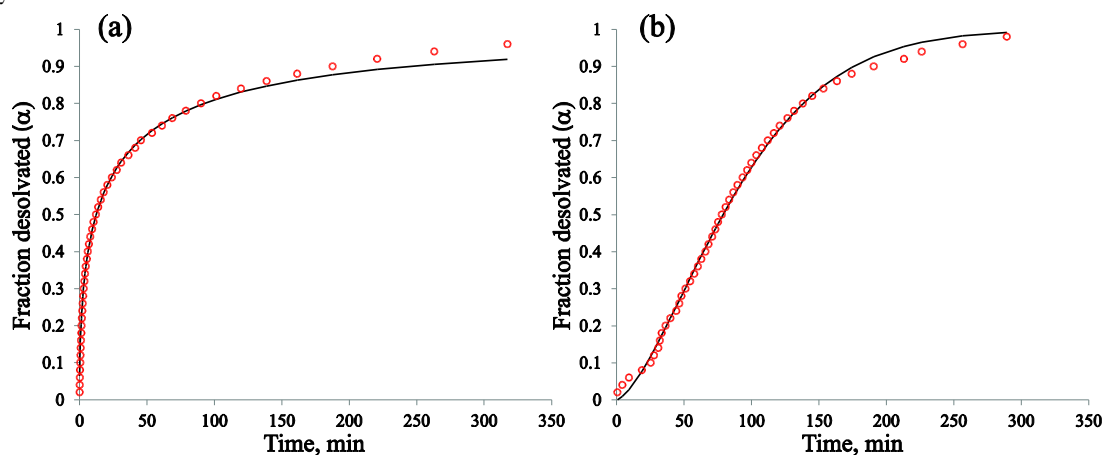


Fig. S12. Fit of the desolvation kinetic curves of droperidol solvate samples with different kinetic models in isothermal mode: a) desolvation of **S_{Me} Powder I** at 55 °C fitted with D5 model, and b) desolvation of **S_{Et} Small crystals** at 80 °C fitted with A3/2 model.

Interestingly, crystals of **S_{Me}** and **S_{Et}** had different shape of the desolvation curves (see Fig. S7) which reflected also in the different dehydration kinetic model (A3/2 or R2) determined for these samples (see Table S3). Moreover, particularly these two samples had lower E_a values (20-45 kJ·mol⁻¹, see Fig. S8) than the other samples of these solvates. Different kinetic model determined for crystalline **S_{Me}** and **S_{Et}** samples suggested that the desolvation process of these samples could be limited by different mechanism than the diffusion. However, dehydration mechanism of **NSH** crystals did not differ from that of the powdered **NSH** samples.

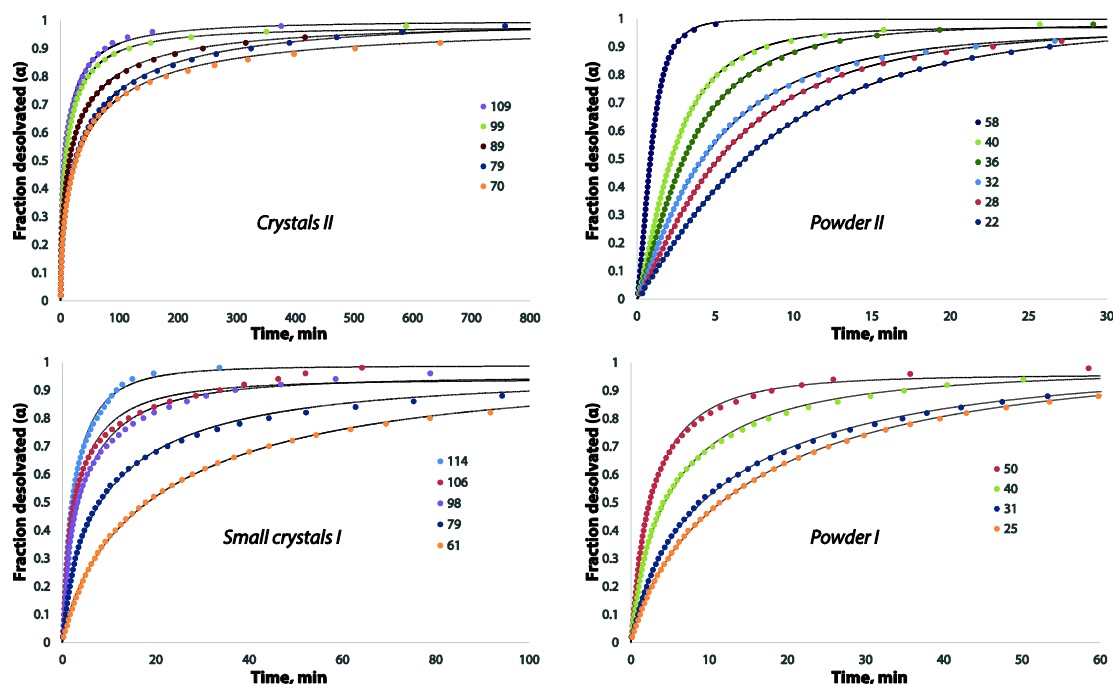


Fig. S13. Dehydration kinetic curves of different **NSH** samples at different temperatures in isothermal mode. Theoretical curves calculated using the modified D5 model (Eq. 1) are shown with black lines.

Possible explanation for the observed differences in the exact diffusion mechanism between the solvates can be the presence of different interactions between the solvent and the droperidol molecules, which could also explain the fact that the desolvation curves of organic solvates were more similar if compared with those of the **NSH**. The differences arising between the different samples could result from the different particle size distribution of the samples and/or different solvent content in the channels. Besides, also very differing particle size could introduce the changes in the diffusion mechanism (as observed for different **NSH** samples), because the channel length and the crystal shape can be very different. Although apparent deviations from the classical diffusion mechanisms could result from a wide particle size distribution, this would not result as different kinetic curves as observed for **NSH**.

For the kinetic curves best described with original D5 model, constant n in Eq. 1 was close to 1, whereas for curves best described by reaction order models F, n increased up to 3.

Table S5. Parameters for the modified D5 kinetic model (Eq. 1) providing the fit with different **NSH** sample dehydration kinetic curves

Crystals II	T, °C	70	79	89	99	109	
	k, min ⁻¹	0.00188	0.00161	0.00341	0.00511	0.00786	
	n	1.12	1.15	1.11	1.24	1.17	
	N	0.979	1.012	0.991	0.976	0.998	
Small crystals I	T, °C	61	79	98	106	114	
	k, min ⁻¹	0.000923	0.00430	0.0118	0.0182	0.0192	
	n	1.52	1.40	1.52	1.54	1.76	
	N	0.959	0.948	0.948	0.939	0.986	
Powder I	T, °C	25	31	40	50		
	k, min ⁻¹	0.00123	0.00224	0.00742	0.0160		
	n	1.62	1.54	1.56	1.77		
	N	1.016	1.003	0.975	0.957		
Powder II	T, °C	22	28	32	36	40	58
	k, min ⁻¹	0.000840	0.00164	0.00323	0.00501	0.0102	0.109
	n	2.29	2.31	2.22	2.43	2.52	2.90
	N	0.989	0.967	0.957	0.978	0.969	0.998

Table S6. Parameters for the modified D5 kinetic model (Eq. 1) providing the fit with different droperidol solvate sample desolvation kinetic curves

	T, °C	41	52	61	70	79	88	104
S _{Me} powder II	k, min ⁻¹	0.000962	0.00185	0.00408	0.00502	0.00755	0.0132	0.0331
	n	1.01	1.07	1.10	1.18	1.17	1.29	1.54
	N	1.137	1.125	1.026	1.062	1.054	0.989	0.957
	T, °C	52	62	66	71	80	99	106
S _{Et} powder	k, min ⁻¹	0.000753	0.00131	0.00204	0.00255	0.00611	0.0157	0.0244
	n	1.00	0.96	0.97	1.06	1.13	1.05	1.23
	N	1.120	1.172	1.135	1.093	1.042	1.021	0.973
	T, °C	89	94	109	114			
S _{ACN} powder	k, min ⁻¹	0.00372	0.00658	0.0154	0.0157			
	n	1.08	1.09	1.17	1.66			
	N	1.166	1.076	1.030	1.058			
	T, °C	89	98	103	108			
S _{NM} suspension	k, min ⁻¹	0.000702	0.00142	0.00125	0.00123			
	n	1.07	1.09	1.19	2.09			
	N	1.126	1.250	1.378	1.118			

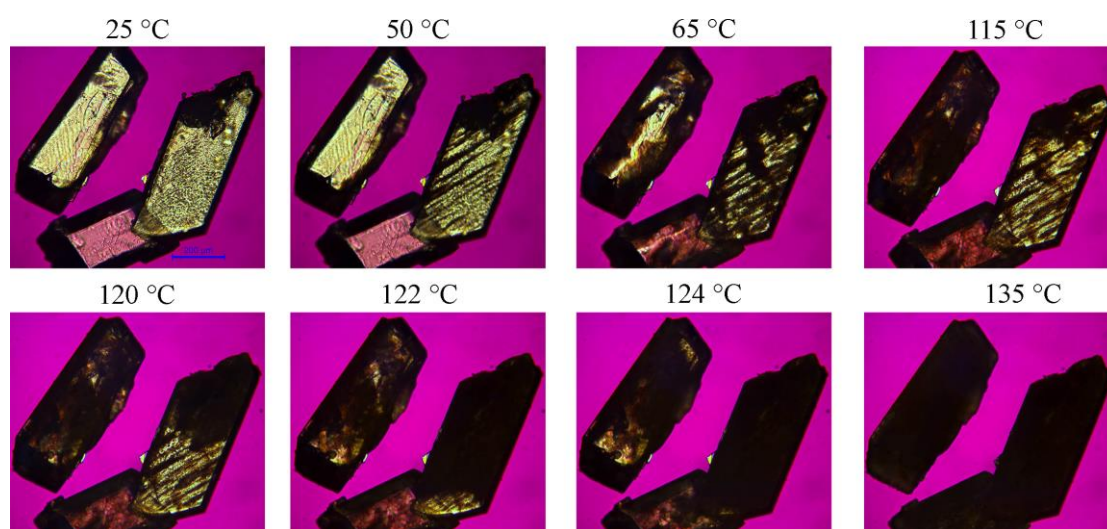


Figure S14. Hot stage photomicrographs revealing the changes during the dehydration process of **NSH** and its transformation to polymorph **I**.

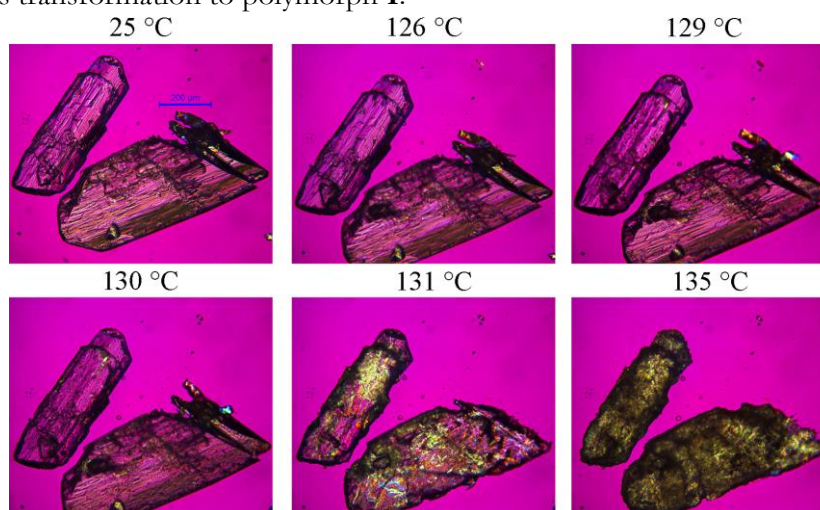


Figure S15. Hot stage photomicrographs revealing the changes during the desolvation process of **SMe** and its transformation to polymorph **I**.

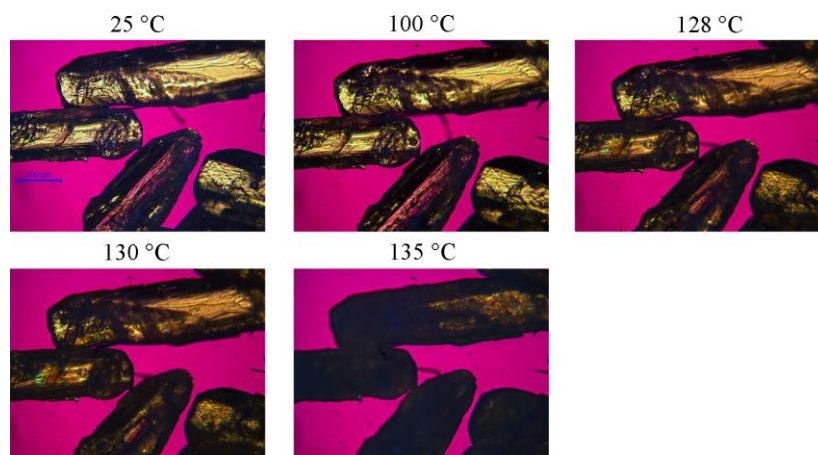


Figure S16. Hot stage photomicrographs revealing the changes during the desolvation process of S_{Et} and its transformation to polymorph I.

When the melting point solvate was reached, either fast transition or melt with a rapid desolvation and following recrystallization occurred by producing polymorph I, as already reported¹.

In the HSM study it was observed that the desolvation of S_{Me} and S_{Et} crystals are not controlled by the nucleation and nuclei growth or the phase boundary advance, as determined from the analysis of the desolvation kinetic curves. As for now, we do not have any explanation for this observation, but the most reasonable possibility is that the kinetic curves are strongly distorted due to a cause associated with the sample, but not yet identified.

THERMAL STABILITY OF THE SOLVATES

In the nonisothermal mode solvate which had reached higher fraction desolvated at a certain temperature using the same heating rate was considered to be less stable, whereas in isothermal mode solvate which desolvated faster at a given temperature was indicated to be less stable. When solvate stability was compared using PXRD patterns, time necessary for complete desolvation was identified by the match of the sample PXRD patterns to that of the **ISD**. These times are given in Table S8.

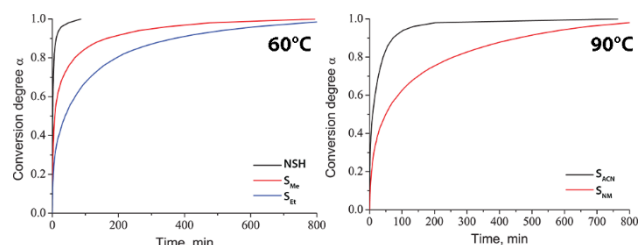


Figure S17. Desolvation kinetic curves of ground droperdiol isostructural solvate samples in isothermal mode at 60 °C and 90 °C temperature.

Slightly different order of stability was determined from the nonisothermal measurements recorded during the desolvation kinetic study (see Table S8). In these experiments S_{NM} desolvated at lower temperature than S_{ACN} , S_{Et} and S_{Me} . However, results from all of the other measurements performed with different S_{NM} samples confirmed that the stability of the S_{NM} is higher than that of all the other solvates. Incompatibility of this results most probably is associated with the differences in sample preparation or possible changes of the sample during the storage processes as this particular kinetic study was performed with only one sample.

Table S7. Characterization of droperidol solvate thermal stability from nonisothermal kinetic TG curves and PXRD patterns recorded during the isothermal desolvation

	NSH	S_{Me}	S_{Et}	S_{ACN}	S_{NM}
	T _{α=0.5^a} in nonisothermal kinetic curves, °C				
1 °·min ⁻¹	32	63	68	71	55
2 °·min ⁻¹	34	72	82	86	63
	Time for complete desolvation as determined from the PXRD measurements				
80°C	<0.5 h	1 h	-	-	-
100°C	-	-	4 h	5 h	48 h

^a – Temperature at which fraction desolvated (α)=0.5 was reached.

COMPARISON OF CRYSTAL STRUCTURES AFTER THE GEOMETRY OPTIMIZATION

Crystal structures obtained after the geometry optimization with different methods was compared based on: a) lattice parameters after full unit cell (UC) optimization, b) solvent arrangement in the channels and c) all intermolecular interaction geometry.

As already pointed out, it is essential to use the dispersion correction if full unit cell optimization is performed⁹, because proper description of dispersion interactions is crucial for correct description of the intermolecular interactions¹⁰⁻¹². Optimization of droperidol solvate crystal structures with pure PBE functional in *CASTEP* increased the unit cell volume by more than 20%, which was already reported for other organic crystal structures⁹. It can be seen that the cell volume was closest to the experimental one when PBE+TS (-3%) method was used (as already reported for other organic crystal structures⁹), while the optimization with B3LYP-D* (-6%) and PBE+G06 (-7.5%) resulted in slightly larger volume reduction (see Table S9).

Table S8. Comparison of the unit cell parameter changes of droperidol solvates and ISD introduced by different optimization methods

	a, Å	b, Å	c, Å	α, °	β, °	γ, °	V, Å ³
ACN	6.09	10.22	16.26	101.2	92.7	96.8	982.8
B3LYP	-2.0	-1.0	-2.6	-0.7	2.0	-0.5	-5.4
PBE+TS	-0.7	-0.9	-2.0	-1.4	0.4	0.0	-3.0
PBE+G06	-1.4	-1.0	-4.8	-1.3	1.8	0.8	-7.1
NM	6.07	10.19	16.42	99.8	92.3	95.6	993.9
B3LYP	-1.9	-1.1	-2.9	-1.0	2.4	-0.4	-5.7
PBE+TS	-0.5	-0.7	-2.3	-1.3	0.0	-0.2	-3.1
PBE+G06	-1.4	-0.9	-4.8	-1.8	1.1	0.5	-6.7
ET	6.08	10.30	16.17	100.9	92.6	95.9	987.3
B3LYP	-1.9	-1.1	-2.9	-1.0	1.2	-0.2	-5.6
PBE+TS	-0.5	-0.6	-2.5	-1.1	0.2	0.1	-3.3
PBE+G06	-1.2	-1.1	-5.6	-1.8	1.7	1.0	-7.6
ME	6.07	10.22	16.21	101.3	93.2	97.0	974.7
B3LYP	-2.5	-0.5	-3.1	-0.5	2.4	-0.5	-6.0
PBE+TS	-0.8	-0.5	-1.7	-0.7	0.6	0.0	-2.9
PBE+G06	-1.4	-0.8	-4.9	-1.2	1.6	0.5	-6.9
NSH 298 K	6.28	10.15	16.19	102.6	91.9	99.3	991.6
B3LYP	-3.8	0.7	-3.5	0.1	5.3	-2.1	-6.9
PBE+TS	0.2	-0.6	-4.3	-1.6	0.0	0.1	-4.1
PBE+G06	-3.5	-0.1	-7.2	-4.3	0.6	-2.3	-8.7
NSH 173 K	6.29	10.17	15.92	102.6	91.9	99.9	976.4
PBE+TS	0.5	-0.2	-2.9	-0.8	0.5	-0.2	-2.3
ISD^a	6.27	10.13	16.23	102.7	92.6	99.2	989.0
B3LYP	-2.2	0.3	-4.7	0.1	2.7	0.0	-6.9
PBE+TS	0.0	-0.1	-4.0	-1.2	0.6	-0.1	-3.6
PBE+G06	-1.1	-0.8	-6.7	-2.3	2.1	0.0	-7.9

^a - from PXRD data at ambient temperature

By comparing the individual lattice parameter changes after the optimization, it can be seen that all of the optimization schemes performed similarly by reducing a, b, c and α while not changing or slightly increasing angles β and γ. The changes introduced to the lattice parameters were almost the same for all solvates except

for the **NSH** which showed different behaviour of the unit cell parameter changes. Similar changes of the lattice parameters and volume was observed also for the isostructural desolvate **ISD**, for which calculated values were compared with lattice parameters determined from PXRD data at ambient temperature.

Evaluation of the changes introduced by HO and ALL structure optimization procedures was possible by comparing the geometry of intramolecular interactions and the solvent molecule arrangement in the crystal structure. Such a comparison is given in the Table S10 where only selected intermolecular interactions of the solvent molecules are given.

Table S9. Geometrical parameters of the selected solvent-droperidol intramolecular interactions (by using solvent-droperidol interaction labelling as given in Figure 6) in the droperidol solvate crystal structures after different geometry optimization procedures.

Solvate	Interaction	Parameter	B3LYP-D*	PBE+G06	PBE+TS	PBE+TS	PBE+TS
					UC	ALL	HO
S_{ACN}	N4···H-C5A	D···A, Å	3.565	3.6	3.603	3.642	3.704
	γ	D-H···A, °	161.2	162.6	162.4	161.9	161.3
	C24-H···H-C4A	D···A, Å	3.039	2.915	3.082	3.09	3.094
	α	D-H···A, °	126.3	122.9	127.6	128.4	128.2
	C24-H···π	D···A, Å	3.817	3.799	3.841	3.914	3.91
ε	D-H···A, °	158.9	167.1	165.6	168.3	169.5	
S_{NM}	O3···H-C4A	D···A, Å	3.195	3.325	3.362	3.395	3.44
	α	D-H···A, °	143.1	138.7	140.9	141.6	142.3
	O4···H-C5B	D···A, Å	3.147	3.184	3.202	3.258	3.269
	η	D-H···A, °	126	120.6	122.8	121.65	121.5
	C23-H···O1A	D···A, Å	3.307	3.371	3.309	3.335	3.32
δ	D-H···A, °	155.3	156.3	156.7	145.9	143.9	
S_{Et}	C24-H···π	D···A, Å	3.72	3.731	3.737	3.808	3.83
	δ	D-H···A, °	161.5	151.9	151.6	151.9	147.7
	O3-H···O1	D···A, Å	2.77	2.748	2.759	2.776	2.823
	ε	D-H···A, °	167.9	165.1	165.7	165.8	167.6
	O3···H-C5	D···A, Å	3.292	3.332	3.446	3.464	3.454
γ	D-H···A, °	133.4	139.9	129.1	127.9	129.7	
S_{Me}	O3-H···O1	D···A, Å	3.552	2.791	2.798	2.834	2.955
	ε	D-H···A, °	161.3	165.9	164.5	162.5	159.5
	C23-H···O1	D···A, Å	3.332	3.42	3.387	3.411	3.248
	δ	D-H···A, °	134	158.4	152.6	150.7	149.9
	C23-H···H3	D···A, Å	2.854	2.919	2.971	2.979	2.97
α	D-H···A, °	118.2	130	133.5	134.8	129	
NSH	O3-H···O1	D···A, Å			2.754	2.763	2.85
	ε	D-H···A, °			166.4	166.5	167.2
	O3···H-C9	D···A, Å	3.143	3.23	3.217	3.274	3.446
	ζ	D-H···A, °	168.4	121.2	128.9	128.6	126
	O3H···O3	D···A, Å	2.944	3.029	2.897	2.904	2.757
κ	D-H···A, °	104.4	112.4	121	121.3	119.6	

By comparing the solvent molecule arrangement and geometrical parameters of intermolecular interactions it was concluded that there were almost no differences for crystal structures of **S_{ACN}**, **S_{NM}** and **S_{Et}**. However, in **S_{Me}** similar location of the methanol methyl group, but completely different direction of the O-H bond was observed after the optimization with B3LYP-D* if compared with other optimization techniques (see Figure S18). This difference was a result of the bad initial position of the O-H hydrogen atom (not forming the hydrogen bond with benzimidazolone moiety). In **NSH** water molecules did not form any hydrogen bonds with droperidol molecules after geometry optimization with B3LYP-D* and PBE+G06, whereas after the structure optimization with PBE+TS water arrangement corresponded to that observed in the experimental **NSH** structure determined at 120 K¹ and there was a hydrogen bonding between the water molecule and the benzimidazolone moiety of droperidol molecule (See Figure S19).

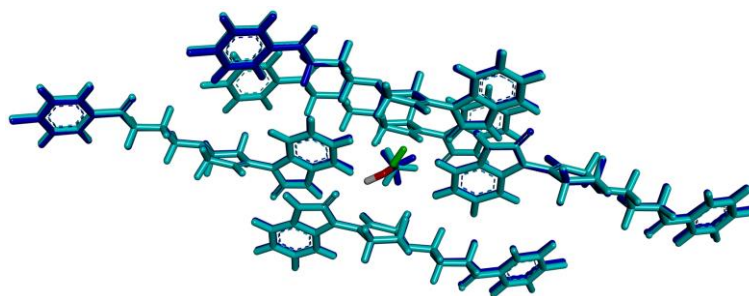


Figure S18. Overlay of **S_{Me}** crystal structure after UC geometry optimization procedure at the PBE+TS level in *CASTEP* (in dark blue, methanol OH group coloured by elements) and B3LYP-D level in *CRYSTAL09* (in cyan, methanol OH group coloured dark green).

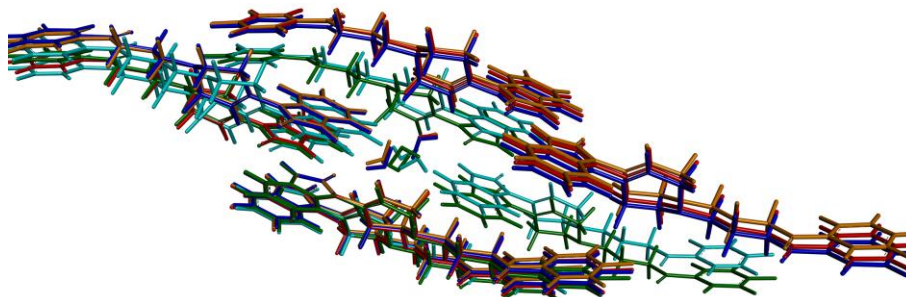


Figure S19. Overlay of **NSH** crystal structure after geometry optimization at the PBE+TS (UC in dark blue, ALL – red, HO – orange) and PBE+G06 (UC in green) level in *CASTEP* and B3LYP-D* level in *CRYSTAL09* (UC in cyan).

It was noticed that interatomic distances after ALL and HO optimization procedures generally were larger than those after UC optimization procedures because of the more compact molecule arrangement after the reduction of unit cell volume after the UC optimization.

By comparing the geometry of droperidol-droperidol intermolecular interactions it was concluded that there were no significant differences between the structures after different optimization procedures, and also between different solvates and even the **ISD**.

DROPEIDOL-DROPERIDOL INTERMOLECULAR INTERACTION ENERGY

Droperidol-droperidol intermolecular interaction energy in all solvates was compared for all of the optimized crystal structures to explore the possible differences introduced by the presence of different solvent molecules and to explore the effect of different structure optimization methods on the obtained results. In this analysis droperidol molecule pairs where droperidol-droperidol interactions with interatomic distance shorter than sum of atom Van der Waals radii were included. It was not checked whether interactions with other molecules were not relevant for the total interaction energy because the objective of this analysis was only to compare the differences between different solvents and results after different geometry optimization procedures and analysis of selected interactions was enough to reach this goal. Intermolecular interactions present in the selected droperidol molecule pairs A – G are given in the Table S11.

Table S10. Intermolecular interactions present in the droperidol molecule pairs A - G selected for the calculation of intermolecular interaction energy

Molecule pair	Interaction	Graph set
A	N2-H···O1	$R_2^2(8)$
B	C13-H···O2, $\pi \cdots \pi$	
C	C21-H···N3, C2-H··· π	
D	$\pi \cdots \pi$	
E	C18-H···O2	$R_2^2(10)$
F	C11-H···F1	
G	C19-H···F1	$R_2^2(8)$

It should be pointed out that after the geometry optimization in organic solvates basically there were two symmetrically independent droperidol molecules in the unit cell and interaction energies were evaluated only for one of these molecules. However, the droperidol molecules themselves are related by the inversion centre. Nevertheless, slight variations due to the presence of the solvate molecule most probably were introduced and thus could affect the calculated droperidol interaction energy.

Intermolecular interaction energy of droperidol molecule pairs were calculated at the B3LYP-D* level from a) all five solvate and **ISD** structures after UC optimization in *CASTEP* (PBE+G06) and *CRYSTAL09* (B3LYP-D*), b) **S_{ACN}**, **S_{Et}**, **NSH** and **ISD** structures after all three optimization procedures in *CASTEP* (PBE+TS), and c) **S_{NM}** and **S_{Me}** structures after ALL and UC optimization procedures in *CASTEP* (PBE+TS). Droperidol molecule pair interaction energy for all five solvate structures after UC optimisation in *CASTEP* (PBE+G06 and PBE+TS) was also calculated at the M06-2X level, while for **NSH** and **ISD** structures these calculations were also performed using semi-empirical *PIXEL*¹³ methodology (code provided in the CLP software suite). Empirical parameters were used as provided in the literature¹³. Hydrogen atom positions were kept as optimized with *CASTEP* or *CRYSTAL09*. Molecular electron density calculations were performed in *Gaussian 09*¹⁴ at the MP2/6-31G(d,p) level using standard grid parameters. Condensation level 4 was used.

From all of the calculations it was concluded that the intermolecular interactions between droperidol molecules as well as their energy were almost the same for all solvates and did not depend on the crystal structure optimization method. By comparing the results from different crystal structure optimization procedures it was determined that the most sensitive interaction was for the hydrogen bonded droperidol molecule dimer (A) where interaction energy varied by up to 1 kcal·mol⁻¹ for all structures and up to 0.8 kcal·mol⁻¹ for UC optimized structures (with the exception of **NSH**, which showed higher structure differences depending on the optimization method as discussed later, and thus interaction energy varied up to 1.5 kcal·mol⁻¹). By comparing the interaction energy of an individual molecule pairs from all of the structures, differences up to 1.7 kcal·mol⁻¹ was observed. However, also in this case extreme values were obtained for **NSH** and **ISD** crystal structures and thus can be related with an important differences in the arrangement of the solvent molecules in the channels. Calculated interaction energies between the droperidol dimers in each solvate after all performed geometry optimization procedures are given in Table S12 to S17.

Table S11. Interaction energy of droperidol-droperidol molecule pairs (in kcal·mol⁻¹) in **S_{ACN}** structure after different geometry optimization procedures

Molecule pair	B3LYP-D					M06-2X	
	TS, ALL	TS, HO	TS, UC	G06, UC	B3LYP-D*, UC	TS, UC	G06, UC
A	-21.84	-21.39	-21.73	-21.67	-21.11	-19.61	-19.55
B	-11.95	-11.62	-12.07	-12.1	-12.55	-7.65	-7.82
C	-11.8	-11.81	-12.04	-11.8	-11.87	-10.09	-10.33
D	-10.51	-10.54	-10.53	-10.69	-10.97	-8.91	-9.8
E	-6.06	-5.94	-6.02	-6.2	-5.98	-4.47	-4.72
F	-3.09	-3.06	-3.27	-3.22	-3.34	-1.33	-1.24
G	-2.7	-2.67	-2.74	-2.68	-2.63	-1.63	-1.63
Total	-94.79	-93.52	-95.78	-95.47	-96.21	-72.75	-74.48

Table S12. Interaction energy of droperidol-droperidol molecule pairs (in kcal·mol⁻¹) in **S_{NM}** structure after different geometry optimization procedures

Molecule pair	B3LYP-D				M06-2X	
	G06, UC	B3LYP-D*, UC	TS, ALL	TS, UC	TS, UC	G06, UC
A	-21.5	-20.81	-21.8	-21.85	-19.77	-19.44
B	-11.5	-11.85	-11.53	-11.48	-7.04	-7.27
C	-11.76	-11.98	-11.7	-11.92	-9.78	-10.11
D	-10.64	-10.92	-10.37	-10.5	-9.04	-9.76
E	-6.07	-5.95	-5.99	-6.03	-4.47	-4.58
F	-3.38	-3.38	-3.17	-3.32	-1.41	-1.37
G	-2.71	-2.68	-2.71	-2.74	-1.62	-1.64
Total	-94.2	-94.78	-93.67	-94.56	-71.36	-72.92

Table S13. Interaction energy of droperidol-droperidol molecule pairs (in kcal·mol⁻¹) in **S_{E1}** structure after different geometry optimization procedures

Molecule pair	B3LYP-D					M06-2X	
	TS, ALL	TS, HO	TS, UC	G06, UC	B3LYP-D*, UC	TS, UC	G06, UC
A	-22.02	-21.44	-22.06	-21.82	-21.37	-19.94	-19.73
B	-11.58	-11.63	-11.67	-11.73	-11.94	-7.28	-7.55
C	-11.74	-11.74	-11.94	-11.58	-11.73	-10.17	-10.28
D	-10.38	-10.58	-10.71	-10.84	-11.04	-9.33	-10.09
E	-5.98	-5.83	-6.01	-6.01	-5.93	-4.46	-4.54
F	-3.11	-3.1	-3.25	-3.31	-3.33	-1.31	-1.28
G	-2.69	-2.66	-2.69	-2.6	-2.67	-1.61	-1.6
Total	-93.93	-93.45	-95.18	-94.51	-95.01	-72.86	-74.18

Table S14. Interaction energy of droperidol-droperidol molecule pairs (in kcal·mol⁻¹) in **S_{Me}** structure after different geometry optimization procedures

Molecule pair	B3LYP-D				M06-2X	
	G06, UC	B3LYP-D*, UC	TS, ALL	TS, UC	TS, UC	G06, UC
A	-22.04	-21.12	-22.09	-22.22	-20.13	-19.95
B	-11.98	-12.73	-12.17	-12.4	-8.02	-7.84
C	-11.58	-11.49	-11.65	-11.66	-9.71	-10.14
D	-10.63	-10.79	-10.27	-10.56	-9.04	-9.78
E	-6.18	-5.98	-6.09	-6.12	-4.57	-4.71
F	-3.27	-3.33	-3.14	-3.29	-1.34	-1.29
G	-2.71	-2.69	-2.73	-2.74	-1.62	-1.63
Total	-95.23	-95.68	-95.1	-96.34	-73.5	-74.62

Table S15. Interaction energy of droperidol-droperidol molecule pairs (in kcal·mol⁻¹) in **NSH** structure after different geometry optimization procedures

Molecule pair	B3LYP-D			M06-2X			PIXEL	
	TS, ALL	TS, HO	TS, UC	TS, ALL	TS, HO	TS, UC	TS, ALL	TS, UC
A	-22.29	-21.4	-22.4	-20.2	-19.28	-20.33	-16.11	-16.85
B	-11.48	-11.42	-11.37	-6.83	-6.68	-6.77	-8.94	-8.89
C	-11.86	-11.88	-11.99	-9.6	-9.48	-9.98	-9.89	-9.56
D	-10.66	-10.84	-11.25	-8.48	-8.68	-9.47	-7.58	-7.74
E	-6.14	-6.02	-6.18	-4.65	-4.51	-4.72	-5.23	-5.35
F	-2.92	-2.25	-3.02	-1.26	-0.5	-1.3	-1.82	-1.86
G	-2.67	-2.59	-2.62	-1.6	-1.56	-1.59	-2.20	-2.10
Total	-94.28	-91.95	-95.22	-70.31	-67.35	-72.21	-72.42	-72.68

Table S16. Interaction energy of droperidol-droperidol molecule pairs (in kcal·mol⁻¹) in **ISD** structure after different geometry optimization procedures

Molecule pair	B3LYP-D					PIXEL	
	TS, ALL	TS, HO	TS, UC	G06, UC	B3LYP-D*, UC	TS, ALL	TS, UC
A	-21.62	-22	-21.59	-21.26	-20.77	-16.20	-17.57
B	-11.61	-11.5	-11.69	-11.83	-12.48	-9.25	-9.20
C	-11.84	-11.66	-12	-11.8	-11.84	-9.75	-9.49
D	-10.41	-10.42	-11.15	-11.2	-11.2	-7.34	-7.29
E	-6.12	-5.91	-6.25	-6.19	-6.13	-5.04	-5.16
F	-2.9	-2.84	-3.07	-3.16	-3.14	-2.08	-2.27
G	-2.73	-2.62	-2.66	-2.67	-2.68	-2.22	-2.17
Total	-93.59	-92.96	-95.17	-94.89	-95.71	-72.97	-74.12

The total droperidol interaction energy (a sum from all ten dimers, see Table S18) calculated at the B3LYP-D level varied up to 2.8 kcal·mol⁻¹ for different optimization methods (but only 0.8 kcal·mol⁻¹ for UC optimization procedures) within the same solvate (with the exception of **NSH** where changes up to 3.5 kcal·mol⁻¹ for all and 3.0 kcal·mol⁻¹ for UC optimization procedures were obtained). By comparing the total interaction energies from all solvates (excluding the **NSH**) with every optimization procedure, maximal differences were 3.3 kcal·mol⁻¹ for all and only 2.0 kcal·mol⁻¹ for UC optimization procedures.

Although similar conclusions were drawn also for interaction energy calculated at the M06-2X level, differences between different structures were higher: for UC optimized structures individual droperidol pair interaction energy varied by up to 1.4 kcal·mol⁻¹ and the total interaction energy varied by 3.3 kcal·mol⁻¹.

Table S17. Total droperidol-droperidol interaction energies (in kcal·mol⁻¹) calculated as a sum from the interaction energy of ten droperidol molecule pairs in the droperidol solvates after all used geometry optimization procedures

Solvate	B3LYP					M06-2X	
	TS, ALL	TS, HO	TS, UC	G06, UC	B3LYP-D*, UC	TS, UC	G06, UC
S_{ACN}	-94.79	-93.52	-95.78	-95.47	-96.21	-72.75	-74.48
S_{Et}	-93.93	-93.45	-95.18	-94.51	-95.01	-72.86	-74.18
S_{Me}	-95.1		-96.34	-95.23	-95.68	-73.5	-74.62
S_{NM}	-93.67		-94.56	-94.2	-94.78	-71.36	-72.92
NSH	-94.28	-91.95	-95.22			-72.21	
ISD	-93.59	-92.96	-95.17	-94.89	-95.71		

As already mentioned, droperidol interaction energies of **NSH** were calculated at the M06-2X level, while those of **NSH** and **ISD** were also calculated with semi-empirical PIXEL code. Interaction energy calculated at the M06-2X level was by 1 to 4.7 kcal·mol⁻¹ lower than that calculated at the B3LYP-D level. The difference could not be associated with the magnitude of the interaction energy and the biggest difference was observed for droperidol molecule pair B. Resulting total droperidol interaction energy was 23-25 kcal·mol⁻¹ lower than that calculated at the B3LYP-D level. In PIXEL calculated interaction energy was 0.5 to 6.2 kcal·mol⁻¹ lower than that calculated at the B3LYP-D level with the biggest difference observed for hydrogen bonded droperidol molecule pair A. Although the difference between energy calculated at the M06-2X level and in PIXEL varied from -4 to +2 kcal·mol⁻¹, total droperidol interaction energy between these two methods differed only 0.5 to 2 kcal·mol⁻¹.

SOLVENT INTERMOLECULAR INTERACTION ENERGY

It was determined that for all of the solvates it was enough to include the solvent interactions with droperidol molecules for which the shortest interatomic distance was below Van der Waals radii + 0.6 Å (for most of the solvents smaller distances were enough to obtain the same solvent-droperidol interactions, whereas this value had to be used for **NSH** because of the smaller size of water molecules if compared to the other solvent molecules) and the interactions with the closest solvent molecules. It was also confirmed that no other droperidol molecule had an intramolecular interaction with the solvent molecule even if the cutoff value for interatomic distance was increased to Van der Waals radii + 1.5 Å, and it was proved that if the solvent molecule in a particular solvate formed intramolecular interaction with distance longer than Van der Waals radii + 0.6 Å, interaction between these molecules was energetically irrelevant and did not change the total solvent interaction energy.

It was confirmed that the geometry of strong hydrogen bond O3-H···O1 in **NSH**, **S_{Me}** and **S_{Et}** with a droperidol molecule was almost identical and was not disturbed by different geometry optimization procedures (with the exception of **NSH** structure after geometry optimization at the PBE+G06 level in *CASTEP* and B3LYP-D* level in *CRYSTAL09*).

Solvent molecule interaction energy for all crystal structures was calculated at both B3LYP-D and M06-2X levels. Obtained results are presented in Table S19 to S23.

Table S18. Interaction energy of solvent-droperidol and solvent-solvent molecule pairs (in kcal·mol⁻¹) in **S_{ACN}** structure after different geometry optimization procedures

Molecule pair	B3LYP-D					M06-2X				
	TS, ALL	TS, HO	TS, UC	B3LYP-D*, UC	G06, UC	TS, ALL	TS, HO	TS, UC	B3LYP-D*, UC	G06, UC
α	-0.72	-0.75	-0.75	-0.74	-0.54	-0.03	-0.05	-0.07	-0.11	0.02
β	-0.97	-0.96	-1	-0.99	-0.96	-0.1	-0.09	-0.07	-0.03	0.07
γ	-2.52	-2.44	-2.54	-2.41	-2.61	-2.08	-2	-2.11	-1.96	-2.18
δ	-6.53	-6.4	-6.61	-6.18	-6.31	-5.79	-5.57	-6.06	-5.64	-5.85
ϵ	-2.4	-2.39	-2.5	-2.81	-2.25	-1.54	-1.5	-1.68	-2	-1.52
ζ	-1.34	-1.39	-1.24	-1.13	-1.09	-0.83	-0.84	-0.73	-0.62	-0.63
η	-2.78	-2.78	-2.8	-2.71	-2.81	-2.34	-2.28	-2.34	-2.22	-2.41
θ	0.4			0.34	0.41	0.93			0.97	0.88
ι	-2.62	-2.55	-2.65	-2.75	-2.71	-2.52	-2.44	-2.56	-2.64	-2.68

Table S19. Interaction energy of solvent-droperidol and solvent-solvent molecule pairs (in kcal·mol⁻¹) in **S_{NM}** structure after different geometry optimization procedures

Molecule pair	B3LYP-D					M06-2X				
	TS, ALL	TS, HO	TS, UC	B3LYP-D*, UC	G06, UC	TS, ALL	TS, HO	TS, UC	B3LYP-D*, UC	G06, UC
α	-1.03	-1.14	-0.89	-0.53	-0.58	-0.27	-0.39	-0.16	0.16	0.07
β	-1.03	-0.99	-1.06	-1.09	-1.01	-0.09	-0.06	-0.02	0.01	0.12
γ	-2.39	-2.72	-2.49	-2.33	-2.54	-1.91	-2.3	-2.01	-1.82	-2.06
δ	-8	-8.76	-8.28	-8.52	-7.65	-7.16	-7.99	-7.62	-7.83	-7.01
ϵ	-3.66	-3.34	-3.64	-3.7	-3.75	-2.63	-2.26	-2.66	-2.79	-2.92
ζ	-1.91	-1.77	-1.9	-1.33	-1.8	-1.32	-1.06	-1.29	-0.63	-1.27
η	-2.42	-2.36	-2.38	-2.35	-2.34	-2.02	-1.88	-2.02	-2	-1.97
θ	0.61			0.59	0.62	1.14			1.11	1.07
ι	-1.92	-1.94	-2.02	-2.19	-2.12	-1.91	-1.93	-2.02	-2.12	-2.17

Table S20. Interaction energy of solvent-droperidol and solvent-solvent molecule pairs (in kcal·mol⁻¹) in **S_{E_t}** structure after different geometry optimization procedures

Molecule pair	B3LYP-D					M06-2X				
	TS, ALL	TS, HO	TS, UC	B3LYP-D*, UC	G06, UC	TS, ALL	TS, HO	TS, UC	B3LYP-D*, UC	G06, UC
α	-2.31	-2.4	-2.35	-2.34	-2.38	-1.76	-1.81	-1.8	-1.81	-1.91
β	-1.26	-1.26	-1.24	-1.06	-1.14	-0.46	-0.48	-0.43	-0.29	-0.37
γ	-1.18	-0.78	-1.17	-1.24	-1.06	-0.41	0.04	-0.41	-0.39	-0.28
δ	-5.28	-4.68	-5.39	-5.66	-5.32	-4.47	-3.87	-4.73	-4.99	-4.96
ϵ	-8.4	-9.48	-8.25	-8.33	-7.95	-7.2	-8.38	-7.08	-7.19	-7.06
ζ	-1.63	-1.63	-1.68	-1.61	-1.33	-0.51	-0.53	-0.54	-0.42	-0.2
η	-1.38	-1.48	-1.35	-1.31	-1.16	-0.76	-0.87	-0.77	-0.75	-0.69
θ	-0.53	-0.61	-0.52	-0.53	-0.51	0.02	-0.09	0.05	0.03	0.06
ι	-0.44	-0.37	-0.46	-0.46	-0.46	-0.35	-0.29	-0.37	-0.37	-0.37

Table S21. Interaction energy of solvent-droperidol and solvent-solvent molecule pairs (in kcal·mol⁻¹) in **S_{Me}** structure after different geometry optimization procedures

Molecule pair	B3LYP-D					M06-2X				
	TS, ALL	TS, HO	TS, UC	B3LYP-D*, UC	G06, UC	TS, ALL	TS, HO	TS, UC	B3LYP-D*, UC	G06, UC
α	-1.46	-1.56	-1.5	-1.62	-0.28	-0.87	-0.98	-0.93	0.01	-1.43
β	-1	-1.09	-1.05	-0.83	-1.57	-0.34	-0.38	-0.35	-0.31	-1.12
γ	-0.41			-1.15	-1.08	-0.12			-0.34	-0.29
δ	-3.27	-3.17	-3.37	-5.74	-3.13	-2.29	-2.28	-2.41	-4.68	-2.16
ϵ	-9.23	-9.27	-9.23	-1.15	-9.08	-8.4	-8.4	-8.45	-0.34	-8.55
ζ	-1.83	-1.69	-1.79	-5.74	-1.65	-1.25	-1.12	-1.19	-4.68	-1.05
η	-1.95	-1.88	-1.94	-1.62	-2	-1.65	-1.57	-1.65	-1.15	-1.7
θ	-0.23		0.16	-0.17	-0.25				0.15	0.23
ι	-0.35	-0.38	-0.37	-0.12	-0.38	-0.32	-0.35	-0.35	-0.37	-0.04

Table S22. Interaction energy of solvent-droperidol and solvent-solvent molecule pairs (in kcal·mol⁻¹) in **NSH** structure after different geometry optimization procedures

Molecule pair	B3LYP-D					M06-2X				
	TS, ALL	TS, HO	TS, UC	B3LYP-D*, UC	G06, UC	TS, ALL	TS, HO	TS, UC	B3LYP-D*, UC	G06, UC
α	-0.42	-0.65	-0.35	-0.27	0.28	0.04	-0.19	0.1	0.07	-0.2
β	-1.42	-1.49	-1.72	1.27	-1.83	-0.86	-0.83	-1.08	0.38	-1.48
γ	-0.83	-0.75	-0.82	-2.26	-2.39	-0.3	-0.08	-0.27	-1.97	-2.16
δ	0.1			0.29	0.2	0.22			0.29	0.37
ϵ	-7.98	-7.47	-8.15	-3.86	-3.1	-7.51	-6.93	-7.7	-3.23	-2.4
ζ	-1.91	-1.51	-2.04	-0.49	0.08	-1.62	-1.1	-1.79	-0.14	0.5
η	-1.68	-1.7	-1.62	-1.43	-0.1	-1.54	-1.56	-1.48	-0.92	1.47
θ	0.11			-1.29	-2.23	0.18			-1.15	-2.1
κ	-3.85	-3.43	-3.77	-4.16	-4.18	-3.77	-3.57	-3.69	-4.12	-3.99
ι	0.05	0.67	0.07	-4.39	-3.94	0.1	0.74	0.11	-4.17	-3.64

For **NSH** water molecule interaction energy calculation was also performed with PIXEL. In contrast to the droperidol-droperidol interactions, the total water interaction energy calculated with PIXEL was almost identical to that calculated at the B3LYP-D in *Gaussian 09*, although the energy calculated for particular molecule pairs differed by up to 1 kcal·mol⁻¹.

Exclusion of the solvent-solvent intermolecular interaction energy from the total solvent intermolecular interaction energy significantly reduced its value for **S_{ACN}** and **S_{NM}**, by changing the order of the solvates sorted with respect to this parameter and making the differences between the total solvent interaction energy smaller if compared with the case where all of the solvent interactions were taken into account (see Fig. S20).

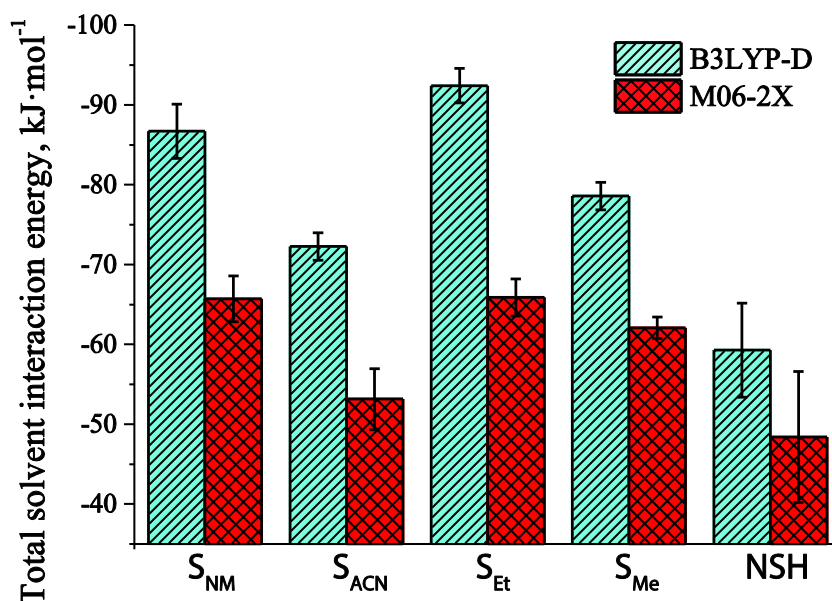


Fig. S20. Average total solvent interaction energy excluding solvent-solvent interaction energy calculated in *Gaussian 09* after the structure optimization at the PBE+TS level in *CASTEP* for all droperidol solvates.

By adding together the energy for all the interactions present in the unit cell (from two droperidol molecules and from one solvent molecule in organic solvates and two water molecules in **NSH**, by taking into account correction for the double summation of droperidol-droperidol and water-water interactions), it was observed that the interaction efficiency calculated at the B3LYP-D level changed in the same order as observed when only the total solvent interaction energy was calculated at the M06-2X level (see Fig. S21). The only exception was the more negative energy of the **S_{ACN}** if compared with that of **S_{NM}**, because of the more efficient droperidol-droperidol molecule interactions in **S_{ACN}**. This was also observed when the interaction energy was calculated at the M06-2X level. This most probably is due to the fact that nitromethane is the largest of all the analyzed solvent molecules, and particularly its size perpendicular to the channel direction is larger than that for other solvent molecules. However, for **S_{Me}** at the M06-2X level calculated total droperidol-droperidol and solvent interaction energy was more negative than that in **S_{Et}** and even in **S_{NM}** by thus changing the order of the solvates sorted by this parameter. This could probably be because small size of the methanol molecules allowed more efficient packing and thus the interaction between the droperidol molecules. This effect was not observed in the **NSH** structure, which could be explained by the formation of monohydrate, while the methanol formed hemimethanolate.

However, the presence of two water molecules in the unit cell of **NSH** resulted the total droperidol-droperidol and solvent interaction energy of this solvate to be the most negative one (see Fig. S21).

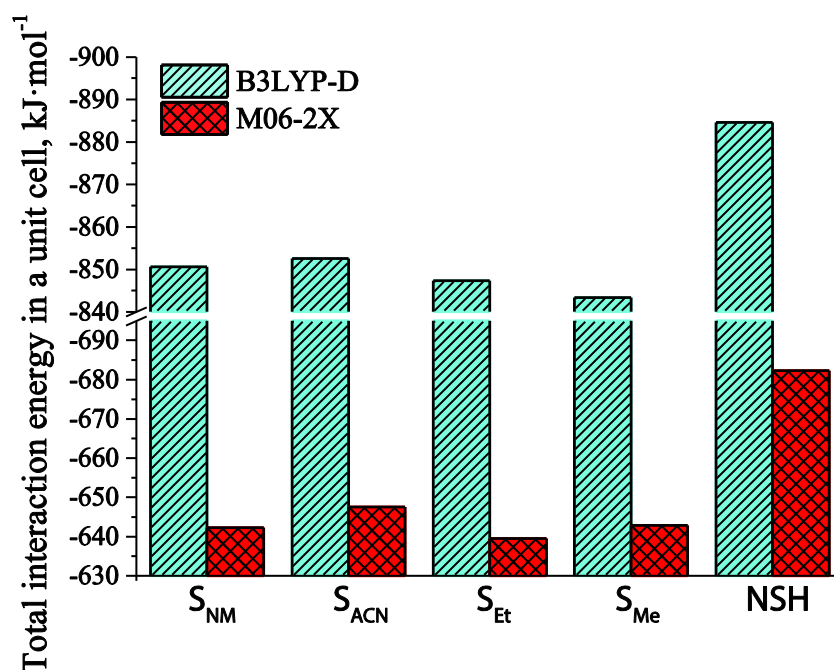


Fig. S21. Total droperidol-droperidol and solvent interaction energy in the unit cell calculated in *Gaussian 09* after the structure optimization at the PBE+TS level with UC optimization procedure in *CASTEP* for all droperidol solvates.

EFFECT OF THE REORIENTATION OF THE ALCOHOL MOLECULES

In order to confirm the validity of the ordered solvent model for alcohol solvates, the effect of the reorientation of the alcohol molecule to the opposite direction than that of the adjacent molecules on the interaction energy was evaluated.

The unit cell of these solvates was doubled in the solvent channel (*a*-axis) direction and one of the solvent molecules was flipped to the opposite direction by obtaining the “*opposite direction*” structure. Geometry optimization of this structure was performed in *CASTEP* (PBE+TS, ALL). Solvent-droperidol and solvent-solvent interaction energies were calculated for both different alcohol molecules in the “*opposite direction*” unit cell. Comparison of the total solvent interaction energy in “*same direction*” structure to that in “*opposite direction*” structure revealed that this value was the same for **S_{Et}**, and was only slightly less effective for **S_{Me}**. By analyzing the interaction energies for individual molecule pairs it was found that the variable most affecting the total solvent interaction energy in **S_{Me}** was the interactions between two adjacent alcohol molecules (see Table S24).

These results and the observation that the alcohol-alcohol interaction energy in **S_{Me}** and **S_{Et}** had only minor contribution in the total solvent interaction energy justified that it was reasonable to approximate the disordered **S_{Me}** and **S_{Et}** structures with the ordered ones.

Table S23. From individual molecule pairs calculated total solvent interaction energy and solvent-solvent interaction energy in “*same direction*” and “*opposite direction*” droperidol alcohol solvate structures (in kJ·mol⁻¹)

	“ <i>same direction</i> ”		“ <i>opposite direction</i> ”			
	Total	Solvent pair ^a	Total ₁	Total ₂ ^b	Solvent pair ₁ ^a	Solvent pair ₂ ^{a,b}
S_{Et}	-68.0	-1.2	-69.0	-69.0	-2.3	-1.0
S_{Me}	-64.6	-1.5	-58.2	-58.5	0.0	3.1

^a – interaction energy between two adjacent alcohol molecules.

^b – there are two different alcohol molecules in the “*opposite direction*” structure.

SOLVENT SORPTION ISOTHERMS OF DROPERIDOL ISOSTRUCTURAL SOLVATES

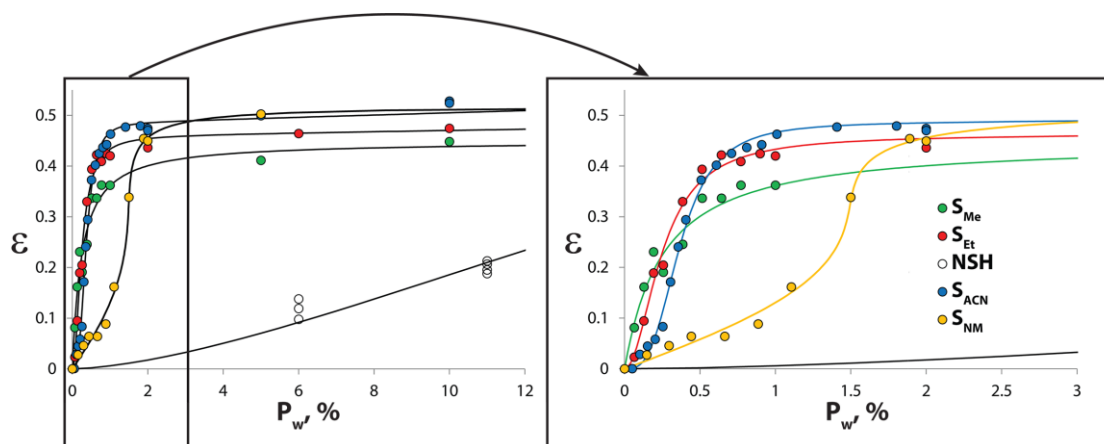


Fig. S22. Initial part of the droperidol isostructural solvate sorption-desorption isotherms¹.

REFERENCES

- (1) Bērziņš, A.; Skarbulis, E.; Reķis, T.; Actiņš, A. *Cryst. Growth Des.* **2014**, 14, (5), 2654-2664.
- (2) Khawam, A.; Flanagan, D. R. *J. Pharm. Sci.* **2006**, 95, (3), 472-498.
- (3) Khawam, A.; Flanagan, D. R. *J. Phys. Chem. B* **2006**, 110, (35), 17315-17328.
- (4) Koradia, V.; de Diego, H. L.; Elema, M. R.; Rantanen, J. *J. Pharm. Sci.* **2010**, 99, (9), 3966-3976.
- (5) Sheth, A. R.; Zhou, D.; Muller, F. X.; Grant, D. J. W. *J. Pharm. Sci.* **2004**, 93, (12), 3013-3026.
- (6) Dickinson, C. F.; Heal, G. R. *Thermochim. Acta* **1999**, 340-341, (0), 89-103.
- (7) Galwey, A. K.; Brown, M. E., *Thermal Decomposition of Ionic Solids*. ed.; Elsevier: Amsterdam, 1999; p 598.
- (8) Ortega, A. *Thermochim. Acta* **2008**, 474, (1-2), 81-86.
- (9) Dudenko, D. V.; Yates, J. R.; Harris, K. D. M.; Brown, S. P. *CrystEngComm* **2013**, 15, (43), 8797-8807.
- (10) Moellmann, J.; Grimme, S. *Phys. Chem. Chem. Phys.* **2010**, 12, (30), 8500-8504.
- (11) Heitmann, D.; Pape, T.; Hepp, A.; Mück-Lichtenfeld, C.; Grimme, S.; Hahn, F. E. *J. Am. Chem. Soc.* **2011**, 133, (29), 11118-11120.
- (12) Reckien, W.; Bredow, T. *Chem. Phys. Lett.* **2011**, 508, (1-3), 54-58.
- (13) Gavezzotti, A. *New J. Chem.* **2011**, 35, (7), 1360-1368.
- (14) Frisch, M. J.; Trucks, G. W.; Schlegel, H. B.; Scuseria, G. E.; Robb, M. A.; Cheeseman, J. R.; Scalmani, G.; Barone, V.; Mennucci, B.; Petersson, G. A.; Nakatsuji, H.; Caricato, M.; Li, X.; Hratchian, H. P.; Izmaylov, A. F.; Bloino, J.; Zheng, G.; Sonnenberg, J. L.; Hada, M.; Ehara, M.; Toyota, K.; Fukuda, R.; Hasegawa, J.; Ishida, M.; Nakajima, T.; Honda, Y.; Kitao, O.; Nakai, H.; Vreven, T.; Montgomery, J. A. J.; Peralta, J. E.; Ogliaro, F.; Bearpark, M.; Heyd, J. J.; Brothers, E.; Kudin, K. N.; Staroverov, V. N.; Kobayashi, R.; Normand, J.; Raghavachari, K.; Rendell, A.; Burant, J. C.; Iyengar, S. S.; Tomasi, J.; Cossi, M.; Rega, N.; Millam, J. M.; Klene, M.; Knox, J. E.; Cross, J. B.; Bakken, V.; Adamo, C.; Jaramillo, J.; Gomperts, R.; Stratmann, R. E.; Yazyev, O.; Austin, A. J.; Cammi, R.; Pomelli, C.; Ochterski, J. W.; Martin, R. L.; Morokuma, K.; Zakrzewski, V. G.; Voth, G. A.; Salvador, P.; Dannenberg, J. J.; Dapprich, S.; Daniels, A. D.; Farkas, O.; Foresman, J. B.; Ortiz, J. V.; Cioslowski, J.; Fox, D. J. *Gaussian 09*, Gaussian Inc., Wallingford, CT: 2009.

Appendix 10. Supplementary Information for publication “Solid-state NMR and computational investigation of solvent molecule arrangement and dynamics in isostructural solvates of droperidol”

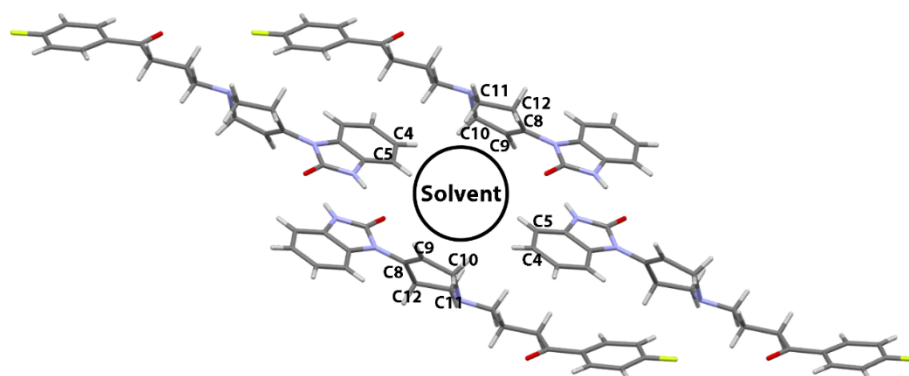


Fig. S1. Molecular packing in the droperidol isostructural solvates showing the carbon atoms in proximity to the solvent molecules.

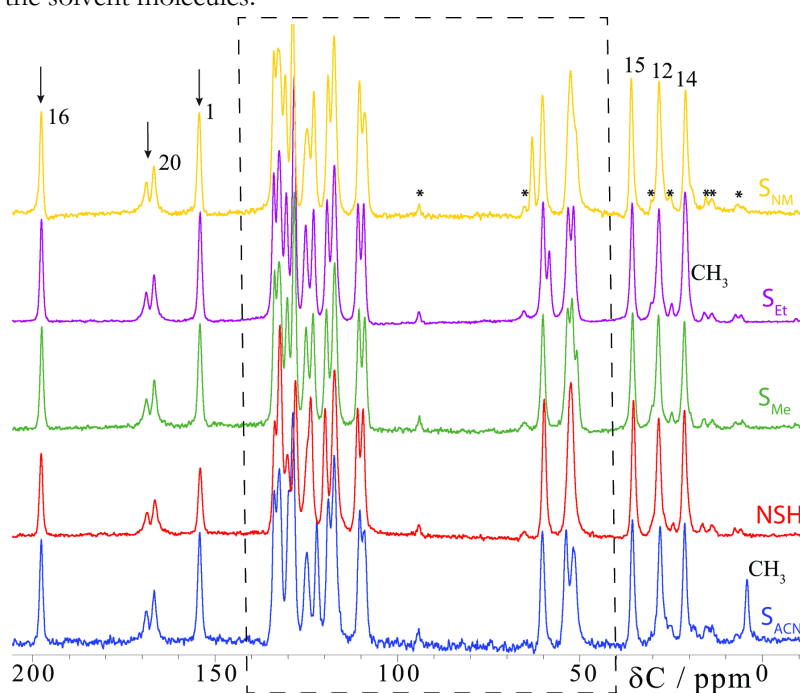


Figure S2. Full ¹³C CPMAS spectra of the droperidol isostructural solvates, together with peak assignment. Spinning sidebands are marked with asterisks, signals that disappear in short CP contact time experiments are marked with arrows. The dashed rectangle marked region is enlarged in Figure 2.

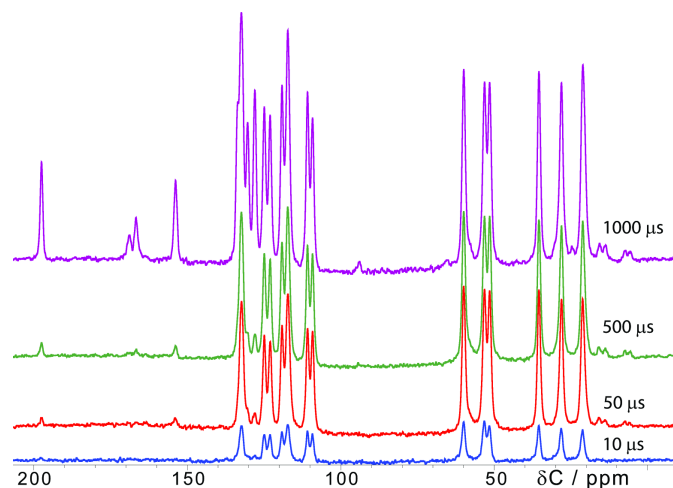


Fig. S3. ¹³C CPMAS spectra for S_{Et} using different contact times at -40 °C.

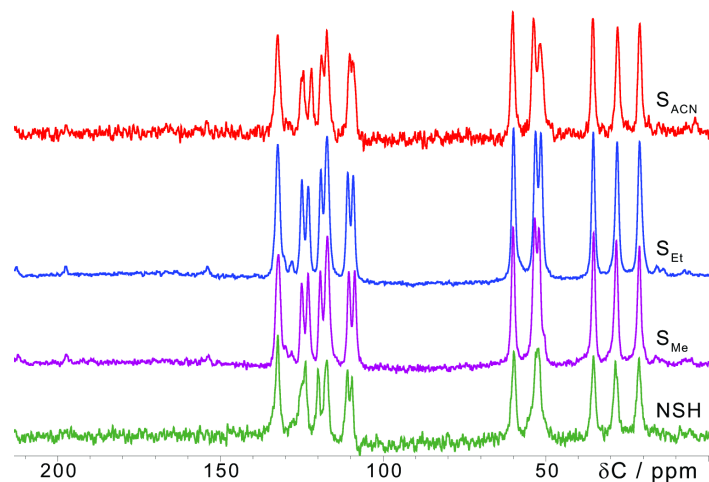


Fig. S4. ^{13}C CPMAS spectra for droperidol solvates using 50 μs contact time.

Table S1. Rescaled average calculated ^{13}C chemical shifts (in ppm) after optimisation of only hydrogen atoms, plus the difference between the same carbon atom in two molecules in the unit cell.

Assig	S_{Me}			S_{Et}		S_{ACN}		S_{NM}	
	δ_{HO}	δ_{HO}	dif.	δ_{HO}	dif.	δ_{HO}	dif.	δ_{HO}	dif.
C16	200.2	199.1	5.8	200.8	0.3	200.3	3.2	200.6	0.2
C20	170.6	170.6	5.9	171.4	2.1	171.5	3.5	170.3	4.2
C1	149.9	150.9	0.3	147.4	1.4	148.4	1.4	147.7	0.9
C17/C8	137.4	135.5	6.0	134.1	3.8	134.4	3.7	134.6	4.7
C18	133.1	132.1	4.4	133.5	0.4	134.7	0.7	134.7	1.3
C22	132.7	131.0	5.8	132.8	1.9	134.6	1.2	134.1	1.5
C17/C8	131.7	131.1	4.4	132.5	0.2	132.1	0.7	132.7	2.7
C6	128.4	127.5	1.1	128.0	0.0	127.6	1.1	129.8	3.7
C7	127.5	125.9	3.6	126.2	3.0	126.8	3.5	126.3	3.9
C9	122.3	128.6	1.5	127.6	4.1	127.1	5.2	125.8	6.5
C4	121.7	124.5	4.5	120.9	3.2	123.0	2.1	121.7	2.8
C3	117.9	116.2	5.3	117.7	2.4	117.4	2.0	115.7	5.1
C19	115.8	117.5	0.2	119.2	2.6	117.0	3.3	117.6	0.2
C21	115.8	115.6	6.6	115.5	4.4	116.9	1.8	117.5	1.9
C2	109.4	109.8	0.4	109.2	2.2	109.2	1.8	108.0	0.2
C5	105.6	105.9	3.6	107.4	2.4	107.8	3.7	106.9	5.5
C13	62.6	61.1	1.7	60.5	1.8	61.4	0.6	61.1	0.9
C11	54.5	53.4	1.5	53.5	1.8	54.7	0.2	54.5	0.4
C10	54.2	53.2	1.1	51.9	4.4	52.4	0.9	54.3	0.4
C15	35.1	35.4	0.9	37.7	0.8	36.1	1.7	37.0	1.2
C12	27.8	27.8	1.0	29.1	0.5	28.6	0.1	29.2	1.1
C14	21.1	20.5	0.2	20.7	2.3	20.8	0.9	21.3	0.7
CH₃^{solv}		53.8		22.3		4.1		59.3	
CH₂/CN^{solv}				56.5		120.6			
RMSD	2.16	1.87		2.18		2.54		2.27	

Droperidol dihydrate, **DH**, was prepared by dissolving droperidol in acetone at 50 °C, cooling the solution to ~10 °C, slowly adding similar volume of water and then slowly partially evaporating the resulting solution at 5 °C. Droperidol polymorph **II** was obtained by recrystallizing the sample from acetone at 50 °C [1]. ^{13}C CP/MAS spectra of **II** and **DH** were recorded with the same conditions as described in the main text, using a 120 s recycle delay.

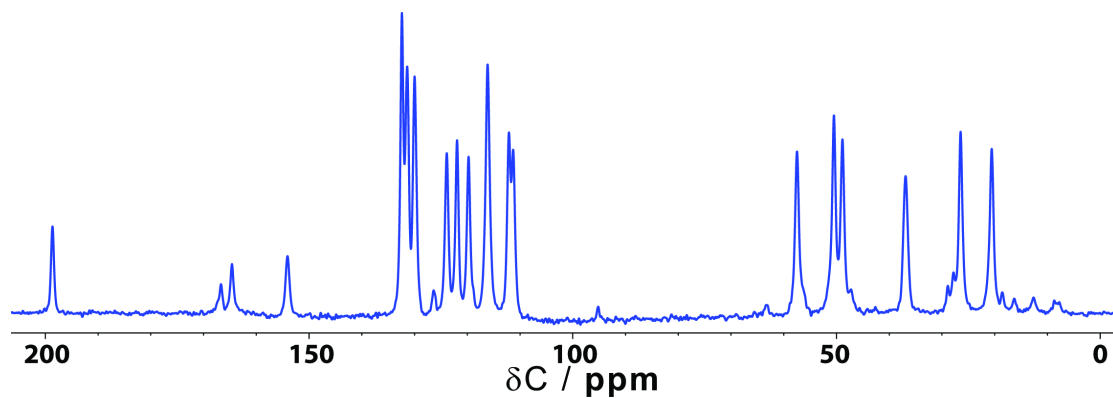


Fig. S5. ^{13}C CPMAS spectra of droperidol dihydrate **DH**.

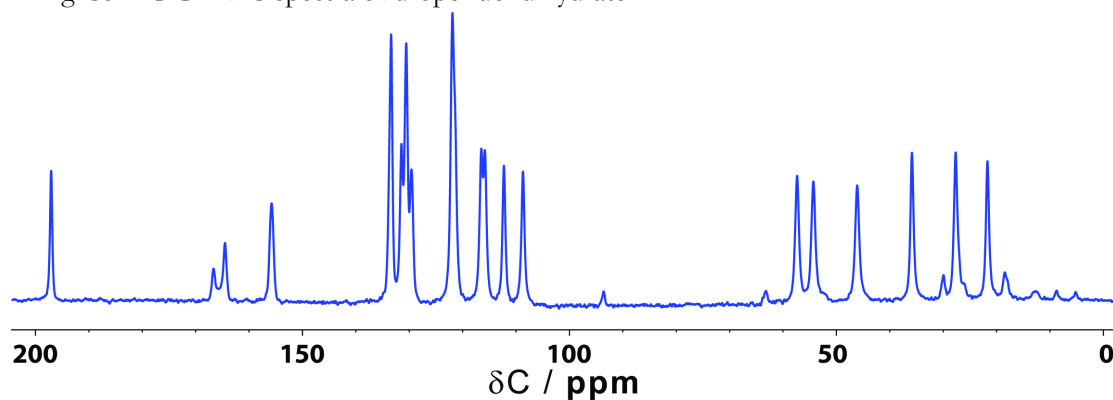


Fig. S6. ^{13}C CPMAS spectra of droperidol polymorph **II**.

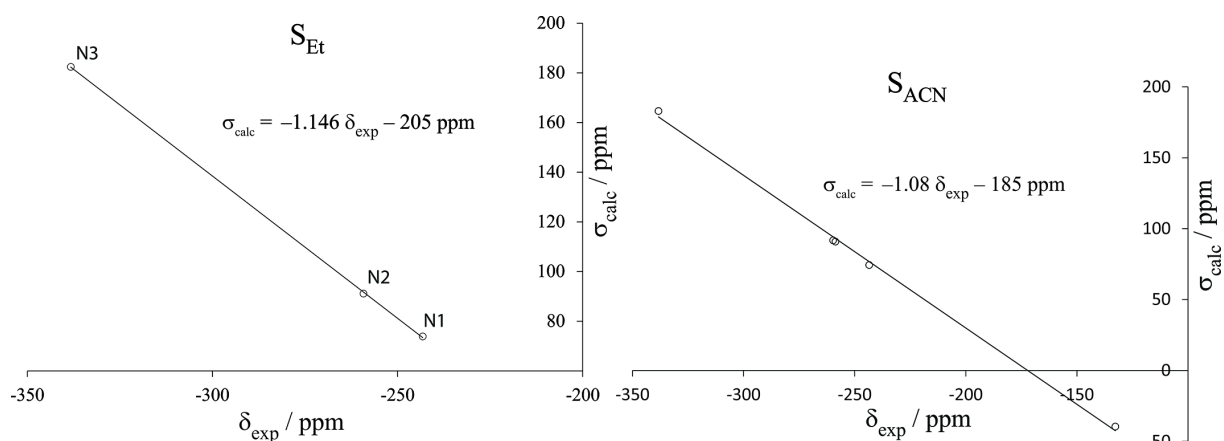


Fig. S7. Plot of the experimental ^{15}N chemical shifts versus the calculated shieldings in S_{Et} and S_{ACN} after optimization of all atoms.

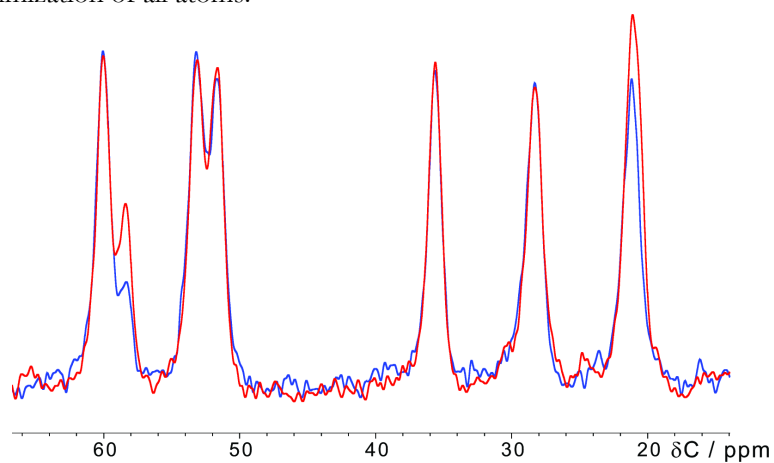


Fig. S8. Overlay of S_{Et} ^{13}C CPMAS spectra at 20 °C using 50 μs (blue) and 1000 μs (red) contact time (intensities are scaled to match the peaks from droperidol CH_2 groups).

Table S2. ^{13}C spin-lattice relaxation times determined for solvent molecule carbon atoms in droperidol solvates from ^{13}C direct-excitation experiments.

$T / ^\circ\text{C}$	S_{Et}		S_{Me}	S_{ACN}
	$T_1(\text{CH}_2) / \text{s}^{\text{a}}$	$T_1(\text{CH}_3) / \text{s}^{\text{a,b}}$	$T_1(\text{CH}_3) / \text{s}^{\text{c}}$	$T_1(\text{CH}_3) / \text{s}^{\text{c}}$
20	1.04	0.8	5.2	17
10	1.05	0.6		
0	1.23	0.5	7.0	
-10	1.55	0.35		
-20	1.44	0.3		
-30	1.37	0.2		
-40	0.94	0.2	7.6	32

^a – determined from saturation recovery experiments.

^b – values can be considered only as estimates due to NOE effects (see below), and were calculated by fitting only the initial intensity rise.

^c – estimates from simple experiments using different delay times.

Figure S9 shows that the peak intensity of ethanol CH_3 group carbon in saturation recovery experiments reached a maximum as a function of the recovery time, τ , and then decreased to an intensity similar to that observed for the ethanol CH_2 group. The same pattern was observed when the recycle delay was increased in ^{13}C direct-excitation experiments. This phenomenon can be explained by the magnetization transfer from ^1H atoms by transient Nuclear Overhauser effects; at short recycle delays the ^1H nuclei have insufficient time to reach the thermal equilibrium before applying the next pulse after the applied decoupling [2]. This effect slightly differed when the temperature was changed, which no doubt reflects the temperature dependence of ^{13}C and ^1H relaxation times (in turn largely dependent on methyl group orientation).

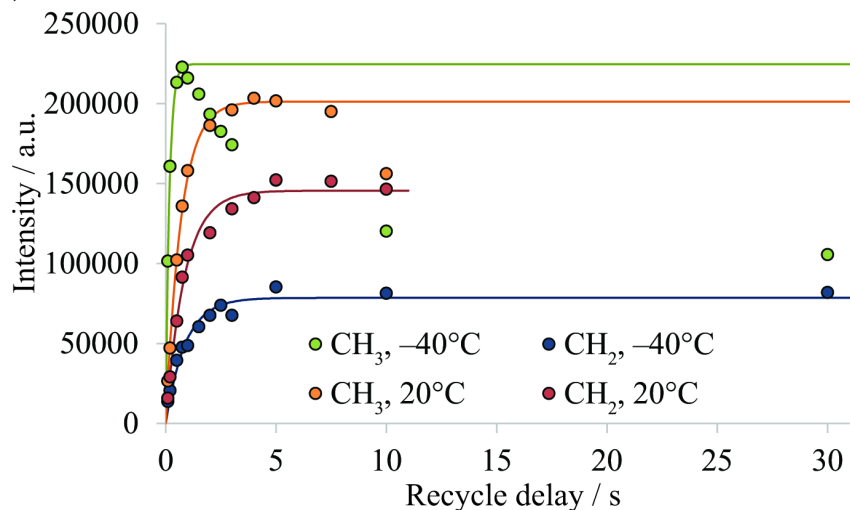


Figure S9. Intensity of ethanol ^{13}C signals as a function of recovery time in ^{13}C saturation recovery experiments at 20 and -40°C .

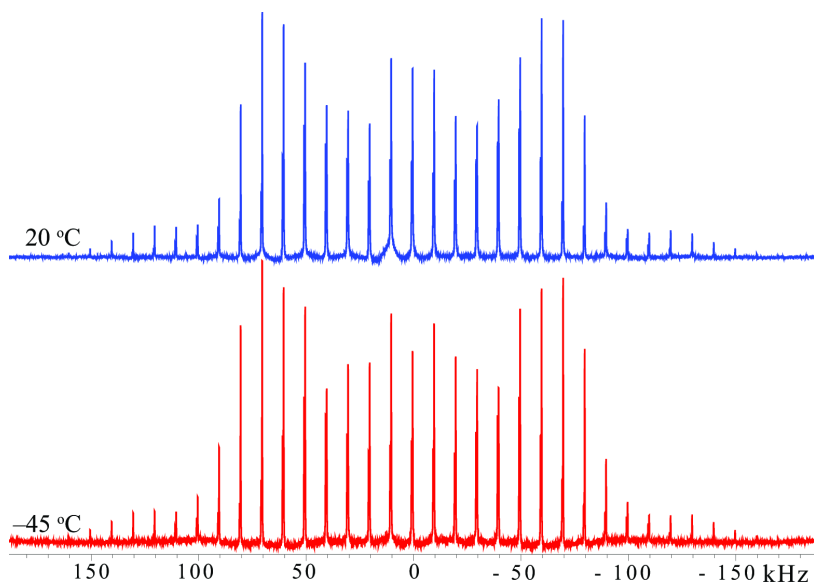


Fig. S10. ^2H MAS spectra at a spinning rate of 10 kHz of S_{Me} at 20 and -45 °C.

Table S3. Fitted quadrupolar coupling parameters for ^2H MAS spectra of droperidol solvates at different temperatures.

Solvate	Temperature	N-D site		Solvent site	
		χ / kHz	η	χ / kHz	η
S_{Et}	20 °C	166 ^a	0.22 ^a	207	0.20
	-45 °C	153 ^b	0.26 ^b	222	0.15
S_{Me}	20 °C	162	0.23	206	0.14
	-45 °C	160	0.23	213	0.15
NSH 32% RH	20 °C	165	0.21	83	0.62
	-45 °C	162	0.26	86	0.8 ^c
NSH 100% RH	20 °C	172	0.20	81	0.87
	-10 °C	165	0.26	87	0.88
	-30 °C	169	0.19	87	1.0 ^c
	-45 °C	161 ^b	0.33 ^b	89	1.0 ^c

^a –typical estimated uncertainty from repeat bandshape fittings using different methods / baseline roll suppression (see Experimental) is 2 kHz for χ and 0.02 for η . The statistical uncertainties returned by fitting, which assume a perfect model, are much lower, typically <0.1 kHz and <0.002 , and unrealistically small.

^b –fit was unsatisfactory (most likely due to exchange effects) and so parameters obtained should be interpreted cautiously.

^c – very low intensity of the peaks from the water sites prevented accurate determination of η .

Table S4. ^2H spin-lattice relaxation times T_1 determined for solvent hydroxyl and droperidol amide hydrogen atoms.

Solvate	Temperature	N-D site	Solvent site
NSH 32% RH	20 °C	1.33	<0.1
	-45 °C	2.51	<0.1
S_{Et}	20 °C	1.60	0.11
	-45 °C	1.93	0.27
S_{Me}	20 °C	0.63	0.11
	-45 °C	1.71	0.15

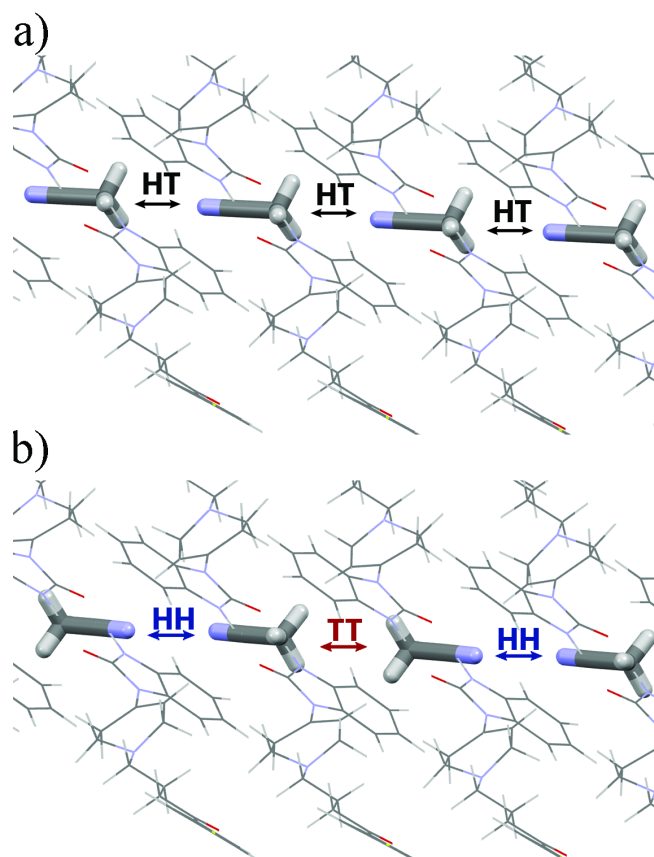


Fig. S11. Solvent orientations in the channels in (a) “same direction” and (b) “opposite direction” S_{ACN} crystal structures, showing one type of solvent-solvent interaction (“head-to-tail” (HT) with black arrows) in “same direction” structure, and two types of solvent-solvent interactions (HH with blue arrow and TT with brown arrow) in “opposite direction” structure.

Table S5. Total pair-wise interaction energies of solvent molecules and solvent-solvent interaction energies (in kJ mol^{-1}) in “same direction” and “opposite direction” droperidol solvate structures.

	“same direction”		“opposite direction”			Solvent-solvent contribution ^b
	Total	Solvent-solvent HT	Total ^a	Solvent-solvent HH	Solvent-solvent TT	
S_{Et}	-68.0	-1.2	-69.0	-2.3	-1.0	–
S_{Me}	-64.6	-1.5	-58.4	0.0	3.1	96
S_{NM}	-80.4	-8.1	-51.6	4.7	4.4	87
S_{ACN}	-74.3	-10.2	-38.5	7.7	2.9	88

^a - Total interaction energies for the “opposite direction” structures are averages over both of the solvent orientations. The largest differences between total interaction energies for both orientations were 0.8 kJ mol^{-1} for S_{NM} and 0.3 kJ mol^{-1} for S_{Me} .

^b - Percentage contribution of the change of solvent-solvent interaction to the change of the total pairwise interaction energies.

References

- [1] A. Bērziņš, E. Skarbulis, T. Reķis, and A. Actiņš, On the formation of droperidol solvates: characterization of structure and properties. *Cryst. Growth Des.* 14 (2014) 2654-2664.
- [2] A. Findlay, and R.K. Harris, Measurement of nuclear overhauser enhancements in polymeric films. *J. Magn. Reson.* 87 (1990) 605-609.

PREPARATION AND CHARACTERIZATION OF BENPERIDOL SOLVATES AND POLYMORPHS

Table S1. Crystal forms obtained after the crystallization of droperidol from different solvents.

Solvent	Classification ¹	Group ²	Temperature, °C	Obtained phase
<i>n</i> -hexane	AAA	1	60 ^a	I
<i>n</i> -heptane	AAA	1	70 ^a	I
carbon tetrachloride	HBD	1	70	(S_{TCC}) ^b
Ethyl acetate	AP	2	70	I/ S_{EtOAc} ^c
butyl acetate	AP	2	80	I
tetrahydrofuran	EPD	2	60	I
<i>tert</i> -butyl methyl ether	EPD/AAA	2	50 ^a	I
isopropyl acetate	AP	2	80	I
1-butanol	HBD	3	80	I
2-propanol	HBD	3	70	I/II
1-propanol	HBD	3	80	I
isobutanol	HBD	3	80	I
ethanol	HBD	3	70	S_{Et}
methanol	HBD	3	60	S_{Me}
toluene	AALP	4	80	I/ HH ^d
<i>o</i> -xylene	AALP	4	80	I/ HH ^d
cyclohexanone	AP	5	120	I
butanone	AP	5	70	I
3-pentanone	AP	5	80	I
acetone	AP	5	50	I
N,N-dimethylformamide	AP	6	120	I
dimethylsulfoxide	AP	6	120	no crystallization
chloroform	EPD/HBD/AP	7	50	(S_{CLF}) ^b
dichloromethane	AP	7	40	I
1,1-dichloroethane	AP	7	70	I
acetonitrile	AP	9	80	S_{ACN} /I
nitromethane	AP	9	80	I/ S_{NM} ^e
benzyl alcohol	AALP	10	100 ^f	S_{Benz}
1,4-dioxane	AP/EPD	11	80	S_{DIOX}
water	HBD	15	- ^g	DH
cyclohexanol	HBD	-	120	I

^a - solution was partially evaporated at 50 °C temperature

^b – Obtained products typically contained impurities and/or PXRD patterns differed significantly.

^c – Mainly polymorph **I** was obtained, but slow crystallization at low temperatures produced **S_{EtOAc}**.

^d – Hemihydrate (**HH**) formed only when solvents contained traces of water.

^e – **S_{NM}** was obtained only once and all repeated crystallizations produced only polymorph **I**.

^f – Crystallization was very slow and occurred either at 20° or at -5°C.

^g – Solvent exchange method was used either at ambient temperature or at 50 °C.

Classifications: AP = aprotic polar, AALP = aromatic apolar or lightly polar, EPD = electron pair donors, HBD = hydrogen bond donors, AAA = aliphatic aprotic apolar.

Groups are based on cluster analysis of following solvent parameters: hydrogen bond acceptor propensity, hydrogen bond donor propensity, polarity/dipolarity, dipole moment, and dielectric constant, and contain various solvents with similar properties (except for: group 13 = diethylamine, group 14 = glycerol, and group 15 = water).

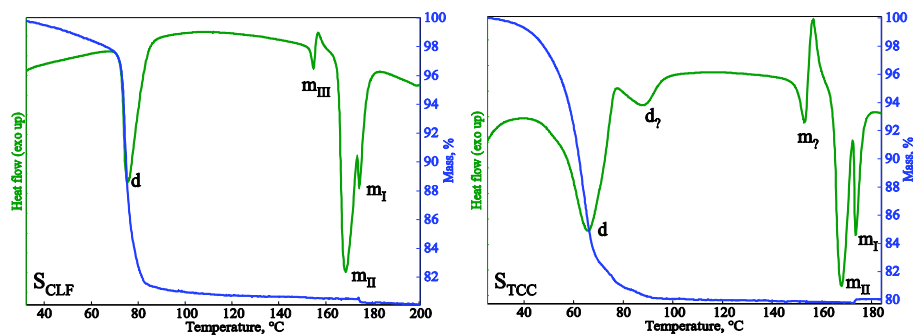


Figure S1. The DTA and TG curves of the benperidol solvates. d – desolvation,, m – melting of polymorphs.

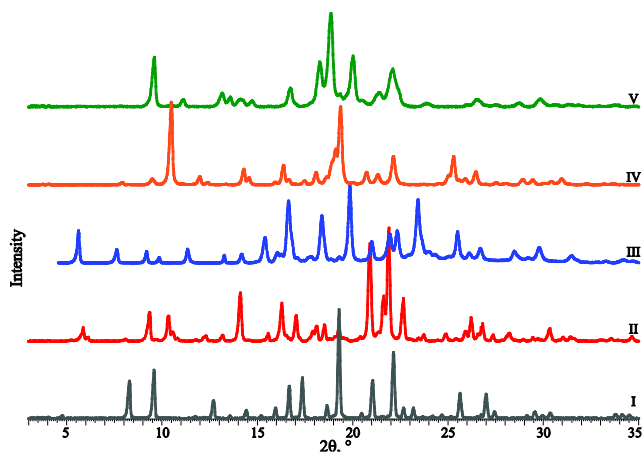


Figure S2. PXRD patterns of the benperidol polymorphs.

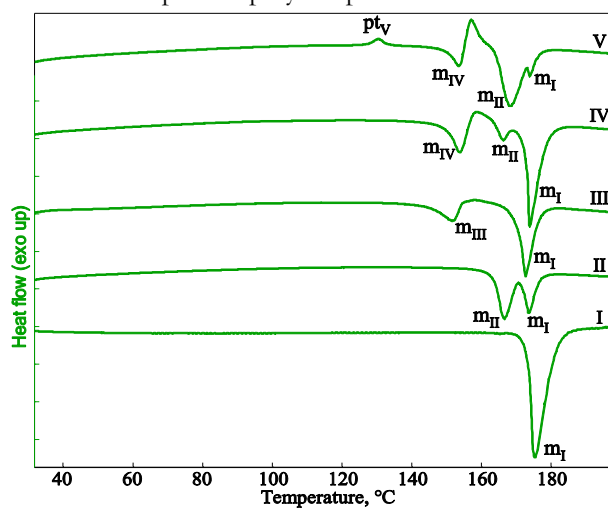


Figure S3. The DTA curves of the benperidol polymorphs. m – melting of polymorphs, pt – phase transition.

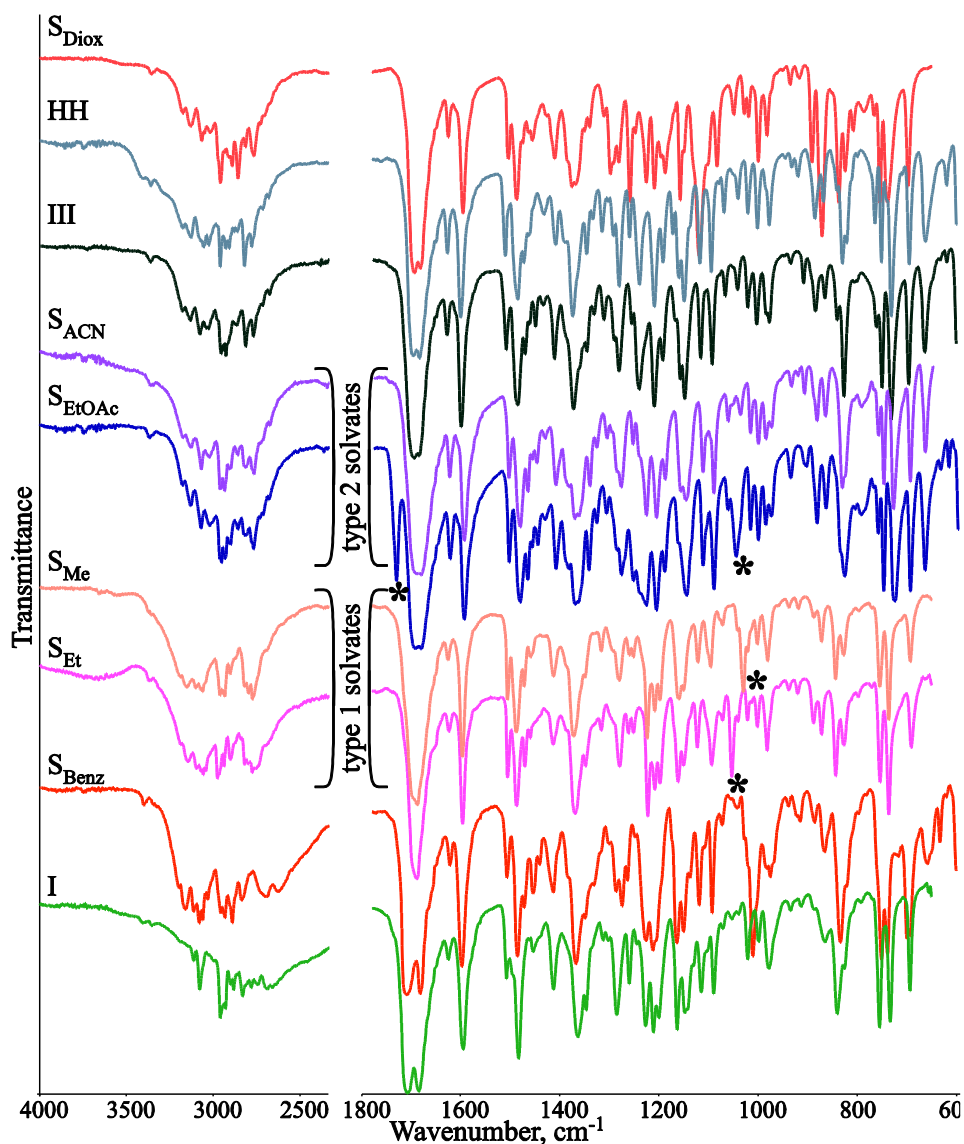


Figure S4. FTIR spectra of the benperidol solvates and polymorphs **I** and **III**. Asterisks marks the most characteristic bands from the solvent molecules in isostructural solvates.

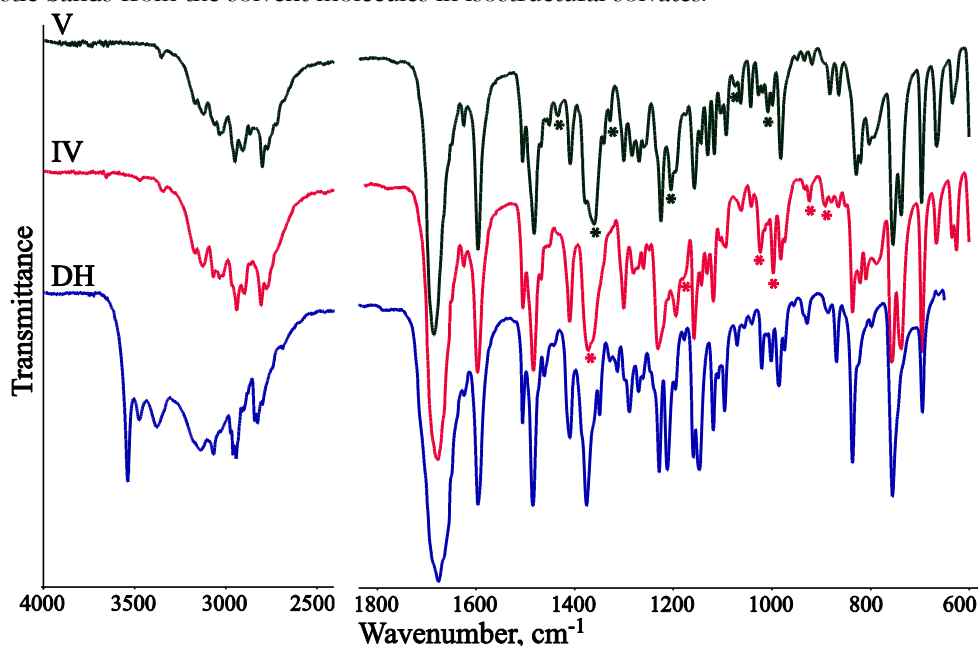


Figure S5. FTIR spectra of the benperidol **DH** and polymorphs **IV** and **V**. The peaks showing most characteristic differences between **IV** and **V** are designated with asterisks.

EVALUATION OF THE THERMODYNAMIC STABILITY OF BENPERIDOL POLYMORPHS

From the melting points of **I** (171 °C) and **II** (161 °C) and from slurry bridging experiment in isopropanol of the mixture of polymorphs **I** and **II** at 50 °C it was determined that thermodynamically stable polymorph at elevated temperatures is polymorph **I**. Interestingly, slurry bridging experiments of the same mixture in acetone at ambient temperature showed the transformation of polymorph **I** to polymorph **II**, while no phase change occurred in isopropanol. This could show that **II** is thermodynamically stable at ambient and lower temperatures. This, however, was not supported by computational calculations, as total energy calculated in *CATSEP* of **I** is by 2.5 kJ·mol⁻¹ lower than that of **II**. This was calculated after relaxation of all atom positions for crystal structures determined at 173 K.

The melting points of polymorphs **III** (146 °C) and **IV** (149 °C) indicates that both of these phases have lower thermodynamic stability than **I** and **II** in high temperatures, while the same stability relationship at lower temperatures was confirmed by the observed conversation of **III** and **IV** to polymorph **I** in slurry bridging experiment in 2-propanol and tetrahydrofuran at 50 °C.

The exothermic peak corresponding of phase transition from **V** to **IV** at 127 °C proves monotropic relation between these polymorphs with **V** being thermodynamically less stable in all temperatures.

DETERMINATION OF CRYSTAL STRUCTURES OF BENPERIDOL SOLVATES AND POLYMORPHS

Table S2. Crystallographic data for the benperidol phases **II**, **DH**, **S_{Et}**, **S_{Me}**, **S_{ACN}**, **S_{EtOAc}**, **HH**, **S_{Benz}** and **III**.

Solvate	II	DH	S_{Et}	S_{Me}	S_{ACN}	S_{EtOAc}	HH	S_{Benz}	III
Empirical formula	C ₂₂ H ₂₄ FN ₃ O ₂	C ₂₂ H ₂₄ FN ₃ O ₂ ·2H ₂ O	C ₂₂ H ₂₄ FN ₃ O ₂ ·C ₂ H ₆ O	C ₂₂ H ₂₄ FN ₃ O ₂ ·CH ₄ O	C ₂₂ H ₂₄ FN ₃ O ₂ ·C ₂ H ₅ N	C ₂₂ H ₂₄ FN ₃ O ₂ ·0.5C ₄ H ₈ O ₂	C ₂₂ H ₂₄ FN ₃ O ₂ ·0.5H ₂ O	C ₂₂ H ₂₄ FN ₃ O ₂ ·C ₇ H ₈ O	C ₂₂ H ₂₄ FN ₃ O ₂
Mr	381.44	417.48	427.51	413.48	422.49	425.49	390.45	489.58	381.44
Crystal system	triclinic	monoclinic	monoclinic	monoclinic	triclinic	triclinic	monoclinic	orthorombic	triclinic
Space group	$\bar{P}1$	$P2_1/n$	$P2_1/c$	$P2_1/c$	$\bar{P}1$	$\bar{P}1$	$C2/c$	$Pbca$	$\bar{P}1$
a (Å)	10.8417(3)	11.0595(3)	15.0684(3)	15.1097(4)	5.56500(10)	5.4228(3)	36.7342(7)	13.7193(4)	15.61501(10)
b (Å)	16.2903(4)	9.3896(2)	10.8602(3)	10.7200(3)	14.1256(4)	14.6014(8)	5.58581(10)	51.6467(20)	11.48189(8)
c (Å)	17.9497(5)	20.4456(6)	15.2555(4)	15.3070(5)	15.0478(5)	14.8045(10)	23.6629(5)	7.43071(20)	5.45694(30)
α (°)	66.7233(11)	90	90	90	109.2583(13)	109.936(3)	90	90	86.627(3)
β (°)	87.0069(10)	91.7206(11)	117.6353(9)	119.3538(13)	90.9875(13)	90.199(2)	124.8680(8)	90	96.618(6)
γ (°)	85.0074(16)	90	90	90	100.071(2)	100.322(3)	90	90	94.435(5)
V (Å ³)	2900.55(13)	2122.20(10)	2211.69(9)	2161.04(11)	1095.91(5)	1081.50(11)	3983.71(14)	5265.07(30)	967.71(6)
Z/Z'	6/3	4/1	4/1	4/1	2/1	2/1	8/1	8/1	2/1
T, K	173(2)	173(2)	173(2)	173(2)	173(2)	100(2)	298(3)	298(3)	298(3)
μ (mm ⁻¹)	0.092	0.096	0.091	0.091	0.089	0.090			
D _{calc} (g cm ⁻³)	1.310	1.307	1.284	1.271	1.280	1.264			
no. of parameters	757	271	286	273	285	276			
reflns collected	13138	5709	5900	5753	4973	3659	6407	6603	6407
reflns (I > 2 σ) ^a	6787	3734	4081	3503	3730	2532			
wR (all data)	0.1616	0.196	0.1415	0.1997	0.1126	0.1992			
final R (I > 2 σ) ^a	0.0765	0.048	0.0543	0.0644	0.0460	0.0751			
GOF	1.013	1.243	1.028	0.972	1.018	1.030			
ΔQ_{\max} (e ⁻ Å ⁻³)	0.244	0.59	0.293	0.265	0.212	0.603			
ΔQ_{\min} (e ⁻ Å ⁻³)	-0.285	-0.63	-0.251	-0.287	-0.189	-0.543			
R _{wp}							0.02897	0.03356	0.03686
R _p							0.01721	0.02427	0.0243
R _{exp}							0.00520	0.00734	0.00816
final R (all data)							0.1203	0.0787	0.0660
GOF							5.57	4.57	4.52
Pacing coef.	0.682	0.689	0.684	0.672	0.681	0.690	0.675	0.651	0.681

^a – For **DH** I > 3 σ

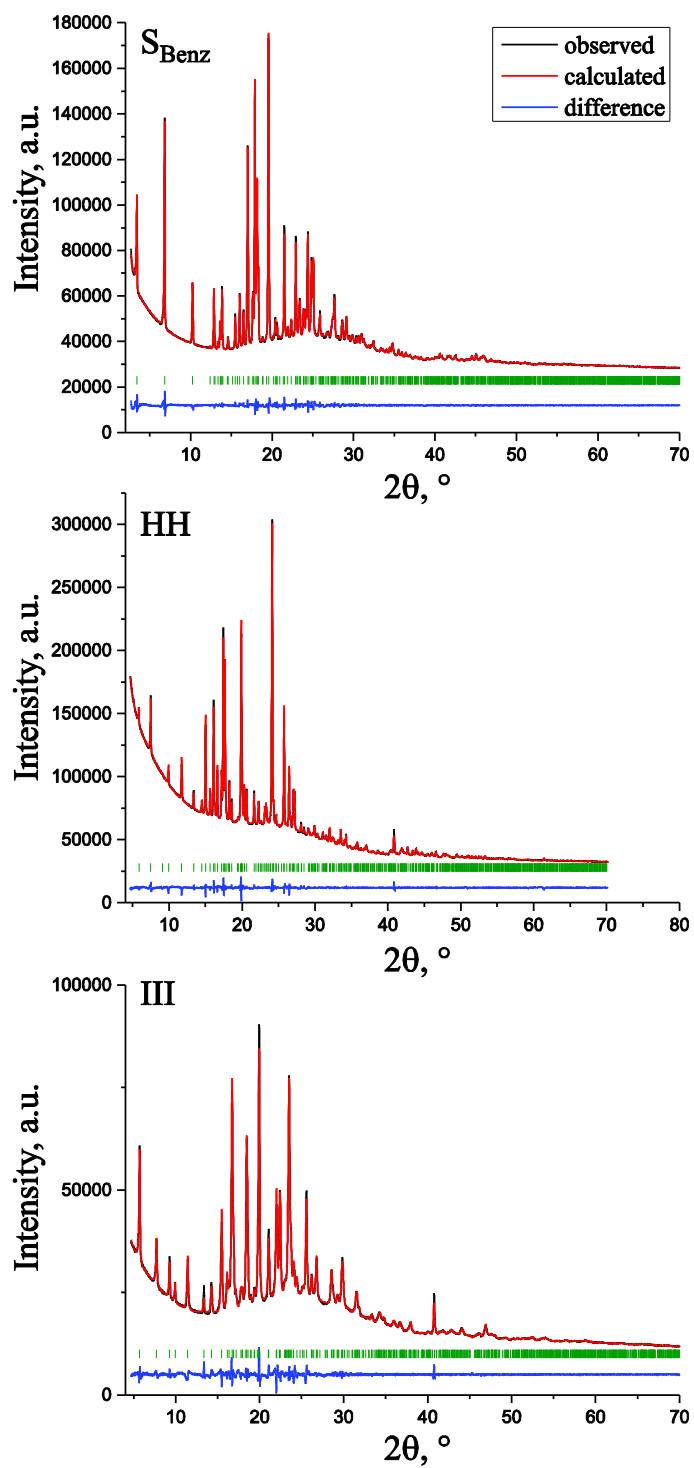


Figure S6. Experimental (black), calculated (red), and difference (dark-blue) PXR D profiles from the final Le Bail refinement of different benperidol forms.

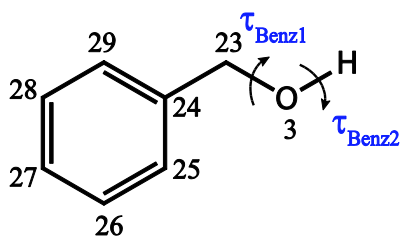


Figure S7. Molecular structure of benzyl alcohol with the numbering of non-hydrogen atoms and labelling of flexible torsion angles.

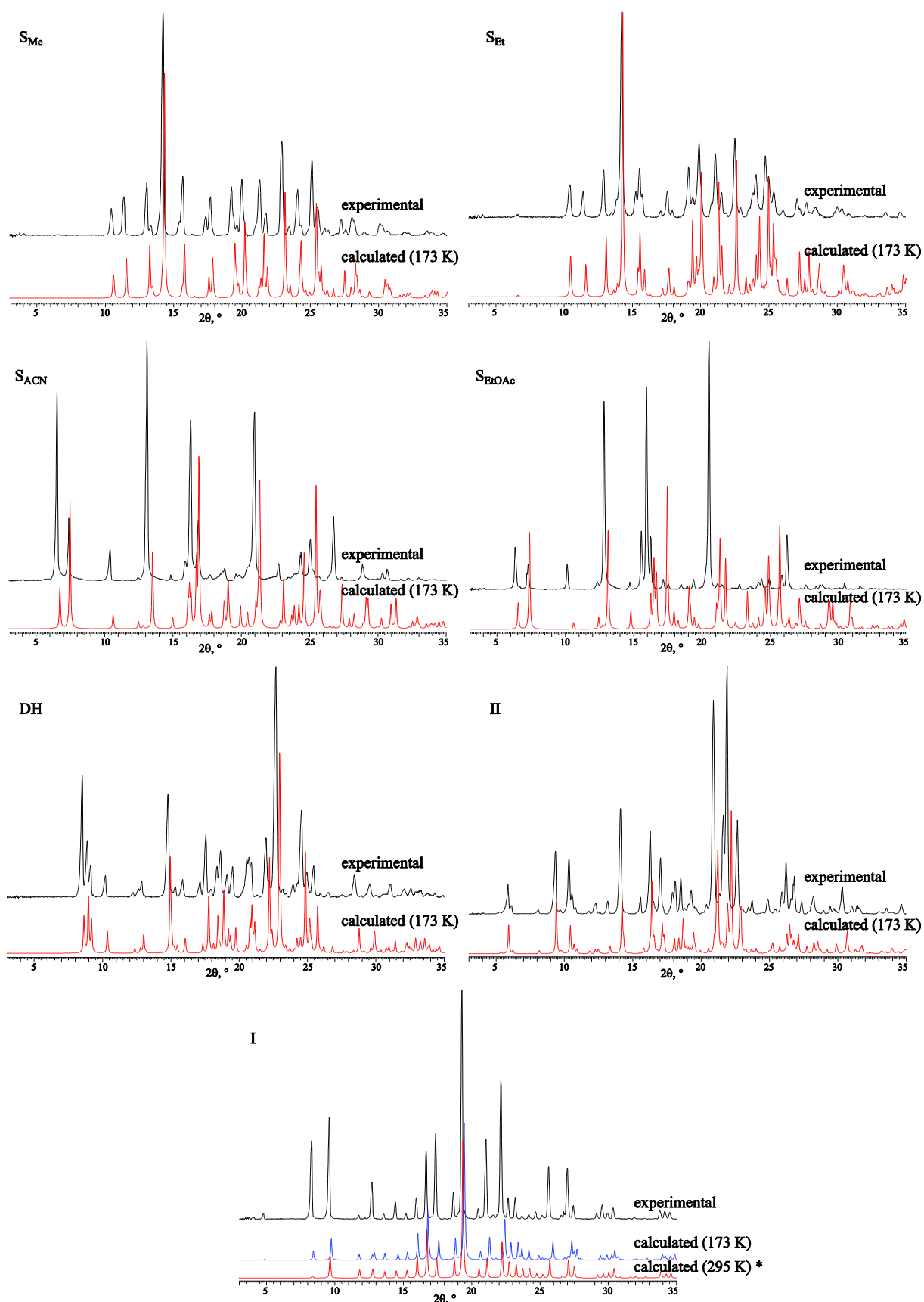


Figure S8. Overlay of the experimental and from crystal structure data simulated PXRD patterns for benperidol solvates and polymorphs. Observed differences in peak positions were due to the different temperature used for the crystal structure determination and experimental PXRD measurements, whereas the intensity differences between calculated and experimental PXRD patterns suggested the presence of preferred orientation.

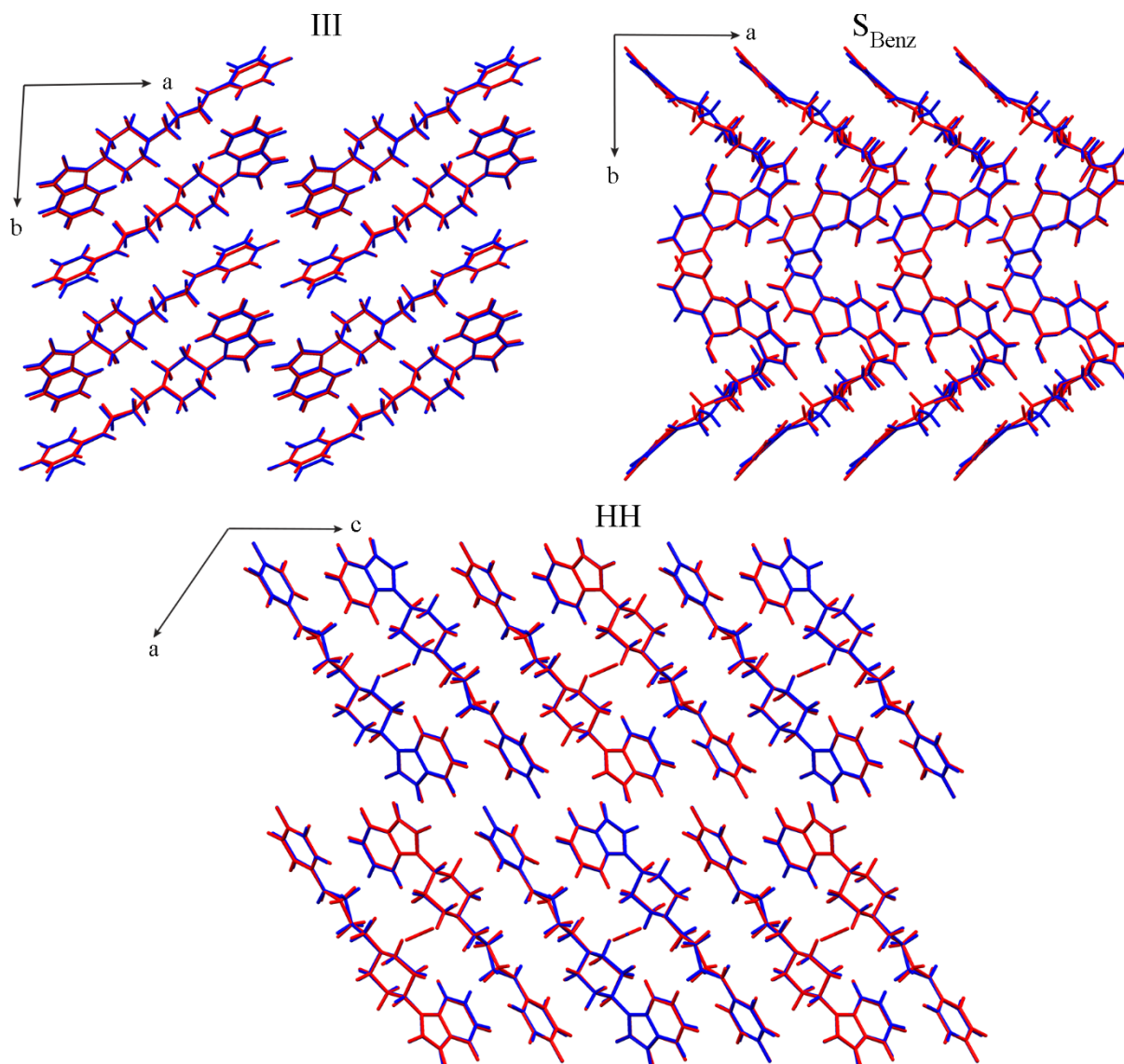


Figure S9. Overlay of crystal structures after final Rietveld refinement and geometry optimization in CASTEP.

ANALYSIS OF CRYSTAL STRUCTURES OF BENPERIDOL SOLVATES AND POLYMORPHS

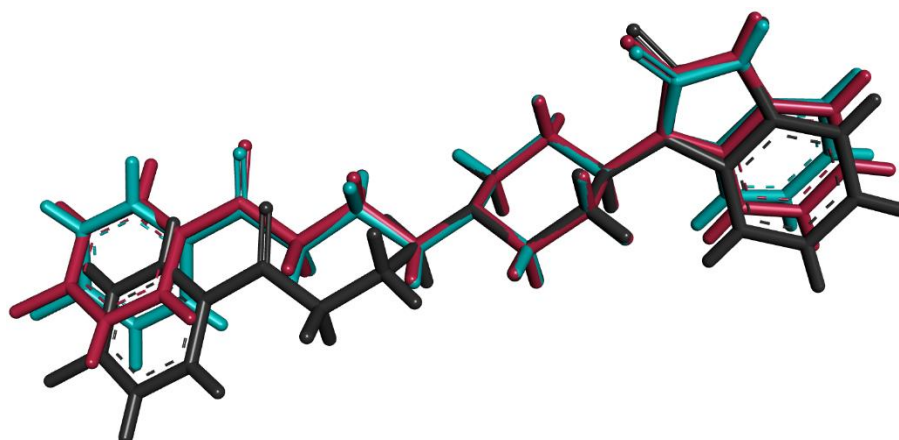


Figure S10. Overlay of the benperidol molecules in polymorph II. II_A: red, II_B: dark grey, II_C: cyan.

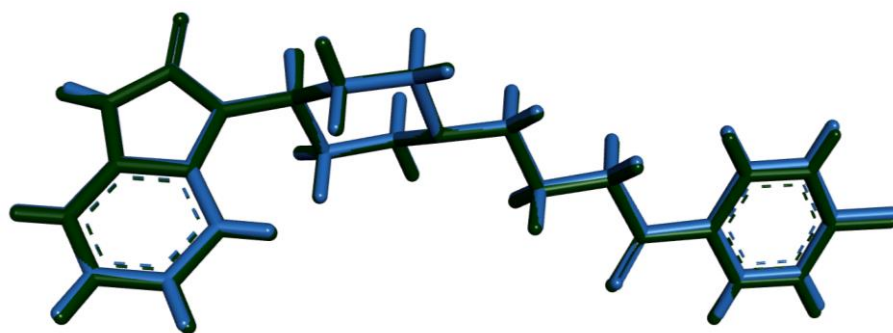


Figure S11. Overlay of the benperidol molecules in type 1 solvates. S_{Et} – dark green, S_{Me} – light blue

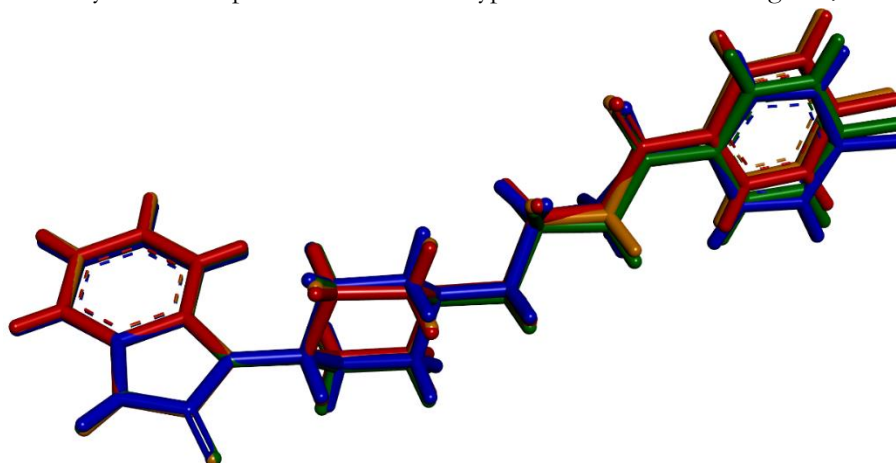


Figure S12. Overlay of the benperidol molecules in type 2 solvates, HH and polymorph III . III – red, S_{EtOAc} – green, HH – blue, and S_{ACN} – orange.

Table S3. Torsion angles (in degrees) of benperidol in its solvates S_{Me} and S_{EtOAc} .

	S_{Me}	S_{EtOAc}
τ_1	-107.02	-114.25
τ_2	-72.92	-71.26
τ_3	-176.56	-169.89
τ_4	178.26	-170.85
τ_5	-179.87	-176.10
τ_6	178.40	-177.23

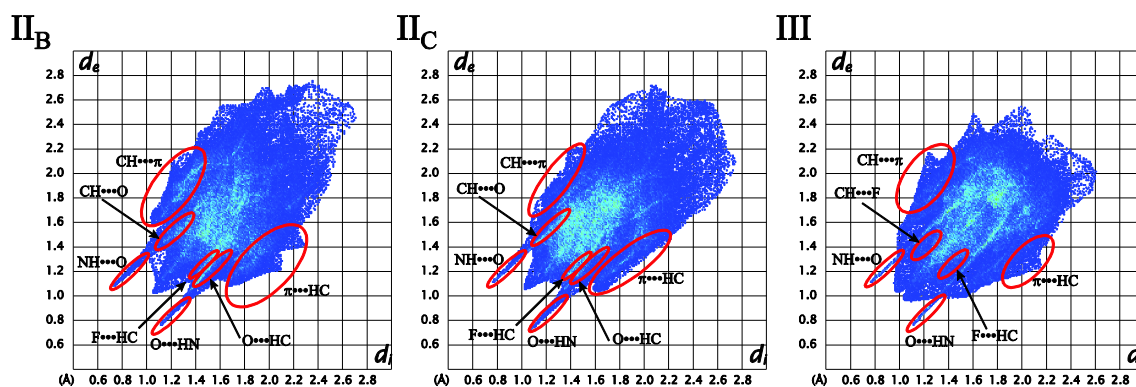


Figure S13. 2D fingerprint plots of Hirshfeld surface for benperidol molecules in polymorphs II and III .

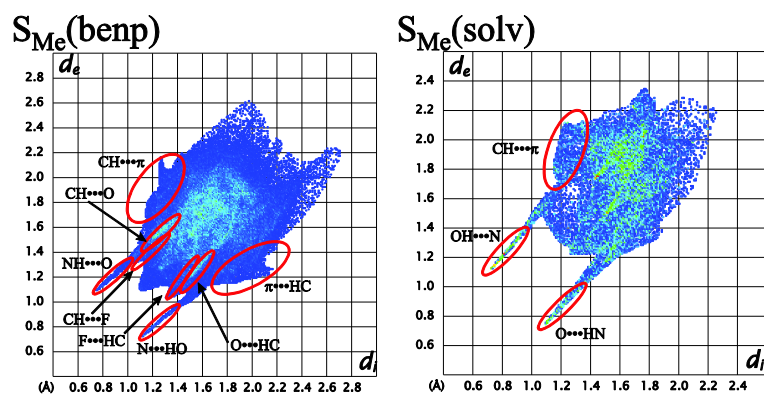


Figure S14. 2D fingerprint plots of Hirshfeld surface for benperidol solvate S_{Me} .

Slight differences in small spikes corresponding to $CH\cdots F$ interaction was observed for S_{Me} and S_{Et} due to different hydrogen bond geometry. Besides, closer molecule packing in S_{Me} was identified from smaller d_i and d_e distances for central spike corresponding to $H\cdots H$ contacts. This is due to smaller size of the methanol molecule and this increase of benperidol molecule separation possibly explains the reason for not observing isostructural solvates with bigger alcohol molecules.

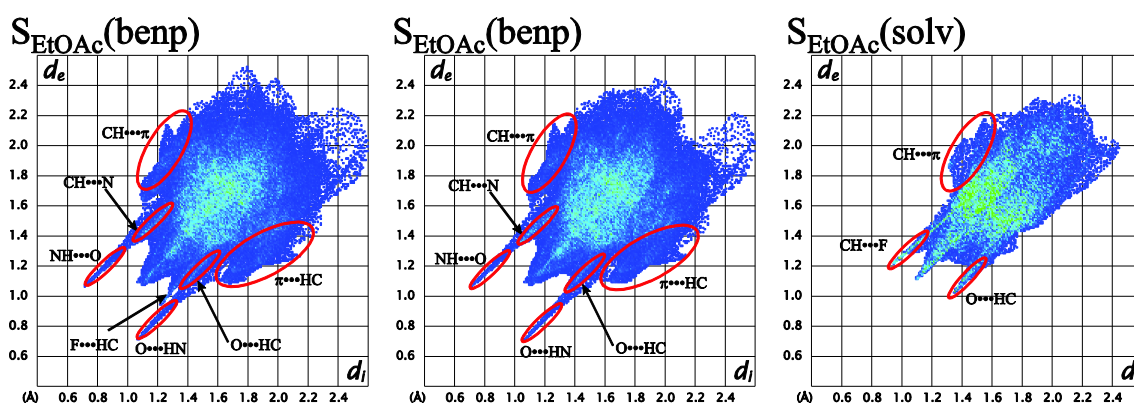


Figure S15. 2D fingerprint plots of Hirshfeld surface for benperidol solvate S_{EtOAc} .

Most noticeable differences observed in plots of benperidol molecules in S_{ACN} and S_{EtOAc} is associated with differences in interactions with the solvent molecules.

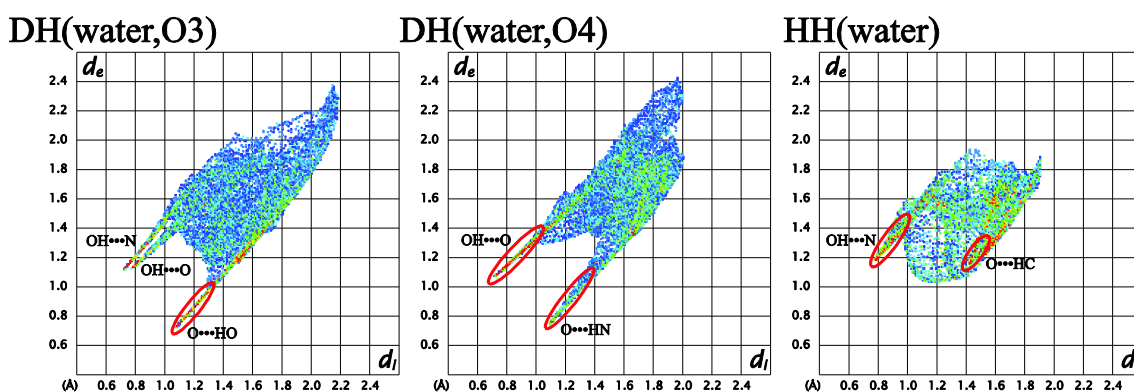


Figure S16. 2D fingerprint plots of Hirshfeld surface for water molecules in both benperidol hydrates.

Table S4. Geometrical parameters for all intermolecular interactions (with D...A distance lower than vdW radii – 0.1 Å) in benperidol polymorphs and solvates.

Phase	Interaction	Distance, Å			D-H...A (°)	Graph set
		X-H	H...A	D...A		
I	N2-H...N3			2.883		$R_6^6(48)$
	C21-H...O2			3.140		C(6)
	C21-H...O1			3.235		$R_6^6(84)$
	C15-H...O1			3.454		$R_6^6(66)$
II	N2A-H...O1A	0.86	1.96	2.800(3)	165	$R_2^2(8)$
	N2B-H...O1C	0.86	1.95	2.779(3)	161	$R_2^2(8)$
	N2C-H...O1B	0.86	2.03	2.881(3)	171	$R_2^2(8)$
	O2A...H-C2B	0.93	2.48	3.389(4)	165	
	C18A-H...O2B	0.93	2.50	3.217(4)	134	
	C13A-H...O1C	0.97	2.50	3.348(4)	146	
	C2A-H...O2C	0.93	2.42	3.347(4)	178	
	C22A-H...O1B	0.93	2.62	3.499(4)	158	
	C10A-H...F1C	0.97	2.53	3.409(4)	151	
	C21A-H...F1A	0.93	2.53	3.265(4)	136	
	O2B...H-C15C	0.97	2.52	3.469(4)	165	
	O1B...H-C9C	0.97	2.61	5.514(4)	155	
S _{Me}	N2-H...O3	0.86	1.97	2.783(3)	157	$C_2^2(10)$
	O3-H...N3	0.82	2.00	2.806(3)	169	
	C11-H...O1	0.97	2.51	3.420(3)	156	
	C19-H...O1	0.93	2.48	3.191(3)	133	C(15)
	C4-H...F1	0.93	2.48	3.332(3)	152	C(19)
	C15-H...F1	0.97	2.51	3.420(3)	156	C(8)
S _{Et}	N2-H...O3	0.90(2)	1.91(2)	2.7872(19)	163.9(18)	$C_2^2(10)$
	O3-H...N3	0.82	1.98	2.7931(19)	175	
	C11-H...O1	0.97	2.56	3.444(2)	152	
	C19-H...O1	0.93	2.53	3.249(2)	134	C(15)
	C21-H...O1	0.93	2.62	3.498(2)	158	C(15)
	C15-H...F1	0.97	2.45	3.365(2)	158	C(8)
S _{ACN}	N2-H...O1	0.89(2)	1.906(19)	2.7978(16)	177.1(14)	$R_2^2(8)$
	C18-H...O2	0.93	2.45	3.246(2)	143	$R_2^2(10)$
	C21-H...N4	0.93	2.60	3.511(2)	165	D
S _{EtOAc}	N2-H...O1	0.86(4)	1.93(4)	2.776(4)	172(4)	$R_2^2(8)$
	C18-H...O2	0.93	2.50	3.238(5)	137	
	C15-H...O2	0.97	2.61	3.511(5)	155	
	F1...H-C23	1.08	2.16	3.232(4)	172	
	F1...H-C25	1.08	2.33	3.065(5)	124	
	O3...H-C5	0.93	2.61	3.352(5)	137	
	O3...H-C21	0.93	2.52	3.411(5)	162	
DH	O4-H...O3	0.92	1.85	2.7271(19)	159	
	O4-H...O2	0.85	2.02	2.8597(19)	168	
	N2-H...O4	0.97	1.86	2.7629(18)	153	
	O3-H...O1	0.9	1.98	2.8385(17)	159	
	O3-H...N3	0.87	1.95	2.8122(18)	174	
	C3-H...O2	0.96	2.60	3.382(2)	139	
	C12-H...O1	0.96	2.54	3.434(2)	156	
	C15-H...O1	0.96	2.48	3.384(2)	157	
III	N2-H...O1	0.91	1.97	2.866(9)	167	$R_2^2(8)$
	C5-H...F1	0.93	2.50	3.113(10)	124	
S _{Benz}	N2-H...O3	0.86	1.99	2.841(7)	169	$C_2^2(10)$
	O3-H...N3	0.90	1.75	2.625(8)	162	
	C15-H...O1	0.96	2.57	3.470(7)	155	
	C21-H...O2	0.93	2.27	3.190(6)	171	
	C19-H...F1	0.93	2.43	3.173(6)	136	
HH	N2-H...O1	0.90	1.90	2.787(8)	165	$R_2^2(8)$
	O3-H...N3			3.005(15)		D_2^2
	C11-H...O3	0.96	2.60	3.23(2)	124	

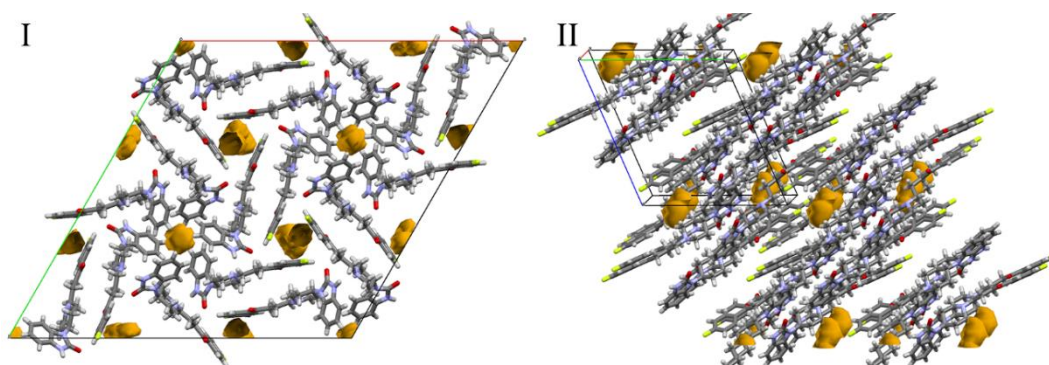


Figure S17. Packing of benperidol molecules in polymorphs **I** and **II** showing structural voids.

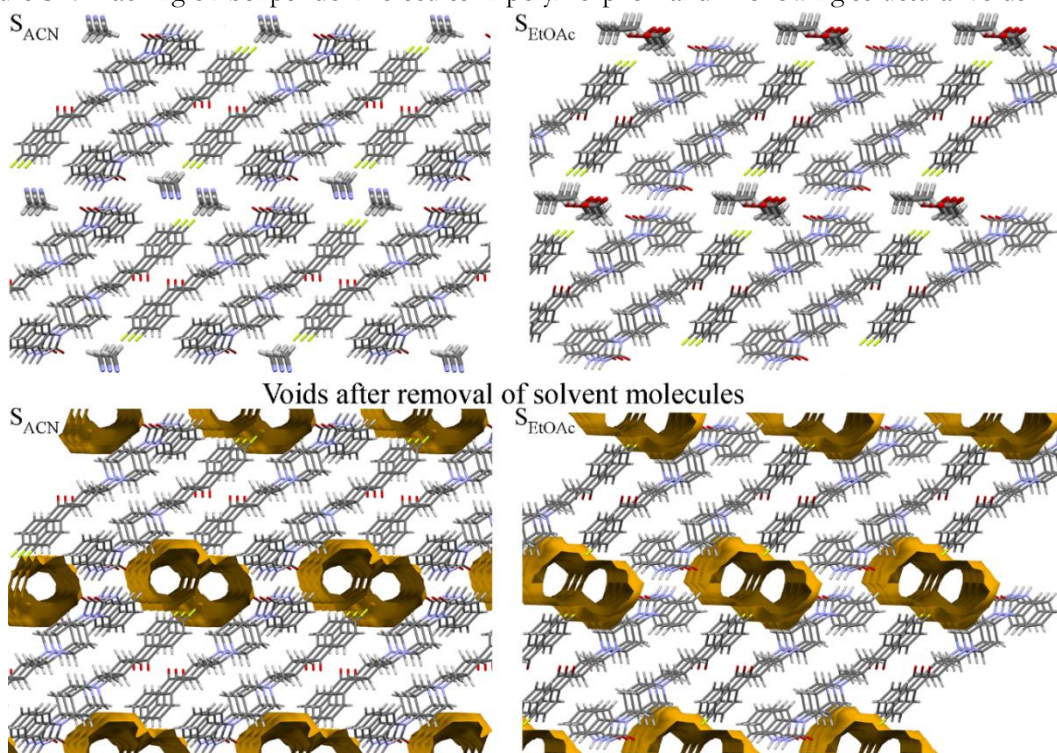


Figure S18. Arrangement of solvent molecules in the channels of type 2 solvates.

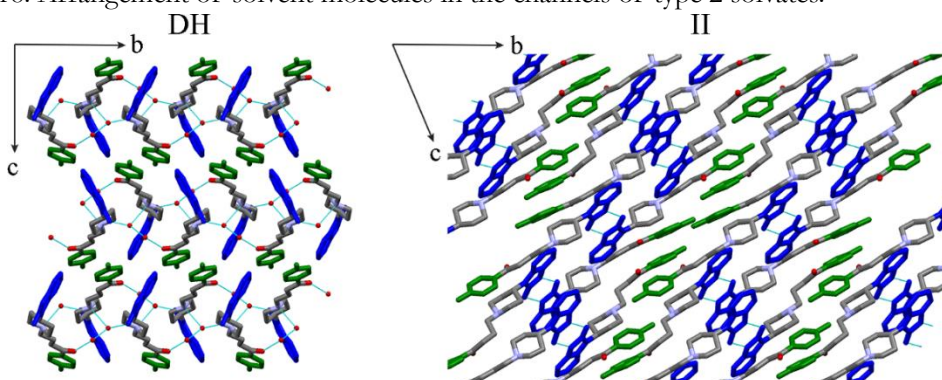


Figure S19. Molecular packing in benperidol polymorphs and solvates.

Besides the identified packing similarities, some additional minor similarities of packing between individual molecule moieties associated with the presence of a particular identical intermolecular interactions was found using XPac code³. Most similar feature was identified in the crystal structures of type 1 and type 2 solvates, which contains identical 0D supramolecular construct: a benperidol molecule dimer. Identical 0D supramolecular construct (benperidol molecule dimer) was found also in polymorph **II** and in the structures of type 2 solvates, **HH**, **III** as well as in **DH**. However, packing of these dimers in crystal structures is completely different.

Using crystal structures of **S**_{ACN} and **S**_{EtOAc} crystal structure of isostructural **S**_{NM} was modelled. Firstly lattice parameters were determined from ambient temperature PXRD pattern using *LP-Search* indexing algorithm implemented in TOPAS v4.2. After that crystal structure of **S**_{ACN} was modified by setting the determined lattice parameters and replacing the acetonitrile molecule with the nitromethane molecule (extracted from crystal structure of droperidol nitromethane solvate). Then the obtained structure was used as input for geometry optimization (by relaxing all atom positions) in CASTEP. It was determined that **S**_{NM} should exist in a form of monosolvate as the size of nitromethane (48.1 cm³·mol⁻¹) is only slightly larger than that of acetonitrile (37.9 cm³·mol⁻¹) and it is able to position in one channel.

COMPUTATIONAL SIMULATION OF INFRARED SPECTRA

Interestingly, based on the presence of a single carbonyl stretching band at 1685 cm⁻¹ in the IR spectra, it has been stated that benperidol in **II** and **S**_{Et} has ionized and exists in the zwitterionic form, whereas the presence of two carbonyl stretching bands at 1685 cm⁻¹ and 1710 cm⁻¹ in **I** benperidol has been associated with its existence in a neutral state. However, crystal structure data rejects this statement (see Table S5). Also it was stated that polymorph **III** actually is a mixture of **I** and **II**⁴, despite unique PXRD peak positions have been given elsewhere⁵.

Table S5. Lengths of the selected bonds as well as the location of hydrogen atom H5 in crystal structures of benperidol solvates and polymorphs.

Phase	C1-O1	N2-C1	Hydrogen attached to:
I	1.211	1.369	
II ^a	1.238-1.247	1.363-1.374	
SEtOH	1.233	1.366	N2
SACN	1.237	1.358	
DH	1.235	1.365	

^a – maximum and minimum value for three molecules in the asymmetric unit.

Table S6. Experimental and calculated IR frequencies and their intensities for both carbonyl groups in different benperidol solvates and polymorphs.

Band	Experimental, cm ⁻¹	Calculated*, cm ⁻¹
Polymorph I		
C=O _{amide}	1707 (100%)	1728 (100%)
C=O _{ketone}	1685 (98%)	1706 (25%)
S_{Benz}		
C=O _{amide}	1709 (100%)	1721 (100%)
C=O _{ketone}	1682 (100%)	1702 (40%)
Polymorph II		
C=O _{amide}	1696 (90%)	1708 (100%)
C=O _{ketone}	1683 (100%)	1701 (30%)
Type I solvates		
C=O _{amide}	1689 (100%)	1706 (100%)
C=O _{ketone}		1692 (30%)
Type II solvates		
C=O _{amide}	1695 (98%)	1708 (100%)
C=O _{ketone}	1683 (100%)	1700 (30%)
HH		
C=O _{amide}	1696 (96%)	1704 (100%)
C=O _{ketone}	1683 (100%)	1699 (20%)

Calculated at pm6 level and rescaled by multiplying with scale factor 0.953.

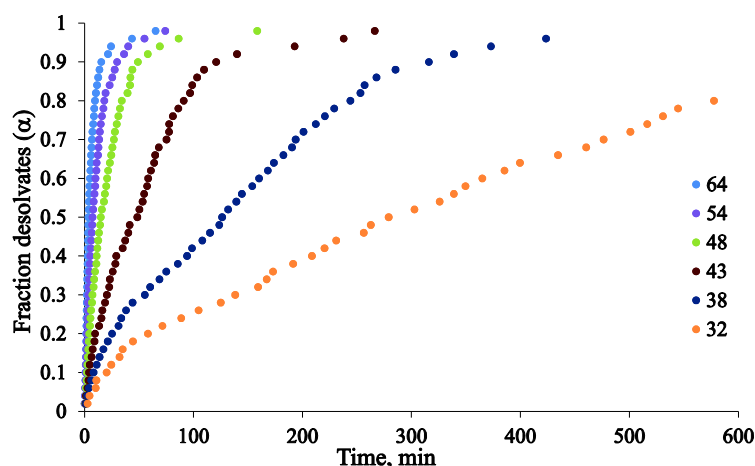
STUDY OF DEHYDRATION PROCESS AND KINETICS OF BENPERIDOL SOLVATES

For studying the desolvation kinetics, TG analysis in open aluminium pans was performed with Exstar6000 TG/DTA6300 (SII Nanotechnology). Desolvation kinetics were studied in the isothermal mode at the temperature range from 30 to 110°C with a step of 5 °C. The heater unit was preset to the required temperature before the insertion of the sample. For each sample, desolvation was performed at four to eight

different temperatures selected according to the desolvation rate, which depended on the analysed solvate and the particle size. The sample weight was 5.0 ± 0.5 mg and the nitrogen flow rate was 100 ± 10 mL·min⁻¹.

The desolvation activation energy and kinetic model were determined using a model-free approach⁶. The data sets of fraction desolvated (α) – time were obtained with $\Delta\alpha = 0.02$ for each temperature. E_a was calculated from the Arrhenius equation with isoconversional methods⁷⁻⁹: Friedman (FR)¹⁰ and average linear integral method (ALIM)¹¹. The E_a was calculated from the slope of the line in the corresponding coordinates for α values with step size 0.02^{10, 11}, and identical E_a values were obtained. The confidence intervals for the calculated E_a values were evaluated from the slope error of the line used for calculation of E_a with the FR method. Kinetic model determination was performed with ALIM¹¹ and also with the reaction progress reconstruction in the coordinates $g(\alpha) - \alpha$ ^{12, 13} and $f(\alpha) - \alpha$ ^{9, 12, 13}. Besides, kinetic model determination was performed with reduced time plots¹⁴. The most often used solid state kinetic models were included in the analysis^{7-9, 15-17}.

Dihydrate. Dehydration kinetics of **DH** powder was studied in isothermal mode. It was determined that the dehydration $E_a = 120 \pm 20$ kJ·mol⁻¹, and the dehydration is limited by the phase boundary movement, with the most suitable kinetic model being R2 in particular. Hot-stage microscopy (HSM) analysis of the dehydration of a single crystal, however, showed the nucleation and nuclei growth, which could explain the formation of polymorphs **II** and **I** in the dehydration process of a crystal.



S20. Dehydration kinetic curves of **DH** at different temperatures in isothermal mode.

Type 1 solvates. A study of the desolvation kinetics of grinded type 1 solvate samples in isothermal mode was performed and it was determined that the desolvation E_a is 100 ± 20 kJ·mol⁻¹ for **S_{Me}** and 120 ± 20 kJ·mol⁻¹ for **S_{Et}**. Nevertheless, the desolvation curves were complicated by fast desolvation up to desolvation degree $\alpha = 0.5$ and then relatively slow desolvation at higher α values due to already described difference in the desolvation rates for solvate with different distance from the surface of the particles. The desolvation curves resembled those of diffusion models (D5 in particular), meaning that the rate limiting step is a diffusion, which agrees with the observation that the escape of the solvent across the product layers is difficult and able to significantly slow down the desolvation process.

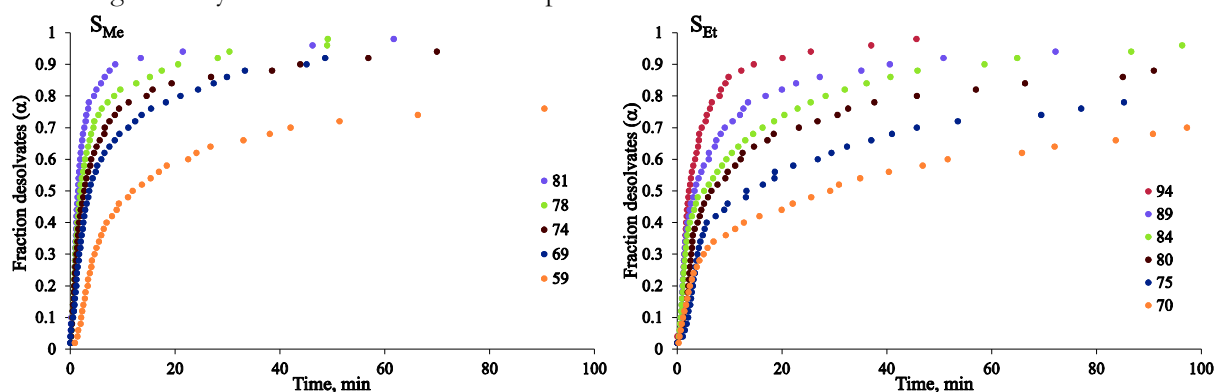


Figure S21. Desolvation kinetic curves of type 1 solvates at different temperatures in isothermal mode.

Type 2 solvates. Desolvation E_a for both S_{ACN} and S_{EtOAc} was determined to be $150 \pm 30 \text{ kJ} \cdot \text{mol}^{-1}$ and desolvation appeared to be limited by the phase boundary movement. HSM analysis revealed that desolvation of S_{ACN} crystal occurred by the appearance of dark spots oriented along the crystal longest dimension, which, based on the morphology prediction in *Mercury*, is along a -axis in the direction of the solvent channels. Both of these observations support the assumption that the desolvation occurs by the solvent escape via the channels.

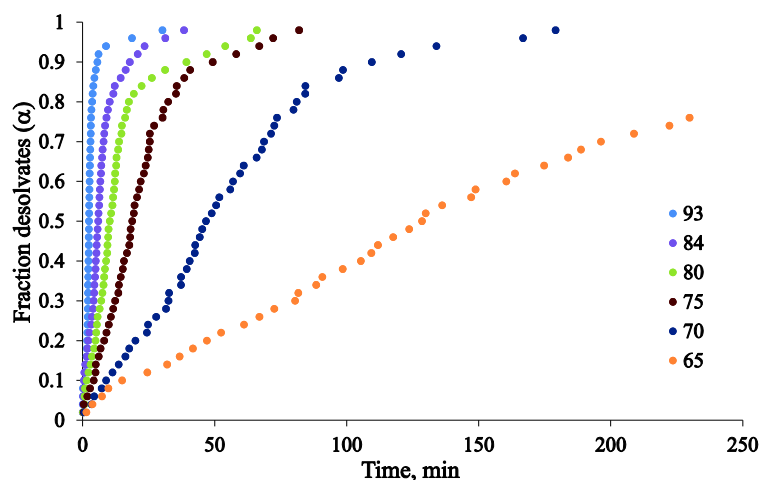


Figure S22. Desolvation kinetic curves of S_{ACN} at different temperatures in isothermal mode.

Benzyl alcohol solvate. It was determined that the desolvation $E_a = 100 \pm 10 \text{ kJ} \cdot \text{mol}^{-1}$, and the desolvation is limited by the phase boundary movement, with the most suitable kinetic model being R3 in particular.

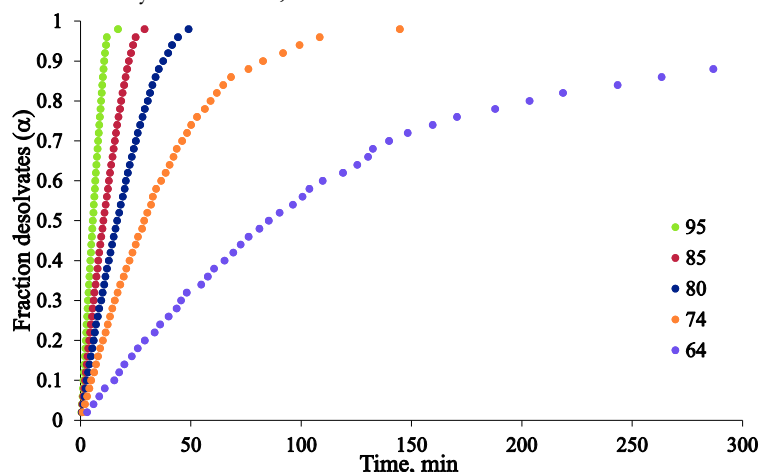


Figure S23. Desolvation kinetic curves of S_{Benz} at different temperatures in isothermal mode.

Dioxane solvate. The desolvation of S_{DIOX} at elevated temperature produced mainly polymorph **III**, although typically also impurities of **I** were observed. Desolvation analysis with VT-PXRD showed that poorly crystalline **III** was the initial desolvation product with the following transformation to more crystalline **III**. More complex desolvation occurred at ambient conditions, see Figures S24. In the first step the intensity of peaks characteristic to S_{DIOX} decreased, followed by the appearance of new peaks, position for part of which corresponded to that of polymorph **III**. Further reduction of the intensity for peaks not corresponding to the polymorph **III** occurred, and after 22 days only peaks corresponding to **HH** was present. Parallel to PXRD analysis thermal analysis was carried out (see Figures S25) and showed the reduction of the solvent content by increasing the time. This confirms the presence of two phases after the desolvation and suggests that the disappearing phase probably is a lower stoichiometry dioxane solvate (designated as S_{DIOX2} in Figure 11), while phase present after 22 days is pure **HH**.

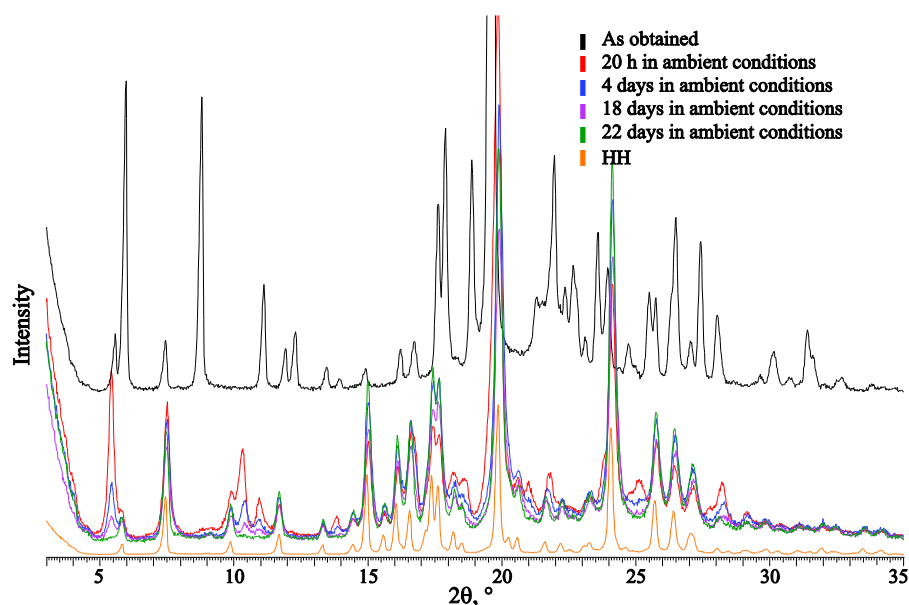


Figure S24. PXRD patterns recorded during storage of S_{DIOX} in ambient conditions.

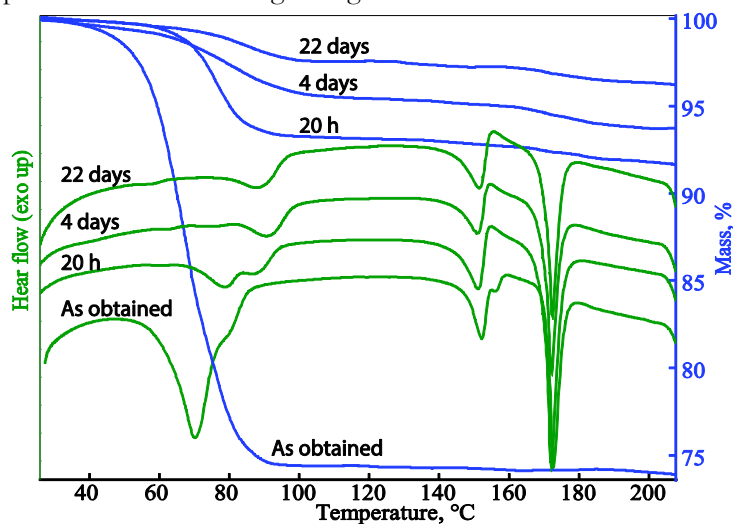


Figure S25. DTA/TG patterns recorded during storage of S_{DIOX} in ambient conditions.

REFERENCES

- (1) Gramatica, P.; Navas, N.; Todeschini, R., Classification of organic solvents and modelling of their physico-chemical properties by chemometric methods using different sets of molecular descriptors. *Trends Anal. Chem.* **1999**, 18, (7), 461-471.
- (2) Gu, C.-H.; Li, H.; Gandhi, R. B.; Raghavan, K., Grouping solvents by statistical analysis of solvent property parameters: implication to polymorph screening. *Int. J. Pharm.* **2004**, 283, (1-2), 117-125.
- (3) Gelbrich, T., The Xpac program for comparing molecular packing. *IUCr Newslett.* **2006**, (7), 39-44.
- (4) Gassim, A. E. H.; Girgis Takia, P.; James, K. C., Polymorphism and possible intramolecular bonding in benperidol. *Int. J. Pharm.* **1986**, 34, (1-2), 23-28.
- (5) Azibi, M.; Draguet-Brughmas, M.; Bouche, R., Polymorphisme des butyrophenones: benperidol et droperidol. *Pharm. Acta Helv.* **1982**, 57, (7), 182-188.
- (6) Vyazovkin, S.; Burnham, A. K.; Criado, J. M.; Pérez-Maqueda, L. A.; Popescu, C.; Sbirrazzuoli, N., ICTAC Kinetics Committee recommendations for performing kinetic computations on thermal analysis data. *Thermochim. Acta* **2011**, 520, (1-2), 1-19.
- (7) Khawam, A.; Flanagan, D. R., Basics and applications of solid-state kinetics: A pharmaceutical perspective. *J. Pharm. Sci.* **2006**, 95, (3), 472-498.

- (8) Koradia, V.; de Diego, H. L.; Elema, M. R.; Rantanen, J., Integrated approach to study the dehydration kinetics of nitrofurantoin monohydrate. *J. Pharm. Sci.* **2010**, 99, (9), 3966-3976.
- (9) Sheth, A. R.; Zhou, D.; Muller, F. X.; Grant, D. J. W., Dehydration kinetics of piroxicam monohydrate and relationship to lattice energy and structure. *J. Pharm. Sci.* **2004**, 93, (12), 3013-3026.
- (10) Friedman, H. L., Kinetics of thermal degradation of char-forming plastics from thermogravimetry. Application to a phenolic plastic. *J. Polym. Sci. C* **1964**, 6, 183-195.
- (11) Ortega, A., A simple and precise linear integral method for isoconversional data. *Thermochim. Acta* **2008**, 474, (1-2), 81-86.
- (12) Zhou, D.; Schmitt, E. A.; Zhang, G. G. Z.; Law, D.; Wight, C. A.; Vyazovkin, S.; Grant, D. J. W., Model-free treatment of the dehydration kinetics of nedocromil sodium trihydrate. *J. Pharm. Sci.* **2003**, 92, (7), 1367-1376.
- (13) Vyazovkin, S.; Wight, C. A., Kinetics in Solids. *Annu. Rev. Phys. Chem.* **1997**, 48, (1), 125-149.
- (14) Bamford, C. H.; Tipper, C. F. H., *Reactions in the Solid State*. ed.; Elsevier: Amsterdam, 1980; p 340.
- (15) Khawam, A.; Flanagan, D. R., Solid-State Kinetic Models: Basics and Mathematical Fundamentals. *J. Phys. Chem. B* **2006**, 110, (35), 17315-17328.
- (16) Dickinson, C. F.; Heal, G. R., Solid-liquid diffusion controlled rate equations. *Thermochim. Acta* **1999**, 340-341, (0), 89-103.
- (17) Galwey, A. K.; Brown, M. E., *Thermal Decomposition of Ionic Solids*. ed.; Elsevier: Amsterdam, 1999; p 598.

I hereby declare and confirm with my signature that the doctoral dissertation “**On the rationalization of the formation, stability and phase transitions of pharmaceutically active solid substance solvates**” is exclusively the result of my own autonomous work based on my research and literature published, which is seen in the list of original publications and bibliography used. I also declare that no part of the paper submitted has been made in an inappropriate way, whether by plagiarizing or infringing on any third person's copyright. Finally, I declare that no part of the thesis submitted has been used for any other thesis in another higher education institution, research institution or educational institution.

Author: Agris Bērziņš

Signature _____

Supervisor: Prof., Dr. Chem. Andris Actiņš

Signature _____

Thesis submitted in the Promotion Council in Chemistry of University of Latvia for the commencement of the degree of Doctor of Chemistry on _____.

Secretary of the Promotion Council: Vita Rudoviča _____

Thesis defended at the session of Promotion Council in Chemistry of University of Latvia for the commencement of the degree of Doctor of Chemistry on June 27, 2015, protocol No. _____

Secretary of the Promotion Council: Vita Rudoviča _____

SCIENTIFIC ARTICLES

Dehydration of mildronate dihydrate: a study of structural transformations and kinetics†

Cite this: *CrystEngComm*, 2014, 16, 3926

Agris Bērziņš* and Andris Actiņš

The dehydration of mildronate dihydrate (3-(1,1,1-trimethylhydrazin-1-ium-2-yl)propionate dihydrate) was investigated by powder X-ray diffraction, thermal analysis, hot-stage microscopy, water sorption–desorption studies and dehydration kinetic studies. It was determined that mildronate dihydrate dehydrated in a single step, directly transforming into the anhydrous form. In order to understand the reasons for a one step dehydration mechanism, crystal structures of dihydrate, monohydrate and anhydrous forms were compared, proving the similarity of the dihydrate and anhydrous forms. In order to understand the reasons for molecule reorganization during dehydration, the energy of the anhydrous form was compared with that of a theoretical dihydrate structure without water molecules. It was proven that the experimentally observed anhydrous phase AP was thermodynamically more stable. By analyzing the effect of the particle size and sample weight on the dehydration kinetic parameters it was determined that besides the main rate limiting step, phase boundary advancement, contribution from the water diffusion outside the crystal and the water diffusion outside the powdered sample also appeared to affect the dehydration kinetics and contribution from these processes could be changed by changing the aforementioned factors.

Received 14th October 2013,
Accepted 21st February 2014

DOI: 10.1039/c3ce42077a

www.rsc.org/crystengcomm

Introduction

It has been shown that many active pharmaceutical ingredients (APIs) can exist in hydrated forms.¹ Changes in the hydration state of API can occur during crystallization, drying, wet granulation, milling, freeze drying, tableting, or even during storage and transportation.^{1,2} Such changes result in modification of API physicochemical properties, such as solubility, dissolution rate and bioavailability,² so it is important to identify possible phase transitions and to determine the conditions in these transitions before undertaking routine manufacturing. One of the main factors affecting hydrate stability is the role played by water molecules in the crystal structure, and it has been pointed out³ that besides investigating the conditions for hydrate stability and phase transitions it is also important to understand and explain these phenomena from a structural point of view, thus enabling the prediction of hydrate stability and changes using crystal structures as the only starting information.

The most common techniques for studying dehydration or desolvation are powder X-ray diffraction (PXRD),^{4–6} differential scanning calorimetry (DSC),^{6–9} thermogravimetry (TG),^{10,11}

hot-stage microscopy (HSM),^{4,12–14} differential thermal analysis (DTA),⁹ infrared and Raman spectroscopy^{15–17} and nuclear magnetic resonance spectroscopy.^{16,18} By using these methods it is possible to explore the dehydration behaviour of a hydrate. However, these techniques alone are insufficient for understanding the reasons for changes if structural analysis of the crystals is not performed. Thus, the crystal structures of hydrate and dehydration products should be compared. That includes comparison of structures¹⁹ by using packing analysis,^{20–22} investigation of molecular conformation²³ and intermolecular interactions.^{24–26}

An additional tool to better understand dehydration mechanisms is the determination of dehydration kinetic parameters: kinetic model and activation energy (E_a).^{5,27} Although it is known that there are a lot of factors affecting the dehydration kinetics and there are cases where these effects can be very important,²⁸ it is generally accepted that the crystal structure is usually the dominant factor.^{16,29,30} Therefore, by knowing the crystal structure of a hydrate and its dehydration kinetic parameters, it is possible to understand the mechanism of the dehydration process.^{4,5,14,27,29–31}

Mildronate (3-(1,1,1-trimethylhydrazin-1-ium-2-yl)propionate; Fig. 1) is a γ -butyrobetaine analogue, an inhibitor of γ -butyrobetaine hydroxylase, and used as an anti-ischemic drug.^{32,33} It is known to exist in the form of dihydrate,³⁴ monohydrate or anhydrous phase.³⁵ The crystal structures of all of these phases are known. Dihydrate DH belongs to the $P2_1/c$ space group,^{34,36} the monohydrate MH crystallizes in the $P\bar{1}$ space group,³⁷ and both hydrates contain water molecules in

Faculty of Chemistry, University of Latvia, Rīga, Kr. Valdemāra iela 48, LV-1013, Latvia. E-mail: agris.berzins@lu.lv; Tel: +(371) 67372576

† Electronic supplementary information (ESI) available: Additional experimental details, more detailed analysis of DH dehydration process, mildronate crystal structures, potential energy surface scans, molecular conformation energy, intermolecular interaction energy and results from crystal structure optimization, and optimized crystal structures of AP and MH. See DOI: 10.1039/c3ce42077a

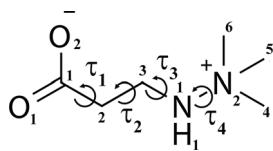


Fig. 1 Molecular structure of mildronate showing the atom numbering scheme and dihedral angle designations used in this work.

structural channels. The anhydrous phase AP belongs to the $P2_1/n$ space group with empty channels present in the structure.³⁷ Mildronate is hygroscopic and deliquesces if kept in high humidity. When heated in dry air, mildronate DH transforms into AP, whereas at high temperature and relatively high humidity it transforms into MH.³⁵ However, the dehydration mechanism of the DH, the only stable mildronate form in ambient conditions, has not yet been examined. Understanding the mechanism of such dehydration is important for the systematic study of the dehydration processes of pharmaceutical materials.³⁸

The aims of this study were: a) to determine the dehydration mechanism of mildronate DH; b) to establish the reasons for the observed one step dehydration process of mildronate DH directly to the AP, c) to understand the observed dehydration product formation by calculating the conformation and crystal structure energy, and d) to calculate the dehydration kinetic parameters and relate them to the dehydration mechanism and the crystal structure of DH.

Experimental section

Sample preparation and storage

Mildronate was provided by JSC Grindeks, Riga, Latvia, and was confirmed as pure DH by PXRD. A sample was prepared by slowly crystallizing mildronate from water at 30 °C. The obtained product was then fractionated according to the particle size by pushing through sieves with mesh sizes of 1300, 700, 350, 150, 67 and 40 μm, thus obtaining 6 fractions (the obtained particle size distribution for different fractions is given in Fig. S1†). The sample was stored above the saturated solution of potassium acetate (relative humidity of 22.5%).

Powder X-ray diffraction

PXRD patterns were measured on a D8 Advance (Bruker) diffractometer using copper radiation ($\text{CuK}\alpha$) at a wavelength of 1.54180 Å. The tube voltage and current were set to 40 kV and 40 mA, respectively. The divergence and antiscattering slits were set at 1.0 mm, and the receiving slit was set at 0.6 mm. The diffraction patterns were recorded with a scintillation detector using a scanning speed of 0.5 s/0.02° from 3° to 30° in the 2θ scale. When necessary, to prevent the atmospheric humidity effect, samples were covered with a 10 μm polyethylene film.

For variable temperature PXRD (VT-PXRD), a D8 Advance (Bruker) diffractometer equipped with a MRI heating stage, a Sol-X energy dispersive detector, automatically adjustable

slits (1.0, 1.0 and 0.1 mm) and Soller collimators were used. The diffraction patterns were recorded using a scanning speed of 4 s/0.02° from 10° to 25° in the 2θ scale. A stepwise temperature increase of 1 °C per diffraction pattern was used from 30 to 60 °C, and then 5 °C per diffraction pattern was used up to 80 °C.

Thermal analysis

DSC patterns were recorded with a DSC 823e apparatus (Mettler Toledo), and 5–10 mg of each sample was used for analysis. Samples were heated in sealed aluminium pans at a heating rate of 1 °C min⁻¹ or 5 °C min⁻¹ from 30 °C to 120 °C in static air atmosphere. Some of the samples were pinholed with a hole diameter 0.5 mm.

DTA/TG analysis was performed with an Exstar6000 TG/DTA6300 (SII) apparatus. Open aluminum pans were used. Sample heating from 30 to 120 °C was performed at heating rates of 0.5, 1, 2, 3, 4 and 5° min⁻¹. A sample mass of 7.0 ± 0.5 mg and nitrogen flow with a rate of 80 ± 10 mL min⁻¹ were used.

Dehydration kinetics was analyzed isothermally in a temperature range of 25 to 80 °C with a step of 5 °C using an Exstar6000 TG/DTA6300 (SII) apparatus. The heater unit was preset to the required temperature allowing fast stabilization of the necessary temperature at the start of the experiment. For each sample, dehydration was performed at eight different temperatures selected according to the dehydration rate. The sample mass was 7.0 ± 0.5 mg, and the nitrogen flow rate was 80 ± 10 mL min⁻¹. The effect of the sample mass was determined at additional data points, where the sample mass was 2, 4, 6, 8, 10 mg.

For HSM, a Laborlux 12 PolS (Leitz) polarized light microscope equipped with a heating stage and a Newtronic heating control module was used. The heating rate was 5° min⁻¹. Images were collected with Leica Application Suite software from a DFC450 (Leica) digital microscope camera.

Energy calculation and geometry optimization

Single molecule and molecular cluster energy calculation and geometry optimization were performed in *Gaussian09*.³⁹ Energy calculation and geometry optimization of crystal structures were performed in *CRYSTAL09*⁴⁰ at the B3LYP-D*^{41,42} level using a 6-31G(d,p) basis set.^{43,44} DFT-D dispersion correction was performed with a Grimme dispersion correction model⁴⁵ modified as described in the literature.^{42,46,47} Detailed parameters used for calculations in *CRYSTAL09* are given in the ESI†. For calculations crystal structures of DH (determined from SCXRD data³⁶) and AP (determined from PXRD data,³⁷ corrected in *Gaussian09* at the B3LYP/6-31G level. See ESI†) were used. All of the obtained energies were corrected for the basis set superposition error by the counterpoise method.⁴⁸ Infrared frequency calculation^{49,50} was performed for structures after the full geometry optimization in order to calculate the zero-point vibration correction and thermal correction on the total energy.

Hydrogen bonded dimer and lattice energy calculation in CLP suite

Lattice energy calculations were performed with semi-empirical PIXEL⁵¹ methodology (code provided in the CLP software suite). Empirical parameters were used as provided in the literature.^{51,52} The atom positions for the purposes of this calculation were obtained by standard procedure using *RETCIF* and *RETCOR* modules. Hydrogen atom positions were renormalized. Molecular electron density calculations were performed in *Gaussian09*³⁹ at the MP2/6-31G(d,p) level using standard grid parameters. Condensation at level 4 and a calculation cutoff value of 35 Å were used.

Calculation of kinetic parameters

Data sets of conversion degree (α)-time were obtained with $\Delta\alpha = 0.02$ at each temperature. E_a was calculated using model fitting methods: the kinetic model was determined from linearization of experimental points in coordinates $g(\alpha)$ -time, and the model with the best linear fit was selected from the list of the most often used solid-state kinetic models.^{4,27,53,54} The dehydration rate constants were subsequently determined by plotting experimental data points in the coordinates α -time and fitting theoretical lines modelled from selected kinetic models to the experimental points. The sum of the squared differences between practical and theoretically calculated α values was minimized with MS Excel Solver. If more than one model was selected for this procedure, then the best model was identified by the smallest sum of the least squares. The E_a values were then determined from the Arrhenius plot.

Results and discussion

Characterization of mildronate dihydrate dehydration

It was determined that at a 25 °C temperature DH was stable in the relative humidity interval from 6 to 50%, but dehydrated to AP at humidity below 6%. Thus it was confirmed that MH was not thermodynamically stable at any of the examined conditions (see ESI†). It was observed that the dehydration of DH at various temperatures gave AP as the only product, implying that the dehydration of DH was a one step process. In order to confirm this dehydration mechanism, we analyzed the dehydration of DH with VT-PXRD under air atmosphere. The temperature in the range where dehydration was observed in other experiments was raised with a 1 °C step size per diffraction pattern, until complete dehydration was observed. Diffraction patterns for those temperatures where phase transition was observed are given in Fig. 2. It can be seen that at $p(\text{H}_2\text{O}) = 1.1$ kPa, with relative humidity of 40% at 22 °C, dehydration started at the 57 °C temperature, which was identified by appearance of the AP peaks (marked with blue triangles). Formation of MH was not observed in this experiment, nor in other similar experiments. The characteristic diffraction peak position for MH would be at 12.0° and 16.6° in the 2θ scale (as illustrated in Fig. S3†).

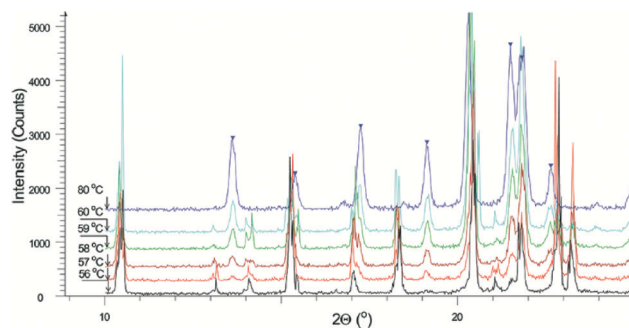


Fig. 2 VT-PXRD patterns of mildronate DH dehydration.

Dehydration of DH samples was analyzed with DSC in closed or pinholed sample holders and with DTA/TG in open pans under nitrogen flow. In DTA analysis one or two overlapping endothermic peaks appeared with dehydration starting at 45–55 °C. The second endothermic effect was always observed as a relatively narrow peak at 86–88 °C and above this temperature the weight loss rate noticeably decreased. The temperature of the first peak was affected by the heating rate and the particle size, whereas these parameters did not affect the temperature of the second peak (see Fig. 3 and S4†). When DH samples were analyzed with DSC, dehydration was observed as a narrow signal with peak temperatures of 88–90 °C, regardless of the hole in the container (see Fig. S4†). From various experiments (9 scans for particle size fractions from <40 μm up to 350–700 μm) the enthalpy of the observed process was calculated as 31.8 ± 0.9 kJ mol⁻¹.

From the obtained data it can be concluded that the observed endothermic process in the DSC scans under static air atmosphere was melting/peritectic decomposition of the DH. This explains the observed enthalpy value (31.8 ± 0.9 kJ mol⁻¹), which was too low even for the evaporation of two water molecules (the vaporization enthalpy of water at the corresponding temperature is 41.6 kJ mol⁻¹⁵⁵). This was obvious for closed pans, and the explanation for pinholed pans was that the size of the hole was too small for evaporation of the evolved water during the analysis. However, when

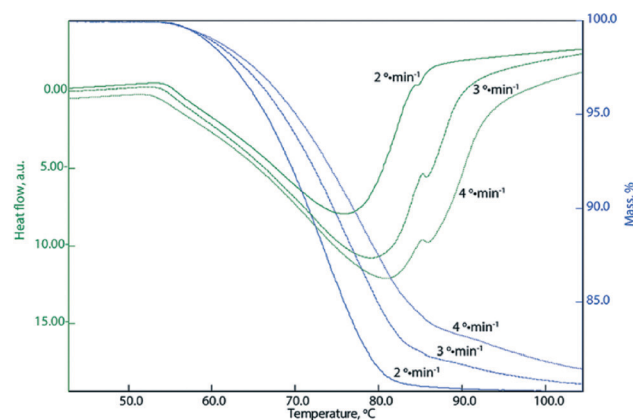


Fig. 3 DTA/TG curves of mildronate DH fraction 67–150 μm at various heating rates.

DH was heated in a DTA/TG instrument on open pans, nucleation of AP started at lower temperatures and water was lost much more effectively. Thus the dehydration of the DH was finished before reaching the melting temperature in cases when the heating rate was slow enough and/or particles were small enough. By using the DTA data it was calculated that the dehydration enthalpy of the DH was $120 \pm 10 \text{ kJ mol}^{-1}$, corresponding to the sum of the crystal hydrate decomposition and water vaporization enthalpies (DTA was calibrated with substances having known melting and dehydration enthalpy values).

If complete dehydration was not reached until the melting temperature in the DTA scans, then a melting/peritectic decomposition process was also observed. This was supported by the HSM study of two samples with different particle sizes (see ESI†) and by the decrease of the weight loss rate.

Phase composition of the samples obtained after and during DTA/TG analysis was determined with PXRD. It was found that for samples where dehydration was observed as a one step process (complete dehydration was reached below 86–88 °C), the only phase which formed during and after the dehydration was AP. The results of PXRD and thermal analysis thus indicated that AP formed as the only product in a one-step dehydration process. However, when dehydration was slower (and also the melting/peritectic decomposition signal appeared in DTA) during and after the second endothermic dehydration peak (at temperatures above 90 °C), MH was sometimes also detected as one of the phases. Nevertheless, after exceeding the melting temperature, formation of MH occurred due to the crystallization of mildronate from the solution or solid phase transition from the AP in the presence of liquid water. This observation agreed with the previously reported fact that MH was stable only at an elevated temperature.³⁵

The relationship between crystal structures and the observed dehydration mechanism

The dehydration of DH resulted in the formation of AP instead of MH. This observation could be related to the similarity of the crystal structures of DH and AP. To explore this theory, we analyzed the structures of three crystalline phases formed by mildronate.

Mildronate molecules in the structures of DH and MH adopted the same conformation and were characterized by the same hydrogen bonding motif different from that in the AP structure (see ESI†). Thus, from this analysis, the crystal structures of DH and MH appeared to be similar.³⁷

However, analysis of molecular packing in the crystal structures of DH, AP and MH showed that the structures of DH and AP were similar and consisted of four mildronate molecules notated A, B, C and D (each generated by one of four symmetry operations corresponding to the $P2_1/c$ or $P2_1/n$ space group). In DH these molecules were grouped around the hydrogen bonded graph set ring $R_4^4(8)$ formed by water molecules (see Fig. S12†). Each of the four molecules, A, B, C and D, formed a hydrogen bonded molecule pair with the molecules A', B', C' and D', respectively. Similarly arranged four pairs of molecules, A–A', B–B', C–C' and D–D', could be identified in the crystal structure of AP as well (see Fig. 4). However, in the structure between these molecules there was an empty channel, and molecule pairs were packed more tightly. Besides this, there were significant changes in molecular conformation (τ_1 and τ_2 , see ESI†) and hydrogen bonds between the molecule pairs A and A', B and B' *etc.* were lost, but new hydrogen bonds formed between molecules A and D, and between B and C, thus forming C(6) chains (see Fig. S12†). Therefore, inversion-related antiparallel molecule pairs occurred in the crystal structures of DH and AP. Two such antiparallel pairs (A–A' and C–C') were situated perpendicularly to two other (B–B' and C–C').

In the crystal structure of MH, inversion-related antiparallel molecule pairs E–F were packed parallel to other such pairs, resulting in layers of mildronate molecules (see Fig. 4). These layers were interconnected by hydrogen bonds mediated by water molecules (see Fig. S12†). Although hydrogen bonded antiparallel molecule pairs with the same molecular conformation were present in both hydrates, these pairs in the MH structure were packed in a different way. Therefore, the molecular conformation can be associated with hydrogen bonding motif and/or the presence of the hydrogen bonds with water molecules but not with the molecular packing.

Thus, it was shown that the transformation from DH to AP was associated with only minor changes in packing of the mildronate molecules. At the same time, the transformation

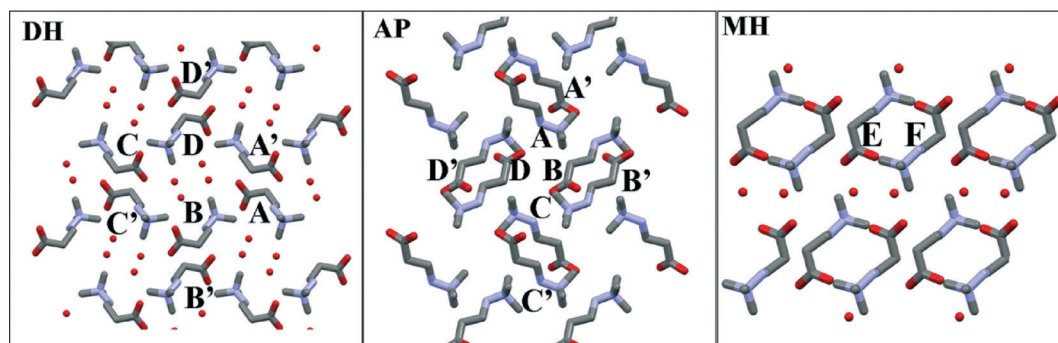


Fig. 4 Molecular packing in the crystalline forms of mildronate (hydrogen atoms have been omitted for clarity).

from the DH structure to MH was connected with important reorganization of mildronate molecular packing, which could occur only during destructive dehydration followed by crystallization of a new phase. Thus it can be seen that transition from DH to AP should be an easy one-step process, and not connected with formation of MH as an intermediate step. However, dehydration did not occur as a single crystal to single crystal transition. It can be concluded that structure reorganization was important enough to introduce cracking and thus AP was produced as a polycrystalline powder.

Based on the structural analyses, we provide a mechanism of water elimination and structure reorganization explaining the observed dehydration of DH to AP. Due to the presence of large channels containing all of the water molecules, it was likely that the first step in the dehydration process represented escape of water by emptying of the channels (see 1 in Fig. 5). After this step, conformation change (2) and molecular translation (3) occurred, forming AP as the final product. Although separated in the Fig. 5 for clarity, most probably both of these processes happened simultaneously and were associated with disappearance of the hydrogen bonded molecule pairs and formation of new hydrogen bonds observed in the AP structure.

Thus, based on the dehydration process classification according to structural changes during the dehydration, dehydration of the DH could be classified as a) a water evolution type WET3 with direct formation of the AP crystalline phase after the dehydration³ and b) cooperative release of water followed by the cooperative rearrangement, thus belonging to the class II-Coop.-Reorg.,⁵⁶ according to the two systems described in the literature.

Analysis of the observed structural changes during the dehydration of mildronate DH

Despite the presented rationalization why the dehydration of DH resulted directly in AP, the observations did not explain why conformation of mildronate changed and why complete rearrangement in the hydrogen bonding network between mildronate molecules was observed during the dehydration. Firstly, conformation energy analysis was performed in order to explain the presence of the observed conformations in AP

and DH structures and to evaluate the energy barriers associated with conformation changes. Secondly, the energy of the AP structure was compared with the energy of the theoretically proposed DH structure without water molecules (DHWW) where molecular conformations and hydrogen bonding patterns were retained as in the DH structure. This structure would be obtained if the water molecules left the channels without introducing major changes to the rest of the structure, as it is observed for typical channel hydrates.^{57,58}

Analysis of molecular conformation in AP and DH.

Intramolecular energy calculation of mildronate molecules extracted from AP and DH structures showed that the energy of both molecular conformations was almost the same. From PES scans (see ESI†) it was determined that the conformations observed in both DH and AP structures did not correspond to the global energy minimum, defined as the molecular conformation with an intramolecular hydrogen bond N–H \cdots O. Both in the DH and AP structures mildronate molecules had weak intramolecular hydrogen bonds C3–H \cdots O2(O1). However, if the intramolecular hydrogen bond N–H \cdots O formed, it would prevent the formation of strong intermolecular hydrogen bonds that dramatically affect the lattice energy. So it may be concluded that the molecular conformations observed in crystal structures correspond to local energy minima, which allow efficient intermolecular interactions.

Reliability of this conclusion and the obtained PES scans was supported by the crystal structures of various salts and co-crystals of mildronate.³⁶ In these crystal structures the τ_1 values clustered around 39° (4 hits) and 179° (9 hits) with one exception, and τ_2 clustered around 70° (4 hits) and 178° (9 hits) with one exception. For the dihedral angle τ_3 there were 11 values in the interval $180 \pm 10^\circ$ and three values lying in the interval $180 \pm 20^\circ$, while the dihedral angle τ_4 in all the cases matched the PES scan minima. In most of the cases weak intramolecular hydrogen bond C3–H \cdots O was observed also in these crystal structures.

From the PES analysis it was determined that the energy necessary for molecular conformation changes in transition from DH to AP was 10–25 kJ mol⁻¹ (see ESI†).

The comparison of intermolecular interaction energy and total energy for AP and DHWW. It was calculated that the

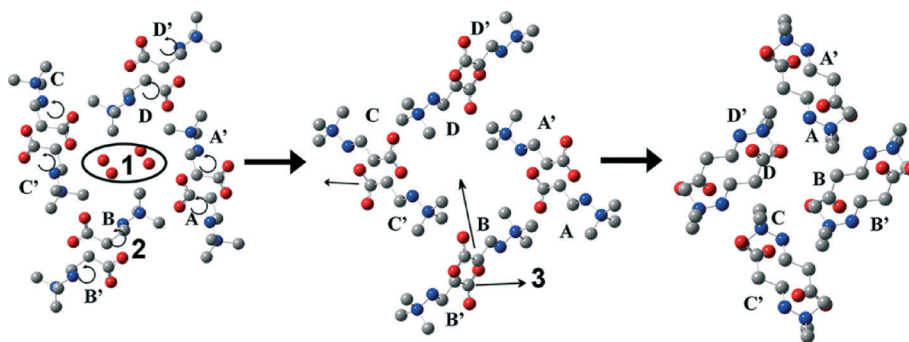


Fig. 5 Schematic representation of structural reorganizations during the transition from DH to AP.

interaction energy of two hydrogen-bonded molecules was more favourable in the DHWW structure (see ESI†). However, after optimization of the crystal structure, AP was found to be energetically favourable by 11.0 kJ mol^{-1} and the lattice energy of the AP structure was energetically favourable by 14 kJ mol^{-1} (see ESI†) thus proving that the role of strong hydrogen bonds does not always determine the stability of the crystal structure, as emphasized recently.^{59,60}

Therefore, the observed molecular reorganization and formation of AP during the dehydration of DH is explained by the fact that the AP structure is energetically more favourable because of more favourable intermolecular interactions.

Kinetic parameters and mechanism of dehydration

Kinetic parameters of dehydration

Particle size. Dehydration of DH was studied for samples with different particle sizes. Particle size distribution for different DH fractions is given in Fig. S1.† PXR was used to determine that in all of the cases AP was obtained as the only dehydration product. The dehydration E_a value for each fraction was calculated from isothermal experiments and are shown in Fig. 6.

From Fig. 6 it can be seen that the E_a of the samples with a particle size of up to $350 \mu\text{m}$ was $75 \pm 3 \text{ kJ mol}^{-1}$, but for particles larger than $350 \mu\text{m}$ there was a significant decrease of the E_a caused by increasing the particle size. Most probably this decrease of the E_a for larger particles was due to diffusion control. When considering water vapor escape through a thick product layer, the rate becomes diffusion limited for some critical particle size, and this effect grows upon further increase in the particle size.

It was determined that the most appropriate kinetic model for dehydration of fractions with a particle size below $150 \mu\text{m}$ was the one-dimensional phase boundary model R1, but for the particle size above $350 \mu\text{m}$ it was the two-dimensional phase boundary model R2. Kinetic models R1 and R2 both describe phase boundary controlled reactions with different dimensionality. This result fits with the observations from hot stage microscopy where the dehydration process initiated on the single crystal surface and then reaction boundary

progressed inwards to the crystal interior (as shown in Fig. S8†). It has been mentioned in the literature³ that the typical thickness of the reaction interface is $10\text{--}150 \mu\text{m}$, so for smaller particles the only rate limiting step can be the formation and advancement of this interface towards the crystal interior from only one energetically more favourable direction. However, the formation of the phase boundary for bigger particles (applicable in this case where the average particle diameter was above $350 \mu\text{m}$) was complete when there was still a lot of DH present. Thus the rate limiting step could also involve reaction interface advancement from other crystal faces, which could be described by a two dimensional phase boundary mechanism.

Sample weight. Dehydration of DH $<40 \mu\text{m}$ fraction was studied for samples with different weight. It was determined that the dehydration rate decreased when the sample weight was increased. The reason for the decrease of the rate constant by increasing the sample weight can be due to the slower vapor diffusion through the sample layer, which limits the total dehydration rate. Dehydration E_a dependence on the sample weight was calculated as well and the obtained results are shown in Fig. 7. It is apparent that the E_a decreased by increasing the sample weight. Such an effect can be the result of increased contribution from the bulk diffusion effect upon increasing the sample weight as the E_a of the diffusion step typically is smaller than that of the phase boundary reaction and more contribution from the diffusion would be observed by increasing the sample weight.

Dehydration mechanism. There are large channels containing water molecules along the a -axis^{34,36} in the DH structure. Thus, we suggested that during the dehydration of mildronate DH, water molecules escaped through these channels. It has been postulated that if the dehydration environment is controlled by nitrogen flow with relative humidity close to zero, then the water molecule diffusion to the crystal surface should not control the dehydration rate,³¹ as it appeared for mildronate DH where dehydration kinetics were described by models R1 and R2. Thus it can be concluded that the rate limiting step should be hydrogen bond dissociation and/or molecular conformation change and reorganization. From the PES analysis it was determined that the energy

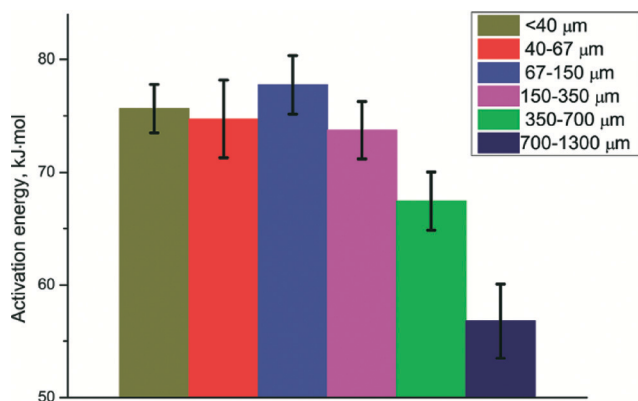


Fig. 6 Dehydration activation energy for different fractions of DH.

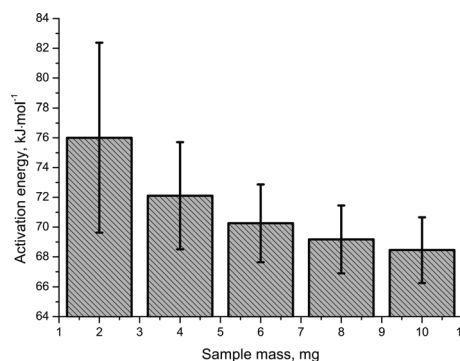


Fig. 7 Dehydration activation energy dependence on sample weight for the $<40 \mu\text{m}$ fraction.

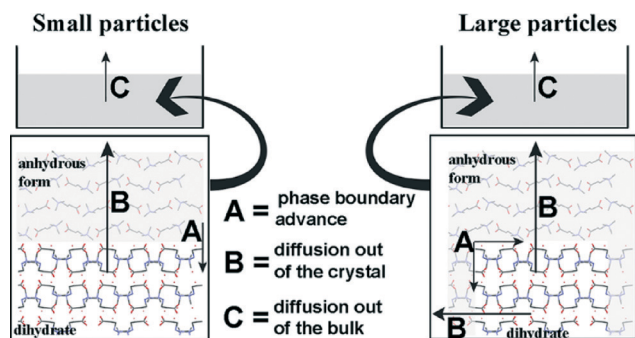


Fig. 8 Schematic representation of the dehydration process and the rate limiting steps.

necessary for molecular conformation changes was at least three times lower than the dehydration E_a (see ESI†). Thus it can be predicted that the rate limiting step most probably is the disruption of the hydrogen bonding network, or separation of mildronate molecules paired through hydrogen bonds in the crystal structure of DH.³⁴

However, it was also found that besides phase boundary advancement other factors limited the rate of dehydration: a) the diffusion rate of water outside the crystal and b) diffusion of water from the inside of the powder. By changing the particle size and sample weight the influence of these rate limiting steps could be modified. However, based on the results from kinetic model determination, phase boundary advancement was the main rate limiting step.

Based on the crystal structure it can be suggested that for small particles the phase boundary advancement during the dehydration of DH occurred along the a -axis and complete dehydration was reached by phase boundary advancement only in this direction. The dehydration rate could thus be described with a one-dimensional phase boundary reaction model. However, for particles with a size larger than 350 μm , dehydration most probably occurred also in the second energetically favourable direction. This can be described by the movement of the reaction interface also perpendicular to the channels where water molecules are situated in the DH crystal structure. As a result the dehydration could be described by a two-dimensional phase boundary reaction model. It is possible that evolving of water in the direction perpendicular to the water channels is hindered, thus contribution from the diffusion increased in this case, and the dehydration E_a decreased as observed for samples where R2 was determined as the most appropriate kinetic model. Schematic representation of the dehydration process and the rate limiting steps are given in Fig. 8.

Conclusions

The mechanism of mildronate dihydrate (DH) dehydration was analyzed according to various experimental methods, and it was determined that dehydration of the DH is a single-step process leading directly to the anhydrous form (AP). By analyzing the crystal structures of the DH, MH and AP it was

determined that, in addition to the similar molecular conformation and hydrogen bonding patterns in DH and MH, molecular packing in the DH and AP structures was also similar, thus explaining the one-step dehydration of the DH directly to AP.

The dehydration of the mildronate DH was linked to the escape of water molecules through structural channels, as molecular conformation changes and molecular translation. Thus, dehydration of the DH could be classified as a) WET3 with direct formation of the AP crystalline phase after the dehydration³ and b) class II-Coop.-Reorg.⁵⁶

The dehydration E_a of DH was $75 \pm 3 \text{ kJ mol}^{-1}$ for particles with a diameter below 350 μm but it decreased for larger particles due to the increasing effect of water diffusion out of the particle. The kinetic model best describing the dehydration of particles smaller than 150 μm was R1, while for particles larger than 350 μm it was the R2 model. This change was associated with the altered dimensionality of the phase boundary movement towards the center of the crystal.

By analyzing the sample weight effect on the dehydration, a decrease of the reaction rate and the dehydration E_a were observed by increasing the sample weight. This decrease was associated with increasing contribution from the water diffusion out of the powdered sample.

Acknowledgements

This work was supported by the European Social Fund within the project "Support for Doctoral Studies at University of Latvia". We wish to thank the University of Latvia Institute of Solid State Physics for the possibility to carry out calculations with *CRYSTAL09* software on the Latvian SuperCluster computers, and the Riga Technical University Institute of Inorganic Chemistry for the possibility to carry out VT-PXRD measurements, as well as the Riga Technical University Institute of Polymer Materials for the possibility to carry out hot-stage microscopy measurements, and Dr. Anatolijs Mišņovs for kindly supplying the crystal structure data of mildronate salts and co-crystals, and Inese Sarceviča for helpful consultations.

Notes and references

- 1 R. Hilfiker, *Polymorphism in the pharmaceutical industry*, Wiley-VCH Verlag GmbH & Co, KGaA., Weinheim, 2006.
- 2 R. Khankari and D. Grant, *Thermochim. Acta*, 1995, 248, 61–79.
- 3 A. Galwey, *Thermochim. Acta*, 2000, 355, 181–238.
- 4 V. Koradia, H. L. de Diego, M. R. Elema and J. Rantanen, *J. Pharm. Sci.*, 2010, 99, 3966–3976.
- 5 L. Malaj, R. Censi and P. D. Martino, *Cryst. Growth Des.*, 2009, 9, 2128–2136.
- 6 C. Guguta, H. Meeke and R. de Gelder, *J. Pharm. Biomed. Anal.*, 2008, 46, 617–624.
- 7 P. Chakravarty, R. T. Berendt, E. J. Munson, V. G. Young, R. Govindarajan and R. Suryanarayanan, *J. Pharm. Sci.*, 2010, 99, 1882–1895.

- 8 D. E. Braun, T. Gelbrich, V. Kahlenberg, R. Tessadri, J. Wieser and U. J. Griesser, *Cryst. Growth Des.*, 2009, 9, 1054–1065.
- 9 K. Fujii, H. Uekusa, N. Itoda, G. Hasegawa, E. Yonemochi, K. Terada, Z. Pan and K. D. M. Harris, *J. Phys. Chem. C*, 2009, 114, 580–586.
- 10 D. E. Braun, T. Gelbrich, R. K. R. Jetti, V. Kahlenberg, S. L. Price and U. J. Griesser, *Cryst. Growth Des.*, 2008, 8, 1977–1989.
- 11 F. Kang, F. G. Vogt, J. Brum, R. Forcino, R. C. B. Copley, G. Williams and R. Carlton, *Cryst. Growth Des.*, 2011, 12, 60–74.
- 12 P. Chakravarty, R. T. Berendt, E. J. Munson, V. G. Young, R. Govindarajan and R. Suryanarayanan, *J. Pharm. Sci.*, 2010, 99, 816–827.
- 13 N. Zencirci, E. Gstrein, C. Langes and U. Griesser, *Thermochim. Acta*, 2009, 485, 33–42.
- 14 A. Z. Zellelow, K.-H. Kim, R. E. Sours and J. A. Swift, *Cryst. Growth Des.*, 2010, 10, 418–425.
- 15 K. Kachrimanis and U. Griesser, *Pharm. Res.*, 2012, 29, 1143–1157.
- 16 F. G. Vogt, J. Brum, L. M. Katrincic, A. Flach, J. M. Socha, R. M. Goodman and R. C. Haltiwanger, *Cryst. Growth Des.*, 2006, 6, 2333–2354.
- 17 A. Zimmermann, F. Tian, H. L. de Diego, K. Frydenvang, J. Rantanen, M. R. Elema and L. Hovgaard, *J. Pharm. Sci.*, 2009, 98, 3596–3607.
- 18 C. Guguta, E. R. H. van Eck and R. de Gelder, *Cryst. Growth Des.*, 2009, 9, 3384–3395.
- 19 J. Bernstein, in *Polymorphism in Molecular Crystals*, ed. J. Bernstein, Oxford University Press, Oxford, 2002, pp. 29–65.
- 20 T. Gelbrich, *IUCr Newsletter*, 2006, pp. 39–44.
- 21 T. Gelbrich and M. B. Hursthouse, *CrystEngComm*, 2005, 7, 324–336.
- 22 K. Fujii, M. Aoki and H. Uekusa, *Cryst. Growth Des.*, 2013, 13, 2060–2066.
- 23 C. Guguta, H. Meekes and R. de Gelder, *Cryst. Growth Des.*, 2006, 6, 2686–2692.
- 24 J. J. McKinnon, M. A. Spackman and A. S. Mitchell, *Acta Crystallogr., Sect. B: Struct. Sci.*, 2004, 60, 627–668.
- 25 M. A. Spackman and D. Jayatilaka, *CrystEngComm*, 2009, 11, 19–32.
- 26 J. Martí-Rujas, A. Morte-Ródenas, F. Guo, N. Thomas, K. Fujii, B. M. Kariuki and K. D. M. Harris, *Cryst. Growth Des.*, 2010, 10, 3176–3181.
- 27 A. R. Sheth, D. Zhou, F. X. Muller and D. J. W. Grant, *J. Pharm. Sci.*, 2004, 93, 3013–3026.
- 28 M. E. Brown and R. E. Brown, *Thermochim. Acta*, 2000, 357, 133–140.
- 29 S. R. Byrn, R. R. Pfeiffer and J. G. Stowell, *Solid State Chemistry of Drugs*, SSCI, Inc., West Lafayette, IN, 2nd edn, 1999.
- 30 P. Perrier and S. R. Byrn, *J. Org. Chem.*, 1982, 47, 4671–4676.
- 31 Z. Dong, J. S. Salisbury, D. Zhou, E. J. Munson, S. A. Schroeder, I. Prakash, S. Vyazovkin, C. A. Wight and D. J. W. Grant, *J. Pharm. Sci.*, 2002, 91, 1423–1431.
- 32 I. Kalviņš and I. Stonāns, *WO Patent*, WO/2009/071586, 2009.
- 33 B. Z. Simkhovich, Z. V. Shutenko, D. V. Meirena, K. B. Khagi, R. J. Mezapuke, T. N. Molodchina, I. J. Kalvins and E. Lukevics, *Biochem. Pharmacol.*, 1988, 37, 195–202.
- 34 A. Kemme, J. Bleidelis, I. Kalvins and A. Eremeev, *Latv. PSR Zinat. Akad. Vestis*, 1983, 2, 215.
- 35 K. Veldre, A. Actiņš and A. Kalniņa, *Thermal Stability of 3-(2,2,2-trimethylhydrazine)propionate*, *Solid State Chemistry 2010*, Prague, 2010.
- 36 A. Mishnev, I. Kalvins, L. Aleksejeva and A. Lebedev, *Structure of Mildronate, its Pharmaceutical Salts and Cocrystals*, XXII Congress and General Assembly of the International Union of Crystallography, Madrid, Spain, 2011.
- 37 A. Zvirgzdiņš, K. Veldre and A. Actiņš, *Latv. J. Chem.*, 2011, 50, 64–72.
- 38 K. Fujii, H. Uekusa, N. Itoda, E. Yonemochi and K. Terada, *Cryst. Growth Des.*, 2012, 12, 6165–6172.
- 39 M. J. Frisch, G. W. Trucks, H. B. Schlegel, G. E. Scuseria, M. A. Robb, J. R. Cheeseman, G. Scalmani, V. Barone, B. Mennucci, G. A. Petersson, H. Nakatsuji, M. Caricato, X. Li, H. P. Hratchian, A. F. Izmaylov, J. Bloino, G. Zheng, J. L. Sonnenberg, M. Hada, M. Ehara, K. Toyota, R. Fukuda, J. Hasegawa, M. Ishida, T. Nakajima, Y. Honda, O. Kitao, H. Nakai, T. Vreven, J. A. J. Montgomery, J. E. Peralta, F. Ogliaro, M. Bearpark, J. J. Heyd, E. Brothers, K. N. Kudin, V. N. Staroverov, R. Kobayashi, J. Normand, K. Raghavachari, A. Rendell, J. C. Burant, S. S. Iyengar, J. Tomasi, M. Cossi, N. Rega, J. M. Millam, M. Klene, J. E. Knox, J. B. Cross, V. Bakken, C. Adamo, J. Jaramillo, R. Gomperts, R. E. Stratmann, O. Yazyev, A. J. Austin, R. Cammi, C. Pomelli, J. W. Ochterski, R. L. Martin, K. Morokuma, V. G. Zakrzewski, G. A. Voth, P. Salvador, J. J. Dannenberg, S. Dapprich, A. D. Daniels, O. Farkas, J. B. Foresman, J. V. Ortiz, J. Cioslowski and D. J. Fox, *Gaussian 09*, Gaussian Inc., Wallingford, CT, 2009.
- 40 R. Dovesi, V. Saunders, C. Roetti, R. Orlando, C. Zicovich-Wilson, F. Pascale, B. Civalleri, K. Doll, N. Harrison and I. Bush, *CRYSTAL09*, University of Torino, Torino, Italy, 2009.
- 41 A. Coelho, *J. Appl. Crystallogr.*, 2003, 36, 86–95.
- 42 B. Civalleri, C. M. Zicovich-Wilson, L. Valenzano and P. Ugliengo, *CrystEngComm*, 2008, 10, 405–410.
- 43 C. Gatti, V. R. Saunders and C. Roetti, *J. Chem. Phys.*, 1994, 101, 10686–10696.
- 44 M. A. Spackman and A. S. Mitchell, *Phys. Chem. Chem. Phys.*, 2001, 3, 1518–1523.
- 45 S. Grimme, *J. Comput. Chem.*, 2006, 27, 1787–1799.
- 46 L. Maschio, B. Civalleri, P. Ugliengo and A. Gavezzotti, *J. Phys. Chem. A*, 2011, 115, 11179–11186.
- 47 C. M. Zicovich-Wilson, B. Kirtman, B. Civalleri and A. Ramirez-Solis, *Phys. Chem. Chem. Phys.*, 2010, 12, 3289–3293.
- 48 S. F. Boys and F. Bernardi, *Mol. Phys.*, 1970, 19, 553–566.
- 49 F. Pascale, C. M. Zicovich-Wilson, F. López Gejo, B. Civalleri, R. Orlando and R. Dovesi, *J. Comput. Chem.*, 2004, 25, 888–897.

- 50 C. M. Zicovich-Wilson, F. Pascale, C. Roetti, V. R. Saunders, R. Orlando and R. Dovesi, *J. Comput. Chem.*, 2004, **25**, 1873–1881.
- 51 A. Gavezzotti, *New J. Chem.*, 2011, **35**, 1360–1368.
- 52 A. Gavezzotti, *The Coulomb - London - Pauli (CLP) model of intermolecular interaction*, Description and user's manual, 2012.
- 53 A. Khawam and D. R. Flanagan, *J. Pharm. Sci.*, 2006, **95**, 472–498.
- 54 A. Khawam and D. R. Flanagan, *J. Phys. Chem. B*, 2006, **110**, 17315–17328.
- 55 *CRC Handbook of Chemistry and Physics*, ed. D. Lide, Taylor & Francis Group, London, 87th edn, 2006.
- 56 S. Petit and G. Coquerel, *Chem. Mater.*, 1996, **8**, 2247–2258.
- 57 G. Stephenson, E. Groleau, R. Kleemann, W. Xu and D. Rigsbee, *J. Pharm. Sci.*, 1998, **87**, 536–542.
- 58 G. A. Stephenson and B. A. Diserod, *Int. J. Pharm.*, 2000, **198**, 167–177.
- 59 A. Gavezzotti, *Top. Curr. Chem.*, 2012, **315**, 1–32.
- 60 J. D. Dunitz and A. Gavezzotti, *Angew. Chem., Int. Ed.*, 2005, **44**, 1766–1787.

Effect of Experimental and Sample Factors on Dehydration Kinetics of Mildronate Dihydrate: Mechanism of Dehydration and Determination of Kinetic Parameters

AGRIS BĒRZIŅŠ, ANDRIS ACTIŅŠ

Faculty of Chemistry, University of Latvia, Rīga LV-1013, Latvia

Received 6 January 2014; revised 4 March 2014; accepted 25 March 2014

Published online 11 April 2014 in Wiley Online Library (wileyonlinelibrary.com). DOI 10.1002/jps.23972

ABSTRACT: The dehydration kinetics of mildronate dihydrate [3-(1,1,1-trimethylhydrazin-1-ium-2-yl)propionate dihydrate] was analyzed in isothermal and nonisothermal modes. The particle size, sample preparation and storage, sample weight, nitrogen flow rate, relative humidity, and sample history were varied in order to evaluate the effect of these factors and to more accurately interpret the data obtained from such analysis. It was determined that comparable kinetic parameters can be obtained in both isothermal and nonisothermal mode. However, dehydration activation energy values obtained in nonisothermal mode showed variation with conversion degree because of different rate-limiting step energy at higher temperature. Moreover, carrying out experiments in this mode required consideration of additional experimental complications. Our study of the different sample and experimental factor effect revealed information about changes of the dehydration rate-limiting step energy, variable contribution from different rate limiting steps, as well as clarified the dehydration mechanism. Procedures for convenient and fast determination of dehydration kinetic parameters were offered. © 2014 Wiley Periodicals, Inc. and the American Pharmacists Association *J Pharm Sci* 103:1747–1755, 2014

Keywords: dehydration; kinetics; thermal analysis; particle size; mathematical model; kinetic model; isoconversional methods

INTRODUCTION

It is known that many organic compounds can exist in hydrated forms^{1,2} and a variety of active pharmaceutical ingredients (APIs) are produced as hydrates.² The determination of the hydrate stability is thus important both from industrial and scientific point of view. Typically hydrate stability is evaluated by characterizing the dehydration conditions and observed phase changes. The most common techniques for studying dehydration are powder X-ray diffraction (PXRD),^{3–7} thermal analysis,^{3,5,6,8–14} spectroscopic methods,^{8,12,15–17} and particle morphology and particle size characterization of the original and dehydrated products.^{18–20} By using these methods, it is possible to determine the dehydration conditions and understand the behavior of hydrate upon dehydration. An additional tool for the better understanding of dehydration mechanisms is the determination of dehydration kinetic parameters: kinetic model and activation energy (E_a).^{4,21}

Although it is generally accepted that the crystal structure in most cases determines the dehydration kinetics,^{17,22,23} several other factors may contribute significantly.²⁴ Determination of the dehydration reaction kinetic parameters has been thoroughly explored, and a lot of studies can be found in the literature for organic compound hydrates, especially for API, for example,^{3,11,15} because of the practical interest in these compounds.² However, determination of the API hydrate dehydration kinetic parameters under various experimental

modes and under different conditions has not been sufficiently studied.

As already mentioned, it has been observed that the dehydration kinetic parameters can be strongly affected by various sample and experimental factors.^{25–27} Differences of the sample particle size,^{28–32} crystal habit,³³ sample history,²⁵ and crystal defect distribution²⁴ can result in different dehydration rates, E_a variation, and even change the kinetic model. Besides these factors, all the mentioned kinetic parameters can be affected by the relative humidity,^{31,32,34–36} inert gas flow rate,^{31,34} and sample weight.^{28,37} Thus, for the better understanding of the dehydration process and calculated kinetic parameters, the effects of sample and experimental factors should be evaluated.

Mildronate [3-(1,1,1-trimethylhydrazin-1-ium-2-yl)propionate; Fig. 1] is a γ -butyrobetaine analogue, inhibitor of γ -butyrobetaine hydroxylase, and used as an anti-ischemic drug.^{38,39} It is known to exist in a form of dihydrate DH,^{40,41} monohydrate MH, and anhydrous phase AP.⁴² Water molecules in the DH and MH are situated in structural channels,^{40,41,43} whereas in the structure of the AP, empty channels are present.⁴³ Dehydration of the DH is a single-step process resulting directly in the formation of AP.⁴⁴ The effects of some sample and experimental factors on the dehydration kinetic parameters have already been reported. However, only limited number of factors were studied for one sample in isothermal mode.⁴⁴

In this study, (1) the possibilities of determining the dehydration kinetic parameters of mildronate hydrate DH (the form used as API) by both isothermal and nonisothermal methods were explored, (2) the effect of various sample and experimental factors on the dehydration activation energy and kinetic model were studied in depth, (3) variations of kinetic parameters were used for understanding the dehydration mechanism,

Correspondence to: Agris Bērziņš (Telephone: +371-67372576; Fax: +371-67378736; E-mail: agris.berzins@lu.lv)

This article contains supplementary material available from the authors upon request or via the Internet at <http://onlinelibrary.wiley.com/>.

Journal of Pharmaceutical Sciences, Vol. 103, 1747–1755 (2014)

© 2014 Wiley Periodicals, Inc. and the American Pharmacists Association

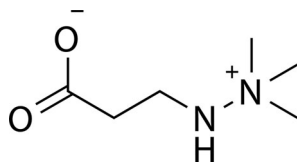


Figure 1. Molecular structure of mildronate.

and (4) optimal conditions for determining the dehydration kinetic parameters were selected.

Although the effects of various sample and experimental factors on the dehydration process of API hydrates have been investigated in a number of papers,^{14,18,28–30,45,46} in this study the effect of multiple factors on a single system was examined, so the magnitude and direction of each effect could be analyzed and explained. Investigation of the sample and experimental factors in both isothermal and nonisothermal modes allowed us to compare the influence of each factor on the results obtained in both modes. Moreover, evaluation of various factors allowed the identification of the most appropriate sample and experimental factors for performing reliable determination of the dehydration kinetic parameters.

EXPERIMENTAL

Sample Preparation and Storage

Mildronate DH was provided by JSC Grindeks (Riga, Latvia). The sample was confirmed as pure DH by PXRD. Four samples differing by the preparation procedure and/or storage conditions were used in this study. Samples were prepared by slowly crystallizing mildronate from water at 30°C or by drying a paste obtained by adding a small amount of water to mildronate in mortar. The obtained samples were fractionated by pushing through sieves with mesh size 1300, 700, 350, 150, 67, and 40 μm , yielding a maximum of seven fractions (the obtained particle size distribution for different fractions is given in Fig. S3). Part of the 150–350 and 350–700 μm fractions was slightly ground and then fractionated by pushing through sieves with mesh size 350, 150, 67, and 40 μm , and five fractions were thus obtained. Samples were stored at ambient temperature above saturated solutions of potassium acetate (relative humidity 22.5%) or magnesium chloride [relative humidity 34%, see Supporting Information (SI)]. All of the samples were used for determination of the dehydration kinetic parameters. Inorganic salts for humidity control were purchased from commercial suppliers and used as received. More details of sample preparation procedures are given in the SI.

For studying the effect of mechanical compression on the dehydration kinetics of DH, approximately 30 mg of sample was inserted in a die with 13 mm diameter, and then compressed at 130, 370, and 740 MPa for 1 min. Manual hydraulic press was used for compression of the samples. Right after the compression, the obtained tablet was either gently ground to obtain powder or divided into smaller pieces suitable for analysis with thermogravimetric (TG). Dehydration analyses were started immediately afterwards.

For studying the effect of prior history of dehydration/rehydration, the initial DH sample was dehydrated at 50°C temperature under N_2 flow. Then, the dehydrated sample was stored at the ambient temperature in 22.5% relative humidity.

Powder X-Ray Diffraction

Powder X-ray diffraction patterns were measured on a D8 Advance (Bruker AXS GmbH, Karlsruhe, Germany) diffractometer using copper radiation (CuK_α) at a wavelength of 1.54180 Å. The tube voltage and current were set to 40 kV and 40 mA. The divergence slit was set at 0.6 mm, and the antiscattering slit was set at 8.0 mm. The diffraction pattern was recorded using a 0.2 s/0.02° scanning speed from 3° to 30° in 2 θ scale and a LynxEye position sensitive detector. To prevent the atmosphere humidity effect, samples were covered with a 10 μm polyethylene film.

Particle Size Analysis

A Mastersizer 2000 (Malvern Instruments Ltd., Malvern, UK) laser diffraction instrument was used for particle size analysis. Integration time was 3000 ms. The measurement range was set to 0.020–2000 μm , and 59 counting channels were used. For sample dispersion, nitrogen with 1.0 bar pressure was used. All measurements were carried out three times and the average particle size distribution was calculated.

Thermal Analysis

For studying the dehydration kinetics of mildronate DH, TG analysis was performed with Exstar6000 TG/DTA6300 (SII Nanotechnology Inc., Chiba, Japan). The samples were heated in nonisothermal mode from 30°C to 120°C temperature with heating rates of 0.5, 1, 2, 3, 4, and 5°C/min. Open aluminum pans were used. The sample weight was 7.0 ± 0.5 mg, and nitrogen flow rate was 80 ± 10 mL/min. The effects of sample size and nitrogen flow rate were determined at additional data points, where the sample weight was 3 or 15 mg and nitrogen flow rate was 30 or 300 mL/min.

Dehydration was also analyzed isothermally at the temperature range from 25°C to 80°C with a step of 5°C. The heater unit was preset to the required temperature before the insertion of the sample. For each sample, dehydration was performed at eight different temperatures selected according to the dehydration rate. The sample weight was 7.0 ± 0.5 mg, and nitrogen flow rate was 80 ± 10 mL/min. The effects of sample weight and nitrogen flow rate were determined at additional data points, where the sample weight was 2, 4, 6, 8, and 10 mg, and nitrogen flow rate was 0, 45, 200, and 300 mL/min.

For studying dehydration at controlled water vapor pressure, a system previously described in the literature⁴⁵ was used for providing specific water vapor activity. Dry and moist nitrogen gas was mixed in a gas controller unit (SII) at selected flow rates. The combined flow rate was 300 mL/min. The relative humidity was measured with a TFH 620 (Ebro) humidity meter, which was previously calibrated using saturated solutions of NaCl and MgCl_2 .

Methods for Kinetic Parameter Determination

For isothermal experiments, both model-free and model-based methods were used, but for nonisothermal experiments only model-free kinetic analysis was performed.⁴⁷ For isothermal experiments, data sets of α -time were obtained with $\Delta\alpha = 0.02$ at each temperature. Temperature stability during the reaction was evaluated and further analysis was performed in the conversion degree region where temperature change was smaller than 0.3° for all used temperatures. For nonisothermal experiments, data sets of α -temperature and time were

obtained with $\Delta\alpha = 0.02$ for each heating rate. By using results from both experimental modes, E_a was calculated with isoconversional methods: Friedman (FR),⁴⁸ average linear integral method (ALIM),⁴⁹ and advanced isoconversional method (AIC).^{50,51} For the first two methods, E_a was calculated from the slope of the line in corresponding coordinates for α values with step size 0.02,^{48,49} but for AIC method, the parameter $\Phi(E_a)$ was minimized with MS Excel Solver, obtaining E_a for α values with step size 0.1.^{50,51} Confidence intervals for the calculated E_a values were evaluated from the slope error of the line used for calculation of E_a with the FR method. Kinetic model determination was performed with ALIM⁴⁹ and reaction progress was reconstructed in the coordinates $g(\alpha)-\alpha$ ^{30,52} and $f(\alpha)-\alpha$.^{21,30,52} Besides, kinetic model determination for isothermal experiments was performed with reduced time plots,³⁵ but for nonisothermal experiments, from master plots using the parameter $Z(\alpha)$.⁵³ Most often used solid-state kinetic models were included in the analysis.^{3,21,54,55}

For isothermal experiments, model-fitting methods were used as well. The kinetic model was determined from linearization of the experimental points in coordinates $g(\alpha)$ -time, and model with the best linear fit was selected from the list of the most often used solid-state kinetic models.^{3,21,54,55} The dehydration rate constants were subsequently determined by plotting experimental data points in the coordinates α -time and fitting theoretical lines modeled from selected kinetic models to the experimental points. The sum of squared differences between experimental and theoretically calculated α values was minimized with MS Excel Solver. If more than one model was selected for this procedure, then the best model was identified by the smallest sum of least squares. The E_a values were then determined from the Arrhenius plot.

RESULTS AND DISCUSSION

As mentioned in the *Experimental* section, E_a and the kinetic model were determined by more than one method. Matching E_a values were obtained with all the calculation methods for each sample in each particular experiment. For representation of the model-free method results, E_a values calculated with FR's method were used in this paper. In each of the cases, a certain kinetic model was determined as the most appropriate according to all methods, unless stated otherwise.

Powder X-ray diffraction was used to determine that AP was obtained as a dehydration product. However, in samples where the dehydration continued after the melting/peritectic decomposition point, MH was also detected, even though its formation was not associated with direct dehydration of the DH⁴⁴ (see SI).

It was determined that sample preparation procedure and storage conditions had no effect on the examined kinetic parameters. For example, the similarity of the dehydration E_a for fractions up to 150–350 μm of all the samples can be evaluated from Figure S4. Thus, the sample designations given in the SI were not used in the text. The sample particle size is reported in this article according to the mesh sizes used for their preparation.

Particle Size Effects Evaluated from Dehydration in Isothermal and Nonisothermal Modes

To evaluate the possibility of determining the dehydration kinetics of DH under isothermal and nonisothermal modes, as

well as for the evaluation of the particle size effects, E_a and kinetic models from dehydration experiments of different DH particle size fractions in both modes were calculated and compared. Particle size distribution for different DH fractions is given in Figure S3. The particle size effects on the dehydration rate for different fractions in isothermal mode at 45°C temperature and in nonisothermal mode at the heating rate of 1°C/min are shown in Figure S5. It can be seen that by increasing the particle size, the dehydration process slowed, and the dehydration rate constant correspondingly decreased in isothermal mode, whereas the dehydration starting and finishing temperatures increased in the nonisothermal mode. This is because of the fact that for smaller particles there was more surface area accessible to dehydration than that for larger particles. Nevertheless, it was observed that the dehydration rate expressed as fraction converted per 1° was similar for all sample fractions in the nonisothermal mode (See Fig. S5b). However, more detailed study identified that the fraction of less than 40 μm showed an exception from these trends (see SI).

It has already been reported that dehydration E_a of the DH samples with particle size up to 350 μm is almost the same, but for particles larger than 350 μm there is a significant decrease of the E_a by increasing the particle size, explained by diffusion control.⁴⁴ In this study, the dehydration E_a was calculated with isoconversional methods from both isothermal and nonisothermal experiments. The obtained dehydration E_a as a function of conversion degree α for samples with various particle sizes is shown in Figure 2.

From the isothermal experiments shown in Figure 2a, it was confirmed that E_a of the samples with particle size up to 350 μm was the same, whereas it decreased by further increasing the particle size. From the nonisothermal experiments shown in Figure 2b, it was possible to identify differences in the final part of the E_a - α plots for fractions with particle size up to 350 μm .

In Figure 3, the dehydration E_a - α plots calculated from isothermal and nonisothermal experiments for the 40–67 μm fraction are shown. It can be seen that the E_a values calculated from both modes were the same at the start of the reaction, within the limits of experimental error, and a small decrease in the values was observed by increasing the conversion degree. This decrease was explained by the fact that the higher dehydration E_a at the start of the reaction was caused by nucleation of the product phase³ or by the reversibility of the dehydration reaction.⁵²

After this initial decrease, E_a values calculated from isothermal experiments in the α interval from 0.2 to 0.8 were almost constant. However, the E_a values obtained from nonisothermal experiment were constant only for a small α interval and after that started to decrease slowly by increasing α . This decrease became faster when the conversion degree approached 1.

Similar results were obtained also when other fractions were compared, although there typically was some divergence of the E_a values at the beginning of the dehydration reaction. Comparison of the obtained E_a values in isothermal and nonisothermal experiments for the fractions from less than 40 μm up to 150–350 μm is given in Figure 4. In this diagram, the bottom and the top of the presented column corresponds to the lowest and highest dehydration E_a values in α interval from 0.2 to 0.7. The color change point corresponds to the average E_a value in this interval.

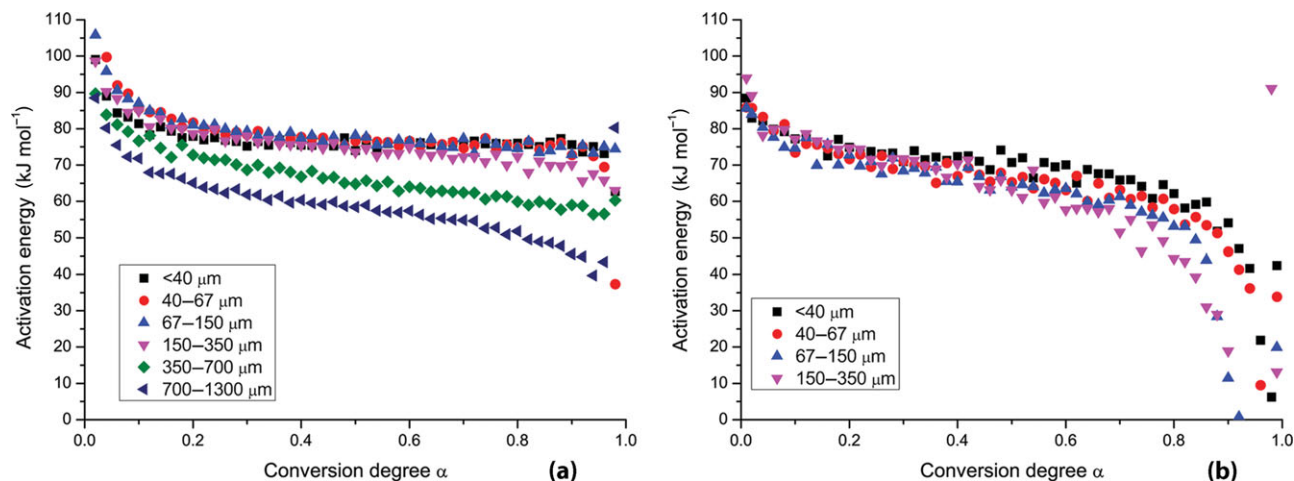


Figure 2. Dehydration activation energy–conversion degree plot for various DH fractions obtained (a) from isothermal experiments and (b) from nonisothermal experiments.

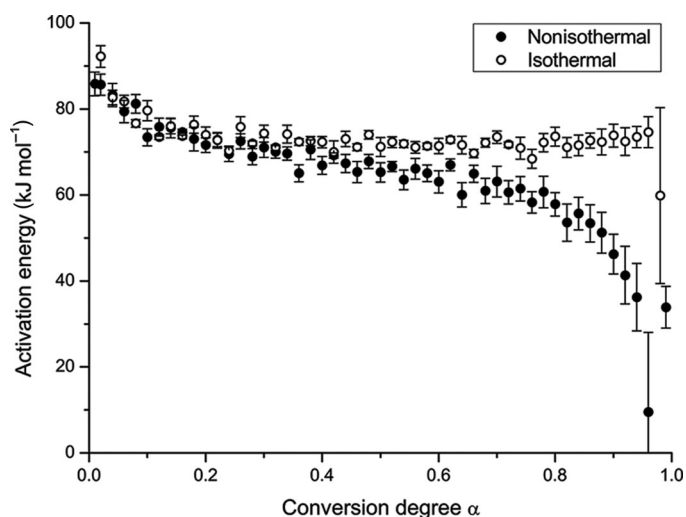


Figure 3. An activation energy–conversion degree plot for dehydration of the 40–67 μm fraction calculated from isothermal and nonisothermal experiments.

Figure 4 clearly illustrates that in all cases, the average, minimum, and maximum values of dehydration E_a were higher for isothermal experiments. Also, for nonisothermal experiments, the E_a value changed more within the conversion degree interval from 0.2 to 0.7, because E_a decreased at higher conversion degree, as presented in Figures 2b and 3. Moreover, in nonisothermal experiments, the range of E_a values in this α interval became wider by increasing the particle size. These results can easily be connected with Figure 2, where the E_a values are constant for fractions up to 150–350 μm in isothermal experiments and decrease in nonisothermal experiments. Furthermore, this decrease was faster for larger particles.

The temperature range at which the dehydration reaction was examined in both experimental modes for each DH fraction is given in Table S1. It is evident that higher temperatures were used in nonisothermal experiments. Moreover, the E_a values for nonisothermal experiments at high conversion degrees were calculated from data measured at higher temperatures, explaining the differences in E_a values presented in Figure 3.

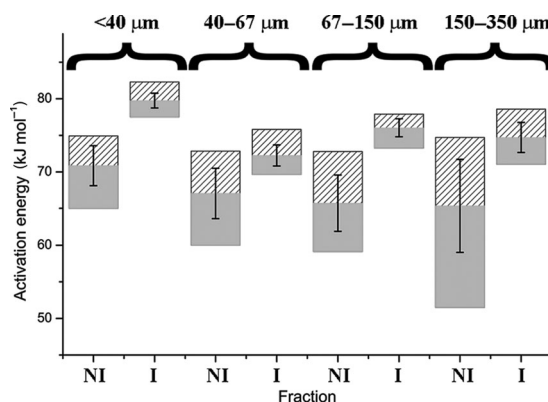


Figure 4. Minimum, maximum, and the average value of the dehydration activation energy calculated from nonisothermal and isothermal experiments for the less than 40, 40–67, 67–150, and 150–350 μm fractions.

Thus, the decrease of E_a by increasing α suggested that at higher temperatures the energy of the rate-limiting step was different, or contribution from a different rate-limiting step became apparent. The more pronounced decrease of the E_a for larger particles in nonisothermal experiments could easily be associated with slower dehydration, which led to higher dehydration temperature. Moreover, in order to reach complete dehydration at every experimentally used heating rate for the fractions with 67–150 and 150–350 μm particle size, samples were heated above the melting/peritectic decomposition point at 88°C–92°C.⁴⁴ The conversion degree at which this point was reached for the fastest heating rate is given in Table S1. It is clear that data obtained above melting point cannot be used for calculation of the dehydration E_a . Thus, E_a obtained above this conversion degree could not be considered purely as dehydration E_a , because some of the data used for its calculation was not actually from the dehydration process. For the 150–350 μm fraction, this α value was as low as 0.55, thus explaining the significantly lower minimum E_a value in Figure 4.

Thus, also for nonisothermal experiments, E_a was not dependent on the particle size for fractions with particle size up to 350 μm . Unfortunately, it was not possible to reliably

Table 1. The Most Appropriate Dehydration Kinetic Model for Different DH Fractions, Determined by Studying the Effect of Various Sample and Experimental Factors

Study	Less Than 40 to 67–150 μm	150–350 μm	350–700 μm	700–1300 μm , More Than 1300 μm
Isothermal mode ^a	R1	R1/R2	R2	R2
Nonisothermal mode ^a	R1	R2	R2	-
Sample weight	R1	R1	R2	-
Atmosphere	R1	-	-	-
Dehydration/rehydration	R1	-	-	-
Mechanical compression ^b	R1	-	-	-

^aStudy of the particle size effect.^bResults from dehydration of the powdered sample under isothermal mode.

calculate the E_a of the samples with particle size above 350 μm , because the evolution of water above the melting point caused problems in most of the experiments. Thus, E_a decrease for fractions with particle size above 350 μm was not demonstrated in nonisothermal experiments.

As can be seen from Figure 2a, small decrease of the E_a by increasing the α was observed in isothermal experiments for the 350–700 and 700–1300 μm fractions. This cannot be explained by the higher temperature, because dehydration of the 350–700 μm fraction was examined at the same conditions as the fractions with smaller particle size. As already mentioned, decrease of the average E_a for these two fractions was associated with the increased diffusion of water out of the particles.⁴⁴ Thus, it was possible that the diffusion effect slightly increased during the dehydration, and in this way E_a decreased by increasing α , as shown in Figure 2a. Therefore, the decrease of the E_a resulting from increased contribution of water diffusion was because of the fact that water molecules had to travel a longer distance to leave the particle, or because of the possible phase boundary advance in directions perpendicular to the water channels,⁴⁴ which was observed for larger particles, especially at the end of the reaction when all of the hydrate was surrounded by a thick AP layer.

The most appropriate kinetic models for the dehydration process were determined for all of the samples with various particle sizes under both isothermal and nonisothermal conditions, as well as for samples where the influence of other factors was examined. The obtained results are presented in Table 1. It is visible that the dehydration of fractions with particle size below 150 μm was best described by the one-dimensional phase boundary model R1, whereas that of fractions with particle size above 350 μm was best described by the two-dimensional phase boundary model R2. This was consistent with our previous work.⁴⁴ The other examined experimental and sample factors did not change the dehydration kinetic model. However, for all of the analyzed samples, there were deviations from the most appropriate kinetic model at the beginning and the end of the dehydration process. Deviations at the beginning can be associated with stabilization of the temperature or heating rate, whereas at the end, there may have been actual deviations from the chosen model associated with either (1) a certain degree of diffusion control or (2) the fact that the escape of the last water molecules can occur in other directions rather than those associated with the main movement of the phase boundary.³⁰ The reason for different kinetic models determined for different particle size fractions is associated with change of the dimensionality of the phase boundary movement.⁴⁴

Although it can be seen that the same dehydration kinetic model for all of the analyzed samples was found both from isothermal and nonisothermal experiments, determination of the kinetic model from isothermal experiments was more straightforward and it was possible to make a selection more convincingly.

Effect of the Sample Weight

It was already reported that the dehydration rate of the DH decreased for larger samples, because of the slower vapor diffusion through the sample layer.⁴⁴ By carrying out more detailed investigation, it was observed that the reciprocal dehydration rate constant determined with model fitting methods was linearly dependent on the sample weight (see Fig. 5, the slopes and intercept points of these lines are given in Fig. S6). It can be seen that the slope was decreasing if the temperature was raised, showing that the sample weight had a more pronounced effect on the dehydration rate constant at lower temperatures. This probably was because of slower water diffusion from the sample volume at lower temperatures. However, it was concluded that the particle size did not have an effect on the slope, although the slopes determined for 40–67 and 350–700 μm fractions were different than that for the rest of the fractions. For the 40–67 μm fraction, this could be because of random errors, but for the 350–700 μm fraction, this was because of the different kinetic model used, producing different rate constant values and thus changing the slope (see Table 1). Increase of the intercept (thus decrease of the dehydration rate) by increasing the particle size was because of the slower dehydration rate of the larger particles, as discussed previously.

It also has been reported that the dehydration E_a determined under isothermal conditions decreased by increasing the sample weight because of the increasing contribution from the bulk diffusion effect.⁴⁴ In this work, the effect of the sample weight on the dehydration E_a was measured in both isothermal and nonisothermal conditions, and the obtained E_a dependence on α for samples of various weight is shown in Figure 6.

Decrease of the dehydration E_a by increasing the sample weight was observed in both experimental modes. By changing the sample weight from 2 to 15 mg, dehydration E_a changed from 84 to 64 kJ/mol. These E_a values were in accordance with our previous study⁴⁴ and showed that larger samples gave even smaller dehydration E_a . From the obtained results, it was evaluated that sample weights of 2, 3, and 4 mg were not appropriate for accurate study of the dehydration kinetics because of the elevated random error in calculated E_a values. However, by

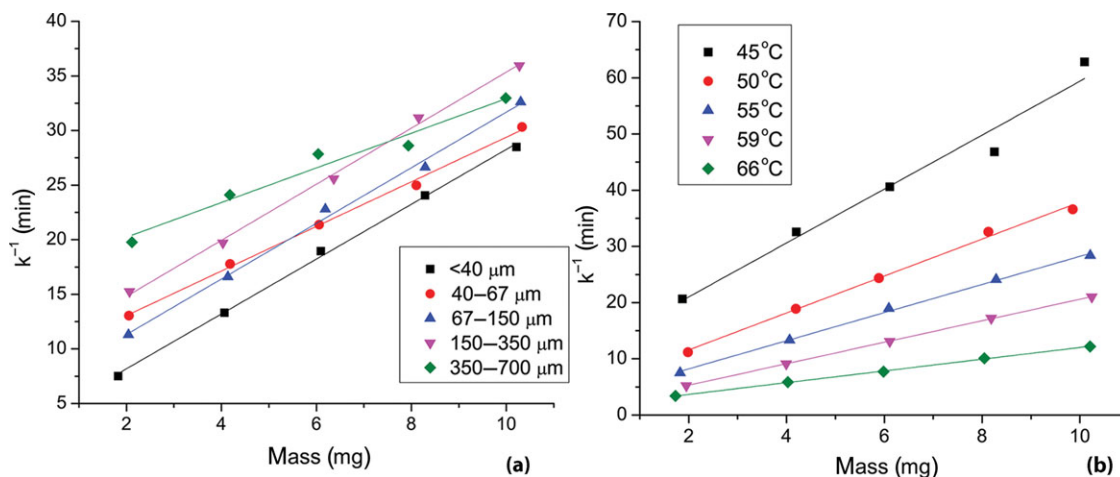


Figure 5. Sample weight effect on the reciprocal dehydration rate constant of mildronate DH: (a) different fractions at 55°C temperature and (b) less than $40\ \mu\text{m}$ fraction at different temperatures.

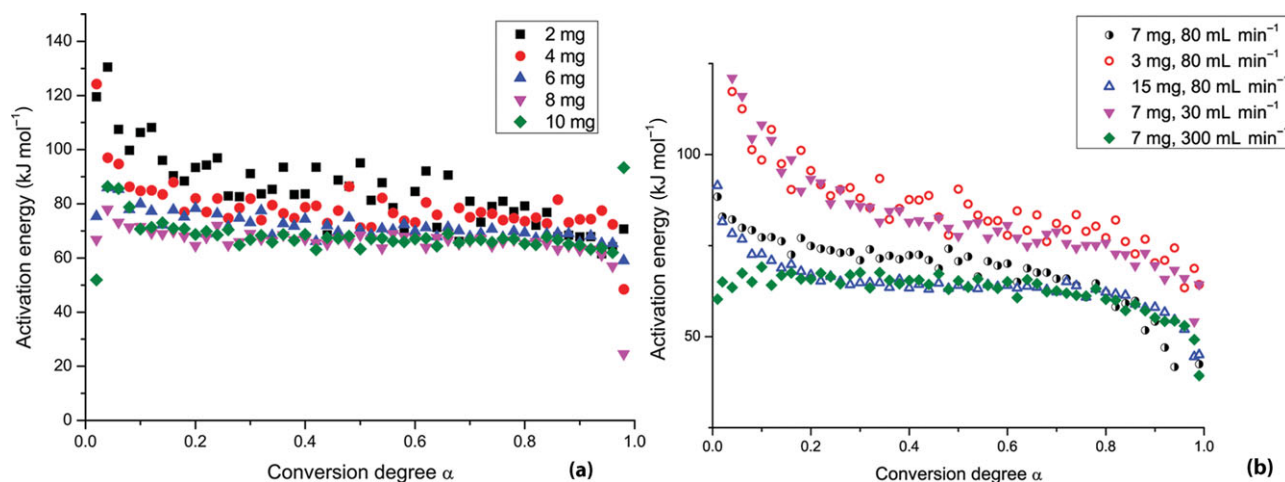


Figure 6. Dehydration activation energy dependence on (a) sample weight for the less than $40\ \mu\text{m}$ fraction in isothermal experiments and (b) sample weight (empty markers) and nitrogen flow rate (filled markers) for the less than $40\ \mu\text{m}$ fraction in nonisothermal experiments.

using excessively large samples, unacceptable diffusion effects would appear, so samples of moderate weight are preferable. Thus, both experimental modes could easily be used for the evaluation of the sample weight effect on the dehydration rate and E_a , although results obtained under nonisothermal mode were complicated by the sample weight unrelated E_a changes, the reason for which is already discussed.

Effect of the Atmosphere

Experiments with dehydration of DH less than $40\ \mu\text{m}$ fraction were carried out under nitrogen gas flow at various flow rates. It was determined that by increasing the N_2 flow rate increased the dehydration reaction rate as shown for isothermal experiments in Figure S7. This is because the rate of reversible dehydration was enhanced noticeably when the evolved vapor was promptly removed from the sample. The same effect was found in nonisothermal mode as well. However, changes of the nitrogen flow had less effect on the dehydration rate, compared with changes in other factors (like particle size, sample weight, and water vapor content in the atmosphere). From the results obtained under nonisothermal conditions, dehydration E_a was

calculated and the obtained results are shown in Figure 6b. Although the increase of the nitrogen flow resulted in faster dehydration, it did not noticeably reduce the contribution from the step associated with the water diffusion out of the sample that would result in a lower E_a value. On the contrary, the dehydration E_a decreased when the N_2 flow rate was increased. The magnitude of the E_a changes was similar to that introduced by the sample weight variation. These results suggested that the increased N_2 flow provided for a more efficient removal of water from the bulk of DH particles, most probably resulting in an increase of the contribution from the water vapor diffusion from the DH particles. Thus, the observed total dehydration E_a decreased because the E_a of water vapor diffusion from the particles was lower than that of the phase boundary advance. Figure 6b indicates that with 300 mL/min N_2 flow the calculated dehydration E_a values did not show initial decrease at low α values as observed in all the other cases. This initial decrease was therefore most probably associated with the reversibility of the dehydration reaction, and faster nitrogen flow precluded this effect.

The effect of variable water vapor pressure on the dehydration of DH was evaluated as well. It was observed that the

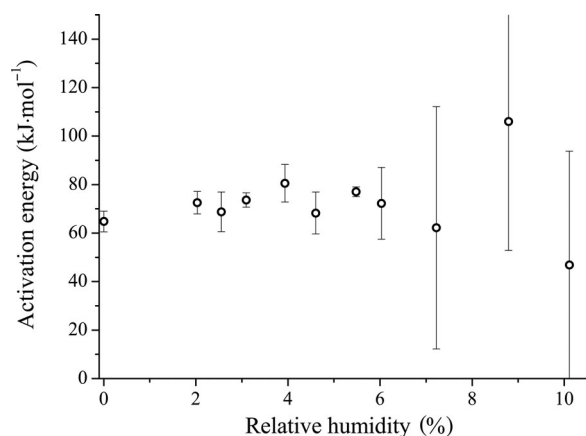


Figure 7. The dependence of the dehydration activation energy on the relative humidity for the less than 40 μm fraction.

dehydration rate decreased with increasing water vapor pressure at a given temperature, and the rate constant dependence on water vapor pressure could be approximated with straight line (see Fig. S8). This observation can be associated with the reversibility of the dehydration reaction. The observation of a linear dehydration rate decrease suggested that the presence of water in the vapor phase did not change the dehydration mechanism. By using dehydration curves recorded at different temperatures for a particular relative humidity, the dehydration E_a dependence on the relative humidity was calculated, and the results are shown in Figure 7. It is visible that the dehydration E_a did not depend on the relative humidity. This confirms that the presence of water did not change the dehydration mechanism and did not introduce any changes in the dehydration rate-limiting step energy at the reaction interface. However, the three highest relative humidity levels used had a high uncertainty, which could be related to slow dehydration where other factors could play a major role in the determination of the dehydration rate and the fact that the AP and DH phase boundary has a slight temperature dependence.⁴²

Effect of the Sample History

The considered aspects of sample history were (1) previous dehydration/rehydration of the sample and (2) mechanical compression. It was observed that repeated dehydration of previously dehydrated/rehydrated samples occurred faster and the dehydration E_a was lower (See Fig. S9). This effect could result from the cracking of the crystals and formation of channels through which water escape was facilitated during the repeated dehydration as well as because of the formation of internal defects allowing for an easier phase boundary advance. Also, it was possible that previous dehydration/rehydration reduced the particle size, allowing faster dehydration in the second dehydration cycle.⁴⁶ However, reduction of the particle size alone would not explain the decrease of the dehydration E_a .

It was observed that the mechanical compression (in terms of enhanced crystal defects and stress) had no effect on the dehydration E_a and the kinetic model. However, these defects promoted the initiation of the dehydration process, which was clearly observed as lower dehydration starting temperatures in nonisothermal experiments. When dehydration of compressed tablets was performed, water evolution from samples was more

difficult compared with powdered samples; thus, the dehydration rate was reduced, as observed both in isothermal and nonisothermal experiments. Extended discussion about the obtained results for mechanically compressed samples can be found in the SI.

CONCLUSIONS

It was possible to obtain comparable E_a values and the same kinetic model for the dehydration of mildronate DH in both isothermal and nonisothermal mode. However, both the obtained results and experimental procedures were more complicated when experiments were performed in nonisothermal mode. First, there was a decrease of dehydration E_a at high conversion degree values, either because of different contributions from various rate-limiting steps at different temperatures, or because of altered E_a of rate-limiting step at high temperatures. Second, dehydration process should be complete before reaching the melting/peritectic decomposition point for every employed heating rate. Thus, in nonisothermal mode, it was possible to analyze only sufficiently small particles; therefore, the possibility to study the particle size effect was limited. Moreover, obtained results were complicated by the E_a changes not directly caused by the change of the particle size. For fast identification of the possible complications and for setting up the dehydration kinetic study, results obtained from thermal analysis should be used to get insight about the appropriate temperature interval for the study.

Particle size influenced both the dehydration rate and E_a . This factor should therefore be controlled and sample with narrow particle size distribution would be preferred for the dehydration kinetic study. Although in isothermal mode it was possible to study the dehydration of all prepared fractions, small variation in dehydration E_a was observed for particles with size above 350 μm , because of the changing diffusion contribution, and less than 40 μm fraction showed deviation from typical dehydration behavior.

Study of the experimental factor effects revealed that very low-sample weight resulted in elevated random error for dehydration E_a , whereas very high-sample weight increased the diffusion contribution. Increase in the nitrogen flow decreased the dehydration E_a , suggesting that the contribution from water diffusion out of the particles was possibly increased by this change. Relative humidity did not affect the dehydration E_a , thus the presence of water at the reaction interface did not change the energy of the dehydration rate-limiting step.

Although sample preparation and storage did not show an effect on the examined dehydration parameters, sample history did. Thus, in order to perform a kinetic study, the sample should be handled carefully prior to dehydration experiments, in order not to induce any physical changes.

As the dehydration E_a is affected by the diffusion of the water out of the particle and the kinetic model is affected by the phase boundary advance in other directions than those along the water channels,⁴⁴ the particle morphology can be an important factor affecting these kinetic parameters. In this study, we used samples with particles lacking a characteristic morphology, which had crystallized as a particle aggregate. However, it is possible that other crystallization procedures can produce particles with different characteristic morphologies showing different dehydration kinetics.

For the determination of diffusion-independent kinetic parameters characterizing the main DH dehydration mechanism, an isothermal experimental mode should be selected, with moderate particle size (narrow range within 40–150 μm) and sample weight (6–8 mg), and nitrogen flow providing effective removal of the evolved water (~ 100 mL/min) should be used. Sample preparation and handling should be performed carefully. Such conditions would preclude the detection of the sample property and experimental factor effects, thus limiting the study of the dehydration mechanism. However, parameters obtained through such approach would be characteristic of the DH dehydration. Nevertheless, if one wants to study the dehydration mechanism, effects of various sample and experimental factors should be investigated.

Of course, the study of dehydration mechanisms through the influence of various sample and experimental factors on the kinetic parameters is not limited to mildronate DH. Thus, a similar study could easily reveal essential information about the dehydration mechanism of other organic and inorganic hydrates, as well as provide conditions for determining the main dehydration mechanism characterizing dehydration kinetic parameters.

ACKNOWLEDGMENTS

This work has been supported by the European Social Fund within the project “Support for Doctoral Studies at the University of Latvia.”

REFERENCES

- Infantes L, Fabian L, Motherwell WDS. 2007. Organic crystal hydrates: What are the important factors for formation. *Cryst Eng Comm* 9(1):65–71.
- Hilfiker R. 2006. Polymorphism in the pharmaceutical industry. Weinheim: Wiley-VCH Verlag GmbH & Co, KGaA, pp 414.
- Koradia V, de Diego HL, Elema MR, Rantanen J. 2010. Integrated approach to study the dehydration kinetics of nitrofurantoin monohydrate. *J Pharm Sci* 99(9):3966–3976.
- Malaj L, Censi R, Martino PD. 2009. Mechanisms for dehydration of three sodium naproxen hydrates. *Cryst Growth Des* 9(5):2128–2136.
- Guguta C, Meekes H, de Gelder R. 2008. The hydration/dehydration behavior of aspartame revisited. *J Pharm Biomed Anal* 46(4):617–624.
- Fujii K, Uekusa H, Itoda N, Hasegawa G, Yonemochi E, Terada K, Pan Z, Harris KDM. 2009. Physicochemical understanding of polymorphism and solid-state dehydration/rehydration processes for the pharmaceutical material acrinol, by ab initio powder X-ray diffraction analysis and other techniques. *J Phys Chem C* 114(1):580–586.
- Fujii K, Uekusa H, Itoda N, Yonemochi E, Terada K. 2012. Mechanism of dehydration–hydration processes of lisinopril dihydrate investigated by ab initio powder X-ray diffraction analysis. *Cryst Growth Des* 12(12):6165–6172.
- Chakravarty P, Berendt RT, Munson EJ, Young VG, Govindarajan R, Suryanarayanan R. 2010. Insights into the dehydration behavior of thiamine hydrochloride (vitamin B1) hydrates: Part II. *J Pharm Sci* 99(4):1882–1895.
- Braun DE, Gelbrich T, Kahlenberg V, Tessadri R, Wieser J, Griesser UJ. 2009. Stability of solvates and packing systematics of nine crystal forms of the antipsychotic drug aripiprazole. *Cryst Growth Des* 9(2):1054–1065.
- Braun DE, Gelbrich T, Jetli RKR, Kahlenberg V, Price SL, Griesser UJ. 2008. Colored polymorphs: Thermochemical and structural features of N-picryl-p-toluidine polymorphs and solvates. *Cryst Growth Des* 8(6):1977–1989.
- Kang F, Vogt FG, Brum J, Forcino R, Copley RCB, Williams G, Carlton R. 2011. Effect of particle size and morphology on the dehydration mechanism of a non-stoichiometric hydrate. *Cryst Growth Des* 12(1):60–74.
- Chakravarty P, Berendt RT, Munson EJ, Young VG, Govindarajan R, Suryanarayanan R. 2010. Insights into the dehydration behavior of thiamine hydrochloride (vitamin B1) hydrates: Part I. *J Pharm Sci* 99(2):816–827.
- Zencirci N, Gstrein E, Langes C, Griesser U. 2009. Temperature- and moisture-dependent phase changes in crystal forms of barbituric acid. *Thermochim Acta* 485(1–2):33–42.
- Zellelow AZ, Kim K-H, Sours RE, Swift JA. 2010. Solid-state dehydration of uric acid dihydrate. *Cryst Growth Des* 10(1):418–425.
- Kachrimanis K, Griesser U. 2012. Dehydration kinetics and crystal water dynamics of carbamazepine dihydrate. *Pharm Res* 29(4):1143–1157.
- Guguta C, van Eck ERH, de Gelder R. 2009. Structural insight into the dehydration and hydration behavior of naltrexone and naloxone hydrochloride. dehydration-induced expansion versus contraction. *Cryst Growth Des* 9(8):3384–3395.
- Vogt FG, Brum J, Katrincic LM, Flach A, Socha JM, Goodman RM, Haltiwanger RC. 2006. Physical, crystallographic, and spectroscopic characterization of a crystalline pharmaceutical hydrate: understanding the role of water. *Cryst Growth Des* 6(10):2333–2354.
- Khoo JY, Williams DR, Heng JYY. 2010. Dehydration kinetics of pharmaceutical hydrate: Effects of environmental conditions and crystal forms. *Dry Technol* 28(10–12):1164–1169.
- Jones MD, Hooton JC, Dawson ML, Ferrie AR, Price R. 2006. Dehydration of trehalose dihydrate at low relative humidity and ambient temperature. *Int J Pharm* 313(1–2):87–98.
- Li H, Stowell JG, He X, Morris KR, Byrn SR. 2007. Investigations on solid–solid phase transformation of 5-methyl-2-[(4-methyl-2-nitrophenyl)amino]-3-thiophenecarbonitrile. *J Pharm Sci* 96(5):1079–1089.
- Sheth AR, Zhou D, Muller FX, Grant DJW. 2004. Dehydration kinetics of piroxicam monohydrate and relationship to lattice energy and structure. *J Pharm Sci* 93(12):3013–3026.
- Byrn SR, Pfeiffer RR, Stowell JG. 1999. Solid state chemistry of drugs. 2nd ed. West Lafayette, Indiana: SSCI, Inc., pp 754.
- Perrier P, Byrn SR. 1982. Influence of crystal packing on the solid-state desolvation of purine and pyrimidine hydrates: Loss of water of crystallization from thymine monohydrate, cytosine monohydrate, 5-nitouracil monohydrate, and 2'-deoxyadenosine monohydrate. *J Org Chem* 47(24):4671–4676.
- Brown ME, Brown RE. 2000. Kinetic aspects of the thermal stability of ionic solids. *Thermochim Acta* 357:133–140.
- Galwey A. 2008. What can we learn about the mechanisms of thermal decompositions of solids from kinetic measurements? *J Therm Anal Calorim* 92(3):967–983.
- Galwey A, Brown M. 2000. Solid-state decompositions—stagnation or progress? *J Therm Anal Calorim* 60(3):863–877.
- Galwey AK. 2004. Is the science of thermal analysis kinetics based on solid foundations?: A literature appraisal. *Thermochim Acta* 413(1–2):139–183.
- Agbada CO, York P. 1994. Dehydration of theophylline monohydrate powder—Effects of particle size and sample weight. *Int J Pharm* 106(1):33–40.
- Taylor L, York P. 1998. Effect of particle size and temperature on the dehydration kinetics of trehalose dihydrate. *Int J Pharm* 167(1–2):215–221.
- Zhou D, Schmitt EA, Zhang GGZ, Law D, Wight CA, Vyazovkin S, Grant DJW. 2003. Model-free treatment of the dehydration kinetics of nedocromil sodium trihydrate. *J Pharm Sci* 92(7):1367–1376.
- Okoth MO, Vrcelj RM, Sheen DB, Sherwood JN. 2012. Hydration studies of a simple molecular solid. *Cryst Eng Comm* 14(5):1602–1612.

32. Okoth MO, Vrcelj RM, Sheen DB, Sherwood JN. 2013. Dehydration mechanism of a small molecular solid: 5-Nitouracil hydrate. *Cryst Eng Comm* 15(40):8202–8213.
33. Burnett DJ, Malde N, Naderi M, Acharya M. 2010. 11th International conference on pharmacy and applied physical chemistry. Innsbruck, Austria.
34. Galwey AK, Brown ME. 1999. Thermal decomposition of ionic solids. Amsterdam, The Netherlands: Elsevier, pp 598.
35. Bamford CH, Tipper CFH. 1980. Reactions in the solid state. Amsterdam, The Netherlands: Elsevier, pp 340.
36. Han J, Suryanarayanan R. 1999. A method for the rapid evaluation of the physical stability of pharmaceutical hydrates. *Thermochim Acta* 329(2):163–170.
37. L'Vov BV, Novichikhin AV, Dyakov AO. 1998. Mechanism of thermal decomposition of magnesium hydroxide. *Thermochim Acta* 315(2):135–143.
38. Kalviņš I, Stonāns I. 2009. 3-(2, 2, 2-trimethylhydrazinium) propionate salts for treating ischemic heart disease. Patent WO/2009/071586.1-6.
39. Simkhovich BZ, Shutenko ZV, Meirena DV, Khagi KB, Mezapuke RJ, Molodchina TN, Kalvlins IJ, Lukevics E. 1988. 3-(2,2,2-Trimethylhydrazinium)propionate(thp)-a novel [gamma]-butyrobetaine hydroxylase inhibitor with cardioprotective properties. *Biochem Pharmacol* 37(2):195–202.
40. Mishnev A, Kalvins I, Aleksejeva L, Lebedev A. 2011. XXII Congress and General Assembly of the International Union of Crystallography, Madrid, Spain, 22–30 August 2011, pp MS53.P23.
41. Kemme A, Bleidelis J, Kalvinsh I, Ereemeev A. 1983. Molecular-crystalline structure of 3-(2,2, 2-trimethylhydrazinio)propionate dihydrate C₆H₁₄N₂O₂·2H₂O. *Latv PSR Zinat Akad Vestis* 2:215.
42. Veldre K, Actiņš A, Kalniņa A. 2010. Solid state chemistry 2010, Book of Abstract. Prague. pp. 231.
43. Zvirgzdiņš A, Veldre K, Actiņš A. 2011. Structures of mildronate polymorphic and pseudopolymorphic forms. *Latv J Chem* 50(1):64–72.
44. Bērziņš A, Actiņš A. 2014. Dehydration of mildronate dihydrate: A study of structural transformations and kinetics. *CrystEngComm*. [Epub ahead of print.]
45. Han J, Suryanarayanan R. 1998. Influence of environmental conditions on the kinetics and mechanism of dehydration of carbamazepine dihydrate. *Pharm Dev Technol* 3(4):587–596.
46. Zhu H, Grant DJW. 2001. Dehydration behavior of nedocromil magnesium pentahydrate. *Int J Pharm* 215(1–2):251–262.
47. Vyazovkin S, Burnham AK, Criado JM, Pérez-Maqueda LA, Popescu C, Sbirrazzuoli N. 2011. ICTAC kinetics committee recommendations for performing kinetic computations on thermal analysis data. *Thermochim Acta* 520(1–2):1–19.
48. Friedman HL. 1964. Kinetics of thermal degradation of char-forming plastics from thermogravimetry. Application to a phenolic plastic. *J Polym Sci C* 6:183–195.
49. Ortega A. 2008. A simple and precise linear integral method for isoconversional data. *Thermochim Acta* 474(1–2):81–86.
50. Vyazovkin S. 1997. Evaluation of activation energy of thermally stimulated solid-state reactions under arbitrary variation of temperature. *J Comput Chem* 18(3):393–402.
51. Vyazovkin S. 2001. Modification of the integral isoconversional method to account for variation in the activation energy. *J Comput Chem* 22(2):178–183.
52. Vyazovkin S, Wight CA. 1997. Kinetics in solids. *Annu Rev Phys Chem* 48(1):125–149.
53. Ortega A. 2002. The kinetics of solid-state reactions toward consensus, Part 2: Fitting kinetics data in dynamic conventional thermal analysis. *Int J Chem Kinet* 34(3):193–208.
54. Khawam A, Flanagan DR. 2006. Basics and applications of solid-state kinetics: A pharmaceutical perspective. *J Pharm Sci* 95(3):472–498.
55. Khawam A, Flanagan DR. 2006. Solid-state kinetic models: Basics and mathematical fundamentals. *J Phys Chem B* 110(35):17315–17328.

On the Formation of Droperidol Solvates: Characterization of Structure and Properties

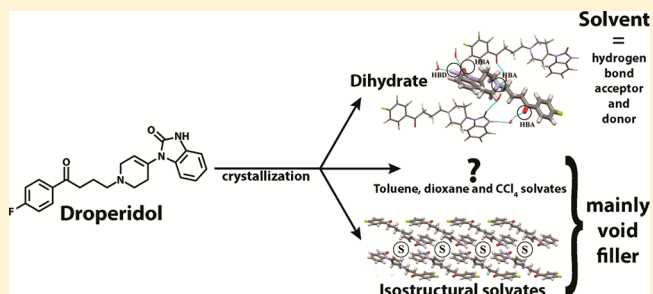
Agris Bērziņš,^{*,†,‡} Edgars Skarbulis,[†] Toms Reķis,[†] and Andris Actiņš[†]

[†]Faculty of Chemistry, University of Latvia, Kr. Valdemara 48, Riga, LV-1013, Latvia

[‡]Department of Chemistry, Durham University, South Road, Durham, U.K., DH1 3LE

Supporting Information

ABSTRACT: A solvate screening and characterization of the obtained solvates was performed to rationalize and understand the solvate formation of active pharmaceutical ingredient droperidol. The solvate screening revealed that droperidol can form 11 different solvates. The analysis of the crystal structures and molecular properties revealed that droperidol solvate formation is mainly driven by the inability of droperidol molecules to pack efficiently. The obtained droperidol solvates were characterized by X-ray diffraction and thermal analysis. It was found that droperidol forms seven nonstoichiometric isostructural solvates, and the crystal structures were determined for five of these solvates. To better understand the structure of these five solvates, their solvent sorption–desorption isotherms were recorded, and lattice parameter dependence on the solvent content was determined. This revealed a different behavior of the nonstoichiometric hydrate, which was explained by the simultaneous insertion of two hydrogen-bonded water molecules. Isostructural solvates were formed with sufficiently small solvent molecules providing effective intermolecular interactions, and solvate formation was rationalized based on already presented solvent classification. The lack of solvent specificity in isostructural solvates was explained by the very effective interactions between droperidol molecules. Desolvation of stoichiometric droperidol solvates produced one of the four droperidol polymorphs, whereas that of nonstoichiometric solvates produced an isostructural desolvate.



INTRODUCTION

The investigation of solid phase diversity of pharmaceutical molecules has clearly shown the formation of different phases, including polymorphs and solvates.^{1,2} The fact that different polymorphs and solvates have different stability,³ mechanical properties,^{4–6} and bioavailability (because of different solubility⁷) makes solid form screening an essential step during drug development, in order to prevent unexpected solid form appearance after the approval of a drug.^{8,9} Moreover, the ability of a compound to form numerous polymorphs³ and, as reported, more than 100 solvates² makes it necessary to include various research techniques in the screening process and to carefully choose the commercial form and its storage conditions.

Solvates typically appear during the active pharmaceutical ingredient (API) purification stage or the API processing stages, such as mixing and blending, wet granulation, lyophilization, spray drying, etc., when APIs are exposed to solvents or solvent vapors.^{10–13} Moreover, solvates tend to crystallize more easily than solvent-free polymorphs because of the more efficient packing together with solvent molecules.¹⁴ However, the stability of the solvates under an atmosphere without the corresponding solvent vapor is typically limited. During the desolvation, unstable polymorphs can form, which can make formation of the solvate either undesirable or

advantageous, as polymorphs inaccessible by crystallization can be obtained in such cases.^{15–18}

Therefore, the understanding of the reasons for solvate formation is important in order to enable prediction of their formation and even stability. Currently, it would be the most reasonable to make solvate predictions based on the solvent and host properties, as computational structure predictions have been successful only for polymorphs^{19–23} and relatively simple hydrate systems.^{20,24–26}

Although structural features leading to the solvate formation have not been completely identified, there are two main scenarios in which solvent molecules tend to incorporate into the crystal lattice by forming solvates:¹ (a) potential intermolecular interactions between the molecules of the compound are not well satisfied and the incorporation of solvent molecules provides a strong intermolecular interaction, or (b) solvent inclusion in the crystal decreases the void space. In the first scenario, the solvate selectivity is typically based on their functionality, whereas it does not have to be so for the second scenario. However, most solvates include contributions from both of these driving forces, which can be viewed as

Received: March 10, 2014

Revised: April 10, 2014

Published: April 16, 2014

lowering the crystal free energy primarily through electrostatic and van der Waals interactions, respectively. In more specific cases the solvent molecules can act as bridges between polar and apolar structure regions and/or serve the role of ligands completing the coordination around a metal ion.¹² It has also been concluded that solvate ability to involve multipoint recognition through hydrogen bonds strongly facilitates its stability.²⁷

More challenging is understanding the reason for the formation of isostructural solvates, where the same host structure can incorporate different solvent molecules. There are cases where the formation of isostructural solvates can occur only from solvents with some specific interaction^{28,29} or molecular shape,³⁰ although it is common that such solvates form with very different solvent molecules located in structural channels.^{18,31,32} It has been found that in some cases even empty host structures can be thermodynamically stable if compared to polymorphs,³³ although more typically they are unstable.³⁴ In many cases, however, host structure collapses immediately after the removal of the guest despite the weak nature of the host–guest interactions.^{35,36}

To understand the solvate formation, it is necessary to study and understand both the structural features of the solvates as well as their stability and phase transitions occurring at different conditions.^{17,18,37–39}

Droperidol, 1- $\{1-[4-(4\text{-fluorophenyl})-4\text{-oxobutyl}]-1,2,3,6\text{-tetrahydro-4-pyridyl}\}-1,3\text{-dihydro-2H-benzimidazol-2-one}$ (Figure 1) is a neuroleptic pharmaceutical. It is reported to exist in two

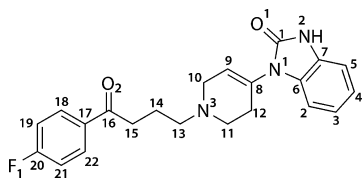


Figure 1. Molecular structure of droperidol.

polymorphic forms I and II (also labeled as z)^{40,41} and three solvated forms: dihydrate **DH**,^{41,42} nonstoichiometric hydrate **NSH** (also labeled as x),^{40,41,43} and ethanol solvate **S_{Et}**.⁴⁴ The crystal structures of the **DH**, **S_{Et}**, **NSH**, and the polymorph **II** have been reported, and it was determined that the **NSH** and **S_{Et}** are isostructural.⁴³ Although **NSH** is reported as hemihydrate,⁴⁰ it is nonstoichiometric and the water content in its structure can change freely from 0 to 1.⁴³ In the polymorph **II** and in isostructural solvates, droperidol forms hydrogen bonded amide homodimers. Additional structural stability in **II** is provided by two weak hydrogen bonds formed by a carbonyl group, whereas the isostructural solvate structures are stabilized by three weak hydrogen bonds formed by a carbonyl group, a tertiary nitrogen and fluorine, as well as by the hydrogen bond between the amide carbonyl group and the solvent molecules. However, in **DH** the structure is stabilized by a strong hydrogen bond network mediated by water molecules employing all the strong hydrogen bond donor and acceptor sites of droperidol.

In this work we tried to understand and rationalize the solvate formation of droperidol. Therefore, we crystallized droperidol from solvents belonging to different solvent classes to investigate the possibility of forming new solvates, and we also characterized the structure and physicochemical properties of all droperidol solvates. We tried to rationalize solvate

formation based on the solvate structure and solvent and droperidol properties. Besides, we characterized the solvent role and interactions in solvate structures and the water molecule arrangement in a partially filled **NSH** structure.

EXPERIMENTAL SECTION

Materials. Droperidol (purity >99%) was obtained from JSC Grindeks (Riga, Latvia). The sample consisted of polymorph **II**. Inorganic compounds and organic solvents of analytical grade were purchased from commercial sources and used without further purification.

Preparation of the Crystal Forms. The most popular solvents chosen from different solvent classes^{45,46} (grouped according to physical and physicochemical properties) were selected for the crystallization of droperidol. Saturated or concentrated solutions of droperidol in all of the solvents were prepared at 40–130 °C depending on the boiling point of the solvent (see Table S1, Supporting Information). The obtained solutions were then cooled down to –5 °C. In the cases when no crystallization was observed, the solutions were slowly evaporated at 40 or 50 °C, while preventing a complete evaporation. The obtained products were collected by filtration, air-dried, and characterized. Depending on the procedure, both of the previously known hydrates were obtained from crystallization in the presence of water (see Supporting Information).

Single Crystal X-ray Diffraction (SCXRD). The single-crystal X-ray diffraction data for droperidol solvates were collected either at 173 K on a Bruker-Nonius Kappa CCD diffractometer or at 120 K, or 333 K on a Bruker SMART CCD 6000 diffractometer, both using Mo $K\alpha$ radiation (graphite monochromator, $\lambda = 0.71073$ Å) and Oxford Cryostream (Oxford Cryosystems) open-flow nitrogen cryostat for sample temperature control. The structure was solved by direct method and refined by full-matrix least-squares on F^2 for all data using SHELXTL⁴⁷ and OLEX2⁴⁸ software or SHELX-97 suite.⁴⁷ All nondisordered non-hydrogen atoms were refined anisotropically. For disordered alcohol molecules fixed SOF = 0.5 was used.

The packing coefficients for crystal structures were calculated by PLATON.⁴⁹ Mercury 3.3 software⁵⁰ was used for crystal structure analysis and simulation of powder X-ray diffraction patterns based on crystal structure data.

Powder X-ray Diffraction (PXRD). PXRD patterns were measured at ambient temperature on a D8 Advance (Bruker) diffractometer using copper radiation (Cu $K\alpha$) at the wavelength of 1.54180 Å, equipped with a LynxEye position sensitive detector. The tube voltage and current were set to 40 kV and 40 mA. The divergence slit was set at 0.6 mm, and the antiscattering slit was set at 8.0 mm. The diffraction patterns were recorded using a 0.2 s/0.02° scanning speed (for phase identification) or 0.5 s/0.02° (for lattice parameter determination) from 3° to 35° in 2θ scale. To prevent the atmospheric humidity effect and decomposition of the solvates, when necessary the samples were covered during the analysis with a 10 μm polyethylene film.

Differential Thermal Analysis/Thermogravimetry (DTA/TG). DTA/TG analysis was performed with Exstar6000 TG/DTA6300 (SII). Open aluminum pans were used. Heating of samples from 30 to 200 °C was performed at a 5°·min^{–1} heating rate. Samples of 5–10 mg mass were used, and the nitrogen flow rate was 100 \pm 10 mL·min^{–1}.

Gravimetric Determination of Solvent Content. Solvent content was determined for nonstoichiometric solvates stored in desiccators with controlled solvent activity in the vapor phase. To provide a variety of relative humidity (RH) values for determination of water content in **NSH**, saturated salt solutions and P₂O₅ were used. The salts used for this experiment and the corresponding RH values were LiBr (6%), LiCl (11%), CH₃CO₂K (23%), MgCl₂ (32%), NaBr (56%), KI (68%), NaCl (75%), KCl (84%), K₂SO₄ (97%), and also P₂O₅ (~0%).⁵¹ To provide a variety of ethanol, methanol, acetonitrile, and nitromethane vapor activity, solutions with different compositions of the corresponding solvents and glycerol for methanol and ethanol, and glycerol and dimethylformamide for acetonitrile and nitromethane were prepared. The solvent activity in the vapor phase was estimated

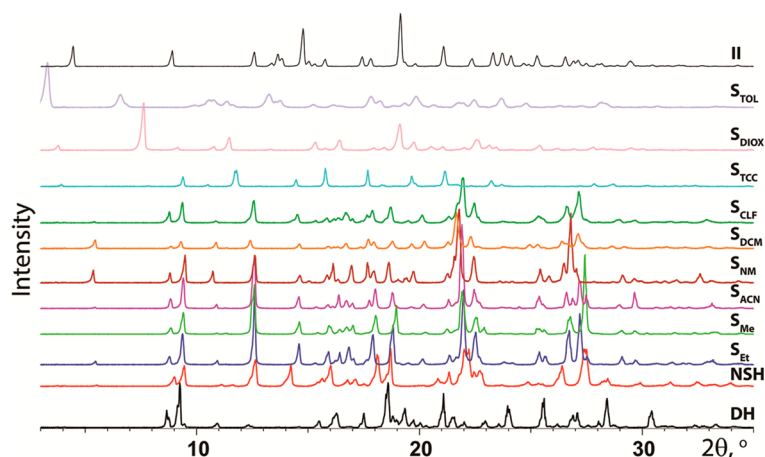


Figure 2. PXRD patterns of the droperidol solvates and polymorph II.

Table 1. Crystallographic Data for the Droperidol Solvates (S_{ACN} , S_{NM} , S_{Me} , NSH, ISD, and S_{Et})

solvate	S_{ACN}	S_{NM}	S_{Me}	NSH-mono	NSH-hemi	ISD
empirical formula	$(C_{22}H_{22}FN_3O_2)_2 \cdot C_2H_3N$	$(C_{22}H_{22}FN_3O_2)_2 \cdot CH_3NO_2$	$C_{22}H_{22}FN_3O_{22} \cdot 0.5CH_4O$	$C_{22}H_{22}FN_3O_2 \cdot H_2O$	$C_{22}H_{22}FN_3O_2 \cdot 0.5H_2O$	$C_{22}H_{22}FN_3O_2$
M_r	399.96	409.95	395.45	397.44	388.43	379.43
crystal system	triclinic	triclinic	triclinic	triclinic	triclinic	triclinic
space group	$P1$	$P1$	$\bar{P}1$	$\bar{P}1$	$\bar{P}1$	$\bar{P}1$
temperature	173	173	120	120	120	333
a (Å)	6.0870(2)	6.06730(10)	6.0504(5)	6.3199(4)	6.2743(3)	6.2780(3)
b (Å)	10.2177(3)	10.1884(3)	10.2207(8)	10.1525(7)	10.1560(6)	10.0865(4)
c (Å)	16.2642(6)	16.4237(5)	16.1100(14)	15.7463(11)	15.7786(9)	16.3969(7)
α (deg)	101.2051(11)	99.8303(13)	101.397(2)	102.691(2)	102.253(2)	103.0980(10)
β (deg)	92.7447(10)	92.2880(12)	93.445(3)	91.775(2)	92.501(2)	92.8550(10)
γ (deg)	96.7569(19)	95.6243(18)	97.022(2)	100.403(2)	99.460(2)	99.4190(10)
V (Å ³)	982.78(6)	993.86(4)	965.62(14)	966.81(11)	965.95(9)	993.57(7)
Z^a	2	2	2	2	2	2
μ (mm ⁻¹)	0.094	0.099	0.096	0.098	0.095	0.089
D_{calc} (g cm ⁻³)	1.352	1.370	1.360	1.365	1.335	1.268
no. of parameters	533	542	350	353	353	342
refl. collected	5243	5245	16 568	12 518	12 520	11 524
refl. ($I > 2\sigma$)	3644	3649	5392	5357	5375	4788
wR (all data)	0.1285	0.1346	0.1512	0.1721	0.1635	0.1558
final R ($I > 2\sigma$)	0.0526	0.0546	0.0534	0.0600	0.0556	0.0486
GOF	1.012	1.023	1.011	1.073	1.030	1.020
packing coeff	0.705	0.704	0.717 ^b	0.714		0.659

^aOn the basis of droperidol as the molecular entity. ^bCalculated for structure where solvent molecules were ordered.

by Raoult's Law. All desiccators were thermostated at 30 ± 0.5 °C temperature, and the sample containers were weighed on analytical balance ($d = 0.1$ mg). Further experimental details are given in Supporting Information.

Determination of Lattice Parameters of Solvates with Different Solvent Content. The PXRD patterns were determined for solvates with different solvent content. Samples identical to those used for gravimetric solvent content determination were used. Both samples were stored together, and thus the solvent content was assumed to be identical. The lattice parameters of the fully solvated nonstoichiometric solvates was determined at ambient temperature with *LP-Search* algorithm in *TOPAS 4.2*⁵² using lattice parameters determined at 173 K in SCXRD measurements as the initial guess. The lattice parameters of the nonstoichiometric solvates with different solvent content were determined by performing the Pawley refinement in *TOPAS 4.2* by relaxing the lattice parameters and the crystallite size parameter.

Fourier Transform (FTIR) Infrared Spectroscopy. The ATR-FTIR spectra were collected for neat solids on a PerkinElmer Frontier

FTIR spectrometer equipped with a Universal ATR Sampling Accessory with a diamond window. The spectra were recorded from 650 to 4000 cm^{-1} at a 2 cm^{-1} spectral resolution with 16 scans.

Theoretical Calculations. The geometry optimization and energy calculation for crystal structures were performed using *CASTEP*⁵³ with the PBE⁵⁴ functional using on-the-fly generated ultrasoft pseudopotentials and a cutoff energy of 600 eV. In *CASTEP* calculations, disorder could not be taken into account, and therefore the structures of S_{Me} and S_{Et} with one of the possible solvent orientations were used, thus creating a structure in the $P1$ space group with two symmetrically individual droperidol molecules. When lattice parameters were relaxed, Tkatchenko–Scheffler dispersion correction scheme⁵⁵ was used.

The molar volumes of selected solvent molecules were calculated in *Gaussian09*⁵⁶ after the geometry optimization at the B3LYP/6-311G(d,p) level using Grimme's dispersion correction.⁵⁷

Lattice energy calculations were performed with the semiempirical *PIXEL*⁵⁸ methodology. Hydrogen atom positions were optimized by *CASTEP*.

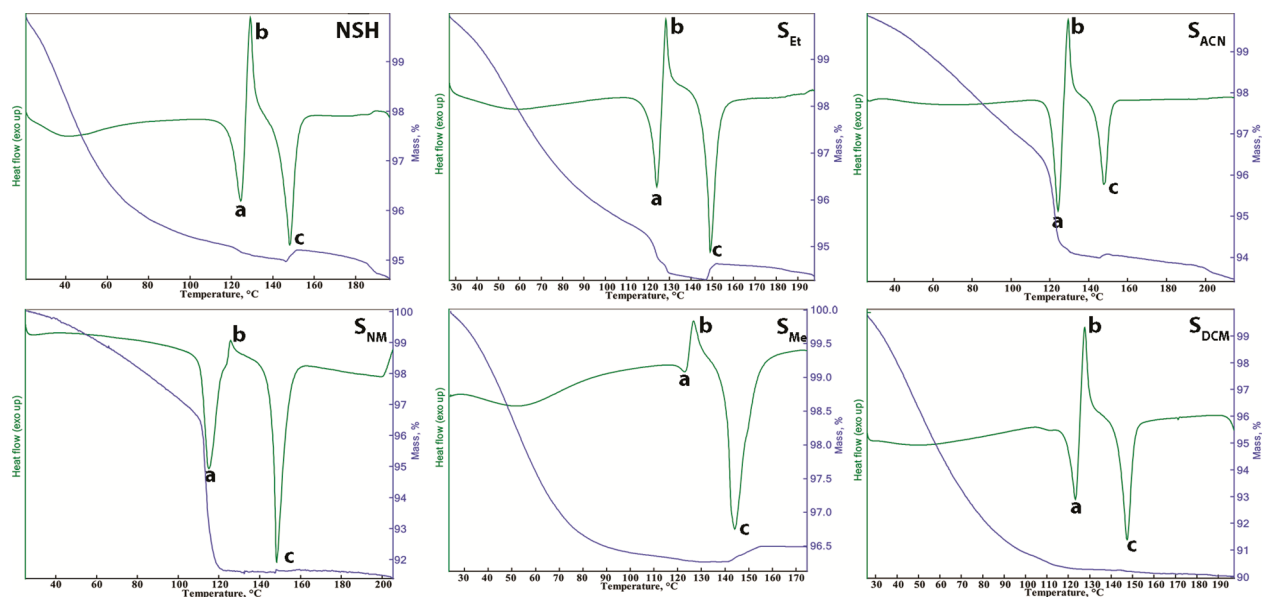


Figure 3. The DTA and TG curves of the droperidol isostructural solvates showing (a) the melting of solvate and/or ISD, (b) recrystallization, and (c) melting of the resulting polymorph I.

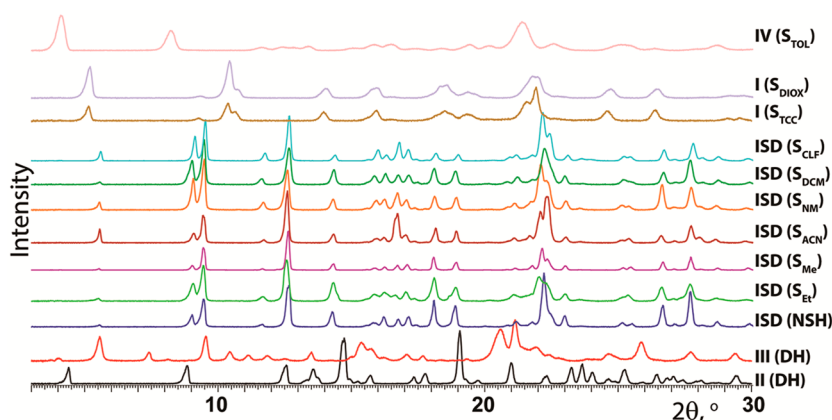


Figure 4. PXRD patterns of the desolvation products of the droperidol solvates.

RESULTS AND DISCUSSION

Solvate Screening. A crystal form screening of droperidol was performed by selecting the most commonly used solvents covering different solvent classes based on classification according to statistical analysis of four molecular descriptors⁴⁵ and hydrogen bond acceptor and donor propensity, polarity/dipolarity, dipole moment, and dielectric constant.⁴⁶ Solvents used for the screening and the crystal forms obtained after the crystallization are given in Table S1, Supporting Information. It can be seen that besides the already known polymorphic forms I and II, hydrates NSH and DH, and the ethanol solvate S_{Et} , eight new crystalline forms were obtained from methanol, acetonitrile, nitromethane, chloroform, dichloromethane, carbon tetrachloride, 1,4-dioxane, and toluene. All of the obtained crystal forms were characterized by PXRD and thermal methods and were found to be droperidol solvates and were labeled as S_{Me} , S_{ACN} , S_{NM} , S_{CLF} , S_{DCM} , S_{TCC} , S_{DIOX} , and S_{TOL} respectively. Crystals suitable for SCXRD analyses were obtained only from methanol, acetonitrile, and nitromethane. Besides, all of the analyses were performed also with the poorly characterized solvated forms NSH, S_{Et} , and DH.

X-ray Diffraction. PXRD patterns of all the obtained solvated forms are given in Figure 2. It can be seen that the diffraction peak positions of the new solvates S_{Me} , S_{ACN} , S_{NM} , S_{DCM} , and S_{CLF} were very similar and almost matched those of NSH and S_{Et} , suggesting the isostructurality of all these solvated forms. However, PXRD patterns of S_{TCC} , S_{DIOX} , and S_{TOL} exhibited different characteristic features and differed also from the PXRD patterns of all other known droperidol forms.

A crystal structure determination for the newly prepared S_{Me} , S_{ACN} , S_{NM} , and also S_{Et} and NSH was performed, and the obtained crystallographic data are given in Tables 1 and S3, Supporting Information. The crystal structures of NSH and S_{Et} were consistent with those already reported,^{40,44} and the newly prepared solvates S_{Me} , S_{ACN} , and S_{NM} were isostructural to NSH and S_{Et} as already suggested by the PXRD patterns (a more detailed discussion is given further). In this study the NSH was determined to be of monohydrate stoichiometry (the previously published hemihydrate stoichiometry⁴⁰ is explained by its nonstoichiometric behavior⁴³), whereas S_{Et} , S_{Me} , S_{ACN} , and S_{NM} crystallized as hemisolvates (although monoethanol solvate was reported,⁴⁴ both the published⁴⁴ and our

determined crystal structures corresponded to a hemioethanol solvate).

An overlay of the PXRD patterns obtained experimentally and simulated from crystal structure data (see Figure S1, Supporting Information) confirmed the identity of the polycrystalline phases.

Thermal Characterization. The DTA/TG curves of all isostructural solvates were almost the same (see Figure 3 and Figure S3): desolvation of these solvates occurred over a wide temperature range, which started at ambient temperature without a characteristic sharp endothermic effect associated with the desolvation process, thus suggesting that all of these solvates are nonstoichiometric. When the temperature was increased to 115–130 °C, melting occurred as confirmed by hot stage microscopy (HSM) (see Figure S4). Desolvation of these solvates occurred at different rates, and at the heating rate 5°·min⁻¹ the forms S_{Et}, S_{ACN}, S_{NM}, and S_{CLF} were not completely desolvated before melting, and thus the melting endotherm appeared together with a rapid loss of the rest of solvent. After the melting, recrystallization occurred by forming polymorph I as identified by the melting point in the DTA curves. The recrystallization was also observed in the HSM study (see Figure S4, Supporting Information).

Desolvation products of all the solvates were analyzed with PXRD, and the obtained diffraction patterns are given in Figure 4. By combining the PXRD and DTA/TG data, it was determined that all of the isostructural solvates can be desolvated before melting (by heating at 100 °C for a maximum of 2 days).

From Figure 4 it can be identified that desolvation of isostructural solvates produced a phase with only a slightly different PXRD pattern: the isostructural desolvate (ISD). This was confirmed also by the structure determination of completely dehydrated NSH crystals (see Table 1). The formation of isostructural desolvate supports the fact that isostructural solvates are nonstoichiometric.

Solvent stoichiometry was determined from TG curves (see Figures 3 and S3, Supporting Information), and the obtained results are given in Table 2. The obtained results were

Table 2. Physicochemical Data for the Droperidol Isostructural Solvates

solvate	calculated weight loss, %	observed weight loss, %	T _{desolvation} ^a , °C (peak)	resulting phase
NSH	4.5 ^b	2.5–4.8 ^c	124	ISD
S _{Me}	4.2 ^d	3.5–4.5	124	ISD
S _{Et}	6.1 ^d	5.1–6.6	125–127	ISD
S _{ACN}	5.4 ^d	4.9–6.0	124–129	ISD
S _{NM}	8.0 ^d	8.2–8.9	113–115	ISD
S _{DCM}	11.2 ^d	5.5–11.0	123–124	ISD
S _{CLF}	15.7 ^d	5.5–9.5	123–126	ISD

^aMelting peak of the solvate or resulting ISD. ^bFor monosolvate stoichiometry. ^cDepended on the storage conditions. ^dFor hemisolvate stoichiometry.

consistent with the solvent stoichiometry determined by SCXRD. The differences between the observed and calculated solvent content in isostructural solvates are associated with their nonstoichiometric behavior. The stoichiometry of S_{DCM} and S_{CLF} was determined only from TG data. On the basis of measurements from at least three different samples, S_{DCM} was found to be a hemisolvate, whereas the stoichiometry of S_{CLF}

was unclear because the highest obtained solvent/droperidol ratio was only 1:3.

Desolvation of S_{TCC} and S_{DIOX} produced the polymorph I, S_{TOL} produced a new polymorph IV and that of DH depended on the sample and produced either the polymorph II or a new polymorph III. Results from thermal analysis of these solvates are given in the Supporting Information.

Schematic representation of solvate preparation and phase transformations upon heating is given in Figure 5.

Crystal Structures of Isostructural Solvates. NSH, S_{Et}, and S_{Me} crystallize in $P\bar{1}$ space group (see Table 1 and Table S3, Supporting Information) with one droperidol molecule and a water molecule or half of a disordered alcohol molecule respectively, in agreement with the already reported structures.^{35,36} However, S_{ACN} and S_{NM} crystallize in the *P1* space group with two droperidol molecules and a solvent molecule in the unit cell. Both droperidol molecules in these two solvates are inversion related; thus only the asymmetric solvent molecule breaks centrosymmetry of the whole crystal structure. Therefore, the conformation of both droperidol molecules in the unit cell is the same (by taking into account the inversion symmetry, see Figure S6 and Table S4, Supporting Information). As already mentioned, despite the different space groups, all these droperidol solvates are isostructural (see Figure 6 and Figures S8 and S9, Supporting Information), and the solvent molecules are situated in the channels positioned along the *a*-axis (see Figure S7, Supporting Information).

In these solvates all of the acetonitrile and nitromethane molecules pointed in only one direction. Although the methanol and ethanol molecules are asymmetric, the disorder of these solvent molecules allowed description of S_{Et} and S_{Me} in the $P\bar{1}$ space group. The type of structural disorder with regard to the solvent molecules and its causes were further investigated using solid-state NMR and theoretical calculations and is a topic for our next study.

The 2D fingerprint plots (calculated from the Hirshfeld surfaces^{59,60} in *CrystalExplorer 3.1*⁶¹) of droperidol molecules from all of the solvates were almost the same and were dominated by the interactions between the droperidol molecules themselves (see Figure S11, Supporting Information). Thus, the solvent had only a minor role in the crystal structure, and therefore it was reasonable that isostructural solvates with quite different solvent molecules could form.

The Interactions of Solvent Molecules in Isostructural Solvates. In order to understand the differences between the isostructural solvates, as well as the reasons for their stability, intermolecular interactions of solvent molecules were analyzed. Solvates can be divided based on the presence (in NSH, S_{Me}, and S_{Et}) or absence (in S_{ACN} and S_{NM}) of strong hydrogen bonds between the solvent and the droperidol molecule oxygen atom O1 in the benzimidazolone moiety. Although the disorder of solvent molecules complicated the characterization of this interaction in S_{Me} and S_{Et} hydrogen bond parameters were characteristic to a strong hydrogen bond with the O1...O3 distance of 2.81–2.91 Å, where the longest distance was in S_{Me} (see Tables 3 and S5). There were slightly different interactions between alkyl residues of alcohol molecules and droperidol molecules: in both solvates the O3 atom was an acceptor of hydrogen bond from different droperidol hydrogen atoms, and the methyl group of the methanol was a hydrogen bond donor for a much shorter interaction than in ethanol (see Table 3).

There was no strong hydrogen bond between droperidol and acetonitrile or nitromethane. Nevertheless, these molecules

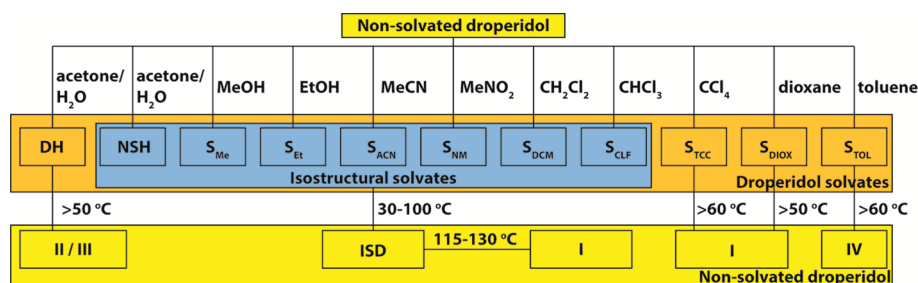


Figure 5. Schematic representation of the droperidol solvate preparation and phase transformations upon their heating.

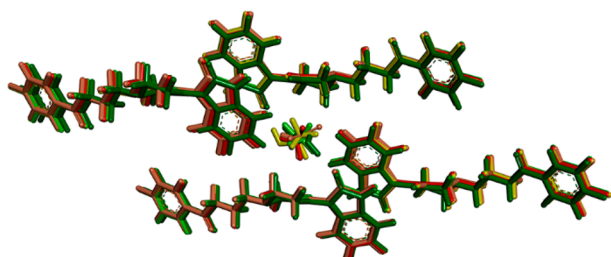


Figure 6. Overlay of the crystal structures of isostructural droperidol solvates.

Table 3. Geometrical Parameters for the Intermolecular Interactions of Solvent Molecules in Droperidol Solvates S_{Me} , S_{Et} , S_{ACN} , S_{NM} , and NSH^a

	interaction ^b	X–H (Å)	H...A (Å)	D...A (Å)	D–H...A (deg)
S_{Me}	O3–H...O1 ^b	1.13	1.87	2.91	150
	O3...H–C9 ^c	0.97	2.80	3.51	130
	C23–H...O1 ^d	0.96	2.46	3.36	156
S_{Et}	O3–H...O1 ^d	0.82	2.53	2.81	102
	O3...H–C5 ^e	0.93	2.64	3.41	140
	C24–H...C9 ^f	0.95	2.99	3.85	151
S_{ACN}	C24–H...O1 ^f	0.97	2.92	3.51	120
	C23–H...O1 ^g	0.96	2.68	3.41	133
	C23–H...C9 ^b	0.96	2.97	3.92	169
S_{NM}	N4...H–C5 ^c	0.93	2.80	3.70	162
	N4...H–C5 ^g	0.93	2.83	3.60	140
	C23–H...O1 ^h	0.96	2.44	3.31	150
	C23–H...C9 ^b	0.96	2.90	3.86	178
	O3...H–C5 ^a	0.93	2.70	3.42	135
	O3...H–C10 ^h	0.97	2.52	3.29	135
	O3...H–C11 ^h	0.97	2.66	3.51	147
	O3...H–C4 ^e	0.93	2.64	3.42	143
	O4...H–C9 ^c	0.93	2.66	3.16	115
	O4...H–C10 ^c	0.97	2.72	3.13	106
NSH	O4...H–C4 ^g	0.93	2.67	3.28	124
	O4...H–C5 ^g	0.93	2.66	3.26	123
	O3–H...O1 ^b	0.85	1.99	2.83	171
	O3–H...O3 ⁱ	0.85	2.22	2.86	131
	O3...H–C9 ^c	0.95	2.73	3.38	127

^aSymmetry codes: (b) x, y, z . (c) $1+x, y, z$. (d) $1-x, 1-y, -z$. (e) $-1+x, y, z$. (f) $-1+x, -1+y, z$. (g) $1+x, 1+y, z$. (h) $x, 1+y, z$. (i) $2-x, -y, -z$. ^bCutoff parameter: van der Waals radii +0.1 Å.

formed numerous weak hydrogen bonds and dispersion interaction with droperidol molecules (see Table 3), therefore providing sufficient interactions to allow the formation of a stable solvate.

The only strong intermolecular interaction between solvent molecules was observed in NSH where two water molecules formed hydrogen bond by connecting two droperidol molecules via an $O1...O3...O3...O1$ linkage⁴⁰ across the channel.

Hirshfeld surface 2D fingerprint plots of the solvent molecules representing the intermolecular interactions are given in Figure 7. For this analysis crystal structures of S_{Me} and S_{Et} with ordered solvent molecules after optimization of hydrogen atom positions were used.

From the solvent molecule 2D fingerprint plots, it was possible to determined that interactions of both alcohol molecules were different, although both were dominated by

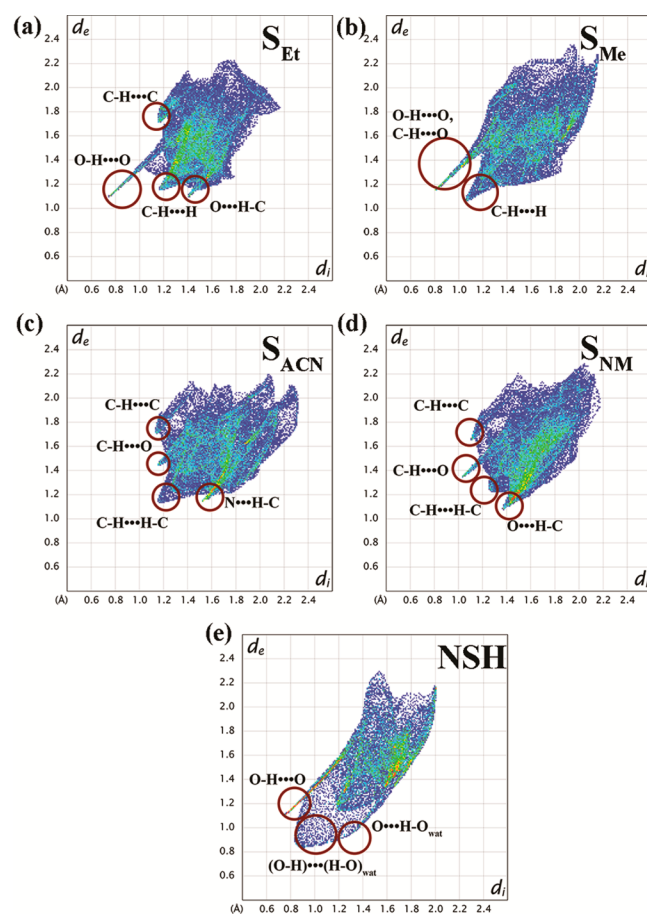


Figure 7. Hirshfeld surface 2D fingerprint plots of solvent molecules in droperidol isostructural solvates, where d_e is the distance from a point on the surface to the nearest nucleus outside the surface and d_i represents the distance from a point on the surface to the nearest nucleus inside the surface.^{57,58}

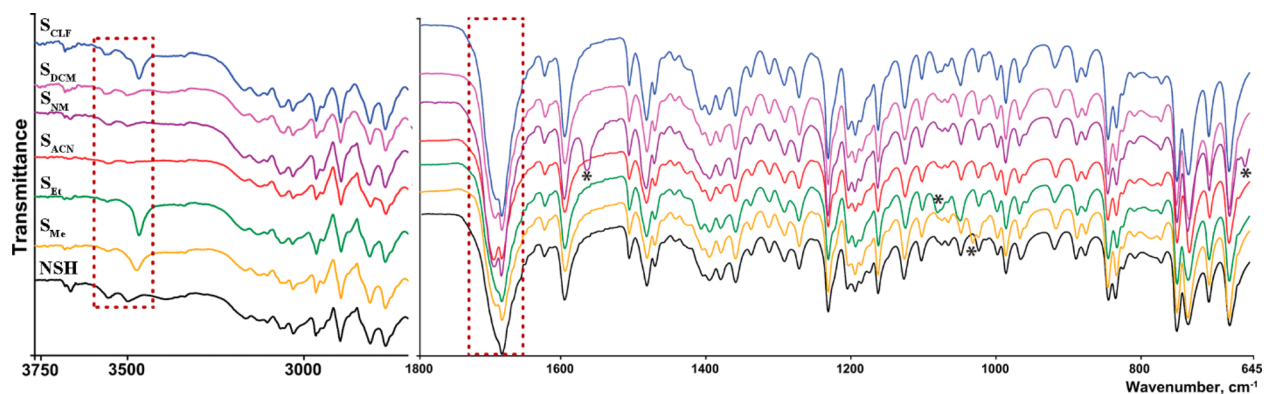


Figure 8. FTIR spectra of the droperidol isostructural solvates with dashed rectangle highlighting the most differing spectral regions and asterisks marking the bands due to the solvent molecules.

the strong hydrogen bond O3–H···O1. Despite the different functional groups in acetonitrile and nitromethane, and the seemingly different interactions of nitrile and nitro groups (see Table 3), the interactions represented in 2D fingerprint plots, although differently shaped, were very similar. This suggests that the properties of S_{ACN} and S_{NM} could be similar. Therefore, besides a strong hydrogen bond connecting alcohols in S_{Me} and S_{EV} the stability of these solvates and that of S_{ACN} and S_{NM} was provided by weak hydrogen bonds and dispersion interactions. As could be expected, interactions of water molecules in NSH were dominated only by strong hydrogen bonds. However, unusual relative arrangement of water molecules (see Figure S14, Supporting Information) introduced unusually shaped broad representation of hydrogen–hydrogen interactions between both water molecules.

Fourier-Transform Infrared Spectroscopy. ATR-FTIR spectra of the solvates are presented in Figure 8. Besides the few peaks appearing due to the presence of different solvent molecules, the spectra of these solvates were almost identical, confirming their isostructurality. However, noticeable differences characterizing the structure of solvates appeared in the carboxyl group stretching and O–H stretching regions. There were two distinct peaks with almost the same intensity in the carboxyl group stretching region for S_{NM} , S_{ACN} , and S_{DCM} (see Figure S17a, Supporting Information). However, the higher frequency peak ($\sim 1692\text{ cm}^{-1}$) was observed as a shoulder on the lower frequency peak ($\sim 1682\text{ cm}^{-1}$) for S_{Me} , S_{CLF} , S_{EV} and NSH . At the same time there was sharp peak at $3468\text{--}3475\text{ cm}^{-1}$ for S_{EV} , S_{Me} , and S_{CLF} , and at 3499 cm^{-1} for NSH corresponding to the O–H (in alcohols and water) and C–H (in chloroform) stretching bands, respectively.

Thus, based on the similarities in IR spectra in the O–H and C–H stretching regions and in the C=O stretching region, it can be concluded that chloroform molecule also forms hydrogen bond with droperidol molecules similarly to water and alcohol molecules, whereas the solvent interactions in S_{DCM} are more similar to those in S_{NM} and S_{ACN} .

Characterization of Solvent Content in Isostructural Solvates at Different Solvent Activity. The nonstoichiometric behavior of the solvates and the presence of solvent channels suggested that solvent content in the structure (ϵ) should be dependent on the solvent activity.⁶² To investigate this, NSH , S_{EV} , S_{Me} , S_{ACN} , and S_{NM} were stored under atmosphere with different solvent activity, obtaining the sorption–desorption isotherms of the corresponding solvents. Water sorption–desorption isotherm of NSH is shown in

Figure 9. The highest water content corresponds to monohydrate stoichiometry and lowering of the RH gradually

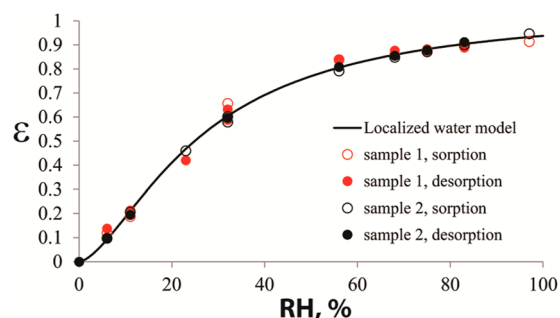


Figure 9. Water sorption–desorption isotherm of NSH from two sample sorption and desorption cycles, and localized water model describing the experimental points.

decreased the water content ϵ by completely dehydrating the NSH and obtaining ISD at $\approx 0\%$ RH.

A study of the other four solvate sorption–desorption isotherms revealed that uptake of the solvent also was gradual but occurred at much lower solvent activity: most of the solvent uptake had already had taken place when solvent activity reached 0.02 and maximum solvate stoichiometry ($\epsilon \approx 0.5$) was reached at solvent activity 0.1. The resulting sorption–desorption isotherm of S_{Me} is given in Figure 10, but those of S_{EV} , S_{ACN} , and S_{NM} are in Figures S20 and S23, Supporting Information. The initial parts of the isotherms for all solvates are given in Figure 11.

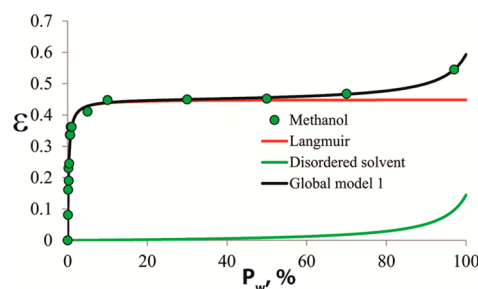


Figure 10. Methanol sorption–desorption isotherm of S_{Me} . The black line corresponds to global isotherm model formed by combination of Langmuir isotherm (red line) and disordered solvent model⁶³ (green line).

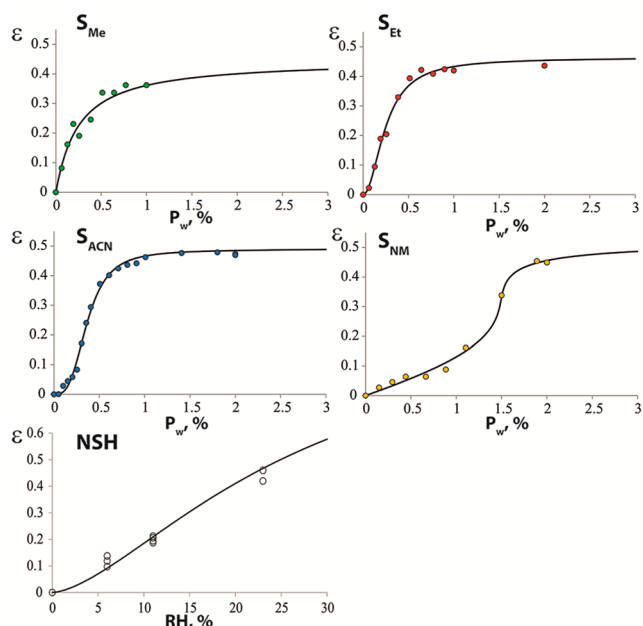


Figure 11. Initial part of the droperidol isostructural solvate sorption–desorption isotherms where circles indicate experimental solvent content ε and lines represent the best theoretical model (Langmuir isotherm (S_{Me}) and general localized solvent model⁶³ with constant activity coefficients (NSH , S_{Et} and S_{ACN}) or activity coefficients described by third-order Margules equation (S_{NM})). For NSH a 10 times larger solvent activity region is shown.

In order to compare the obtained isotherms, thermodynamic models were used to describe the obtained data points, thus characterizing the thermodynamics of the solvates themselves.⁶³ The sorption–desorption isotherm of NSH was fitted with general localized water model with constant activity coefficients (see Figure 9, parameters used for all the fittings are given in Tables S5–S8), whereas those of all organic solvates were described as a combination of (a) localized solvent model describing solvent in the structural channels and (b) disordered solvent model describing the adsorbed solvent⁶³ (see Supporting Information). Localized solvent in the sorption–desorption isotherm of S_{Me} was fitted with Langmuir isotherm and that in S_{Et} with general localized solvent model with constant activity coefficients. The sorption–desorption isotherms of S_{ACN} and S_{NM} clearly did not correspond to Langmuir isotherm because of the hindered solvent absorption at very low solvent activity and thus sigmoidal shape (see Figure 11). The S_{ACN} isotherm was fitted with a general localized solvent model (usage of variable activity coefficients only slightly improved the fit), whereas that of S_{NM} could be fitted only using localized solvent model with variable activity coefficients described by Margules equations (see Figure S24, Supporting Information). The differences between the isotherms are associated with the presence or absence of interactions between solvent molecules in two adjacent solvent sites positioned along the a -axis as well as the solvent molecule size differences (see Supporting Information). As the solvent molecules have well located crystallographic sites, the use of the Langmuir model or localized solvent model for describing the change of these molecules in the channels is in accordance with the assumptions for these models.

Characterization of Changes in Isostructural Solvate Structure at Various Solvent Content. The PXRD patterns

of solvates with various solvent content were recorded. By increasing the solvent content, continuous displacement of diffraction peaks to mostly lower 2θ values occurred (insertion of the solvent molecules increased the cell volume and thus the interplanar spacing), and continuous intensity changes of some peaks were observed. The peak positions changed gradually, thus confirming the continuity of structural changes (see Figures S25–S29, Supporting Information), and it was possible to calculate the dependence of lattice parameters on the solvent content (ε) for these solvates. The obtained results confirmed gradual changes of the crystal structure (see Figure 12). The

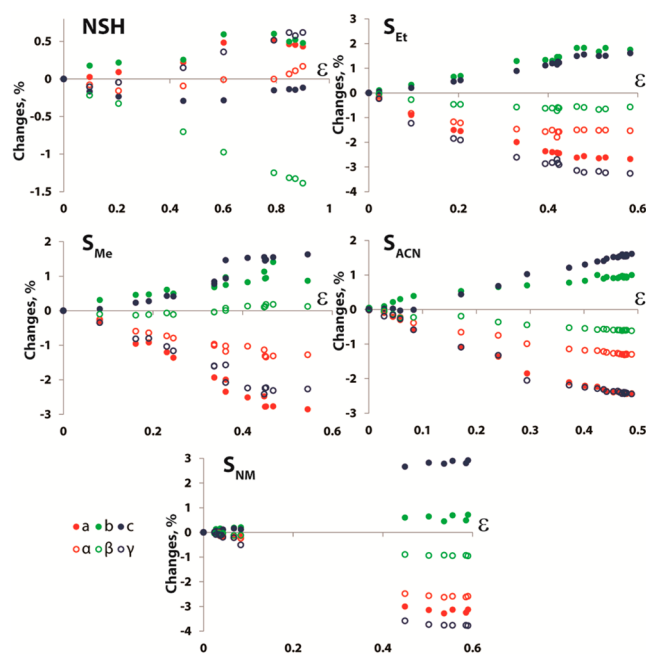


Figure 12. Lattice parameter dependence on the solvent content (ε) in the isostructural solvates of droperidol.

differences between NSH and other solvates already observed from changes of the diffraction peak positions (see Supporting Information) were reflected in the calculated lattice parameters: the direction and amplitude of the lattice parameter changes was almost identical for all solvates except for the NSH (see Figure 12).

These differences of the lattice parameter change clearly could be associated with the formation of hydrogen bonds mediated by water molecules, with these bonds providing links between droperidol molecules situated across structural channels. Therefore, the decrease of the cell length c and the angle α , with concurrent increase of the angle γ in NSH was due to the geometric effects driven by the formation of this linkage. The decrease of the cell length a for other solvates most probably can be associated with the presence of solvent–solvent interactions in the channels, but the size of the solvent molecules caused the increase of the cell lengths b and c .

Water Arrangement in a Partially Filled NSH Structure. In this study the crystal structures of NSH with three different levels of water content were determined: the monohydrate (120 K, obtained from synthesis), the hemihydrate (120 K, obtained by storing a sample at 30–40% RH), and the anhydrous form or ISD (333 K, obtained by storing a sample at 0% RH, or heating the sample). As can be seen in Table S12, Supporting Information, the intermolecular

interaction geometry of droperidol molecules was only slightly affected by the water content.

The hydrogen bonding parameters determined for water mediated hydrogen bond linkage O1...O3...O3...O1 are given in Table 4. In this study, both of the hydrogen atoms were

Table 4. Geometrical Parameters for the Hydrogen Bond Linkage Provided by Water Molecules in NSH with Mono- and Hemihydrate Stoichiometry

ϵ	temp, K	O1...O3, Å	O3...O3, Å	O1–O3–O3, °	O1...O1, Å
1	120	2.83	2.86	109	7.11
	173	2.85	2.83	109	7.14
0.5	120	2.85	2.86	108	7.13
	298 ⁴⁰	2.85	2.76	111	7.16

located for the case of monohydrate stoichiometry, therefore confirming that between two water molecules there is a hydrogen bond with unusual geometry (see Figure S14, Supporting Information).

The geometrical parameters for the O3–H...O1 and O3–H...O3 hydrogen bonds were the same for both stoichiometries. Therefore, the removal of water occurred by simultaneously losing both hydrogen bonded water molecules from some of the channel sites instead of losing water molecules from one of the O3 positions and thus losing hydrogen bond linkage across the channel. This water molecule arrangement in NSH with stoichiometry below 1 was also supported by the absence of a significant increase in the equivalent isotropic displacement parameter of water oxygen for hemihydrate stoichiometry (thus confirming that water retains two hydrogen bonds also for this stoichiometry), by the energy calculations (hemihydrate structure with hydrogen bonded water molecules was energetically favorable by 2–4.5 kJ per mole of water), lattice parameter changes (this arrangement explained the observed lattice parameter changes), and the recorded sorption–desorption isotherms corresponding to the presence of only equivalent water absorption sites in the structure. More details are given in the Supporting Information.

We therefore conclude that the difference observed in the solvent uptake at a given solvent activity in the NSH sorption–desorption isotherm (see Figure 11) can be associated with the absorption of water through an insertion of two hydrogen-bonded molecules at one site, which theoretically is a lower probability process compared to the absorption of one solvent molecule, as in the rest of the solvates.

Analysis of the Droperidol Solvate Formation. While it should not be assumed that all of the potentially existing solvates have been identified, the crystallization from 30 solvents selected from various solvent classes should ensure the discovery of most of the stable solvated forms. Interestingly, five of the newly prepared solvated phases were isostructural to the already known NSH and S_{Et}. Thus, although droperidol solvates can be obtained with 10 solvents, only five distinct solvated crystal structures were obtained: DH, S_{TCC}, S_{DIOX}, S_{TOL}, and the “isostructural solvate”, where the latter one formed from a variety of different solvents. Therefore, three questions can be raised to understand the solvate formation of droperidol: (a) what is the reason for the formation of only these five structures, (b) why were the isostructural solvates obtained from such a wide range of solvents, and (c) which solvents can form isostructural solvates?

Unfortunately, the lack of information regarding the S_{TCC}, S_{DIOX} and S_{TOL} crystal structures prevents a thorough answer to the first question. It is stated that one of the driving forces for solvate formation can be a mismatch of the hydrogen bond donors and acceptors in a molecule.⁶⁴ Although the molecule of droperidol contains three strong hydrogen bond acceptors (HBA) and only one hydrogen bond donor (HBD), this HBD deficiency was compensated only in the DH structure. In isostructural solvates, the solvent molecules did not compensate the HBD deficiency, and it is not theoretically possible also in the structures of S_{TCC}, S_{DIOX} and S_{TOL}. Therefore, it can be concluded that the formation of droperidol solvates can be associated with the fact that molecules cannot pack with a sufficient efficiency and solvent molecules act as void fillers in these structures. This is supported by the fact that the packing index of the thermodynamically stable polymorph II is 0.675, which is only slightly higher than that of ISD at 333 K (0.659) where there are empty channels, but significantly lower than that of the isostructural solvates (0.704–0.717).

The reason for the formation of isostructural solvates is the stability of this structure. The calculation of both the total and lattice energy showed that the structures of II and ISD have almost the same energy at 0 K (the energy of ISD is even slightly favorable, see Table S13, Supporting Information), and only the higher density of the polymorph II makes it thermodynamically stable at elevated temperature. Therefore, this structure is not necessarily characterized by a high solvent selectivity, and the criteria for solvate formation most probably are (a) the ability to form sufficiently efficient droperidol–solvent interactions, and (b) the solvent molecules should fit into the channels by not significantly disturbing the packing of droperidol molecules.

By evaluating the properties of solvents forming isostructural solvates, it was noticed that three solvates formed with aprotic polar solvents (acetonitrile, nitromethane, and dichloromethane), three formed with hydrogen bond donors (water, methanol, and ethanol), and the last one formed with chloroform that can be classified both as a hydrogen bond donor and aprotic polar solvent, depending on the classification scheme.⁴⁵ However, the classification of solvents according to these two groups clearly is not the main factor affecting the formation of the solvates (see Table S1, Supporting Information), although the formation of strong hydrogen bonds apparently is one of the driving forces. A better explanation of isostructural solvate formation can be achieved by taking into account a more detailed solvent classification based on various physical and physicochemical properties.⁴⁶ Isostructural solvates were obtained from solvents belonging to groups 3 (mostly alcohols), 7 (mostly halocarbons), 9 (nitriles and nitromethane), and 15 (water).⁴⁶ Therefore, only solvents from these groups were able to form energetically favorable interactions with the functional groups of droperidol molecules located around the structure channel.

Nevertheless, the second important factor for the formation of isostructural solvates clearly is the size (and shape) of solvent molecules. Thus, only the smallest molecules from the solvent groups 3, 7, and 9 formed isostructural solvates, which was confirmed by the calculation of molar volume (see Table S14, Supporting Information). The largest solvent molecule forming an isostructural solvate with droperidol is chloroform (the size of which is even higher than that of some solvents not able to form isostructural solvates with droperidol), explaining the solvent content in the S_{CLF} phase observed by TG measure-

ments to be below 0.5 stoichiometry. In contrast, the small size of water molecule and its ability to form interwater hydrogen bonds enabled the formation of a monohydrate.

CONCLUSIONS

Crystallization of droperidol from 30 different solvents produced eight new solvates from methanol, acetonitrile, nitromethane, chloroform, dichloromethane, carbon tetrachloride, 1,4-dioxane, and toluene, while the desolvation of droperidol solvates produced two new polymorphs III and IV. Droperidol solvates obtained from methanol, ethanol, acetonitrile, nitromethane, dichloromethane, chloroform, and water are nonstoichiometric and isostructural. The solvent content in these solvates can reach up to 0.5 equiv (with the exception of NSH, that can reach monohydrate stoichiometry), and desolvation of these solvates produces an isostructural desolvate.

The crystal structures of five of these solvates were determined, proving that the droperidol molecule arrangement was isostructural despite the crystal structure description in both the centrosymmetric $P\bar{1}$ (NSH, S_{Me} , and S_{Et}) and non-centrosymmetric $P1$ (S_{ACN} and S_{NM}) space group. The different space group determined for solvates with organic solvents was due to the disorder of methanol and ethanol molecules. The stability of isostructural solvates was mainly provided by the interactions between droperidol molecules themselves, while the solvent molecules were located in the structural channels and formed strong and/or weak hydrogen bonds with the droperidol molecules. On the basis of the IR spectra, it was concluded that the chloroform molecules in S_{CLF} formed hydrogen bonds with droperidol molecules.

The solvent sorption–desorption isotherms of NSH, S_{Me} , S_{Et} , S_{ACN} , and S_{NM} showed that the solvent molecule content in the solvate could be described with a localized solvent model and there was no interaction between the solvent sites in S_{Me} . For NSH, S_{Et} , S_{ACN} , and S_{NM} the solvent interactions and the larger molecule size complicated the shape of the sorption isotherm. It was proved that the solvent content variation in the channels resulted in linear changes of the lattice parameters; therefore the transformation of the crystal structure was gradual. The lattice parameter changes and the solvent uptake at a given solvent activity in NSH significantly differed from those in the rest of the solvates. This was due to the formation of water molecule mediated hydrogen bond linkage across the structural channels and the simultaneous occupation of both of these hydrogen bonded water molecule positions.

The analysis of the solvate formation revealed that the driving force for droperidol solvate formation was the inability of droperidol molecules to pack efficiently; thus the solvent molecules acted as a void fillers, with the exception of DH, where water molecules provided an HBD function matching the excess HBA functions in the molecule of droperidol. The stability of the isostructural solvate structure was rationalized by the very effective interactions between droperidol molecules, explaining the fact that no specific interaction with solvate was necessary to maintain the crystal structure of the isostructural solvate. Therefore, isostructural solvates can be obtained with solvents fitting in the channels and providing sufficiently effective intermolecular interactions with droperidol. By analyzing the solvent classification, it was concluded that these solvates can be obtained with the smallest solvent molecules from the solvent groups 3, 7, and 9, as well as from

water,⁴⁶ and the formation of strong hydrogen bonds is one of the driving forces for solvate formation.

ASSOCIATED CONTENT

Supporting Information

More detailed analysis and results of droperidol solvate synthesis, crystal structures, solvent sorption–desorption isotherms, solvent content effect on solvate crystal structures, and solvate formation, along with X-ray crystallographic information files (CIF), additional results from PXRD, DTA/TG, HSM, and FTIR characterization of droperidol solvates and polymorphs, and additional crystallographic data. This material is available free of charge via the Internet at <http://pubs.acs.org/>. Crystallographic information files are also available from the Cambridge Crystallographic Data Center (CCDC) upon request (<http://www.ccdc.cam.ac.uk>, CCDC deposition numbers 990349–990351 and 990471–990474).

AUTHOR INFORMATION

Corresponding Author

*E-mail: agris.berzins@lu.lv. Telephone: +(371)-67372576.

Notes

The authors declare no competing financial interest.

ACKNOWLEDGMENTS

This work was supported by the European Social Fund within the project “Support for Doctoral Studies at the University of Latvia”. We wish to thank the Riga Technical University Institute of Polymer Materials for the provided opportunity to carry out hot-stage microscopy measurements and Inese Sarceviča for the help with crystal structure determination.

REFERENCES

- (1) Price, C. P.; Glick, G. D.; Matzger, A. J. *Angew. Chem., Int. Ed.* **2006**, *45*, 2062.
- (2) Bingham, A. L.; Hughes, D. S.; Hursthouse, M. B.; Lancaster, R. W.; Tavener, S.; Threlfall, T. L. *Chem. Commun.* **2001**, 603.
- (3) Yu, L.; Stephenson, G. A.; Mitchell, C. A.; Bunnell, C. A.; Snorek, S. V.; Bowyer, J. J.; Borchardt, T. B.; Stowell, J. G.; Byrn, S. R. *J. Am. Chem. Soc.* **2000**, *122*, 585.
- (4) Sun, C.; Grant, D. J. W. *Pharm. Res.* **2001**, *18*, 274.
- (5) Khomane, K. S.; More, P. K.; Bansal, A. K. *J. Pharm. Sci.* **2012**, *101*, 2408.
- (6) Picker-Freyer, K. M.; Liao, X.; Zhang, G.; Wiedmann, T. S. *J. Pharm. Sci.* **2007**, *96*, 2111.
- (7) Pudipeddi, M.; Serajuddin, A. T. M. *J. Pharm. Sci.* **2005**, *94*, 929.
- (8) Bauer, J.; Spanton, S.; Henry, R.; Quick, J.; Dziki, W.; Porter, W.; Morris, J. *Pharm. Res.* **2001**, *18*, 859.
- (9) Morissette, S. L.; Soukasene, S.; Levinson, D.; Cima, M. J.; Almarsson, Ö. *Proc. Natl. Acad. Sci. U. S. A.* **2003**, *100*, 2180.
- (10) Chavez, K. J.; Guevara, M.; Rousseau, R. W. *Cryst. Growth Des.* **2010**, *10*, 3372.
- (11) Fujii, K.; Aoki, M.; Uekusa, H. *Cryst. Growth Des.* **2013**, *13*, 2060.
- (12) Guguta, C.; Eeuwijk, I.; Smits, J. M. M.; de Gelder, R. *Cryst. Growth Des.* **2008**, *8*, 823.
- (13) Herbstein, F. H. *Cryst. Growth Des.* **2004**, *4*, 1419.
- (14) Vippagunta, S. R.; Brittain, H. G.; Grant, D. J. W. *Adv. Drug Delivery Rev.* **2001**, *48*, 3.
- (15) Schmidt, A. C.; Niederwanger, V.; Griesser, U. J. *J. Therm. Anal. Calorim.* **2004**, *77*, 639.
- (16) Giron, D. *Thermochim. Acta* **1995**, *248*, 1.
- (17) Braun, D. E.; Kahlenberg, V.; Gelbrich, T.; Ludescher, J.; Griesser, U. J. *CrystEngComm* **2008**, *10*, 1617.

- (18) Braun, D. E.; Gelbrich, T.; Kahlenberg, V.; Tessadri, R.; Wieser, J.; Griesser, U. J. *Cryst. Growth Des.* **2009**, *9*, 1054.
- (19) Kazantsev, A. V.; Karamertzanis, P. G.; Adjiman, C. S.; Pantelides, C. C.; Price, S. L.; Galek, P. T. A.; Day, G. M.; Cruz-Cabeza, A. J. *Int. J. Pharm.* **2011**, *418*, 168.
- (20) Bardwell, D. A.; Adjiman, C. S.; Arnautova, Y. A.; Bartashevich, E.; Boerrigter, S. X. M.; Braun, D. E.; Cruz-Cabeza, A. J.; Day, G. M.; Della Valle, R. G.; Desiraju, G. R.; van Eijck, B. P.; Facelli, J. C.; Ferraro, M. B.; Grillo, D.; Habgood, M.; Hofmann, D. W. M.; Hofmann, F.; Jose, K. V. J.; Karamertzanis, P. G.; Kazantsev, A. V.; Kendrick, J.; Kuleshova, L. N.; Leusen, F. J. J.; Maleev, A. V.; Misquitta, A. J.; Mohamed, S.; Needs, R. J.; Neumann, M. A.; Nikylov, D.; Orendt, A. M.; Pal, R.; Pantelides, C. C.; Pickard, C. J.; Price, L. S.; Price, S. L.; Scheraga, H. A.; van de Streek, J.; Thakur, T. S.; Tiwari, S.; Venuti, E.; Zhitkov, I. K. *Acta Crystallogr., Sect. B* **2011**, *67*, 535.
- (21) Price, S. L. *Chem. Soc. Rev.* **2014**, *43*, 2098.
- (22) Ismail, S. Z.; Anderton, C. L.; Copley, R. C. B.; Price, L. S.; Price, S. L. *Cryst. Growth Des.* **2013**, *13*, 2396.
- (23) Kendrick, J.; Stephenson, G. A.; Neumann, M. A.; Leusen, F. J. *J. Cryst. Growth Des.* **2013**, *13*, 581.
- (24) Braun, D. E.; Tocher, D. A.; Price, S. L.; Griesser, U. J. *J. Phys. Chem. B* **2012**, *116*, 3961.
- (25) Braun, D. E.; Karamertzanis, P. G.; Price, S. L. *Chem. Commun.* **2011**, *47*, 5443.
- (26) Hulme, A. T.; Price, S. L. *J. Chem. Theory Comput.* **2007**, *3*, 1597.
- (27) Nangia, A.; Desiraju, G. *Chem. Commun.* **1999**, 1999, 605.
- (28) Stieger, N.; Liebenberg, W.; Wessels, J.; Samsodien, H.; Caira, M. *Struct. Chem.* **2010**, *21*, 771.
- (29) Caira, M. R.; Bettinetti, G.; Sorrenti, M. *J. Pharm. Sci.* **2002**, *91*, 467.
- (30) Hosokawa, T.; Datta, S.; Sheth, A. R.; Brooks, N. R.; Young, V. G., Jr.; Grant, D. J. W. *Cryst. Growth Des.* **2004**, *4*, 1195.
- (31) Banerjee, R.; Bhatt, P. M.; Desiraju, G. R. *Cryst. Growth Des.* **2006**, *6*, 1468.
- (32) Zhang, Q.; Lu, L.; Dai, W.; Mei, X. *CrystEngComm* **2014**, *16*, 1919.
- (33) Murphy, B. J.; Casteel, M. J.; Samas, B.; Krzyzaniak, J. F. *J. Pharm. Sci.* **2012**, *101*, 1486.
- (34) Stephenson, G.; Groleau, E.; Kleemann, R.; Xu, W.; Rigsbee, D. *J. Pharm. Sci.* **1998**, *87*, 536.
- (35) Byard, S.; Abraham, A.; T. Boulton, P. J.; Harris, R. K.; Hodgkinson, P. *J. Pharm. Sci.* **2012**, *101*, 176.
- (36) Nassimbeni, L. R. *Acc. Chem. Res.* **2003**, *36*, 631.
- (37) Kamiński, D. M.; Hoser, A. A.; Gagoś, M.; Matwijczuk, A.; Arczewska, M.; Niewiadomy, A.; Woźniak, K. *Cryst. Growth Des.* **2010**, *10*, 3480.
- (38) Aitipamula, S.; Chow, P. S.; Tan, R. B. H. *J. Mol. Struct.* **2011**, *1005*, 134.
- (39) Aitipamula, S.; Chow, P. S.; Tan, R. B. H. *CrystEngComm* **2011**, *13*, 1037.
- (40) Actins, A.; Araj, R.; Belakovs, S.; Orola, L.; Veidis, M. *J. Chem. Crystallogr.* **2008**, *38*, 169.
- (41) Azibi, M.; Draguet-Brughmas, M.; Bouche, R. *Pharm. Acta Helv.* **1982**, *57*, 182.
- (42) Blaton, N. M.; Peeters, O. M.; De Ranter, C. J. *Acta Crystallogr., Sect. B* **1980**, *36*, 2828.
- (43) Orola, L. Ph.D. thesis, Riga Technical University: 2010.
- (44) Klein, C. L.; Welch, J.; Southall, L. C. *Acta Crystallogr., Sect. C* **1989**, *45*, 650.
- (45) Gramatica, P.; Navas, N.; Todeschini, R. *Trends Anal. Chem.* **1999**, *18*, 461.
- (46) Gu, C.-H.; Li, H.; Gandhi, R. B.; Raghavan, K. *Int. J. Pharm.* **2004**, *283*, 117.
- (47) Sheldrick, G. *Acta Crystallogr., Sect. A* **2008**, *64*, 112.
- (48) Dolomanov, O. V.; Bourhis, L. J.; Gildea, R. J.; Howard, J. A. K.; Puschmann, H. *J. Appl. Crystallogr.* **2009**, *42*, 339.
- (49) Spek, A. L. *Acta Crystallogr., Sect. D* **2009**, *65*, 148.
- (50) Macrae, C. F.; Bruno, I. J.; Chisholm, J. A.; Edgington, P. R.; McCabe, P.; Pidcock, E.; Rodriguez-Monge, L.; Taylor, R.; van de Streek, J.; Wood, P. A. *J. Appl. Crystallogr.* **2008**, *41*, 466.
- (51) Greenspan, L. *J. Res. Natl. Bur. Stand., Sect. A* **1977**, *81A*, 89.
- (52) TOPAS, version 4.2; Bruker AXS: Karlsruhe, Germany, 2009.
- (53) Clark, S. J.; Segall, M. D.; Pickard, C. J.; Hasnip, P. J.; Probert, M. I.; Refson, K.; Payne, M. C. *Z. Kristallogr.* **2005**, *220*, 567.
- (54) Perdew, J. P.; Burke, K.; Ernzerhof, M. *Phys. Rev. Lett.* **1996**, *77*, 3865.
- (55) Tkatchenko, A.; Scheffler, M. *Phys. Rev. Lett.* **2009**, *102*, 073005.
- (56) Frisch, M. J.; Trucks, G. W.; Schlegel, H. B.; Scuseria, G. E.; Robb, M. A.; Cheeseman, J. R.; Scalmani, G.; Barone, V.; Mennucci, B.; Petersson, G. A.; Nakatsuji, H.; Caricato, M.; Li, X.; Hratchian, H. P.; Izmaylov, A. F.; Bloino, J.; Zheng, G.; Sonnenberg, J. L.; Hada, M.; Ehara, M.; Toyota, K.; Fukuda, R.; Hasegawa, J.; Ishida, M.; Nakajima, T.; Honda, Y.; Kitao, O.; Nakai, H.; Vreven, T.; Montgomery, J. A. J.; Peralta, J. E.; Ogliaro, F.; Bearpark, M.; Heyd, J. J.; Brothers, E.; Kudin, K. N.; Staroverov, V. N.; Kobayashi, R.; Normand, J.; Raghavachari, K.; Rendell, A.; Burant, J. C.; Iyengar, S. S.; Tomasi, J.; Cossi, M.; Rega, N.; Millam, J. M.; Klene, M.; Knox, J. E.; Cross, J. B.; Bakken, V.; Adamo, C.; Jaramillo, J.; Gomperts, R.; Stratmann, R. E.; Yazyev, O.; Austin, A. J.; Cammi, R.; Pomelli, C.; Ochterski, J. W.; Martin, R. L.; Morokuma, K.; Zakrzewski, V. G.; Voth, G. A.; Salvador, P.; Dannenberg, J. J.; Dapprich, S.; Daniels, A. D.; Farkas, O.; Foresman, J. B.; Ortiz, J. V.; Cioslowski, J.; Fox, D. J. *Gaussian 09, Revision D.01*; Gaussian Inc.: Wallingford, CT, 2009.
- (57) Grimme, S.; Antony, J.; Ehrlich, S.; Krieg, H. *J. Chem. Phys.* **2010**, *132*, 154104.
- (58) Gavezzotti, A. *New J. Chem.* **2011**, *35*, 1360.
- (59) McKinnon, J. J.; Jayatilaka, D.; Spackman, M. A. *Chem. Commun.* **2007**, 3814.
- (60) Spackman, M. A.; Jayatilaka, D. *CrystEngComm* **2009**, *11*, 19.
- (61) Wolff, S. K.; Grimwood, D. J.; McKinnon, J. J.; Turner, M. J.; Jayatilaka, D.; Spackman, M. A.; *CrystalExplorer*, version 3.1; University of Western Australia: Perth, 2012.
- (62) Brittain, H. G.; Morris, K. R.; Boerrigter, S. X. M. In *Polymorphism in Pharmaceutical Solids*; Brittain, H. G., Ed.; Informa Healthcare: New York, 2009; p 233.
- (63) Authelin, J. *Int. J. Pharm.* **2005**, *303*, 37.
- (64) Tessler, L.; Goldberg, I. *J. Inclusion Phenom. Macrocyclic Chem.* **2006**, *55*, 255.

Comparison and Rationalization of Droperidol Isostructural Solvate Stability: An Experimental and Computational Study

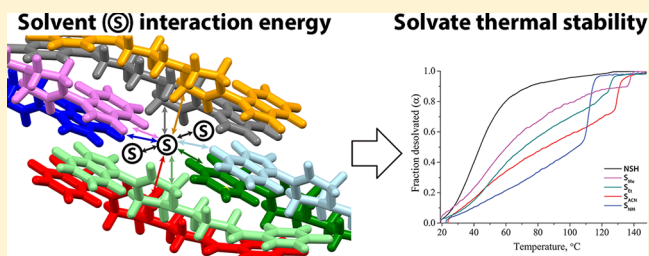
Agris Bērziņš,^{*,†,‡} Toms Reķis,[†] and Andris Actiņš[†]

[†]Faculty of Chemistry, University of Latvia, Kr. Valdemāra iela 48, Rīga, LV-1013, Latvia

[‡]Department of Chemistry, Durham University, South Road, Durham, U.K., DH1 3LE

S Supporting Information

ABSTRACT: In order to find a tool for comparison of solvate stability and to rationalize their relative stability, droperidol nonstoichiometric isostructural solvates were characterized experimentally and computationally. For the experimental evaluation of stability, three comparison tools were considered: thermal stability characterized by the desolvation rate, desolvation activation energy, and solvent sorption–desorption isotherms. It was found that the desolvation process was limited by diffusion, and the same activation energy values were obtained for all of the characterized solvates, while the solvent content in the sorption isotherm was determined by the steric factors. Therefore, the only criterion characterizing the solvate stability in this particular system was the thermal stability. It was found that computationally obtained solvent–droperidol and solvent–solvent interaction energies could be used for the rationalization of the isostructural solvate stability in this system and that the solvent–solvent interaction energy has a crucial role in determining the stability of solvates.



1. INTRODUCTION

The investigation of solid phase diversity of pharmaceutical molecules has frequently shown the formation of different phases, including polymorphs and solvates.^{1,2} The fact that different polymorphs and solvates have different stability,³ mechanical properties,^{4–6} and bioavailability (because of different solubility⁷) makes understanding the solid form stability and phase transitions a crucial step for the characterization of drug compounds. Determination of the relative stability of polymorphs is relatively simple, and there are numerous reports employing different techniques,^{8–11} with a growing number of computational stability predictions,^{10–12} including the calculation of crystal energy landscape where the stability of theoretical structures is also calculated.^{13–17} The same experimental and computational methods can also be used for the identical stoichiometry solvates^{17–19} with the same solvent, although the desolvation temperature predictions are not straightforward. The comparison of solvate stability with different solvents is cumbersome because of the lack of an unambiguous comparison parameter. The stability of solvates can be assessed by comparing the thermal stability, desolvation activation energy, or solvent sorption–desorption isotherms.

Most commonly, the thermal stability is compared by using the desolvation onset temperature or the desolvation rate at a given temperature or heating rate. In general, thermal stability should be a function of all the host–guest interactions, host–host interactions, and the intrinsic properties of the guest itself.²⁰ Surely, the first aspect is avoided if the host structure is identical for all the compared solvates. Although it is stated²⁰ and shown experimentally^{21,22} that the thermal stability

correlates with the normal boiling point of the solvent, this can be true only if the solvent molecules are weakly bound to the host material and situated in open voids. In other cases, the solvate stability should strongly depend on the solvent molecule accommodation in the host structure: the interaction energy between solvent and host molecules and the spatial characteristics.²¹ This is supported by the experimentally obtained order of the isostructural solvate thermal stability not matching the order of solvent boiling points^{23,24} and explained by the presence of different solvent–host intermolecular interactions,^{25–28} tight binding of the solvent molecules in the crystal cavities,^{29,30} or steric effects hindering the desolvation.³¹

The desolvation activation energy could also be used as a comparison tool if the desolvation mechanism of all the compared solvates is identical. However, this approach is rarely employed.³² In principle, also the solvent sorption–desorption isotherms could be compared by evaluating the phase composition at a given solvent activity. However, we have not found any example where this approach has been applied to pharmaceutical molecules, probably due to the possible experimental difficulties and the relatively complicated experimental procedure.

Here, we have tried to rationalize the solvate stability with respect to the desolvation based on their crystal structures and to select an appropriate tool for experimental comparison of the

Received: April 30, 2014

Revised: June 12, 2014

Published: June 13, 2014

solvate stability. Solvate stability was compared theoretically by calculating the intermolecular interactions in the solvate structure and experimentally by determining the solvate thermal stability and desolvation kinetics and by analyzing previously reported solvent sorption–desorption isotherms.³³ In order to avoid the effects of any other factors on the solvate stability and desolvation process, for this study, we selected isostructural solvates of droperidol that retain the crystal structure after the desolvation.

Droperidol, 1-[1-[4-(4-fluorophenyl)-4-oxobutyl]-1,2,3,6-tetrahydro-4-pyridyl]-1,3-dihydro-2H-benzimidazol-2-one (Figure 1), is a neuroleptic pharmaceutical. It is reported to exist in four

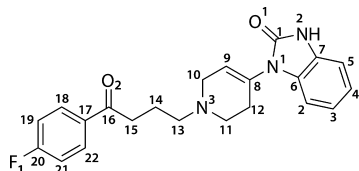


Figure 1. Molecular structure of droperidol.

polymorphic forms, I–IV,^{33–35} and 11 solvated forms: dihydrate DH,^{35,36} nonstoichiometric hydrate NSH,^{34,35,37} and solvates with ethanol,³⁸ methanol, acetonitrile, nitromethane, chloroform, dichloromethane, carbon tetrachloride, 1,4-dioxane, and toluene³³ (S_{Ev} , S_{Me} , S_{ACN} , S_{NM} , S_{CLF} , S_{DCM} , S_{CTC} , S_{DIOX} , and S_{TOL} , respectively). It is determined that the NSH, S_{Ev} , S_{Me} , S_{ACN} , S_{NM} , S_{CLF} , and S_{DCM} are nonstoichiometric isostructural solvates,^{33,37} but the crystal structures have been determined only for the first five of them (see Table S1, Supporting Information).^{33,34,38} The unit cell of these solvates consists of two droperidol molecules and one (for organic solvates) or two (for NSH) solvent molecules.^{33,34,38} The solvent molecules are situated in the structural channels oriented along the *a* axis (see Figure S1, Supporting Information) and in NSH, S_{Ev} and S_{Me} form strong hydrogen bonds with the droperidol molecule, while the solvent and droperidol molecules in S_{ACN} and S_{NM} are connected by weak hydrogen bonds and dispersion interactions.³³ It is also reported that the desolvation of all of these droperidol solvates occurs without changes of the droperidol molecule structure and produces the isostructural desolvate ISD.³³

Although nonstoichiometric in that the solvent content is dependent on the partial pressure of solvent in the atmosphere—up to 1 equiv of water per droperidol for NSH, and 0.5 equiv of solvent for the other solvates—samples produced from crystallization are always fully solvated and are relatively stable with respect to desolvation if stored in the mother liquor or in a desiccator with the relative vapor pressure of the corresponding solvent above 20%.³³

2. EXPERIMENTAL SECTION

2.1. Materials and Preparation of Solvates. Droperidol (purity > 99%) was obtained from JSC Grindeks (Riga, Latvia). The sample consisted of polymorph II, as determined by powder X-ray diffraction (PXRD) pattern.^{34,35} Organic solvents of analytical grade were purchased from commercial sources and used without further purification.

2.2. Preparation of Solvate Samples. For studying the thermal stability of solvates, samples were prepared as follows: saturated solutions of droperidol in methanol, ethanol, acetonitrile, and nitromethane were prepared at 60–90 °C depending on the boiling

point of the solvent. The solutions were then cooled down to –5 °C, giving S_{Me} , S_{Ev} , S_{ACN} , and S_{NM} , respectively. A small amount of water (5–10%) was added to droperidol solution in acetone, and the resulting solution was slowly partially evaporated at 50 °C temperature, giving NSH. Solvates were stored in the mother liquor, filtered, dried, and ground in a mortar for 30 s immediately before the analysis.

For a study of the desolvation kinetics, different sample preparation procedures were used. Four different types of NSH samples were obtained similarly as described above by adding 5–50% of water (relative to the final volume). Samples labeled as *Crystals I–IV* (the size of all of the dimensions was higher than 100 μm) were obtained by slowly evaporating the solution in a 100 mL conical flask, and samples labeled *Small crystals I–III* (with the size below 100 μm for at least one of the dimensions) were obtained by evaporating the solution in a 250 mL conical flask, while samples labeled *Powder I–II* (with the size below 40 μm for all of the dimensions) were obtained when the solution was evaporated at 25 °C temperature from a Petri dish. The fourth type of samples was obtained by grinding the *Crystals II* in a mortar. More details on the preparation of each sample are given in Table S2 (Supporting Information).

Organic solvates used for the kinetic study were prepared by obtaining saturated solutions of droperidol in the respective solvents at 60–90 °C (depending on the boiling point of the solvent) and then cooling to –10 °C either slowly (obtaining crystals with the size of at least one of the dimensions below 100 μm , labeled *Small crystals*) or rapidly (obtaining powder samples with the particle size below 40 μm for all of the dimensions, and labeled *Powder*). Alternatively, well-ground polymorph II was suspended in the corresponding solvent at 50 °C for 24 h, producing powdered solvate samples labeled *Suspension*. For the study of the desolvation kinetics of organic solvates under nonisothermal conditions, *Small crystals* were ground in a mortar for 1 min.

Prior to the analysis, samples were stored at ambient temperature in desiccators above saturated solution of K_2SO_4 (97% relative humidity) for NSH and 90% solution (mole fraction) of the corresponding solvent with glycerol (for alcohol solvates) or DMF (for acetonitrile and nitromethane solvates). The identity of all droperidol solvates was confirmed using PXRD³³ (see Figure S2, Supporting Information).

2.3. Differential Thermal Analysis/Thermogravimetry (DTA/TG). DTA/TG analysis was performed with Exstar6000 TG/DTA6300 (SII). Open aluminum pans were used. Samples of 7.0 ± 0.5 mg in mass were used. For studying the thermal stability of the solvates, heating of samples from 30 to 180 °C was performed at a $5^\circ\text{C}\cdot\text{min}^{-1}$ heating rate. The nitrogen flow rate was 100 ± 10 $\text{mL}\cdot\text{min}^{-1}$.

For studying the desolvation kinetics in nonisothermal mode, samples were heated with variable heating rates in the range from 0.1 to 3 $^\circ\text{C}\cdot\text{min}^{-1}$. The nitrogen flow rate was 300 ± 20 $\text{mL}\cdot\text{min}^{-1}$. Desolvation kinetics were studied also in the isothermal mode at 20–125 °C temperatures with an average step of 5 °C. The heater unit was preset to the required temperature before the insertion of the sample. For each sample, desolvation was performed at four to eight different temperatures selected according to the dehydration rate, which depended on the analyzed solvate and the particle size; see Tables S2 and S3 (Supporting Information). The nitrogen flow rate was 100 ± 10 $\text{mL}\cdot\text{min}^{-1}$.

2.4. Powder X-ray Diffraction (PXRD). PXRD patterns were measured on a D8 Advance (Bruker) diffractometer equipped with a LynxEye position sensitive detector, using copper radiation ($\text{Cu K}\alpha$) at the wavelength of 1.54180 Å. The tube voltage and current were set to 40 kV and 40 mA. The divergence slit was set at 0.6 mm, and the antiscattering slit was set at 8.0 mm. The diffraction patterns were recorded using a 0.2 s/0.02° scanning speed from 3° to 35° on a 2θ scale. To prevent the atmospheric humidity effect, the samples were covered during the analysis with a 10 μm polyethylene film.

2.5. Hot-Stage Microscopy (HSM). For HSM, a Laborlux 12 PolS (Leitz) polarized light microscope equipped with a heating stage and a Newtronic heating control module was used. The heating rate was $5^\circ\text{C}\cdot\text{min}^{-1}$. Images were acquired with Leica Application Suite software from a DFC450 (Leica) digital microscope camera.

2.6. Methods for Kinetic Parameter Determination. The desolvation activation energy and kinetic model were determined using a model-free approach.³⁹ The data sets of fraction desolvated (α) – time (for isothermal experiments) and α – temperature (for nonisothermal experiments) were obtained with $\Delta\alpha = 0.02$ for each temperature or heating rate. By using results from both experimental modes, E_a was calculated from the Arrhenius equation with isoconversional methods:^{40–42} Friedman (FR)⁴³ and average linear integral method (ALIM).⁴⁴ The E_a was calculated from the slope of the line in the corresponding coordinates for α values with a step size of 0.02,^{43,44} and identical E_a values were obtained. The confidence intervals for the calculated E_a values were evaluated from the slope error of the line used for calculation of E_a with the FR method. Kinetic model determination was performed with ALIM⁴⁴ and also with the reaction progress reconstruction in the coordinates $g(\alpha) - \alpha^{45,46}$ and $f(\alpha) - \alpha^{42,45,46}$. Besides, kinetic model determination for isothermal experiments was performed with reduced time plots.⁴⁷ The most often used solid-state kinetic models were included in the analysis (see Table S4, Supporting Information).^{40–42,48–50}

For isothermal experiments, the selection of the kinetic model was also evaluated by plotting the experimental data points in the coordinates α – time and fitting the theoretical lines modeled from the selected kinetic models to these experimental points. The sum of squared differences between experimental and theoretically calculated α values was minimized with MS Excel Solver. The best model was identified by the smallest sum of least-squares.

2.7. Geometry Optimization of the Crystal Structures. The starting geometries of droperidol solvates were obtained from a previously published crystal structure report.³³ Since the solvent molecules in S_{Me} and S_{Et} are disordered over two orientations related by inversion symmetry,³³ the starting geometries of S_{Me} and S_{Et} without disorder were prepared by discarding one of the solvent molecule orientations. The starting geometry for **ISD** was obtained by removing the water molecules from the **NSH** structure. Geometry optimization of these crystal structures were performed in CRYSTAL09⁵¹ and in CASTEP.⁵² Calculations in CRYSTAL09 were performed at the B3LYP-D*^{53,54} level using the 6-31G(d,p) basis set,^{55,56} and dispersion was corrected by the Grimme dispersion correction model⁵⁷ modified as described in the literature.^{54,58,59} The calculations in CASTEP were performed with the PBE⁶⁰ functional using on-the-fly generated ultrasoft pseudopotentials and a cutoff energy of 600 eV. Dispersion interactions were treated using semiempirical dispersion correction schemes G06⁵⁷ and TS.⁶¹ Crystal structure optimization was performed by employing three different procedures—by relaxing only the hydrogen atoms (HO), by relaxing all atoms (ALL), and by relaxing all atoms and the unit cell parameters (UC)—for three different calculation methods: PBE+TS (HO, ALL, and UC) and PBE+G06 (UC) in CASTEP, as well as B3LYP-D* (UC) in CRYSTAL09. Identical input geometries were used for all of the calculation methods.

The validity of the ordered model of S_{Me} and S_{Et} structures was confirmed by optimizing the geometry of S_{Me} and S_{Et} structures where adjacent alcohol molecules were oriented in opposite directions and calculating the intermolecular interaction energy of the solvent molecules (see the Supporting Information).

2.8. Calculation of the Intermolecular Interaction Energy. The interaction energies between pairs of molecules were calculated in Gaussian 09⁶² using the B3LYP and M06-2X⁶³ functionals and the 6-311G(d,p) basis set to molecular geometries directly extracted from the crystal structures after the geometry optimization. The basis set superposition error was corrected using the counterpoise method. For B3LYP calculations, the Grimme dispersion correction method was used.⁶⁴ The interaction energy was calculated as the difference between the total energy of the dimer and the corresponding isolated molecules. The total solvent interaction energy was calculated as a sum of all solvent–droperidol and solvent–solvent interaction energies.

3. RESULTS AND DISCUSSION

3.1. Desolvation Kinetics of Droperidol Solvates. First, the stability of droperidol isostructural solvates was compared by determining their desolvation kinetic parameters. The desolvation kinetics was studied in both isothermal and nonisothermal modes. Various samples were analyzed in the isothermal mode (including the crystals of **NSH**, S_{Me} , and S_{Et}), whereas, in the nonisothermal conditions, only a well-ground sample was analyzed for each solvate. The E_a values were calculated by using an isoconversional method only, to allow the identification and characterization of possible complexity of the desolvation process³⁹ and to identify the possible complications and errors associated with the experimental variables (most importantly, the sample, its mass and packing),⁴⁰ which can easily affect the results, especially for the desolvation process of nonstoichiometric solvates.

3.1.1. Desolvation Activation Energy. A total of 11 different **NSH** samples were analyzed in isothermal mode, and the calculated activation energy values had a relatively high dispersion (see Table 1). However, no direct relationship

Table 1. Summary of the NSH Desolvation Kinetic Parameters in Isothermal Mode

sample	E_a , kJ·mol ⁻¹	kinetic model ^a	temperatures used, °C
Crystals I	38 ± 20	F3/2, D5	60–100
Crystals II	55 ± 20	D5, D3	70–110
Crystals III	47 ± 13	F1	40–90
Crystals IV	49 ± 10	F3/2, D3, D5	50–100
Small crystals I	54 ± 11	F2, D5	60–120
Small crystals II	66 ± 7	F3/2, F1	25–50
Small crystals III	60 ± 20	F1	35–60
Crystals II ground for 10 s	68 ± 7	D5, F2	25–70
Crystals II ground for 1 min	65 ± 10	F3/2, F2	25–70
Powder I	54 ± 12	F2, F3/2	25–50
Powder II	56 ± 10	F3/2, F1	20–60
summary	56 ± 10	modified D5	20–120

^aFor each individual sample, only commonly used kinetic models were included in the selection (see Table S4, Supporting Information).

between the dehydration E_a (or kinetic model) and the sample particle size was observed. It was confirmed that the samples with smaller particle size dehydrated faster at a given temperature (see Figure S3, Supporting Information, and Table 1), and it was determined that unground samples showed higher variation of apparent E_a with α , while the average E_a values were in the same range as those determined for samples without E_a variation (see Table S2 and Figure S5, Supporting Information). The average dehydration E_a of **NSH** was calculated to be 56 ± 10 kJ·mol⁻¹.

The determination of the desolvation E_a was less straightforward for the organic solvates of droperidol. First, for some of the samples, complications arose due to almost identical desolvation rates at each temperature in the beginning of the reaction. This was observed for the samples with the smallest particles and could be due to the rapid escape of the solvent molecules close to the surface and with only minor temperature dependence, and for small particles, there were many such solvent molecules. Second, a higher E_a variation from sample to sample and also higher apparent variation by the fraction desolvated was observed (see Table S3 and Figure

S6, Supporting Information). This most probably was a result of lower reproducibility of the sample conditions and a stronger effect of different sample and experimental factors on the obtained results. Third, the desolvation of S_{ACN} and S_{NM} in the selected conditions could be analyzed only at temperatures very close to the melting point of these solvates.³³ This resulted in a very high desolvation rate dependence on the temperature, which produced unexpectedly high calculated E_a values. This most probably was a result of the change of the desolvation mechanism at temperatures close to the melting point; therefore, the calculated E_a values most probably did not actually represent the activation energy of the desolvation process. This assumption was supported by the relatively lower E_a values obtained for the S_{ACN} sample that was analyzed at slightly lower temperatures (see Table S3). The average desolvation E_a values for all droperidol solvates are given in Table 2.

Table 2. Kinetic Parameters for the Desolvation of Droperidol Solvates

solvate	isothermal mode		nonisothermal mode	
	E_a , $\text{kJ}\cdot\text{mol}^{-1}$	model	E_a , $\text{kJ}\cdot\text{mol}^{-1}$	model
NSH	56 ± 10			
S_{Me}	50 ± 13		65 ± 10	D5
S_{Et}	53 ± 15	modified D5	51 ± 15	D1, D4
S_{NM}	^a		57 ± 5	D5
S_{ACN}	^a		60 ± 15	D5

^aDesolvation mechanism changed at a temperature close to the melting point of the solvate.

In order to bring more clarity about the desolvation kinetics of droperidol solvates with organic molecules, these solvates were studied also in nonisothermal mode using well-ground samples and a higher nitrogen flow rate. Although these results were also complicated by the apparent variation of E_a with the fraction desolvated and by the high uncertainty of the E_a values (see Figure S10, Supporting Information), the determined average desolvation E_a value for all four solvates was similar

(50–65 $\text{kJ}\cdot\text{mol}^{-1}$) and almost the same as that of NSH in the isothermal mode (see Table 2). Therefore, it was concluded that (a) the desolvation activation energy of all the droperidol solvates is almost the same and is $57 \pm 15 \text{ kJ}\cdot\text{mol}^{-1}$, and (b) in isothermal mode, very high E_a calculated for desolvation of S_{ACN} and S_{NM} was due to the analysis at the temperatures close to the melting point and not because of actually higher desolvation E_a .

The identical desolvation E_a values did not allow us to use this parameter for the comparison of solvate stability.

3.1.2. Kinetic Model. Determination of the desolvation kinetic model of droperidol solvates was not straightforward, and none of the commonly cited^{41,48–50,65} kinetic models (see Table S4, Supporting Information) derived from the rate dependence on the nuclei formation and growth, interface advance, diffusion, and/or geometrical shape of the particles were able to convincingly and satisfactorily describe the desolvation kinetic curves recorded in isothermal mode. However, the shape of the desolvation kinetic curves was similar to those of diffusion (D5 and D3) and reaction order (F3/2, F1, and F2) models. The arrangement of the solvent molecules in the structural channels, the absence of structural changes during the desolvation,³³ and the similarity of the shape of diffusion and reaction order model kinetic curves suggested that the rate-limiting step in the desolvation process for all droperidol solvates was the diffusion of the solvent molecules out of the crystals. However, the exact diffusion mechanism appeared to be slightly different for different solvates, different samples, or even different conditions used. The deviation from the classical diffusion mechanisms could be due to the lattice parameter shrinkage during the loss of the solvent, resulting in the reduction of the channel cross-sectional area, which could change the diffusion coefficient during the desolvation process.

Besides, it was observed that the desolvation kinetic curves of S_{ACN} and S_{NM} at the highest used temperatures were significantly different from diffusion-controlled kinetic curves and could be fitted by the nucleation and nuclei growth models (see Table S3, Supporting Information). This observation

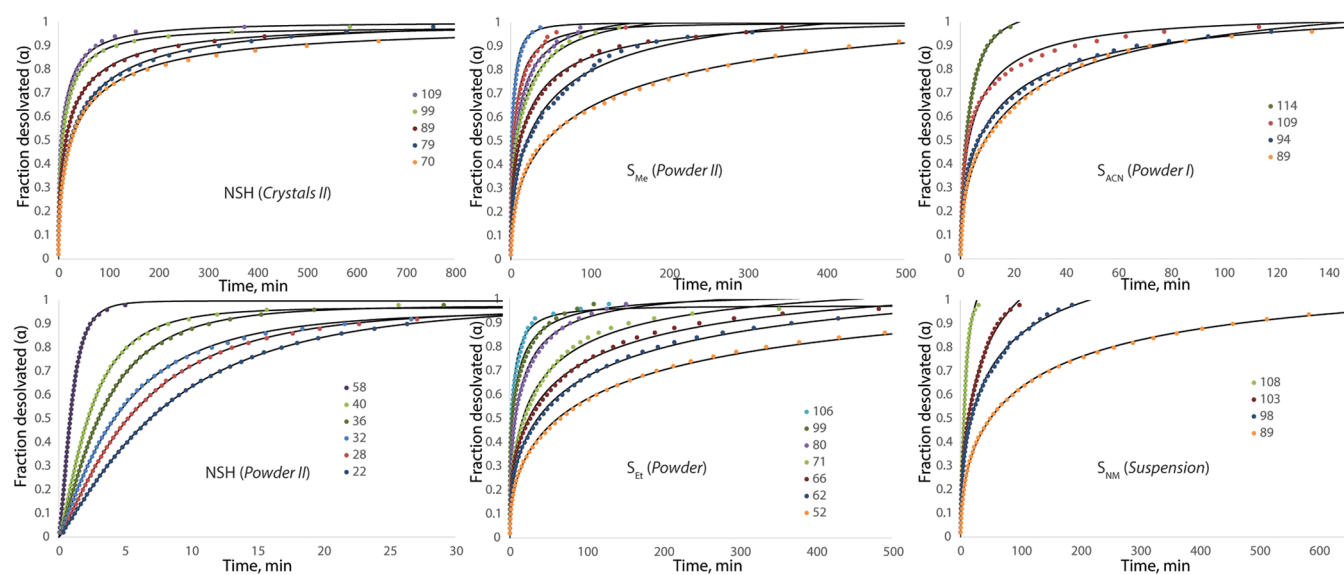


Figure 2. Desolvation kinetic curves of droperidol isostructural solvate samples at various temperatures (in $^{\circ}\text{C}$) in the isothermal mode. Theoretical curves calculated using the modified D5 model (eq 1) are shown with black lines.

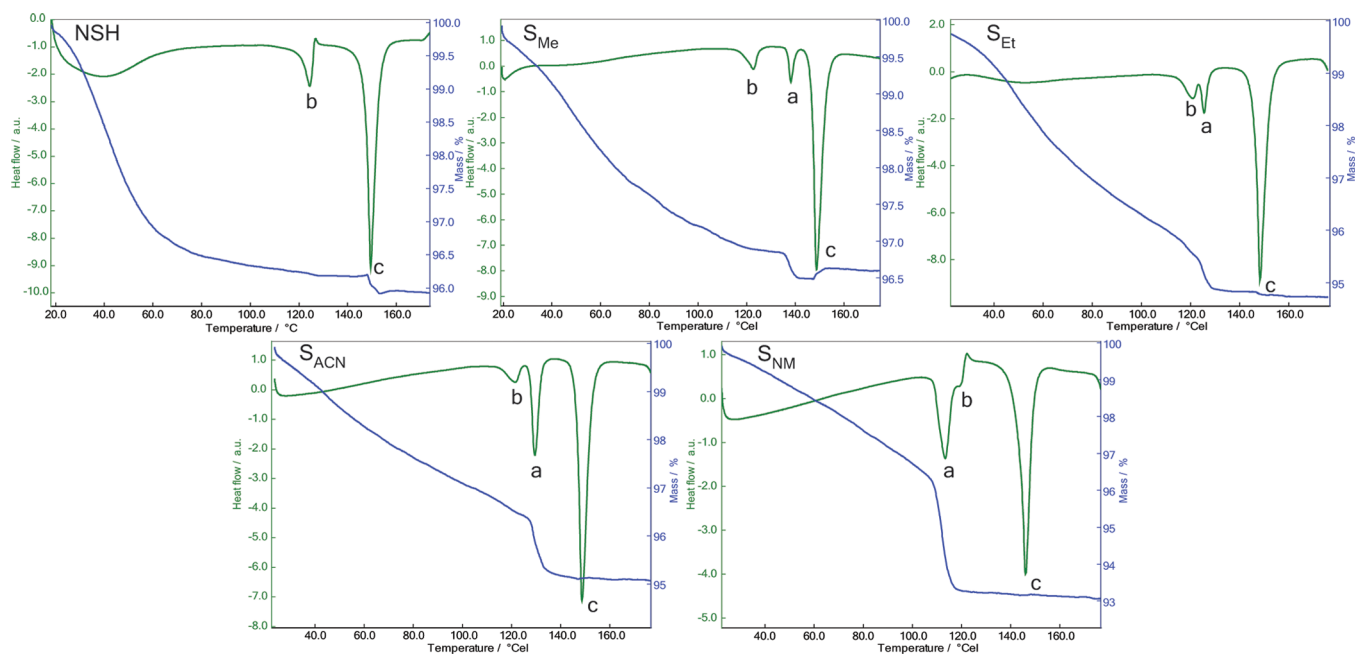


Figure 3. DTA and TG curves of the droperidol isostructural solvates showing (a) the melting of solvate, (b) the melting of ISD or its phase transition to I, and (c) the melting of the resulting polymorph I.

confirmed the already stated hypothesis that, at temperatures close to the melting point, the desolvation mechanism of these solvates differed from that at the lower temperatures. Moreover, at temperatures close to the melting temperature, partial melting of the sample and desolvation from the melt could occur, thus changing the desolvation mechanism.

Nevertheless, the most appropriate kinetic model fitting most of the kinetic curves was the Zhuravlev equation DS.^{66,67} This kinetic model has been modified^{68,69} based on the changing diffusion activation energy during the reaction, giving eq 1.

$$N \cdot [(1 - \alpha)^{-1/3} - 1]^2 = kt^n \quad (1)$$

This modification, however, could as well represent the changing diffusion coefficient during the reaction or even the effect of a hindered conversion of the largest particles appearing due to a broad particle size distribution. It was found that all of the kinetic curves describing the desolvation of droperidol solvates in isothermal mode could be fitted with this modified Zhuravlev equation (see Figure 2 and Figure S13 with the corresponding fitting parameters given in Tables S6 and S7; see the Supporting Information). Note that an additional normalization constant N was introduced in this equation in order to compensate for the possible effects from either slight absorption of the solvent at the surface or a very slow approach to complete conversion due to the presence of a few very large particles.

Although the fit of the data with eq 1 could as well be empirical, the obtained description of desolvation of all droperidol solvates cannot be a coincidence, proving that the rate-limiting step in this desolvation process is the diffusion. This conclusion is also supported by the fact that the desolvation E_a of all of the solvates was the same, which can easily be true for diffusion limited desolvation, but is less likely to be true for other rate controlling mechanisms, because of the different interaction energy between the solvent and the droperidol molecules. Furthermore, also in the nonisothermal

mode, the desolvation process was best described by diffusion models, with the most appropriate one being D5, in particular.

Moreover, the diffusion as the rate-limiting step was also confirmed by analyzing the desolvation of NSH, S_{Me} , and S_{Et} crystals by HSM (see Figures S14–S16, Supporting Information), as the desolvation before melting (up to 120 °C) did not introduce any apparent changes to the crystal, except for the appearance of defects due to the cracking of the crystals or slight distortion of the molecular layers close to the crystal surface, which was most probably associated with the reduction of the unit cell size.

3.2. Thermal Stability of Droperidol Solvates. Although the desolvation kinetic parameters were almost the same for all droperidol isostructural solvates, the solvate thermal stability was not equal. It was not possible to compare the desolvation onset temperature as the desolvation occurred over a wide temperature range and the nonstoichiometric behavior produced a very broad and indistinct desolvation endotherm (see Figure 3). Therefore, the thermal stability of the droperidol solvates was evaluated from the experimental results characterizing the desolvation rate of the solvates in both isothermal and nonisothermal modes using TG curves and PXRD patterns recorded during the desolvation. The determination of the solvate stability in nonisothermal mode was complicated by the solvate melting due to the relatively slow desolvation process, during which a complete rapid desolvation from the melt occurred (see Figure 3). In this study, it was possible to identify separate melting peaks for the solvates (a in Figure 3) and the melting or phase transition peak of ISD (b in Figure 3). Although, in our previous study, both of these processes were not distinguishable, the reported melting points were consistent with those determined in this study.³³ It was observed that S_{NM} had the lowest melting point, whereas S_{Me} had the highest melting point. Therefore, the thermal stability of the solvates was evaluated from the desolvation curves before the melting point of solvate, as the

melting point did not characterize the thermal stability of solvate with respect to the desolvation.

Although the criteria for evaluation of the thermal stability were straightforward (see the Supporting Information), the sample preparation appeared to be the crucial aspect to determine the thermal stability (as can be identified from the dehydration kinetic curves of different NSH samples at 60 °C in Figure S3, Supporting Information). Thus, the obtained results were not completely unambiguous, although identical sample preparation was used to obtain all of the data for this comparison. Nevertheless, the presented conclusions are based on separate experiments using different samples and, therefore, are reliable.

Nonisothermal (Figure 4) and isothermal (Figure S17, Supporting Information) heating of ground droperidol

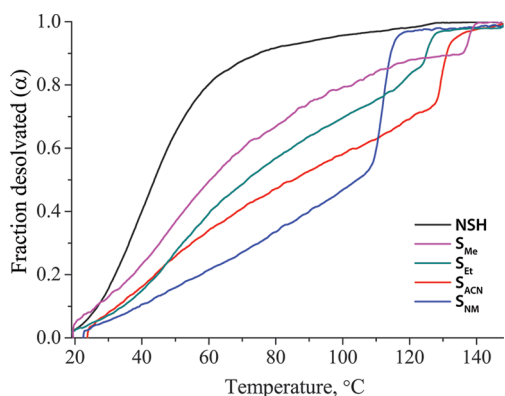


Figure 4. Desolvation kinetic curves of droperidol isostructural solvates in nonisothermal mode at the heating rate of 5°min^{-1} .

isostructural solvates showed that it is possible to rationalize their thermal stability: the least stable was NSH, whereas the most stable was S_{NM} . Although the thermal stability of S_{Me} , S_{Et} , and S_{ACN} was more similar and the established stability order slightly differed in some of the experiments, most of the experiments showed that, from these three phases, the least stable was S_{Me} and the most stable was S_{ACN} .

The same order of thermal stability was confirmed also by monitoring the PXRD patterns during the isothermal solvate desolvation and by analyzing the curves recorded during the study of the desolvation kinetics in the nonisothermal mode (see the Supporting Information). Therefore, on the basis of the data obtained from all of the performed experiments, it was possible to determine the relative thermal stability of droperidol isostructural solvates, which increased in the following order:



3.3. Quantitative Comparison of Solvate Stability Based on the Crystal Structure. In the crystal structure of droperidol solvates, the solvent molecules and droperidol molecules are connected with strong and/or weak hydrogen bonds. It is clear that the stability of the solvates cannot be associated with the presence of strong hydrogen bonds, because, in the most stable solvates S_{ACN} and S_{NM} , the acetonitrile and nitromethane molecules form only weak hydrogen bonds with the droperidol molecules. Therefore, in order to rationalize the relative stability of the droperidol solvates, solvent–droperidol, solvent–solvent, and also droperidol–droperidol intermolecular interaction energy values were calculated in Gaussian 09. Before the calculation of the

interaction energy, geometry optimization of the crystal structures was performed. To obtain comparable results, crystal structures of all five solvates determined at 173 K were used for the calculations. As it is not possible to take into account the degree of disorder, the alcohol molecules in the crystal structures of S_{Me} and S_{Et} were oriented in one of their two possible positions for crystal structure optimization and calculation of the interaction energy.

3.3.1. Characterization of the Droperidol–Droperidol Intermolecular Interaction Energy. Droperidol–droperidol interaction energy in all solvates was evaluated based on droperidol molecule interactions with 10 closest droperidol molecules designated by the letters A–G (see Figure 5;

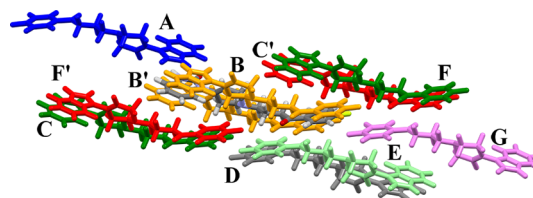


Figure 5. Arrangement of the central droperidol molecule and 10 closest droperidol molecules surrounding it, which was used for the evaluation of pairwise droperidol–droperidol interaction energy values in the droperidol isostructural solvates.

symmetrically equivalent interactions were designated with the same letter). The calculated interaction energy for these droperidol molecule pairs, as well as the total droperidol–droperidol interaction energy from these 10 interactions, is given in the Supporting Information. From these calculations, it was concluded that the intermolecular interactions between droperidol molecules as well as their energy were almost the same in all of these solvates and did not depend on the crystal structure optimization method. Therefore, different solvent molecules in the channels did not introduce significant changes in the droperidol–droperidol molecule arrangement, although some minor differences of the interaction energy values occurred (see the Supporting Information).

3.3.2. Characterization of the Intermolecular Interaction Energy of Solvent Molecules. The presence of various functional groups in the solvent molecules and different arrangements of these molecules in the crystal structure prevented a direct comparison of the intermolecular interaction energy for solvent–droperidol molecule pairs in different solvates. Nevertheless, the interaction energy was calculated between the solvent molecule and up to 8 droperidol molecules, as well as the closest solvent molecules. These interactions with droperidol molecules were designated by Greek alphabet letters α to θ , and solvent–solvent interactions were designated by ι and κ (see Figure 6), and the calculated values are given in the Supporting Information.

Most of the molecule pairs were characterized by negative interaction energy and, therefore, corresponded to energetically favorable interactions, whereas few pairs were characterized by slightly positive interaction energy and corresponded to energetically unfavorable interactions, which was shown to be a common phenomenon and was explained by the existence of a crystal structure in a state where the energy minimum was reached for the whole multimolecular system, and not individual molecule pairs.⁷⁰

It was observed that the calculated interaction energy for all of the molecule pairs at the B3LYP-D level was more negative

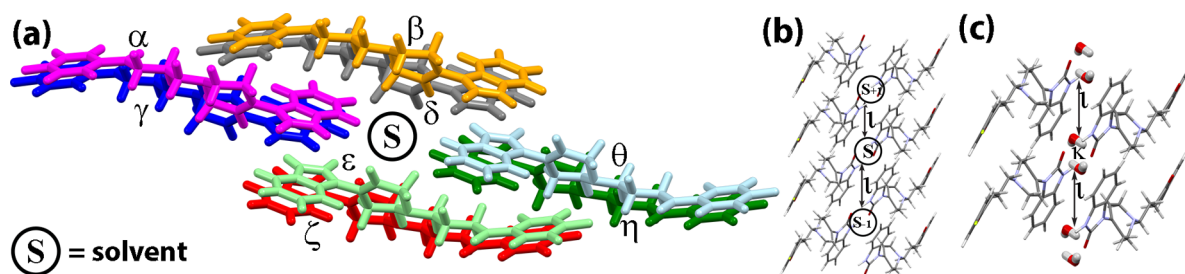


Figure 6. Arrangement of (a) solvent–droperidol molecule pairs and solvent–solvent molecule pairs in (b) organic solvates and (c) NSH, corresponding to all energetically relevant solvent interactions in the droperidol isostructural solvates.

than that calculated at the M06-2X level. This difference for interactions between droperidol and solvent molecules was less than $6.5 \text{ kJ}\cdot\text{mol}^{-1}$ with no direct correlation with the magnitude of the interaction energy (although it was noticed that B3LYP-D typically overestimated the magnitude of the interaction energy for pairs in which it was small). Therefore, the total solvent interaction energy (a sum of all solvent–droperidol and solvent–solvent interaction energies) calculated at the M06-2X level was also less negative (see Table 3). The results obtained

Table 3. Total Solvent Interaction Energy (in $\text{kJ}\cdot\text{mol}^{-1}$) Values Calculated in Gaussian 09 after Different Structure Optimization Methods for Isostructural Solvates of Droperidol^a

		S_{NM}	S_{ACN}	S_{Et}	S_{Me}	NSH
B3LYP-D	1	-104.4	-92.9	-96.5	-81.3	-71.1
	2	-101.6	-94.1	-95.6	-82.3	-75.7
	3	-103.3	-95.1	-95.7	-81.4	-77.3
	4	-97.4	-90.3	-91.1	-82.8	-72.0
	5	-98.9	-92.6	-96.2	-76.4	-69.4
M06-2X	1	-82.8	-72.0	-69.3	-64.6	-59.7
	2	-80.4	-74.3	-68.0	-64.6	-65.1
	3	-82.9	-76.1	-68.8	-65.6	-66.6
	4	-76.6	-71.0	-67.6	-67.6	-57.0
	5	-75.4	-70.7	-69.2	-50.5	-62.6

^a1: PBE+TS HO in CASTEP; 2: PBE+TS ALL in CASTEP; 3: PBE+TS UC in CASTEP; 4: PBE+G06 UC in CASTEP; and 5: B3LYP-D* UC in CRYSTAL09.

by using M06-2X are considered to be more accurate, as it has been shown that this empirical exchange–correlation functional performs better for the description of the noncovalent interactions, compared to the more commonly used dispersion corrected B3LYP-D functional.^{71,72} Moreover, the better accuracy of the interaction energies calculated at the M06-2X level also was supported by a better agreement to the interaction energy values calculated with PIXEL code (see the Supporting Information). Unfortunately, it was not possible to use the PIXEL code for the calculation of the intermolecular interaction energy in droperidol organic solvates due to the presence of three symmetry independent molecules in the unit cell.

The differences in crystal structure geometry obtained after different optimization methods (see the Supporting Information) were also reflected in the calculated interaction energy values. Therefore, there were only slight differences of interaction energy values for the individual molecule pairs (typically below $2.0 \text{ kJ}\cdot\text{mol}^{-1}$; see the Supporting Information) and for total solvent interaction energy (below $6.4 \text{ kJ}\cdot\text{mol}^{-1}$) in

S_{ACN} , S_{NM} , and S_{Et} structures after all structure optimization methods (see Table 3). The same applied also to the differently optimized structures of S_{Me} , except for that optimized at the B3LYP-D* level. The different water molecule arrangements in NSH after different geometry optimization methods also showed up as differences in the water interaction energy values. Further discussion is given in the Supporting Information.

From all three optimization procedures at the PBE+TS level in CASTEP, the calculated average total solvent interaction energy per 1 mol of solvent for all droperidol solvates is presented in Figure 7. From these results, it follows that the

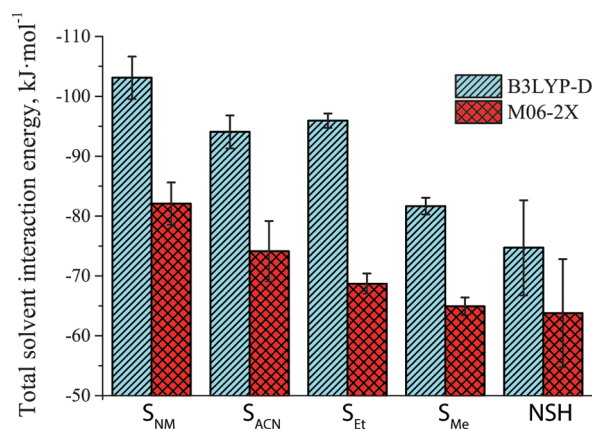


Figure 7. Average total solvent interaction energy calculated in Gaussian 09 after geometry optimization at the PBE+TS level in CASTEP for all isostructural solvates of droperidol.

total solvent interaction energy becomes more negative in the following order

$$\text{NSH} > S_{\text{Me}} > (S_{\text{Et}}, S_{\text{ACN}}) > S_{\text{NM}}$$

where the sequence between the S_{Et} and S_{ACN} depended on the interaction energy calculation level (at the B3LYP-D level, the calculated total solvent intermolecular interaction energy was higher in S_{Et} , whereas, at the M06-2X level, the calculated energy was higher in S_{ACN}), but not on the crystal structure optimization method (although full relaxation of the crystal structure reduced at the B3LYP-D level calculated energy difference between S_{Et} and S_{ACN}). Therefore, the S_{NM} was predicted to be the most stable solvate with respect to the loss of the solvent molecule, as this process would require disruption of energetically favored interactions, while the NSH was predicted to be the least stable one.

It was also noticed that, in S_{NM} and S_{ACN} , an important contribution to the total solvent interaction energy was

provided by the solvent–solvent interactions, whereas they had only a minor contribution for the alcohol solvates (see Table 4). This is logical, as the acetonitrile and nitromethane

Table 4. Average Solvent–Solvent Interaction Energy (in $\text{kJ}\cdot\text{mol}^{-1}$) and Its Contribution to the Total Solvent Interaction Energy Calculated in Gaussian 09 at the M06-2X Level after the Structure Optimization at the PBE+TS Level in CASTEP for Isostructural Solvates of Droperidol

		S_{NM}	S_{ACN}	S_{Et}	S_{Me}	NSH
B3LYP-D	E (solv–solv)	−8.5	−11.1	−1.8	−1.3	−15.4
	contribution, %	16.9	23.9	3.9	3.3	20.6
M06-2X	E (solv–solv)	−8.5	−10.7	−1.5	−1.2	−15.4
	contribution, %	21.4	29.5	4.3	4.0	24.2

molecules have the greatest length and do not have a specific orientation of the polar end (in alcohol molecules, this end is hydrogen-bonded to the benzimidazolone moiety of droperidol). Besides, the contribution from the interactions with other solvent molecules in the total interaction energy increased when the interaction energy calculation level was changed from B3LYP-D to M06-2X, which appeared to be one of the main factors affecting the change of the order of the total solvent interaction energy for S_{ACN} and S_{Et} .

Logically, due to the presence of a strong hydrogen bond between two water molecules, water–water interaction energy had a relatively high contribution to the total interactions involving water molecules.

3.3.3. Summary and Comparison to the Experimental Results. The calculated total solvent interaction energy at the M06-2X level became more negative in the following order:

$$\text{NSH} > S_{\text{Me}} > S_{\text{Et}} > S_{\text{ACN}} > S_{\text{NM}}$$

Thus, the theoretically predicted order of the stability of solvates based on the total solvent interaction energy at the M06-2X level is opposite, compared to this sequence. This order is identical to that observed for the thermal stability of these solvates, which should not come as a surprise, as, during the desolvation, only solvent–droperidol and solvent–solvent interactions are disrupted, while the rest of the crystal structure is maintained. Therefore, the calculation of the total solvent interaction energy at the M06-2X level in this system can be used to rationalize and predict the thermal stability of solvates.

Although the total solvent interaction energy in NSH was very similar to that of S_{Me} , the thermal stability of these two solvates was quite different. This most probably could be associated with the small size of water molecules allowing an easier dehydration and the fact that the dehydration occurs by simultaneously losing the hydrogen-bonded molecule pair;³³ therefore, the water–water interaction between the hydrogen-bonded water molecules actually did not stabilize the NSH against the dehydration.

Interestingly, it was noted that the order of the solvate melting points correlated with the calculated total droperidol–droperidol interaction energy values (see Table S18, Supporting Information). Although such a small interaction energy value difference ($8\text{--}9 \text{ kJ}\cdot\text{mol}^{-1}$) is unlikely to introduce significant melting point differences ($>20 \text{ }^\circ\text{C}$), it would be reasonable that the solvate melting point would be associated with the droperidol–droperidol interactions and, therefore, the stability of the crystal lattice.

Although the thermal stability of the organic solvates increased in the same order as the boiling points of the respective solvents, this should be considered only a coincidence as the interactions of solvent molecules in the solvates are completely different than those in their liquid states.

Although the experimental stability of the solvates can also be compared using the sorption–desorption isotherms, which would provide an information about the thermodynamic stability, the solvent content in the initial part of the isotherm representing the solvent sorption at a given solvent vapor activity increased in the order $\text{NSH} < S_{\text{NM}} < S_{\text{ACN}} < S_{\text{Et}} < S_{\text{Me}}$ ³³ (see Figure S22, Supporting Information). Therefore, it appeared that the solvent content was determined by the steric factors of solvent molecules, and not by the intermolecular interactions. The only exception was the NSH, which had the lowest solvent content at any given activity, although the significant difference, if compared to other solvents, cannot be explained exclusively by the lower total energy of intermolecular interactions involving water molecules.

4. CONCLUSIONS

The study of the desolvation kinetics of droperidol isostructural solvates revealed that the desolvation activation energy of all of these solvates was almost the same ($57 \pm 15 \text{ kJ}\cdot\text{mol}^{-1}$) and the desolvation process was diffusion limited, and the desolvation curves could be fitted using the modified Zhuravlev equation.

The thermal stability of the solvates determined from the desolvation rate in both isothermal and nonisothermal modes could be successfully used as a solvate stability comparison and ranging tool for the droperidol solvates. The calculation of the intermolecular interaction energies in droperidol solvates showed that it was possible to rationalize and predict the thermal stability order of solvates by using a sum of the solvate–droperidol and solvate–solvate interaction energies.

Although this solvate system can be used to understand the general trends in the characterization and rationalization of the solvate stability, we conclude that (a) crystal structure does not substantially change during the desolvation, and (b) droperidol–droperidol interaction energy in all solvates is almost the same, which makes this system a relatively simple model. Complications associated with (a) different host–host interaction energy and (b) the energy necessary for the crystal structure change during the desolvation will arise when a general stoichiometric solvate system is considered. Therefore, additional studies are necessary to obtain a more general understanding of the solvate stability.

■ ASSOCIATED CONTENT

📄 Supporting Information

More detailed results from the desolvation kinetic study, comparison of the solvate thermal stability, comparison of the crystal structures after different geometry optimization procedures, and calculations of the intermolecular interaction energy, as well as the solvent sorption–desorption isotherms are given in the Supporting Information. This material is available free of charge via the Internet at <http://pubs.acs.org>.

■ AUTHOR INFORMATION

Corresponding Author

*E-mail: agris.berzins@lu.lv. Phone: +(371)-67372576.

Notes

The authors declare no competing financial interest.

ACKNOWLEDGMENTS

This work was supported by the European Social Fund within the project “Support for Doctoral Studies at the University of Latvia”. We wish to thank the Riga Technical University Institute of Polymer Materials for the provided opportunity to carry out hot-stage microscopy measurements and the University of Latvia Institute of Solid State Physics for the possibility to carry out calculations with CRYSTAL09 software on the Latvian SuperCluster computers.

REFERENCES

- (1) Price, C. P.; Glick, G. D.; Matzger, A. J. *Angew. Chem., Int. Ed.* **2006**, *45* (13), 2062–2066.
- (2) Bingham, A. L.; Hughes, D. S.; Hursthouse, M. B.; Lancaster, R. W.; Tavener, S.; Threlfall, T. L. *Chem. Commun.* **2001**, 603–604.
- (3) Yu, L.; Stephenson, G. A.; Mitchell, C. A.; Bunnell, C. A.; Snorek, S. V.; Bowyer, J. J.; Borchardt, T. B.; Stowell, J. G.; Byrn, S. R. *J. Am. Chem. Soc.* **2000**, *122* (4), 585–591.
- (4) Sun, C.; Grant, D. J. W. *Pharm. Res.* **2001**, *18*, 274–280.
- (5) Khomane, K. S.; More, P. K.; Bansal, A. K. *J. Pharm. Sci.* **2012**, *101* (7), 2408–2416.
- (6) Picker-Freyer, K. M.; Liao, X.; Zhang, G.; Wiedmann, T. S. *J. Pharm. Sci.* **2007**, *96* (8), 2111–2124.
- (7) Pudipeddi, M.; Serajuddin, A. T. M. *J. Pharm. Sci.* **2005**, *94* (5), 929–939.
- (8) Zencirci, N.; Griesser, U. J.; Gelbrich, T.; Apperley, D. C.; Harris, R. K. *Mol. Pharmacol.* **2013**, *11* (1), 338–350.
- (9) Zeidan, T. A.; Trotta, J. T.; Chiarella, R. A.; Oliveira, M. A.; Hickey, M. B.; Almarsson, Ö.; Remenar, J. F. *Cryst. Growth Des.* **2013**, *13* (5), 2036–2046.
- (10) Perlovich, G. L.; Ryzhakov, A. M.; Tkachev, V. V.; Hansen, L. K.; Raevsky, O. A. *Cryst. Growth Des.* **2013**, *13* (9), 4002–4016.
- (11) Simões, R. G.; Bernardes, C. E. S.; da Piedade, M. E. M. *Cryst. Growth Des.* **2013**, *13* (7), 2803–2814.
- (12) Surov, A. O.; Bui, C. T.; Proshin, A. N.; Roussel, P.; Idrissi, A.; Perlovich, G. L. *J. Phys. Chem. B* **2013**, *117* (36), 10414–10429.
- (13) Ismail, S. Z.; Anderton, C. L.; Copley, R. C. B.; Price, S. L. *Cryst. Growth Des.* **2013**, *13* (6), 2396–2406.
- (14) Price, S. L. *Chem. Soc. Rev.* **2014**, 2098–2111.
- (15) Kendrick, J.; Stephenson, G. A.; Neumann, M. A.; Leusen, F. J. *Cryst. Growth Des.* **2013**, *13* (2), 581–589.
- (16) Braun, D. E.; McMahon, J. A.; Koztecki, L. H.; Price, S. L.; Reutzel-Edens, S. M. *Cryst. Growth Des.* **2014**, *14* (4), 2056–2072.
- (17) Braun, D. E.; Tocher, D. A.; Price, S. L.; Griesser, U. J. *J. Phys. Chem. B* **2012**, *116* (13), 3961–3972.
- (18) Hoser, A. A.; Kaminski, D. M.; Matwijczuk, A.; Niewiadomy, A.; Gagos, M.; Wozniak, K. *CrystEngComm* **2013**, *15* (10), 1978–1988.
- (19) Braun, D. E.; Bhardwaj, R. M.; Florence, A. J.; Tocher, D. A.; Price, S. L. *Cryst. Growth Des.* **2012**, *13* (1), 19–23.
- (20) Nassimbeni, L. R. *Acc. Chem. Res.* **2003**, *36* (8), 631–637.
- (21) Zencirci, N.; Griesser, U. J.; Gelbrich, T.; Kahlenberg, V.; Jetty, R. K. R.; Apperley, D. C.; Harris, R. K. *J. Phys. Chem. B* **2014**, *118* (12), 3267–3280.
- (22) Aitipamula, S.; Chow, P. S.; Tan, R. B. H. *J. Mol. Struct.* **2011**, *1005* (1–3), 134–140.
- (23) Braun, D. E.; Gelbrich, T.; Jetty, R. K. R.; Kahlenberg, V.; Price, S. L.; Griesser, U. J. *Cryst. Growth Des.* **2008**, *8* (6), 1977–1989.
- (24) Byard, S.; Abraham, A.; Boulton, P. J. T.; Harris, R. K.; Hodgkinson, P. J. *Pharm. Sci.* **2012**, *101* (1), 176–186.
- (25) Aitipamula, S.; Chow, P. S.; Tan, R. B. H. *CrystEngComm* **2011**, *13* (3), 1037–1045.
- (26) Aitipamula, S.; Chow, P. S.; Tan, R. B. H. *Cryst. Growth Des.* **2010**, *10* (5), 2229–2238.
- (27) Bettinetti, G. P.; Caira, M. R.; Sorrenti, M.; Catenacci, L.; Ghirardi, M.; Fábrián, L. *J. Therm. Anal. Calorim.* **2004**, *77* (2), 695–708.
- (28) Caira, M. R.; Bettinetti, G.; Sorrenti, M. *J. Pharm. Sci.* **2002**, *91* (2), 467–481.
- (29) Banerjee, R.; Bhatt, P. M.; Desiraju, G. R. *Cryst. Growth Des.* **2006**, *6* (6), 1468–1478.
- (30) Braun, D. E.; Gelbrich, T.; Kahlenberg, V.; Tessadri, R.; Wieser, J.; Griesser, U. J. *Cryst. Growth Des.* **2009**, *9* (2), 1054–1065.
- (31) Zhang, Q.; Lu, L.; Dai, W.; Mei, X. *CrystEngComm* **2014**, *16*, 1919–1926.
- (32) Joshi, V.; Morris, K. R.; Byrn, S. R.; Carvajal, M. T. *Cryst. Growth Des.* **2009**, *9* (8), 3359–3366.
- (33) Bērziņš, A.; Skarbulis, E.; Rekis, T.; Actiņš, A. *Cryst. Growth Des.* **2014**, *14* (5), 2654–2664.
- (34) Actins, A.; Arajs, R.; Belakovs, S.; Orola, L.; Veidis, M. *J. Chem. Crystallogr.* **2008**, *38* (3), 169–174.
- (35) Azibi, M.; Dragnet-Brughmas, M.; Bouche, R. *Pharm. Acta Helv.* **1982**, *57* (7), 182–188.
- (36) Blaton, N. M.; Peeters, O. M.; De Ranter, C. J. *Acta Crystallogr., Sect. B* **1980**, *36* (11), 2828–2830.
- (37) Orola, L. Synthesis, structure and properties of crystalline forms of some active pharmaceutical ingredients. Ph.D. Thesis, Riga Technical University, Riga, Latvia, 2010.
- (38) Klein, C. L.; Welch, J.; Southall, L. C. *Acta Crystallogr., Sect. C* **1989**, *45* (4), 650–653.
- (39) Vyazovkin, S.; Burnham, A. K.; Criado, J. M.; Pérez-Maqueda, L. A.; Popescu, C.; Sbirrazzuoli, N. *Thermochim. Acta* **2011**, *520* (1–2), 1–19.
- (40) Khawam, A.; Flanagan, D. R. *J. Pharm. Sci.* **2006**, *95* (3), 472–498.
- (41) Koradia, V.; de Diego, H. L.; Elema, M. R.; Rantanen, J. *J. Pharm. Sci.* **2010**, *99* (9), 3966–3976.
- (42) Sheth, A. R.; Zhou, D.; Muller, F. X.; Grant, D. J. W. *J. Pharm. Sci.* **2004**, *93* (12), 3013–3026.
- (43) Friedman, H. L. *J. Polym. Sci., Part C* **1964**, *6*, 183–195.
- (44) Ortega, A. *Thermochim. Acta* **2008**, *474* (1–2), 81–86.
- (45) Zhou, D.; Schmitt, E. A.; Zhang, G. G. Z.; Law, D.; Wight, C. A.; Vyazovkin, S.; Grant, D. J. W. *J. Pharm. Sci.* **2003**, *92* (7), 1367–1376.
- (46) Vyazovkin, S.; Wight, C. A. *Annu. Rev. Phys. Chem.* **1997**, *48* (1), 125–149.
- (47) Bamford, C. H.; Tipper, C. F. H. *Reactions in the Solid State*; Elsevier: Amsterdam, 1980; p 340.
- (48) Khawam, A.; Flanagan, D. R. *J. Phys. Chem. B* **2006**, *110* (35), 17315–17328.
- (49) Dickinson, C. F.; Heal, G. R. *Thermochim. Acta* **1999**, *340*–341, 89–103.
- (50) Galwey, A. K.; Brown, M. E. *Thermal Decomposition of Ionic Solids*; Elsevier: Amsterdam, 1999; p 598.
- (51) Dovesi, R.; Saunders, V.; Roetti, C.; Orlando, R.; Zicovich-Wilson, C.; Pascale, F.; Civalleri, B.; Doll, K.; Harrison, N.; Bush, I. CRYSTAL09; University of Torino: Torino, Italy, 2009.
- (52) Clark, S. J.; Segall, M. D.; Pickard, C. J.; Hasnip, P. J.; Probert, M. I.; Refson, K.; Payne, M. C. *Z. Kristallogr.* **2005**, *220*, 567–570.
- (53) Coelho, A. J. *Appl. Crystallogr.* **2003**, *36* (1), 86–95.
- (54) Civalleri, B.; Zicovich-Wilson, C. M.; Valenzano, L.; Ugliengo, P. *CrystEngComm* **2008**, *10* (4), 405–410.
- (55) Gatti, C.; Saunders, V. R.; Roetti, C. *J. Chem. Phys.* **1994**, *101* (12), 10686–10696.
- (56) Spackman, M. A.; Mitchell, A. S. *Phys. Chem. Chem. Phys.* **2001**, *3* (8), 1518–1523.
- (57) Grimme, S. *J. Comput. Chem.* **2006**, *27* (15), 1787–1799.
- (58) Maschio, L.; Civalleri, B.; Ugliengo, P.; Gavezzotti, A. *J. Phys. Chem. A* **2011**, *115* (41), 11179–11186.
- (59) Zicovich-Wilson, C. M.; Kirtman, B.; Civalleri, B.; Ramirez-Solis, A. *Phys. Chem. Chem. Phys.* **2010**, *12* (13), 3289–3293.
- (60) Perdew, J. P.; Burke, K.; Ernzerhof, M. *Phys. Rev. Lett.* **1996**, *77* (18), 3865–3868.

- (61) Tkatchenko, A.; Scheffler, M. *Phys. Rev. Lett.* **2009**, *102* (7), 073005.
- (62) Frisch, M. J.; Trucks, G. W.; Schlegel, H. B.; Scuseria, G. E.; Robb, M. A.; Cheeseman, J. R.; Scalmani, G.; Barone, V.; Mennucci, B.; Petersson, G. A.; Nakatsuji, H.; Caricato, M.; Li, X.; Hratchian, H. P.; Izmaylov, A. F.; Bloino, J.; Zheng, G.; Sonnenberg, J. L.; Hada, M.; Ehara, M.; Toyota, K.; Fukuda, R.; Hasegawa, J.; Ishida, M.; Nakajima, T.; Honda, Y.; Kitao, O.; Nakai, H.; Vreven, T.; Montgomery, J. A., Jr.; Peralta, J. E.; Ogliaro, F.; Bearpark, M.; Heyd, J. J.; Brothers, E.; Kudin, K. N.; Staroverov, V. N.; Kobayashi, R.; Normand, J.; Raghavachari, K.; Rendell, A.; Burant, J. C.; Iyengar, S. S.; Tomasi, J.; Cossi, M.; Rega, N.; Millam, J. M.; Klene, M.; Knox, J. E.; Cross, J. B.; Bakken, V.; Adamo, C.; Jaramillo, J.; Gomperts, R.; Stratmann, R. E.; Yazyev, O.; Austin, A. J.; Cammi, R.; Pomelli, C.; Ochterski, J. W.; Martin, R. L.; Morokuma, K.; Zakrzewski, V. G.; Voth, G. A.; Salvador, P.; Dannenberg, J. J.; Dapprich, S.; Daniels, A. D.; Farkas, O.; Foresman, J. B.; Ortiz, J. V.; Cioslowski, J.; Fox, D. J. *Gaussian 09*; Gaussian Inc.: Wallingford, CT, 2009.
- (63) Zhao, Y.; Truhlar, D. *Theor. Chem. Acc.* **2008**, *120* (1–3), 215–241.
- (64) Grimme, S.; Antony, J.; Ehrlich, S.; Krieg, H. *J. Chem. Phys.* **2010**, *132* (15), 154104.
- (65) Zellelow, A. Z.; Kim, K.-H.; Sours, R. E.; Swift, J. A. *Cryst. Growth Des.* **2010**, *10* (1), 418–425.
- (66) Zhuravlev, V. F.; Lesokhin, I. G.; Templeman, R. G. *J. Appl. Chem. (USSR)* **1948**, *21*, 887–902.
- (67) Šesták, J.; Šatava, V.; Wendlandt, W. W. *Thermochim. Acta* **1973**, *7* (5), 333–556.
- (68) Malecki, A.; Komornicki, S.; Prochowska-Klisch, B. *Bull. Pol. Acad. Sci., Chemistry* **1981**, *29*, 455.
- (69) Malecki, A.; Prochowska-Klisch, B.; Gajerski, R. *J. Therm. Anal. Calorim.* **1998**, *54* (1), 25–34.
- (70) Gavezzotti, A. *Acta Crystallogr., Sect. B* **2010**, *66* (3), 396–406.
- (71) Maranzana, A.; Giordana, A.; Indarto, A.; Tonachini, G.; Barone, V.; Causà, M.; Pavone, M. *J. Chem. Phys.* **2013**, *139* (24), 244306.
- (72) Zhao, Y.; Truhlar, D. G. *Acc. Chem. Res.* **2008**, *41* (2), 157–167.



ELSEVIER

Contents lists available at ScienceDirect

Solid State Nuclear Magnetic Resonance

journal homepage: www.elsevier.com/locate/ssnmr

Solid-state NMR and computational investigation of solvent molecule arrangement and dynamics in isostructural solvates of droperidol

Agris Bērziņš^{a,b,*}, Paul Hodgkinson^b^a Faculty of Chemistry, University of Latvia, Kr. Valdemara iela 48, Rīga LV-1013, Latvia^b Department of Chemistry, Durham University, South Road, Durham DH1 3LE, UK

ARTICLE INFO

Article history:

Received 7 June 2014

Received in revised form

2 September 2014

Accepted 7 September 2014

Available online 17 September 2014

Keywords:

Droperidol

Solid-state NMR

Hydrates/solvates

Isostructural solvates

Solvent dynamics

Spin–lattice relaxation

Motional broadening

Ab initio calculations

ABSTRACT

¹³C, ¹⁵N and ²H solid-state NMR spectroscopy have been used to rationalize arrangement and dynamics of solvent molecules in a set of isostructural solvates of droperidol. The solvent molecules are determined to be dynamically disordered in the methanol and ethanol solvates, while they are ordered in the acetonitrile and nitromethane solvates. ²H NMR spectra of deuterium-labelled samples allowed the characterization of the solvent molecule dynamics in the alcohol solvates and the non-stoichiometric hydrate. The likely motion of the alcohol molecules is rapid libration within a site, plus occasional exchange into an equivalent site related by the inversion symmetry, while the water molecules are more strongly disordered. DFT calculations strongly suggest that the differences in dynamics between the solvates are related to differences in the energetic penalty for reversing the orientation of a solvent molecule.

© 2014 Elsevier Inc. All rights reserved.

1. Introduction

Solid-form screening of pharmaceutical molecules has demonstrated their propensity to adopt different forms, including polymorphs and solvates [1,2]. It is not unusual for a pharmaceutical molecule to form more than five polymorphs [3–5] and, as reported, even in excess of one hundred solvates [2]. Understanding and characterizing these forms is essential for the pharmaceutical industry.

Solvates are typically divided in stoichiometric or non-stoichiometric solvates [6]. It is common that the same host structure can incorporate different solvent molecules to form a set of isostructural solvates. This phenomenon is typical for non-stoichiometric channel solvates [7,8], but is not limited to non-stoichiometric solvates [9–11] nor to channel solvates [12]. The formation of isostructural solvates is typically driven by the presence of specific solvent–host interactions [9,12] or by the specific shape of the solvent molecule [7]. It is also possible to form mixed isostructural solvates, where solvent molecules can be exchanged in only a subset of the crystallographic sites [13,14].

Although empty host structures can be stable [15], they are typically unstable [16] or collapse immediately after the removal of the guest, despite the weak nature of the host–guest interactions [17].

Droperidol, 1-[1-[4-(4-fluorophenyl)-4-oxobutyl]-1,2,3,6-tetrahydro-4-pyridyl]-1,3-dihydro-2H-benzimidazol-2-one, Fig. 1, is a neuroleptic pharmaceutical. It is reported to exist in four polymorphic forms I–IV [18–20] and eleven solvated forms [18–23]. The solvates with methanol, ethanol, acetonitrile, nitromethane, chloroform, dichloromethane as well as the nonstoichiometric hydrate (**S_{Me}**, **S_{Et}**, **S_{ACN}**, **S_{NM}**, **S_{CLF}**, **S_{DCM}** and **NSH** respectively) are isostructural, as observed by PXRD, and crystallize in the *P*1 or *P*1̄ space group (depending on the solvent symmetry and ordering), with two droperidol molecules in the unit cell. It has not, however, been possible to obtain diffraction quality crystals for **S_{CLF}** and **S_{DCM}** [20]. Although non-stoichiometric in that the solvent content is dependent on the partial pressure of solvent in the atmosphere – up to one equivalent of water per droperidol for **NSH**, and 0.5 equivalents of solvent for the other solvates – samples produced from crystallization are always fully solvated and are relatively stable with respect to desolvation if stored in closed containers.

Although isostructural in terms of the host droperidol structure, these solvates are unusual in that they fall into three categories. Firstly, the **NSH** crystal structure is centrosymmetric

* Corresponding author. Tel.: +371 67372576.

E-mail addresses: agris.berzins@lu.lv (A. Bērziņš), paul.hodgkinson@durham.ac.uk (P. Hodgkinson).

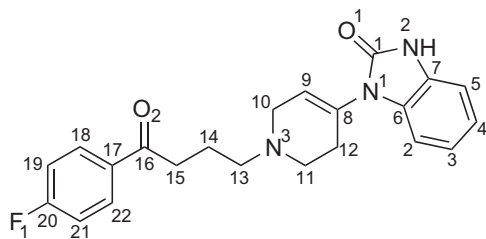


Fig. 1. Molecular structure of droperidol with the numbering of non-hydrogen atoms.

with one droperidol and one water molecule in the asymmetric unit. The water molecules occupy two nearby hydrogen-bonded positions in the channel, forming hydrogen bonds with the carboxyl group in the benzimidazolone moiety of droperidol. The isotropic displacement parameter for the water oxygen at 120 K is three times higher than for other non-hydrogen atoms, and it was not possible to locate all the water hydrogen atoms for structures determined at 173 K or above [20], suggesting that the water molecules are slightly disordered. Secondly, the S_{Me} and S_{Et} structures refine with centrosymmetry, with one droperidol and half a disordered alcohol molecule in the asymmetric unit. The alcohol molecule has the same hydrogen bond arrangement with droperidol as the water does in **NSH**. In contrast to the **NSH**, however, only one of the two droperidols in the unit cell is hydrogen bonded to the alcohol molecule, and taking into account disorder between two orientations related by inversion symmetry is necessary for a satisfactory refinement within the $P\bar{1}$ space group. Thirdly, the S_{ACN} and S_{NM} are non-centrosymmetric, with two droperidol and one ordered solvent molecules in the asymmetric unit, and there are no strong hydrogen bonds between the solvent and droperidol.

Solid-state NMR is now widely used in the field of pharmaceutical molecule characterization [24]. The main advantage of this method is its ability to characterize the molecular-level structure and identify possible dynamics using powdered rather than single-crystal samples [25–31]. It can be used to support or complement the information from X-ray diffraction methods [32,33]. Although organic solvates [32,34–36], including isostructural solvates [13,17,37], have been previously studied using solid-state NMR, the behaviour and dynamics of solvent molecules in isostructural solvates has not been the subject of detailed research. Typically, the NMR spectra of isostructural channel solvates are only slightly affected by changing the solvent molecules [13], as the solvent molecules introduce only minor differences in chemical environment of the host molecules, although such spectra can still be used for solvate identification [38]. Similarly, only slight changes are typically observed in NMR spectra of non-stoichiometric hydrates as function of water content [39–41], although some structural variations can be inferred [42–44].

In this study we use ^{13}C , ^{15}N and 2H solid-state NMR to determine and characterize the differences between these five droperidol isostructural solvates. This includes the identification and characterization of the molecular motion in **NSH**, S_{Me} and S_{Et} to explain the slight disorder of water molecule in **NSH** and to distinguish between static vs. dynamic disorder in the alcohol solvates. Theoretical calculations are used to rationalize the differences in the molecular motion of the solvent molecules.

2. Experimental

2.1. Sample preparation

Droperidol (purity > 99%) was obtained from JSC Grindeks (Riga, Latvia). Droperidol **NSH** was obtained by dissolving droperidol in

acetone at 50 °C, adding a small amount of water and then slowly partially evaporating the resulting solution at 50 °C [20]. Droperidol solvates S_{Me} , S_{Et} , S_{ACN} and S_{NM} were obtained by dissolving droperidol in the corresponding solvent at 60–75 °C (depending on solvent boiling point) and then cooling the solution to –20 °C [20]. Solvates were stored in the mother liquor and filtered and dried immediately before packing into rotors.

Deuterium-labelled solvates were prepared by grinding and then desolvating the original solvate at 50 °C above P_2O_5 . The resulting sample was then placed in a closed container with saturated D_2O or d_1 -alcohol vapour. **NSH** with different D_2O contents was obtained by storing the deuterium-labelled sample above D_2O to obtain monohydrate stoichiometry or above a saturated solution of $MgCl_2$ in D_2O to obtain approximately hemihydrate stoichiometry. These stoichiometries were estimated from previously measured sorption–desorption isotherms [20].

All of the solvents, $MgCl_2$ and P_2O_5 were purchased from commercial suppliers and used without further purification. The identity of all droperidol solvates was confirmed using PXRD [20].

2.2. Solid-state NMR

High-resolution solid-state NMR spectra were obtained using either a Bruker Avance III HD spectrometer (Bruker, Germany) operating at 125.67 MHz for ^{13}C (499.72 MHz for 1H) and 76.71 MHz for 2H with a 4.0 mm (rotor o.d.) MAS probe, or a Varian VNMRS 400 spectrometer (Varian Inc., USA), operating at 40.53 MHz for ^{15}N (399.88 MHz for 1H) with a 6.0 mm (rotor o.d.) MAS probe. ^{15}N spectra were recorded at ambient temperature, whereas ^{13}C and 2H spectra were recorded at controlled temperatures from 20 °C down to –45 °C. Note that these are set temperatures that do not attempt to correct for sample heating under magic-angle spinning; these are estimated to be of the order of +5, +8 and +15 °C for the 2H , ^{15}N and ^{13}C spectra respectively.

^{13}C and ^{15}N spectra were obtained under MAS conditions using cross polarization (CP) with the following conditions: recycle delay 7–30 s for **NSH**, S_{Me} and S_{Et} , and 120–180 s for S_{ACN} , and S_{NM} , contact time 0.5–2 ms, a sample spin rate of 13 kHz for ^{13}C and 6.8 kHz for ^{15}N spectra, and acquiring 300–1000 transients for ^{13}C and 440–3600 transients for ^{15}N (depending on relaxation delays). SPINAL64 with 78 kHz 1H nutation rate and TPPM with 55.6 kHz nutation rate were used for heteronuclear decoupling of the ^{13}C and ^{15}N spectra respectively. Spectra were referenced with respect to external neat TMS for ^{13}C or neat nitromethane for ^{15}N by setting the high-frequency signal from a replacement sample of adamantane to 38.4 ppm or the nitrate signal from a replacement sample of solid ammonium nitrate to –5.1 ppm, and typically processed with an apodisation function corresponding to a 20 Hz Lorentzian line-broadening prior to Fourier transformation. ^{13}C linewidths were determined by fitting the peaks to a mixed Lorentzian/Gaussian lineshape in the Bruker TopSpin software.

Carbon-13 T_1 values were estimated from direct-excitation spectra with recycle delays of 0.2–180 s, while more accurate measurements were made using saturation-recovery experiments with recovery delays of 0.1 ms to 90 s. 12 Pulses separated with a 10 ms delay were used for saturation of the ^{13}C magnetization. 200–240 Repetitions were accumulated, with a spinning rate of 13 kHz and 1H decoupling nutation rate of 71 kHz. T_1 values from variable recycle delay experiments were calculated by fitting peak heights to a simple rising exponential function using Excel Solver. T_1 values from saturation-recovery experiments were determined in TopSpin by fitting integrated peak areas to a rising exponential. Note that measurement of the relaxation times for the CH_3 of S_{Et} in particular was complicated by transient Nuclear Overhauser effects [45]; this is discussed further in the Supplementary information.

^2H MAS spectra were acquired without proton decoupling with 10 kHz spinning rate and 10 s recycle delay, acquiring 1000–10,000 transients (depending on time available). T_1 relaxation times were estimated with short experiments (50–100 repetitions) with the recycle delay varying up to 10 s or 30 s using 7–9 increments. T_1 values were estimated by fitting peak heights to a simple rising exponential function as above. Bandshape analysis of the spinning sidebands was performed in Gsim [46]/pNMRsim [47] by simultaneously fitting the peak linewidths (using a Lorentzian lineshape function) and quadrupolar coupling parameters from both ND and solvent sites. Flat baselines, which are significant for fitting, were typically obtained by discarding the data points before the first rotary echo for signals obtained on-resonance. Alternatively, the baseline roll was suppressed using spline fitting in TopSpin.

2.3. First-principles computation

Chemical shift calculations were carried out using the GIPAW method implemented in CASTEP 6.0 [48–51], after geometry optimization of the droperidol crystal structures determined at 173 K [20]. Since the first principles calculations cannot be applied to disordered structures, starting structures of S_{Me} and S_{Et} without disorder were prepared in two ways: (a) both structures were solved in the $P1$ space group with ordered solvent and (b) $P1$ structures were derived from the reported $P\bar{1}$ structures by discarding one of the solvent molecule orientations. Calculations were performed with the PBE [52] functional using on-the-fly generated ultrasoft pseudopotentials and a cut-off energy of 600 eV, with integrals taken over the Brillouin zone using a Monkhorst-Pack grid of a minimum k -point sampling of 0.05 \AA^{-1} . Two approaches were used for geometry optimization: optimization of hydrogen atom positions only and optimization of all atomic positions. Unit cell parameters were fixed to the values determined from X-ray diffraction studies in both cases. The computed ^{13}C and ^{15}N chemical shifts were referenced by linear regression of computed shielding values to the experimental shifts [50]. Geometry optimizations of doubled unit cells (see below) with adjacent solvent molecules in the same or opposing directions were performed both with the pure PBE functional and also using the Tkatchenko–Scheffler (TS) dispersion correction scheme [53]. The orientation of the solvent molecule was inverted by manually adjusting the atomic coordinates on one solvent molecule prior to full geometry optimization.

Interaction energies between pairs of molecules were calculated in Gaussian 09 [54] using the M06-2X [55] functional for molecular geometries directly extracted from the crystal structures after optimization of all atom positions in CASTEP. Basis set superposition error was corrected using the counterpoise method. The pairs involved a given solvent molecule and either adjacent solvent molecules in the channels or adjacent droperidol molecules (see further Section 3.4).

3. Results and discussion

3.1. Solvate characterization using ^{13}C CPMAS spectra

Fig. 2 shows the ^{13}C CPMAS spectra of the solvates, with the peak positions given in Table 1. The resonances of the solvent molecules are readily identified (see labels), except for the methyl group signal of ethanol and the quaternary carbon of acetonitrile, as these overlap with the peaks of droperidol. Bearing in mind that the spectra were recorded under CP conditions, and so are not strictly quantitative, the intensity of the solvent peaks is consistently around two times lower than that of the droperidol CH_2 peaks, consistent with a 0.5 solvate stoichiometry. CP spectra with

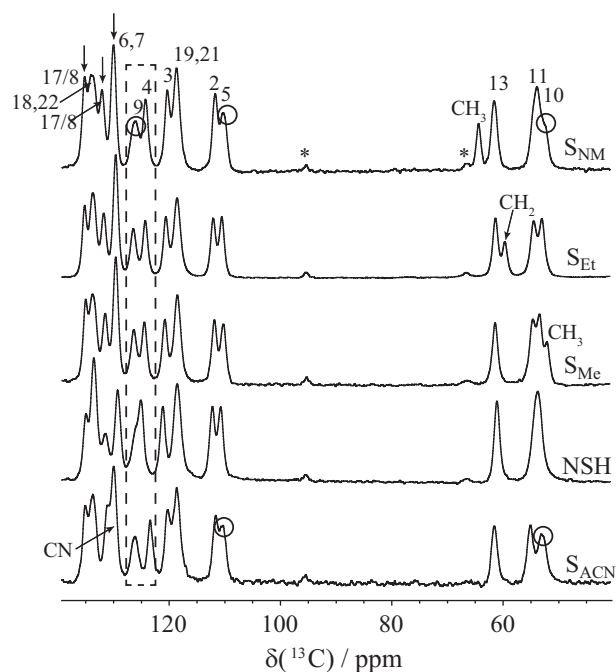


Fig. 2. 50–135 ppm region of the ^{13}C CPMAS spectra of the droperidol isostructural solvates together with peak assignment. Spinning sidebands are marked with asterisks, signals absent in short CP contact time experiments are marked with arrows, and signals in the S_{ACN} and S_{NM} spectra showing evidence of splitting are circled. Full spectra are given in Fig. S2.

short (10–50 μs) contact times were recorded (see Fig. S3) to identify the carbon atoms directly attached to hydrogen; the peaks absent in these spectra and thus associated with quaternary carbon atoms are marked with arrows in Fig. 2.

As would be expected, the NSH spectrum is consistent with one unique droperidol molecule in the asymmetric unit. However, the S_{Me} and S_{Et} spectra also do not show clear evidence of distinct droperidol molecules in the crystal structure, one hydrogen-bonded to the solvent, and one not. Only slight splitting of some peaks, circled in Fig. 2, is observed in the spectra of S_{ACN} and S_{NM} , which would be consistent with having two slightly different droperidol molecules in the asymmetric unit.

To help assign the peaks, GIPAW calculations of the NMR parameters were performed for all solvates after geometry optimization. The results, after rescaling each set of the calculated shieldings against the experimental chemical shifts, are presented in Table 1. Different isotropic shielding values were calculated for the same carbon atom where inequivalent droperidol molecules are present in the asymmetric unit (S_{Me} , S_{Et} , S_{ACN} and S_{NM}). It was observed that these differences were quite large (up to 6.8 ppm, with an average difference of 2–3 ppm, depending on the solvate) when only hydrogen atom positions were relaxed for structures solved in the $P1$ space group. Relaxing all atomic positions during the geometry optimization decreased the average difference to 0.5 ppm. Since this is clearly in better agreement with the experimental results, only the structures obtained by all atom optimization were used in further calculations, and average values of the calculated shieldings of corresponding atoms were used when making comparisons with experimental data. The maximum difference of up to 2–3 ppm is observed for C9 and C10, which is consistent with their proximity to the solvent molecules, see Fig. S1. These results imply that solution of the XRD results in $P1$ has “exaggerated” the asymmetry between the droperidol molecules; relaxing all the atomic positions results in increased local symmetry and better agreement with the experimental NMR data.

Table 1Assigned experimental peak maxima (in ppm) in ^{13}C CPMAS spectra and (rescaled) average calculated ^{13}C chemical shifts after all atom optimization.

Carbon	NSH		S_{Me}		Diff. ^a	S_{Et}		Diff. ^a	S_{ACN}		Diff. ^a	S_{NM}		Diff. ^a	$\Delta\delta_{\text{calc}}^b$
	δ_{Exp}	δ_{all}	δ_{Exp}	δ_{all}		δ_{Exp}	δ_{all}		δ_{Exp}	δ_{all}		δ_{Exp}	δ_{all}		
C16 ^c	197.6	199.9	197.5	199.9	0.1	197.5	199.8	0.1	197.6	200.2	0.2	197.5	199.7	0.0	0.5
C20 ^{c,d}	167.5	171.5	167.7	171.7	0.0	167.7	171.6	0.1	167.7	171.9	0.0	167.6	171.6	0.0	0.4
C1 ^c	154.0	149.2	154.1	149.5	0.3	154.1	149.3	0.1	154.1	149.8	0.2	154.2	149.7	0.4	0.6
C17/C8 ^{c,e}	133.6	131.4 ^f	133.6	131.4 ^g	1.4	133.8	132.1 ^g	0.6	133.7	131.4 ^f	0.0	133.9	132.9 ^g	0.8	0.1 ^f
C18	132.2	132.7	132.4 ^h	133.0	0.2	132.4	132.9	0.2	132.3	132.8	0.0	132.7 ^h	133.3	0.1	0.5
C22		132.4		132.6	0.1		132.7	0.4		133.3	0.0		132.6	0.2	0.9
C17/C8 ^{c,e}	130.1	130.0 ^g	130.2	131.3 ^f	0.1	130.4	131.4 ^f	0.0	129.8	131.3 ^g	0.2	130.7	131.5 ^f	0.0	3.0 ^g
C6 ^c	127.9	127.1	128.3	127.1	0.4	128.3	127.0	0.4	128.6	127.2	0.5	128.6	127.4	0.2	0.4
C7 ^c		126.3		126.6	0.1		126.7	0.3		127.2	0.3		127.3	0.3	1.1
C9	124.7	130.0	125.0	128.4	3.2	125.1	128.2	1.2	124.8	128.0	1.3	124.6 ^h	127.3	2.1	2.7
C4	123.7	122.9	123.1	122.0	1.3	123.0	122.1	0.9	122.1	121.0	0.2	122.9	122.3	0.3	1.8
C3	119.8	118.1	119.4	118.0	0.3	119.3	117.9	0.3	118.9	117.4	0.1	119.0	117.5	0.0	0.6
C19	117.2	117.3	117.2	117.6	0.5	117.3	117.4	0.5	117.3	117.6	0.0	117.3	117.6	0.3	0.3
C21		116.5		116.7	0.0		116.7	0.4		116.8	0.0		116.8	0.0	0.4
C2 ⁱ	110.9	108.7	110.5	108.9	0.6	110.8	109.2	0.6	110.3	108.6	0.1	110.4	108.8	0.2	0.6
C5 ^j	109.4	109.0	108.9	107.5	1.3	109.2	108.3	1.1	109.0 ^h	107.7	0.7	108.9 ^h	107.7	0.9	1.5
C13	59.8	60.3	60.1	60.1	0.0	60.0	60.1	1.2	60.3	60.2	0.5	60.3	60.5	1.1	0.4
C11 ⁱ	52.4	53.8	53.3	53.6	1.0	52.3	53.4	0.6	53.7	53.9	0.4	52.6 ^h	53.2	1.2	0.7
C10 ⁱ		53.2	52.1	53.0	0.6	51.7	53.2	2.1	51.8 ^h	51.8	1.0		52.9	2.1	1.5
C15	35.3	36.1	35.5	36.1	0.0	35.6	36.6	0.0	35.6	36.5	0.0	35.9	37.2	0.1	1.1
C12	28.4	28.2	28.4	28.8	0.2	28.3	28.7	0.2	28.0	28.0	0.2	28.4	29.1	0.3	1.1
C14	21.3	21.0	21.3	21.0	0.2	21.1	21.1	0.0	21.2	20.9	0.0	21.1	21.2	0.0	0.3
CH ₃ ^{solv}			50.8	52.2		21.1	19.8		4.2	6.0		63.1	62.5		
CH ₂ /CN ^{solv}						58.3	60.9		128.6/129.8 ^k	128.3					
RMSD ^k		2.06		1.83			1.79				1.81		1.65		

^a Difference in calculated chemical shift between two chemically equivalent atoms in the unit cell. Significant differences greater than 0.7 ppm are in italics and those larger than 2 ppm are in bold.

^b Difference between the highest and lowest calculated chemical shifts from the same atom in all five solvates.

^c Non-protonated carbons identified from short contact time CP spectrum.

^d Signal split by J -coupling to ^{19}F , with $^1J_{\text{CF}}=278\text{--}280\text{ Hz}$ in NSH, S_{Me} , S_{Et} and S_{ACN} and $^1J_{\text{CF}}=265\text{ Hz}$ in S_{NM} .

^e High variation in CASTEP calculated chemical shifts for these two atoms in different solvates prevents unambiguous assignment.

^f Given value is for C17 (calculated).

^g Given value is for C8 (calculated).

^h Signal is slightly split.

ⁱ Peak separation of C2 and C5, as well as that of C10 and C11 is too small for unambiguous assignment, but consistent relative position in GIPAW calculations for all solvates (with the exception of C2 and C5 in NSH) and the splitting of C5 and C10 peaks support this assignment.

^j Experimental peak position uncertain, but peak intensities and GIPAW calculations suggest that nitrile carbon corresponds to one of these peaks.

^k Root mean square difference between experimental and calculated chemical shifts.

As might be expected, the situation was reversed for the structures originally solved in $P\bar{1}$ space group (S_{Me} and S_{Et}). With only optimization of the hydrogen atom positions, the droperidol environments remain essentially identical and only small maximal (1.6–2.2 ppm) and average (0.3–0.45 ppm) differences were observed for equivalent carbon shifts in the two droperidol molecules. Several of these shifts, both for solvent and droperidol sites, however, deviated significantly from the experimentally observed values. Relaxation of all atoms resulted in almost identical chemical shifts to those calculated after all-atom optimization of structures solved in $P1$.

The most significant differences between the ^{13}C spectra are observed for the C4 and C9, marked by a dashed rectangle in Fig. 2; these again are close to the solvent molecules. This observation was consistent with the GIPAW calculations, where the highest difference between the average chemical shifts for different solvates were predicted to be for C9 (2.7 ppm), C4 (1.8 ppm) as well as for C8 (3.0 ppm), see Table 1. Overall, however, the spectra of solvates are very similar, showing that the different solvent molecules introduce significant changes in the local chemical environment of the droperidol molecules.

Taking into account the previously identified signals from quaternary carbons and solvent atoms, the obtained shielding values after all atom optimization were plotted versus the observed chemical shifts, illustrated in Fig. 3 for S_{Et} . As observed previously [37,50] and justified theoretically [56], these plots had a non-unity slope. Linear regression

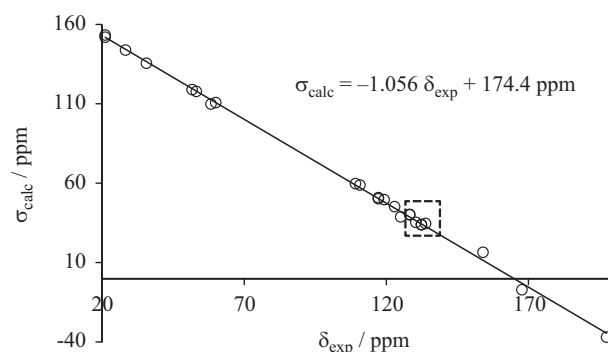


Fig. 3. Calculated ^{13}C isotropic shielding (averaged over equivalent carbons) values versus observed chemical shifts in droperidol S_{Et} . The dashed rectangle marks the region where the peak assignment is ambiguous.

was used to reference the mean experimental shift to the mean computed shielding, and to rescale the calculated shifts. These plots allowed the majority of the signals to be assigned, as indicated in Fig. 2, with the exceptions of strongly overlapped peaks in the region 127–135 ppm, indicated by the rectangle in Fig. 3. These ambiguities are not, however, significant for the purposes of this study. Further details of the assignment are given in Table 1. In each case, a smaller RMS deviation between calculated and experimental values was observed when all atomic positions were refined, see Tables 1 and S1.

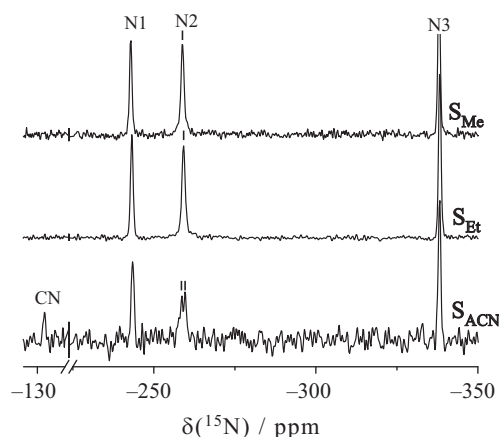


Fig. 4. ^{15}N CPMAS spectra of droperidol solvates S_{Et} , S_{Me} and S_{ACN} , showing the splitting of the N2 peak in the spectrum of S_{ACN} . The lower signal-to-noise ratio of the S_{ACN} spectrum reflects the much longer recycle delay needed for this sample (120 s, compared to 15 and 25 s for S_{Et} and S_{Me} respectively) and consequently a much reduced number of acquisitions compared to the alcohol solvates (440 compared to 3628 and 2308 respectively).

The experimental spectra show only slight evidence of splitting for a few peaks in S_{ACN} and S_{NM} corresponding to carbon atoms C5, C9 and C10, which are all close to the solvent molecules. The differences between peak maxima were at most 0.5 ppm, but these particular carbon atoms also show the highest splitting in the GIPAW-calculated chemical shifts, see Table 1. Observing the line splitting is complicated by the relatively broad linewidths; the widths of the peaks in the spectra of droperidol isostructural solvates were 0.75–1.15 ppm, whereas peak widths in the ^{13}C spectra of droperidol dihydrate and form II (see Figs. S5 and S6) were only 0.32–0.70 ppm under the same conditions. This difference in linewidths cannot be explained by the presence of two slightly different droperidol molecules in the unit cell, as the linewidths of the organic solvates was identical to that of NSH , where there is a single droperidol molecule in the asymmetric unit. The “line-broadening factors” associated with the anisotropy of the bulk magnetic susceptibility (ABMS) for powder samples [57] were determined using the magnetic susceptibility tensor calculated by CASTEP-NMR. This was found to be ~ 3.6 ppm for the isostructural solvates and ~ 1.7 ppm for both form II and dihydrate, suggesting that the width of the lines in the solvate spectra is associated with a large ABMS, making it intrinsically difficult to resolve overlapped resonances.

3.2. Solvate characterization using ^{15}N CPMAS spectra

As shown in Fig. 4, ^{15}N CPMAS spectra were recorded for the S_{Et} , S_{Me} and S_{ACN} solvates, and peaks assigned based on the GIPAW calculations. Both S_{Et} and S_{Me} show sharp lines from all three nitrogen atoms, whereas the line from N2 – the only nitrogen atom close to the solvent – was split (or significantly broadened) in S_{ACN} , indicating two distinct local environments. This confirms that the acetonitrile breaks the local symmetry of droperidol molecules, consistent with the determined crystal structure [20]. The experimental and GIPAW-calculated ^{15}N chemical shift differences are almost the same, 1.0 and 0.8 ppm respectively. The alcohol molecules are strongly hydrogen-bonded with the droperidol O1 atom, thus affecting the strength of the intermolecular hydrogen bond between droperidol molecules $\text{N2-H}\cdots\text{O1}$, and the calculated chemical shift difference for N2 is significantly higher in S_{Me} and S_{Et} , 1.6 and 3.2 ppm respectively. In contrast to S_{ACN} , only one, somewhat broader, line is observed in the ^{15}N spectrum for the alcohol solvates (45–50 Hz for N2 compared to 35–40 Hz for other nitrogen resonances). This strongly suggests that the alcohol molecules in S_{Me} and S_{Et} are dynamically disordered, resulting in a single resonance.

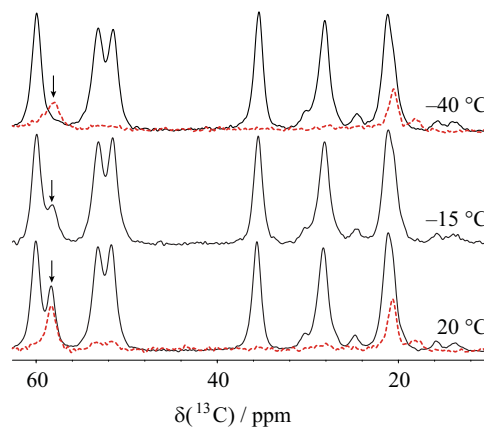


Fig. 5. ^{13}C CPMAS (solid lines) and direct-excitation (dashed lines, 20 °C and –40 °C) spectra of S_{Et} at different temperatures. The signal from ethanol CH_2 is marked with an arrow.

Although the ^{15}N spectra were much more demanding to acquire, they are more sensitive in this case to the very subtle symmetry breaking involved. It is also worth noting in this context that ^{14}N shifts can also be very sensitive to changes in local environment as they are also dependent (via the quadrupolar 2nd order isotropic shift) on local differences in electric field gradient [58].

3.3. Characterization of solvent dynamics in droperidol isostructural solvates

The evidence from the ^{13}C and ^{15}N CPMAS spectra acquired at ambient temperature, combined with the crystal structure determinations, suggests that the solvent molecules are dynamic in S_{Me} and S_{Et} . The crystal structure of NSH also shows evidence of disordered water molecules. ^{13}C and ^2H MAS spectra of S_{Et} , S_{Me} and NSH as a function of temperature are used here to try to characterize the solvent dynamics.

3.3.1. Solvates with organic solvents

It can be seen in Fig. 5 that the ethanol CH_2 group signal (highlighted with an arrow) in the CPMAS spectrum (solid lines) of S_{Et} broadens when the temperature is reduced to –15 °C and has lost most of its intensity at –40 °C. These changes are reversible and consistent with the presence of dynamics. Experiments with different contact times, see Fig. S3, confirmed that the low intensity of this peak is related to its broad nature rather than, for example, rapid $T_{1\rho}$ relaxation. The broad CH_2 peak is more easily observed in the ^{13}C direct-excitation spectra (dashed lines). The most likely mechanism for the broadening is interference between the modulation of NMR parameters by dynamics and the ^1H decoupling [31,59], implying that the dynamics of the ethanol CH_2 are on the order of 10 s/kHz around –40 °C. It was also noticed that the build-up of the ethanol CH_2 group signal during cross-polarization at 20 °C was significantly slower than that of CH_2 carbons of droperidol (see Fig. S8). This implies that the heteronuclear CH dipolar couplings are partially averaged by dynamics on the timescale of 10 s of kHz or faster.

The ^{13}C T_1 relaxation times measured as a function of temperature provide further insight into the dynamics of the ethanol molecules. These are tabulated in Table S2 and plotted in Fig. 6. The relaxation times of both ethanol carbon atoms are relatively short e.g. 1.04 s for the CH_2 and 0.8 s for the CH_3 at 20 °C, compared to at least 50 s for the carbon atoms in droperidol. The steady decrease in T_1 relaxation time of the CH_3 carbon with decreasing temperature is consistent with the approach towards a

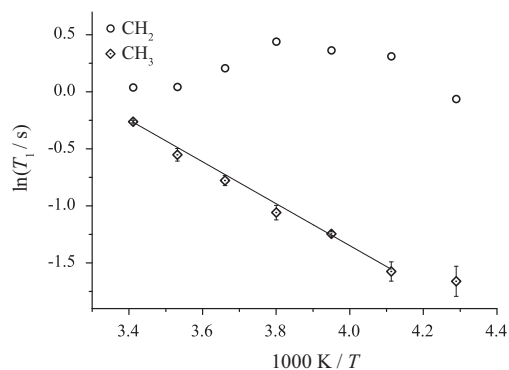


Fig. 6. ^{13}C T_1 relaxation times for the ethanol carbons of S_{Et} as a function of inverse temperature. The one-standard-deviation error bars on the fitting of CH_2 T_1 values are of the order of the size of symbols used.

T_1 minimum. Assuming Arrhenius-type behaviour, fitting the linear regime (i.e. excluding the data point at -40°C) gives an activation barrier, E_a , of $15.1 \pm 0.6 \text{ kJ mol}^{-1}$. This is a typical value for rotational diffusion of the methyl group [29,30,60], although it should be noted that a more extensive data set encompassing the T_1 minimum would provide much more robust figures. The interpretation of the CH_2 carbon data is less straightforward, but its rapid relaxation implies that there are significant local dynamics of the CH_2 over the full temperature range. While ^{13}C relaxation rates will be dominated by dipolar relaxation driven by modulations of the CH heteronuclear couplings, there will also be a contribution from cross-relaxation to any rapidly relaxing ^1H spins. Faster ^1H T_1 relaxation at lower temperatures allowed the recycle delays to be reduced from 12 s at 20°C to 6 s at -40°C , suggesting that the decrease in the ^{13}C T_1 of the CH_2 in the low-temperature limit may be related to faster cross-relaxation to ^1H (associated with the methyl group re-orientation). The ^{13}C T_1 of the CH_2 also decreases in the high temperature limit, where the methyl group dynamics is not contributing so effectively to T_1 relaxation. This suggests that there are additional dynamic processes that become more effective at driving the spin–lattice relaxation in the high temperature regime (and so are likely to have higher activation barrier than methyl rotation). Such processes would need to be of the order of the ^{13}C Larmor frequency (in this case 125 MHz) at 20°C , which could also be consistent with a process that is of the order of 10 s kHz at -40°C (as observed via the spectra).

The T_1 relaxation times of methyl group carbons in methanol and acetonitrile molecules are much longer than in the ethanol solvate, 5.1 and 17 s at 20°C respectively (see Table S2), and show the opposite temperature dependence (i.e. decreasing with increasing temperature). Bearing in mind the difficulties of interpreting relaxation data at some distance from the T_1 minimum, this suggests that the barrier for methyl group re-orientation in these solvates (and the acetonitrile solvate in particular) is significantly higher, and that the T_1 minimum is well above ambient temperature. There is also no evidence for additional high-frequency motions.

The ^2H MAS spectra of the alcohol solvates prepared from d_1 -alcohols were very similar, showing resonances both from the deuterated solvent, at about 4.0 ppm, and the labile NH site of droperidol, at about 10.5 ppm. Fig. 7 shows the spectra for S_{Et} ; the corresponding figure for S_{Me} can be found in the Supplementary information (Fig. S10). Fitting the bandshape from both of the deuterium sites, quadrupolar coupling parameters were determined in pNMRsim [47]. The quadrupolar couplings for the ND site are uninformative, but are tabulated in Table S3. The quadrupolar coupling parameters for the alcohol OD determined from the spectra at 20°C were found to be the same within experimental error, $\chi=206 \text{ kHz}$,

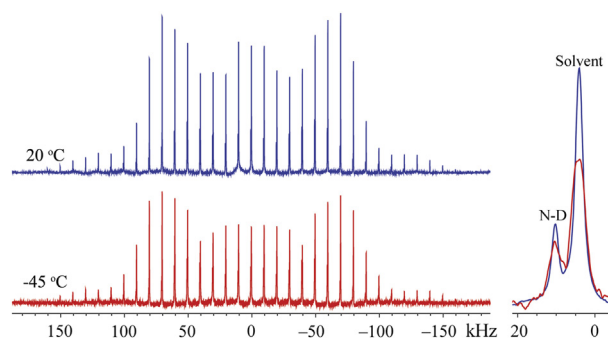


Fig. 7. ^2H MAS spectra at a spinning rate of 10 kHz for S_{Et} at 20 and -45°C , with the centreband region expanded on the right.

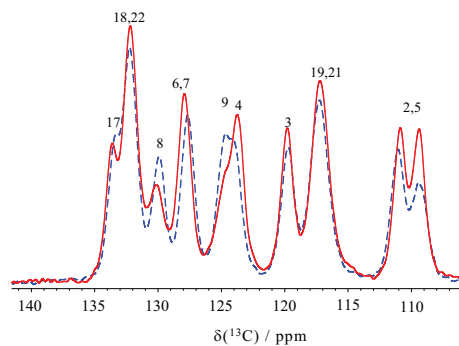


Fig. 8. ^{13}C CPMAS spectra of NSH at 20°C (solid line) and -40°C (dashed line).

$\eta=0.17$. The fitted quadrupolar coupling constants were slightly larger at -45°C : $\chi=211 \text{ kHz}$ for S_{Me} and 222 kHz for S_{Et} , with $\eta=0.17$. The uncertainties on χ and η are estimated to be 2 kHz and 0.02 respectively, on the basis of duplicate measurements and different processing methods used to obtain flat spectral baselines. These parameters are consistent with values calculated by the GIPAW calculations, $\chi=244\text{--}246 \text{ kHz}$, $\eta=0.15$, but reduced by high frequency motions of increasing amplitude as the temperature is increased [61]. Note that flipping of the solvent molecules through the inversion centre will not change the quadrupolar coupling tensor orientation and so would not have a direct effect on the spectrum.

In contrast to the ^2H spectra, which might suggest that the solvent molecules are essentially static, the ^2H T_1 relaxation times for the alcohol OD group were short (estimated to be 0.1–0.3 s) at both measurement temperatures (-45°C and 20°C), see Table S4. Again, a simple flip of solvent molecules through an inversion centre cannot itself explain the fast relaxation, since the quadrupolar tensor is left unchanged. This implies that multiple high-frequency processes are active, resulting in fast relaxation rates that are not significantly temperature dependent, i.e. there is no single motional process creating a well-defined T_1 minimum. We have previously observed small amplitude motions that are large enough to drive relaxation but too small to significantly average the quadrupolar coupling constant [30]. The crystal structure solution and the averaged chemical environments for the droperidol molecules in the unit cell indicate that the solvent molecules are also flipping orientations, but the ^2H NMR data and the ^{13}C relaxation times are not sensitive to this process. The most likely scenario is that the alcohol molecules are relatively dynamic within their lattice sites and also occasionally flip over to the equivalent site related by the inversion symmetry.

3.3.2. Nonstoichiometric hydrate

Reduction of the temperature to -40°C noticeably changed the ^{13}C CPMAS spectra of NSH , Fig. 8. The largest changes are for

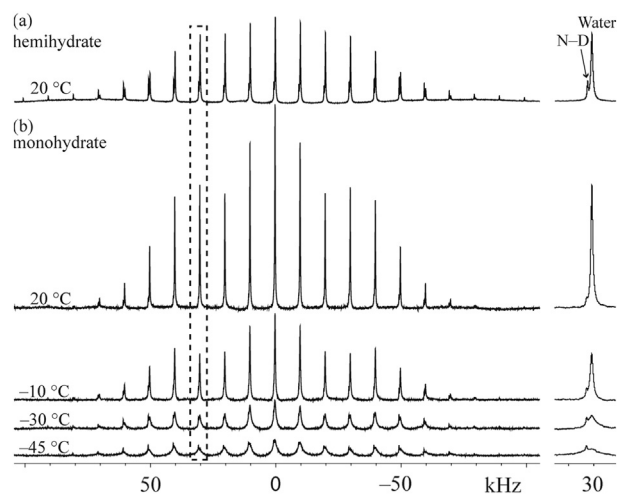


Fig. 9. ^2H MAS spectra at a spinning rate of 10 kHz of **NSH** with (a) hemihydrate stoichiometry at 20 °C, and (b) monohydrate stoichiometry at different temperatures. The insets show the spinning sideband at about 30 kHz (marked with dashed rectangle), as the ND signal is clearer here than in the centreband. The spectra have the same vertical scale.

the signals from C9 and C4, both of which are close to the water molecules – C9 is even weakly hydrogen bonded with the water [18,20] – suggesting changes in the dynamics and/or average structure of the water molecules. The relatively short (largely temperature independent) ^1H T_1 relaxation time of about 15 s observed in the ^{13}C CP experiments is consistent with motion of the water molecules; droperidol phases without mobile solvent molecules, S_{ACN} , S_{NM} , polymorph II and dihydrate, showed T_1 values in excess of 2 min, which is more typical of molecular solids lacking methyl groups to drive relaxation.

Fig. 9 shows ^2H MAS spectra of **NSH** prepared from D_2O as a function of temperature. Very different bands and temperature dependence are observed compared to the alcohol solvates. The water signal in **NSH** has narrower bandshape with partially averaged quadrupolar coupling parameters: χ was 84 ± 3 kHz, while η was more variable, in the range 0.6–1.0, depending both on water content and temperature, see Table S3. This dependence on the water content presumably reflects changes in the overall dynamics with the degree of occupancy of water sites. While the possibility of distinct populations of static vs. dynamic water molecules can be ruled out, it is difficult to distinguish whether there is a distribution of similar water environments or a single averaged water environment with fast exchange between sites. Reducing the temperature clearly broadens the lines corresponding to D_2O , Fig. 9(b), implying the water is highly dynamic at ambient temperature and that some aspect of the dynamics is being slowed to the 10 s kHz frequency scale at -45 °C. The overall quadrupolar coupling constants are somewhat lower than those typically reported for water molecules undergoing rapid C2 flips [62–64], suggesting that the overall dynamics is more complex. Moreover a simple C2 flip motion would produce η values of unity and would not explain the relatively high displacement parameters for water oxygen site observed in XRD [20]. As would be expected, the ^2H T_1 relaxation times for the water sites are very short, estimated to be < 0.1 s from experiments with variable recycle delays. Again, the ND site is relatively uninformative; fitted quadrupolar parameters are tabulated in Table S3. T_1 relaxation times were 1–3 s (see Table S4), comparable to values observed for deuterium sites without high-frequency dynamics. The larger intensity of the ND signal in Fig. 9(a) probably reflects the fact that the hemihydrate sample was stored for longer in the D_2O atmosphere than the monohydrate sample.

To quantify the motional broadening seen in Fig. 9, the line-widths of the D_2O peaks (LW) were determined from the

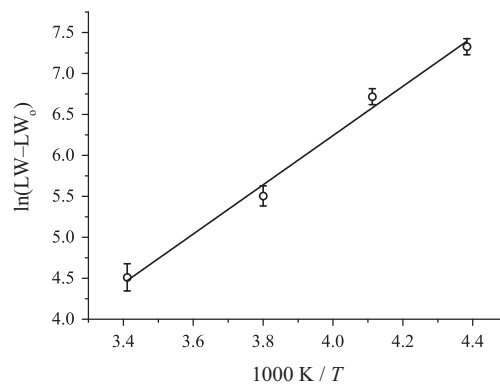


Fig. 10. Estimated motional line broadening of the ^2H D_2O resonance of **NSH** as a function of inverse temperature. The “error bar” indicates the maximum and minimum linewidths observed using different methods for bandshape fitting/baseline roll suppression (see Section 2).

Table 2

Increase in unit cell total energy (in kJ cell^{-1}) of droperidol solvates when adjacent solvent molecules are positioned in the opposite direction, with (+TS) and without dispersion correction.

Solvate	S_{Et}	S_{Me}	S_{NM}	S_{ACN}
PBE	−1.5	2.9	9.9	26.3
PBE+TS	−0.4	3.7	12.6	26.9

bandshape fitting of the spinning sideband manifold. The motional broadening was estimated by subtracting the width of the ND resonance ($\text{LW}_0 = 160$ Hz), which is assumed to be unaffected by the water dynamics. The plot of linewidth due to motional broadening [65] against inverse temperature, Fig. 10, is linear over this temperature range allowing an Arrhenius-type activation barrier to be determined, $E_a = 25 \pm 3$ kJ mol^{-1} . Note that in this fast exchange limit, the constant of proportionality between the motional broadening and the rate of dynamics is related in a non-trivial way to the quadrupolar parameters and motional mechanism. Moreover, the physical significance of the derived activation parameter is limited given both the non-trivial nature of the motion and the restricted temperature range covered.

3.4. Theoretical analysis of the differences in solvent molecule behaviour

In order to rationalize the observed differences in the solvent molecule dynamics between the different droperidol solvates, the energy difference was determined between structures where all the solvent molecules in a channel point in the same direction and where adjacent solvent molecules point in opposite directions. As a first step, the orientation of the solvent molecule in each hemisolvate crystal structure was approximately reversed and geometry optimization in CASTEP used to relax all the atomic positions. The tiny energy differences of up to 0.3 kJ cell^{-1} (equivalent about $3 \cdot 10^{-7}$ of the total cell energy) between the energies of these nominally identical unit cells gives an estimate of the “error bar” in this type of calculation. The unit cell dimensions were then doubled in the solvent channel (a -axis) direction and the orientation of one solvent molecule was reversed. The energy differences (per unit cell/droperidol molecule) between the “same direction” and “opposite direction” structures after full geometry optimization, with and without dispersion correction, are shown in Table 2. It can be seen that the cell energies are essentially the same for S_{Et} , particularly when the dispersion-corrected functional is used. In contrast, the “same direction” structure is slightly

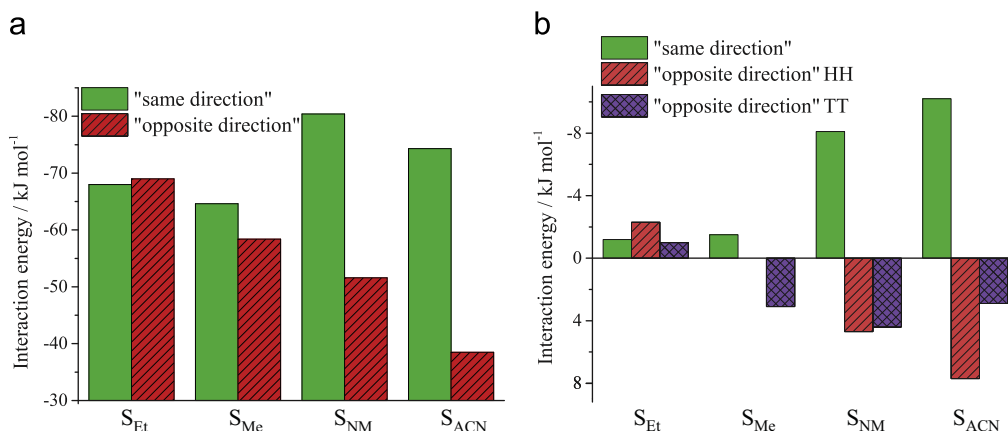


Fig. 11. Calculated (a) total pair-wise interaction energies of solvent molecules and (b) solvent-solvent interaction energies, in "same direction" and "opposite direction" droperidol solvate structures.

energetically more favourable for S_{Me} , and is significantly more energetically favourable for S_{NM} and S_{ACN} .

Pairwise interaction energies were also calculated to provide insight into the energetics of different relative solvent orientations. Interaction energies (the difference in energy between two separated molecules and their dimer) were calculated using *Gaussian 09* between one solvent molecule and the two solvent and eight droperidol molecules that surround the chosen solvent molecule. The co-ordinates of these ten molecular pairs were extracted from the optimized "same direction" and "opposite direction" crystal structures, and the overall interaction energy approximated as the sum of these ten pairwise interaction energies. In the case of the "opposite direction" structure, adjacent solvent molecules can either be oriented "head-to-head" (HH) or "tail-to-tail" (TT), see Fig. S11, along the a -axis direction. As required from the inversion symmetry, the total interaction energy of the solvent with its surroundings is the same, within the calculation accuracy, for the two solvent arrangements in "opposite direction" structure. As shown in Fig. 11, the total interaction energy is essentially identical for the "same direction" and "opposite direction" structures in the case of S_{Et} . In contrast, the interaction energies are much more favourable for the "same direction" structure for S_{NM} and S_{ACN} . These trends are fully consistent with the pattern of total unit cell energies as observed above. As shown in Fig. 11 and tabulated in Table S5, the most significant factor (at least 87%) contributing to the difference in interaction energies are the solvent-solvent interactions. The solvent-solvent interactions are always attractive in the "same direction" structure, whereas the interactions between nitromethane and acetonitrile molecules change by 13–18 kJ mol^{-1} from attractive to repulsive in the "opposite direction" structure.

These results provide a straightforward rationalization of the absence of solvent disorder in the S_{ACN} and S_{NM} solvates – where there is a strong energetic preference for the solvent molecules to be consistently oriented – and the presence of solvent molecule disorder in S_{Me} and S_{Et} , where there is little energetic preference for a consistent orientation.

4. Conclusions

The ^{13}C CPMAS solid-state NMR spectra of a set of isostructural solvates of droperidol (NSH , S_{Me} , S_{Et} , S_{ACN} and S_{NM}) confirm that the solvent molecules have only minor effect on the chemical environment of the droperidol molecules. The relatively broad linewidths, which make it difficult to resolve the inequivalence of

the droperidol molecules in the S_{ACN} and S_{NM} solvates, can be explained by high anisotropy of the bulk magnetic susceptibility. The nature of the disorder was somewhat easier to resolve in the ^{15}N CPMAS spectra, where dynamic disorder in the S_{Me} and S_{Et} results a single sharp set of peaks for the droperidol nitrogen sites.

Variable-temperature ^{13}C and ^2H spectra and measurements of spin-lattice relaxation times allow the characterization of the solvent molecule dynamics in NSH , S_{Me} and S_{Et} . The motion of the alcohol molecules in S_{Me} and S_{Et} contains dynamics of relatively high-frequency (on the order of 10 s MHz to drive ^2H and ^{13}C T_1 relaxation), but of limited amplitude (given the minimal averaging of the ^2H quadrupolar parameters). The absence of well-defined T_1 minima suggests that this is a complex motion. The dynamics also includes components on the 10 s kHz frequency scale (observed via the ^{13}C spectra) and allows for occasional flipping over to the equivalent state related by the inversion symmetry, although the rate of this process cannot be estimated with any precision; the ^{15}N spectra set a lower limit of about 40 Hz at ambient temperature (corresponding to collapsing a frequency difference of about 1 ppm at 40.53 MHz ^{15}N Larmor frequency). The motion of the water molecules in NSH is also expected to be a composite motion, resulting in greater averaging of the NMR parameters than a simple C2 flip between equivalent positions, with an estimated C2 flip rate on the order of 10 s kHz in -45°C temperature, although an Arrhenius-type activation barrier of $E_a = 25 \pm 3 \text{ kJ mol}^{-1}$ could be estimated in this case.

The computational simulations help to rationalize these observations. There is little energy difference between initial and final states for inverting the orientation of the alcohol molecule in the S_{Me} and S_{Et} solvates. Although the barrier to inversion may be relatively high, this means that the solvent molecules appear to be disordered between the two symmetry-equivalent positions over the timescale of the XRD and NMR experiments. In contrast, the unfavourable energetics associated with adjacent acetonitrile and nitromethane molecules having opposite directions means that the S_{ACN} and S_{NM} are strongly ordered on the NMR and XRD timescales. These unfavourable energetics are mostly associated with solvent-solvent interaction energies.

Acknowledgments

This work was supported by the European Social Fund within the project "Support for Doctoral Studies at the University of Latvia" (No. 2009/0138/1DP/1.1.2.1.2/09/IPIA/VIAA/004). We thank David C. Apperley and A. Fraser Maxwell for recording ^{15}N CPMAS spectra and assistance.

Appendix A. Supporting information

Supplementary data associated with this article can be found in the online version at <http://dx.doi.org/10.1016/j.ssnmr.2014.09.001>.

References

- [1] C.P. Price, G.D. Glick, A.J. Matzger, *Angew. Chem. Int. Ed.* 45 (2006) 2062–2066.
- [2] A.L. Bingham, D.S. Hughes, M.B. Hursthouse, R.W. Lancaster, S. Tavener, T.L. Threlfall, *Chem. Commun.* (2001) 603–604.
- [3] L. Yu, G.A. Stephenson, C.A. Mitchell, C.A. Bunnell, S.V. Snorek, J.J. Bowyer, T.B. Borchardt, J.G. Stowell, S.R. Byrn, *J. Am. Chem. Soc.* 122 (2000) 585–591.
- [4] D.E. Braun, T. Gelbrich, V. Kahlenberg, R. Tessadri, J. Wieser, U.J. Griesser, *J. Pharm. Sci.* 98 (2009) 2010–2026.
- [5] J.B. Nanubolu, B. Sridhar, V.S.P. Babu, B. Jagadeesh, K. Ravikumar, *CrystEngComm* 14 (2012) 4677–4685.
- [6] U.J. Griesser, in: R. Hilfiker (Ed.), *Polymorphism in the Pharmaceutical Industry*, Wiley-VCH Verlag GmbH & Co. KGaA, Weinheim, 2006, pp. 211–233.
- [7] T. Hosokawa, S. Datta, A.R. Sheth, N.R. Brooks, V.G. Young Jr, D.J.W. Grant, *Cryst. Growth Des.* 4 (2004) 1195–1201.
- [8] R. Banerjee, P.M. Bhatt, G.R. Desiraju, *Cryst. Growth Des.* 6 (2006) 1468–1478.
- [9] N. Stieger, W. Liebenberg, J. Wessels, H. Samsodien, M. Caira, *Struct. Chem.* 21 (2010) 771–777.
- [10] N. Schultheiss, J.P. Smit, J.A. Hanco, *Eur. J. Pharm. Sci.* 38 (2009) 498–503.
- [11] D.E. Braun, T. Gelbrich, V. Kahlenberg, R. Tessadri, J. Wieser, U.J. Griesser, *Cryst. Growth Des.* 9 (2009) 1054–1065.
- [12] M.R. Caira, G. Bettinetti, M. Sorrenti, *J. Pharm. Sci.* 91 (2002) 467–481.
- [13] A. Othman, J.S.O. Evans, I.R. Evans, R.K. Harris, P. Hodgkinson, *J. Pharm. Sci.* 96 (2007) 1380–1397.
- [14] H. Mimura, S. Kitamura, T. Kitagawa, S. Kohda, *Colloids Surf. B* 26 (2002) 397–406.
- [15] B.J. Murphy, M.J. Casteel, B. Samas, J.F. Krzyzaniak, *J. Pharm. Sci.* 101 (2012) 1486–1495.
- [16] G. Stephenson, E. Groleau, R. Kleemann, W. Xu, D. Rigsbee, *J. Pharm. Sci.* 87 (1998) 536–542.
- [17] S. Byard, A. Abraham, P.J.T. Boulton, R.K. Harris, P. Hodgkinson, *J. Pharm. Sci.* 101 (2012) 176–186.
- [18] A. Actins, R. Arajs, S. Belakovs, L. Orola, M. Veidis, *J. Chem. Crystallogr.* 38 (2008) 169–174.
- [19] M. Azibi, M. Draguet-Brughmas, R. Bouche, *Pharm. Acta Helv.* 57 (1982) 182–188.
- [20] A. Berziņš, E. Skarbulis, T. Rekis, A. Actiņš, *Cryst. Growth Des.* 14 (2014) 2654–2664.
- [21] N.M. Blaton, O.M. Peeters, C.J. De Ranter, *Acta Crystallogr. Sect. B* 36 (1980) 2828–2830.
- [22] L. Orola, *Synthesis, structure and properties of crystalline forms of some active pharmaceutical ingredients (Ph.D. thesis)*, Riga Technical University, Riga, 2010.
- [23] C.L. Klein, J. Welch, L.C. Southall, *Acta Crystallogr. Sect. C* 45 (1989) 650–653.
- [24] F.G. Vogt, *Futur. Med. Chem.* 2 (2010) 915–921.
- [25] M. Geppi, G. Mollica, S. Borsacchi, C.A. Veracini, *Appl. Spectrosc. Rev.* 43 (2008) 202–302.
- [26] R.K. Harris, *J. Pharm. Pharmacol.* 59 (2007) 225–239.
- [27] R.K. Harris, *Analyst* 131 (2006) 351–373.
- [28] P.A. Tishmack, D.E. Bugay, S.R. Byrn, *J. Pharm. Sci.* 92 (2003) 441–474.
- [29] E. Carignani, S. Borsacchi, M. Geppi, *J. Phys. Chem. A* 115 (2011) 8783–8790.
- [30] D.C. Apperley, A.F. Markwell, I. Frantsuzov, A.J. Ilott, R.K. Harris, P. Hodgkinson, *Phys. Chem. Chem. Phys.* 15 (2013) 6422–6430.
- [31] P. Hodgkinson, in: R.K. Harris, R.E. Wasylshen, M.J. Duer (Eds.), *NMR Crystallography*, Wiley, Chichester, 2009.
- [32] F.G. Vogt, D.E. Cohen, J.D. Bowman, G.P. Spoons, G.E. Zuber, G.A. Trescher, P.C. Dell’Orco, L.M. Katrincic, C.W. DeBrosse, R. Curtis Haltiwanger, *J. Pharm. Sci.* 94 (2005) 651–665.
- [33] F.G. Vogt, R.C.B. Copley, R.L. Mueller, G.P. Spoons, T.N. Cacchio, R.A. Carlton, L.M. Katrincic, J.M. Kennady, S. Parsons, O.V. Chetina, *Cryst. Growth Des.* 10 (2010) 2713–2733.
- [34] R.K. Harris, P.Y. Ghi, H. Puschmann, D.C. Apperley, U.J. Griesser, R.B. Hammond, C. Ma, K.J. Roberts, G.J. Pearce, J.R. Yates, C.J. Pickard, *Org. Process Res. Dev.* 9 (2005) 902–910.
- [35] J. Ruiz, V. Rodriguez, N. Cutillas, A. Hoffmann, A.-C. Chamayou, K. Kazmierczak, C. Janiak, *CrystEngComm* 10 (2008) 1928–1938.
- [36] R.K. Harris, P. Hodgkinson, T. Larsson, A. Muruganatham, I. Ymén, D.S. Yufit, V. Zorin, *Cryst. Growth Des.* 8 (2008) 80–90.
- [37] D.C. Apperley, A.F. Markwell, R.K. Harris, P. Hodgkinson, *Magn. Reson. Chem.* 50 (2012) 680–690.
- [38] G.A. Stephenson, J.G. Stowell, P.H. Toma, D.E. Dorman, J.R. Greene, S.R. Byrn, *J. Am. Chem. Soc.* 116 (1994) 5766–5773.
- [39] F.G. Vogt, P.C. Dell’Orco, A.M. Diederich, Q. Su, J.L. Wood, G.E. Zuber, L.M. Katrincic, R.L. Mueller, D.J. Busby, C.W. DeBrosse, *J. Pharm. Biomed. Anal.* 40 (2006) 1080–1088.
- [40] R.L. Te, U.J. Griesser, K.R. Morris, S.R. Byrn, J.G. Stowell, *Cryst. Growth Des.* 3 (2003) 997–1004.
- [41] P. Chakravarty, R.T. Berendt, E.J. Munson, V.G. Young, R. Govindarajan, R. Suryanarayanan, *J. Pharm. Sci.* 99 (2010) 816–827.
- [42] F. Kang, F.G. Vogt, J. Brum, R. Forcino, R.C.B. Copley, G. Williams, R. Carlton, *Cryst. Growth Des.* 12 (2011) 60–74.
- [43] S.M. Reutzel, V.A. Russell, *J. Pharm. Sci.* 87 (1998) 1568–1571.
- [44] D.C. Apperley, P.A. Basford, C.I. Dallman, R.K. Harris, M. Kinns, P.V. Marshall, A.G. Swanson, *J. Pharm. Sci.* 94 (2005) 516–523.
- [45] A. Findlay, R.K. Harris, *J. Magn. Reson.* 87 (1990) 605–609.
- [46] V. Zorin, *Gsim – a visualisation and processing program for solid-state NMR*, URL: (<http://gsim.sourceforge.net>), 2013.
- [47] P. Hodgkinson, *pNMRsim: a general simulation program for large problems in solid-state NMR*, URL: (<http://www.dur.ac.uk/paul.hodgkinson/pNMRsim>), 2013.
- [48] C.J. Pickard, F. Mauri, *Phys. Rev. B* 63 (2001) 245101.
- [49] S.J. Clark, M.D. Segall, C.J. Pickard, P.J. Hasnip, M.I. Probert, K. Refson, M.C. Payne, *Z. Kristallogr.* 220 (2005) 567–570.
- [50] R.K. Harris, P. Hodgkinson, C.J. Pickard, J.R. Yates, V. Zorin, *Magn. Reson. Chem.* 45 (2007) S174–S186.
- [51] J.R. Yates, C.J. Pickard, F. Mauri, *Phys. Rev. B* 76 (2007) 024401.
- [52] J.P. Perdew, K. Burke, M. Ernzerhof, *Phys. Rev. Lett.* 77 (1996) 3865–3868.
- [53] A. Tkatchenko, M. Scheffler, *Phys. Rev. Lett.* 102 (2009) 073005.
- [54] M.J. Frisch, G.W. Trucks, H.B. Schlegel, G.E. Scuseria, M.A. Robb, J.R. Cheeseman, G. Scalmani, V. Barone, B. Mennucci, G.A. Petersson, H. Nakatsuji, M. Caricato, X. Li, H.P. Hratchian, A.F. Izmaylov, J. Bloino, G. Zheng, J.L. Sonnenberg, M. Hada, M. Ehara, K. Toyota, R. Fukuda, J. Hasegawa, M. Ishida, T. Nakajima, Y. Honda, O. Kitao, H. Nakai, T. Vreven, J.A.J. Montgomery, J.E. Peralta, F. Ogliaro, M. Bearpark, J.J. Heyd, E. Brothers, K.N. Kudin, V.N. Staroverov, R. Kobayashi, J. Normand, K. Raghavachari, A. Rendell, J.C. Burant, S.S. Iyengar, J. Tomasi, M. Cossi, N. Rega, J.M. Millam, M. Klene, J.E. Knox, J.B. Cross, V. Bakken, C. Adamo, J. Jaramillo, R. Gomperts, R.E. Stratmann, O. Yazyev, A.J. Austin, R. Cammi, C. Pomelli, J.W. Ochterski, R.L. Martin, K. Morokuma, V.G. Zakrzewski, G.A. Voth, P. Salvador, J.J. Dannenberg, S. Dapprich, A.D. Daniels, O. Farkas, J.B. Foresman, J.V. Ortiz, J. Cioslowski, D.J. Fox, Gaussian 09, Gaussian Inc., Wallingford, CT, 2009.
- [55] Y. Zhao, D. Truhlar, *Theor. Chem. Acc.* 120 (2008) 215–241.
- [56] M. Dračinský, P. Hodgkinson, *Chem. Eur. J.* 20 (2014) 2201–2207.
- [57] A.J. Robbins, W.T.K. Ng, D. Jochym, T.W. Keal, S.J. Clark, D.J. Tozer, P. Hodgkinson, *Phys. Chem. Chem. Phys.* 9 (2007) 2389–2396.
- [58] A.S. Tatton, T.N. Pham, F.G. Vogt, D. Iuga, A.J. Edwards, S.P. Brown, *Mol. Pharm.* 10 (2013) 999–1007.
- [59] W.P. Rothwell, J.S. Waugh, *J. Chem. Phys.* 74 (1981) 2721–2732.
- [60] A.J. Horsewill, *Prog. Nucl. Magn. Reson. Spectrosc.* 35 (1999) 359–389.
- [61] M. Dracinsky, P. Hodgkinson, *CrystEngComm* 15 (2013) 8705–8712.
- [62] R.R. Vold, in: R. Tycko (Ed.), *Nuclear Magnetic Resonance Probes of Molecular Dynamics*, 1994, pp. 27–112.
- [63] G. Soda, T. Chiba, *J. Chem. Phys.* 50 (1969) 439–455.
- [64] T. Chiba, G. Soda, *Bull. Chem. Soc. Jpn.* 44 (1971) 1703–1704.
- [65] N.H.M. Hogg, P.J.T. Boulton, V.E. Zorin, R.K. Harris, P. Hodgkinson, *Chem. Phys. Lett.* 475 (2009) 58–63.

Structural Characterization and Rationalization of Formation, Stability, and Transformations of Benperidol Solvates

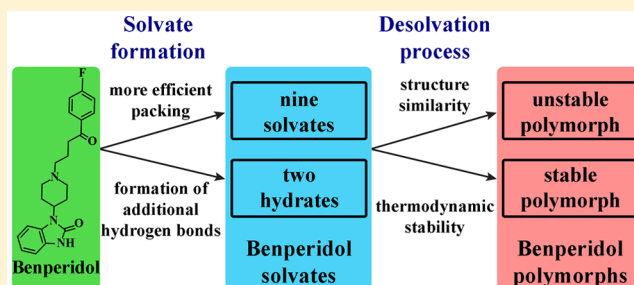
Agris Bērziņš,^{*,†,‡} Edgars Skarbulis,[†] and Andris Actiņš[‡]

[†]Faculty of Chemistry, University of Latvia, Kr. Valdemara 48, Riga, LV-1013, Latvia

[‡]Department of Chemistry, Durham University, South Road, Durham, U.K., DH1 3LE

Supporting Information

ABSTRACT: Experimental and theoretical characterization and studies of phase transitions and stability of the solvates obtained in solvate screening of the pharmaceutical compound benperidol were performed to rationalize and understand the solvate formation, stability, and phase transitions occurring during their desolvation. The solvate screening revealed that benperidol can form 11 solvates, including two sets of isostructural solvates. The analysis of the solvate crystal structures and molecular properties indicated that benperidol solvate formation is mainly driven by the complications during packing of benperidol molecules in an energetically efficient way in the absence of solvent molecules, as well as by the compensation of an insufficient number of hydrogen bond donor moieties. Analysis of solvate structures, particularly those of isostructural solvates, revealed that both the possible interactions and the size and shape of the solvent molecules were important factors in solvate formation. Stability of the solvate was proved to be associated with the intermolecular interaction energies in the crystal structure. Desolvation studies of benperidol solvates identified two forces determining the polymorph obtained after desolvation: structural similarity with the solvate and the thermodynamic stability.



1. INTRODUCTION

Benperidol, 1-[1-[4-(4-fluorophenyl)-4-oxobutyl]piperidin-4-yl]-1,3-dihydro-2H-benzimidazol-2-one (Figure 1), is an

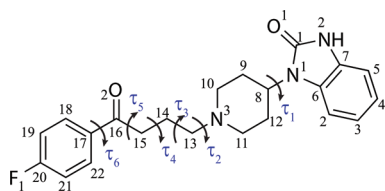


Figure 1. Molecular structure of benperidol with the numbering of non-hydrogen atoms and labeling of flexible dihedral angles.

antipsychotic, used for the treatment of schizophrenia and to control antisocial, hypersexual behavior. It is reported to exist in three polymorphic forms I–III, a dihydrate DH, and an ethanol solvate S_{Et}. These phases have been characterized by powder X-ray diffraction (PXRD) peak positions and melting points,¹ as well as by the IR spectra.² The crystal structure, however, has been reported only for polymorph I,³ which crystallizes in the R $\bar{3}$ space group with Z = 18.

Nevertheless, it has been shown that pharmaceutical molecules tend to form a range of different phases^{4,5} (up to 10 polymorphs^{6,7} and more than 100 solvates⁵), and a recent study of the similar molecule droperidol shows that it exists as four polymorphs and 11 solvates.⁸ Moreover, benperidol has

three strong hydrogen bond acceptors and only one hydrogen bond donor, suggesting it could be a promiscuous solvate former.⁹

Exploration of a solid form landscape is an essential step during the drug development process, as different polymorphs and, particularly, solvates have different stabilities,⁶ mechanical properties,^{10–12} and bioavailability (linked to the different solubility¹³), and such studies are needed to prevent unexpected solid form appearance after the approval of a drug.^{14,15}

The two main structural driving forces leading to the formation of solvates are⁴ (a) unsatisfied potential intermolecular interactions between the molecules, compensated by the incorporation of solvent molecules, the most typical scenario being a misbalance between the hydrogen bond donor and acceptor sites in the molecule,⁹ or (b) solvent inclusion in the crystal decreases the void space and/or leads to more efficient packing.¹⁶ Therefore, only in the first scenario the solvate selectivity is based on their functionality. However, most of the solvates include contributions from both of these driving forces, and the resulting effect for solvate formation is a lowering of the crystal free energy. This principle is well demonstrated by isostructural solvates, which can form only with solvents having

Received: January 31, 2015

Revised: April 13, 2015

Published: April 15, 2015

some specific interactions^{17,18} or molecular shapes,¹⁹ although it is common that such solvates form with different solvent molecules located in structural channels.^{20–22}

A predictable outcome of the desolvation process commonly is the formation of structurally similar nonsolvated phases,^{23–25} which then strongly suggests limited molecule rearrangements caused by the escape of the solvent molecules.^{26,27} However, quite often there is no structural similarity between the solvate and its desolvated form, especially if the solvent molecules have a crucial role in stabilization of the solvate structure,²⁸ and the desolvation results in recrystallization or melting of the desolvated structure.^{29,30}

As it has recently been shown, computational structure prediction tools are successful in the prediction of polymorphs and their relative stability,^{31–40} while the prediction of solvates and, especially, their stability is a lot more challenging and has been successful only for some relatively simple hydrate^{19,41–43} and solvate⁴⁴ systems. Currently, it would be the most reasonable to make solvate predictions based on the solvent and host properties and possible intermolecular interactions.^{45–47} In the recent literature, systematic and comprehensive studies of solvate formation^{8,45} and their properties^{22,48–50} have been reported for some pharmaceutical molecules. However, a general understanding of theoretical prediction of solvate formation based on the molecular structure and prediction of solvate properties based on the crystal structure data have not yet been achieved. Therefore, in this study we tried to understand and rationalize the formation, stability, and phase transformations of benperidol solvates using a comprehensive approach employing experimental, theoretical, and computational analysis of molecular and crystal structure properties. Benperidol was crystallized from solvents belonging to different solvent classes, the obtained solvates were characterized, and their crystal structures, as well as solvent and benperidol properties, were used to rationalize their formation. The desolvation process and products were rationalized based on crystal structure and relative stability of nonsolvated forms. Crystal structures of solvates were compared to rationalize the relative stability of solvates and the observed frequency of the solvate formation in the crystallization experiments. Such a study is a step forward to reaching a general understanding of the solvate formation and properties.

2. EXPERIMENTAL SECTION

2.1. Materials. Benperidol (purity > 99%) was obtained from JSC Grindeks (Riga, Latvia). The sample consisted of polymorph I. Inorganic compounds and organic solvents of analytical grade were purchased from commercial sources and used without further purification.

2.2. Preparation of Known Polymorphs and the Dihydrate. Benperidol polymorph I was prepared by recrystallization from isopropanol, preparing a saturated solution at 70 °C, and rapid cooling to –5 °C. Polymorph II was prepared by slowly evaporating benperidol solution in isopropanol at 50 °C. DH crystals were obtained when a similar volume of water was slowly added to benperidol solution in acetone, and the resulting solution was slowly evaporated at 50 °C. Powdered DH was obtained when benperidol solution in acetone or DMF was poured into a large amount of water, by stirring the obtained suspension.

2.3. Solvent-Based Polymorph and Solvate Screening. The most popular solvents chosen from different solvent classes^{51,52} (grouped according to physical and physicochemical properties) were selected for the crystallization of benperidol. Saturated or concentrated solutions of benperidol in all of the solvents were prepared at 40–120

°C, depending on the boiling point of the solvent (see Table S1, Supporting Information). The obtained solutions were then cooled down to –5 °C. In the cases when no crystallization was observed, the solutions were slowly evaporated at 40 or 50 °C, while preventing a complete evaporation. The obtained products were collected by filtration, air-dried, and characterized.

2.4. Preparation of Solvate Samples. For studying the phase transitions and desolvation kinetics, all solvates were prepared as in the solvate screening experiments by obtaining crystals or powders (for HH and S_{DIOX}). Alternatively, well-ground polymorph I was suspended for 24 h in the corresponding solvent at 50 °C, producing powdered S_{Et}, S_{Me}, and S_{ACN} solvate samples. Fast cooling of the ethanol and methanol solutions produced small solvate crystals (the size of at least one of the dimensions was below 100 μm), while slow evaporation of these solutions at 50 °C produced large crystals (the size of all of the dimensions was higher than 200 μm).

2.5. Study of Solvate Stability. Stability of the solvates was determined at ambient conditions, by storing the solvate sample in a desiccator over P₂O₅ at 30 °C, and at elevated temperatures by heating the samples in air thermostats. The heating temperature was selected based on the recorded differential thermal analysis/thermogravimetry (DTA/TG) curves. Phase transformations were identified using PXRD and, if necessary, DTA/TG as well.

2.6. Single Crystal X-ray Diffraction (SCXRD). The single-crystal X-ray diffraction data for benperidol polymorph II and solvates were collected at 173 K (100 K for S_{EtOAc}) on a Nonius Kappa CCD (Bruker) diffractometer, using Mo–K α radiation (graphite monochromator, $\lambda = 0.71073$ Å) and Oxford Cryostream (Oxford Cryosystems) open-flow nitrogen cryostat for sample temperature control. The structures were solved by direct method and refined by full-matrix least-squares on F² for all data using SHELX-2013 suite⁵³ and OLEX2⁵⁴ software. All nondisordered non-hydrogen atoms were refined anisotropically. For disordered ethyl acetate molecules, a fixed value of SOF = 0.5 was used.

The packing coefficients for crystal structures were calculated by PLATON.⁵⁵ Mercury 3.3 software⁵⁶ was used for crystal structure analysis and simulation of powder X-ray diffraction (PXRD) patterns based on crystal structure data.

2.7. Powder X-ray Diffraction. The PXRD patterns were measured at ambient temperature on a D8 Advance (Bruker) diffractometer using copper radiation (Cu K α) at the wavelength of 1.54180 Å, equipped with a LynxEye position sensitive detector. The tube voltage and current were set to 40 kV and 40 mA. The divergence slit was set at 0.6 mm, and the antiscatter slit was set at 8.0 mm. The diffraction patterns were recorded using a 0.2s/0.02° scanning speed from 3° to 35° on 2 θ scale. To prevent the atmospheric humidity effects and decomposition of the solvates, the samples were covered during the analysis with a 10 μm polyethylene film, when necessary.

For crystal structure determination, PXRD patterns were measured on a D8 Discover (Bruker) diffractometer at transmission geometry using Göbel Mirrors and a capillary sample stage. Other settings and equipment were identical to those used for D8 Advance. Samples were sealed in rotating (60 rpm) borosilicate glass capillaries of 0.5 mm outer diameter (Hilgenberg glass No. 10), and data were collected using 22s/0.01° (III), 25s/0.01° (S_{Benz}), or 36s/0.01° (HH) scanning speed from 2.5° (S_{Benz}) or 4.5° (III and HH) to 70° on 2 θ scale.

2.8. Crystal Structure Determination from PXRD Data. The PXRD patterns were indexed for the first 20–25 peaks, using DICVOL04⁵⁷ (implemented in WinPLOTR software⁵⁸) and SVD indexing algorithms⁵⁹ (implemented in TOPAS v4.2). Space group determination was carried out using a statistical assessment of systematic absences, and Z' was determined based on density considerations. Structure solutions were performed by Monte Carlo/Simulated annealing technique implemented in Expo2014,^{60,61} using a rigid model, flexible about the dihedral angles τ_{1-6} and τ_{Benz1} and τ_{Benz2} (Figure S7, Supporting Information) for benzyl alcohol molecule by also determining the center of mass location and molecular orientation. The initial geometries of benperidol molecule as in crystal structures of polymorph I (for S_{Benz}) and S_{ACN} (for HH and III) were used. For the structure of HH, oxygen atoms of water

molecules were kept in the special positions, and the initial unit cell with water molecules was taken from the CSD (refcode AMCHCA⁶²). The initial geometry of benzyl alcohol molecule was taken from the CSD (refcode FEBCUL⁶³). The final refinements were carried out by the Rietveld method, maintaining the rigid bodies introduced at the structure solution stage. The background was modeled by a 20th-order polynomial function of the Chebyshev type; peak profiles were described by the Pearson VII function, and a common (refinable) isotropic thermal factor was attributed to all non-hydrogen atoms, while that of hydrogen atoms was assumed to be 1.2 times higher.

2.9. Differential Thermal Analysis/Thermogravimetry (DTA/TG). The DTA/TG analysis was performed with Exstar6000 TG/DTA6300 (SII). Open aluminum pans were used. Heating of the samples from 30 to 180 °C was performed at a 5 °·min⁻¹ heating rate. Samples of 5–10 mg mass were used, and the nitrogen flow rate was 100 ± 10 mL·min⁻¹.

2.10. Karl Fischer Titration. A 836 Titrando (Metrohm) Karl Fischer volumetric titrator was used for the determination of water content in the samples. Approximately 100–200 mg portions of each sample were weighed on an analytical balance (*d* = 0.1 mg) and titrated with Hydranal Composite 5 (Fluka).

2.11. Fourier Transform (FTIR) Infrared Spectroscopy. The ATR-FTIR spectra were collected for neat solids on a Frontier FTIR (PerkinElmer) spectrometer equipped with a Universal ATR Sampling Accessory with a diamond window. The spectra were recorded from 650 to 4000 cm⁻¹ at a 2 cm⁻¹ spectral resolution with 16 scans.

2.12. Theoretical Calculations. The geometry optimization was performed in CASTEP⁶⁴ using the PBE⁶⁵ functional and on-the-fly generated ultrasoft pseudopotentials and a cutoff energy of 600 eV (where the lattice parameters and the atom positions were relaxed) or 300 eV (where only the atom positions were relaxed). The Tkatchenko–Scheffler dispersion correction scheme⁶⁶ was used. For these calculations, a structure of S_{EtOAc} with one of the possible solvent orientations was used, thus creating a structure in the P1 space group with two symmetrically individual benperidol molecules.

The lattice energy calculations were performed using semiempirical PIXEL⁶⁷ methodology and classical atom–atom Coulomb–London–Pauli (CLP) model,⁶⁷ both developed by Gavezzotti. Crystal structures were used after geometry optimization in CASTEP.

The interaction energies between pairs of molecules were calculated in Gaussian 09⁶⁸ using the M06-2X⁶⁹ functional and 6-311G(d,p) basis set to molecular geometries directly extracted from the crystal structures after the geometry optimization in CASTEP. The basis set superposition error was corrected using the counterpoise method. The interaction energy was calculated as the difference between the total energy of the dimer and the corresponding isolated molecules. The total interaction energy values were calculated as a sum of all pairwise interaction energies (without the correction for double counting of identical interactions) for molecule pairs having contacts shorter than the given cutoff distance, see Table 5.

The molecular volumes of selected solvent molecules were calculated in Gaussian 09⁶⁸ after the geometry optimization at the B3LYP/6-311G(d,p) level using Grimme's dispersion correction.⁷⁰

Simulation of IR spectra was performed by extracting a characteristic molecular fragment representing the intermolecular interactions (amide homodimers for **II** and S_{ACN}, a ring of six benperidol molecules for **I**, a chain consisting of three benperidol and two alcohol molecules for S_{Me} and S_{Benz}, and a fragment of three benperidol and one water molecule for **HH**). Geometry optimization and frequency calculation were performed at the PM6 level, and the obtained frequencies were multiplied by a scale factor of 0.953.⁷¹

3. RESULTS AND DISCUSSION

3.1. Crystallization. Benperidol was crystallized from a range of solvents selected to represent different solvent classes based on classification according to statistical analysis of four molecular descriptors,⁵¹ as well as hydrogen bond acceptor and donor propensity, polarity/dipolarity, dipole moment, and dielectric constant.⁵² In these experiments no new benperidol

polymorphs were obtained; see Table S1, Supporting Information. Moreover, in our experiments it was not possible to obtain polymorph **III** from *n*-heptane as described in the literature¹ nor from any other solvent. From most of the solvents, polymorph **I** was obtained. In accordance to previous studies,^{1,2} it was possible to crystallize polymorph **II** from isopropanol. However, the precipitation of the solid product from isopropanol usually initiated shortly after cooling the solution, and polymorph **I** was obtained instead.

Nevertheless, besides the already reported solvates **DH** and S_{Et},^{1,2} nine new solvates were obtained in crystallization experiments from methanol, acetonitrile, ethyl acetate, nitromethane, 1,4-dioxane, toluene/*o*-xylene, benzyl alcohol, carbon tetrachloride, and chloroform (labeled as S_{Me}, S_{ACN}, S_{EtOAc}, S_{NM}, S_{DIOX}, **HH**, S_{Benz}, S_{TCC}, and S_{CLF}, respectively). In this study, the first seven of these solvates, as well as the poorly explored solvated forms S_{Et} and **DH** were characterized using PXRD patterns, DTA/TG analysis, and IR spectra, while their desolvation products were also identified, and the desolvation process was characterized. Preparation of solvates S_{TCC} and S_{CLF} was complicated by the formation of side-products and poor reproducibility, so these solvates were characterized only using PXRD and DTA/TG analysis. Crystals suitable for SCXRD measurements were obtained for polymorph **II** and solvates **DH**, S_{Et}, S_{Me}, S_{ACN}, and S_{EtOAc}. Additionally, attempts were made to solve the crystal structures of the rest of the phases by using the recorded PXRD patterns, with success for **HH**, S_{Benz}, and the polymorph **III**.

3.2. X-ray Diffraction and Thermal Characterization of Benperidol Solvates. PXRD patterns of all the obtained solvated forms are given in Figure 2.

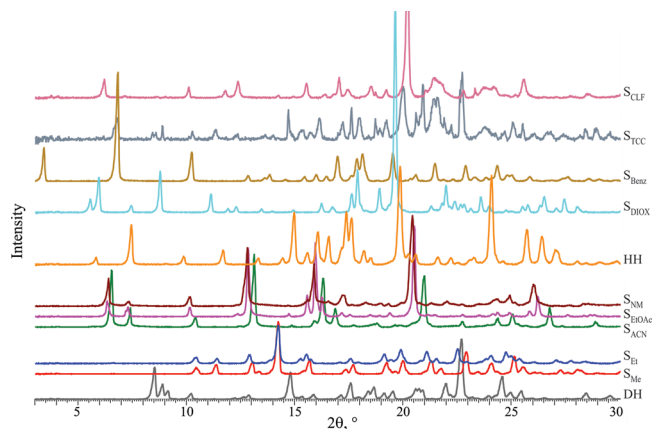


Figure 2. PXRD patterns of the benperidol solvates.

It can be seen that the diffraction peak positions of solvates S_{Me} and S_{Et} were very similar. The same was found also for solvates S_{ACN}, S_{EtOAc}, and S_{NM}. These similarities suggest the formation of two sets of benperidol isostructural solvates: type 1 solvates (S_{Me} and S_{Et}) and type 2 solvates (S_{ACN}, S_{EtOAc}, and S_{NM}). The PXRD patterns of **HH**, S_{Benz}, S_{DIOX}, and S_{TCC}, however, exhibited different characteristic features, which also differed from those in PXRD patterns of all other known benperidol forms. The PXRD pattern of S_{CLF}, however, was similar to that of type 2 solvates, suggesting that this solvate probably also belongs to this type, although the poor quality of the pattern did not allow us to draw an absolute conclusion.

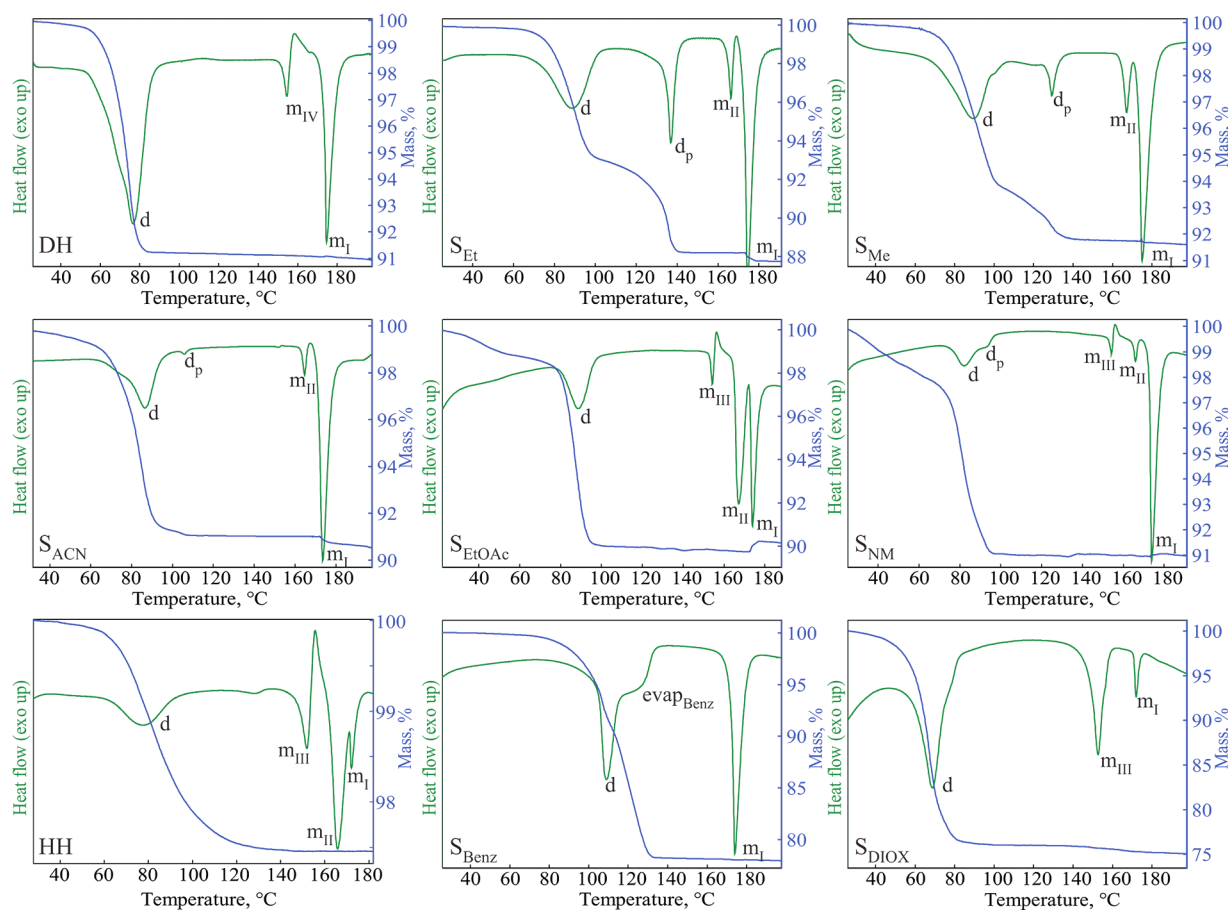


Figure 3. DTA and TG curves of benperidol solvates. d – desolvation, d_p – peritectic desolvation and/or melting, m_{I-IV} – melting of polymorphs I–IV, and $evap_{Benz}$ – evaporation of benzyl alcohol.

Table 1. Weight Loss Observed during the Desolvation of Benperidol Solvates and the Obtained Desolvation Products

solvate	ratio	calculated weight loss, %	observed weight loss, %	$T_{desolvation}$, °C (peak)	resulting phase
DH	1:2	8.6	8.8 (9.0) ^a	77	(V, IV)/(II, I) ^c
S _{Me}	1:1	7.8	7.9	89, 129 ^b	II/I ^c
S _{Et}	1:1	10.8	11.6	87, 137 ^b	
S _{ACN}	1:1	9.7	8.1–9.5 ^d	86, 106 ^b	III/I ^c
S _{NM}	1:0.5	7.4	6.9–9.0 ^d	82, ~95 ^b	
S _{EtOAc}	1:0.5	10.4	8.5–9.8 ^d	88	
HH	1:0.5	2.3	2.0–2.5 (2.1) ^a	89	III/I ^c
S _{Benz}	1:1	22.1	21.8	109	I
S _{DIOX}	1:1.5	25.7	24.5	69	III/I ^c
S _{TCC}	1:1	16.8	16–22	66, 88	IV, V, II, I
S _{CLF}	1:0.5	13.5	10–17	76	III/I

^aThe water content determined by Karl Fischer titration is given in parentheses. ^bThe second value is peritectic decomposition and/or melting temperature. ^cSee discussion in Section 3.5. ^dThe first number is the weight loss after the appearance of the desolvation peak in the DTA, and the second number is the total weight loss.

The DTA/TG curves of the benperidol solvates are shown in Figure 3. Although this method allowed us to confirm S_{TCC} and S_{CLF} as solvates, the obtained curves cannot be assured to be characteristic for pure phases. Nevertheless, for informative purposes they are given in Figure S1, Supporting Information.

The desolvation of DH and HH appeared to be a simple one-step process with a characteristic desolvation endothermic peak associated with the weight loss. The curves of other solvates, however, showed a complex desolvation process. Type 1 and type 2 solvates usually showed two endothermic peaks associated with the weight loss (with larger particle size and

faster heating rate increasing the contribution of the second peak; see Section 3.5). This suggests that the desolvation occurred in two stages, or other complications were encountered during the desolvation. It was shown that the second desolvation peak corresponded to peritectic desolvation and/or melting; see Section 3.5. Although the desolvation of S_{Benz} most probably was also a one-step process, it appeared to be complicated by the difficult evaporation of benzyl alcohol ($T_b = 205.3$ °C).

Desolvation products of the solvates were analyzed using PXRD and are given in Table 1.

Table 2. Crystallographic Data for the Benperidol Phases II, DH, S_{EP}, S_{Me}, S_{ACN}, S_{EtOAc}, HH, S_{Benz} and III

solvent	II	DH	S _{Et}	S _{Me}	S _{ACN}	S _{EtOAc}	HH	S _{Benz}	III
empirical formula	C ₂₂ H ₂₄ FN ₃ O ₂	C ₂₂ H ₂₄ FN ₃ O ₂ · 2H ₂ O	C ₂₂ H ₂₄ FN ₃ O ₂ · C ₃ H ₆ O	C ₂₂ H ₂₄ FN ₃ O ₂ · CH ₄ O	C ₂₂ H ₂₄ FN ₃ O ₂ · C ₃ H ₅ N	C ₂₂ H ₂₄ FN ₃ O ₂ · 0.5C ₄ H ₈ O ₂	C ₂₂ H ₂₄ FN ₃ O ₂ · 0.5H ₂ O	C ₂₂ H ₂₄ FN ₃ O ₂ · C ₂ H ₆ O	C ₂₂ H ₂₄ FN ₃ O ₂
M _r	381.44	417.48	427.51	413.48	422.49	425.49	390.45	489.58	381.44
crystal system	triclinic	monoclinic	monoclinic	monoclinic	triclinic	triclinic	monoclinic	orthorhombic	triclinic
space group	P $\bar{1}$	P2 ₁ /n	P2 ₁ /c	P2 ₁ /c	P $\bar{1}$	P $\bar{1}$	C2/c	Pbca	P $\bar{1}$
a (Å)	10.8417(3)	11.0595(3)	15.0684(3)	15.1097(4)	5.56500(10)	5.4228(3)	36.7342(7)	13.7193(4)	15.61501(10)
b (Å)	16.2903(4)	9.3896(2)	10.8602(3)	10.7200(3)	14.1256(4)	14.6014(8)	5.58581(10)	51.6467(20)	11.48189(8)
c (Å)	17.9497(5)	20.4456(6)	15.2555(4)	15.3070(5)	15.0478(5)	14.8045(10)	23.6629(5)	7.43071(20)	5.45694(30)
α (deg)	66.7233(11)	90	90	90	109.2583(13)	109.936(3)	90	90	86.627(3)
β (deg)	87.0069(10)	91.7206(11)	117.6353(9)	119.3538(13)	90.9875(13)	90.199(2)	124.8680(8)	90	96.618(6)
γ (deg)	85.0074(16)	90	90	90	100.071(2)	100.322(3)	90	90	94.435(5)
V (Å ³)	2900.55(13)	2122.20(10)	2211.69(9)	2161.04(11)	1095.91(5)	1081.50(11)	3983.71(14)	5265.07(30)	967.71(6)
Z/Z'	6/3	4/1	4/1	4/1	2/1	2/1	8/1	8/1	2/1
T, K	173(2)	173(2)	173(2)	173(2)	173(2)	100(2)	298(3)	298(3)	298(3)
wR (all data)	0.1616	0.196	0.1415	0.1997	0.1126	0.1992			
final R (I > 2σ) ^a	0.0765	0.048	0.0543	0.0644	0.0460	0.0751			
GOF	1.013	1.243	1.028	0.972	1.018	1.030			
R _{wp}							0.02897	0.03356	0.03686
R _p							0.01721	0.02427	0.0243
R _{exp}							0.00520	0.00734	0.00816
packing coef	0.682	0.689	0.684	0.672	0.681	0.690	0.675	0.651	0.681

^aFor the DH form I > 3σ.

Besides the polymorphs **I** and **II** obtained in the crystallization, desolvation of type 2 solvates, **HH**, **S_{DIOX}**, and **S_{CLF}** produced the polymorph **III** described in the literature,¹ whereas the desolvation of **DH** produced new polymorphs **IV** and **V**. The PXRD patterns of benperidol polymorphs are given in Figure S2, while the DTA curves are given in Figure S3, Supporting Information.

Therefore, the existence of polymorph **III** as described in the literature¹ has been confirmed,² although it is not clear whether it is possible to obtain it as described,¹ because in our study it was obtained only in the desolvation process.

The stoichiometry of the solvates was calculated from the weight loss in TG curves. The **DH** phase was confirmed to be a dihydrate, whereas **S_{Et}** was determined to be an ethanol monosolvate, in contrast to the reported ethanol disolvate stoichiometry.¹ With regard to the isostructural type 2 solvates, the **S_{ACN}** phase was monosolvate, whereas **S_{NM}** and **S_{EtOAc}** appeared to be hemisolvates. Both TG and KF titration confirmed that **HH** is a hemihydrate. Repeated measurements suggested that **S_{DIOX}** is a sesquisolvate, although this should be interpreted cautiously.

Crystal structures of benperidol polymorph **II**, and solvates **DH**, **S_{Et}**, **S_{Me}**, **S_{ACN}**, and **S_{EtOAc}** were determined from SCXRD measurements at 173 or 100 K (**S_{EtOAc}**), while those of polymorph **III**, as well as solvates **HH** and **S_{Benz}** were determined from PXRD data collected in transmission mode at ambient temperature. The obtained crystallographic data are given in Table 2. An overlay of the experimental data and PXRD patterns simulated from crystal structure data (see Figure S8, Supporting Information) confirmed the identity of the polycrystalline phases. The correctness of the structures calculated from PXRD patterns was confirmed by the good agreement between experimental and calculated diffraction patterns (see Figure 4), as well as by the geometry optimization in CASTEP introducing only small changes in the crystal structure (see Figure S9, Supporting Information). Polymorphs **II** and **III** crystallized in the space group $P\bar{1}$ with three molecules or one molecule in the asymmetric unit, respectively. The **DH** form crystallized in the $P2_1/n$ space group, **S_{Et}** and **S_{Me}** were isostructural and crystallized in the $P2_1/c$ space group, **S_{ACN}** and **S_{EtOAc}** were isostructural and crystallized in the $P\bar{1}$ space group, **HH** crystallized in the $C2/c$ space group, and **S_{Benz}** crystallized in the $Pbca$ space group. The asymmetric units of all solvated forms contained one benperidol molecule and two (**DH**), one (**S_{Me}**, **S_{Et}**, **S_{ACN}**, and **S_{Benz}**), or one-half (**HH** and **S_{EtOAc}**) solvent molecules. In the **HH** form, the oxygen atom of water molecule was at a special position, and the ethyl acetate molecule in **S_{EtOAc}** was disordered over two symmetrically related positions. The solvent stoichiometry determined from this analysis was consistent with that determined from TG analysis.

3.3. Characterization of Benperidol Solvate Crystal Structures. Analysis of the crystal structures revealed that the conformation differences appear as different values of the dihedral angles τ_1 – τ_6 , although the oxobutyl side chain (τ_3 – τ_6) tends to be linear. Interestingly, molecular conformation of benperidol in polymorphs **I** and **III**, as well as that in all of its solvates, is quite similar, but different from all three benperidol molecules in the polymorph **II**, with the most apparent difference observed for the value of τ_1 (see Figure 5a and Table 3). The molecular conformation of all three symmetrically independent molecules in **II** (designated as A, B, and C) was different, with slight variations in the conformations of A and C,

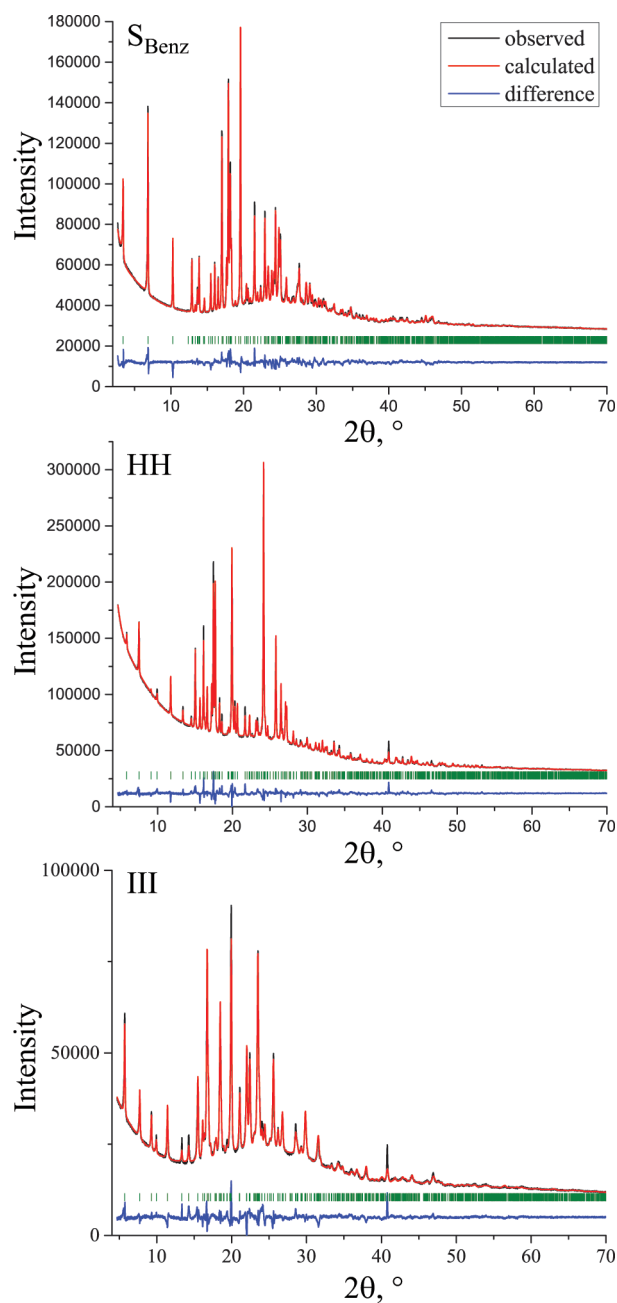


Figure 4. Experimental (black), calculated (red), and difference (dark blue) PXRD profiles from the final Rietveld refinement of various benperidol forms.

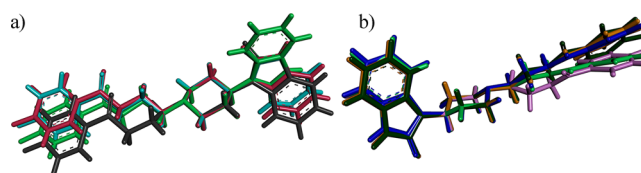


Figure 5. An overlay of benperidol molecules in (a) polymorphs (**I**: green, **II_A**: red, **II_B**: dark gray, **II_C**: cyan), (b) solvates (**DH**: dark blue, **S_{Et}**: dark green, **S_{ACN}**: orange, **S_{Benz}**: pink) and polymorph **I** (green).

and significant variations in the dihedral angles τ_2 and τ_4 for molecule B. As already mentioned, besides the identical conformations observed in the isostructural solvates **S_{Me}** and **S_{Et}** as well as in **S_{ACN}** and **S_{EtOAc}**, the conformations of all

Table 3. Dihedral Angles (in Degrees) of Benperidol in Its Polymorphs and Solvates

	I ³	II _A	II _B	II _C	DH	S _{Et}	S _{ACN}	HH	S _{Benz}	III
τ_1	-124.03	74.00	92.67	64.60	-108.82	-108.29	-113.17	-114.21	-123.07	-108.93
τ_2	-60.75	-157.37	-68.78	-156.47	-60.65	-72.75	-71.46	-72.09	-21.19	-75.32
τ_3	-172.82	175.51	-177.09	-177.98	-167.59	-176.74	-169.39	-148.24	-165.54	-162.38
τ_4	-166.14	171.94	74.07	175.18	-175.91	-179.91	-174.13	-152.45	138.78	-165.18
τ_5	-176.79	-179.31	-172.78	-173.37	179.6	-179.58	-175.07	163.25	172.75	177.45
τ_6	-177.47	155.52	161.46	-177.79	-178.83	178.82	-178.18	169.07	-149.71	170.13

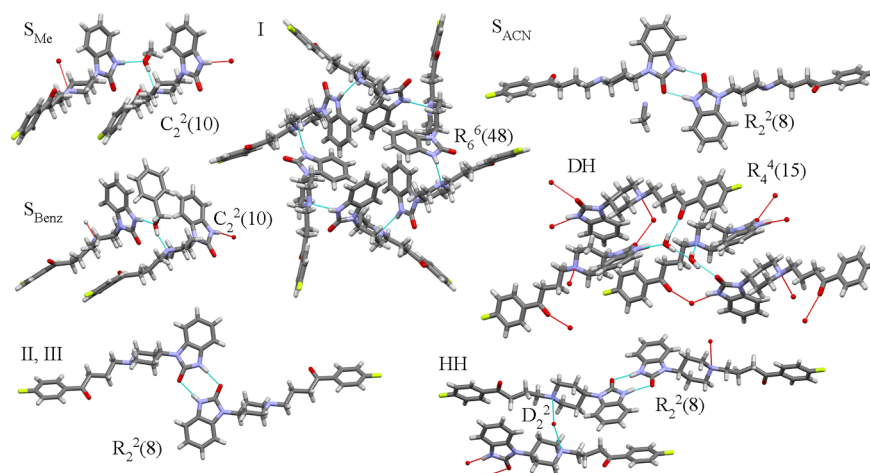


Figure 6. Hydrogen bond patterns observed in crystal forms of benperidol.

Table 4. Geometrical Parameters of the Strong Hydrogen Bonds in Benperidol Polymorphs and Solvates

Phase	Interaction	Distance, Å			D-H...A, °	Graph set
		X-H	H...A	D...A		
I ³	N2-H...N3			2.883		R ₆ ⁶ (48)
II	N2A-H...O1A	0.86	1.96	2.800(3)	165	R ₂ ² (8)
	N2B-H...O1C	0.86	1.95	2.779(3)	161	R ₂ ² (8)
	N2C-H...O1B	0.86	2.03	2.881(3)	171	R ₂ ² (8)
III	N2-H...O1	0.91	1.97	2.866(9)	167	R ₂ ² (8)
S _{Me}	N2-H...O3	0.86	1.97	2.783(3)	157	C ₂ ² (10)
	O3-H...N3	0.82	2.00	2.806(3)	169	
S _{Et}	N2-H...O3	0.90	1.91	2.7872(19)	164	C ₂ ² (10)
	O3-H...N3	0.82	1.98	2.7931(19)	175	
S _{Benz}	N2-H...O3	0.86	1.99	2.841(7)	169	C ₂ ² (10)
	O3-H...N3	0.90	1.75	2.625(8)	162	
S _{ACN}	N2-H...O1	0.89	1.91	2.7978(16)	177	R ₂ ² (8)
S _{EtOAc}	N2-H...O1	0.86	1.93	2.776(4)	172	R ₂ ² (8)
DH	O4-H...O3	0.92	1.85	2.7271(19)	159	} R ₄ ⁴ (15)
	O4-H...O2	0.85	2.02	2.8597(19)	168	
	N2-H...O4	0.97	1.86	2.7629(18)	153	
	O3-H...O1	0.9	1.98	2.8385(17)	159	
	O3-H...N3	0.87	1.95	2.8122(18)	174	
HH	N2-H...O1	0.90	1.90	2.787(8)	165	R ₂ ² (8)
	O3-H...N3			3.005(15)		D ₂ ²

solvates and polymorph III were nearly identical, with the exception of S_{Benz}, which had a noticeable deviation of the dihedral angles τ_2 and τ_4 (see Figure 5b and Table 3). It should, however, be mentioned that the geometry optimization in CASTEP changed the geometry of oxobutyl side chain by making it more similar to that in the rest of the solvates.

Therefore, the overall conformation differences of benperidol were small if compared to other molecules with similar conformational degrees of freedom,^{72,73} and the observed structural diversity resulted from different intermolecular interaction possibilities producing different molecular packing.

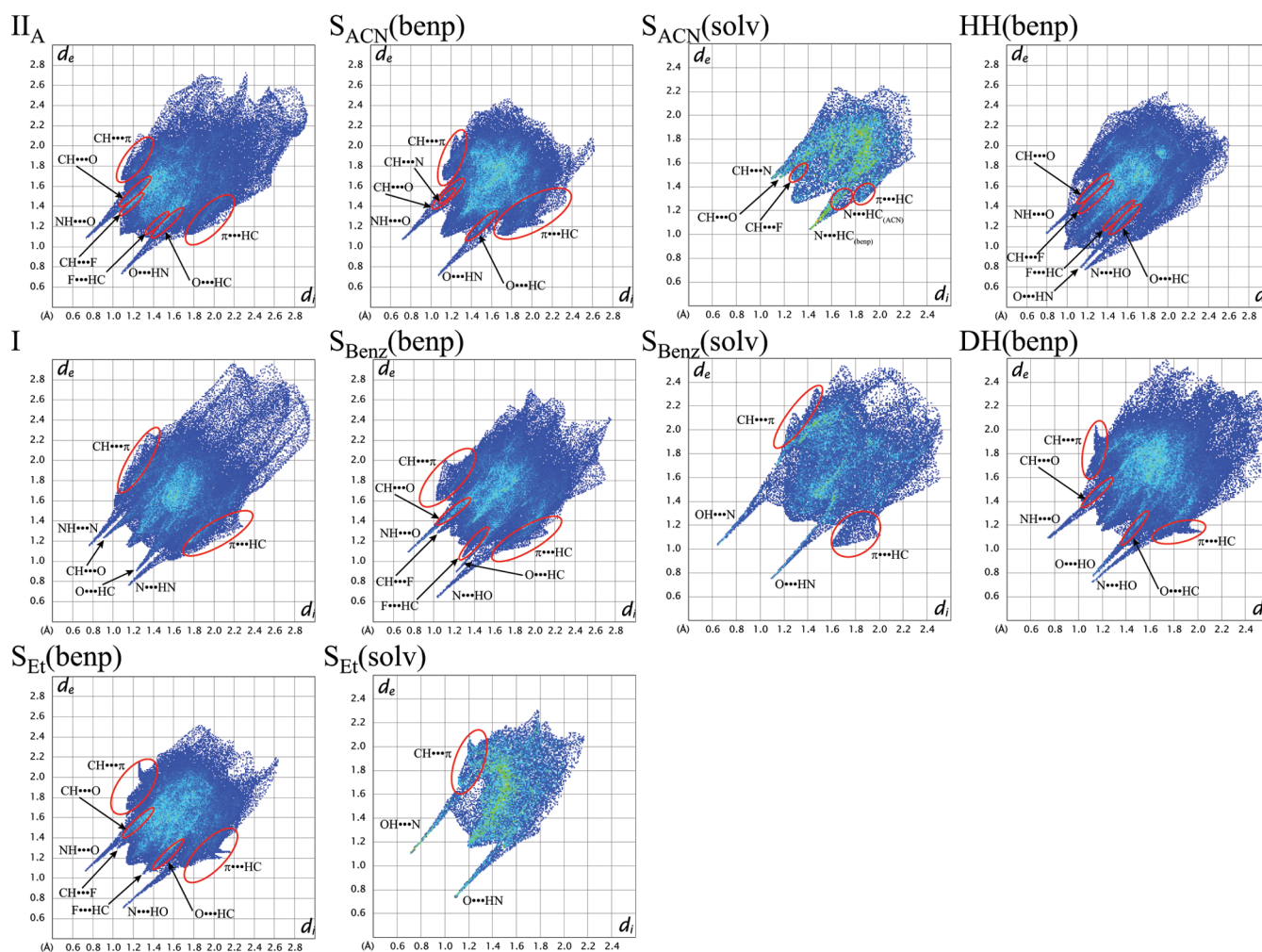


Figure 7. 2D fingerprint plots of Hirshfeld surfaces for selected molecules in benperidol polymorphs and solvates (the remaining plots are given in the Supporting Information).

The analysis of the strong hydrogen bonding pattern showed that benperidol molecules in the polymorph I formed N2–H...N3 bonds creating a ring of six molecules characterized by $R_6^2(48)$ graph set, whereas all three molecules in II formed amide homodimers linked by N2–H...O1 bonds and characterized by $R_2^2(8)$ graph set (see Figure 6 and Table 4). However, the observed conformation differences in benperidol polymorphs could not be purely associated with the difference in strong hydrogen bonds, as benperidol molecules were arranged in amide homodimers also in the form III. Nevertheless, other intermolecular interactions in this form were completely different from those in both II and I (see Table S4, Supporting Information).

Although the incorporation of proton donating alcohol molecules in the crystal lattice can provide a possibility for the formation of additional strong hydrogen bonds, only one hydrogen bond acceptor N3 in both type 1 solvates and in S_{Benz} is employed in similar hydrogen bonding connection with N2–H as observed in form I, with alcohol O–H group inserted between the benperidol molecules, and therefore creating two strong hydrogen bonds. However, infinite hydrogen bonded chains $C_2^2(10)$ are formed in these structures. The alcohol molecules in these solvates are positioned in structural voids which can be joined in zigzag-shaped channels. However, the diameter of the channel in the narrowest place is smaller than

that of the solvent molecules, and alcohol molecules are involved in the formation of the main hydrogen bonding pattern, so these solvates cannot be classified as channel solvates.

In the HH and DH forms, however, the presence of the water molecules provided for the formation of one additional hydrogen bond in HH by employing an additional hydrogen bond acceptor of benperidol molecule, and an efficient hydrogen bonding in DH by employing all hydrogen bond acceptors of benperidol. In the HH form, benperidol molecules existed as amide homodimers, whereas in the DH form benperidol molecules were linked to each other by strong hydrogen bonds via water molecules, and directly interacted only by weak interactions. In these structures, the water molecules were situated in isolated structural cavities, so both the hydrates were isolated site hydrates.

The insertion of acetonitrile and ethyl acetate molecules, however, could not provide a basis for the emergence of additional strong hydrogen bonds. Also, benperidol molecules in type 2 solvates formed amide homodimers characterized by $R_2^2(8)$ graph set. The solvent molecules were located in structural channels and interacted with benperidol molecules only by weak hydrogen bonds (see Table S4, Supporting Information) and dispersion forces. The type 2 solvates thus were typical channel solvates. As ethyl acetate ($81.4 \text{ cm}^3 \cdot \text{mol}^{-1}$)

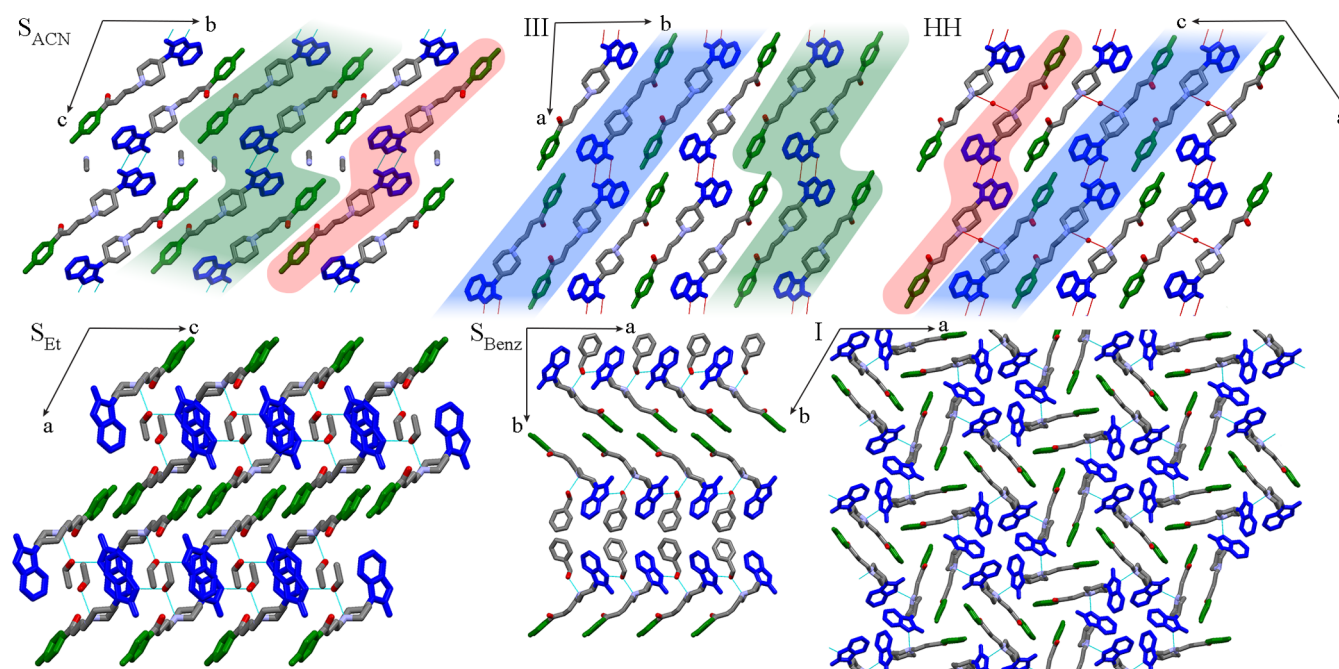


Figure 8. Molecular packing in benperidol polymorphs and solvates. Benzimidazolone moiety is in blue, and fluorophenyl moiety is in green. Green, blue, and red layers represent identical supramolecular constructs identified in the crystal structures. Hydrogen atoms have been omitted for clarity.

molecules are much larger than acetonitrile ($37.9 \text{ cm}^3 \cdot \text{mol}^{-1}$) molecules, the size of the channel apparently is too small to accommodate 1 equiv of ethyl acetate, explaining the different stoichiometry observed in type 2 solvates. Ethyl acetate molecules, however, did not occupy the two adjacent solvent sites in one channel but rather two sites from the nearby partially connected channels; see Figure S18, Supporting Information. Interestingly, the molecular size calculation and computational simulation showed that the crystal structure of S_{NM} should be identical to that of S_{ACN} with monosolvate stoichiometry (see Supporting Information). This could be explained by a partial desolvation before the experiment, which is supported by the slow desolvation at the beginning of the TG curve for type 2 solvates (particularly for S_{NM} , see Figure 3) and can be explained by the fact that solvent molecules are located in the channel and their escape is therefore relatively easy.

A more detailed comparison of the intermolecular interactions was performed through the analysis of weak interactions and 2D fingerprint plots of Hirshfeld surfaces, which summarized the information about intermolecular interactions.^{74,75} The program Crystal Explorer 3.1⁷⁶ was used for calculations; see Figure 7, Table S4, and Figures S13–S16, Supporting Information. Overall, weak hydrogen bonds were the most typical weak intermolecular interactions in crystal structures of benperidol forms, and mostly were formed by O2 (in all structures except type 1 solvates and DH), O1 (in I, type 1 solvates, II, S_{Benz} , and DH), and F1 (in II, III, type 1 solvates, S_{Benz} , and HH), while not by N3 (probably because of the shape and packing of the molecules). In the crystal structure of I, II, DH, and S_{Benz} a noticeable role was played also by other weak interactions (mainly $\text{CH} \cdots \pi$). In the Hirshfeld surface fingerprint plots, a similarity was observed between the benperidol molecules forming amide homodimers in II, III, type 2 solvates, and HH (except for the spike associated with the O3–H \cdots N3 bond). The plot of S_{Benz} is different from those of type 1 solvates, clearly identifying structural differences, whereas it is similar to that of polymorph I, suggesting a

structural similarity with it. The structural similarity between I and S_{Benz} is also identified from the presence of similar weak intermolecular interactions. Because of the dominance of strong hydrogen bonding pattern involving water molecules in DH, its plot completely differs from that of all other phases.

Interestingly, a common feature of the fingerprint plots of polymorphs I and II is the presence of a number of longer contacts (notice the points at high d_i and d_e values in Figure 7) if compared to the solvates, indicating less efficient packing. This is also supported by the presence of small structural voids (2.2% and 1.4% of the volume, respectively, but too small to accommodate residual solvent molecules) in the structure of both of these polymorphs, as determined using PLATON and visualized in Mercury (see Figure S17, Supporting Information).

Analysis of the molecular packing was performed in Mercury and using XPac code.^{77,78} It was determined that the only forms showing clear similarity of molecular packing (except for the isostructural solvates) were III with HH and type 2 solvates, in which the benperidol molecules were packed in a similar manner (see Figure 8) by forming identical 2D supramolecular constructs—infinite layers of molecules parallel to (110) in III, (011) in type 2 solvates, and (201) in HH; see blue and green layers in Figure 8. The similarity of HH and type 2 solvates, however, is lower, and only identical 1D supramolecular construct (finite layers formed from amide homodimers as shown with red in Figure 8) was identified because of the presence of solvent molecules distorting the molecular packing. Similarly formed hydrogen bonded molecular chains forming similar double layers were observed also in all alcohol solvates, with small differences due to different molecular conformations. However, these double layers were stacked differently in S_{Benz} , therefore making these structures different from those of type 1 solvates. Despite the similarity of intermolecular interactions and Hirshfeld surfaces when comparing I and S_{Benz} , no obvious similarity in the molecular packing of these two forms could be identified. All other benperidol forms did not show identifiable

packing similarities; see Figures 8 and S19, Supporting Information.

Interestingly, it was noticed that benperidol molecule layers could be identified in all solvated forms, whereas molecular packing of the two stable polymorphs I and II was more complex.

3.4. Fourier-Transform Infrared Spectroscopy. The FTIR spectra confirmed the already identified isostructurality within type 1, as well as type 2 solvates. Individual solvates, however, could be identified by the presence of particular bands from different solvent molecules; see Figure 9. Also, the already

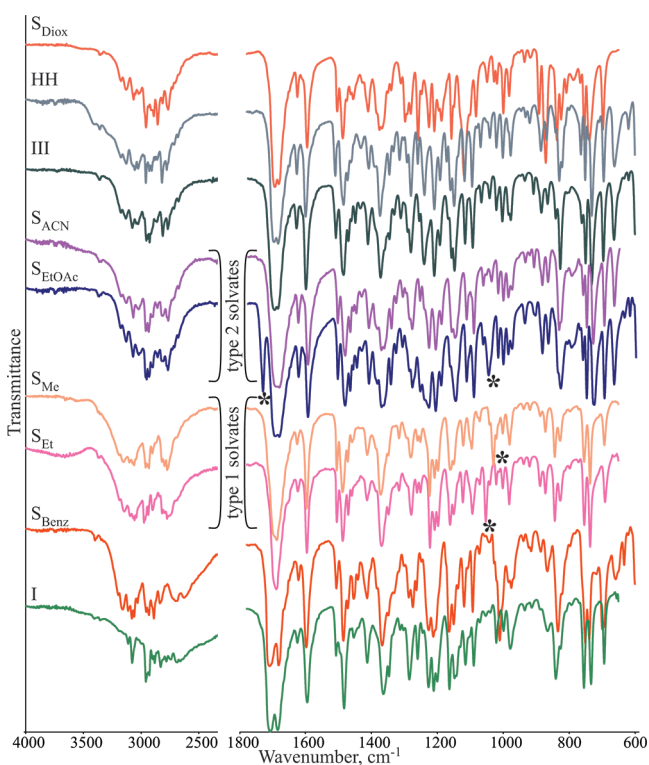


Figure 9. FTIR spectra of the benperidol solvates and polymorphs I and III. Asterisks mark the most characteristic bands from the solvent molecules in isostructural solvates. An enlarged version is given in Figure S4, Supporting Information.

identified similarity of molecular packing in the polymorph III, hydrate HH, and less explicitly in type 2 solvates, as well as similarity between the polymorph I and S_{Benz} identified by intermolecular interaction analysis was reflected as similarity of

their IR spectra. No clear similarities, however, were observed between DH and polymorph V (see Figure S5, Supporting Information), suggesting that there is no direct structural relation between these forms, although this can also be explained by the significant changes introduced in benperidol molecular environment by removal of the water molecules. Interestingly, the IR spectra of polymorphs IV and V are similar, suggesting that structural rearrangements during the transition from V to IV could be quite limited in magnitude; see Figure S5, Supporting Information.

The most easily noticeable difference in the IR spectra was the position of the carbonyl group stretching bands, as two peaks (at ~ 1708 and ~ 1684 cm^{-1}) appearing for the polymorph I and S_{Benz} , whereas two indistinguishable or slightly split peaks (at ~ 1696 – 1683 cm^{-1}) appeared for other polymorphs and solvates. By using computational methods, it was shown that the position of the amide carbonyl stretching band was significantly affected by the hydrogen bonding, with the $\text{N2-H}\cdots\text{N3}$ and $\text{N2-H}\cdots\text{O3}$ hydrogen bonds in I and S_{Benz} observed at ~ 1710 cm^{-1} , while the $\text{N2-H}\cdots\text{O1}$ and $\text{N2-H}\cdots\text{O3}$ hydrogen bonds in other benperidol phases were observed at ~ 1695 cm^{-1} vibrational frequency (see Table S6, Supporting Information).

3.5. Characterization and Rationalization of Benperidol Solvate Desolvation. *Dihydrate.* The TG analysis and PXRD patterns showed that the dehydration of DH occurred in one stage. However, the dehydration products of DH depended on the sample and its preparation. Dehydration of fine DH powder at 30 °C over P_2O_5 resulted in the formation of polymorph V. At elevated temperature (above 40 °C), polymorph V transformed to polymorph IV. However, when DH crystals (the size above 100 μm for all of the dimensions) were dehydrated, polymorph II or a mixture of II and I was obtained. This could be explained by slower water escape from the crystal, which could lead to recrystallization of the product in thermodynamically preferred polymorphs II and I (see Supporting Information). These polymorphs also typically appeared when powdered DH obtained by grinding its crystals was dehydrated and could be explained by the nucleation of polymorphs II and I during grinding. The fact that water molecules had a crucial role in the stabilization of the crystal structure implies that the dehydration most probably involved complete structural collapse, followed by recrystallization to a completely different crystal structure, which explains the possibility of forming different dehydration products.

Type 1 Solvates. The PXRD measurements and crystal structure analysis indicated that the presence of two endothermic peaks in the desolvation process of S_{Me} and S_{Et}

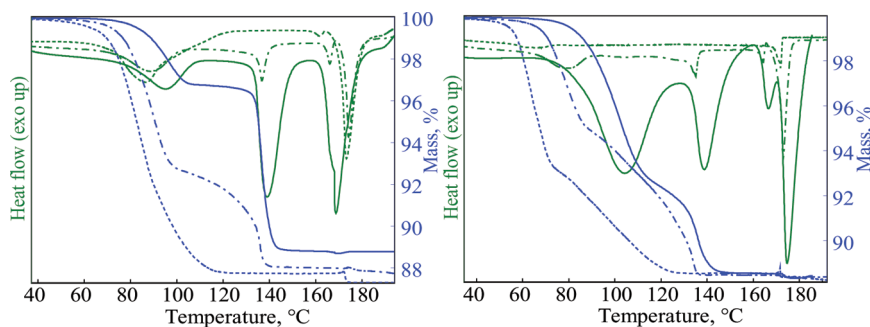


Figure 10. Effect of particle size (on the left, solid lines – large crystals, dashed – small crystals, dotted – well ground powder) and the heating rate (on the right, solid lines – $20^\circ\cdot\text{min}^{-1}$, dashed – $2^\circ\cdot\text{min}^{-1}$, dotted – $0.2^\circ\cdot\text{min}^{-1}$) on the desolvation of S_{Et} .

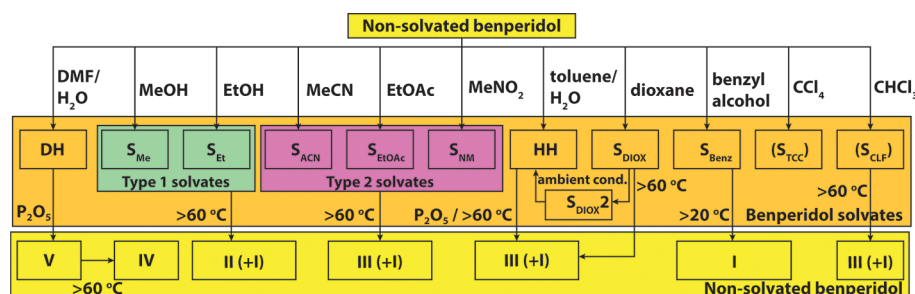


Figure 11. A schematic representation of benperidol solvate preparation and the phase transformations occurring during their desolvation.

(Figure 3) cannot be associated with the formation of a desolvation intermediate. Besides, a change of the sample particle size affected the contribution from each peak. Therefore, the appearance of two peaks apparently resulted from different desolvation rates associated with the molecules located at different distances from the surface of the crystals. The first peak was associated with the desolvation of solvate close to the surface, for which the escape of solvent molecules was relatively easy. The amount of solvate desolvated in this way depended on the particle size. The further desolvation, however, slowed down because of the hindered escape of solvent molecules through the product phase. Nevertheless, the desolvation slowly continued at increased temperature. The second desolvation peak appeared when a fast and complete desolvation occurred by reaching the peritectic decomposition/melting point of the solvate at 129 °C for S_{Me} , and at 137 °C for S_{Et} . Therefore, the desolvation profile depended both on the particle size and on the heating rate (see Figure 10).

The desolvation product in most cases was the structurally different polymorph **II**. Nevertheless, when desolvation was performed with solvates prepared by a suspending technique, or with large solvate crystals, a mixture of polymorphs **II** and **I** was obtained in both desolvation stages, although it was noticed that slow desolvation at low temperature facilitated the formation of polymorph **II**, while fast desolvation at high temperature facilitated the formation of **I**. The formation of polymorph **I** can be explained by the presence of small nuclei of **I** in the solvates obtained by suspending technique, as well as the recrystallization from retained or condensed solvent in large crystals, as **I** is the thermodynamically stable polymorph at temperatures required for the desolvation process; see Supporting Information. This was supported by the observation that seeding of S_{Me} with 5% of **I** led to the formation of pure **I** after desolvation. Moreover, the crystallization of polymorph **I** from ethanol solution, as well as the occurrence of peritectic decomposition and/or melting was confirmed by a hot-stage microscopy experiment.

Type 2 Solvates. Similarly to the type 1 solvates, thermal analysis of S_{ACN} with various particle sizes showed that the second desolvation peak (at 106 °C in Figure 3) corresponded to the peritectic melting and/or decomposition of this solvate. The desolvation process of these solvates usually produced a mixture of polymorphs **III** and **I**, with a smaller particle size and lower temperatures facilitating the formation of **III**. The desolvation of these solvates was easy and occurred even by grinding at ambient conditions in a mortar, producing **III** with low crystallinity. This relatively easy desolvation can be explained by the presence of solvent channels and the absence of strong benperidol–solvent interactions facilitating the solvent removal process. The appearance of polymorph **I** as a

desolvation product most probably occurred in the presence of nuclei of this thermodynamically stable polymorph or in a recrystallization process from acetonitrile solution in the case when large crystals were desolvated.

Other Solvates. Dehydration of **HH** over P_2O_5 at 30 °C produced pure **III**, while dehydration at elevated temperature produced besides **III** also the polymorph **I**. Desolvation of S_{Benz} both at elevated temperature and at ambient temperature produced only the polymorph **I**. Desolvation of S_{DIOX} produced the polymorph **III** or **HH**, depending on the conditions (see Supporting Information).

Structural Characterization of Benperidol Solvate Desolvation. A summary of the most characteristic phase transitions occurring during the desolvation of solvates is given in Figure 11.

By analyzing these phase transitions in association with the crystal structure data and phase stability of polymorphs, it was concluded that two driving forces determined the obtained desolvation product: (a) structural similarity between the solvate and the obtained polymorph and (b) thermodynamic stability of the resulting polymorph. The only solvate clearly producing only one desolvation product was S_{Benz} , which formed only the thermodynamically stable polymorph **I** (see Supporting Information). Besides, a strong similarity of intermolecular interactions was observed in both of these phases. Although type 2 solvates and **HH** showed clear structural similarity with polymorph **III**, which usually was their main desolvation product, it hardly ever appeared without polymorph **I** as a minor component. The formation of polymorph **I** was enhanced in situations facilitating the formation of thermodynamically stable polymorph: at high temperatures and in the case of large solvate crystals, when recrystallization from trapped solvent was possible. Similar effects facilitating the formation of **I** were observed also in the desolvation of type 1 solvates, and in that case further supported by the observation that seeding with **I** produced **I** as the only desolvation product. For type 1 solvates, however, no structural similarities with the main desolvation product **II** could be observed.

Similar observations as for type 2 solvates were made also for the desolvation of **DH**, although in that case the main desolvation product was the unstable polymorph **V**, and the thermodynamically stable byproducts were polymorphs **II** and **I**. In this case, however, a structural similarity between **DH** and **V** could not be determined.

3.6. Rationalization of Solvate Stability and Frequency of Solvate Formation in Crystallization. The solvate stability was compared using the lattice energies and pairwise intermolecular interaction energies. The results obtained for structures where atom positions were relaxed in

CASTEP are given in Table 5. As shown previously, the results from the semiempirical PIXEL code had accuracy similar to

Table 5. Lattice Energy and Total Pairwise Interaction Energy (in $\text{kJ}\cdot\text{mol}^{-1}$) for Benperidol Solvates

solvate	lattice energy		total pairwise interaction energy	
	PIXEL	AA-CLP	benperidol ^a	solvent ^b
DH		−99.3	−227.1	−86.1/−79.4 ^c
HH	−84.3	−65.6	−269.7	−44.7
S _{Benz}	−130.7	−109.5	−167.8	−151.9
			Type 1	
S _{Me}	−119.9	−107.4	−245.7	−92.9
S _{Et}	−124.3	−121.9	−223.0	−104.9
			Type 2	
S _{ACN}	−110.7	−116.0	−295.6	−53.5
S _{EtOAc}		−137.6	−301.1/−301.8 ^c	−60.9
S _{NM}	−108.2	−119.7	−273.5	−75.8

^aThe sum of all pairwise benperidol-benperidol interaction energies with cutoff distance equal to the sum of vdW radii +0.3 Å. ^bThe sum of all pairwise solvent-benperidol and solvent-solvent interaction energies with cutoff distance equal to the sum of vdW radii +1.6 Å. ^cFor each water molecule (in DH) or benperidol molecule (in S_{EtOAc}) in the asymmetric unit.

those from DFT-D methods,⁷⁹ while results from empirical AA-CLP are less accurate and are given only to compare the lattice energy of solvates with more than two molecules in the asymmetric unit. Total pairwise interaction energy values were less conclusive than the lattice energies, especially those calculated for benperidol-benperidol interactions, as they did not take into account the energetically relevant long-range interactions. However, they allowed an approximate evaluation of the contribution from benperidol and solvent molecule interactions in the lattice energies and gave a fast insight into the relative stability of solvates with similar structures.

The higher lattice energy of S_{Et} compared to that of S_{Me} apparently explains the higher stability of this solvate, as observed by its higher peritectic desolvation and/or melting point (see Table 1) and higher desolvation E_d , see Supporting Information.

Logically, by comparing the interaction energies in type 1 solvates with those in S_{Benz} it is observed that an increase in the size of the solvent molecule increases the contribution of the total pairwise solvent interaction energy to the lattice energy, while the contribution from the total pairwise benperidol interaction energy decreases due to the larger separation of these molecules.

Although the thermal stability of type 2 solvates is very similar, crystallization from acetonitrile always resulted in the formation of S_{ACN}, whereas crystallization from ethyl acetate mainly produced pure polymorph I. Moreover, S_{NM} was obtained only once. Besides, S_{ACN} was obtained also in slurry experiments, whereas preparation of the other two solvates using this approach was not possible. The lattice energy of S_{ACN} was slightly more negative than that of S_{NM}, and the pairwise interaction energies between benperidol molecules in the crystal structure of S_{NM} were less efficient (due to the larger size of nitromethane molecule). This theoretically can lead to hindered formation of S_{NM} as the formation of its crystals is energetically less favored, compared to the formation of S_{ACN} crystals. Because of the different stoichiometries, reliable comparison with S_{EtOAc} was possible only using pairwise

interaction energies, which showed that the ethyl acetate molecule in this structure did not form as efficient interactions as acetonitrile or nitromethane molecules, explaining the complications with its crystallization. Nevertheless, it should not be forgotten that the crystallization product can also be associated with the molecular interactions in the solution, and it is theoretically possible that ethyl acetate and nitromethane somehow facilitate the crystallization of polymorph I.

The easier desolvation of type 2 solvates, compared to the type 1 solvates, is explained by the presence of solvent channels and weaker interaction energies experienced by the solvent molecules.^{48,49}

Although all the strong hydrogen bonds in DH structure are formed with or between water molecules, interactions between benperidol molecules in the form of weak hydrogen bonds and dispersion forces contributed more to the lattice energy. Nevertheless, the overall interactions in DH were energetically more favored than those in HH, which apparently explain the fact that this is the most stable of benperidol hydrates. Therefore, the facile crystallization of DH can be explained by a more efficient hydrogen bond network, while the formation of HH was possible only under the conditions with a very low water activity and in the presence of specific solvent molecules, probably providing for the formation of favorable benperidol molecule associates.

3.7. Analysis of Benperidol Solvate Formation.

Crystallization of benperidol from a range of 31 solvents selected from various solvent classes resulted in the formation of 11 solvates. Nevertheless, S_{EtOAc} and S_{NM} were obtained only in some crystallization experiments from the respective solvents, hemihydrate crystallized only from xylene and toluene containing traces of water, and repeated preparation of S_{CLF} and S_{TCC} was complicated. These observations suggest that discovery of additional benperidol solvates with the studied solvents is theoretically possible. Nevertheless, the obtained amount of solvates and the knowledge of benperidol and solvent properties, as well as the elucidation of solvate crystal structure, allowed us to rationalize the formation of benperidol solvates.

Generally it was concluded that solvates formed with solvent molecules representing different solvent classes: hydrogen bond donors (type 1 solvates, HH, and DH), aprotic polar solvents (type 2 solvates, S_{CLF}), aromatic apolar or lightly polar solvents (S_{Benz}; although benzyl alcohol is a hydrogen bond donor, its ability to form dispersion interactions appeared to be even more important for the formation of this solvate), and aprotic polar electron pair donor (S_{DIOX}). Even though the crystal structures of some of the solvates are not known, it was possible to conclude that the solvent molecules in all solvates employed features (strong or weak hydrogen bonds, dispersion interactions) characteristic of the corresponding solvent class. More detailed classification of solvents did not provide additional clarification for the solvate formation of benperidol, as type 1 solvates formed from solvents belonging to group 3, type 2 solvates from solvents from groups 2 and 9, and other solvates were obtained from solvents belonging to groups 1, 7, 10, 11, and 15⁵² (see Table S1, Supporting Information).

As already mentioned, although the solvates were obtained with four different hydrogen bond donors, only in both hydrates the additional hydrogen bond acceptor sites of benperidol molecule were employed. Therefore, the formation of hydrates was directly explained by the advantages of a more efficient hydrogen bonding network. The formation of alcohol

solvates, however, was not driven purely by this feature, although the presence of strong benperidol–solvent hydrogen bonds definitely provided stability for these structures. The solvent molecules in other solvates could not participate in strong hydrogen bonds, but provided new, weak interactions and allowed energetically favorable packing of benperidol molecules with the solvent molecules. Interestingly, although there were some voids in the crystal structures of both polymorphs I and II, which were not observed in any of the solvate structures, the packing index of solvates was generally the same as that in the polymorphs; see Table 2. Nevertheless, the presence of voids and complex structural patterns in the crystals of stable benperidol polymorphs (six-molecule rings in I, see Figure 6, and $Z' = 3$ for II) suggested that energetically efficient packing is complicated for phases consisting of benperidol molecules only. The presence of certain functional groups in the benperidol molecule, however, provides possibilities for efficient interactions with solvent molecules containing different functional groups. These appear to be the two main reasons for the formation of such a wide range of benperidol solvates with various solvent molecules.

The appearance of two isostructural solvate groups suggests that in the case of some particular solvent properties, solvent molecules are incorporated in identical crystal structures. The comparison of these structures shows that both the specific interactions provided by solvent, as well as the size of the solvent molecules are important factors. Therefore, small hydrogen bond donating alcohol molecules form type 1 solvates, whereas aprotic polar donors and acceptors of weak hydrogen bonds with appropriate molecular size and shape form type 2 solvates.

4. CONCLUSIONS

Crystallization of benperidol from various solvents produced nine new solvates containing methanol, acetonitrile, ethyl acetate, nitromethane, 1,4-dioxane, water, benzyl alcohol, carbon tetrachloride, and chloroform, while the desolvation of benperidol solvates produced two new polymorphs IV and V. It was determined that benperidol forms two sets of isostructural solvates: type 1 (with methanol and ethanol) and type 2 (with acetonitrile, nitromethane, and ethyl acetate). Infrequent formation of some of the solvates, however, showed that the existence of a certain solvate cannot guarantee its facile formation and discovery, even if there are isostructural solvates forming easily.

It was determined that the main reason for the formation of various benperidol crystal structures was the diverse possibilities of molecular packing, resulting in different intermolecular interactions, whereas the molecular conformation of benperidol was typically very similar. A comparison of the crystal structures of benperidol phases showed that the only structures showing clear similarities were the polymorph III, hemihydrate HH, and type 2 solvates, while similarities of intermolecular interactions were observed also for S_{Benz} and polymorph I.

Desolvation studies of benperidol solvates showed that the stability of solvates can be associated with the intermolecular interactions in the crystal structure, while the structures of desolvation products were determined through an interplay of structural similarity and thermodynamic stability of the resulting polymorphs, and each of these factors could become dominant due to sample preparation procedures or experimental conditions.

The inability of benperidol molecules to pack efficiently without solvent was found to be the main reason for solvate formation, whereas the presence of specific functional groups in benperidol molecule enabled the formation of a wide range of stable solvate structures containing various solvent molecules. This is similar to the properties for droperidol solvates, although less structural variation was observed in the case of droperidol solvates.⁸ Nevertheless, theoretical prediction of benperidol solvates would be quite complicated as it would be difficult to predict the energetically favorable packing for each particular solvate. The formation of both benperidol hydrates, however, was driven by the compensation for hydrogen bond donor deficiency.

By using both sets of isostructural solvates it was proved that both the possible interactions and the size of the solvent molecules were important factors in solvate formation. The solvate structures of benperidol, however, were more interaction-specific, if compared to those of droperidol, which formed only one set of isostructural solvates with at least seven very different solvents.⁸ In the formation of type 2 solvates, both the size and shape of the solvent molecules appeared to be relevant, as two nearby partially connected channels could be occupied by smaller molecules in each of the channel (as in S_{ACN} and S_{NM}), or by larger molecules occupying both of the channels (S_{EtOAc}).

■ ASSOCIATED CONTENT

Supporting Information

Additional results from solvate screening, solvate and polymorph characterization using PXRD, DTA/TG, and FTIR, crystal structure analysis, and a study of desolvation process and kinetics, along with X-ray crystallographic information files (CIF). This material is available free of charge via the Internet at <http://pubs.acs.org>. Crystallographic information files are also available from the Cambridge Crystallographic Data Center (CCDC) upon request (<http://www.ccdc.cam.ac.uk>, CCDC deposition numbers 1046550–1046558).

■ AUTHOR INFORMATION

Corresponding Author

*Telephone: +(371)-67372576. E-mail: agris.berzins@lu.lv

Notes

The authors declare no competing financial interest.

■ ACKNOWLEDGMENTS

This work was supported by the European Social Fund within the project “Support for Doctoral Studies at the University of Latvia” and 2014 Ludo Frevel Crystallography Scholarship Award (ICDD). We wish to thank Inese Sarceviča for the help with crystal structure determination, Kirils Oļehnovičs for performing some of the experiments as part of his research project, and the Riga Technical University Institute of Polymer Materials for the provided opportunity to carry out hot-stage microscopy measurements.

■ REFERENCES

- (1) Azibi, M.; Draguet-Brughmas, M.; Bouche, R. *Pharm. Acta Helv.* **1982**, *57*, 182.
- (2) Gassim, A. E. H.; Girgis Takia, P.; James, K. C. *Int. J. Pharm.* **1986**, *34*, 23.
- (3) Declercq, J. P.; Germain, G.; Koch, M. H. J. *Acta Crystallogr., Sect. B* **1973**, *29*, 2311.

- (4) Price, C. P.; Glick, G. D.; Matzger, A. J. *Angew. Chem., Int. Ed.* **2006**, *45*, 2062.
- (5) Bingham, A. L.; Hughes, D. S.; Hursthouse, M. B.; Lancaster, R. W.; Tavener, S.; Threlfall, T. L. *Chem. Commun.* **2001**, 603.
- (6) Yu, L.; Stephenson, G. A.; Mitchell, C. A.; Bunnell, C. A.; Snorek, S. V.; Bowyer, J. J.; Borchardt, T. B.; Stowell, J. G.; Byrn, S. R. *J. Am. Chem. Soc.* **2000**, *122*, 585.
- (7) López-Mejías, V.; Kampf, J. W.; Matzger, A. J. *J. Am. Chem. Soc.* **2012**, *134*, 9872.
- (8) Bērziņš, A.; Skarbulis, E.; Rekis, T.; Actiņš, A. *Cryst. Growth Des.* **2014**, *14*, 2654.
- (9) Tessler, L.; Goldberg, I. J. *Inclusion Phenom. Macrocycl. Chem.* **2006**, *55*, 255.
- (10) Sun, C.; Grant, D. J. W. *Pharm. Res.* **2001**, *18*, 274.
- (11) Khomane, K. S.; More, P. K.; Bansal, A. K. *J. Pharm. Sci.* **2012**, *101*, 2408.
- (12) Picker-Freyer, K. M.; Liao, X.; Zhang, G.; Wiedmann, T. S. *J. Pharm. Sci.* **2007**, *96*, 2111.
- (13) Pudipeddi, M.; Serajuddin, A. T. M. *J. Pharm. Sci.* **2005**, *94*, 929.
- (14) Bauer, J.; Spanton, S.; Henry, R.; Quick, J.; Dziki, W.; Porter, W.; Morris, J. *Pharm. Res.* **2001**, *18*, 859.
- (15) Morissette, S. L.; Soukasene, S.; Levinson, D.; Cima, M. J.; Almarsson, Ö. *Proc. Natl. Acad. Sci. U. S. A.* **2003**, *100*, 2180.
- (16) Vippagunta, S. R.; Brittain, H. G.; Grant, D. J. W. *Adv. Drug Delivery Rev.* **2001**, *48*, 3.
- (17) Stieger, N.; Liebenberg, W.; Wessels, J.; Samsodien, H.; Caira, M. *Struct. Chem.* **2010**, *21*, 771.
- (18) Caira, M. R.; Bettinetti, G.; Sorrenti, M. *J. Pharm. Sci.* **2002**, *91*, 467.
- (19) Hosokawa, T.; Datta, S.; Sheth, A. R.; Brooks, N. R.; Young, V. G., Jr.; Grant, D. J. W. *Cryst. Growth Des.* **2004**, *4*, 1195.
- (20) Braun, D. E.; Gelbrich, T.; Kahlenberg, V.; Tessadri, R.; Wieser, J.; Griesser, U. J. *Cryst. Growth Des.* **2009**, *9*, 1054.
- (21) Banerjee, R.; Bhatt, P. M.; Desiraju, G. R. *Cryst. Growth Des.* **2006**, *6*, 1468.
- (22) Zhang, Q.; Lu, L.; Dai, W.; Mei, X. *CrystEngComm* **2014**, *16*, 1919.
- (23) Shankland, N.; David, W. I. F.; Shankland, K.; Kennedy, A. R.; Frampton, C. S.; Florence, A. J. *Chem. Commun.* **2001**, 2204.
- (24) Stephenson, G. A.; Diserod, B. A. *Int. J. Pharm.* **2000**, *198*, 167.
- (25) Fujii, K.; Uekusa, H.; Itoda, N.; Hasegawa, G.; Yonemochi, E.; Terada, K.; Pan, Z.; Harris, K. D. M. *J. Phys. Chem. C* **2009**, *114*, 580.
- (26) Czapik, A.; Konowalska, H.; Gdaniec, M. *Acta Crystallogr., Sect. C* **2010**, *66*, o128.
- (27) Zencirci, N.; Gstrein, E.; Langes, C.; Griesser, U. *Thermochim. Acta* **2009**, *485*, 33.
- (28) Aitipamula, S.; Chow, P. S.; Tan, R. B. H. *CrystEngComm* **2011**, *13*, 1037.
- (29) Petit, S.; Coquerel, G. *Chem. Mater.* **1996**, *8*, 2247.
- (30) Galwey, A. *Thermochim. Acta* **2000**, *355*, 181.
- (31) Price, S. L. *Chem. Soc. Rev.* **2014**, 2098.
- (32) Day, G. M. *Crystallogr. Rev.* **2011**, *17*, 3.
- (33) Price, S. *Acta Crystallogr., Sect. B* **2013**, *69*, 313.
- (34) Bardwell, D. A.; Adjiman, C. S.; Arnautova, Y. A.; Bartashevich, E.; Boerrigter, S. X. M.; Braun, D. E.; Cruz-Cabeza, A. J.; Day, G. M.; Della Valle, R. G.; Desiraju, G. R.; van Eijck, B. P.; Facelli, J. C.; Ferraro, M. B.; Grillo, D.; Habgood, M.; Hofmann, D. W. M.; Hofmann, F.; Jose, K. V. J.; Karamertzanis, P. G.; Kazantsev, A. V.; Kendrick, J.; Kuleshova, L. N.; Leusen, F. J. J.; Maleev, A. V.; Misquitta, A. J.; Mohamed, S.; Needs, R. J.; Neumann, M. A.; Nikylov, D.; Orendt, A. M.; Pal, R.; Pantelides, C. C.; Pickard, C. J.; Price, L. S.; Price, S. L.; Scheraga, H. A.; van de Streek, J.; Thakur, T. S.; Tiwari, S.; Venuti, E.; Zhitkov, I. K. *Acta Crystallogr., Sect. B* **2011**, *67*, 535.
- (35) Kazantsev, A. V.; Karamertzanis, P. G.; Adjiman, C. S.; Pantelides, C. C.; Price, S. L.; Galek, P. T. A.; Day, G. M.; Cruz-Cabeza, A. J. *Int. J. Pharm.* **2011**, *418*, 168.
- (36) Ismail, S. Z.; Anderton, C. L.; Copley, R. C. B.; Price, L. S.; Price, S. L. *Cryst. Growth Des.* **2013**, *13*, 2396.
- (37) Kendrick, J.; Stephenson, G. A.; Neumann, M. A.; Leusen, F. J. *J. Cryst. Growth Des.* **2013**, *13*, 581.
- (38) Baias, M.; Dumez, J.-N.; Svensson, P. H.; Schantz, S.; Day, G. M.; Emsley, L. *J. Am. Chem. Soc.* **2013**, *135*, 17501.
- (39) Eddleston, M. D.; Hejczyk, K. E.; Bithell, E. G.; Day, G. M.; Jones, W. *Chem.—Eur. J.* **2013**, *19*, 7874.
- (40) Braun, D. E.; McMahon, J. A.; Koztecki, L. H.; Price, S. L.; Reutzel-Edens, S. M. *Cryst. Growth Des.* **2014**, *14*, 2056.
- (41) Braun, D. E.; Karamertzanis, P. G.; Price, S. L. *Chem. Commun.* **2011**, 47, 5443.
- (42) Braun, D. E.; Tocher, D. A.; Price, S. L.; Griesser, U. J. *J. Phys. Chem. B* **2012**, *116*, 3961.
- (43) Hulme, A. T.; Price, S. L. *J. Chem. Theory Comput.* **2007**, *3*, 1597.
- (44) Cruz-Cabeza, A. J.; Karki, S.; Fabian, L.; Friscic, T.; Day, G. M.; Jones, W. *Chem. Commun.* **2010**, 46, 2224.
- (45) Fucke, K.; McIntyre, G. J.; Lemée-Cailleau, M.-H.; Wilkinson, C.; Edwards, A. J.; Howard, J. A. K.; Steed, J. W. *Chem.—Eur. J.* **2015**, *21*, 1036.
- (46) Iwata, K.; Kojima, T.; Ikeda, Y. *Cryst. Growth Des.* **2014**, *14*, 3335.
- (47) Infantes, L.; Fabian, L.; Motherwell, W. D. S. *CrystEngComm* **2007**, *9*, 65.
- (48) Berziņš, A.; Rekis, T.; Actiņš, A. *Cryst. Growth Des.* **2014**, *14*, 3639.
- (49) Zencirci, N.; Griesser, U. J.; Gelbrich, T.; Kahlenberg, V.; Jetli, R. K. R.; Apperley, D. C.; Harris, R. K. *J. Phys. Chem. B* **2014**, *118*, 3267.
- (50) Minkov, V. S.; Beloborodova, A. A.; Drebuschak, V. A.; Boldyreva, E. V. *Cryst. Growth Des.* **2014**, *14*, 513.
- (51) Gramatica, P.; Navas, N.; Todeschini, R. *Trends Anal. Chem.* **1999**, *18*, 461.
- (52) Gu, C.-H.; Li, H.; Gandhi, R. B.; Raghavan, K. *Int. J. Pharm.* **2004**, *283*, 117.
- (53) Sheldrick, G. *Acta Crystallogr., Sect. A* **2008**, *64*, 112.
- (54) Dolomanov, O. V.; Bourhis, L. J.; Gildea, R. J.; Howard, J. A. K.; Puschmann, H. *J. Appl. Crystallogr.* **2009**, *42*, 339.
- (55) Spek, A. L. *Acta Crystallogr., Sect. D* **2009**, *65*, 148.
- (56) Macrae, C. F.; Bruno, I. J.; Chisholm, J. A.; Edgington, P. R.; McCabe, P.; Pidcock, E.; Rodriguez-Monge, L.; Taylor, R.; van de Streek, J.; Wood, P. A. *J. Appl. Crystallogr.* **2008**, *41*, 466.
- (57) Boulouf, A.; Louer, D. *J. Appl. Crystallogr.* **2004**, *37*, 724.
- (58) Roinsel, T.; Rodriguez-Carvajal, J. *Mater. Sci. Forum* **2001**, *378–381*, 118.
- (59) Coelho, A. *J. Appl. Crystallogr.* **2003**, *36*, 86.
- (60) Altomare, A.; Camalli, M.; Cuocci, C.; Giacovazzo, C.; Moliterni, A.; Rizzi, R. *J. Appl. Crystallogr.* **2009**, *42*, 1197.
- (61) Altomare, A.; Cuocci, C.; Giacovazzo, C.; Moliterni, A.; Rizzi, R.; Corriero, N.; Falcicchio, A. *J. Appl. Crystallogr.* **2013**, *46*, 1231.
- (62) Yamazaki, K.; Watanabe, A.; Moroi, R.; Sano, M. *Acta Crystallogr., Sect. B* **1981**, *37*, 1447.
- (63) Kawahata, M.; Yamaguchi, K.; Ishikawa, T. *Cryst. Growth Des.* **2005**, *5*, 373.
- (64) Clark, S. J.; Segall, M. D.; Pickard, C. J.; Hasnip, P. J.; Probert, M. I.; Refson, K.; Payne, M. C. *Z. Kristallogr.* **2005**, *220*, 567.
- (65) Perdew, J. P.; Burke, K.; Ernzerhof, M. *Phys. Rev. Lett.* **1996**, *77*, 3865.
- (66) Tkatchenko, A.; Scheffler, M. *Phys. Rev. Lett.* **2009**, *102*, 073005.
- (67) Gavezzotti, A. *New J. Chem.* **2011**, *35*, 1360.
- (68) Frisch, M. J.; Trucks, G. W.; Schlegel, H. B.; Scuseria, G. E.; Robb, M. A.; Cheeseman, J. R.; Scalmani, G.; Barone, V.; Mennucci, B.; Petersson, G. A.; Nakatsuji, H.; Caricato, M.; Li, X.; Hratchian, H. P.; Izmaylov, A. F.; Bloino, J.; Zheng, G.; Sonnenberg, J. L.; Hada, M.; Ehara, M.; Toyota, K.; Fukuda, R.; Hasegawa, J.; Ishida, M.; Nakajima, T.; Honda, Y.; Kitao, O.; Nakai, H.; Vreven, T.; Montgomery, J. A. J.; Peralta, J. E.; Ogliaro, F.; Bearpark, M.; Heyd, J. J.; Brothers, E.; Kudin, K. N.; Staroverov, V. N.; Kobayashi, R.; Normand, J.; Raghavachari, K.; Rendell, A.; Burant, J. C.; Iyengar, S. S.; Tomasi, J.; Cossi, M.; Rega, N.; Millam, J. M.; Klene, M.; Knox, J. E.; Cross, J. B.; Bakken, V.;

Adamo, C.; Jaramillo, J.; Gomperts, R.; Stratmann, R. E.; Yazyev, O.; Austin, A. J.; Cammi, R.; Pomelli, C.; Ochterski, J. W.; Martin, R. L.; Morokuma, K.; Zakrzewski, V. G.; Voth, G. A.; Salvador, P.; Dannenberg, J. J.; Dapprich, S.; Daniels, A. D.; Farkas, O.; Foresman, J. B.; Ortiz, J. V.; Cioslowski, J.; Fox, D. J.; *Gaussian 09, Revision D.01*; Gaussian Inc.: Wallingford, CT, 2009.

(69) Zhao, Y.; Truhlar, D. *Theor. Chem. Acc.* **2008**, *120*, 215.

(70) Grimme, S.; Antony, J.; Ehrlich, S.; Krieg, H. *J. Chem. Phys.* **2010**, *132*, 154104.

(71) Alecu, I. M.; Zheng, J.; Zhao, Y.; Truhlar, D. G. *J. Chem. Theory Comput.* **2010**, *6*, 2872.

(72) Braun, D. E.; Gelbrich, T.; Kahlenberg, V.; Tessadri, R.; Wieser, J.; Griesser, U. J. *J. Pharm. Sci.* **2009**, *98*, 2010.

(73) Zeidan, T. A.; Trotta, J. T.; Chiarella, R. A.; Oliveira, M. A.; Hickey, M. B.; Almarsson, Ö.; Remenar, J. F. *Cryst. Growth Des.* **2013**, *13*, 2036.

(74) McKinnon, J. J.; Jayatilaka, D.; Spackman, M. A. *Chem. Commun.* **2007**, 3814.

(75) Spackman, M. A.; Jayatilaka, D. *CrystEngComm* **2009**, *11*, 19.

(76) Wolff, S. K.; Grimwood, D. J.; McKinnon, J. J.; Turner, M. J.; Jayatilaka, D.; Spackman, M. A. University of Western Australia: Perth, 2012.

(77) Gelbrich, T. *IUCr Newsl.* **2006**, 39.

(78) Gelbrich, T.; Hursthouse, M. B. *CrystEngComm* **2005**, *7*, 324.

(79) Maschio, L.; Civaleri, B.; Ugliengo, P.; Gavezzotti, A. *J. Phys. Chem. A* **2011**, *115*, 11179.